AD-E300 080

DNA 4377P-2

PROCEEDINGS OF THE DICE THROW SYMPOSIUM 21-23 JUNE 1977

Volume 2

General Electric Company—TEMPO
DASIAC
816 State Street
Santa Barbara, California 93102

July 1977

Proceedings

CONTRACT No. DNA 001-75-C-0023

THIS WORK SPONSORED BY THE DEFENSE NUCLEAR AGENCY
UNDER RDT&E RMSS CODE B337076464P99QAXDC00803H2590D

Prepared for

Director
DEFENSE NUCLEAR AGENCY
Washington, D.C. 20305

UNCLASSIFIED

SECURITY CLASSIFICATION OF THIS PAGE (When Data Entered)

REPORT DOCUMENTATION PAGE

READ INSTRUCTIONS BEFORE COMPLETING FORM

1. REPORT NUMBER: DNA 4377P-2 (18) DNA, SBIE	2. GOVT ACCESSION NO.
3. RECIPIENT'S CATALOG NUMBER: (19) 4377P-2, AD-E300 086	
4. TITLE (and Subtitle): (6) PROCEEDINGS OF THE DICE THROW SYMPOSIUM 21-23 JUNE 1977, VOLUME 2.	5. TYPE OF REPORT & PERIOD COVERED: Proceedings
	6. PERFORMING ORG. REPORT NUMBER
7. AUTHOR(s)	8. CONTRACT OR GRANT NUMBER(s): (15) DNA 001-75-C-0023
9. PERFORMING ORGANIZATION NAME AND ADDRESS: General Electric Company -TEMPO DASIAC 816 State St., Santa Barbara, Ca., 93102	10. PROGRAM ELEMENT, PROJECT, TASK AREA & WORK UNIT NUMBERS: (16) P99QAXDC00803 (17)
11. CONTROLLING OFFICE NAME AND ADDRESS: Director Defense Nuclear Agency Washington, D.C. 20305 (12) 590p.	12. REPORT DATE: (11) July 1977
	13. NUMBER OF PAGES
14. MONITORING AGENCY NAME & ADDRESS (if different from Controlling Office)	15. SECURITY CLASS (of this report): Unclassified
	15a. DECLASSIFICATION/DOWNGRADING SCHEDULE

16. DISTRIBUTION STATEMENT (of this Report)

Approved for public release; distribution unlimited.

17. DISTRIBUTION STATEMENT (of the abstract entered in Block 20, if different from Report)

18. SUPPLEMENTARY NOTES

19. KEY WORDS (Continue on reverse side if necessary and identify by block number)

Airblast
Ammonium Nitrate Fuel Oil
Dice Throw
Ground Motion
High Explosive
Nuclear Weapons Effects
Simulation

20. ABSTRACT (Continue on reverse side if necessary and identify by block number)

This report contains the proceedings of the DICE THROW Symposium held 21-23 June at the Ballistic Research Laboratory, Aberdeen Proving Ground, Maryland. The presentations contained herein describe the experiments conducted, instrumentation used, and results obtained by the various participating projects from detonation of the 600-ton ANFO HE test 6 October 1976 at the White Sands Missile Range, N.M. The DICE THROW Event was sponsored by the Defense Nuclear Agency.

407 445

FOREWORD

This report contains the proceedings of the DICE THROW Symposium held 21-23 June 1977 at the Ballistic Research Laboratory (BRL), Aberdeen Proving Ground, Maryland. The report is divided into four volumes. Volumes 1 through 3 contain the unclassified presentations and Volume 4 contains the classified presentations.

The DICE THROW Event, which was conducted near the Giant Patriot site on the White Sands Missile Range (WSMR), 6 October 1976, was the final test of the DICE THROW Program. The charge for this test was composed of approximately 628 tons (570 metric tons) of ammonium nitrate fuel oil (ANFO). The charge configuration was a right-circular-cylinder base tangent to the surface with a hemispherical top, the same configuration as the second event in the Pre-DICE THROW II Series. The primary objectives of this test were to provide a simulated nuclear blast and shock environment for target response experiments that are vitally needed by the military services and defense agencies concerned with nuclear weapons effects, and to confirm empirical predictions and theoretical calculations for shock response of military structures, equipment, and weapon systems.

A complement of 33 experimenters and support agencies (including foreign governments) participated in Event DICE THROW. For details pertaining to the as-built experiment configurations, site and charge descriptions, and fielding requirements in support of this program, refer to the DICE THROW Test Execution Report, POR 6965.

TABLE OF CONTENTS

VOLUME 1

CONTENTS:

~~VOLUME 2~~

16. GROUP HELMET ARMY PERSONNEL SHELTERS—Golden E. Lane, Jr., Civil Engineering Research Facility.

17. PROJECT C-4, FREE-FLIGHT ~~MEASUREMENT OF THE~~ DRAG FORCES ON CYLINDERS, EVENT DICE THROW—A.W.M. Gibb and D.A. Hill, Defence Research Establishment Suffield.

18. PROJECT C-2, BLAST RESPONSE OF ~~UHF~~ POLEMAST ANTENNA, EVENT DICE THROW—C.G. Coffev and G.V. Price, Defence Research Establishment Suffield.

19. BLAST RESPONSE OF LATTICE MAST, EVENT DICE THROW—B.G. Laidlaw, Defence Research Establishment Suffield.

20. BLAST RESPONSE OF ~~35-FT FIBERGLASS~~ WHIP ANTENNA, EVENT DICE THROW—G.V. Price and C.G. Coffey, Defence Research Establishment Suffield.

21. PROJECT C-5, CANADIAN AIR BLAST MEASUREMENTS, EVENT DICE THROW—F.H. Winfield, Defence Research Establishment Suffield.

22. UHF/SHF TRANSMISSION ~~EXPERIMENT~~—Alan A. Burns, SRI International.

23. DICE THROW DUST CLOUD CALCULATIONS—Major Gary P. Ganong, Susan E. Check, and Charles E. Needham, Air Force Weapons Laboratory.

24. DICE THROW SEISMIC MEASUREMENTS—Laurence S. Melzer, Air Force Weapons Laboratory.

25. ARMY PERSONNEL SHELTERS ~~DNA PROJECT~~ NO. 329—William L. Huff, U.S. Army Engineer Waterways ~~Experiment Station~~.

VOLUME 3

26. NORWEGIAN BLAST DOOR—Golden E. Lane, Jr., Civil Engineering Research Facility.

27. BLAST TESTS OF EXPEDIENT SHELTERS IN THE DICE THROW EVENT—C.H. Kearny, Oak Ridge National Laboratory.

28. EXPERIMENTAL STUDY OF AIRCRAFT STRUCTURAL RESPONSE TO BLAST - DICE THROW PROJECT NO. 118—Rudolf Friedberg and Peter Hughes, Naval Weapons Evaluation Facility.

29. BLAST DISPLACEMENT IN FIELD FORTIFICATIONS—E.R. Fletcher, D.R. Richmond, R.O. Clark, and J.T. Yelverton, Lovelace Biomedical and Environmental Research Institute, Inc.

30. DYNAMIC RESPONSE OF TWO TYPES OF GERMAN HOUSE CONSTRUCTION—C.K. Wiehle, J.R. Rempel, and J.E. Beck, Stanford Research Institute.

31. TEST SUMMARY - NBDS OPTICAL MEASUREMENTS—M. Oberst, Sandia Laboratory Albuquerque.

LIST OF ATTENDEES

ABRAHAMSSON, Eddy - Sweden

ALLISON, W. Don - BRL

ALTER, MAJ William A. - DNA

ALVAREZ, CPT Vicen A. - FCDNA

ATKINS, Marvin C. - DNA

AXELSSON, Hakan - Sweden

BACHMANN, Eberhard - Germany

BALLARD, James - WES

BALSARA, Jimmy P. - WES

BASHANT, MAJ Ronald W. - HQSAC

BELLIVEAU, Louis - HDL

BEZEMER, Ole R. - Canada

BRADSHAW, 1LT Joel C. - AFWL

BREAZEAL, Norman - Sandia Labs

BROWN, Larry L. - DRI

BRUEGMANN, LTC Dieter - Germany

BRYANT, Edward - GE-TEMPO

BURNS, Alan A. - SRI

BUTALA, Edward - NSA

CARLSON, Roland - Boeing

CAULIFIELD, Eugene - USASCA

CHAN, Warren - GE-TEMPO

PRECEDING PAGE BLANK

CHAPYAK, Edward - RDA

CHECK, Susan - AFWL

CLARK, Robert O. - Lovelace

COFFEY, Clayton - Canada

COOPER, Henry - RDA

CRISCIONE, Emanuel - Kaman AviDyne

CRONK, Richard - KOA

DeBOY, William - NSA

DELANY, W. D. - ASWE

DeRAAD, CPT Robert G. - FCDNA

DYSART, Richard - WSMR

EDGERTON, LCDR E. W. - NSSC

EDWARDS, CPT Thomas - SAMSO

ERLEMANN, COL Rudolf - Germany

ETHRIDGE, Noel - BRL

FLATHAU, William - WES

FLETCHER, E. Royce - Lovelace

FLUGER, Alvin - ARRADCOM

FREIBERG, Robert - USAECOM

FRIEDBERG, RUDOLF - NWEF

GANTICK, Noel - FCDNA

GIBB, Allan W. M. - Canada

GOMEZ, COL Robert - BRL

GRANT, G A. - Canada

GREEN, Dale W. - WSMR

GUNBY, MAJ E. Neal - DNA

GUPTA, Aaron - BRL

GURKE, Gerhard - Germany

HAYES, Bernard - LLL

HEGGIE, R. M. - Canada

HEINTZEL, COL Hans-H. - Germany

HUFF, William L. - WES

HUGHES, Peter - NWEF

JACOBSON, John - BRL

JONES, Glen - CERF

KAUFMANN, LTC Ronald - WES/Germany

KEARNY, Cresson - ORNL

KEEFER, John - BRL

KELSO, Jack - GE-TEMPO

KENNEDY, Tom - DNA

KING, Vincent - BRL

KINGERY, Charles - BRL

KL[illegible]MEK, LT Charles - FCDNA

KNOWLES, Cyrus - RDA

LANE, Golden - CERF

LAIDLAW, Bryan - Canada

LINO, MAJ Alan - USAMA

MAYERHOFER, Robert - BRL

McDONNEL, Michael - SAI

MELZER, Steve - AFWL

MESZAROS, Julius J. - BRL

MUELLER, MAJ Edmund - HQDNA

NEEDHAM, Charles - AFWL

NOREN, Brig Gen Gunnar - Sweden

OLIVER, Lawrence - NWEF

PACHUTA, Michael A. - OCPA

PAHL, LTC Hermonn - Germany

PARKER, Hassel - MIG

PASMAN, H. J. - Netherlands

PEARSON, Richard - BRL

PECKHAM, Phillip - NSWC/WOL

PERRY, Gerald - GE-TEMPO

PETERSON, Robert L. - BRL

PICKETT, Stephen - CERF

PETES, Joseph - NSWC/WOL

PFRENGLE, Herman - Germany

PLAMONDON, Maynard A. - AFWL

PYLE, Jay C. - Boeing

QUIGLEY, Ennis - BRL

RALEY, Robert J. - BRL

RAVOTTO, Martin - ARRADCOM

REED, Jack - SLA

REICHENBACH, Heinz - Germany

REISLER, Ralph E. - BRL

ROECKER, Eugene - BRL

RICHMOND, Donald - Lovelace

RIGOTTI, David L. - BRL

RULA, Adam A. - WES

SCHILLING, Robert - Germany

SCHUMACHER, Robert - BRL

SCHUMAN, William J. - BRL

SHELTON, Russell - BRL

SKJELTORP, Arne - Norway

SMITH, Ross - Chrysler

STILL, LTC Edwin T. - DNA

STROOP, LCDR J. D. - FCDNA

SULLIVAN, John - BRL

SWISDAK, Michael - NSWC/WOL

TAYLOR, William - BRL

TEEL, George - BRL

UECKE, MAJ John - USANA

VAULT, William - HDL

VAN KUEREN, E. - RCA

WARD, Robert - EG&G

WARREN, LTC James - AFWL

WATSON, George - BRL

WATT, James - WES

WAXLER, Daniel - ARRADCOM

WEBSTER, Harry - AFWL

WIEHLE, Carl - SRI

WIHERLE, Matthew - BRL

WISOTSKI, John - DRI

WOJCICKI, Alexander - USAOCCS

YORK, Edwin - Boeing

ZAKER, Thomas - DDESB

11. BLAST EFFECTS ON THE CREWS OF U.S. ARMY TACTICAL EQUIPMENT

by

D.R. Richmond, J.T. Yelverton, E.R. Fletcher,
W. Hicks, K. Saunders, and A. Trujillo
Lovelace Biomedical and
Environmental Research Institute, Inc.

D. R. Richmond
J. T Yelverton
E. R. Fletcher
W. Hicks
K. Saunders
A. Trujillo

BLAST EFFECTS ON THE CREWS OF U. S. ARMY TACTICAL EQUIPMENT

FOREWORD

This report presents information obtained by the Lovelace Biomedical and Environmental Research Institute, Inc. in support of U. S. Army projects on Event Dice Throw. Anthropomorphic dummies were placed within U. S. Army equipment items in order to evaluate the blast effects on crew personnel.

The Dice Throw Event was a 600-Ton (ANFO) charge detonated on the surface, October 1976, at White Sands Missile Range, Giant Patriot Site.

Funding was provided to Lovelace by the U. S. Army Ballistic Research Laboratories through an interagency agreement with the U. S. Energy Research and Development Administration, Albuquerque Operations Office.

The underground command post included in the field test was a coordinated effort. The structure was prefabricated at the Lovelace Foundation and funded by the Defense Nuclear Agency, Contract No. DNA 001-75-C-0237.

ACKNOWLEDGMENTS

The excellent support provided to this project by the Test Group Staff of the DNA Field Command is acknowledged.

The authors also wish to acknowledge the valuable assistance of T. Minagawa for preparation of illustrative material and B. Martinez for typing and compiling the report.

INTRODUCTION

The Lovelace Foundation provided support to four Army projects on the Dice Throw Event. The support included providing dummies that were instrumented with peak-g reading gages, placing the dummies inside on, or near the various equipment items, and, from the results, predicting what the blast effects might be on the crew personnel associated with these equipment items. The projects were: (1) U. S. Army Weapon Systems, (2) Command Control and Communication Shelter Systems (Electronic Equipment Shelters), (3) a foreign Vehicle, and (4) a Drone Helicopter.

In evaluating the blast effects on the crew personnel, information obtained from other projects was utilized, i.e., motion-picture films of the dummy motions, electronic accelerometer measurements from inside the dummies, and pressure-time measurements.

PROCEDURES

Dummies

A total of 37 anthropomorphic dummies were used on the test. Each weighed 165 lb and was 5 ft 8 in. tall. Six of the dummies, numbered 1 through 6, were manufactured by Alderson and were of a 1960 vintage. All the other dummies were fabricated at the Lovelace Foundation and were roughly equivalent to the Alderson dummies in the degree of sophistication.

All the dummies contained a skeletal-like structure of steel around which expandable polyurethane foam plastic was cast. There were joints at the neck, shoulder, elbows, wrists, hips, knees, and ankles. The Lovelace dummies did not have ankle joints. The dummy joints were adjustable; e.g., the standing dummies would have the hip and the knee joints tightened more than the dummies that were in a seated position.

Each dummy contained a chest cavity in which accelerometers, electronic and/or passive, could be installed. All the dummies wore G.I. fatigue uniforms and G.I boots. White motorcycle helmets were worn by most of the dummies to simulate those worn by crew members inside vehicles and to provide contrast in the camera viewing field. The few exceptions will be mentioned later.

Impact-O-Graphs®

Omni-g, all-directional g-indicators (Impact-O-Graph® Corporation) were placed on a shelf inside the chest cavity of each dummy. Each gage contained two sets of spring-loaded, steel balls that were held in a recess in the side of a transparent housing formed from impact-resistant plastic. The steel balls would unload if impact or shock forces from any angle exceeded their rated values.

These gages measured peak g only, and according to the manufacturer, they have a frequency response that is virtually flat from zero to 60 Hz. The omni-g Impact-O-graph® must receive a pulse of at least the instrument's rated g for at least 8.4-msec duration to unload the steel balls.

In the laboratory, calibration curves were compiled relating the impact velocity of dummies free falling flat onto a concrete slab to the g level at which the Impact-O-Graphs® located in the chest cavity would unload, Figure A-1, Appendix A. Each dummy contained four gages that spanned the ranges of impact velocities required for no injury up to a high probability of injury for whole-body impact, Table A-1, Appendix A. Higher impact velocities were required to unload an Impact-O-Graph® of a given rating inside the Alderson dummies than inside the Lovelace dummies. The Lovelace ones were constructed of a softer and thicker foam plastic.

Figure A-2 and Table A-2 of Appendix A present blast displacement criteria (Reference 1). One criterion was based on laboratory experiments wherein sheep were dropped in different impact orientations onto a concrete slab. The other criterion, for tumbling impacts, was obtained by blast displacing sheep out of the end of a 6-ft-diameter shocktube over flat ground.

Motion-Picture Cameras

All the dummies were viewed with 16mm-motion-picture cameras during the blast. Motion-picture cameras viewed the equipment items from both the inside and outside. The motion-picture cameras were the responsibility of the Denver Research Institute project.

Film Analysis

The films taken of the dummies during the blast wave were projected onto a small screen and their displacements recorded frame-by-frame. Usually, the head was used as a reference point. Velocities toward ground zero were labeled positive and those away from ground zero labeled negative. Charts giving displacement vs time were prepared for each film. The peak velocity and distance of travel were indicated on each chart.

Electronic Accelerometers

Tri-axial accelerometers (Columbia Model 512) were placed in nine of the dummies located within the Army Weapon Systems. Accelerometer mounts were cemented to the back upper center of the thorax cavity. Signals from the gages were hard wired back to a bunker at the 1370-ft range. The records provide acceleration vs time on three axes (x, y, and z). Because of the way the gage was mounted to the back of the thorax, the directions of the x, y, and z axes differed from those normally used in human and dummy nomenclature. Instead it was the following: x axis was up (-) and down (+); z axis was front (+) and back (-); and y was the lateral axis. Movement to the left would generate a (+) signal and movement to the right a (-) signal.

Dummies numbered 2, 4, 5, 7 through 10, 44, and 45 contained electronic accelerometers inside their chest cavities.

Acceleration measurements were the responsibility of the Nuclear Weapons Effect Branch at White Sands Missile Range (WSMR).

Accelerometers were also placed at selected locations on the weapon systems by the WSMR group.

Pressure-Time Measurements

Pressure transducers were placed on the surface adjacent to most of the Army equipment items. The Nuclear Weapons Effects Branch undertook the P-T measurements in connection with the U. S. Army Weapon Systems, and the Ballistics Research Laboratories (BRL) undertook the measurements in connection with the Electronic Equipment Shelters, Blast Line 2; Foreign Vehicle, Blast Line 3; and Drone Helicopter, Blast Line 1.

Because the free-field airblast measurements were limited within the U. S. Army Weapon Systems layout, those measurements taken in the open along Blast Line 3 by BRL (Reference 2) were applied to and considered to be the blast levels received at the various stations. Blast Line 3 was located along the south edge of the weapon systems layout.

U. S. Army Weapon Systems

A layout drawing for the U. S. Army Weapon Systems appears in Figure B-1, Appendix B, giving the station numbers, dummy numbers, camera locations, along with the ranges and corresponding measured overpressures. The precise bearings of these items on the test bed are listed in Table B-1 in Appendix B.

Station 1 - M60 Main Battle Tank

There were three dummies seated inside the M60 at the 580-ft range: one each in the driver's (no. 1), gunner's (2), and commander's (11) position, Figures B-2 through B-4, Appendix B. In addition, a prone dummy (35) was positioned head-on to the blast adjacent to the M60 at Station 1. Dummy No. 2 was equipped with an electronic accelerometer inside its chest cavity.

Station 2 - M551 Sheridan

There were two dummies seated inside the M551 at the 820-ft range: one in the gunner's (3) and one in the commander's (4) position. In addition, there were two dummies positioned outside the M551: one dummy (36) was standing facing ground zero 7.5 ft from the left side of the vehicle and one dummy (37) was standing 4 ft to the rear of the vehicle, Figure B-5, Appendix B. Dummy No. 4 contained an electronic accelerometer inside its chest cavity.

Station 3 - M109 Self-Propelled Howitzer

There were two dummies inside the M109 at the 740-ft range. One dummy was standing in a gunner's (7) position and the other was standing in back of the gunner as a section chief (S), Figure B-6, Appendix B. Each dummy contained an electronic accelerometer inside its chest cavity. In addition, a dummy (40) was positioned standing 7.5 ft to the rear of the M109, Figure B-7, Appendix B.

Station 4 - Underground Command Post

There were three dummies inside the Underground Command Post at the 740-ft range. One dummy (14) was 5 ft inside and in line with the entryway. The other two dummies (13 and 12) were 5 and 10 ft, respectively, from the upstream wall and to the left of Dummy No. 14, Figure B-8, Appendix B. The personnel chamber was 14 x 14 x 6.5 ft. The roof of the shelter was approximately 2 ft beneath ground level with a 2-ft earth mound. The entryway and entryway tunnel were 2 x 4 ft in cross section. The vertical portion of the entryway was 8.5 ft deep followed by the entryway tunnel that was approximately 10 ft long. The shelter was tested open. A diagram of the Underground Command Post is shown in Figure B-9, Appendix B.

Station 5 - M551 Sheridan 90°

There were two dummies inside the M551 Sheridan that was left-side-on at the 820-ft range One dummy (5) was located in the gunner's seat the the other dummy (6) was in the loader's position. Dummy No. 5 contained an electronic accelerometer inside its chest cavity.

Station 6 - M577 Communications Van

There were two dummies seated inside the M577 communications van which was right-side-on to the blast at the 965-ft range. One dummy was in the driver's (9) and one was in the commander's (10) position. The latter was facing the rear of the vehicle. Both dummies contained electronic accelerometers inside their chest cavities.

Station 7 - M110 Self-Propelled Howitzer

There were three dummies positioned on the M110 at the 965-ft range. One was seated in the gunner's (44) seat and one was in the assistant gunner's (45) position. The third dummy (38) was standing at the right-rear portion of the vehicle facing ground zero. It was held erect by leaning slightly against the folded seat, Figure B-10, Appendix B. Dummy Nos. 44 and 45 contained electronic accelerometers inside their chest cavities.

Station 8 - CLGP Laser-Guided Projectile

A dummy (15) was standing 7.5 ft from the CLGP facing ground zero at the 1050-ft range, Figure B-11, Appendix B.

Station 9 - XM204 Towed Howitzer

A dummy (16) was standing 3.5 ft from the XM204 at the 1112-ft range, Figure B-12, Appendix B.

Station 10 - Forward Observer

A prone dummy (17) was head-on to the blast in the forward observer's position at the 1370-ft range, Figure B-13, Appendix B.

Station 12 - M577 Deployed

There were two dummies positioned beneath the deployed M577 at the 1370-ft range. One dummy (18) was standing face-on to the blast and the other dummy (19) was seated at a table right-side-on to the blast. As seen in Figure B-13, Appendix B, a portion of the canopy was left open.

Station 14 - XM198 Towed Howitzer

One dummy (41) was positioned standing in front of the XM198 at the 2400-ft range, Figure B-14, Appendix B.

All the vehicles were completely closed during the test, except the deployed M577 at Station 12. None of the dummies inside the vehicles wore seat belts and were not restrained in any way. The seated ones could be rocked from side-to-side with a minimum of force. Likewise, the standing ones could easily be pushed over. This demonstrated the fact that they could be expected to topple over with minimal vehicle movement.

The dummies which were standing in the open were held erect by leaning them against an inverted U-shaped pipe structure (goal post). During the blast, their arms were down at their sides and not in front of the goal post as shown in the preshot photographs that were taken a few days before shot time.

Electronic Equipment Shelters

Figure C-1, Appendix C, gives the layout of those shelters that contained dummies. The shelters were all truck-mounted and left-side-on to ground zero. Each shelter contained two dummies, one standing and one sitting. All the dummies were equipped with Impact-O-Graph® gages but not with helmets. The shelters were closed during the blast. The cameras that viewed the dummies were mounted on the rear wall adjacent to the door. The dimensions of the S280 shelters were 7.2 x 12 x 7 ft.

Shelter R1/C10

The S250 retrofit shelter at the 1120-ft range did not contain electronic equipment. Dummy No. 26 was standing facing ground zero with its right arm extended against the upstream wall for support. Dummy No. 27 was seated facing ground zero, Figure C-2, Appendix C.

Shelter 04/C16

The S280 shelter was at the 1370-ft range and contained electronic equipment on racks across the front wall. Dummy No. 28 was standing left side toward ground zero with its right arm extended against the electronic equipment. Dummy No. 29 was seated and faced ground zero.

Shelter 07/C26

This S280 shelter was at the 2000-ft range with electronic equipment in racks along the front wall. Dummy No. 31 was standing left side toward ground zero with its right arm extended against the electronic equipment. Dummy No. 30 was seated and faced ground zero.

Foreign Tactical Vehicle

Figure D-1, Appendix D, gives a layout drawing showing the one foreign vehicle, a Dutch Armored Infantry Fighting Vehicle, on the test bed. Dummies were placed in the driver's (34), commander's (33, and passenger's (32) seats. The commander's hatch was left open for the test with the commander's head extending above the hatch opening, see Figures D-2 and D-3 of Appendix D. The two firing ports on the right side of the vehicle were open during the blast. All three of the dummies were secured in their seats with lap seat belts. The dummies contained Impact-O-Graph® gages only. Dummy No. 32, seated to the right rear side of the vehicle, was viewed with a camera mounted near the left wall. The commander was viewed by a camera outside the vehicle.

Drone Helicopter

The test array for the dummy (39) in the UH1 Drone Helicopter appears in Figure E-1, Appendix E. The helicopter was left-side-on to the blast at the 2750-ft range. The dummy was seated on the left side of the aircraft in the pilot's position and was secured in its seat with the aircraft's restraining harness. The dummy wore a helicopter pilot's helmet with the visor down, Figure E-2, Appendix E. To ensure that the dummy's limbs would not interfere with the controls of the aircraft during its interaction with the blast wave, the arms were placed under the harness straps and the feet were secured with nylon lines to the seat. The motion-picture camera viewed the dummy from the rear of the cabin. In addition to four Impact-O-Graphs®, the chest cavity contained a pressure-time gage.

RESULTS

U. S. Army Weapon Systems

Table B-? lists the pre- and postshot positions of dummies, damage to the dummies themselves as well as to their clothing and the Impact-O-Graphs® that were unloaded. Included in the table are summaries of the dummy motions obtained from the motion-picture analysis. The detailed displacement vs. time curves from the film analysis appear in Figures B-15 through B-26 in Appendix B. In general, the blast-displacement effects exhibited by the dummies that were inside the weapon systems were minimal, and most of the dummies were found in their exact preshot position without damage to themselves or their clothing. The lack of blast-displacement effects on the dummies was substantiated by the Impact-O-Graphs® not unloading and the very low velocities attained by the dummies as determined from the film analysis.

Station 1 - M60 Main Battle Tank

Dummy No. 1, in the driver's seat of the M60 tank, was moved 3 inches in its seat to the left from its original position, and there was a small tear above the right knee of its trousers which was probably caused by the periscope assembly that was blown in by the blast and was found postshot partially on the dummy's arm, Figure B-27, Appendix B. Dummy No. 2, in the gunner's seat, and No. 11, in the commander's seat, were in their exact preshot locations. None of the Impact-O-Graphs® were unloaded in these three dummies.

That the 10-g Impact-O-Graph® was not dislodged in the dummy (11) in the commander's position was remarkable and indicated less than a 10 g acceleration and probably no impacts.

Dummy No. 35 that was prone on the ground outside the M60 tank was displaced 87 ft downstream. Film records were not obtained at station 1. Both the 10-g and 40-g Impact-O-Graphs® were unloaded.

Station 2 - M551 Sheridan

Dummy No. 3 in the gunner's seat shifted a little back and right in its seat from its preshot location and was leaning slightly forward. The film record showed that its head moved forward at 5 ft/sec for 1 inch before being obscured by the dust. The results of other film analysis showed the dummies reached their peak velocities within the first few inches of travel so that 5 ft/sec was probably the peak velocity for that dummy.

The dummy in the commander's (4) seat was undamaged and was in its exact preshot position. The film analysis showed that its head moved forward at 2 ft/sec for 1 inch before being obscured by dust. The Impact-O-Graphs® were not unloaded in either of the dummies.

Outside the Sheridan Tank, Dummy No. 36, that was standing to the left of the vehicle, was displaced about 38 ft downstream by the blast, and the film record showed that it reached a peak velocity of 37 ft/sec, Figure B-28, Appendix B. There was no damage to the dummy or its clothing. The 10-g Impact-O-Graph® was unloaded.

In contrast, Dummy No. 37 that was standing 4 ft to the rear of the vehicle was displaced only 6 ft, Figure B-28, Appendix B. Most of this distance could be attributed to just falling over. The camera view of Dummy 37 was obscured by dust. The 10-g Impact-O-Graph® was unloaded.

Station 3 - M109 Self-Propelled Howitzer

Neither Dummy No. 7 that was standing in the gunner's position nor Dummy No. 8 that was standing in back of the gunner was damaged by the blast. Postshot, Dummy No. 8 was found tilted back against the rear wall and the gunner (7) was leaning against him and the loading ram, Figure B-29 of Appendix B. According to the film record, the heads of both dummies moved initially toward ground zero at 3 ft/sec for just 2 inches and then moved toward the rear of the vehicle without sustaining any impacts in the forward direction.

Dummy No. 40 that was standing 7.5 ft to the rear of the M109 was moved only 5 ft downstream by the blast. The 10-g Impact-O-Graph® was unloaded. There was no damage to the dummy or its clothing. The camera view of this dummy was obscured by dust.

Station 4 - Underground Command Post

Only one dummy (14) was displaced by the blast wave entering the Underground Command Post. The dummy, initially standing 5 ft inside the door, was found on its back against the rear wall, Figure B-30, Appendix B. This dummy sustained a 2-inch-long laceration beneath its chin. The motion-picture films showed that this dummy reached a velocity of 18 ft/sec and impacted the rear wall after its center of mass had moved about 6 ft backwards.

The other two dummies inside the Underground Command Post were not damaged by the entering blast wave. No. 13, standing 5 ft inside the door to the left, simply fell forward. The camera view was obscured by dust in that area of the shelter so the reason for Dummy No. 13 falling over could not be determined. Its head was not damaged because the top center was metal to receive an eye bolt and was the point of contact with the wall, Figure B-31, Appendix B.

Figure B-30, Appendix B, shows Dummy No. 12 remained standing.

Station 5 - M551 Sheridan

Inside the M551 that was left-side-on to the blast, Dummy No. 5 in the gunner's seat moved about 6 inches to the right in its seat and slid forward about 3 inches. The film record showed the dummies head moved initially to the left, toward ground zero, at 2 ft/sec for 3 inches and then to the right at 2 ft/sec for 3 inches with no evidence of impacts. Dummy No. 6, in the loader's seat, was found postshot leaning over in its seat against the commander's step, Figure B-32, Appendix B. Some movement was observed on the motion-picture films, but there were no good reference points from which to obtain displacement data. No impacts were observed. Dummy Nos. 5 and 6 were not damaged, their clothing was intact, and the Impact-O-Graphs® were not dislodged.

Station 6 - M577 Communications Van

Dummy No. 9 in the driver's seat remained in its preshot position. It was not damaged, nor were any of the Impact-O-Graphs® dislodged. The film record did not show movement of this dummy for 25 msec before it was obscured by dust. However, any movement would have begun within this time period. Dummy No. 10 in the commander's seat was not damaged and was found leaning over to the right in its seat. Film analysis showed that its head moved to the left toward ground zero at 3 ft/sec for a distance of 5 inches and then moved to the right at 5 ft/sec for 20 inches as it leaned over in its seat. There were no impacts.

Station 7 - M110 Self-Propelled Howitzer

There was no damage to Dummy No. 44 in the gunner's seat on the upstream side of the M110. This dummy remained in its preshot position and the film record showed that it moved to the right at 8 ft/sec for 11 inches before being obscured by dust. The assistant gunner, 45, on the right side of the weapon, also remained undamaged in its preshot location. No movement was detected in the films for 43 msec when the camera's view was obscured by dust. Again, if movement did occur, it should have started during this relatively long time period. Dummy No. 38 that was standing on the rear portion of the M110 was blown from the vehicle for a distance of about 5 ft. The 10-g Impact-O-Graph® was dislodged and the dummy sustained damage to the soft portion of both hands, along with small lacerations on the right shoulder and left elbow. According to the film record analysis, this dummy attained a velocity of 15 ft/sec and moved 10 inches before dust obscured the camera's view.

Station 8 - Laser-Guided Projectile

The dummy (15) that was standing adjacent to the Laser-Guided Projectile was displaced 11.5 ft by the blast, Figure B-33, Appendix B. The film record analysis showed that its center of mass reached a peak velocity of 17 ft/sec. The dummy was not damaged and the 10-g Impact-O-Graph® was unloaded.

Station 9 - XM204 Towed Howitzer

The dummy (16) at this station was not damaged after being displaced 10 ft by the blast, and according to the film record, it attained a peak velocity of 14 ft/sec, Figure B-34, Appendix B.

Station 10 - Forward Observer

Dummy No. 17 that was prone, face-on to ground zero at this station was not moved by the blast and remained in its exact preshot location, Figure B-35, Appendix B. There was no damage tothe dummy or to its clothing and the Impact-O-Graph® was intact.

Station 12 - M577 Deployed

The dummy (18) that was standing beneath the canopy was displaced 6 ft downstream. In contrast to the other ones standing in the open, it was found face down. The seated one was displaced about 4 ft, Figure B-35, Appendix B. The 10-g Impact-O-Graphs® were unloaded in both dummies. Film records were obtained, but, because the camera positions were upstream and downstream of the station, displacement time was not obtained.

The canopy was first shredded by the blast and then the frame of tubing narrowly missed the dummies as it rotated about 180 degrees to the downstream side of the vehicle.

Station 14 - XM198 Towed Howitzer

Dummy No. 41 that was standing in front of the howitzer facing ground zero was displaced 5 ft 1 inch downstream. The displacement distances were measured from the goal post to the belt buckle of the dummy. Consequently, most of this distance resulted from merely falling over backwards. The dummy's initial velocity was 1-2 ft/sec; and, as the film record showed, in simply falling over backwards in a rigid posture, its center of mass impacted the ground at 13 ft/sec and its head at 21 ft/sec. The 10-g Impact-O-Graph® was dislodged.

Electronic Acceleration Records

Acceleration records from the electronic gages inside the dummies are illustrated in Figures B-36 through B-53, Appendix B. Two sets of records for each gage are included: one nonfiltered and one filtered wherein the signal from the gage was fed through a 200-Hz filter at the time of the recording. The peak-g values for all of the records were read by the Nuclear Effects Group at White Sands Missile Range. The peak-g values are indicated on the illustrated records. Calibration bands were placed on the left side of each record and the time to detonation zero (det. zero) was indicated. The curved line drawn through the initial portion of the nonfiltered records was used in obtaining preliminary peak-g values and does not represent the final. These curved lines do not represent the final peak-g readings and should be ignored.

There was considerable noise evident in all the records whichusually showed the same waveshape on all three axes of a particular gage. The extensive amount of noise on the record made it difficult to distinguish the true shape of the acceleration signal. The duration of the accelerations appears to be on the order of 30 to 40 msec.

The peak-g measurements are summarized in Table B-3, Appendix B. The highest g values were measured in the gunner (44) and assistant gunner (45) on the M110 at Station 7. Less than 10 g was measured inside four of the dummies: No. 2 in the gunner's seat of the M60, No. 4 in the commander's seat of the M551 (Station 2), and Nos. 6 and 10 in the driver's and commander's positions inside the M577 (Station 6).

Pressure Time Measured Inside Vehicles

There were three successful pressure-time measurements taken inside the vehicles by the WSMR Nuclear Effects Group. These waveforms appear in Appendix B, Figure B-54. Inside the M60 Tank a peak pressure of 19 psi was measured by the gage located on the rear wall. The time-to-peak pressure was on the order of 15 msec and the pressure duration was near 220 msec. The outside pressure was 43 psi at the 580-ft range.

Inside the M109 the gage on the left wall recorded 2.5-psi peak pressure, a time-to-peak of 15 msec, and a total pressure duration on the order of 190 msec. The outside pressure at the 740-ft range was 21 psi.

Inside the M577, Station 6, that was at the 965-ft range, a peak pressure of 2.6 psi with a time-to-peak of 20 msec was recorded inside the vehicle on the upstream wall. The outside pressure was 9.2 psi.

Electronic Equipment Shelters

All three of the vehicles with electronic equipment shelters containing dummies were in an upright position postshot. The four dummies inside the two forward shelters at the 1120- and 1370-ft ranges had been displaced as a consequence of the blast. In the shelter at the 2000-ft range, dummy displacements appeared minimal. Table C-1, Appendix C, summarizes the effects on dummies in the electronic equipment shelters and the results of the motion-picture film analysis. Figures C-3 through C-8 give the displacement vs time curves obtained from the film analysis for each dummy.

Shelter R1/C10

In the retrofit shelter, the dummy (26) that was initially standing was lying flat on its back on the floor of the shelter with its feet toward ground zero. There was no damage either to the dummy or to its clothing. The 10-g Impact-O-Graphs® were unloaded. The film analysis showed that this dummy moved forward and its head impacted the upstream wall at 14 ft/sec, then it moved backward and impacted the downstream wall at 12 ft/sec.

Dummy No. 27 was found seated in its chair which was leaning back against a shelf on the downstream wall. This dummy sustained a deep laceration across its forehead and a smaller laceration across the bridge of its nose. The 10-g Impact-O-Graph® was unloaded. The film record showed that the dummy's head impacted the shelf in front of him at 11 ft/sec--which no doubt produced the laceration across its forehead. Then, the subject moved back into the chair and again moved forward striking the shelf at 8 ft/sec.

Shelter 04/C16

Inside ths S280 shelter at the 1370-ft range, Dummy No. 28 initially standing left side toward ground zero was found sitting on the floor with its head leaning against a shelf on the downstream wall, Figure C-9, Appendix C. This dummy sustained several slight lacerations to the back of its head and right shoulder. Both 10-g Impact-O-Graphs® were unloaded. The motion pictures showed this subject moved to its left toward ground zero at 10 ft/sec for 6 in. before dust obscured the camera's view. The dummy then must have rotated 90 degrees to its left and fallen backwards against the downstream wall. As it slid down the wall, bits of expanded plastic from the head became embedded in some wire connectors. The connectors can be seen in Figure C-9, Appendix C, just above the dummy's head.

Dummy No. 29, initially seated facing the blast, was found lying back-down on the floor in the collapsed chair with its feet toward ground zero. The film showed that the dummy was struck by a large metal antenna traveling at 38 ft/sec resulting in a V-shaped laceration on the left side of its face, Figure C-10, Appendix C. Postshot the antenna was found partially dislodged from its mountings on the upstream wall of the shelter as seen in the upper left of Figure C-9, Appendix C. The 10-g Impact-O-Graph® was unloaded. According to the motion-picture the dummy's head moved forward at 5 ft/sec and moved 2 inches before dust obscured the camera's view.

Shelter 07/C26

Inside the S280 shelter at the 2000-ft range there was no damage to either of the dummies or to their clothing and no Impact-O-Graphs® were unloaded. Dummy No. 30 remained in its seat. The legs of the chair were within

0.75 inch of their original position. The film record showed that the head of this dummy moved forward 5 inches (toward ground zero) at 4 ft/sec, then 20 inches backward at 4 ft/sec, and then returned to within 0.5 inch of its original position. There were no impacts.

Dummy No. 31 was still standing postshot and was leaning forward against the instrument panel. Its feet were located 4 inches from their original position as indicated by an outline of its boots traced on the floor preshot.

Results of the film analyses were that its head moved to the left (toward ground zero) at 6 ft/sec for 9 inches, then to the right at 7 ft/sec for 19 inches, and then settled at 10 inches to the right of its original position. There were no impacts.

Figure C-11, Appendix C, gives a postshot view of Dummy Nos. 30 and 31. This photograph could serve as a preshot view of these dummies as well as those in the 04/C16 shelter.

Foreign Vehicles

Table D-1, Appendix D, lists the preshot and post-shot positions of the dummies, the condition of the dummies, and the results of the Impact-O-Graph® gages. Included in the table are the dummy motions taken from the motion-pictures. Figures D-4 and D-5 give the displacement-time curves of Dummy Nos. 32 and 33 obtained from the film analysis. Included in the figures were the peak velocities and distances traveled.

The commander dummy (43) was shifted 2 inches over the left edge in its seat and the upper part of its body was tilted slightly toward ground zero. Its shirt was torn at the right pocket and along the front buttons. Both 10-g Impact-O-Graphs® were unloaded. Remnants of some ejecta were present on the hatch adjacent to the commander. The ejecta narrowly missed the commander's head at impact.

The film record taken by the camera outside the vehicle revealed that the commander dummy's head first moved toward ground zero at 13 ft/sec and stopped after 3 inches of travel. The movement stopped presumably from some other portion of the body impacting the upstream part of the vehicle.

The dummy (32) seated inside the troop compartment was found in its preshot position undamaged. No Impact-O-Graphs were unloaded. The film record taken by the camera inside the troop compartment recorded the dummy's head moved to the right at 5 ft/sec and impacted after 2 inches of travel, then the head moved to the left at 3 ft/sec for 8 inches (no impact), and then to the right at 6 ft/sec with impact 2 inches to the right of the original position.

As seen in Table D-1, Appendix D, the dummy (34) on the driver's seat was not damaged and was found in its original preshot position. One set of balls in the 10-g Impact-O-Graph® was unloaded. The subject was not viewed with a motion-picture camera.

Postshot photographs were not available to this project.

Drone Helicopter

The helicopter remained flying during and after the blast. Dummy No. 39 inside the helicopter remained seated with the harness restraint system intact. As seen in Table E-1, Appendix E, the only findings were five scratches on the top of its helmet that were obviously caused by plexiglas fragments from a small window that shattered in the ceiling of the aircraft. None of the Impact-O-Graphs® were unloaded.

The camera film record showed little movement of the dummy. Its head moved to the left for 2 inches at a velocity of 4 ft/sec and returned to within 0.5 inch of its original position going 2 ft/sec, Table E-1 and Figure E-3, Appendix E.

DISCUSSION

U. S. Army Weapon Systems

Closed Armored Vehicles

Blast displacements. Based on the results of this test, it seems reasonable to predict that the crew personnel inside the five closed armored vehicles would not have been injured as a consequence of blast displacements at corresponding ranges from a 1-KT nuclear surface burst. This applies to the M60 tank, the two Sheridan tanks, the M109 Self-Propelled Howitzer, and the M577 Communications Van that was at the 960-ft range.

The results obtained from the different test methods were consistent with one another in indicating that only minor displacements were encountered. The dummies were not damaged, the Impact-O-Graphs® were not unloaded, and the film records showed initial movements of 5 ft/sec or less with just a few inches of travel without impacts. If the peak-g levels measured by the electronic accelerometers were true, no injuries should result from accelerations of less than 20 g because they were of very short duration--less than 0.05 sec (References 3 and 4).

Only four of the dummies inside the closed armored vehicles had moved noticeably from their preshot positions. The dummy in the loader's seat in the M551 at Station 5 and the one in the commander's seat in the M557 at Station 6 apparently just leaned over in their seats. Likewise, the two standing dummies in the M109 apparently lost their footings after an initial forward movement of just 3 ft/sec after which they merely fell over backwards. As already mentioned, these dummies were not restrained in anyway so that the slightest motion of the vehicle would be all that was necessary to topple them over. Personnel under similar circumstances probably would not fall over.

Direct blast. The direct-overpressure effect mechanism would not be expected to injure personnel inside these vehicles. Peak pressures on the order of 2.5 psi that were recorded inside the M109 and inside the M577 were well below those required for a 1-percent probability of eardrum rupture (3.4 psi). Even the 19 psi recorded inside the M60 tank, if true, would not be expected to injure personnel because of the shape of the pressure-time curve. It has been demonstrated in animal experiments, Reference 5, that wave shapes of that character, having rise times of 15 msec without strong shocks at the leading edge, were far less damaging than those recorded in the open wherein the peak pressures were at the leading edge of the waves, i.e., in the incident shocks. For slow-rising blast waves, peak pressures have to be well over 50 psi to cause lung hemorrhages in dogs and monkeys. The one exception is eardrum rupture which is apparently a function of the peak pressure. However, since the crew members in the M60 would be wearing head sets this should provide protection against eardrum rupture.

Open Armored Vehicles

In regard to the results obtained with dummies on the M110, it could be expected that personnel standing on the vehicle would be swept from the vehicle by blast waves on the order of 10 psi. That the dummies seated in the gunner's and assistant gunner's positions remained in place during the blast suggests that the vehicle itself alters the form of the shockwave and flow at those positions thereby reducing the likelihood of personnel being displaced. Crew members thrown from the M110 vehicle by the blast at a velocity of 15 ft/sec would also develop a downward velocity of approximately 22 ft/sec merely from the freefall of about 7 ft (height of vehicle about 4 ft). The probability of injury would be influenced by the nature of the terrain. As seen in Figure A-2, Appendix A, there would be greater than a 50-percent probability of injury if the impact surface was nonyielding.

The dummies that were standing and sitting beneath the deployed canopy of the M577 at approximately 5 psi were displaced 4 and 6 ft by the blast. The calculated peak velocities were 6 ft/sec and 12 ft/sec which could not be expected to produce injury to personnel unless they collide with rigid objects.

Personnel in the Open

Blast displacement. The peak velocities and total distance of travel measured for the dummies that were standing face-on in the open were in close agreement with those predicted from the model reported in Reference 1. The model was used to calculate the curves in Figure A-3, Appendix A, relating displacement velocity for personnel in the open at different orientations to ground range for a 1-KT nuclear surface burst. The peak overpressures in the ranges between 820 and 1370 ft for the 1-KT nuclear surface burst and the 600-ton charge measured along Line 3 were within 1 psi of each other. Dummy No. 36, subjected to 12.7 psi, attained a peak velocity of 34 ft/sec as measured by the camera compared to 35 ft/sec calculated using the model. According to Figure A-2, Appendix A, there would be a 3-percent probability of significant injuries for tumbling displacements in the open terrain at that velocity.

Dummy No. 15, standing adjacent to the Laser-Guided Projectile subjected to 8.1 psi at the 1050-ft range, had a measured velocity of 17 ft/sec compared to 20 ft/sec based on the model. For tumbling displacements in the open, there would be less than a 1-percent probability of injury. Dummy No. 16 that was at the 1112-ft range next to the XM204 subjected to 6.7 psi was displaced about 10 ft and its measured peak velocity was 14 ft/sec compared to 16 ft/sec calculated from the model. There would be less than a 1-percent probability of injury at this velocity.

Although there would be very little probability of injuries resulting from tumbling across level terrain at velocities of 16-20 ft/sec, if impact against rigid objects were to occur, there would be a high probability of significant injuries, Figure A-2, Appendix A.

Dummy No. 41 that was at the 2400-ft range, subjected to about 2.4 psi (predicted), attained a velocity of just 1-2 ft/sec and merely fell backwards. Personnel at that range probably would not have been knocked down by the blast.

Direct blast. As far as direct-blast effects were concerned, Figure A-4, Appendix A, shows the probability of the different direct-blast injuries in relation to overpressure and range for a 1-KT nuclear surface burst. For standing or prone broadside-oriented personnel inside the 1000-ft rnage, 10-psi level and above, lung damage can be expected. The severity would range from pinhead size petechial hemorrhages at 10 psi to over a 50-percent incidence of serious lung hemorrhage at 27 psi (600-ft range). Eardrum rupture would vary from a 50-percent incidence at [illegible] psi (800-ft range) down to a 1-percent probability at 3.4 psi (2100-ft range). Corresponding overpressure levels and ranges for personnel prone, head-on to the blast, and against a reflecting surface were included in Figure A-4, Appendix A. The overpressures were calculated using equations in Reference 6 and the biological criteria were taken from Reference 7.

Personnel Behind Vehicles

The results obtained with dummies located in the open behind the M109 at 21 psi and the M551 at 12.7 psi suggest that personnel would probably be afforded considerable protection against blast displacements when located on the lee side of the vehicles. This location could also be expected to afford considerable protection against other nuclear weapon effects, including the direct-overpressure effects. Because the ideal shockwave becomes altered in defracting around the vehicle, the overpressure probably rose in several steps to peak. Blast wave forms of this nature have been shown to be less damaging to biological systems than ones having an ideal wave form, Reference 8.

Underground Command Post

The results obtained with dummies inside the Underground Command Post were used as input to a model designed to calculate blast displacement velocities of personnel inside open field fortifications. The model was based on laboratory shock tube studies dealing with scaled models of structures, including the Underground Command Post, containing 1/8-scale dummy men. Predictions based on the model and the results of the field test agreed in that blast displacement occurred only in the area of the personnel chamber that was in line with the entryway. There was little, if any, displacement in other areas of the shelter. Dummy No. 14, standing 5 ft inside the entryway, attained a velocity of 18 ft/sec on the present test and sustained some damage. Corresponding velocities calculated from the displacement prediction model for personnel 5 ft inside the entryway for other surface incident shock levels of equivalent yield were as follows: 13 ft/sec at 15 psi, 9 ft/sec at 10 psi, and 5 ft/sec at 5 psi. According to the model study and the results of a previous field test (Reference 9), personnel prone, head-on and in line with the entryway would not be displaced by blast levels of these magnitudes.

Additional information on blast displacement inside the Underground Command Post may be found in a report presented at this symposium by R. O. Clark _et al_ entitled "Blast Displacement Effects in Field Fortifications on Dice Throw Event," Reference 10.

Electronic Equipment Shelters

Shelter R1/C10

Significant displacement of the two dummies occurred inside the retrofit shelter at the 1120-ft range where the measured overpressure was 6.6 psi. The seated dummy moved toward and struck the upstream wall at 11 ft/sec and the standing dummy impacted the wall at 14 ft/sec. According to Figure A-2, Appendix A, there would be a 20- and 40-percent probability of injury from whole-body impact at these impact velocities. The curves in Figure A-2, Appendix A, strictly apply to a flat, hard surface. The probability of injury would be influenced by the nature of the surface or object struck.

The 10-g Impact-O-Graphs® were unloaded indicating an impact velocity greater than 5 ft/sec and less than 8 ft/sec. Specifically, these calibrations apply to dummies impacting flat against a smooth, rigid surface. Inside the electronic equipment shelters this probably did not occur. If just the head strikes the wall, velocities higher than 5 to 8 ft/sec would be required to unload the 10-g rated Impact-O-Graphs® mounted inside the chest cavities.

Shelter 04/C16

The dummies were displaced inside the S280 shelter at the 1370-ft range, where the measured peak overpressure was 4.7 psi. The standing dummy's initial velocity was 10 ft/sec and the seated dummy's was 5 ft/sec. The probability of injury at these velocities would be 13 and 0.2 percent. The severe laceration on the face of Dummy No. 29 demonstrated that objects inside the shelter dislodged by the blast can become dangerous missiles.

Shelter 07/C26

Only minor displacement effects were noted inside the shelter at the 2000-ft range where the overpressure was measured at 2.8 psi. The dummy velocities were 4 and 6 ft/sec with only 5- and 9-inch distances of travel, respectively. There were no impacts. There would be a very low probability of injury--0.02 and 0.6 percent--even if impact occurred at these velocities.

Foreign Vehicle

Inside the armored infantry fighting vehicle at the 820-ft range with measured overpressures of 12.7 psi there was no damge to the dummies. The initial velocities toward ground zero of the commander and passenger were 13 and 5 ft/sec, respectively. As seen in Figure A-2, Appendix A, there would be an associated probability of injury of 33 and 0.15 percent. As already mentioned, the curve in Figure

A-2, Appendix A, applies to whole-body impact parallel with a flat surface; this curve would not apply to head impacts when helmets were worn.

Drone Helicopter

There would be little or no probability of injuries to the pilot from blast-induced motions of the drone helicopter at the 2750-ft range with measured pressures of 2.5 psi.

The only effect on the dummy was a few scratches on its helmet from the small plexiglas window in the roof of the aircraft that was shattered by the blast. The fragments from the windows present a separate problem and depend on the type of plexiglas, its thickness, etc.

CONCLUSIONS

The following conclusions apply to blast waves from explosive yields equal to or on the order of 1-KT nuclear. Admittedly, the conclusions are based on a very limited amount of data.

1. Crew members of an M60 Main Battle Tank should not be injured by blast waves of 40 psi when the tank is closed and oriented head-on to the blast.

2. The crew inside a closed M109 Howitzer, oriented head-on to the blast, should not be injured from dispalcement at incident overpressure levels of 21 psi.

3. Crew personnel would be unharmed from the blast displacement within closed M551 Sheridan Tanks oriented head-on or side-on to incident overpressures of 13 psi.

4. Personnel inside an M577 Communications Van that is closed should not be injured at incident overpressures as high as 9 psi.

5. At a 9-psi overpressure level, personnel standing on an M110 Howitzer would be blown from the

vehicle at velocities of 15 ft/sec or more. The probability of injury would be near 50 percent if the terrain is hard. Crew members who are standing on the ground near the weapon would be displaced at peak velocities of 25 ft/sec. The probability of injury would range from less than 1 percent, if tumbling decelerations occur over flat terrain, to 90 percent if whole-body impact occurs against nonyielding surfaces.

6. The crew of the XM204 Howitzer subjected to 6.7 psi would be thrown about 10 ft by the blast and would attain a velocity of 14 ft/sec. For tumbling in the open on a smooth surface, there would be an associated 0.01-percent probability of injury. If impact occurs at peak velocity with rigid obstacles, the probability of injury would be near 40 percent.

7. Forward observers, if prone and oriented head-on to the detonation, would not be translated by overpressures of 5 psi.

8. Personnel seated or standing beneath the deployed portion of the M577 Communications Van side-on to a blast of 5 psi would be displaced 4 to 6 ft and would attain velocities of 6 to 12 ft/sec. There would be less than a 1-percent probability of injury unless impact occurs against rigid objects. Movement of the canopy's frame could present a hazard to personnel.

9. Crew members of the XM198 Howitzer should not be injured by blast overpressures of 2.4 psi.

10. There would be a 20- to 40-percent probability of blast displacement injuries among crew members inside closed retrofit electronic equipment shelters side-on to blast overpressures of 6.6 psi.

11. There would be a low probability of injury (<0-13 percent) to the crew members within electronic equipment shelters of the S280 type subjected to 5-psi overpressure.

12. There would be less than a 1-percent probability of any significant injuries to the occupants of the S280 equipment shelters subjected to 3-psi overpressure.

13. Inside an Armored Infantry Fighting Vehicle, oriented 315 degrees to a blast wave of 13 psi, the commander and crew members seated on the upstream side would be subjected to impacts with the wall at velocities of 6-13 ft/sec. For nonhead impacts, there would be a 1-30 percent probability of injury.

14. The pilot would not be injured as a consequence of blast displacements in a UH-1 Helicopter subjected to 2.5 psi while in flight.

RECOMMENDATIONS

1. In general, the cooperation and coordination among groups participating on the projects was very good. It is recommended that the coordination among groups involved in the immediate postshot evaluation of the different facets of the equipment be improved. This includes postshot still photography, assessment of vehicle damage, operation of the vehicle itself, assessment of the exact postshot position of the dummies, and, especially, the control of visitors.

2. It is recommended that the vehicles be left on the test bed for a longer length of time, at least through D+1.

3. More attention should be given to the placement of the Golden Bear dust-retardant on the layout before the shot. In addition to covering the surface in the upstream direction from the target, it should be applied on the downstream side as well to eliminate dust entering the cameras field of view on the negative phase. The film records would be greatly improved if the dust-retardant was placed on the ground underneath the vehicles themselves. In addition, the vehicles should be wet down with water inside and outside late on D-1.

4. The methods used in measuring accelerations inside the dummies with electronic accelerometers should be improved. Laboratory calibration of the gages while inside dummies undergoing impacts would be most desirable.

REFERENCES

1. Fletcher, E. R., J. T. Yelverton, R. A. Hutton, and D. R. Richmond, "Probability of Injury from Airblast Dispalcement as a Function of Yield and Range," Topical Report, DNA 3779T, Director, Defense Nuclear Agency, Washington, D. C., 29 October 1975.

2. Final Free-Field Blast Data, distributed by Defense Nuclear Agency, Field Command, Kirtland Air Force Base, NM, 17 March 1977.

3. White, C. S., I. G. Bowen and D. R. Richmond, "Biological Tolerance to Air Blast and Related Biomedical Criteria," USAEC Civil Effects Test Operations Report, CEX-65.4, Office of Technical Services, Department of Commerce, Washington, D. C., October 18, 1965.

4. Ruff, S., "Brief Acceleration: Less than One Second." In Department of the Air Force, German Aviation Medicine, World War II, Vol. I, Chap. VI-C, pp. 584-597, U. S. Government Printing Office, 1950.

5. Richmond, D. R. and D. E. Kilgore, "Blast Effects Inside Structures," in Proceedings of the Second Conference on Military Applications of Blast Simulators, November 2-5, 1970, Naval Weapons Laboratory, Dahlgren, VA., pp. 781-804, DNA-2775P, Defense Nuclear Agency, Department of Defense, Washington, D. C., 19 May 1972.

6. Bowen, I. G., E. R. Fletcher and D. R. Richmond, "Estimate of Man's Tolerance to the Direct Effects of Air Blast," Technical Progress Report, DASA-2113, Defense Nuclear Agency, Department of Defense, Washington, D. C., October 1968.

. Dolan, P. J. (Editor), The Effects of Nuclear Weapons, rev. ed. 1977, Energy Research and Development Administration (formerly U. S. Atomic Energy Commission), Washington, D. C., in the press.

8. Richmond, D. R., E. R. Fletcher and R. K. Jones, "Project LN401--Blast Protection Afforded by Foxholes and Bunkers," in Event Dial Pack Symposium Report, March 30-April 2, 1971, Vol. II, pp. 581-606, The Technical Cooperation Program, The Defence Research Board of Canada, Ottawa, Ontario, Canada, March 1971.

9. Richmond, D. R. and W. S. Jackson, "Airblast Effects Inside Field Fortifications," Final Project Officer's Report, Mixed Company Event, Project LN403, POR6622-2, Defense Nuclear Agency, Washington, D. C., 18 June 1974.

10. Clark, R. O., E. R. Fletcher, D. R. Richmond, and J. T. Yelverton, "Blast Displacement Effects in Field Fortifications on Dice Throw Event." In Proceedings Dice Throw Symposium, 21-23 June 1977, U. S. Army Ballistic Research Laboratories, Aberdeen, MD, in the press.

APPENDIX A

BLAST CRITERIA

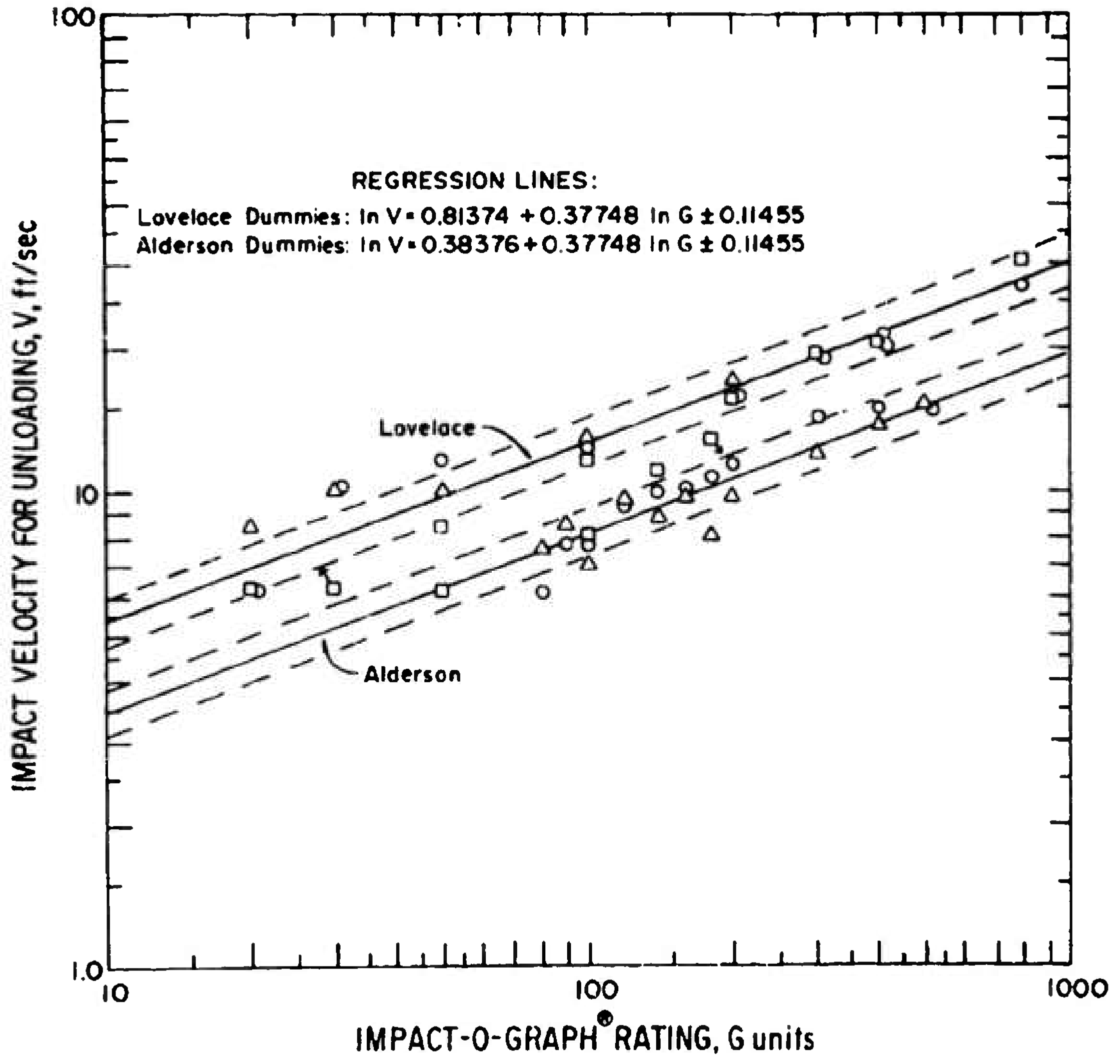

Figure A-1. Impact Velocities Required to Unload Impact-O-Graphs® in Dummies Dropped ○ Back-On, □ Front-On, and △ Side-On Onto a Concrete Slab.

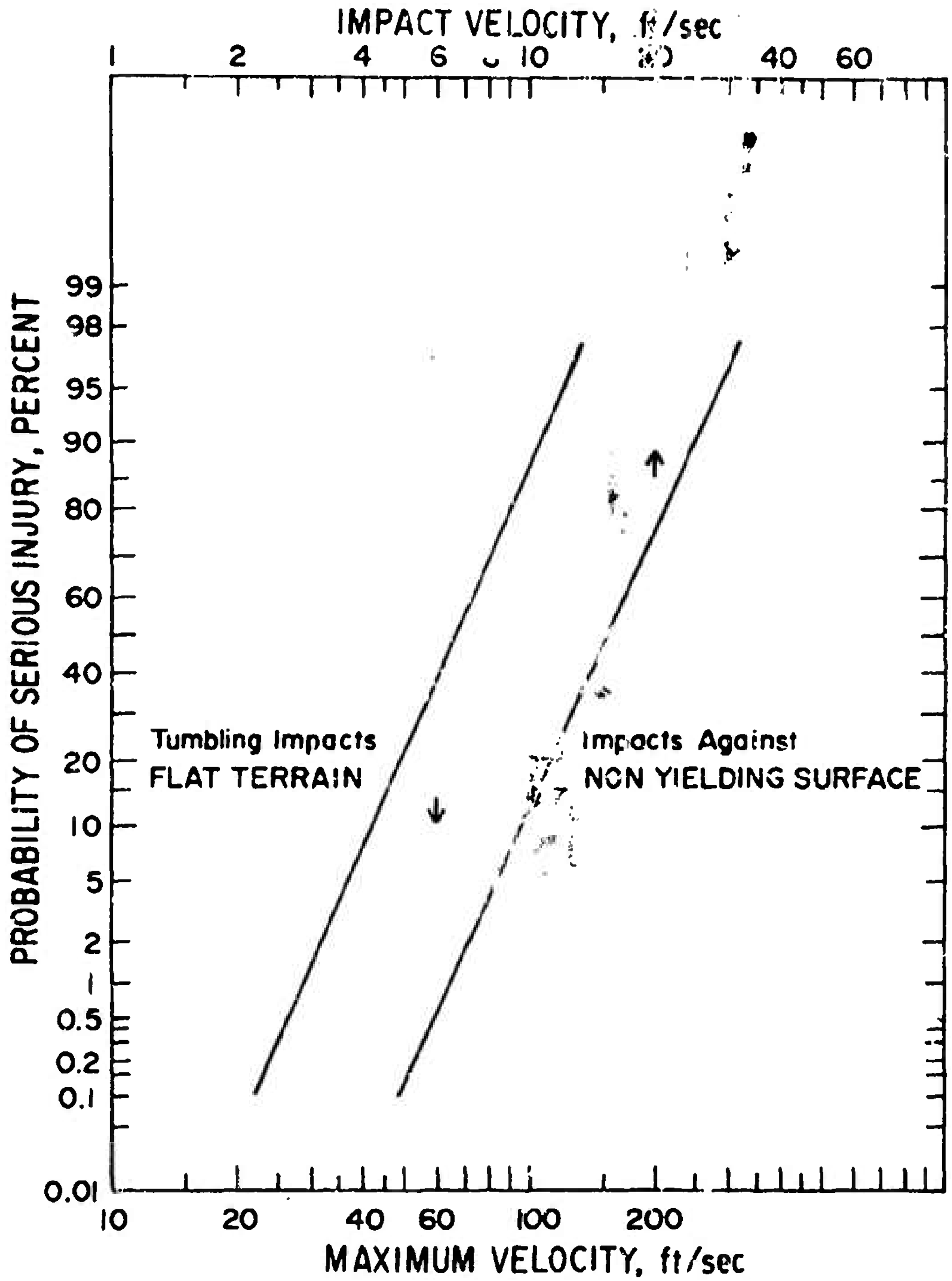

Figure A-2. Probability of Injury as a Function of Blast Displacement.

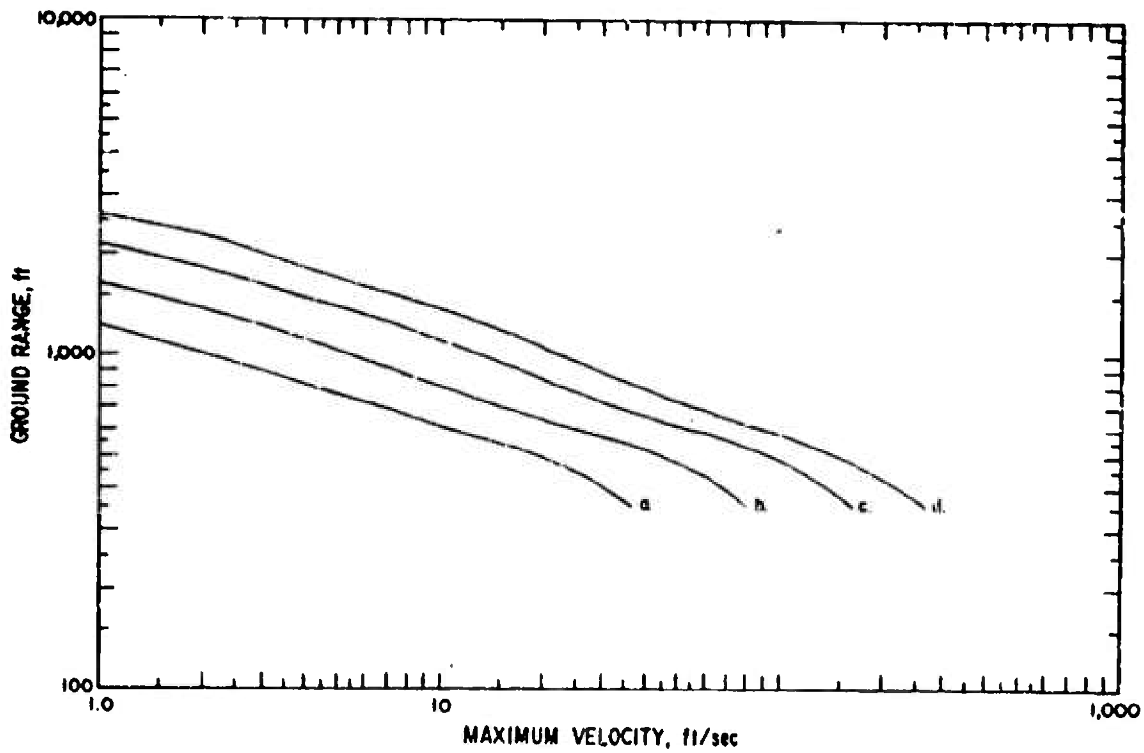

Figure A-3. Blast Displacement Velocity of Personnel in Relation to Ground Range from a 1-KT Nuclear Surface Burst at Sea Level. a. Prone, end-on; b. prone, random; c. prone, side-on; and d. standing, front- or back-on to the blast.

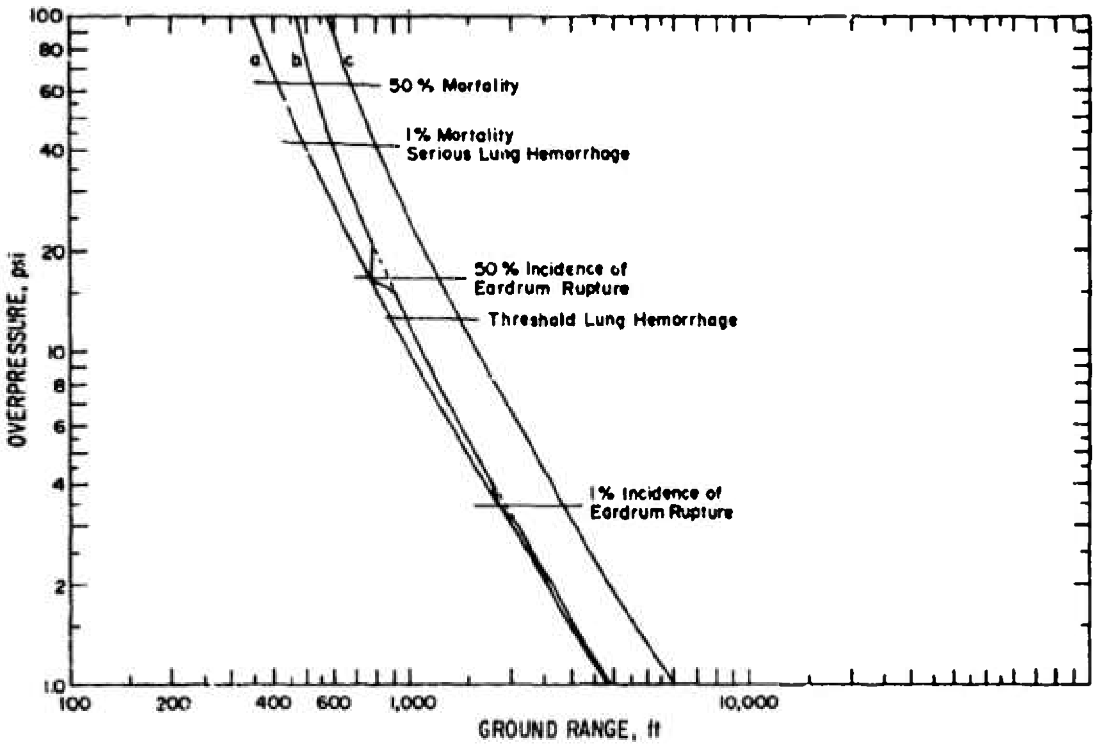

Figure A-4. Direct Blast Injuries in Relation to Overpressure and Ground Range from a 1-KT Nuclear Surface Burst at Sea Level. Orientation to blast: a. prone, head-on; b. prone, side-on or standing; and c. against a reflecting surface.

TABLE A-1

UNLOADING IMPACT VELOCITY FOR VARIOUS G-RATED IMPACT-O-GRAPHS®
IN RELATION TO INCIDENCE OF INJURIES

Impact-O-Graph®, g	Impact Velocity, ft/sec[a]	Incidence of Injuries, %[b]
Lovelace Dummies:		
800	28	95 (2.5% mortality)
200	17	50
40	8	5
10	5	0
Alderson Dummies:		
800	18	70
400	14	40
140	10	11
40	6	<1

[a] Based on the results of dropping dummies onto a concrete slab with Impact-O-Graphs® in the thorax.

[b] Injury based on sheep impact study.

TABLE A-2

BLAST DISPLACEMENT CRITERIA

Probability of Serious Injury, Percent	Impact Velocity, ft/sec, for Normal Incidence Against a Nonyielding, Flat Surface	Maximum Velocity, ft/sec, for Decelerative Tumbling Over Open Terrain
1	6.5 (4.5-8.2)	28.8 (12.7-37.8)
2.5	7.5 (5.4-9.2)	32.9 (16.7-41.4)
5	8.4 (6.3-10.1)	36.8 (21.1-44.8)
50	15.4 (13.5-17.3)	66.4 (58.2-82.9)
95	28.4 (24.8-34.7)	120 (91.8-268)
	$y = -2.384+6.211 \log x$	$y = -6.705+6.423 \log x$

y is the probability of injury in probit units.
x is the velocity.
95% confidence limits for the velocities are given in parentheses.

APPENDIX B

U. S. ARMY WEAPON SYSTEMS

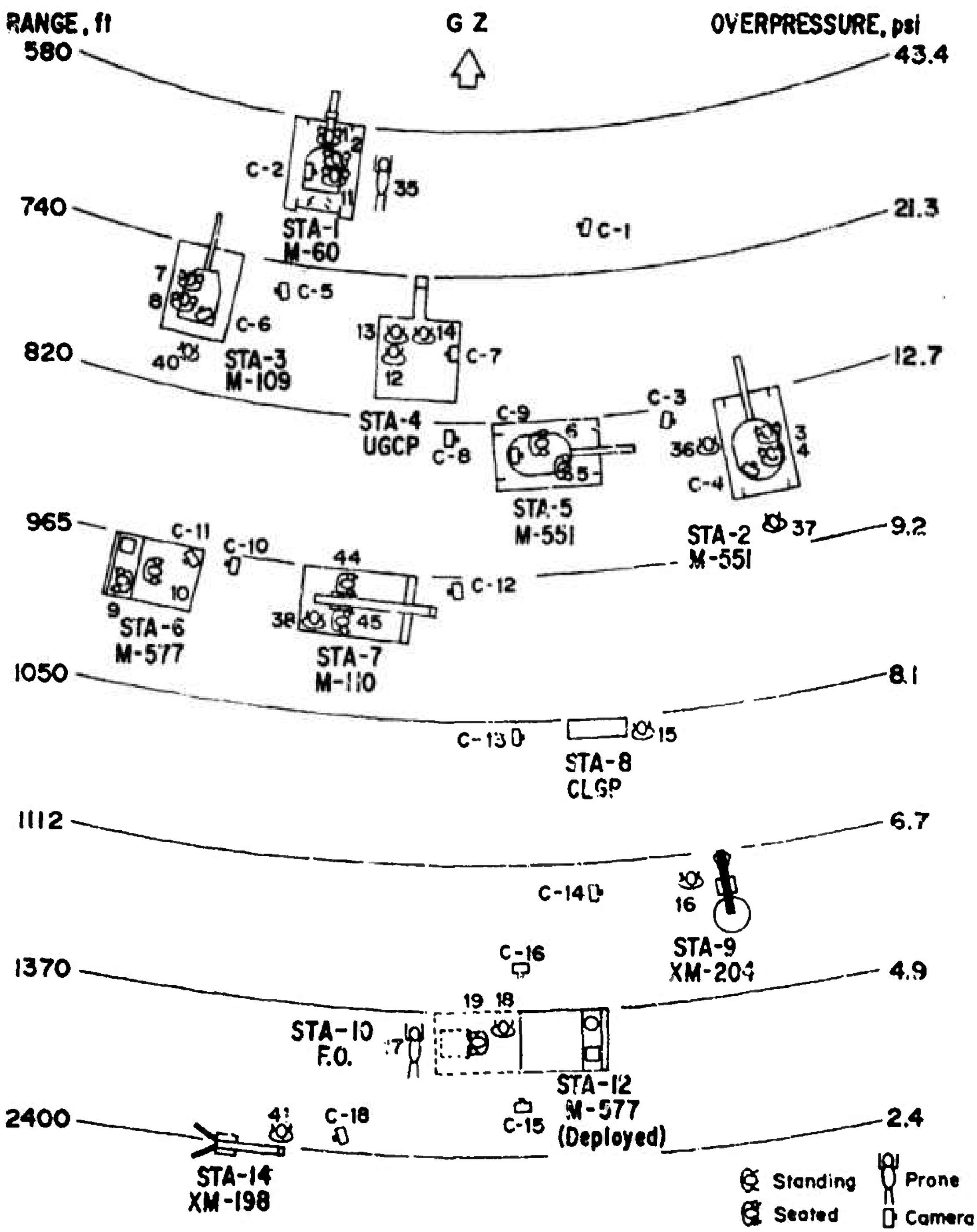

Figure B-1. Layout of U. S. Army Weapon Systems.

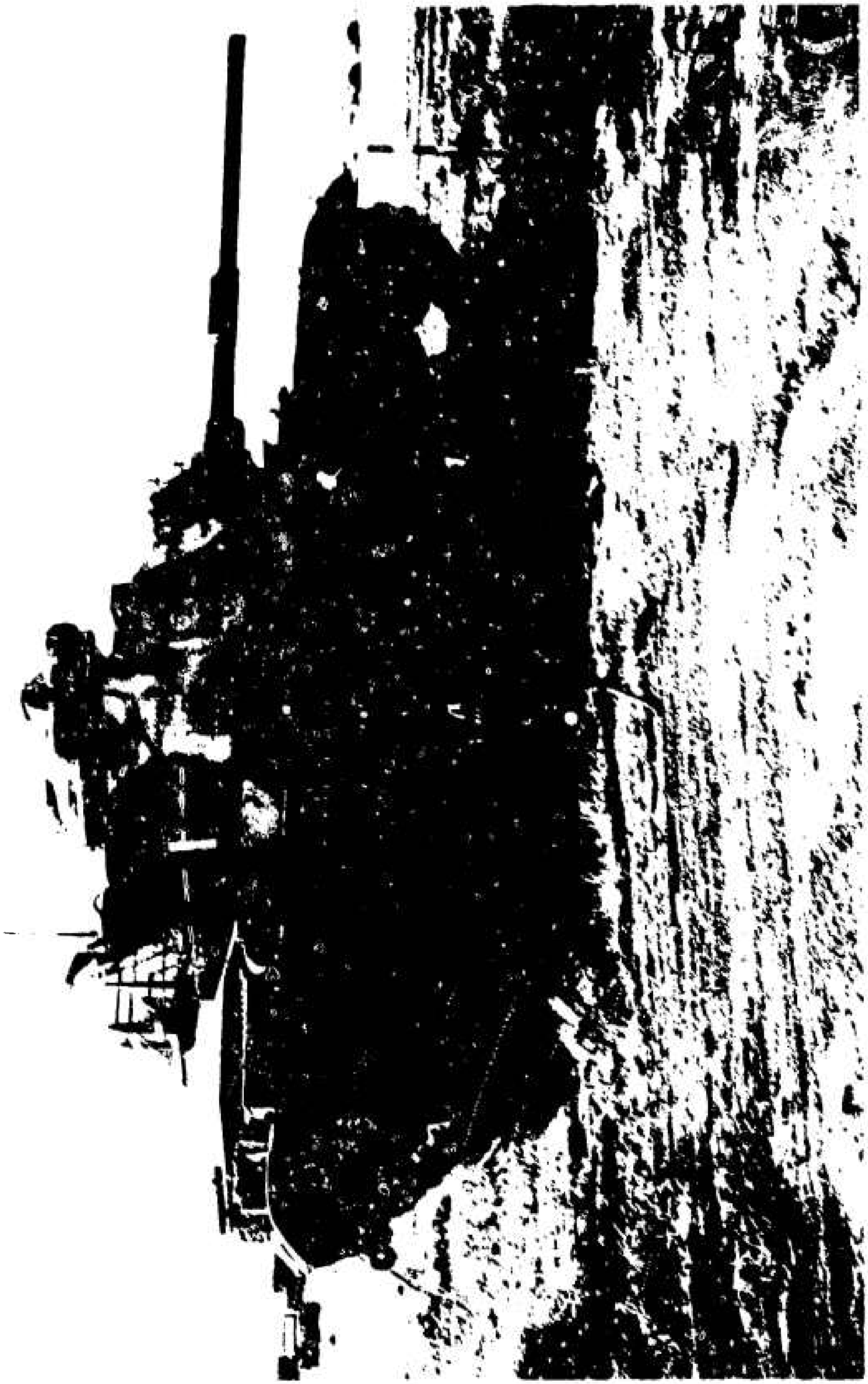

Figure B-2. Station 1 - M60 Main Battle Tank.

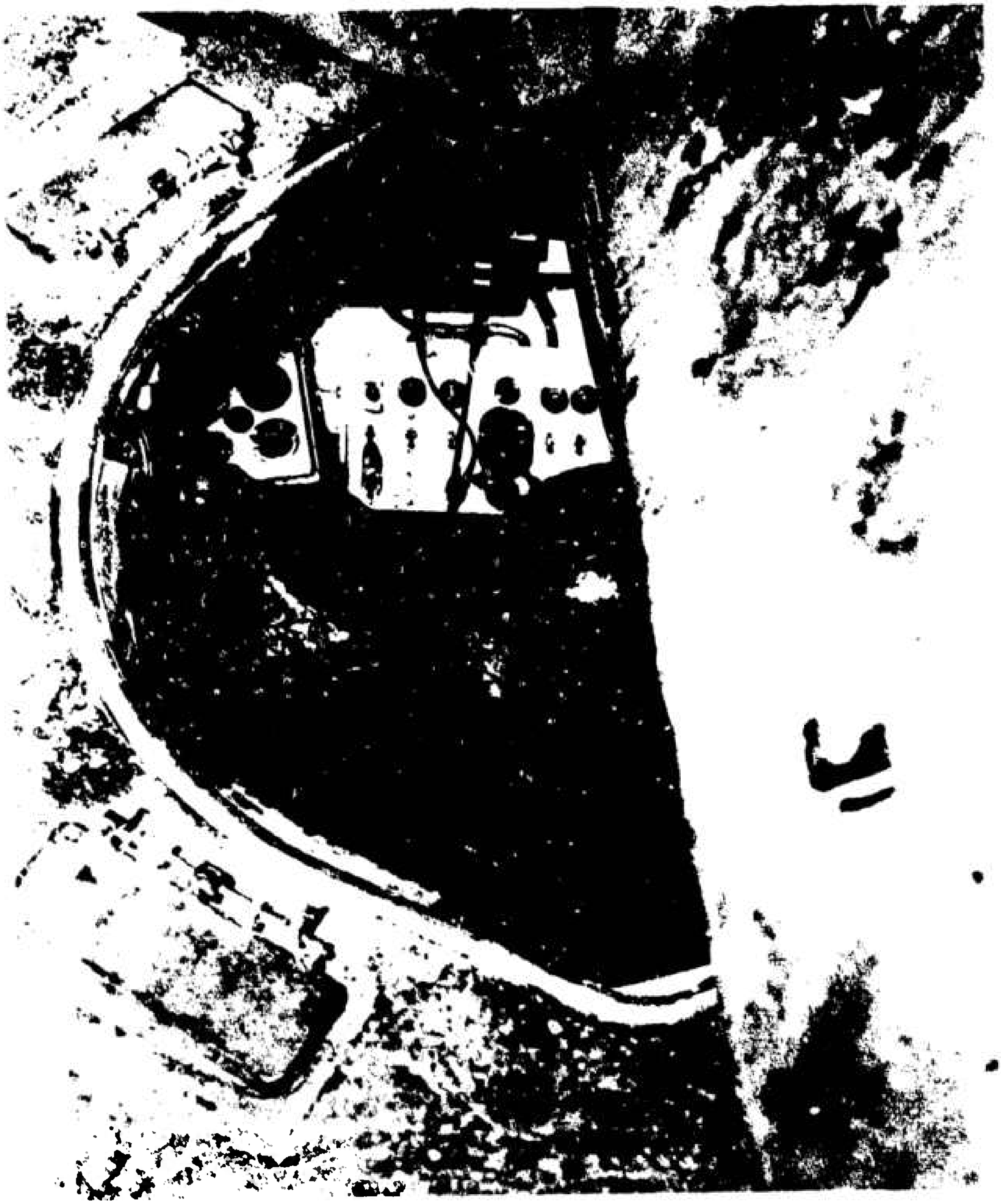

Figure B-3. Dummy No. 1 in Driver's Position, M60 Tank.

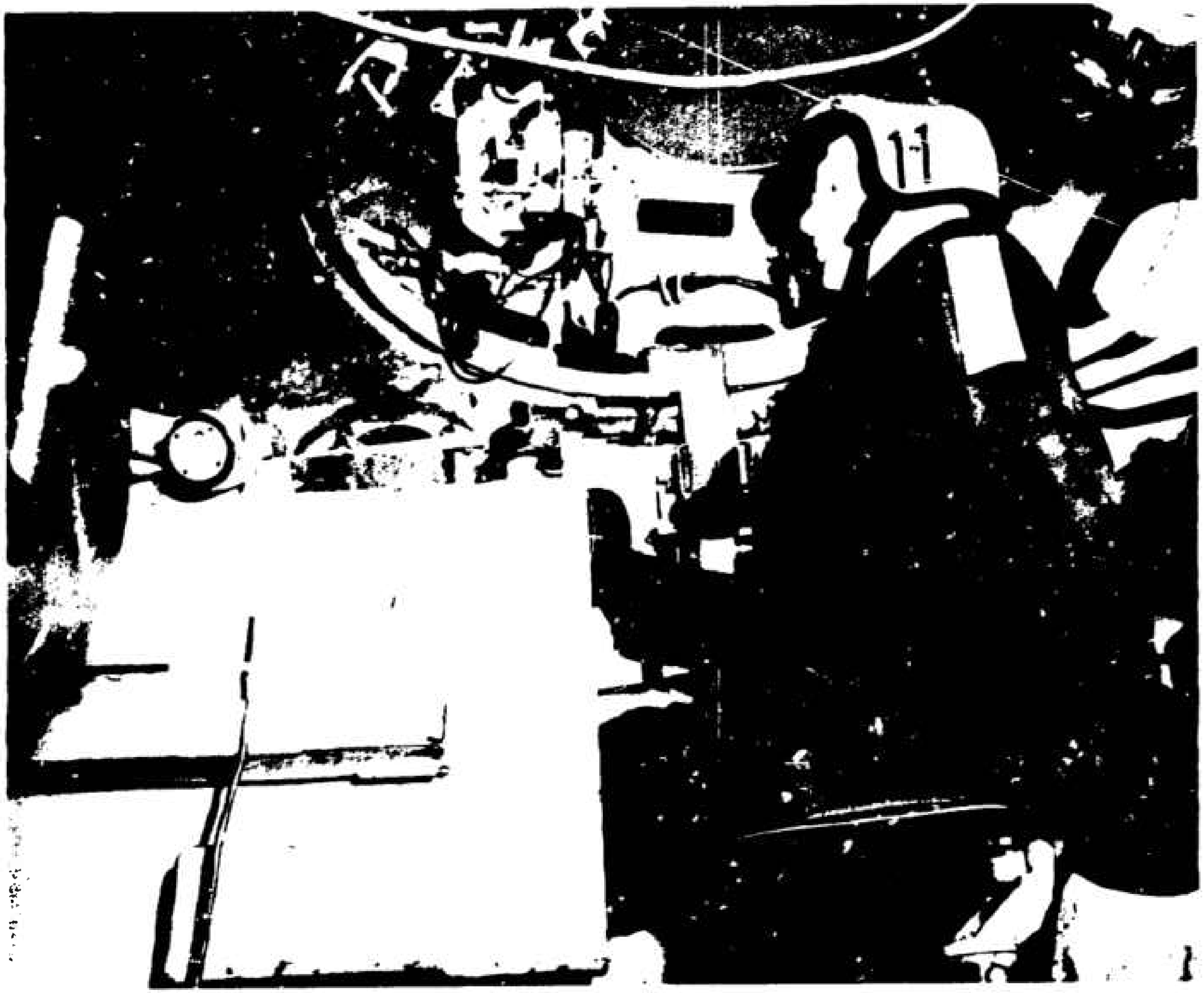

Figure B-4. Dummy No. 11 in Commander's Position, M60 Tank.

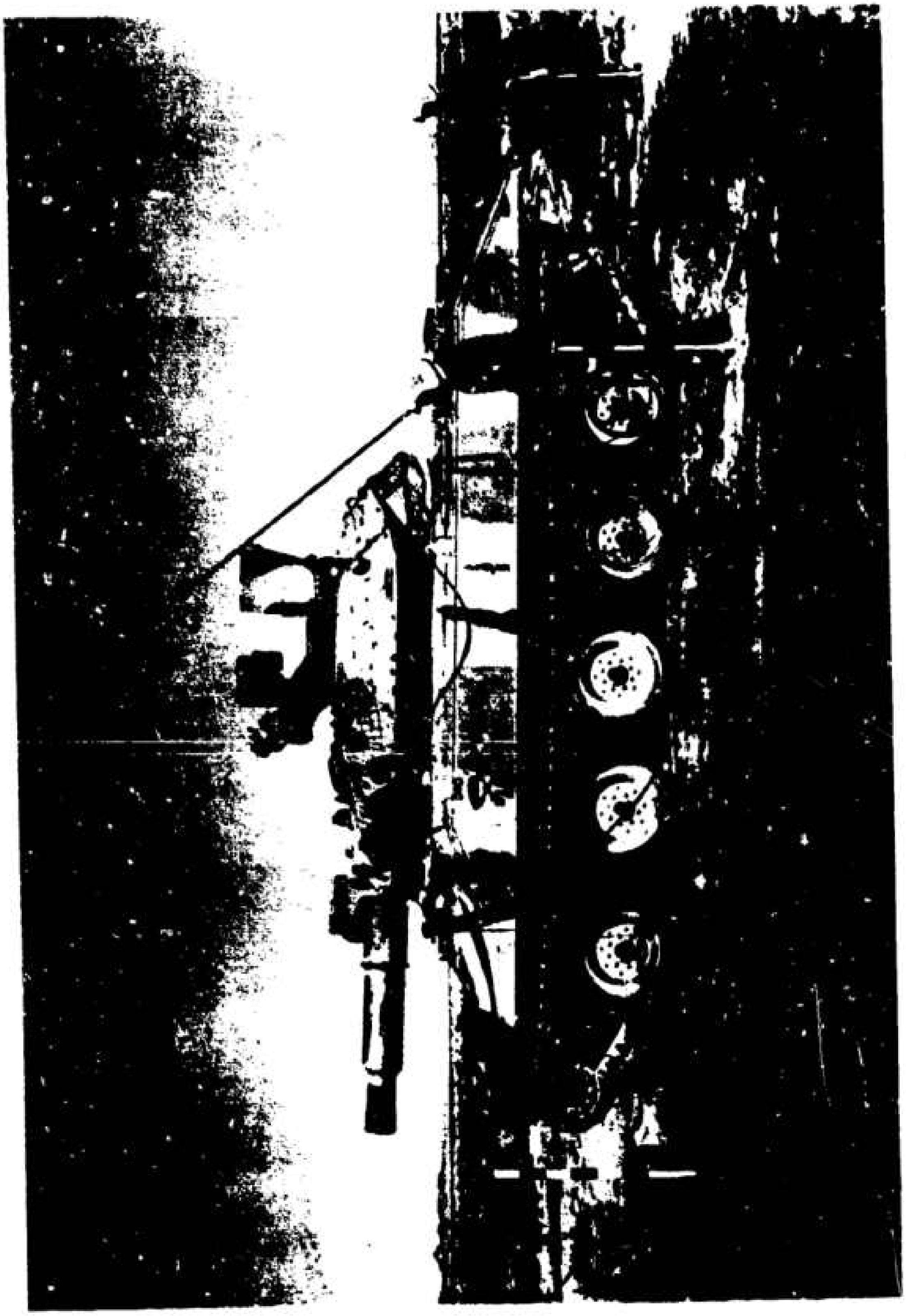

Figure B-5. Station 2 - M551 Sheridan Tank.

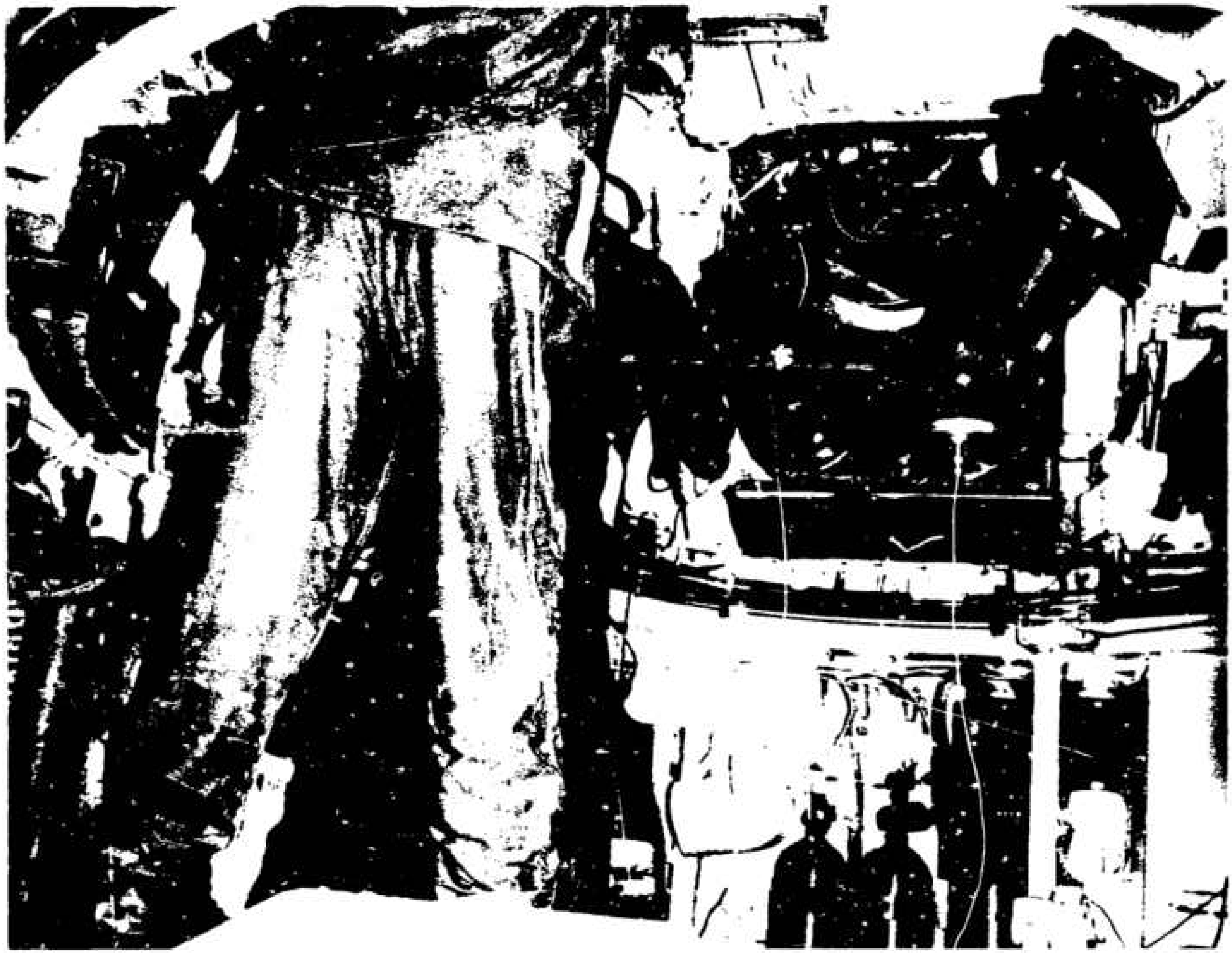

Figure B-6. Dummy Nos. 7 and 8 Inside the M109 Self-Propelled Howitzer Viewed from the Rear Door.

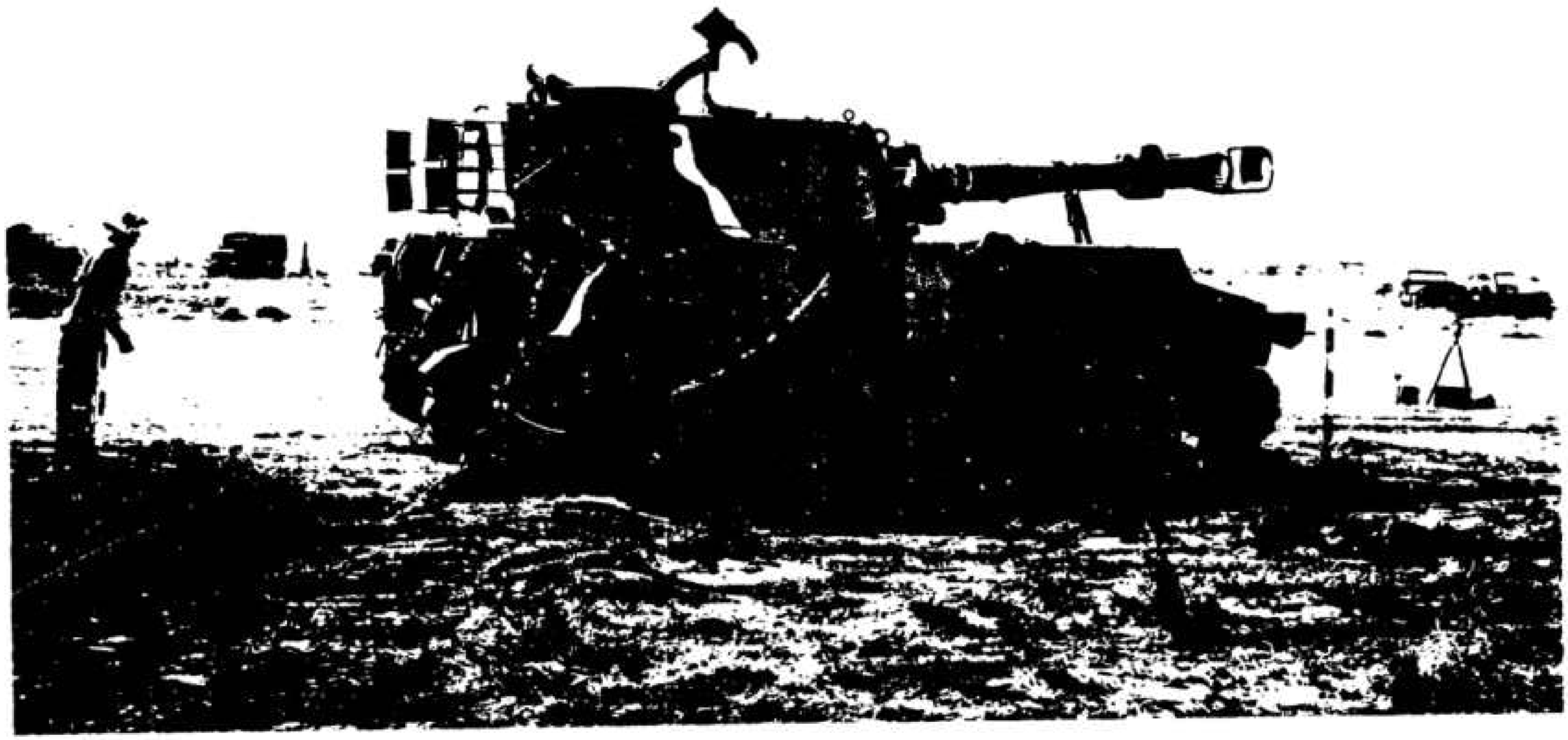

Figure B-7. Station 3 - M109 With Dummy No. 40.

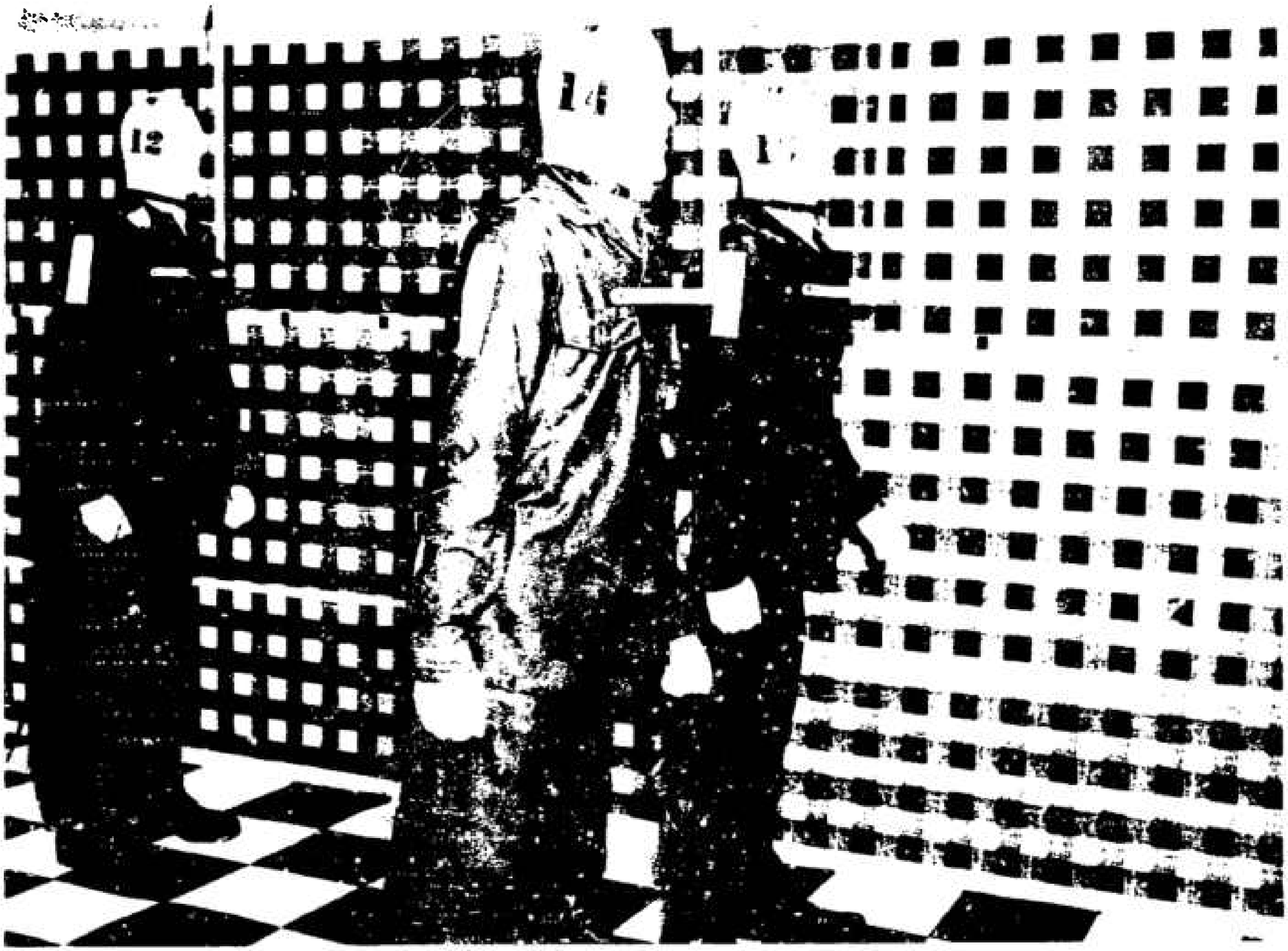

Figure B-8. Station 4 - View of Personnel Chamber of the Underground Command Post.

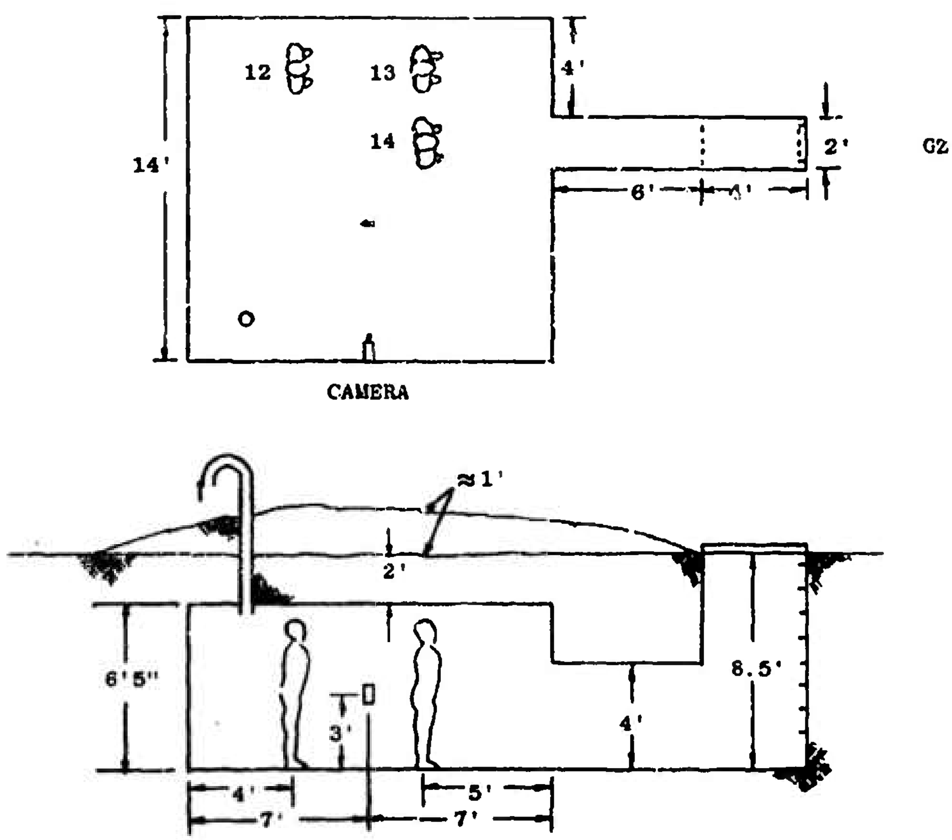

Figure B-9. Dimensions of Underground Command Post.

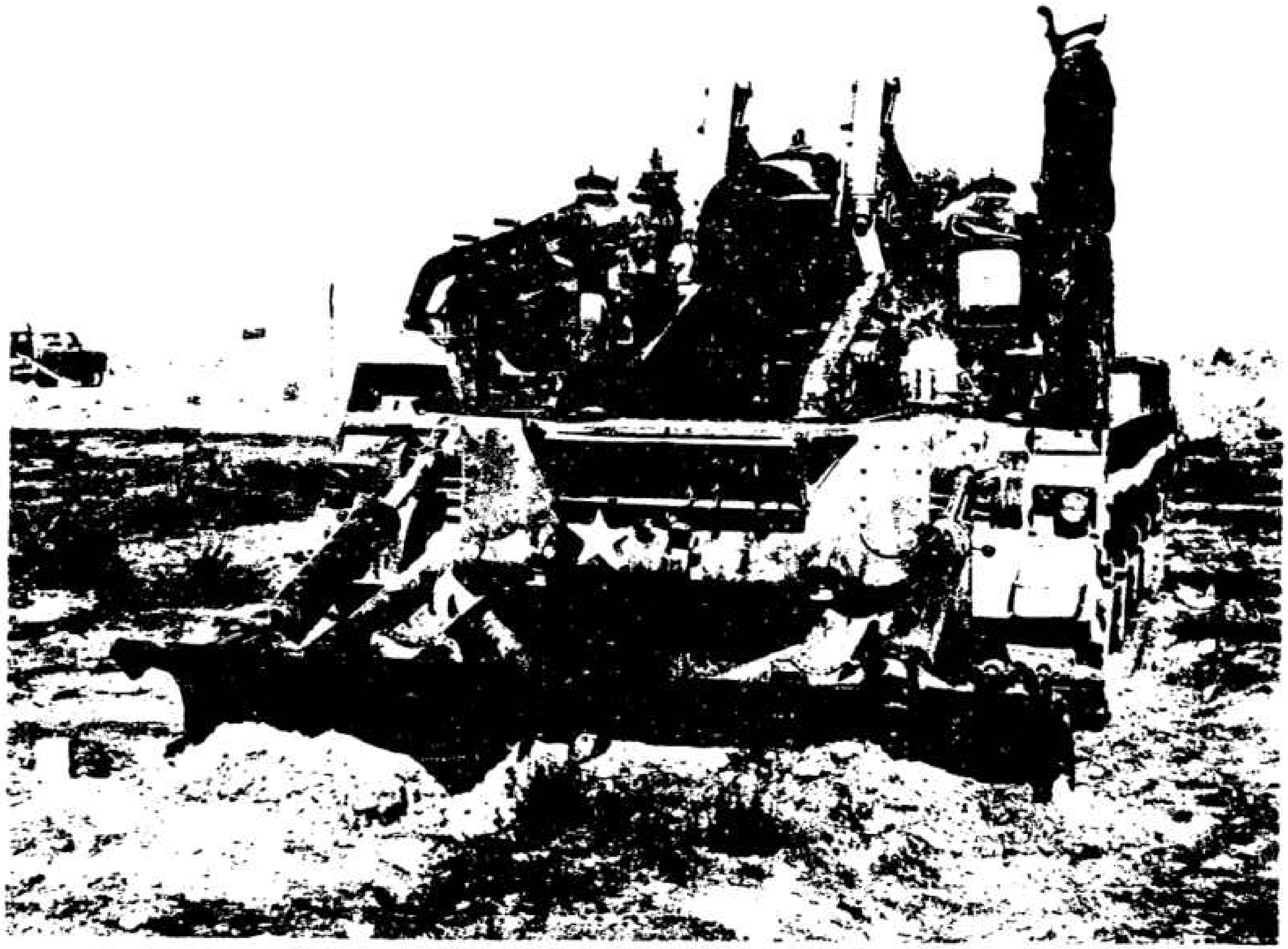

Figure B-10. Station 7 - M110 Self-Propelled Howitzer.

Figure B-11. Station 8 - Dummy No. 15 Adjacent to Laser-Guided Projectile. Before the test the dummy's arms were moved to the backside of the goal post.

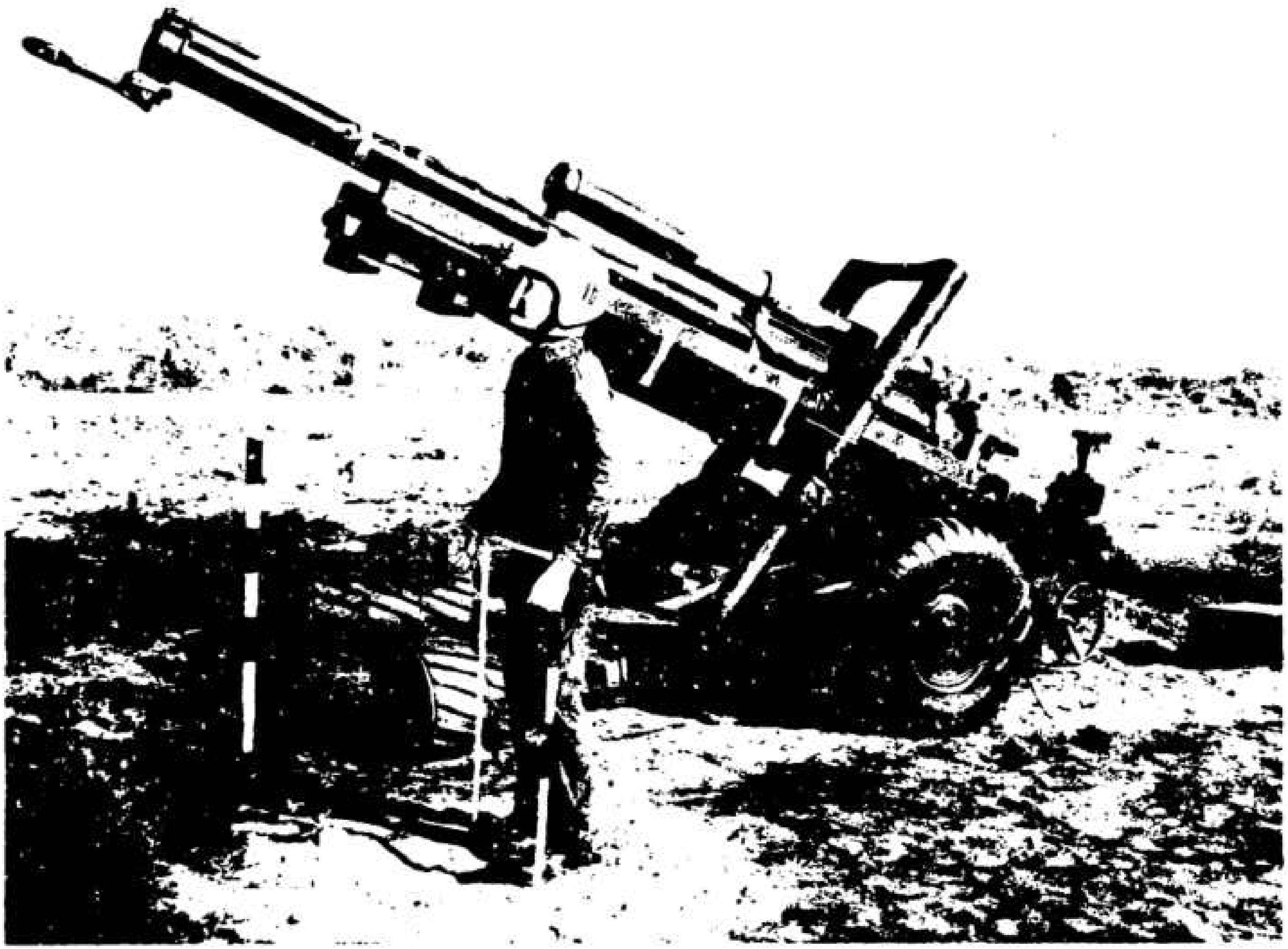

Figure B-12. Station 9 - Dummy No. 16 Adjacent to the XM204.

Figure B-13. Station 10 - Forward Observer and Station 12 - M577 Deployed.

Figure B-14. Station 14 - Dummy No. 41 Adjacent to the XM198.

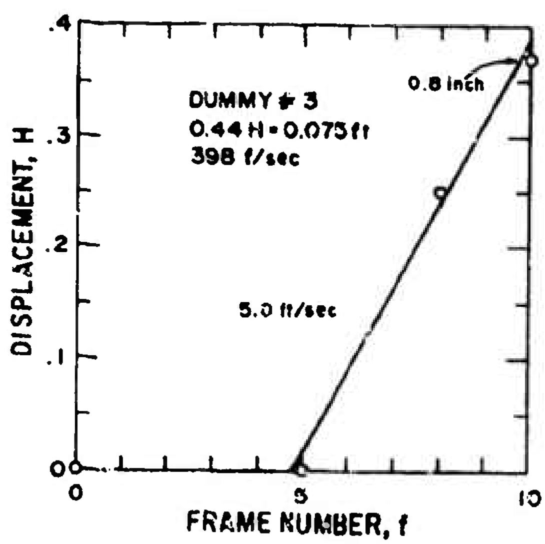

Figure B-15. Displacement vs Time, Dummy No. 3 in Gunner's Seat, M551 Sheridan, Station 2, 820 ft.

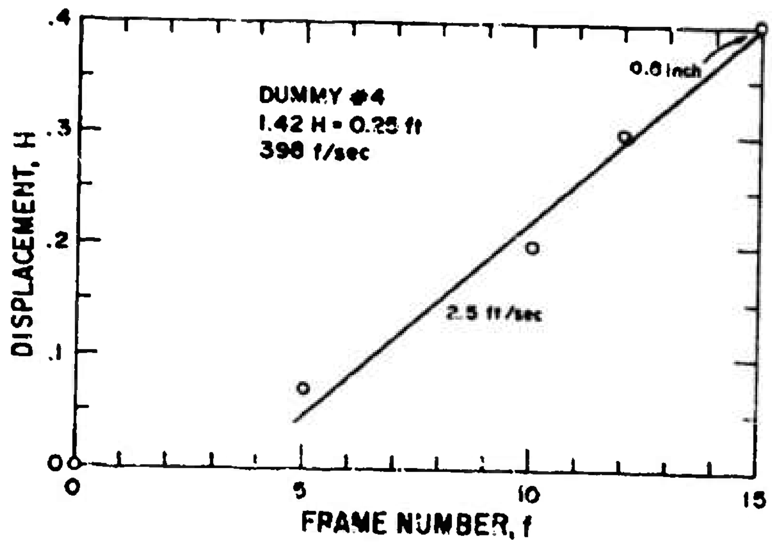

Figure B-16. Displacement vs Time, Dummy No. 4 in Commander's Seat, M551 Sheridan, Station 2, 820 ft.

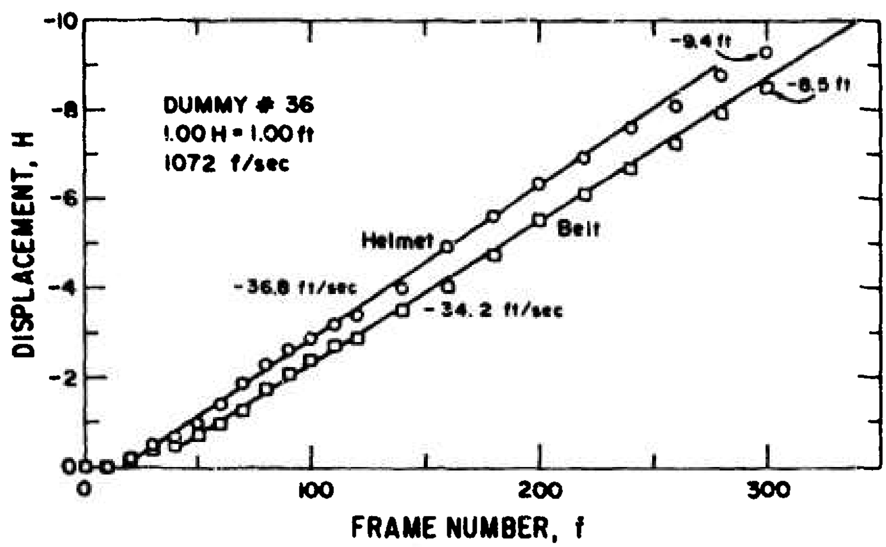

Figure B-17. Displacement vs Time, Dummy No. 36 Standing in Open 7.5 ft to the Left of M551 Sheridan, Station 2, 820 ft.

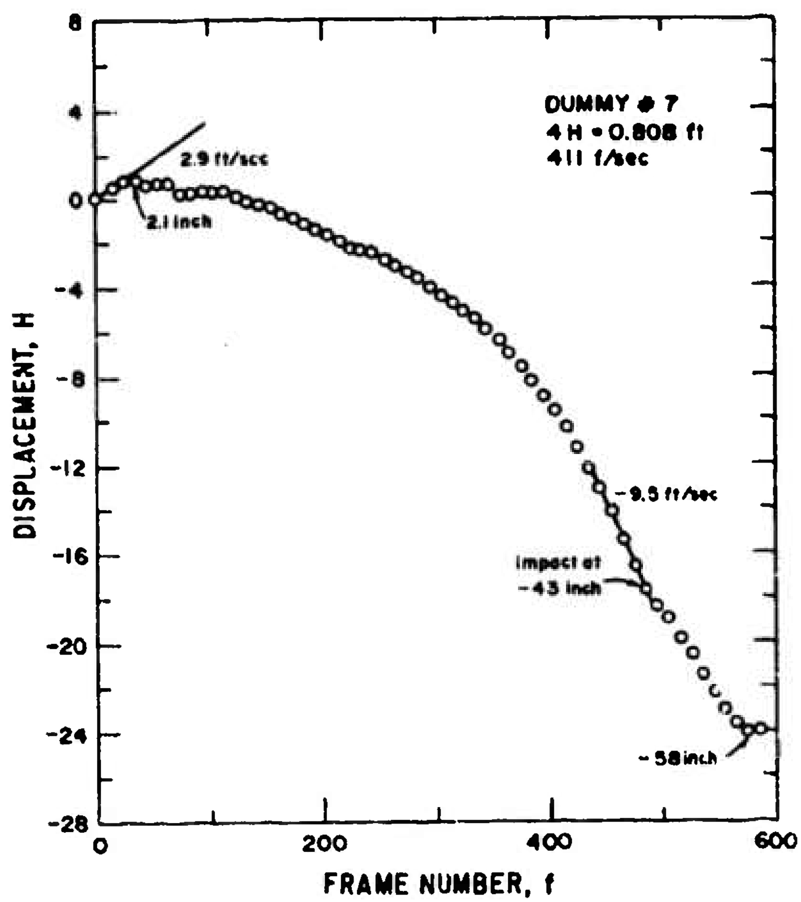

Figure B-18. Displacement vs Time, Dummy No. 7 Standing in Gunner's Position, M109 Self-Propelled Howitzer, Station 3, 740 ft.

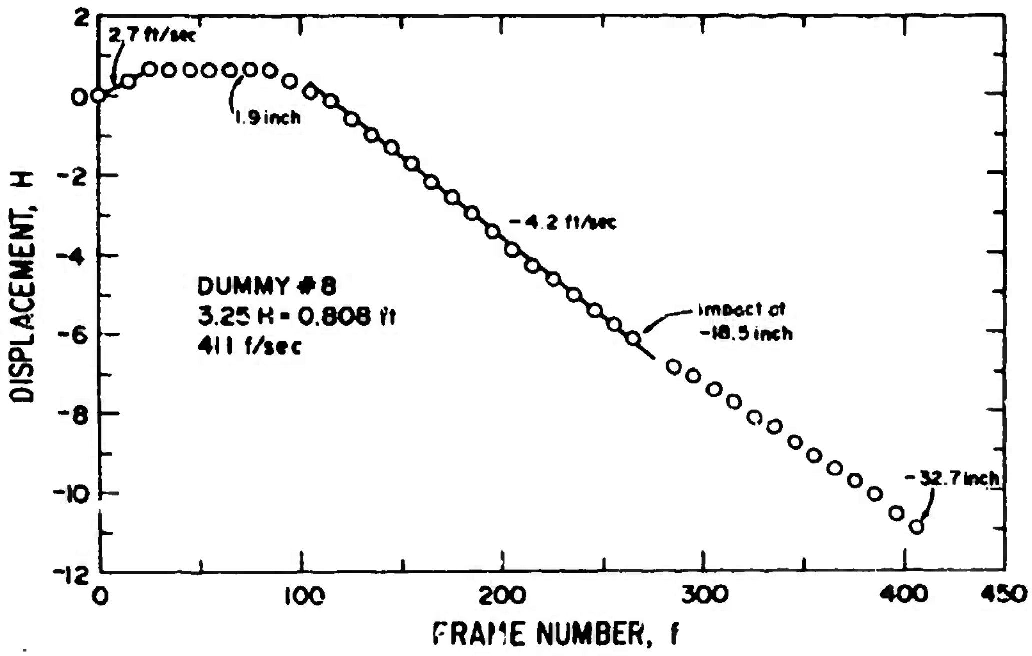

Figure B-19. Displacement vs Time, Dummy No. 8, Chief of Section, Standing in Back of Gunner Dummy, M109 Self-Propelled Howitzer, Station 3, 740 Ft.

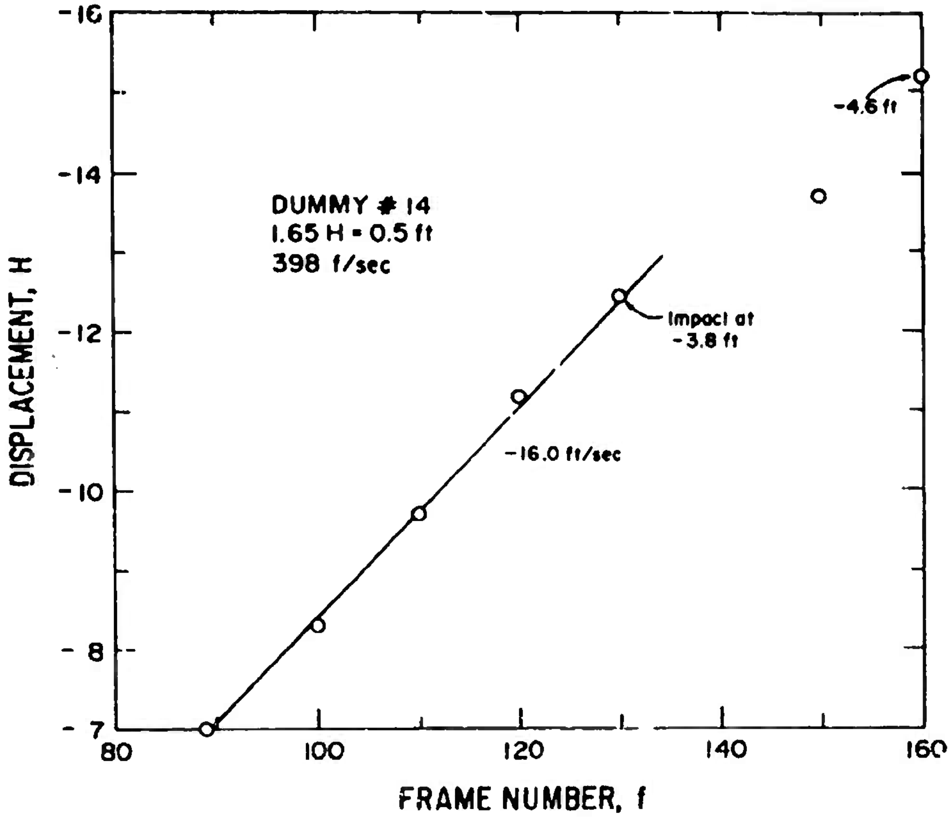

Figure B-20. Displacement vs Time, Dummy No. 14 Standing 5 ft Inside Entryway of Underground Command Post, Station 4, 740 ft.

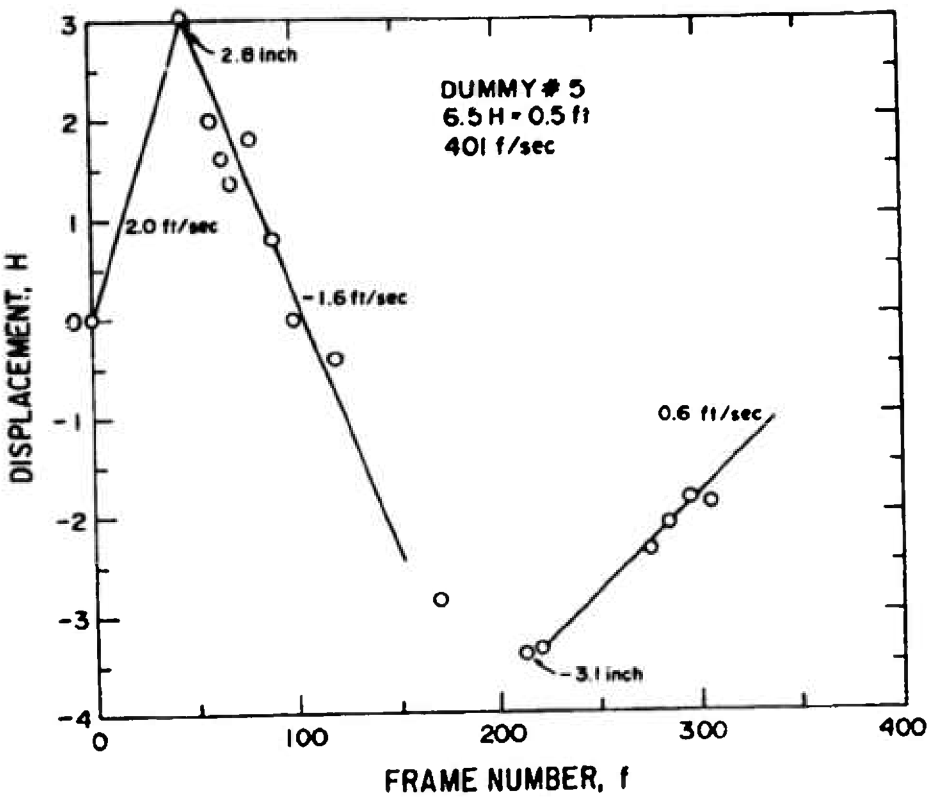

Figure B-21. Displacement vs Time, Dummy No. 5 in Gunner's Seat, M551 Sheridan, Station 5, 820 ft.

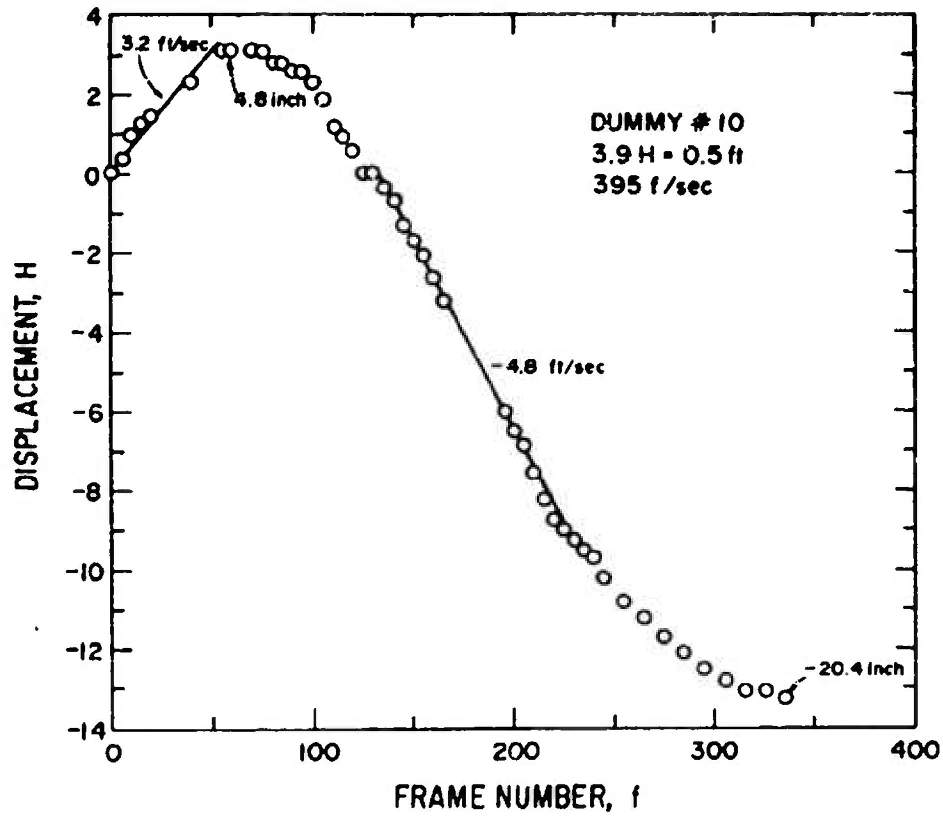

Figure B-22. Displacement vs Time, Dummy No. 10 in Commander's Seat, M577 Communications Van, Station 6, 965 ft.

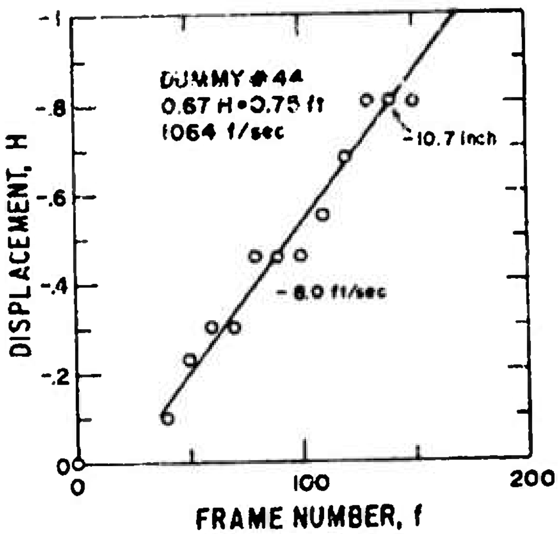

Figure B-23. Displacement vs Time, Dummy No. 44 in Gunner's Seat, M110 Self-Propelled Howitzer, Station 7, 965 ft.

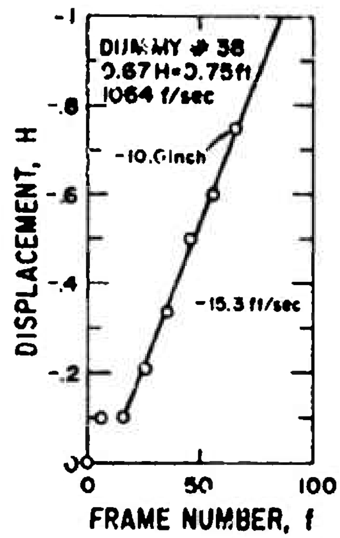

Figure B-24. Displacement vs Time, Dummy No. 38 Standing on M110 Self-Propelled Howitzer, Station 7, 965 ft.

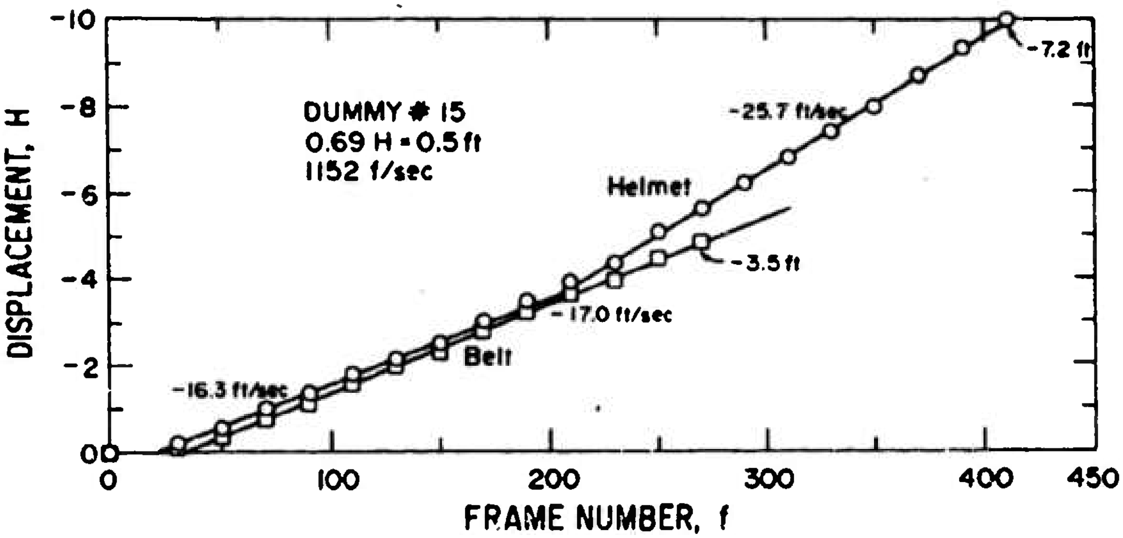

Figure B-25. Displacement vs Time, Dummy No. 15 Standing in the Open Adjacent to the Laser-Guided Projectile, Station 8, 1050 ft.

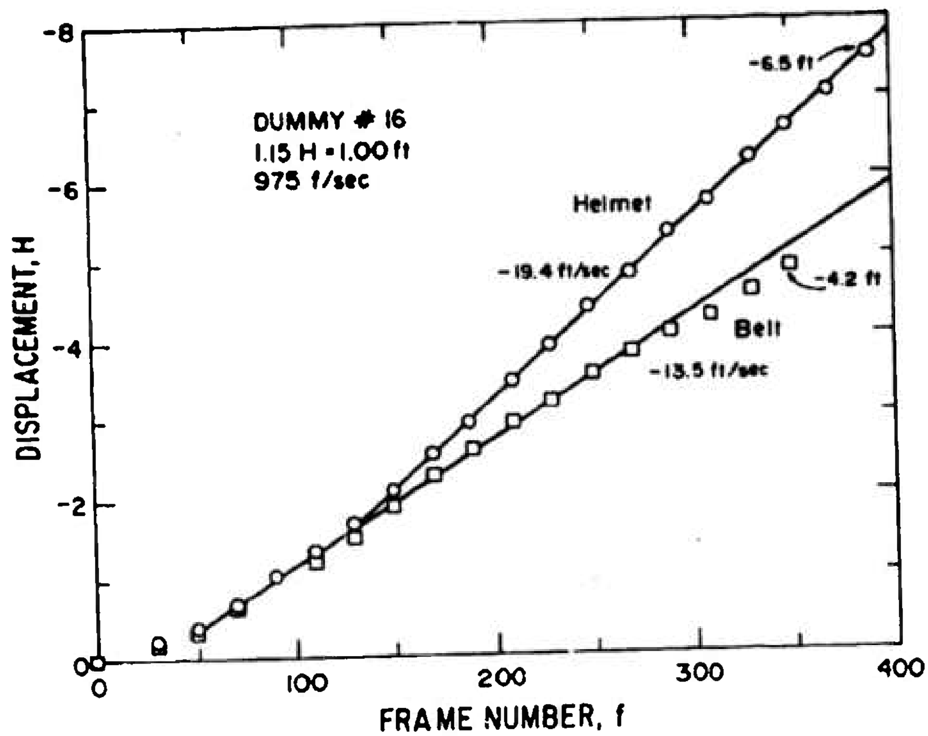

Figure B-26. Displacement vs Time, Dummy No. 16 Standing in the Open Adjacent to the XM204 Towed Howitzer, Station 9, 1112 ft.

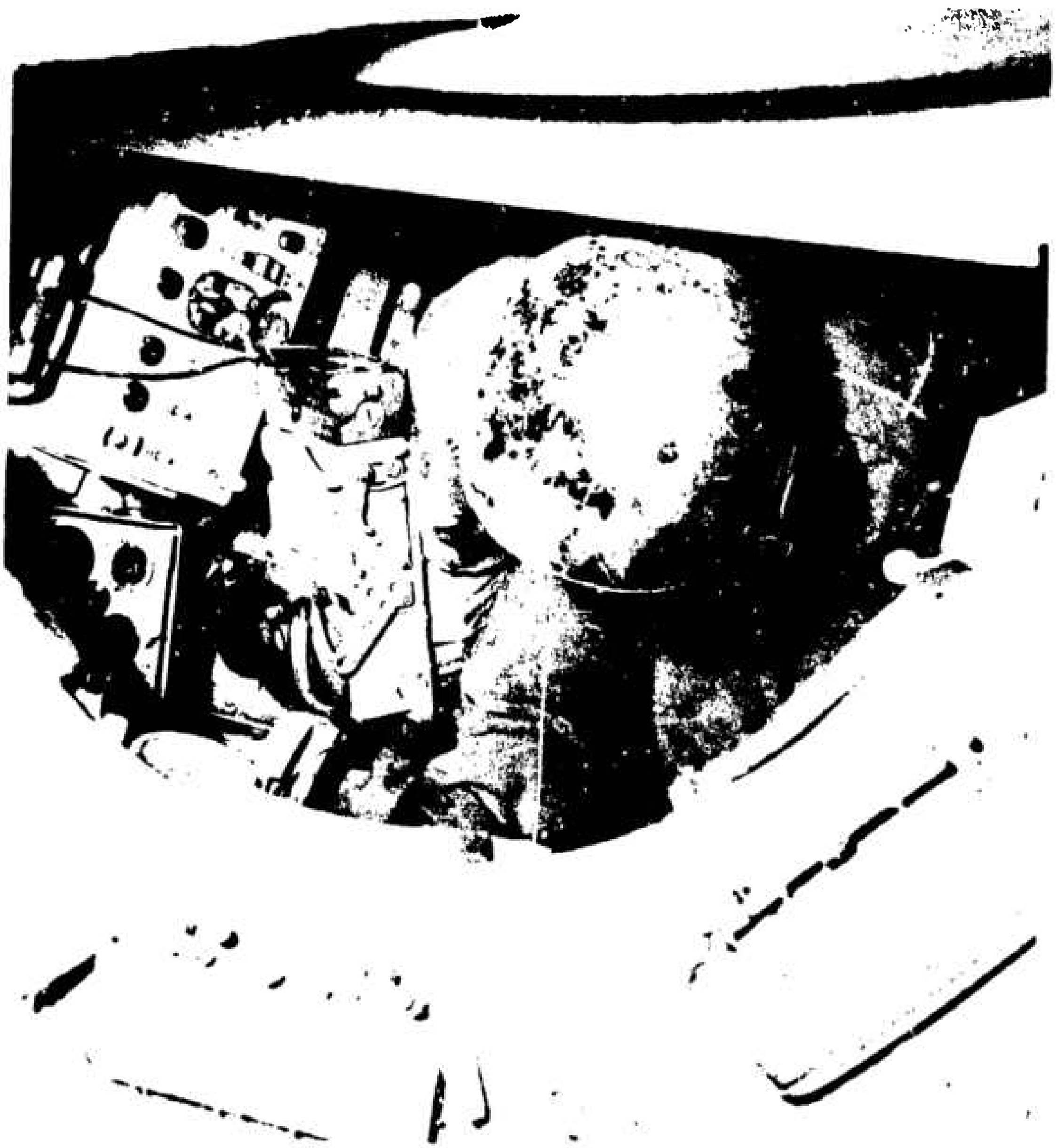

Figure B-27. Postshot View, Station 1, Dummy No. 1 in Driver's Compartment, M60 Tank.

Figure B-28. Postshot View, Station 2, M551 Sheridan Tank.

Figure B-29. Postshot View, Station 3, M109 Self-Propelled Howitzer, Dummy Nos. 7 and 8 View Toward the Rear of the Vehicle.

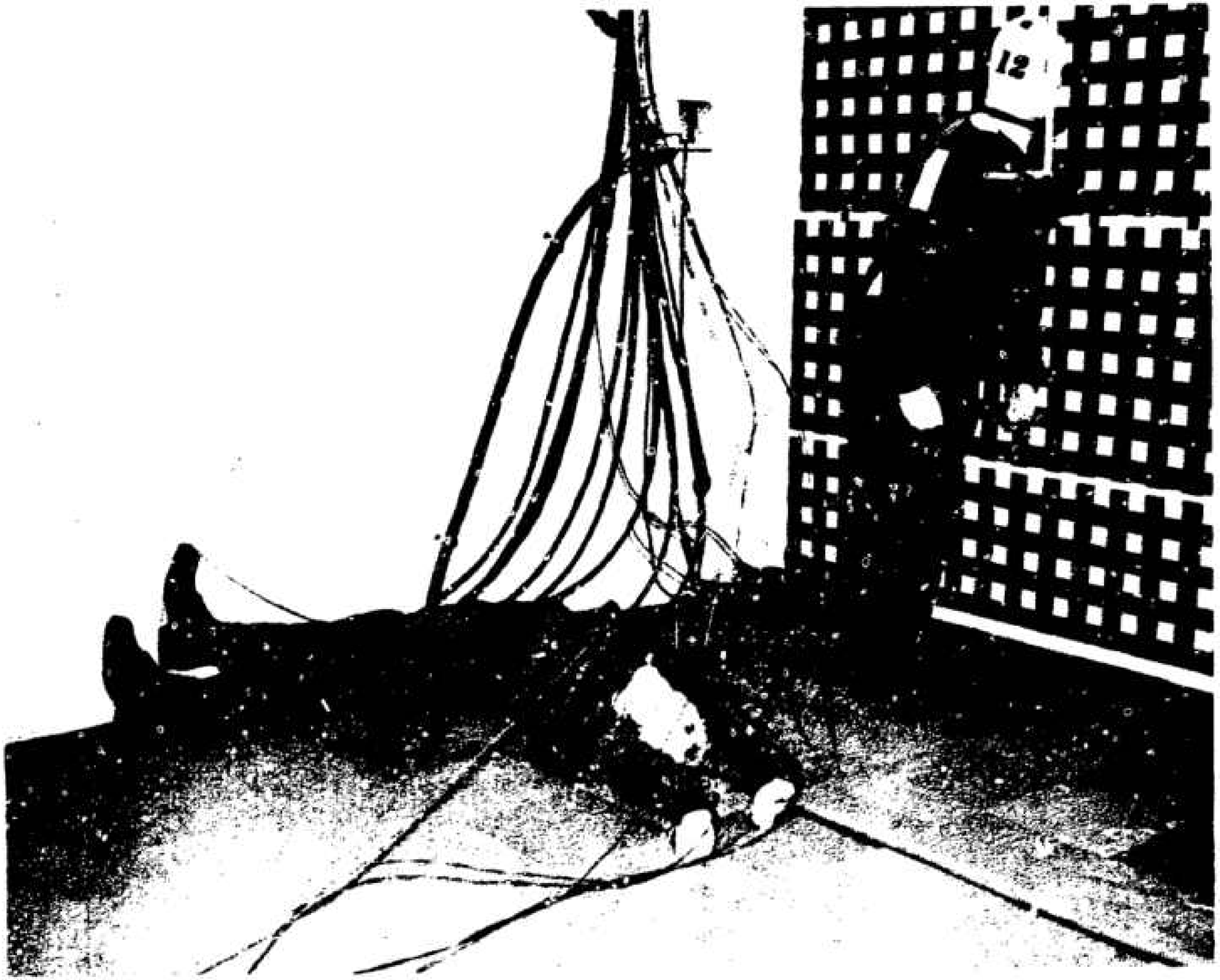

Figure B-30. Postshot View, Station 4, Dummy Nos. 12 and 14, Personnel Chamber Underground Command Post.

Figure B-31. Postshot View, Station 4, Dummy No. 13, Personnel Chamber Underground Command Post.

Figure B-32. Postshot View, Station 5, Dummy No. 6, Loader's Position, M551 Sheridan Tank.

Figure B-33. Postshot View, Station 8, Dummy No. 15.

Figure B-34. Postshot View, Station 9, Dummy No. 16 Adjacent to the XM204.

Figure B-35. Postshot View, Station 10, Forward Observer Dummy No. 17 and Station 12, Dummy Nos. 13 and 19, M577 Deployed.

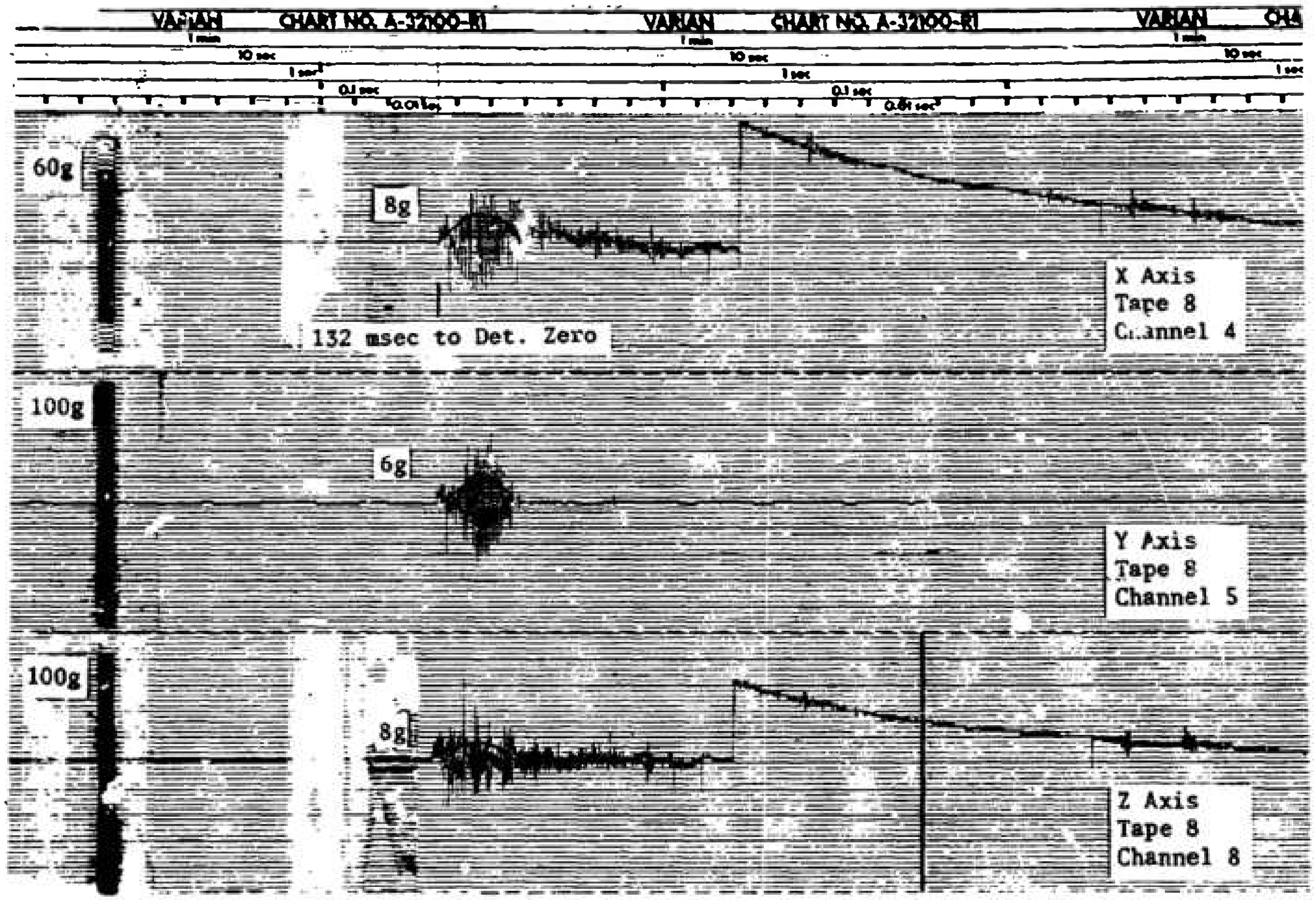

Figure B-36. Station 1, M60 Main Battle Tank. Acceleration record for Dummy No. 2 in gunner's seat.

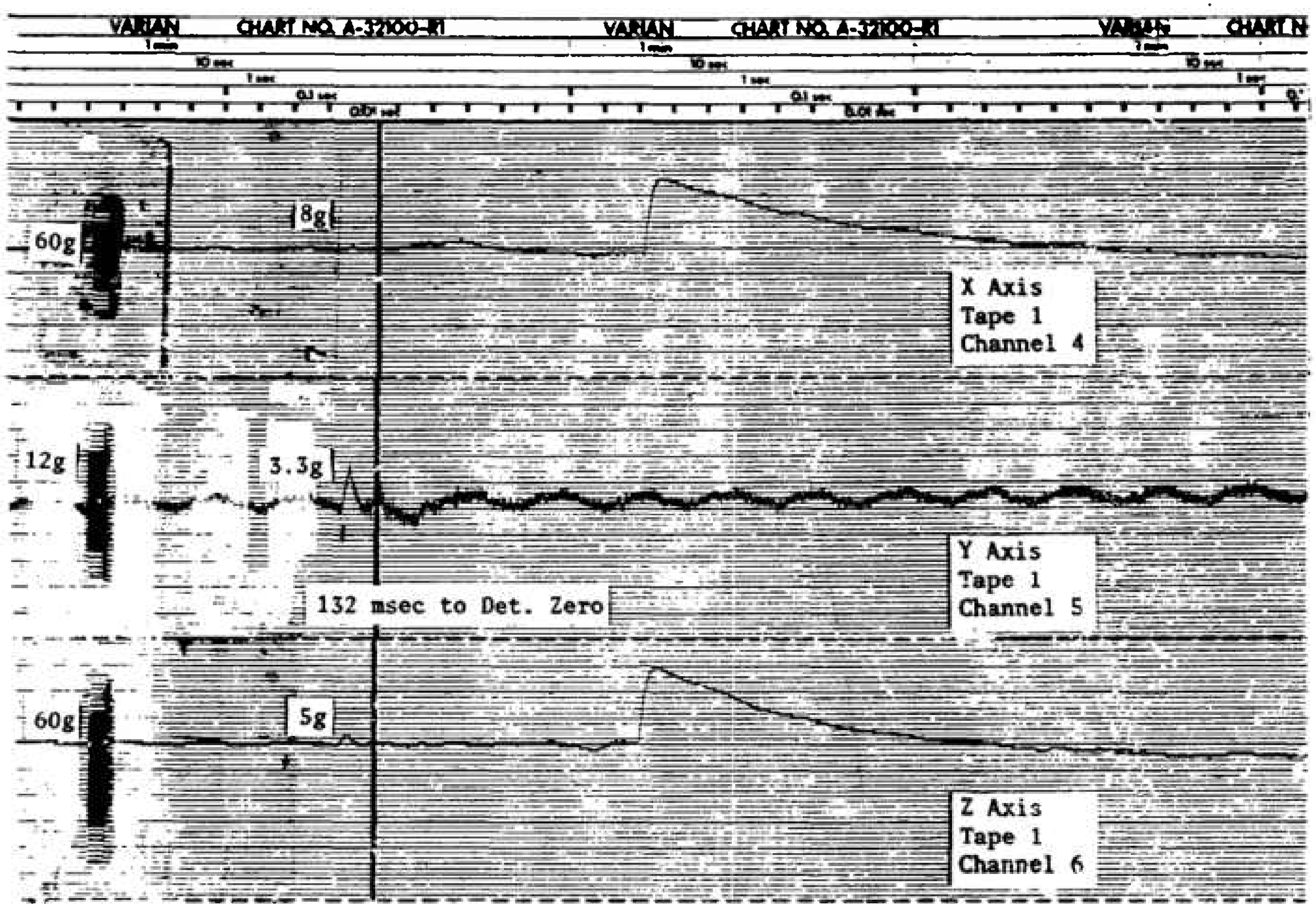

Figure B-37. Station 1, M60 Main Battle Tank. Filtered acceleration record for Dummy No. 2 in gunner's seat.

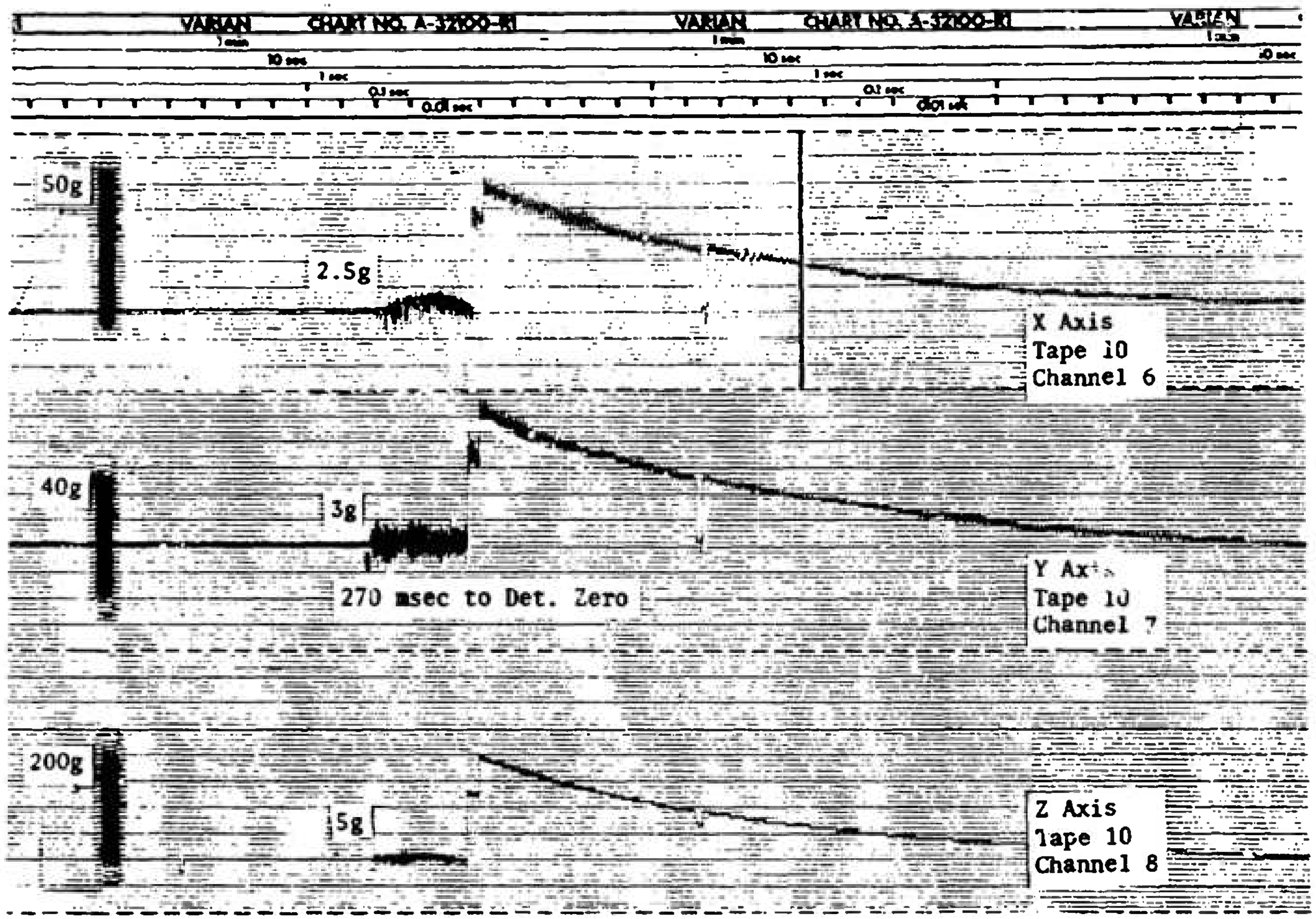

Figure B-38. Station 2, M551 Sheridan. Acceleration record for Dummy No. 4 in commander's seat.

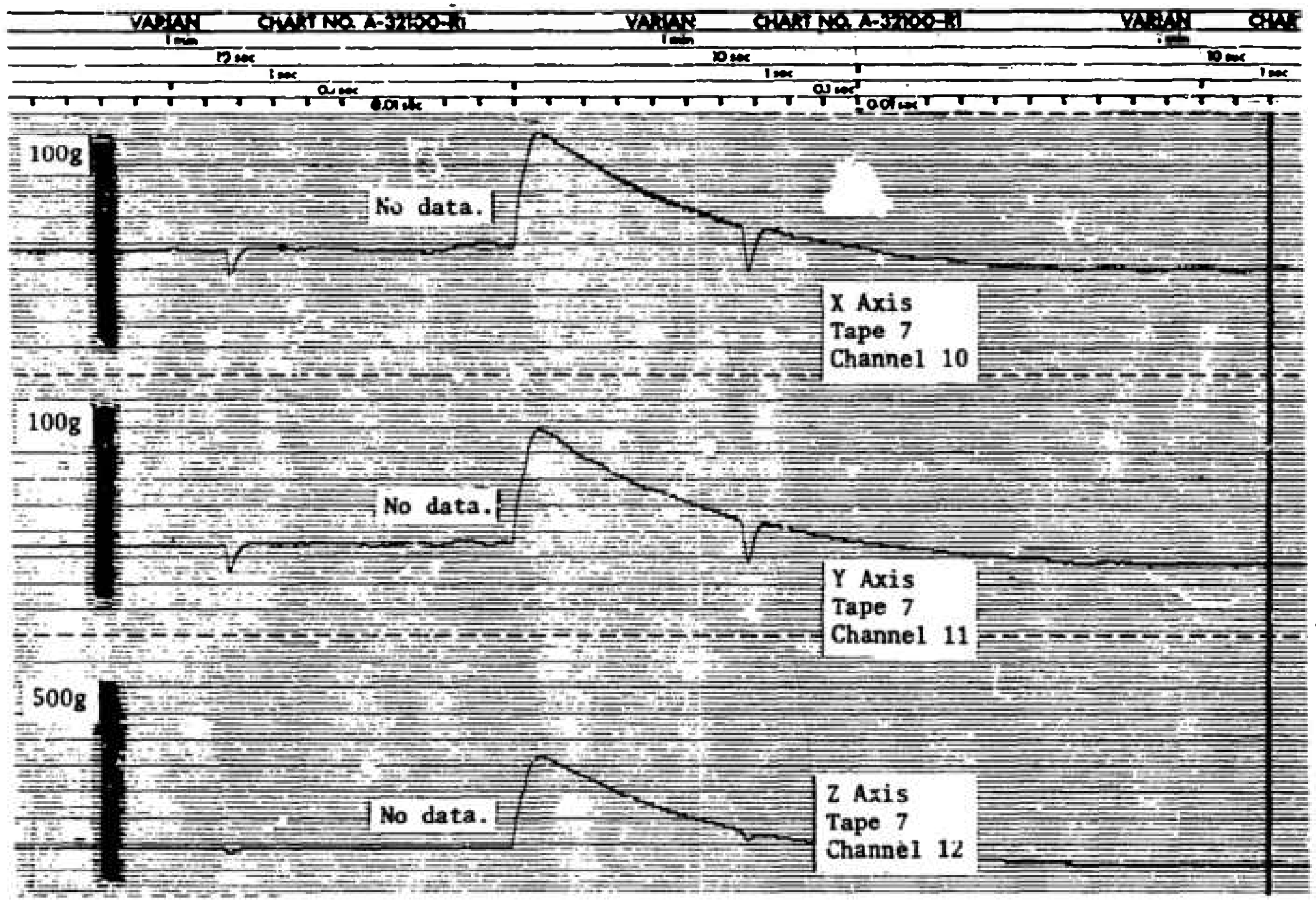

Figure B-39. Station 2, M551 Sheridan. Filtered acceleration record for Dummy No. 4 in commander's seat.

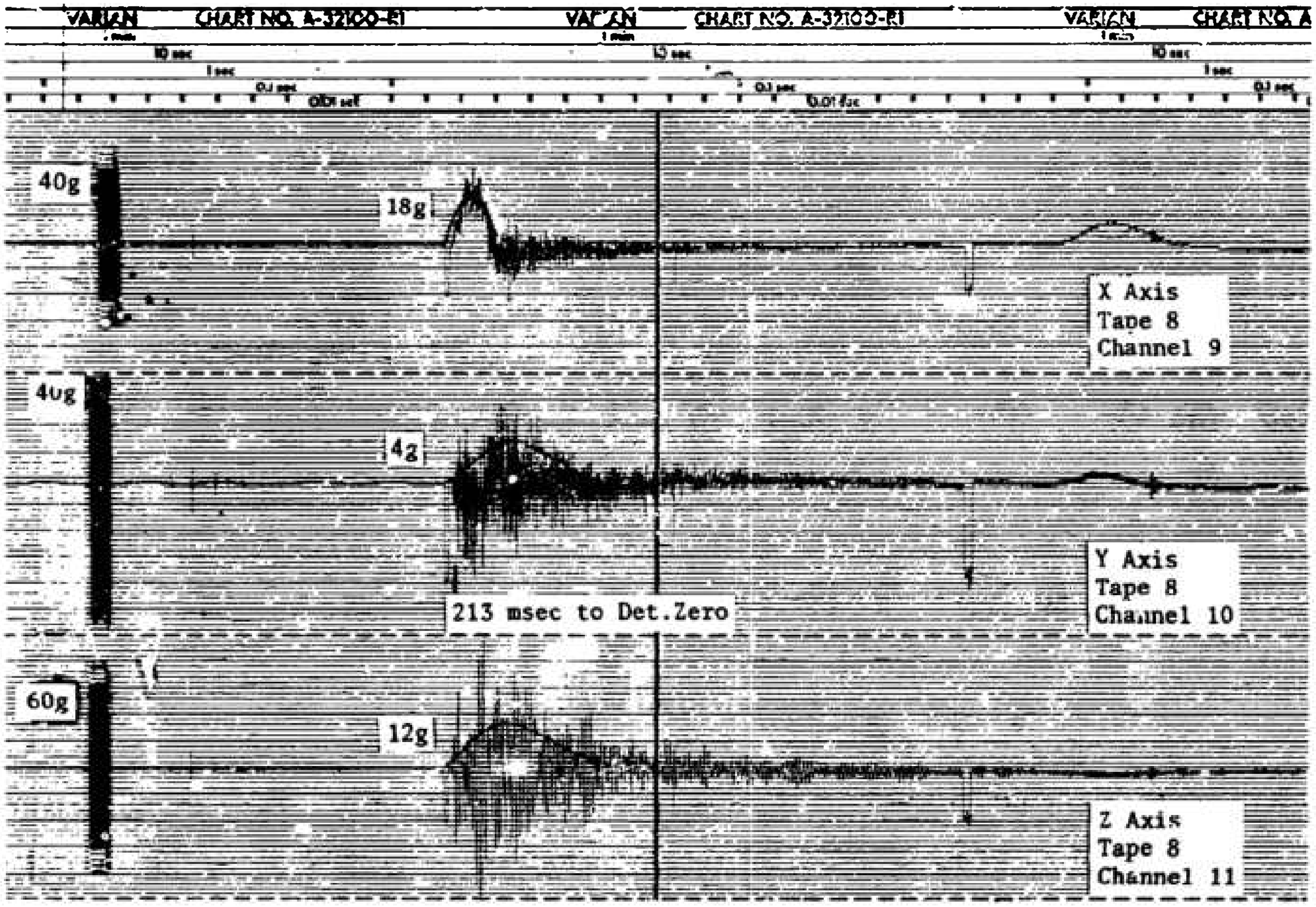

Figure B-40. Station 3, M109 Self-Propelled Howitzer. Acceleration record for Dummy No. 7 standing in gunner's position.

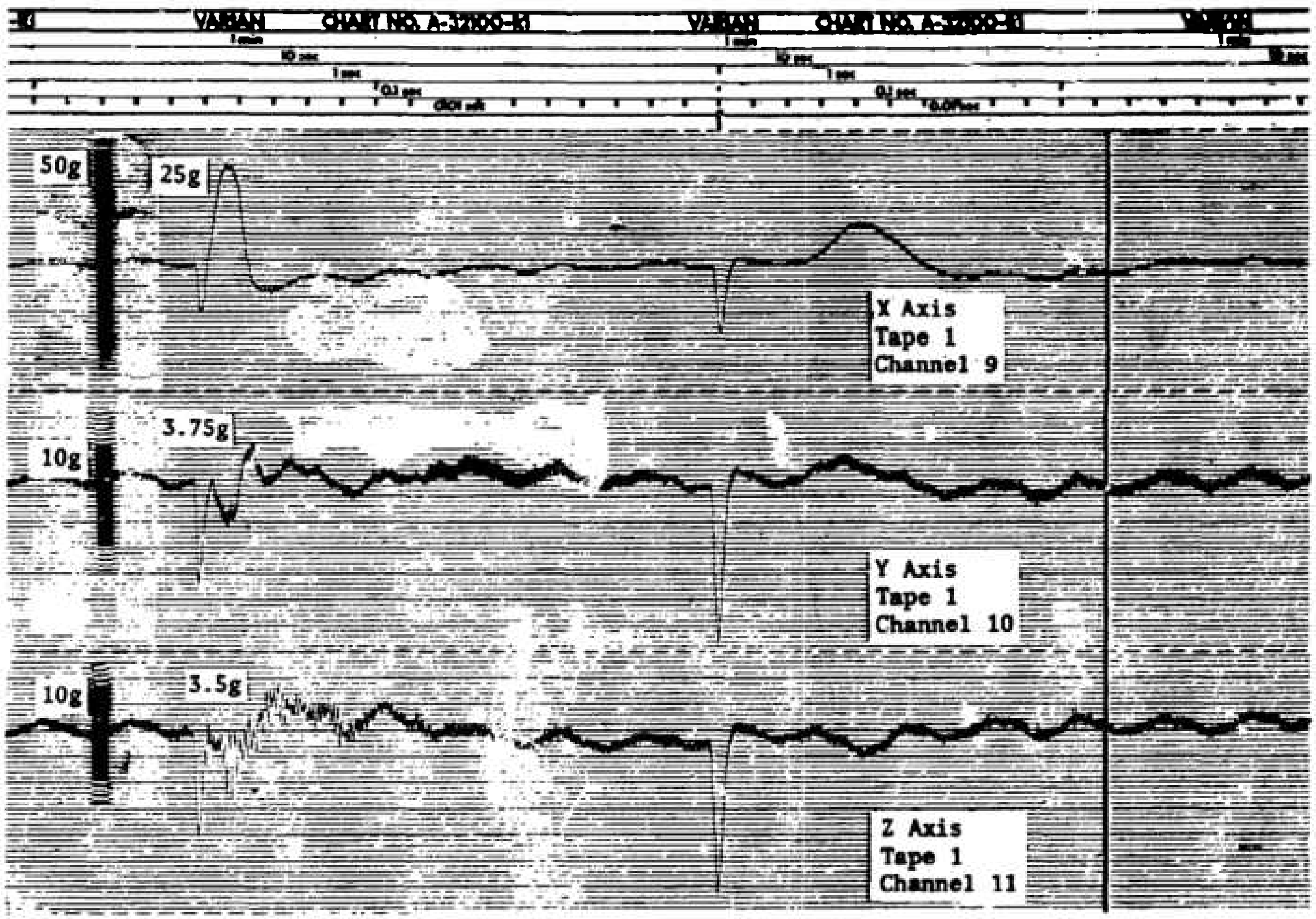

Figure B-41. Station 3, M109 Self-Propelled Howitzer. Filtered acceleration record for Dummy No. 7 standing in gunner's position.

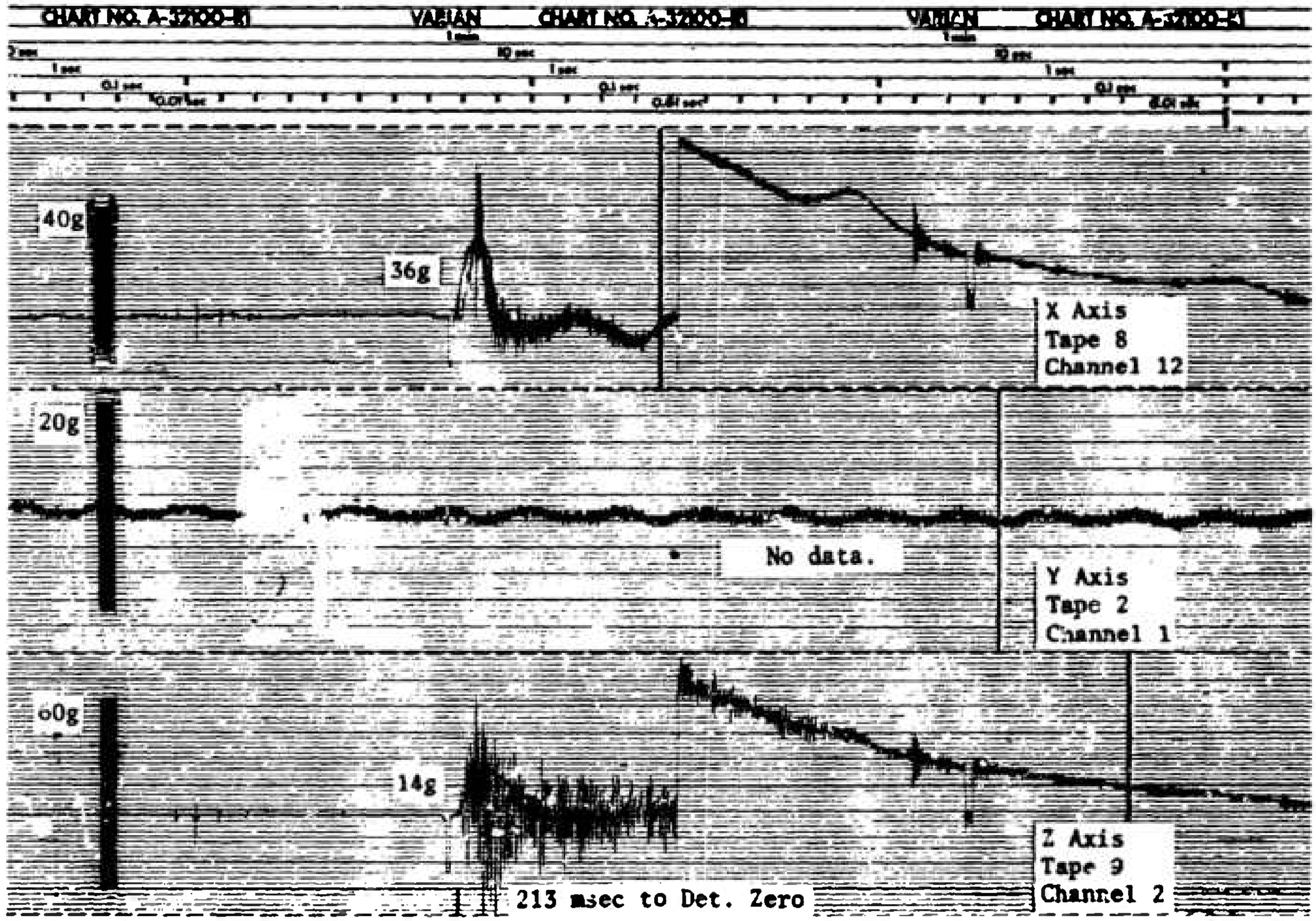

Figure B-42. Station 3, M109 Self-Propelled Howitzer. Acceleration record for Dummy No. 8 standing, chief of section in back of gunner.

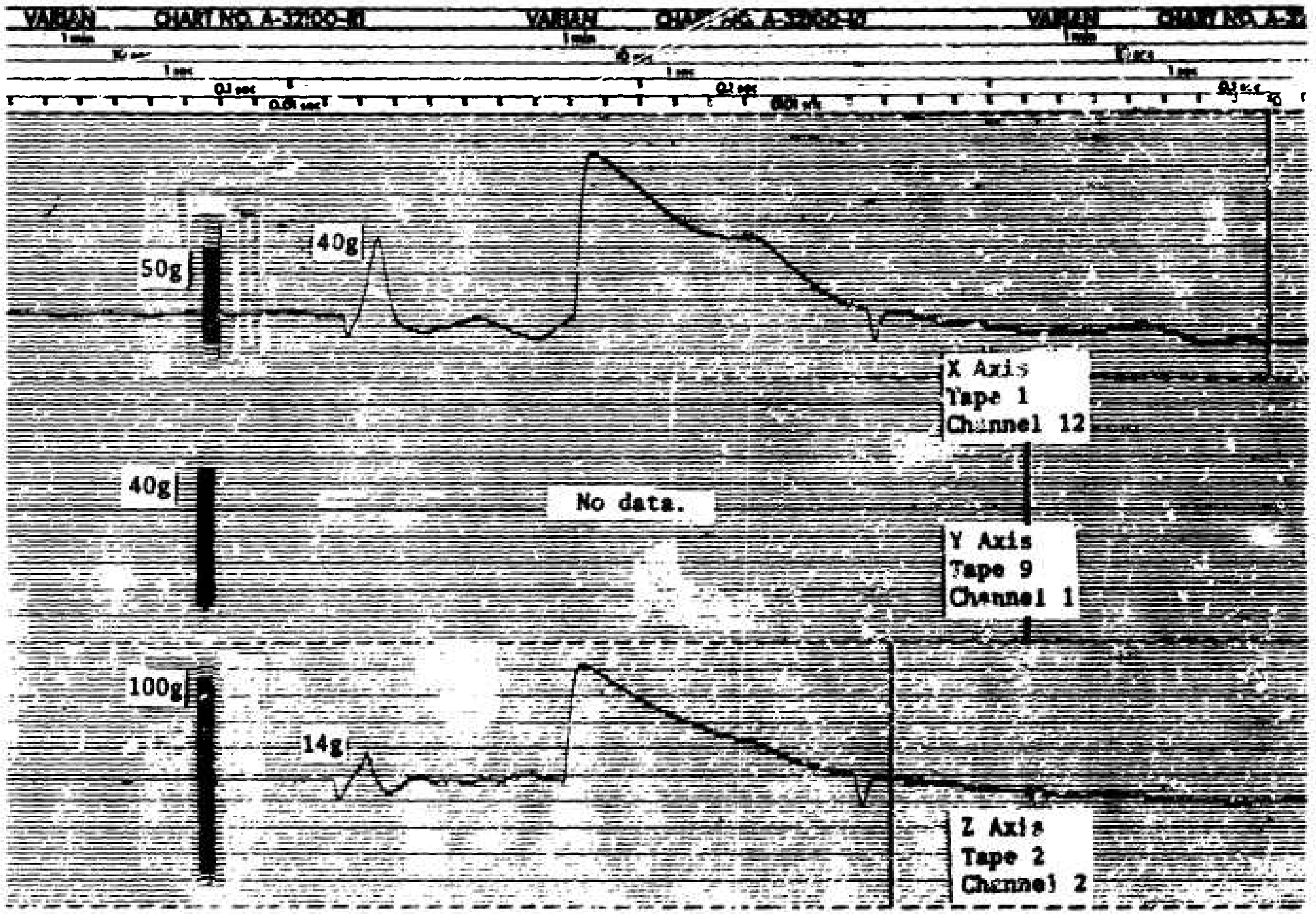

Figure B-43. Station 3, M109 Self-Propelled Howitzer. Filtered acceleration record for Dummy No. 8 standing, chief of section in back of gunner.

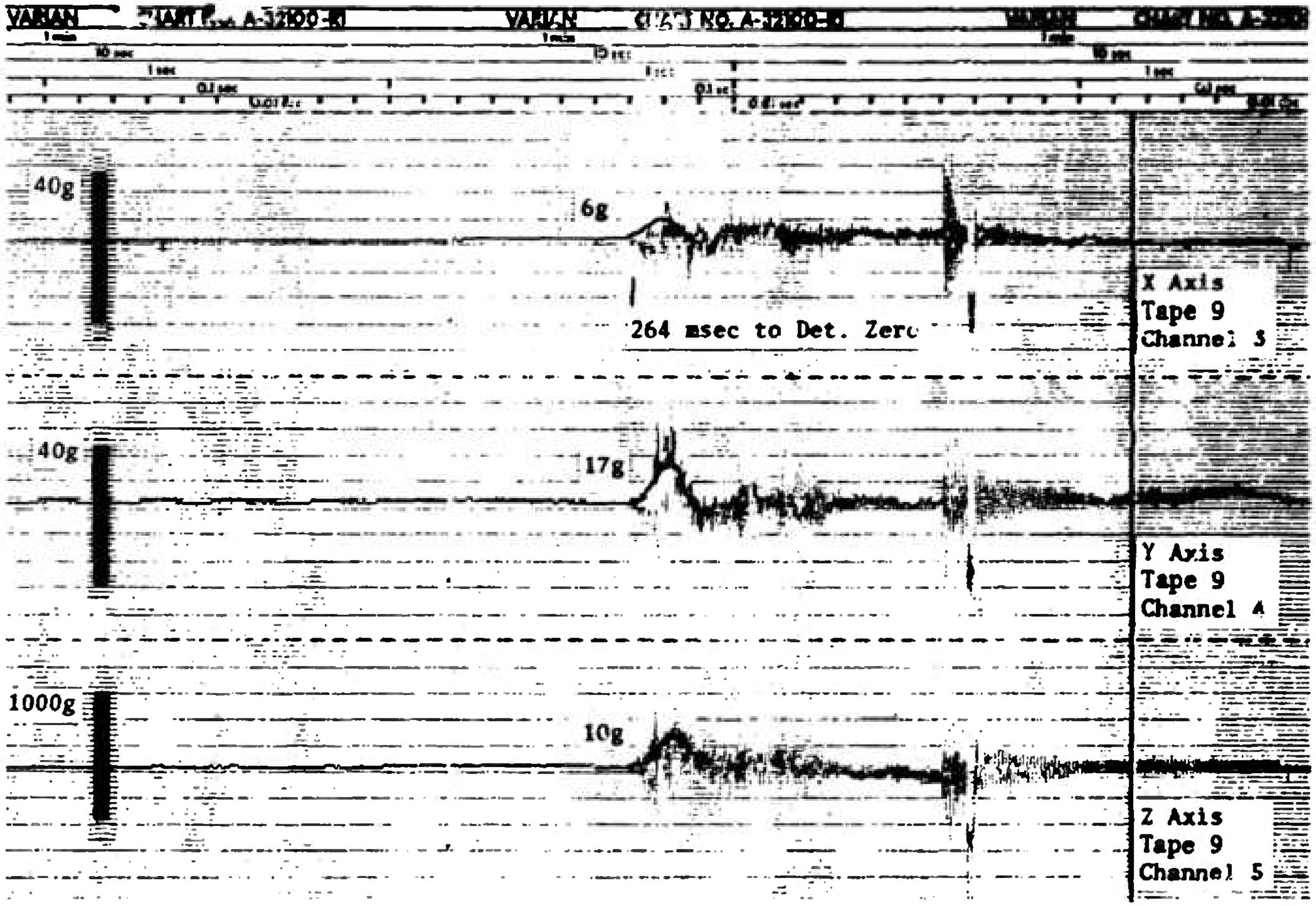

Figure B-44. Station 5, M551 Sheridan 90°. Acceleration record for Dummy No. 5 in gunner's seat.

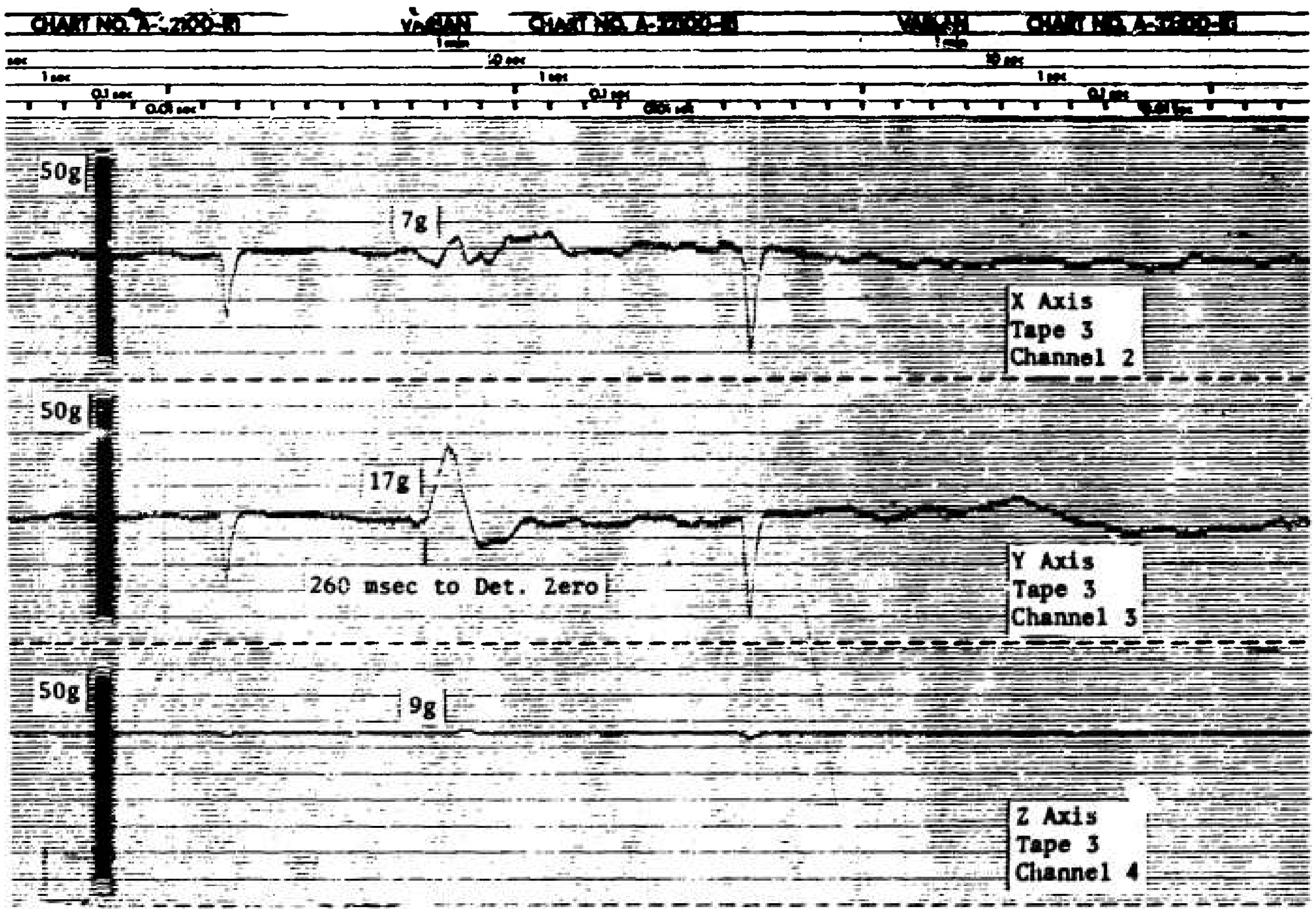

Figure B-45. Station 5, M551 Sheridan 90°. Filtered acceleration record for Dummy No. 5 in gunner's seat.

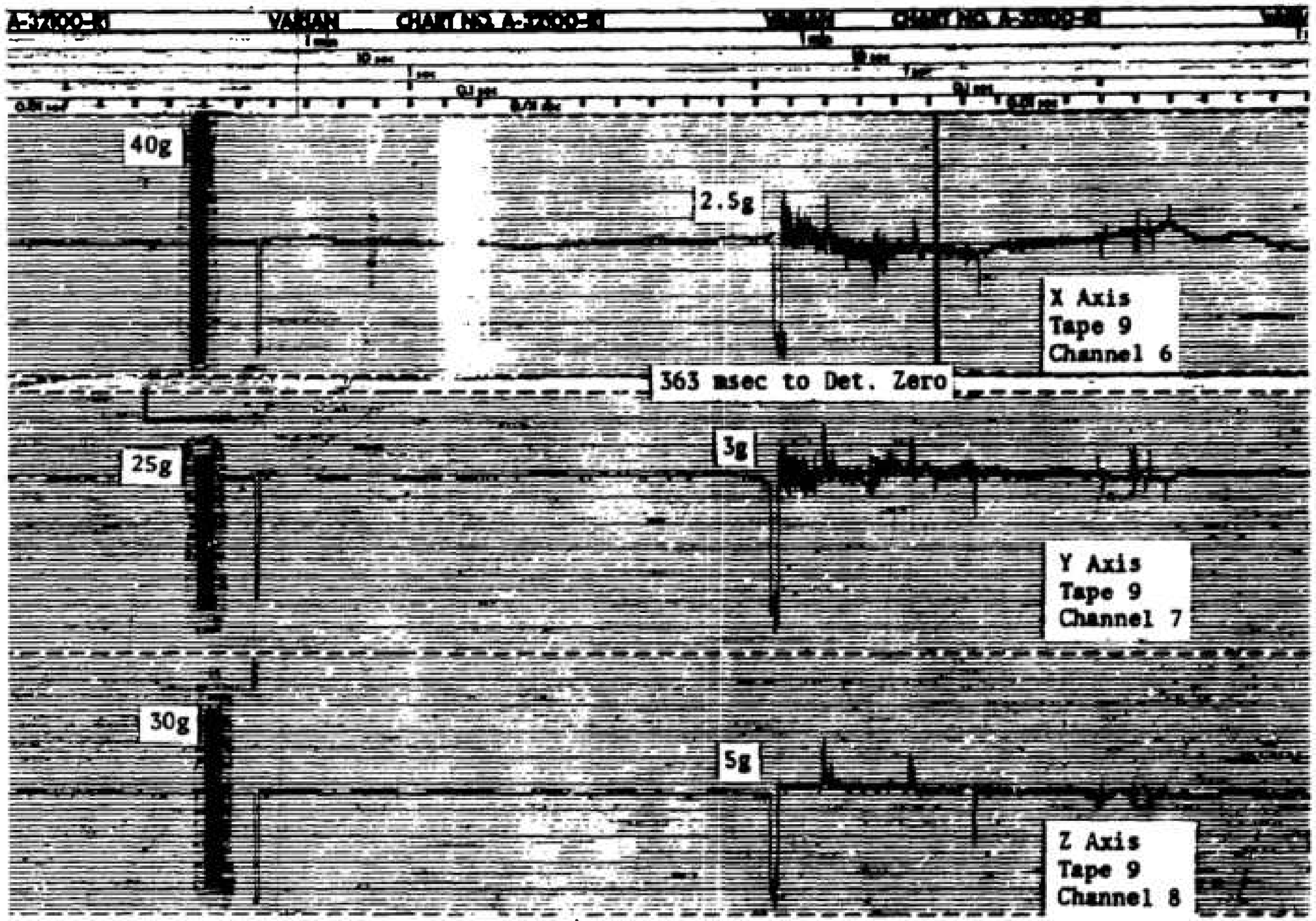

Figure B-46. Station 6, M577 Communication's Van. Acceleration record for Dummy No. 9 in driver's seat.

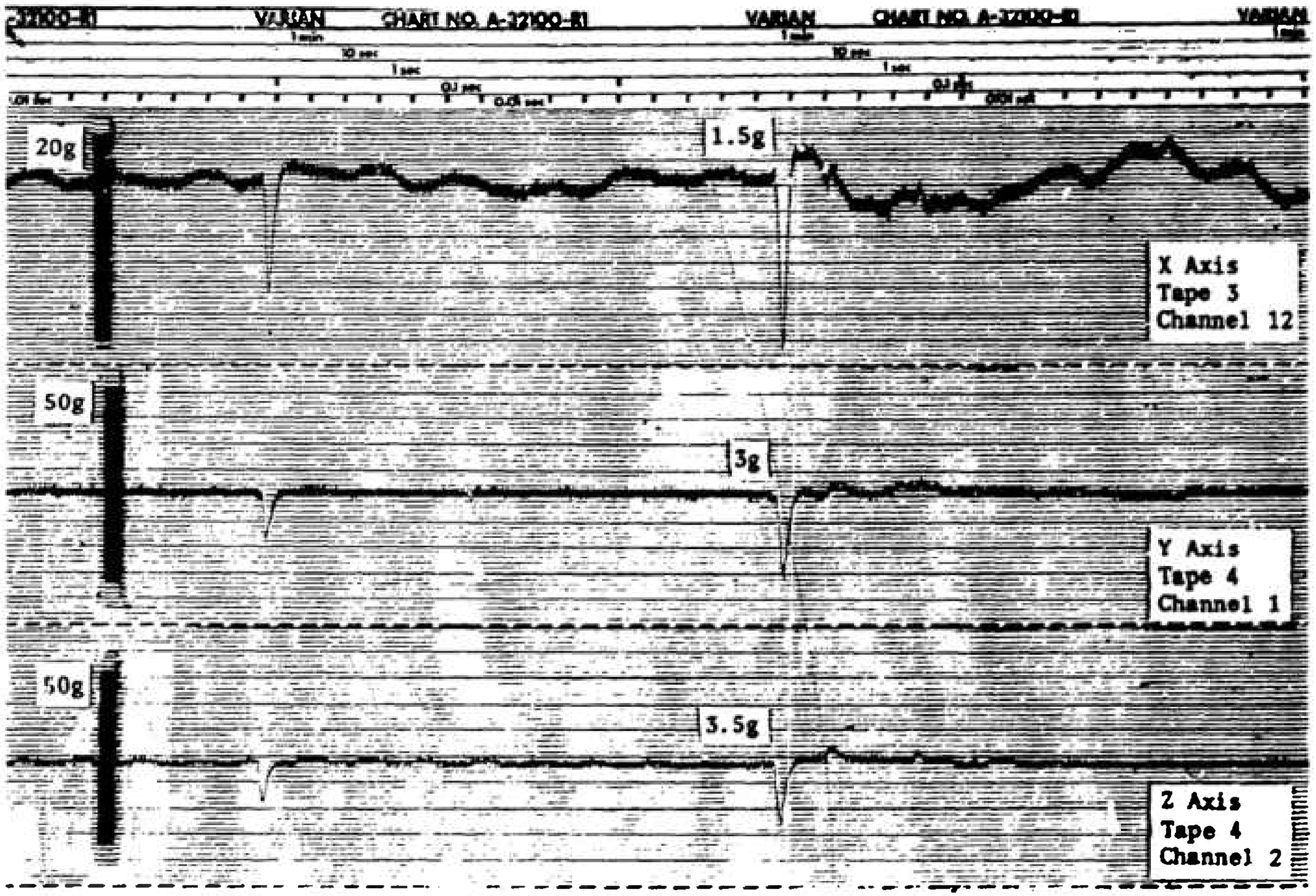

Figure B-47. Station 6, M577 Communications Van. Filtered acceleration record for Dummy No. 9 in driver's seat.

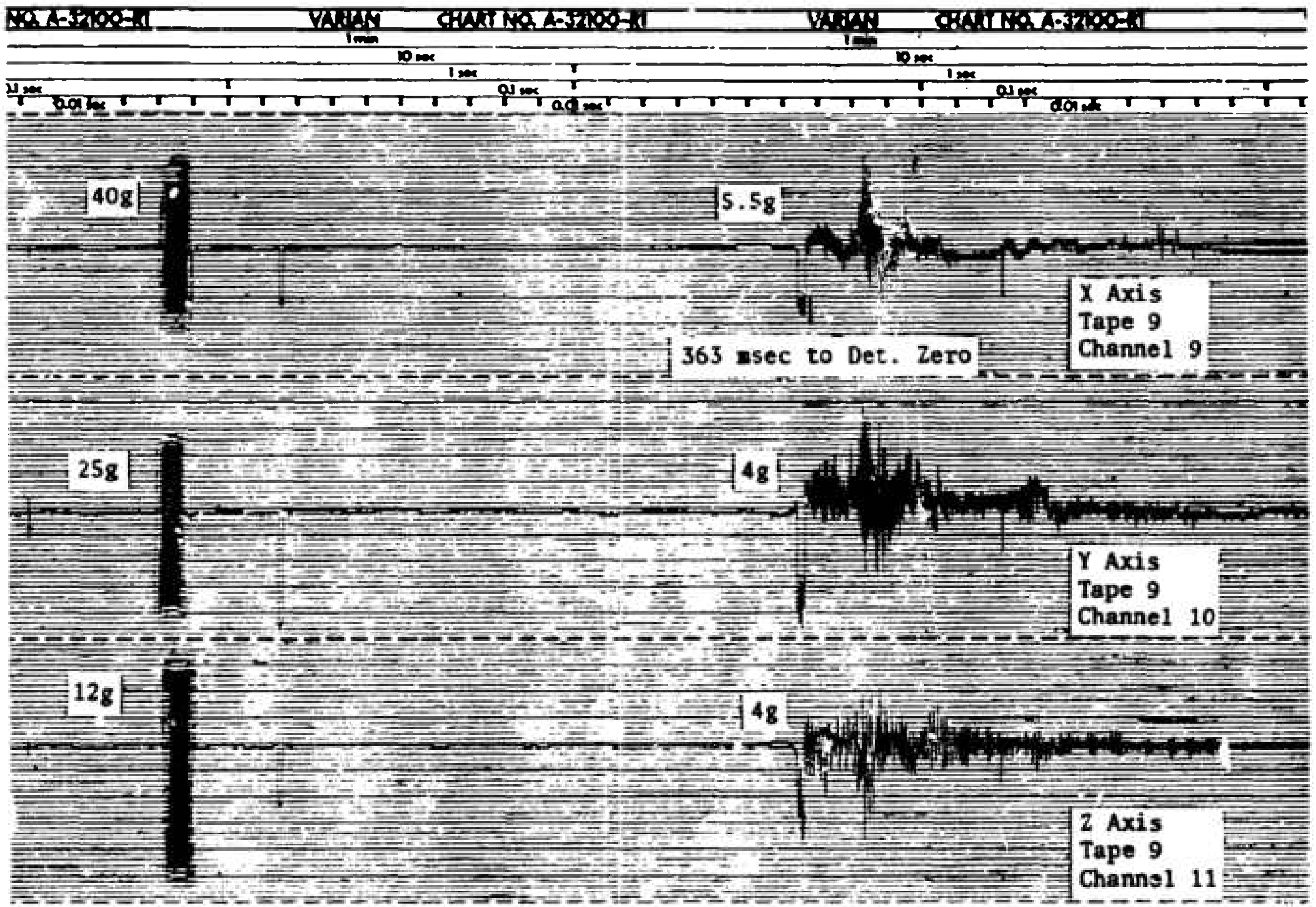

Figure B-48. Station 6, M577 Communications Van. Acceleration record for Dummy No. 10 in commander's seat facing rear of vehicle.

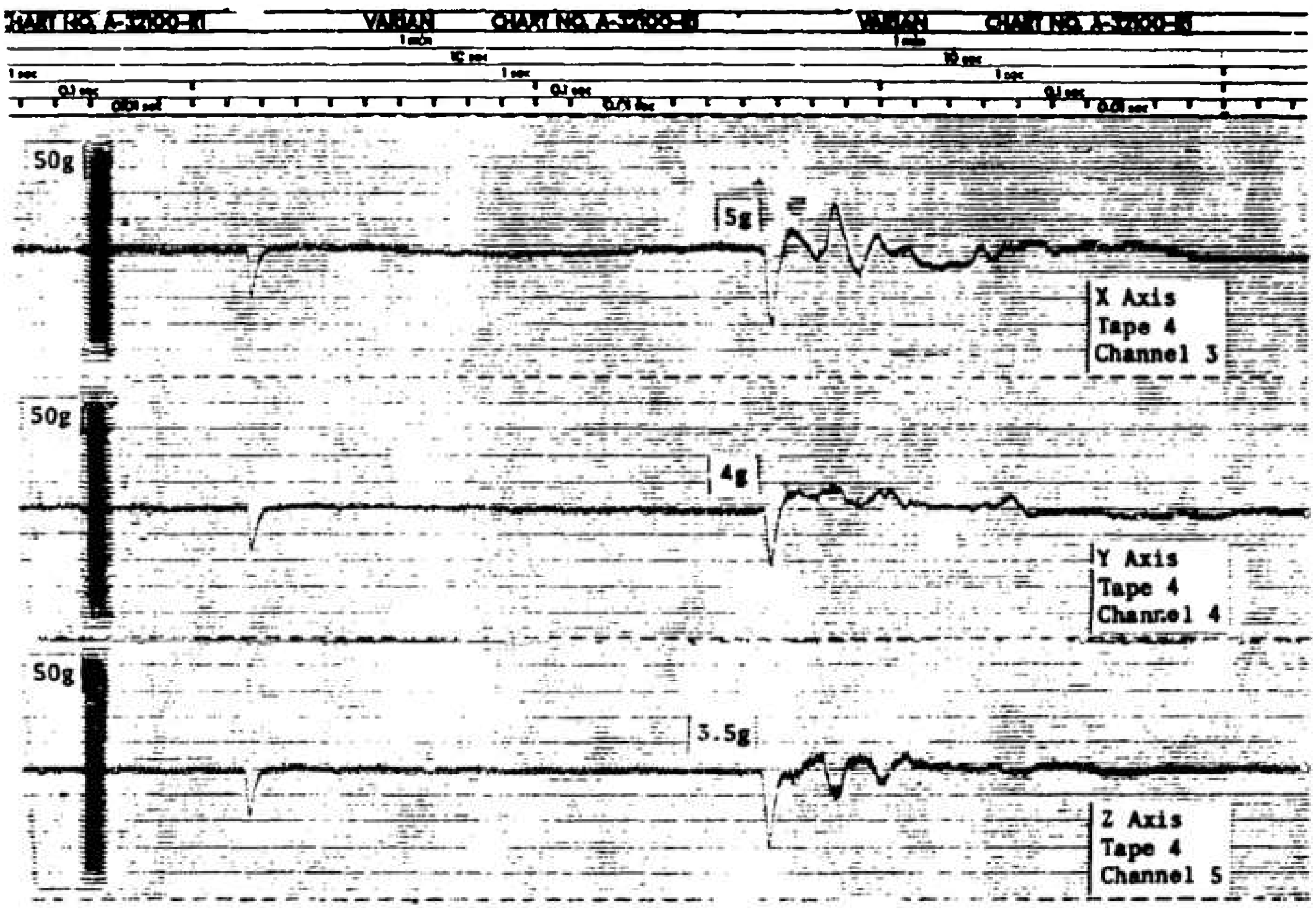

Figure B-49. Station 6, M577 Communications Van. Filtered acceleration record for Dummy No. 10 in commander's seat facing rear of vehicle.

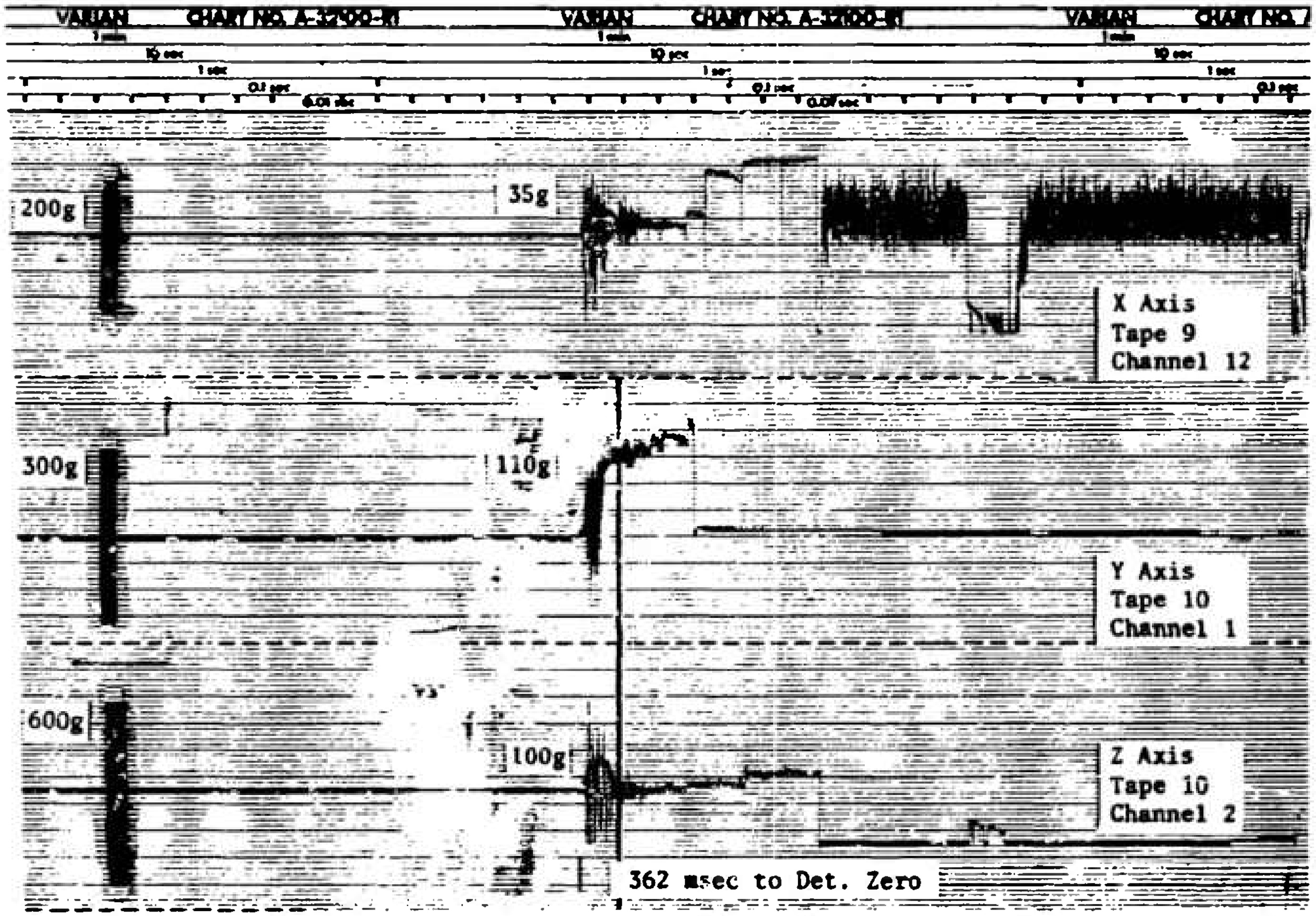

Figure B-50. Station 7, M110 Self-Propelled Howitzer. Acceleration record for Dummy No. 44 in gunner's seat, left side.

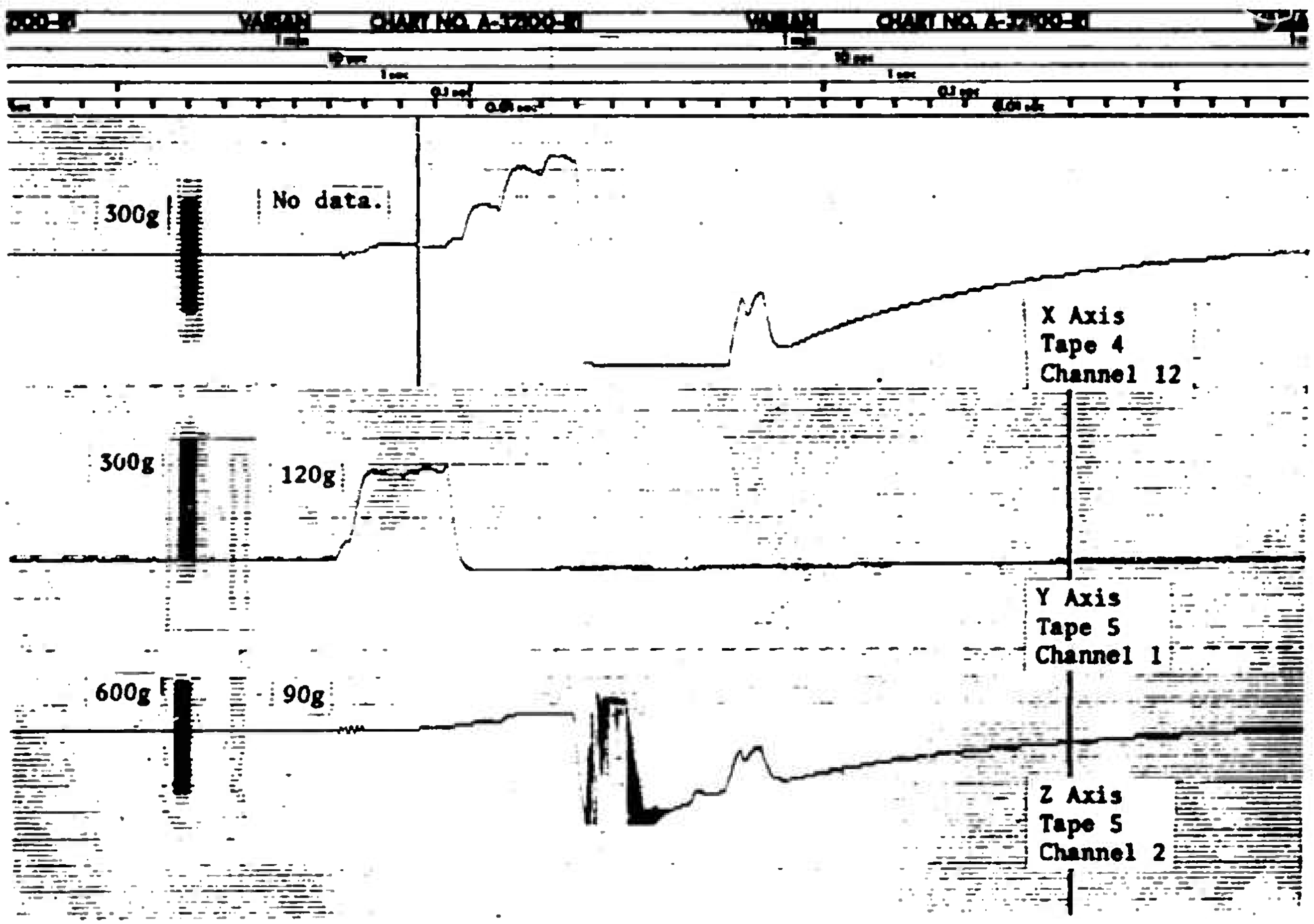

Figure B-51. Station 7, M110 Self-Propelled Howitzer. Filtered acceleration record for Dummy No. 44 in gunner's seat, left side.

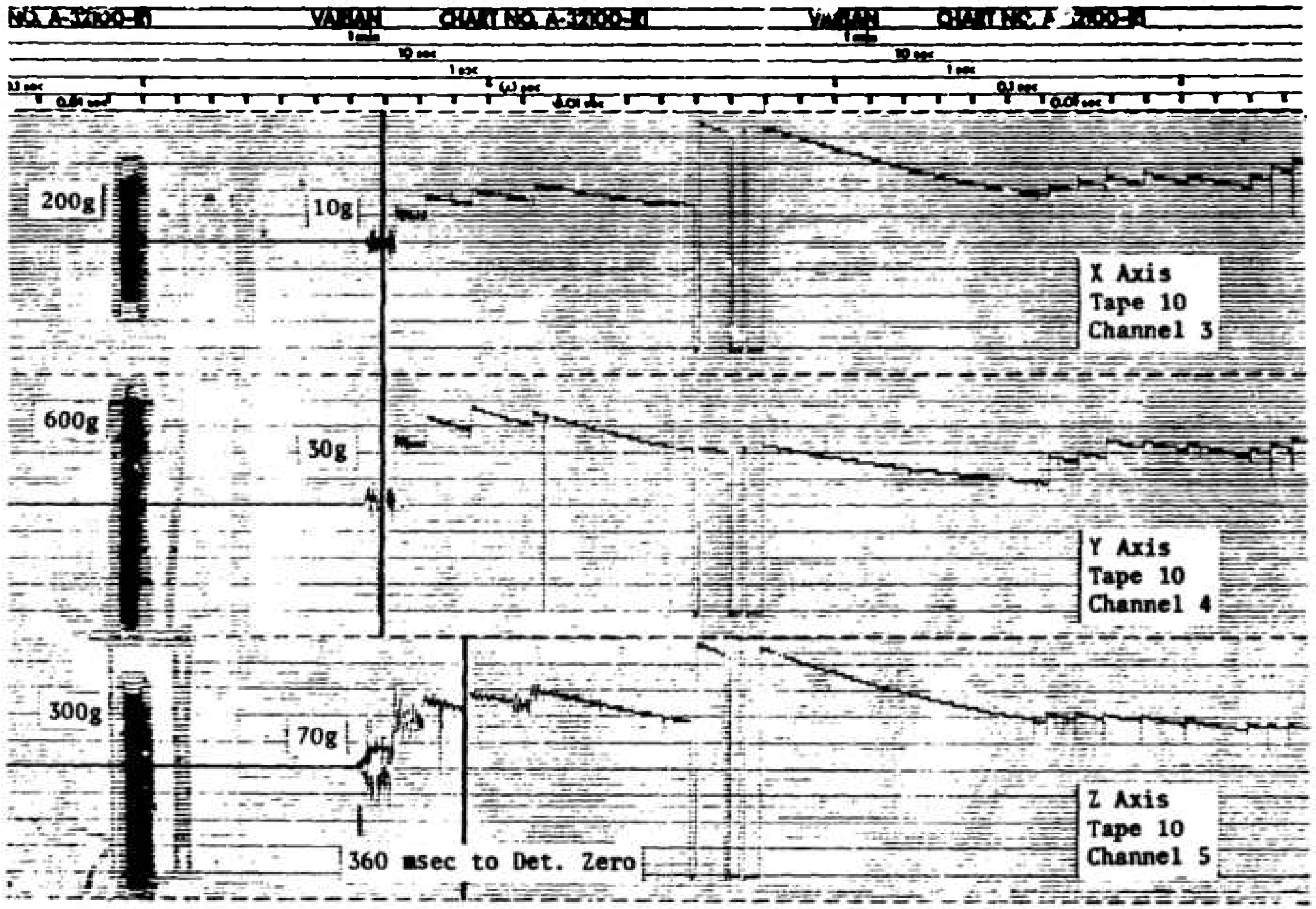

Figure B-52. Station 7, M110 Self-Propelled Howitzer. Acceleration record for Dummy No. 45 in assistant gunner's seat, right side.

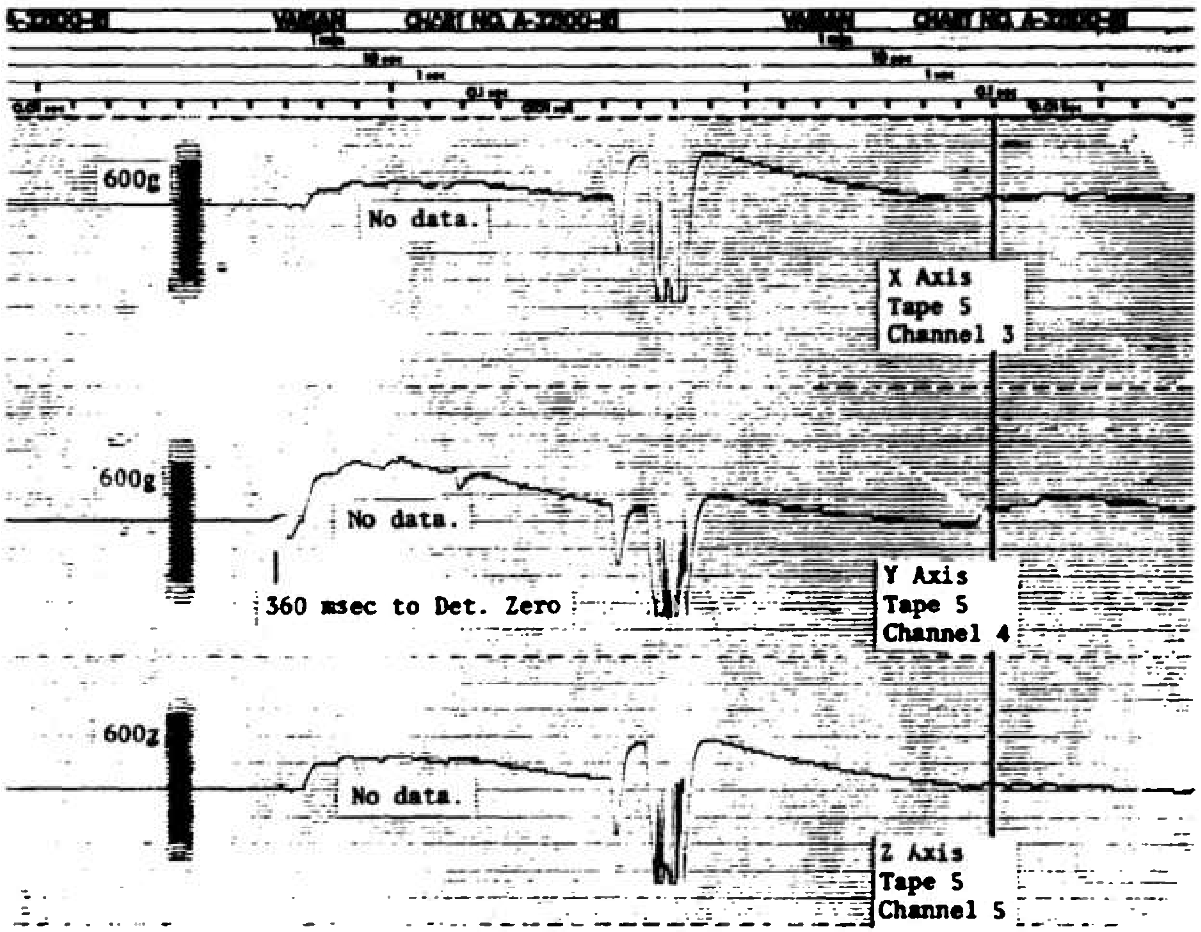

Figure B-53. Station 7, M110 Self-Propelled Howitzer. Filtered acceleration record for Dummy No. 45 in assistant gunner's seat, right side.

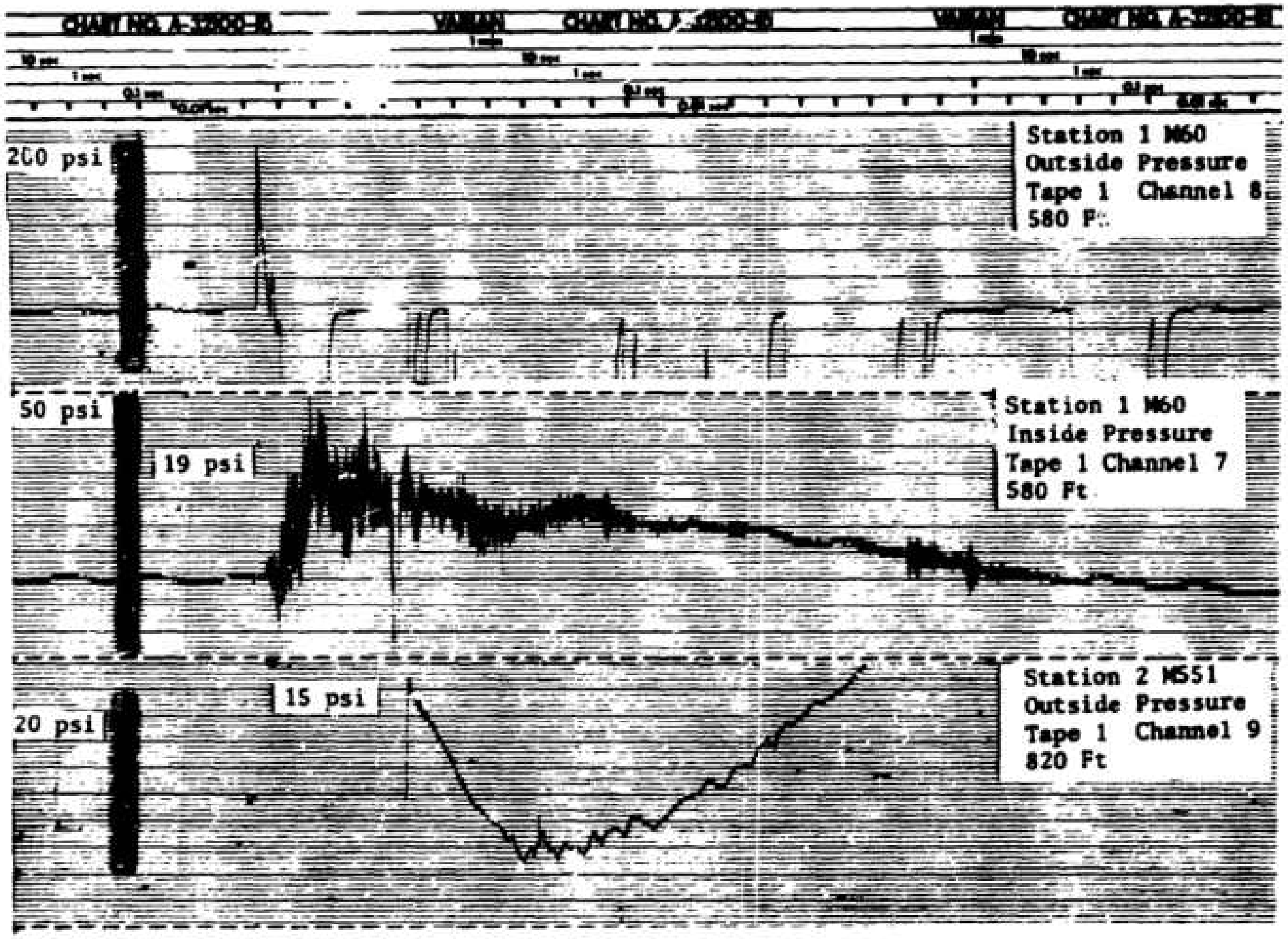

Figure B-54. Pressure-Time Recordings, U. S. Army Weapon Systems. (Sheet 1 of 4)

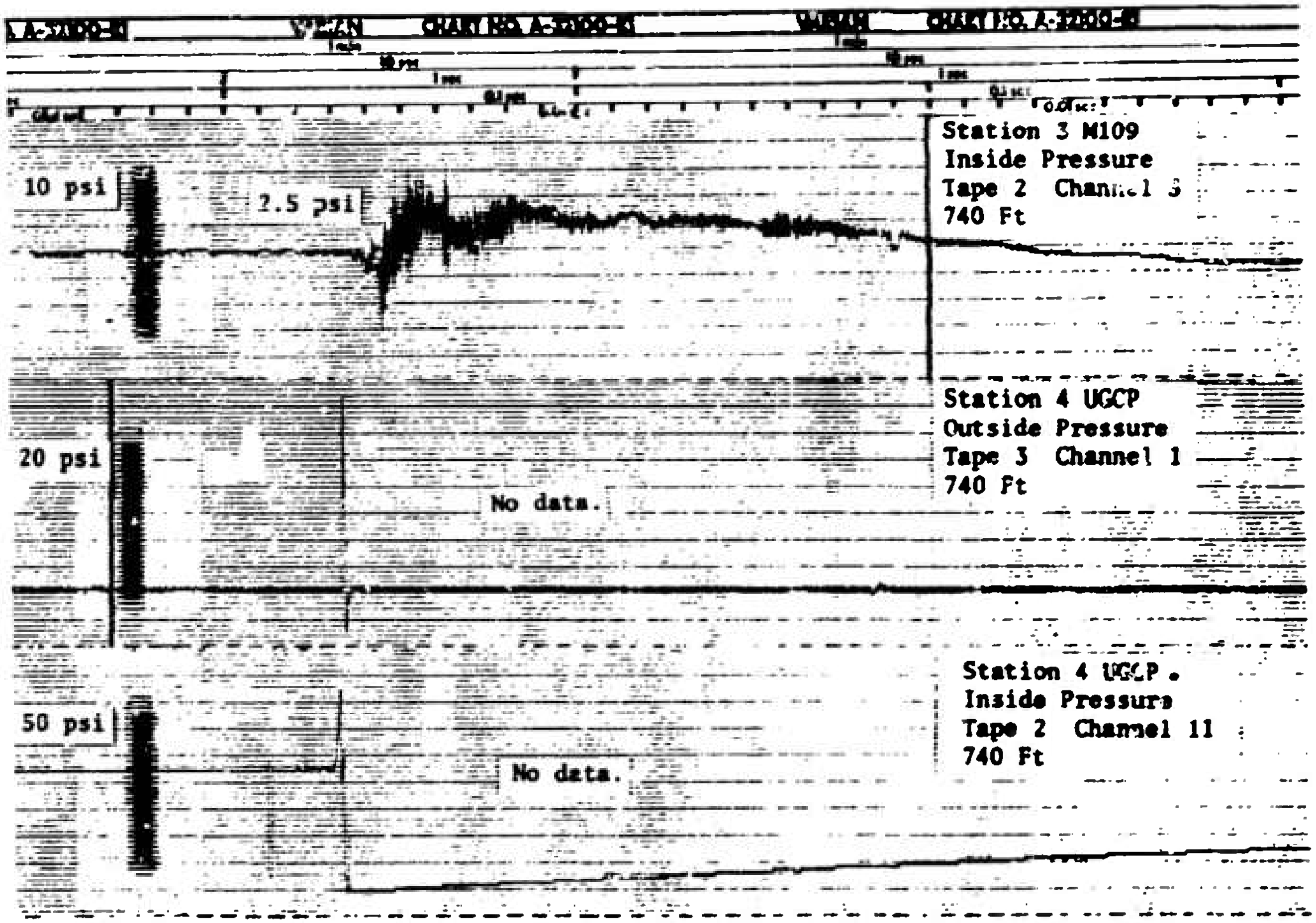

Figure B-34. Pressure-Time Recordings, U. S. Army Weapon Systems. (Sheet 2 of 4)

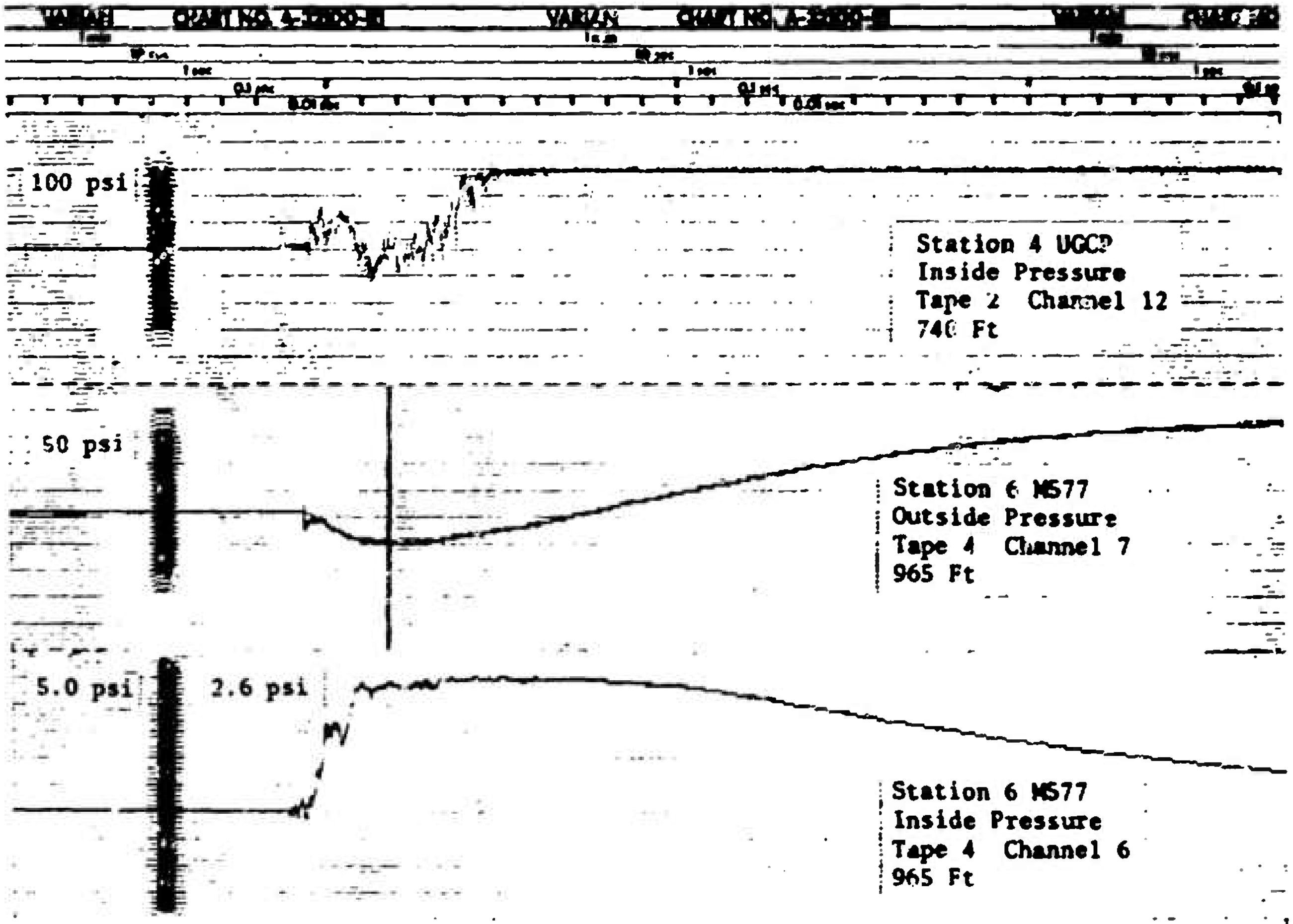

Figure B-54. Pressure-Time Recordings, U. S. Army Weapon Systems.
(Sheet 3 of 4)

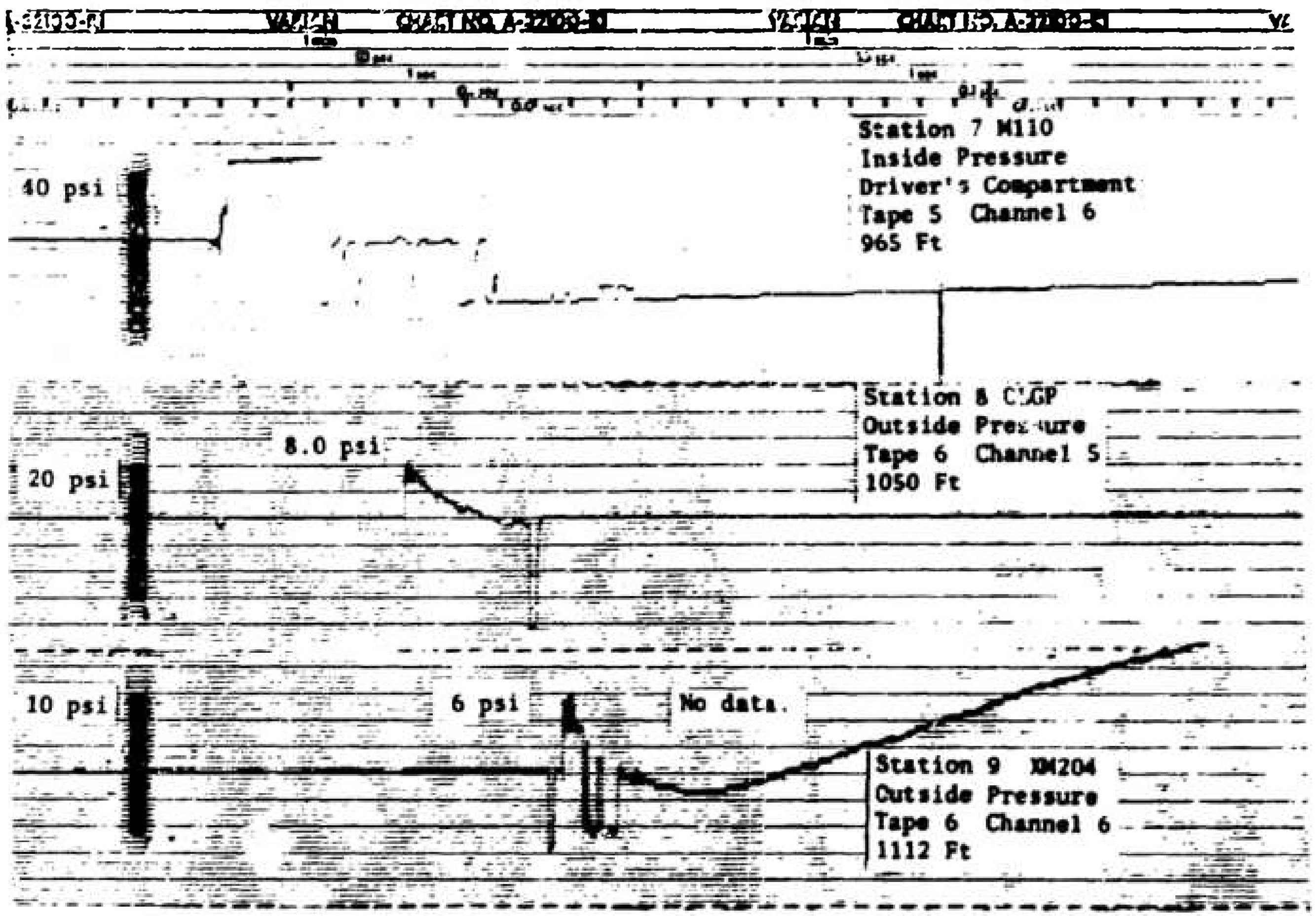

Figure B-54. Pressure-Time Recordings, U. S. Army Weapon Systems.
(Sheet 4 of 4)

TABLE B-1

REFERENCE POINT LOCATIONS—U. S. ARMY WEAPON SYSTEMS

Station No.	Item	Azimuth	Ground Range, ft
1	M60 Main Battle Tank	66°31'00"	580.00
	Camera 1	50°31'38"	740.00
2	M551 Sheridan	55°06'11"	820.00
	Camera 3	58°16'45"	820.00
3	M109 Self-Propelled Howitzer	69°52'18"	740.00
	Camera 5	66°07'04"	740.00
4	Underground Command Post	64°19'54"	740.00
5	M551 Sheridan 90	63°32'04" 61°09'41"	820.00 820.00
	Camera 8	65°55'17"	820.00
6	M577 Communications Van	72°18'59" 71°07'32"	965.00 965.00
	Camera 10	68°44'13"	965.00
7	M110 Self-Propelled Howitzer	67°21'29" 65°40'21"	965.00 965.00
	Camera 12	63°25'51"	965.00
8	CLGP Laser-Guided Projectile	64°07'43"	1050.00
	Camera 13	65°50'07"	1059.63

TABLE B-1—Continued

REFERENCE POINT LOCATIONS—U. S. ARMY WEAPON SYSTEMS

Station No.	Item	Azimuth	Ground Range, ft
9	XM204 Towed Howitzer	62°19'09"	1112.00
	Camera 14	64°55'50"	1112.00
10	Forward Observer	67°56'36"	1370.00
12	M577 Communications Van Deployed	67°23'39"	1370.00
	Camera 15	68°48'08"	1443.34
	Camera 16	68°04'30"	1323.64
14	XM198 Towed Howitzer	73°23'49"	2400.00
	Camera 18	71°50'33"	2400.00

TABLE B-2

BLAST EFFECTS ON DUMMIES - U. S. ARMY WEAPON SYSTEMS

Station	Dummy No.	Dummy Preshot Location	Dummy Postshot Location	Condition of Dummy	Film Analysis
1 M60 Main Battle Tank 580-ft range 43.4 psi overpressure	1[a]	In driver's seat.	Moved 3 in. to left in seat.	No damage to dummy. Helmet strap loose. Clothing torn at right knee and thigh.	No film record.
	2[a]	In gunner's seat.	Same as preshot. Hand still on control.	No damage to dummy or clothing.	-Ditto-
	11[a]	In commander's seat.	Same as preshot. Hand still on control.	No damage to dummy or clothing.	-Ditto-
	35[b]	Prone on ground, head-on adjacent to M60, 12'.	Displaced 87 ft downstream and 8 ft 6 in. to the right.	Soft portions torn off elbow and trunk right side. Right knee joint and left ankle bent in abnormal direction. Right hand bent. Coveralls blown off.	-Ditto-
2 M551 Sheridan 820-ft range 12.7 psi overpressure	3[a]	In gunner's seat.	Moved back and right in seat, leaning over, head against azimuth indicator. Left hand still on control, right arm down to side.	No damage to dummy or clothing.	Head moves forward (toward GZ) @ 5 ft/sec, obscured by dust after moving 1 in.
	4[a]	In commander's seat.	Same as preshot. Hand still on control.	No damage to dummy or clothing.	Head moves forward (toward GZ) @ 2 ft/sec, obscured by dust after moving 1 in.
	36[c]	Standing in open 7.5 ft from left side of M551	Displaced 37 ft 9 in. downstream.	No damage to dummy, 1 in. tear at collar.	Dummy moves backward (away from GZ), rotates head-first, COM @ 34 ft/sec, head @ 37 ft/sec, after 9 ft of travel COM approximately initial height above ground.
	37[c]	Standing in open 4 ft to rear of M551.	Displaced 6 ft	No damage to dummy or clothing.	Obscured by dust.

TABLE B-2 - CONTINUED

BLAST EFFECTS ON DUMMIES - U. S. ARMY WEAPON SYSTEMS

Station	Dummy No.	Dummy Preshot Location	Dummy Postshot Location	Condition of Dummy	Film Analysis
3 M109 Self-Propelled Howitzer 740-ft range 21.3-psi overpressure	7[a]	Standing, gunner's position looking into sight.	Leaning backwards at 30 degree angle against loading ram and chief of section. Feet in original location.	No damage to dummy or clothing.	Head moves forward (toward GZ) @ 3 ft/sec for 2 in. then head moves backward @ 10 ft/sec with an impact @ 43 in., head comes to rest after moving 58 in.
	8[a]	Standing, chief of section in back of gunner.	Leaning back against rear wall. Feet in original location.	No damage to dummy or clothing.	Head moves forward (toward GZ) @ 3 ft/sec for 2 in., then head moves backward @ 4 ft/sec with an impact @ 19 in., head leaves field-of-view after moving 33 in.
	40[c]	Standing in open 7.5 to rear of M109.	Displaced 5 ft 2 in. downstream.	No damage to dummy or clothing.	Obscured by dust.
4 Underground Command Post 740-ft range 21.3-psi overpressure	14[a]	Standing 5 ft inside and in line with entryway of personnel chamber.	Against rear wall on floor.	Two-in.-long laceration under chin, 1 in. deep.	Dummy moves backward, rotates feet first @ 0.8 rev/sec, COM at 18 ft/sec, feet impact on rear wall after COM has moved about 6 ft.
	13[a]	Standing 5 ft inside and to the left of entryway.	Fell forward, face-down.	No damage to dummy or clothing.	Obscured by dust.
	12[a]	Standing 10 ft inside and to the left of entryway.	Same as preshot. No movement.	No damage to dummy or clothing.	Obscured by dust.

TABLE B-2 - CONTINUED

BLAST EFFECTS ON DUMMIES - U. S. ARMY WEAPON SYSTEMS

Station	Dummy No.	Dummy Preshot Location	Dummy Postshot Location	Condition of Dummy	Film Analysis
5 M551 Sheridan 90° 820-ft range 12.7-psi overpressure	5[a]	In gunner's seat.	Moved in seat 6 in. to the right and 3 in. forward. Left hand still on transverse control.	No damage to dummy or clothing.	Head moves to left (toward GZ) @ 2 ft/sec for 3 in., then head moves to right @ 2 ft/sec for 3 in., then head moves to left at 1 ft/sec before being obscured by dust.
	6[a]	Loader.	Leaning over in seat against commander's step.	No damage to dummy or clothing.	Movement observed but no good reference for the motion. No impact.
6 M577 Communications Van 965-ft range 9.2-psi overpressure	9[a]	In driver's seat.	Same as preshot.	No damage to dummy or clothing.	Head did not move for 25 msec. then obscured by dust.
	10[a]	In commander's seat facing rear of vehicle.	Leaning over in seat.	No damage to dummy or clothing.	Head moves to left (toward GZ) @ 3 ft/sec for 5 in., then head moves to right at 5 ft/sec for 20 in. and comes to rest.
7 M110 Self-Propelled Howitzer 965-ft range 9.2-psi overpressure	44[a]	In gunner's seat, left side.	Same as preshot.	No damage to dummy or clothing.	Head moves to right (away GZ) @ 8 ft/sec, obscured by dust after moving 11 in.
	45[a]	In assistant gunner's seat, right side.	Same as preshot.	No damage to dummy or clothing.	Head did not move for 43 msec, then obscured by dust.
	38[c]	Standing, facing GZ on the right rear portion of M110.	Displaced 4 ft 8 in. downstream, face-down on ground.	Damage to soft portions of both hands. Lacerations: 2 in. right shoulder, 3 in. above left elbow.	Head moves backward (away GZ) @ 15 ft/sec, obscured by dust after moving 10 in.

TABLE B-2 - CONTINUED

BLAST EFFECTS ON DUMMIES - U. S. ARMY WEAPON SYSTEMS

Station	Dummy No.	Dummy Preshot Location	Dummy Postshot Location	Condition of Dummy	Film Analysis
8 CLGP Laser-Guided Projectile 1050-ft range 7.6-psi overpressure	15[c]	Standing 7.5 ft from CLGP.	Displaced 11 ft 6 in. downstream on back.	No damage to dummy or clothing.	Dummy moves backward (away GZ), rotates head first, COM @ 17 ft/sec, head @ 26 ft/sec, after 3.5 ft of travel COM approximately initial height above ground.
9 XM204 Towed Howitzer 1112-ft range 6.7-psi overpressure	16[c]	Standing 3.5 ft from XM204.	Displaced 9 ft 11 in. downstream on back.	No damage to dummy or clothing.	Dummy moves backward (away GZ), rotates head first, COM @ 14 ft/sec, head @ 19 ft/sec, after 4.2 ft of travel COM approximately 1 ft below initial height.
10 Forward Observer 1370-ft range 4.9-psi overpressure	17[a]	Prone face-on to ground zero.	Same as preshot.	No damage to dummy or clothing.	Head did not move for 200 msec. then obscured by dust.
12 M577 Deployed 1370-ft range 4.9-psi overpressure	18[c]	Standing beneath deployed portion.	Displaced 6 ft downstream.	No damage to dummy or clothing.	Movement observed but no good reference for the motion.
	19[c]	Seated at table beneath deployed portion. Right side to GZ.	Displaced 4 ft 2 in.	Soft material off right hand.	Movement observed but no good reference for the motion.
14 XM198 Towed Howitzer 2400-ft range 2.4-psi overpressure	41[c]	Standing in front of XM198.	Displaced 5 ft 1 in. downstream.	No damage to dummy or clothing.	Dummy moves backward (away GZ), rotates head first, COM @ 1-2 ft/sec, COM impacts ground @ 13 ft/sec, head impacts ground @ 21 ft/sec.

Impact-O-Graphs® Unloaded

[a] None.

[b] Both leg [illegible] leg

[c] Both leg

TABLE B-3

ACCELERATIONS MEASURED INSIDE DUMMIES
U. S. ARMY WEAPON SYSTEMS

Station	Range, ft	Dummy	Peak g			Peak g (Filtered Record)		
			X-Axis	Y-Axis	Z-Axis	X-Axis	Y-Axis	Z-Axis
1 M60 Main Battle Tank	580	2 In gunner's seat	8	6	8	8	3.3	5
2 M551 Sheridan	820	4 In commander's seat	2.5	3	5	ND	ND	ND
3 M109 Self-Propelled Howitzer	740	7 Standing in gunner's position	18	4	12	25	4	3.5
		8 Standing, section chief	36	ND	14	40	ND	14
5 M551 Sheridan 90°	320	5 In gunner's seat	6	17	10	7	17	9
6 M577 Communications Van	965	9 In driver's seat	2.5	3	5	1.5	3	3.5
		10 In commander's seat	5.5	4	4	5	4	3.5
7 M110 Self-Propelled Howitzer	965	44 In gunner's seat	35	110	100	ND	120	90
		45 In assistant gunner's seat	10	30	70	ND	ND	ND

ND - Indicates no data.

APPENDIX C

ELECTRONIC EQUIPMENT SHELTERS

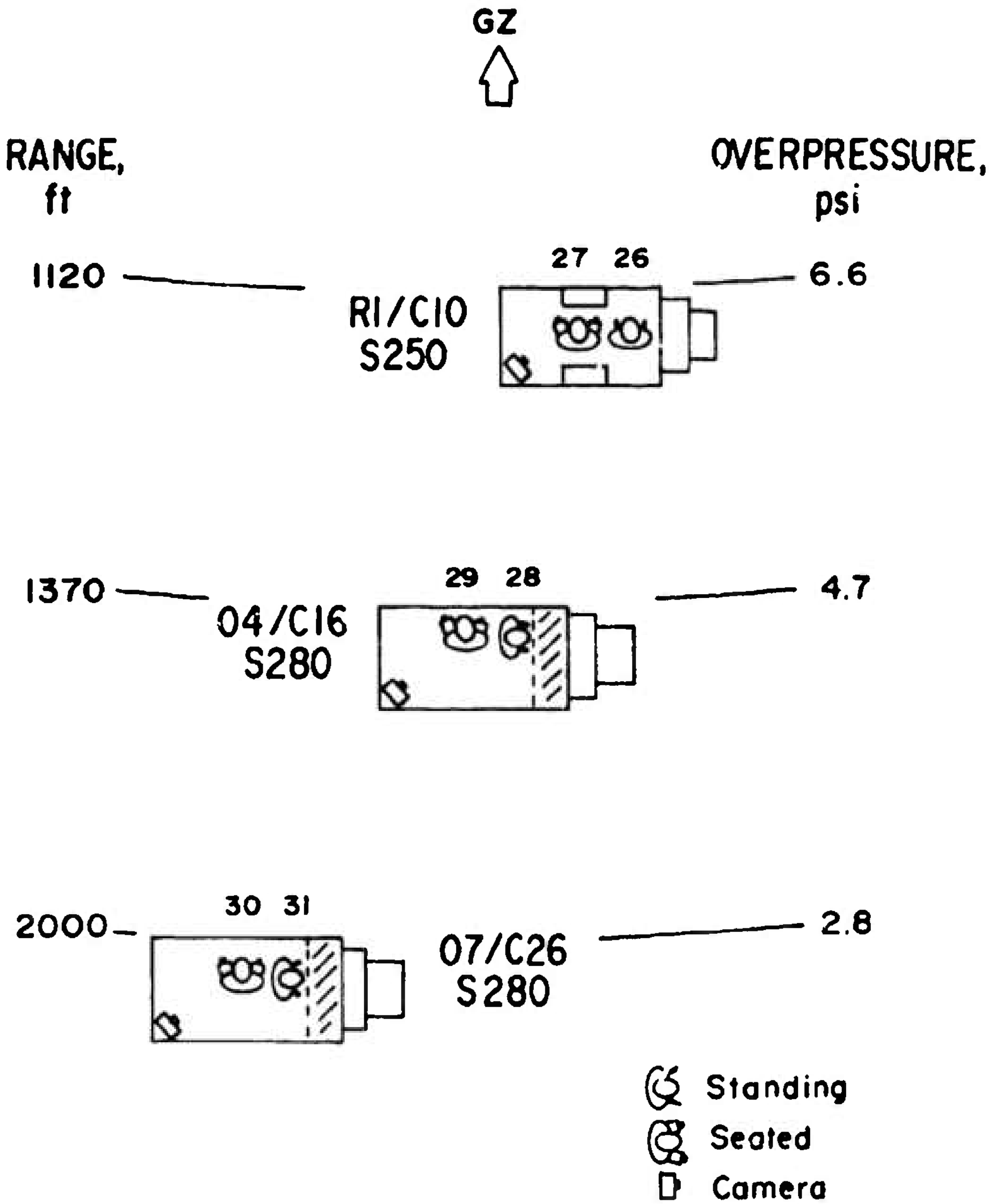

Figure C-1. Layout of Electronic Equipment Shelters.

PRECEDING PAGE BLANK

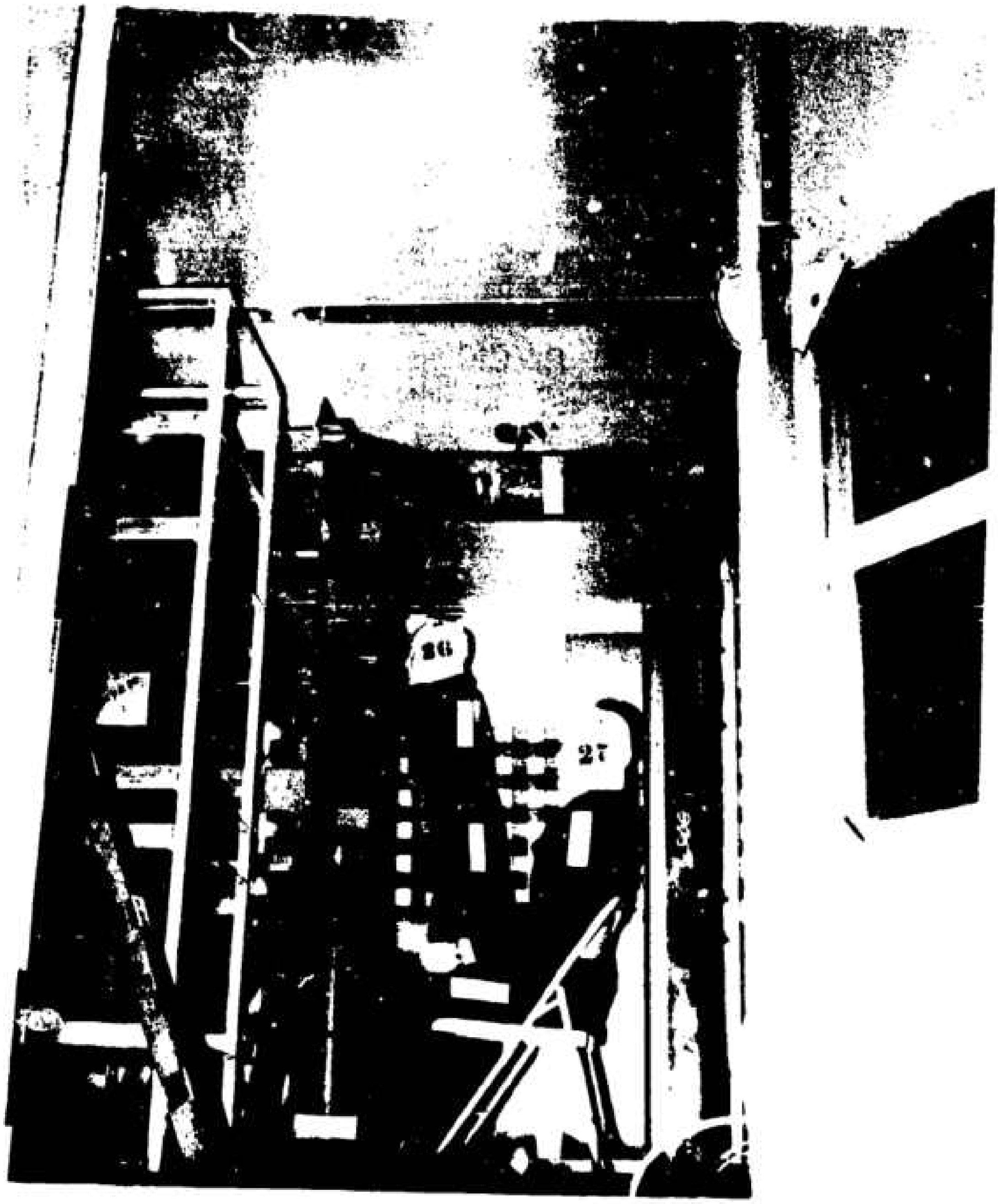

Figure C-2. Dummies in Retrofit Shelter Viewed Through Door, R1/C10, 1120-Ft Range.

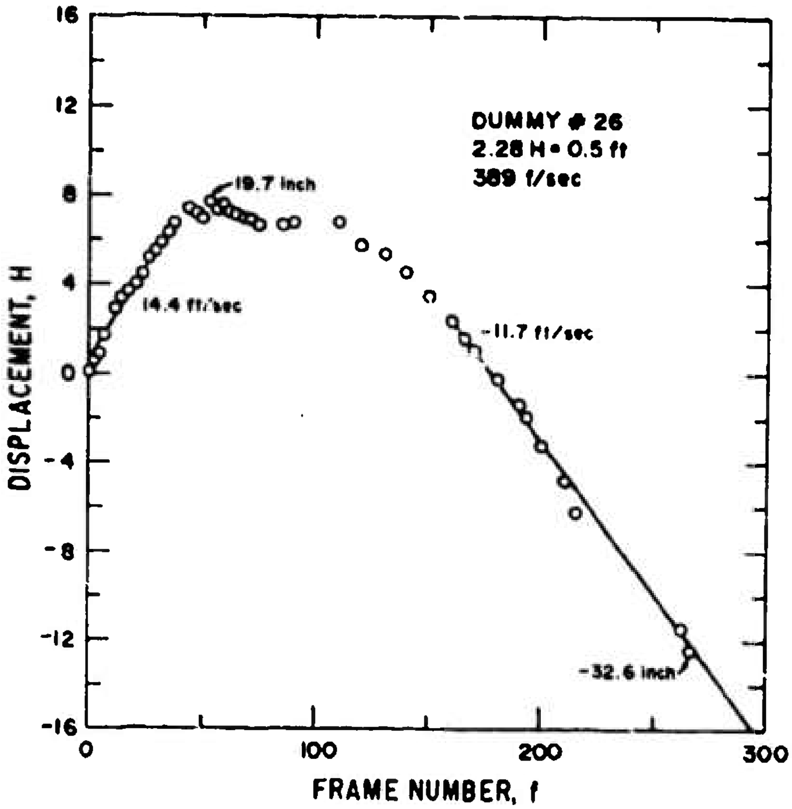

Figure C-3. Displacement vs Time, Dummy No. 26 Standing in S250 Retrofit Shelter R1/C10, 1120 ft.

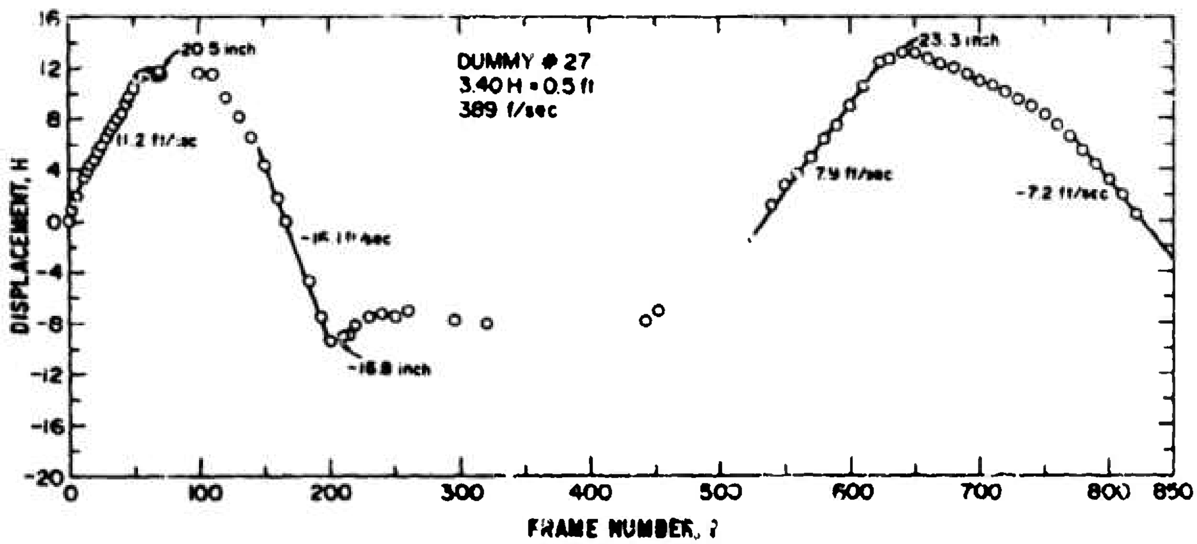

Figure C-4. Displacement vs Time, Dummy No. 27 Seated in Retrofit Shelter R1/C10, 1120 ft.

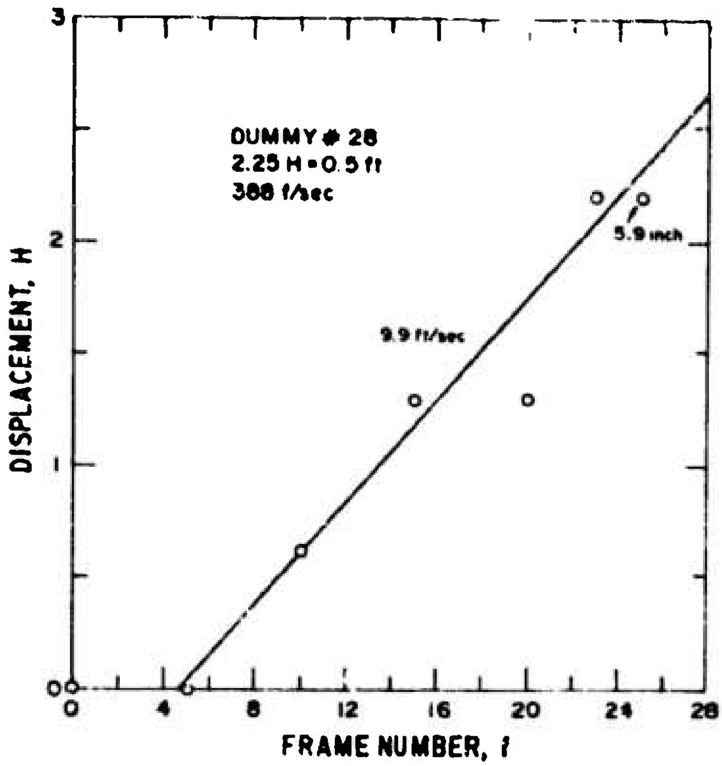

Figure C-5. Displacement vs Time, Dummy No. 28 Standing in S280 Shelter 04/C16, 1370 ft.

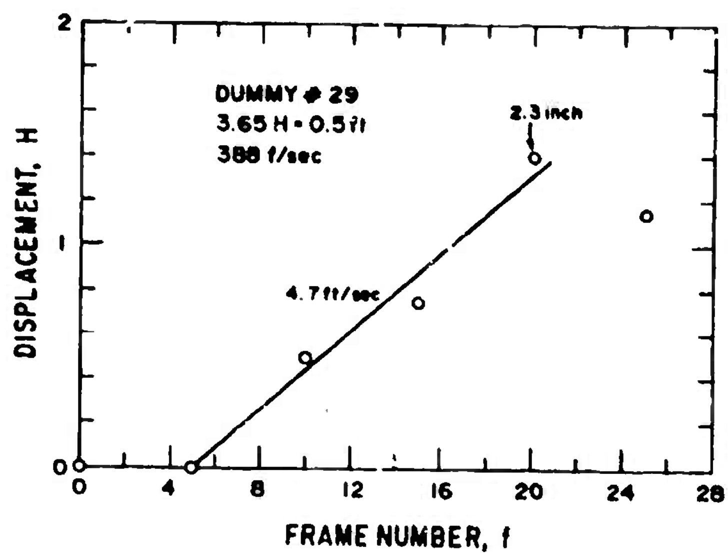

Figure C-6. Displacement vs Time, Dummy No. 29 Seated in S280 Shelter 04/C16, 1370 ft.

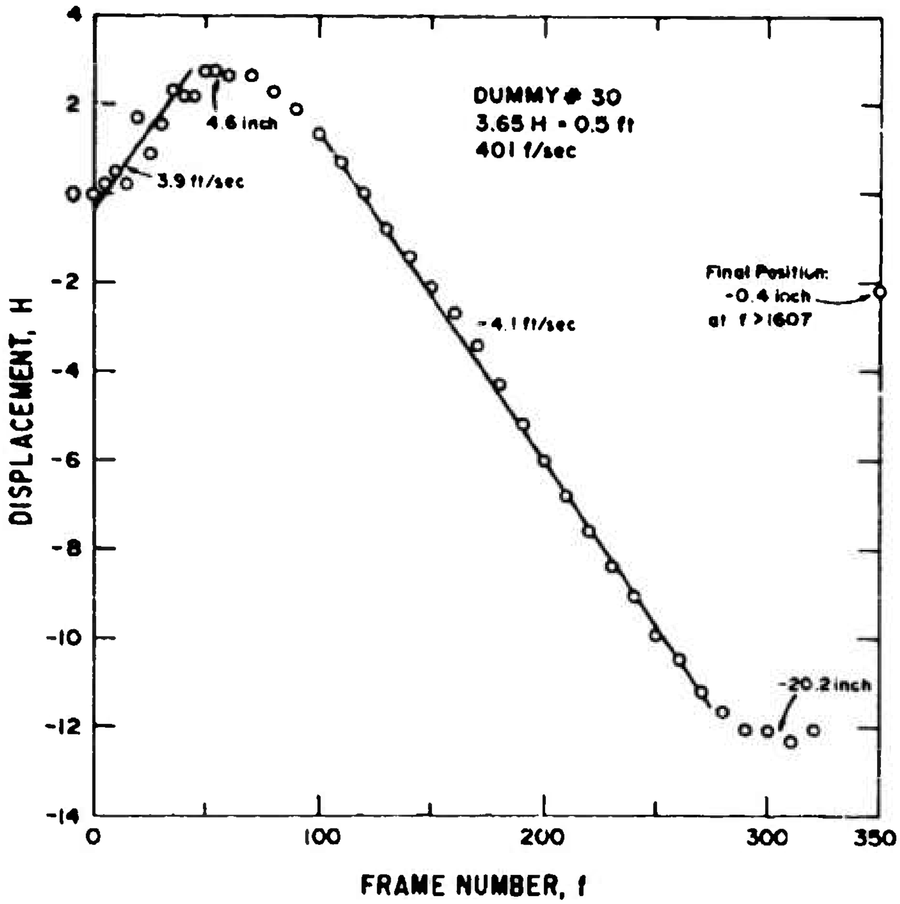

Figure C-7. Displacement vs Time, Dummy No. 30 Seated in S280 Shelter 07/C26, 2000 ft.

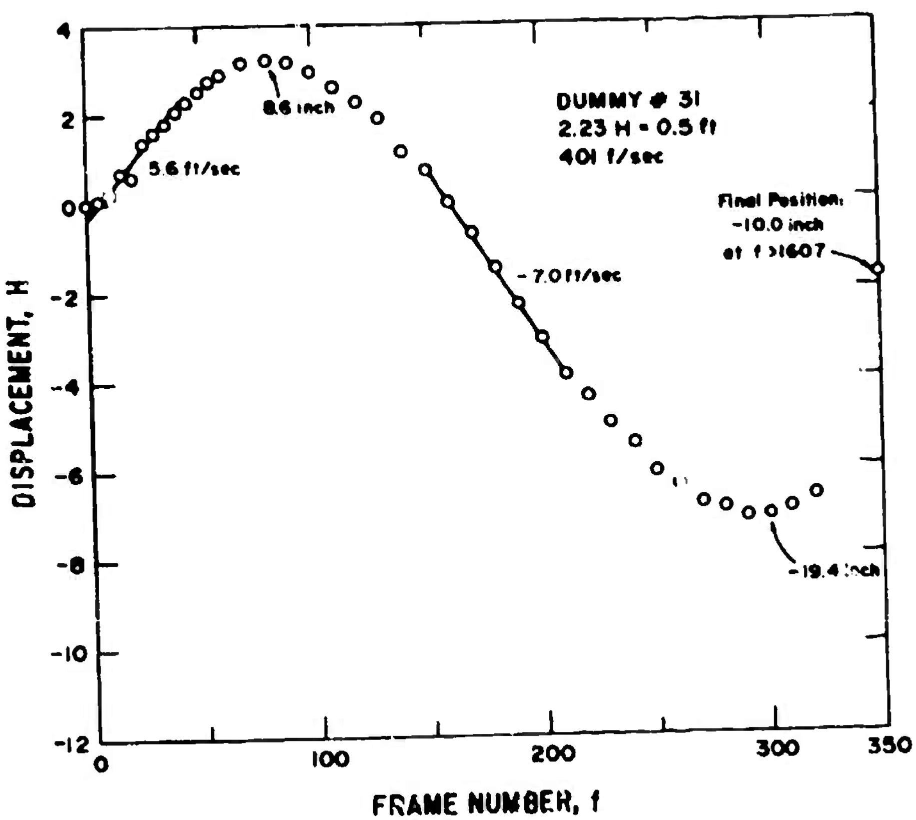

Figure C-8. Displacement vs Time, Dummy No. 31 Standing in S280 Shelter 07/C26, 2000 ft.

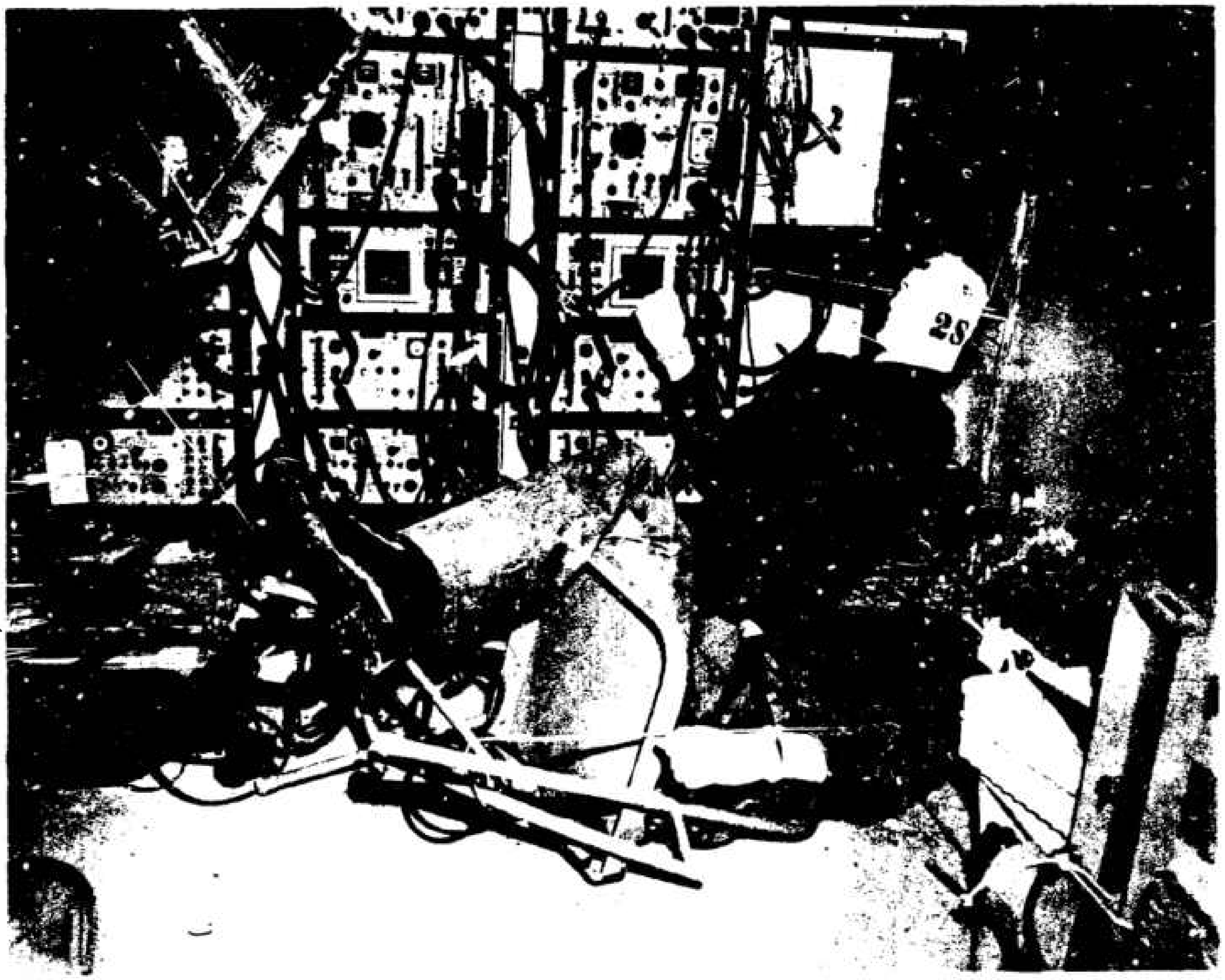

Figure C-9. Postshot View of Dummy Nos. 28 and 29, Shelter 04/C16 at 1370-Ft Range.

Figure C-10. Postshot View of Dummy No. 29 to Show Head Wound.

Figure C-11. Postshot View of Dummy Nos. 30 and 31, Electronic Equipment Shelter 07/C26, 2000-Ft Range.

TABLE C-1

BLAST EFFECTS ON DUMMIES INSIDE ELECTRONIC EQUIPMENT SHELTERS

Station	Dummy No.	Dummy Preshot Location	Dummy Postshot Location	Condition of Dummy	Film Analysis
S-250 Retrofit, R1/C10 1120-ft range 6.5-psi overpressure	26[a]	Standing facing ground zero 23 in. from upstream wall*; right shoulder 8 in. from front wall.	Lying on face feet pointed toward ground zero.	No damage to dummy or clothing.	Dummy moves forward (toward GZ), head hits wall @ 14 ft/sec after traveling 20 in., then dummy moves backward, head hits wall @ 12 ft/sec after traveling 33 in.
	27[b]	Seated between racks facing ground zero, 47 in. from upstream wall.	Remained seated tilted away from ground zero at 45 degree angle leaning against rack.	Laceration 4 in. in length over orbital ridge extending 1.5 in. down both sides of eyes into metal skull, 3/4-in.-laceration over bridge of nose 1/2 in. deep; clothing intact.	Dummy moves forward (toward GZ), head hits shelf @ 11 ft/sec after traveling 20 in., then dummy moves backward and returns to chair, back hits chair @ 16 ft/sec, chair tilts backward, head 17 in. behind original position, then dummy moves forward, head hits shelf @ 8 ft/sec after traveling 23 in., then dummy moves backward and resits in chair, back hits chair @ 7 ft/sec.
S-280, 04/C16 1370-ft range 4.7-psi overpressure	28[a]	Standing, facing and 18 in. from instrument panel; left shoulder 25 in. from upstream wall.	Sitting, head leaning against downstream wall feet toward ground zero.	Three lacerations down back of head: 0.75 in.^{2}, 0.25 in. deep; 1.0 in.^{2}, 0.25 in. deep; 0.75 in.^{2}, 0.50 in. deep. 1.0-in.-long laceration on right shoulder; tear in blouse over right shoulder.	Head moves to left (toward GZ) @ 10 ft/sec, obscured by dust after moving 6 in.
	29[b]	Seated, facing ground zero 30 in. from upstream wall*; right shoulder 27 in. from instrument panel.	Lying on back down on floor, still in chair.	Four-in.-long, V-shaped laceration on left side of face. Clothing torn over both knees.	Head moves forward (toward GZ) @ 5 ft/sec, obscured by dust after moving 2 in.

TABLE C-1 - CONTINUED

BLAST EFFECTS ON DUMMIES INSIDE ELECTRONIC EQUIPMENT SHELTERS

Station	Dummy No.	Dummy Preshot Location	Dummy Postshot Location	Condition of Dummy	Film Analysis
S-280, 07/C26 2000-ft range 2.8-psi overpressure	30[c]	Seated, facing ground zero 32 in. from upstream wall*; right shoulder 25 in. from instrument panel.	Seated upright in chair in preshot position; chair slid 0.75 in. downstream.	No damage to dummy or to clothing.	Head moved forward (toward GZ) @ 4 ft/sec for 5 in. (no impact), then head moved backward @ 4 ft/sec for 20 in. (no impact), then head moved forward and came to rest within 0.4 in. of original position.
	31[c]	Standing, facing and 10 in. from instrument panel; left shoulder 22 in. from upstream wall.	Standing, leaning neck against instrument panel. Foot 4 in. downstream of preshot location.	No damage to dummy or to clothing.	Head moved to left (toward GZ) @ 6 ft/sec for 9 in. (no impact), then head moved to right @ 7 ft/sec for 19 in. (no impact), then hea moved to left and cam to rest 10 in. to right of original position.

Impact-O-Graphs® Unloaded:

[a] Both 10g.

[b] One 10g.

[c] None.

* Measured to center of trunk.

APPENDIX D

FOREIGN VEHICLE

PRECEDING PAGE BLANK

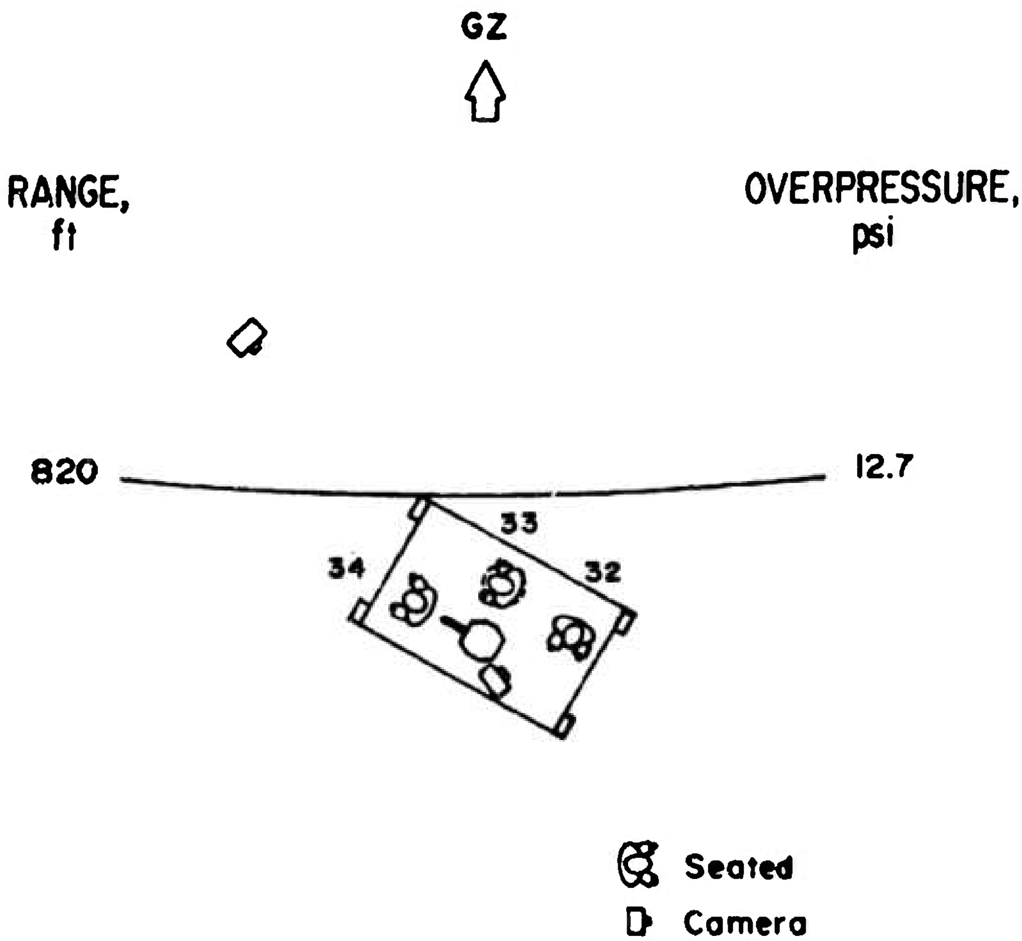

Figure D-1. BRL/Foreign Vehicle Layout Drawing.

Figure D-2. Dummy No. 33 in Commander's Position, Armored Infantry Fighting Vehicle.

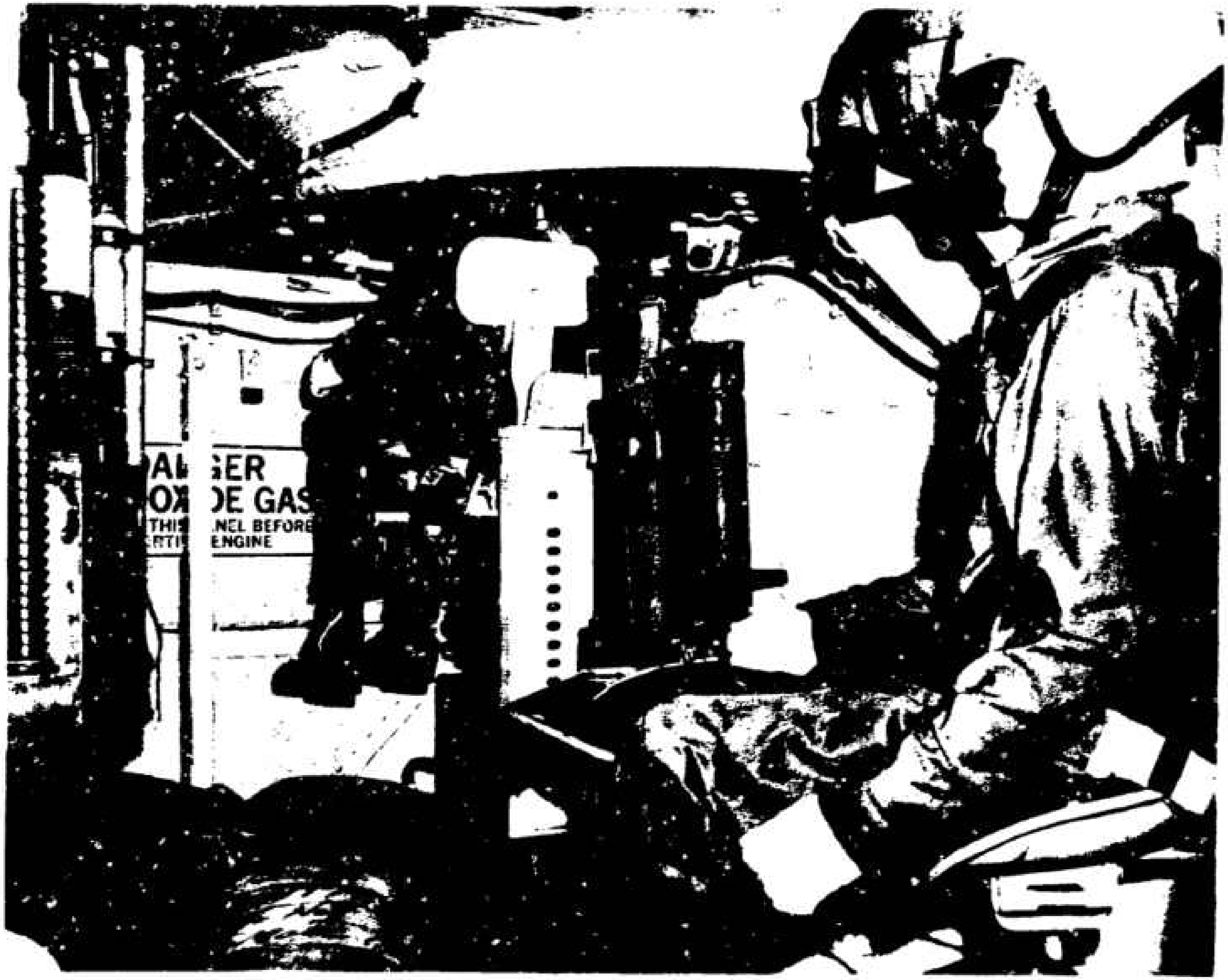

Figure D-3. Dummy No. 32 Seated Inside Troop Compartment and Dummy No. 33 in Commander's Position Viewed from Back Door Preshot.

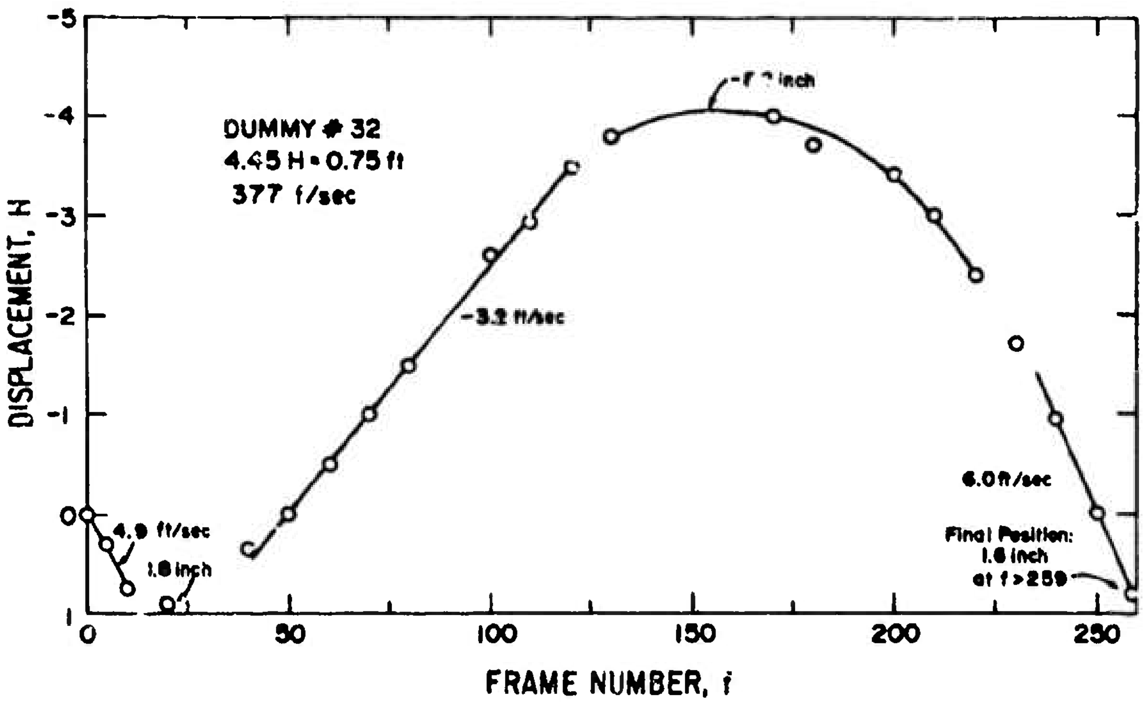

Figure D-4. Displacement vs Time, Dummy No. 32 Seated in Troop Compartment, Armored Infantry Fighting Vehicle GON, 820 ft.

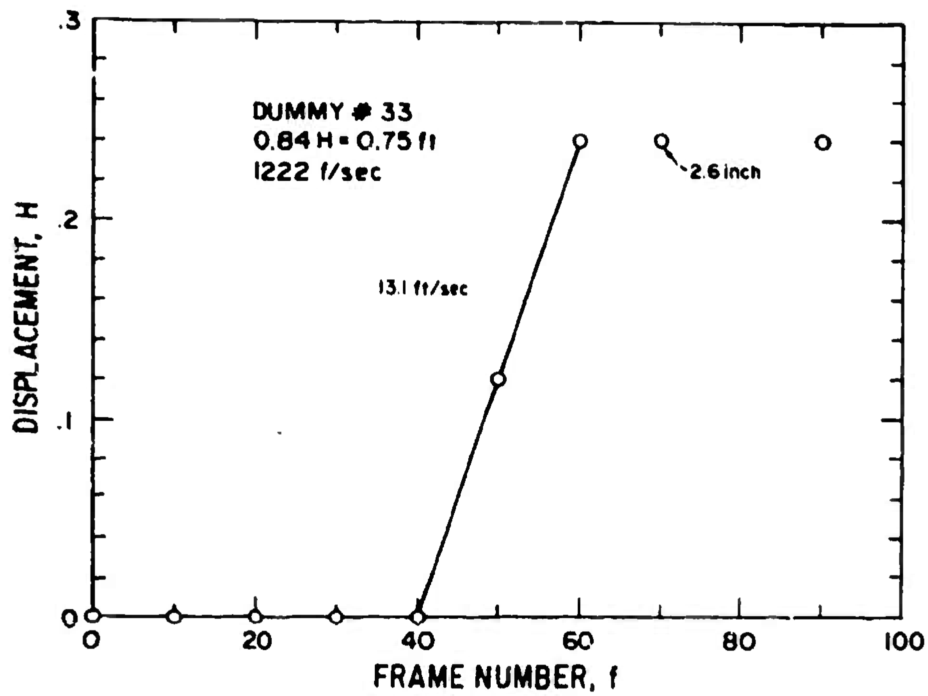

Figure D-5. Displacement vs Time, Dummy No. 33 in Commander's Seat, Armored Infantry Fighting Vehicle.

TABLE D-1

BLAST EFFECTS ON DUMMIES IN FOREIGN VEHICLE

Station	Dummy No.	Dummy Preshot Location	Dummy Postshot Location	Condition of Dummy	Film Analysis
GON AIFV (Armored Infantry Fighting Vehicle) 820-ft range 12.7-psi overpressure	34[a]	Driver's seat (seat belt on).	Same as preshot.	No damage to dummy or clothing.	Not visible in film.
	33[b]	Commander's seat (seat belt on). Head out of open hatch.	2-in. over left of seat; body tilted upstream.	No damage to dummy. Shirt torn at right pocket and at front buttons.	Head moves to right (toward GZ) @ 13 ft/sec, head comes to a sudden stop (as though some other part of dummy impacted) after traveling 3 in.
	32[c]	Seated right side of troop compartment (seat belt on).	Same as preshot.	No damage to dummy or clothing.	Head moves to right (toward GZ) @ 5 ft/sec, impacts after traveling 2 in., then head moves to left 3 ft/sec for 8 in. (no impact), then moves to right @ 6 ft/sec, impact occurs @ same point as before (i.e., 2 in. from original position), dummy comes to rest in this position.

Vehicle oriented 315°degrees to ground zero.

Right front corner of vehicle 6S 21'40".

Impact-O-Graphs® Unloaded:

[a] One 10g.

[b] Both 10g.

[c] None.

APPENDIX E

DRONE HELICOPTER

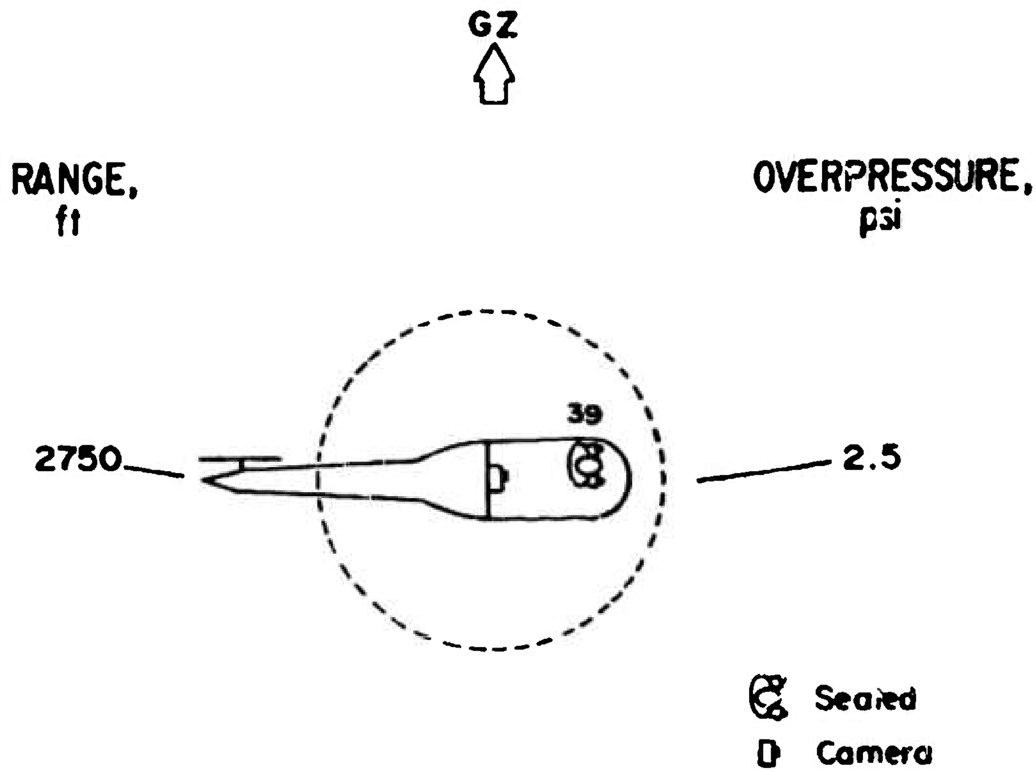

Figure E-1. BRL/Drone Helicopter Layout Drawing.

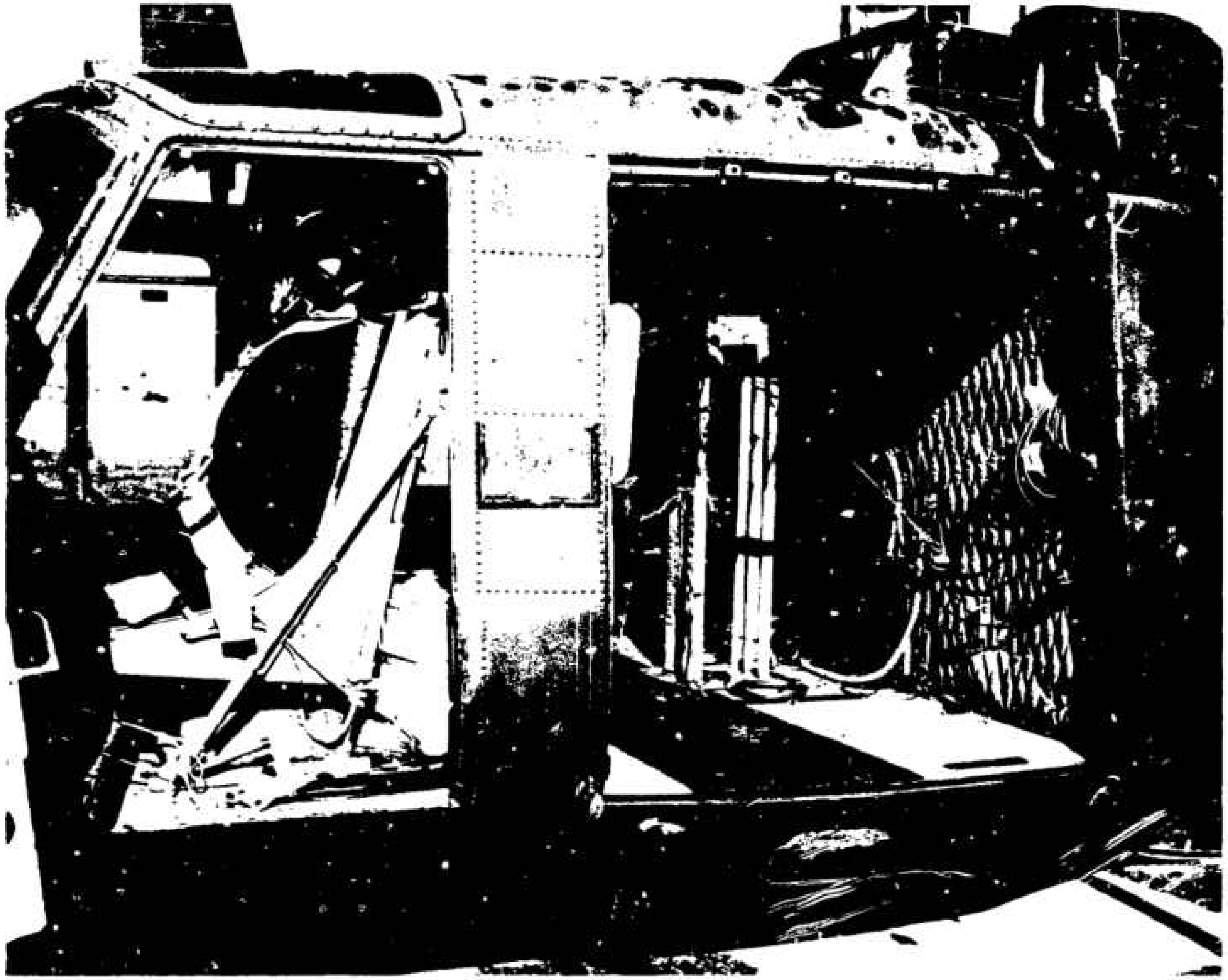

Figure E-2. View of Dummy No. 39 in Drone Helicopter.

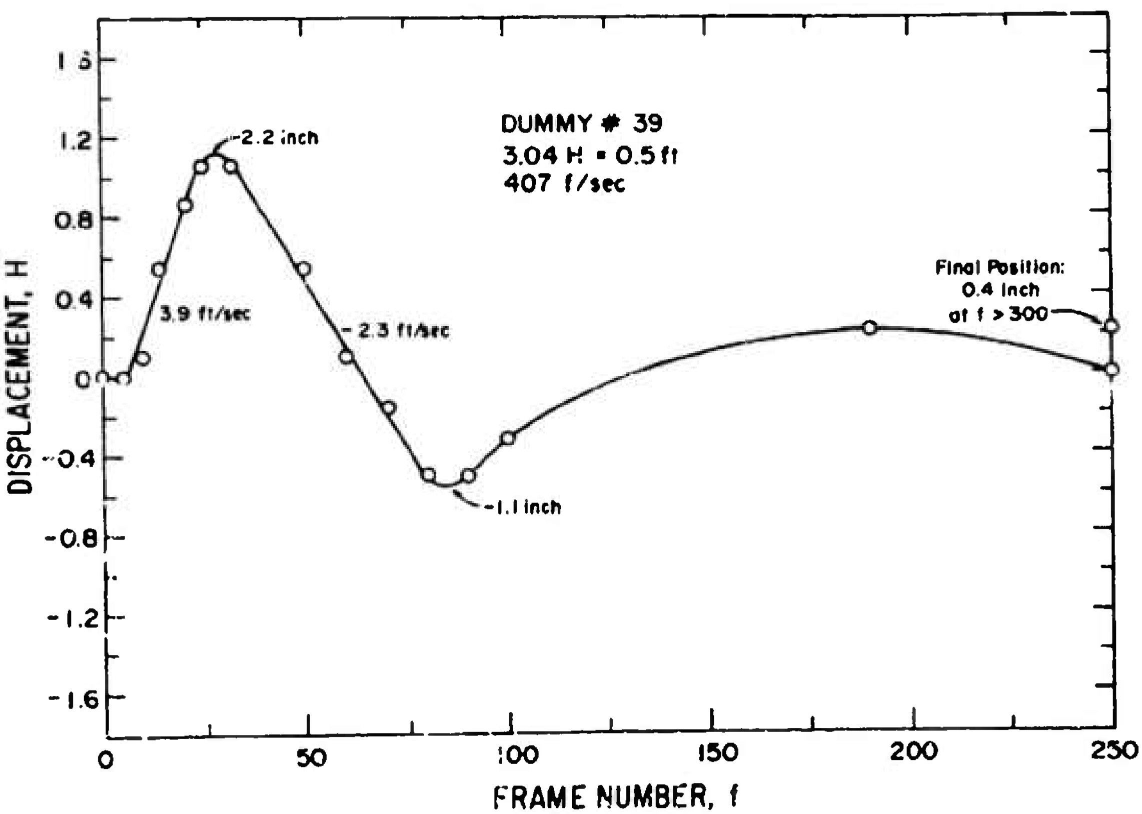

Figure E-3. Displacement vs Time, Dummy No. 39 Seated in Drone Helicopter, 2750 ft.

TABLE E-1

BLAST EFFECTS ON DUMMY IN DRONE HELICOPTER

Station	Dummy No.	Dummy Preshot Location	Dummy Postshot Location	Condition of Dummy	Film Analysis
BRL/HELO (Left Side to Ground Zero) 2750-ft range 2.5-psi overpressure	39[a]	Seated, left front seat. Seat belt harness attached.	Same as preshot.	Five scratches on helmet.[b] No damage to dummy or to clothing.	Head moves to left (toward GZ) @ 4 ft/sec for 2 in., then head moves to right @ 2 ft/sec for 1 in., then head moves to left and comes to rest within 0.5 in. of original position.

[a] Impact-O-Graph® not unloaded.

[b] Small window in ceiling blown in by blast.

Helicopter bearing 286°54'05".

12. DICE THROW OFF-SITE BLAST PREDICTIONS AND MEASUREMENTS

by

" s'. Reed

Sand... ..a'boratories,

Environmental Research Division

"DICE THROW - OFF-SITE BLAST PREDICTIONS AND MEASUREMENTS"*

Final Report on Experiment No. 122

Jack W. Reed
Environmental Research Division
Sandia Laboratories
Albuquerque, New Mexico

ABSTRACT

Predictions and measurements of distant propagations were made of airblasts from Project DICE THROW, including two Pre-DICE THROW events. The purpose was to identify, control, and document the off-site environmental impact from these large explosions. A weather-watch was maintained, using special meteorological observations, to assure that atmospheric acoustic refraction would not cause significant nuisance damage or hazard to surrounding communities. Weak propagation conditions prevailed during the two Pre-DICE THROW events. A moderately strong propagation directed toward the southeast from DICE THROW caused some disturbance in Tularosa and Alamogordo but no damage claims were submitted.

*This work was jointly supported by the Energy Research and Development Administration and the Department of Defense Nuclear Agency.

INTRODUCTION

At the request of the Defense Nuclear Agency Field Command, Sandia Laboratories evaluated the potential for Project DICE THROW airblasts to hazard, damage, or irritate communities surrounding White Sands Missile Range (WSMR). Preliminary evaluations showed that under particular weather conditions, the nuisance damage threshold, often assumed to be near 400-Pa peak-to-peak pressure amplitude, could extend 80 km from the two Pre-DICE THROW calibration shots and over 135 km from the final DICE THROW event. Considering the exposed populations, it appeared that windows could be broken as far away as Albuquerque.

A weather-watch was instituted to determine what propagations could be expected at shot time and provide for delays in case such extreme conditions were encountered. Microbarograph pressure measurements were made in various communities to document the actual wave passage, for use in verification of predictions as well as validation or rejection of any damage claims that resulted.

As it turned out there were no atmospheric propagation problems associated with either calibration event, and only a moderately focused wave was ducted toward Tularosa and Alamogordo from DICE THROW. There may have been some minor damages from this final blast, but no serious claims were made.

Several smaller tasks were also performed for this project. A draft Environmental Impact Assessment [1] was reviewed and corrected. Safe separation distances and altitudes were estimated for project facilities and participating aircraft. Finally, consultant service was provided for evaluating several damage claims that resulted from an associated experiment with 1200 pounds (540 kg) of high-explosives (HE) at Kirtland AFB on March 25, 1975.

SHOT DESCRIPTIONS

Pre-DICE THROW I was a 100-ton (91 Mg) TNT sphere, on and tangent to the ground surface, fired at 1100 MDT (1700Z), August 12, 1975. This explosion ground zero (GZ) was located about 2 km south of the WSMR "Queen 15" Station and 46 km NW of Tularosa, NM.

Pre-DICE THROW II was a 120-ton (109 Mg) ANFO (ammonium nitrate and fuel oil slurry) surface tangent sphere, fired at 1200 MDT (1800Z), September 22, 1975, at a point just east from the previous calibration shot. It was tested to verify that 120-ton ANFO was indeed the equivalent blast generator to 100-ton TNT.

DICE THROW was a 600-ton (544 Mg) ANFO surface tangent sphere, fired at 0800 MDT (1400Z), October 6, 1976. The GZ was located about 5 km west of Trinity Site, thus 56 km SE from Socorro, NM. Various measurements [2] showed that it well simulated the intermediate and distant blast wave phenomena expected from a source of 1-kt NE (nuclear explosion, 4.2TJ) surface burst, or 2-kt NE free-air burst.

DISTANT AIRBLAST PREDICTIONS

Sound or blast waves may be distorted by atmospheric temperature and wind strata. Sound rays are bant away from (toward) ground while passing through layers where sound velocity decreases (increases) with altitude. Sound velocity, a vector, is made up of isotropic sound speed, dependent on temperature, plus a directed wind component. In general, if a directed sound velocity at altitude is greater than at ground level, there will be acoustic ducting or trapping that may considerably amplify airblast overpressures or acoustic amplitudes, above the levels expected from purely spherical (or hemispherical) wave expansion. On the other hand, with a strong gradient of sound velocity with height, much reduced pressures are observed along the ground. More details are available from many sources, a recent one being a Sandia report for Project MIXED COMPANY [3], and will not be repeated here.

Various studies have led to a statistical estimator for window damage as a function of airblast overpressure [4]. Simply stated, $\Delta p(50) = 7.5 \times (2.5)^{\pm 1}$ kPa, or 50 percent of typical window panes are broken by an incident overpressure, Δp, of 7.5 kPa, with a lognormal distribution of failure occurrences and a geometric standard deviation factor of 2.5. Also assumed in damage estimation was an average of 19 window panes per person in a community [5]. Standard explosion overpressure versus distance relations [6] were scaled to yields of calibration shots and DICE THROW as shown in Figure 1 and 2, respectively. Test results have been included for later discussion. Magnifications of 3X for atmospheric boundary layer inversion propagations and 5X for atmospheric focusing were assumed, along with an increased amplitude decay with distance for gradient conditions, for estimating possible window damages to neighboring communities shown in Table I.

Predictions for calibration shots showed that damage levels from airblast focusing on several communities ought to be avoided, lest neighborhood opposition be generated against the much larger final event. The necessary weather restriction was slight, because such focusing at 50-km to 100-km ranges is associated with jet stream winds aloft that are relatively infrequent at this latitude, even in mid-winter.

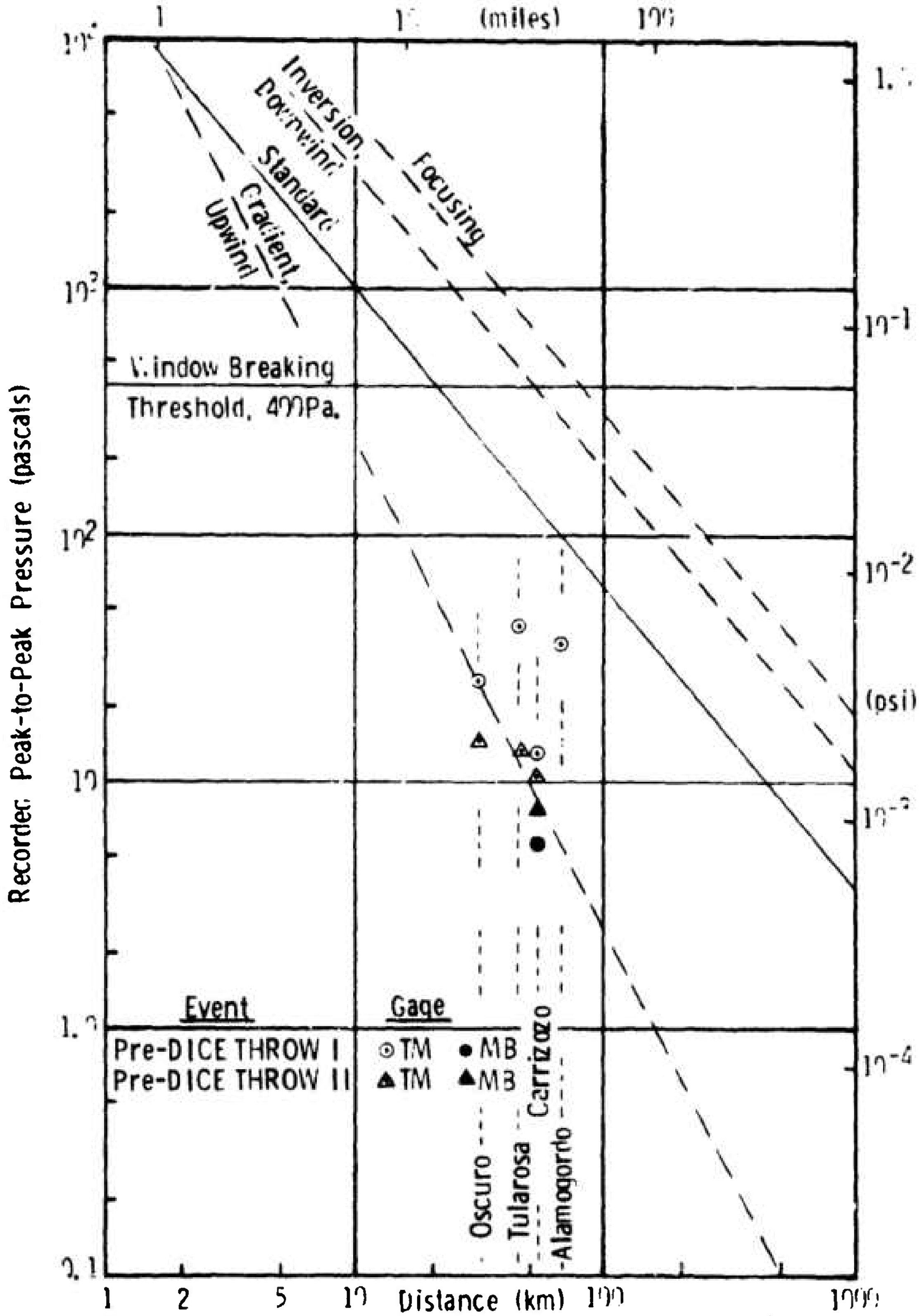

Figure 1. Airblast Pressures from Pre-DICE THROW Events, 100-ton TNT and 120-ton ANFO Surface Bursts.

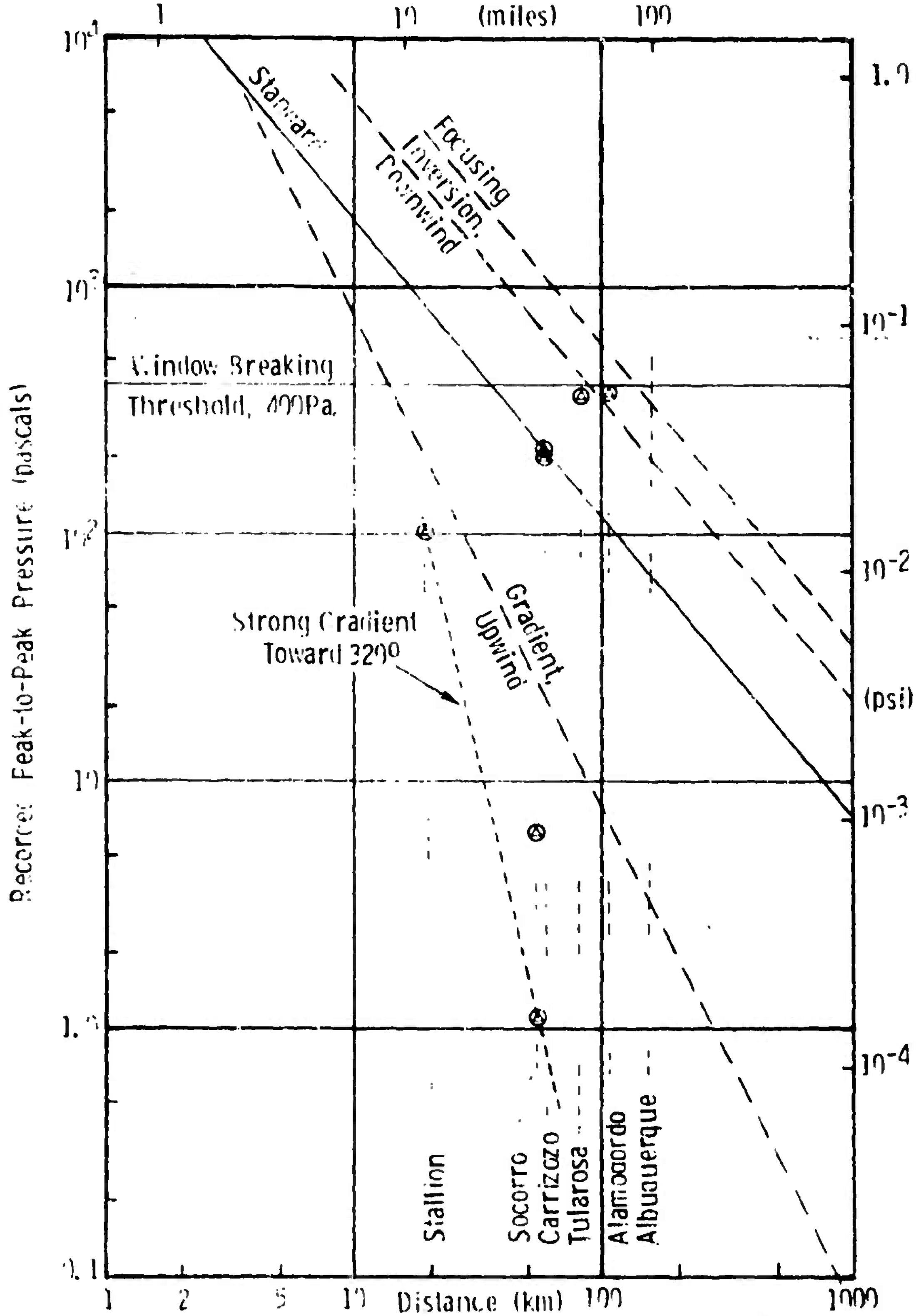

Figure 2. Airblast Pressures from DICE THROW, 600-ton ANFO Surface Burst.

Table I. Predicted Window Damages with Various Airblast Propagations

City:	Alamogordo	Tularosa	Carrizozo	Socorro	Albuquerque
Population (1970):	23, 035	2,851	1,123	4,687	270,000
Atmospheric Propagation Type					
Pre-DICE THROW I, II Distance (km):	66	47	56	91	--
		Broken Panes			
Gradient	0	0	0	0	0
Standard	0	0	0	0	0
Inversion	1	1	0	0	0
Focusing	7	11	2	1	0
DICE THROW Distance (km):	100	81	60	53	155
		Broken Panes			
Gradient	0	0	0	0	0
Standard	0	0	0	1	1
Inversion	0	1	1	13	17
Focusing	38	6	5	51	70

DICE THROW predictions caused more concern in that low level inversion or down-wind propagations could cause numerous complaints and claims from both Socorro and Albuquerque. Lower pressures at the longer range to Albuquerque than to Socorro were counteracted in this damage estimate by the much larger exposed population in Albuquerque. Climatic weather patterns, with south and southwest winds, made delays for weather quite likely, even with mid-day firing and near maximum surface temperatures. Late in field test preparations it was found that at mid-day, very low frequency (VLF) radio noise caused great difficulty with electrical grounding of various experiment recording systems, and an 0800 MDT shot time was established. That made a strong surface temperature inversion likely, with enhanced airblast propagation. As it turned out, this project was very lucky and no delays were needed.

OPERATING PLAN

A blast prediction service was chartered, as Experiment Number 122, which used special WSMR weather observations to establish whether enhanced airblast propagation conditions were occurring toward any of the surrounding communities. Results were relayed to the Test Group Director for consideration in making final firing decisions.

Airblast measurements were made in vulnerable communities to verify predictions and provide bases for validating or rejecting any damage claims that arose. Calibration shots were monitored by pressure gages at Oscuro, Carrizozo, Tularosa, and Alamogordo, connected by radio-telemetry (TM) link to a recording van at D-7 Site, near the test control center. There were problems with line-of-sight TM communications for the DICE THROW plan, so it was monitored by manned microbarograph (MB) units located at Stallion Site, Socorro, Carrizozo, Tularosa, and Alamogordo. These mobile MB units could be moved to more vulnerable locations if warranted by D-1 day weather forecasts.

Meteorological observations were provided by AVCO, a WSMR contractor. A mobile rawinsonde weather balloon facility was operated at SW.70 Site, 5 km southwest of Queen-15, for pre-DICE THROW events. A permanent rawinsonde station at Stallion Site was used for DICE THROW, 19 km north of the test but with a clear view of it over flat terrain, so that representative weather data were assured. A regular balloon ascension is made at WSMR, near the Small Missile Range, daily at 1200Z (0600 MDT) on the international synoptic schedule, and results were made available for early morning planning. For calibration shots, special ascensions from SW.70 were made at H-2.5, H-1, and H hours. Special DICE THROW ascensions from Stallion Site were scheduled for H-4, H-2, H-1 and H hours.

AIRCRAFT SAFE SEPARATION

Explosion wave scaling laws, including the shock strength dependence on ambient pressure at altitude, were used to derive isobar cross-sections in Figure 3 for the two yields. Light aircraft and helicopters are safe from 0.2 psi (1.4 kPa) incident overpressures, although an added safety factor of 2 is often employed for aircraft positioning in association with explosion tests [7]. More substantial jet transports and bombers are safe from 0.5 psi (3.5 kPa), while fighters are safe from 2 psi (14 kPa).

RESULTS

Pre-DICE THROW I:

Distant propagations were expected and verified to be quite weak, so that no disturbance was created among the WSMR neighbors. Rawinsonde measurements, for blast prediction

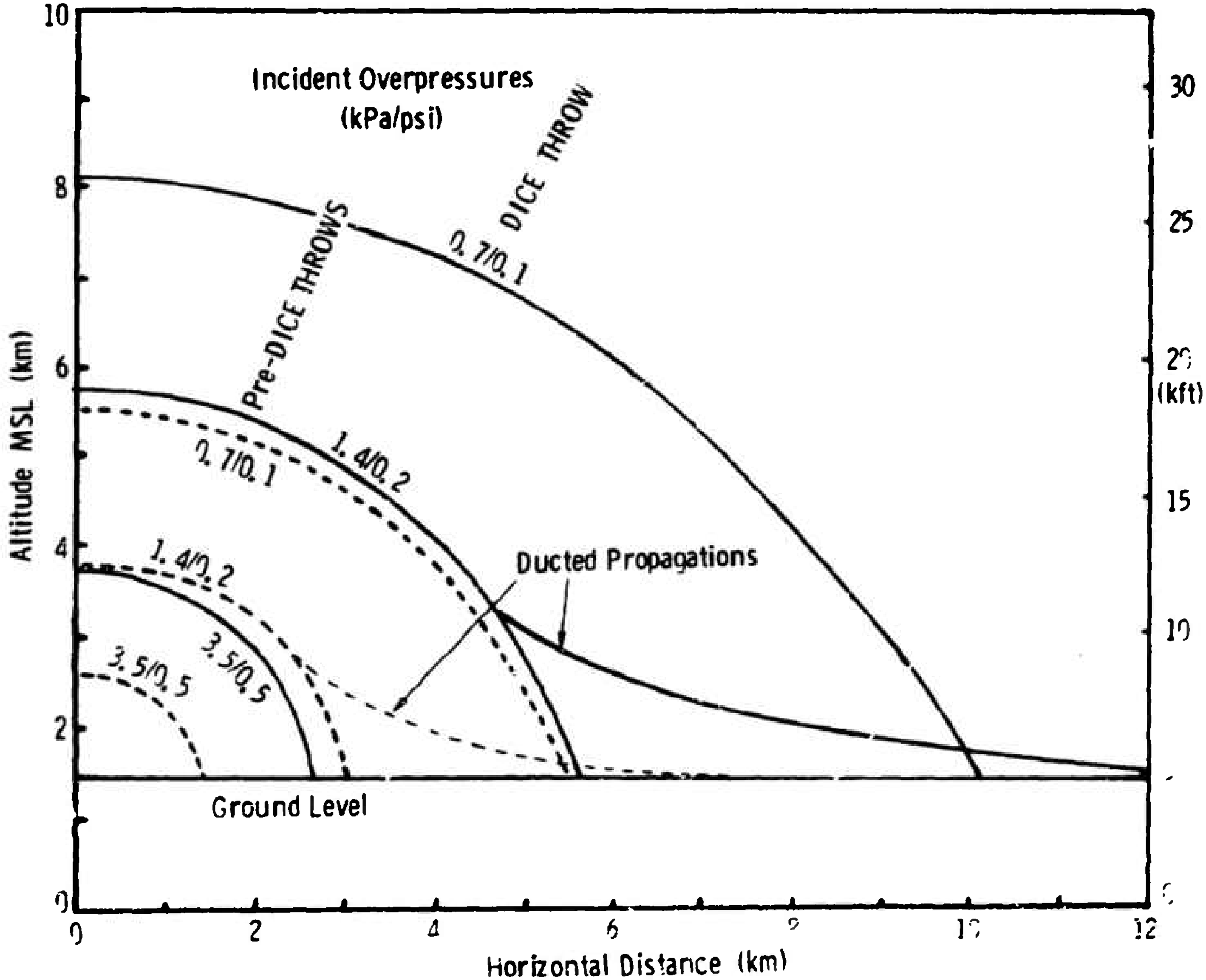

Figure 3. Project DICE THROW Free Air Blast Isobars.

calculations, are listed in Table II for both 8/11/75 (dry run) and 8/12/75 (live run). On Monday (8/11) there was a layer of northerly winds at 2.7-3.6 km MSL (above mean sea level) that would have ducted, and possibly focused, relatively strong airblasts toward Tularosa and Alamogordo.

On test day (8/12) there was never any indication of blast ducting toward either NE or SE directions of concern, after the night-time temperature inversion had been destroyed by solar heating. Sound velocity versus height functions from pre-test (H-2.5, H-1 hours) and shot time (1100 MDT) soundings are shown toward NE in Figure 4 and toward SE in Figure 5. The strong gradient of sound velocity toward NE was expected to give relatively weak propagations in that direction. Toward SE, less upward blast refraction was expected because of an inversion at 2.1-2.6 km MSL, but no strong blast could be refracted into the surface high velocity layer.

Recorder traces from the TM gage network are reproduced in Figure 6. with numerical results shown in Table III. The microbarograph at Carrizozo disagreed with the TM amplitude, but both weak signals were difficult to distinguish from ambient noise. This discrepancy was not significant. Peak amplitudes were shown in Figure 1 for comparison with various prediction curves. Propagations toward NE, to Oscuro and Carrizozo, were indeed as expected from the strong gradient shown in Figure 4. Stronger SE propagations toward Tularosa and Alamogordo, resulted from the weaker overall gradient of Figure 5, as could well be expected.

In summary, predictions, measurements, and off-site protection from nuisance airblasts were all successful.

TABLE II. PRE-DICE THROW I RAWINSONDE UPPER AIR REPORTS

Temperatures (K); Winds (deg./ms^{-1})
Shot Time Surface Pressure: 86.75 kPa

DAY:		8/11/75, DRY RUN						8/12/75, LIVE RUN					
TIME (Z)*		1500		1630		1815		1430		1555		1707 (Shot)	
Temperature/Wind		T	W	T	W	T	W	T	W	T	W	T	W
Altitude MSL (km)													
Surface	1.341	295.2	CALM	299.5	180/8.2	301.2	190/7.2	295.3	180/3.1	298.0	186/4.1	301.6	[illegible]
	1.524	294.6	180/5.1	296.9	190/6.7	277.9	200/6.2	293.5	180/3.6	296.1	175/4.1	299.9	[illegible]/7.7
	1.829	293.1	185.9.3	293.8	190/7.2	295.1	200/6.7	291.7	185/4.1	292.5	185/5.1	295.2	[illegible]/7.2
	2.134	290.5	185/7.7	290.8	190/7.7	292.4	190/6.7	289.8	195/4.1	290.3	[illegible]/6.2	292.9	[illegible]/6.7
	2.438	288.6	190/5.1	288.2	240/7.2	289.4	190/6.2	[illegible]	[illegible]/4.1	[illegible]	190/4.6	[illegible]	[illegible]
	2.743	276.6	245/2.6	285.9	020/7.7	287.2	150/3.1	285.8	250/4.1	286.3	220/3.6	[illegible]	[illegible]/7.1
	3.048	284.5	325/3.1	284.8	035/4.6	285.5	035/3.1	274.0	270/5.7	284.2	235/5.1	284.4	270/5.6
	3.658	281.2	040/6.7	280.5	015/4.1	281.0	040/4.1	279.8	280/4.1	279.4	305/3.1	280.9	325/3.1
	4.267	278.1	080/6.7	276.3	050/2.1	276.8	065/4.1	275.5	075/2.6	274.8	135/[illegible]	276.0	[illegible]
	4.877	274.4	060/4.6	274.1	095/3.6	274.8	045/4.1	270.3	080/6.2	270.4	145/6.2	270.3	125/4.6
	5.486	270.4	050/4.6	270.1	040/5.7	270.6	050/6.2	268.2	200/2.1	267.0	310/4.1	266.6	030/2.1
	6.096	266.3	055/6.2	265.6	050/6.2	266.6	050/6.7	263.5	140/2.1	263.1	070/2.6	[illegible]	025/[illegible]

*Greenwich Time (Z) - 6 hours = Mountain Daylight Savings Time (MDT)

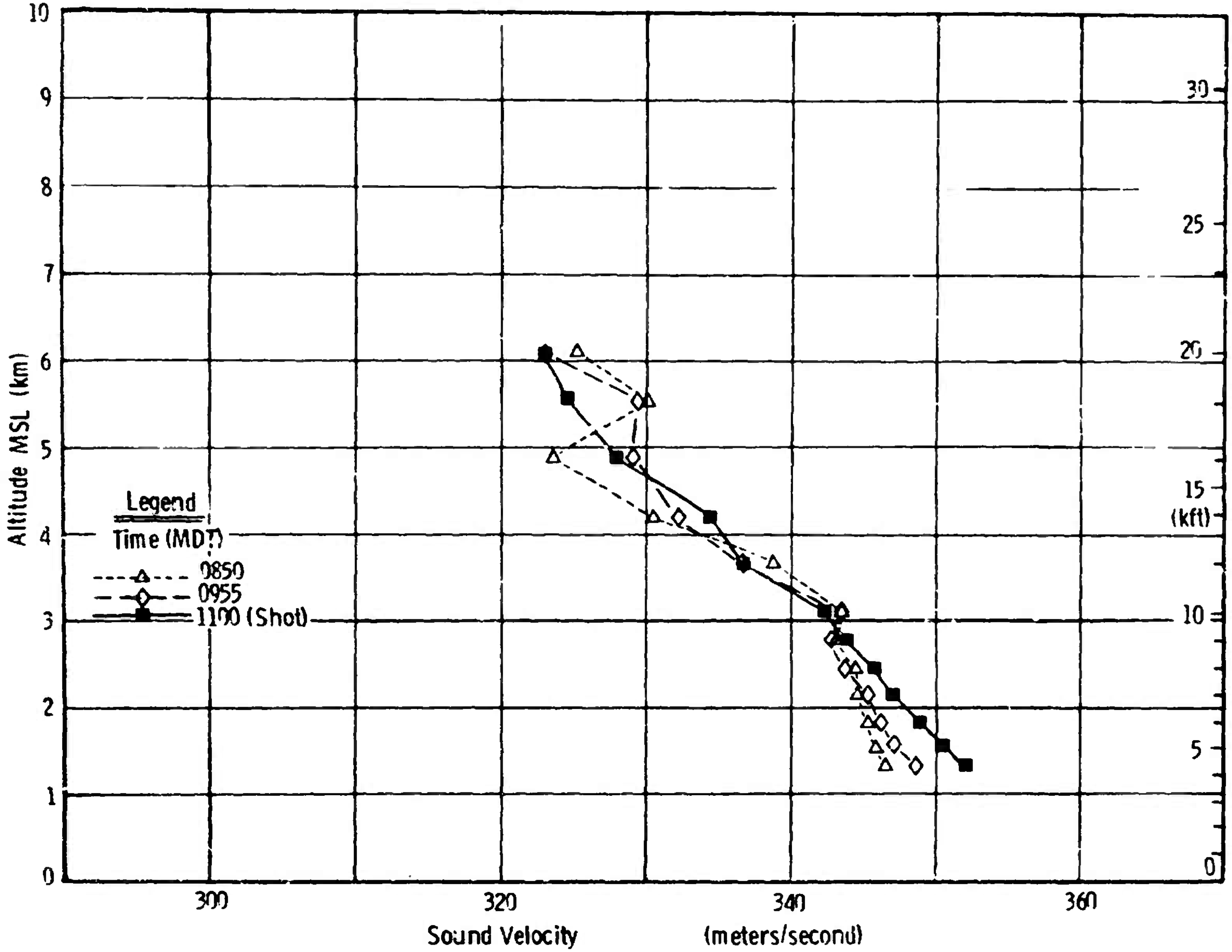

Figure 4. Pre-DICE THROW I Sound Velocities Toward 063° Direction of Oscuro and Carrizozo.

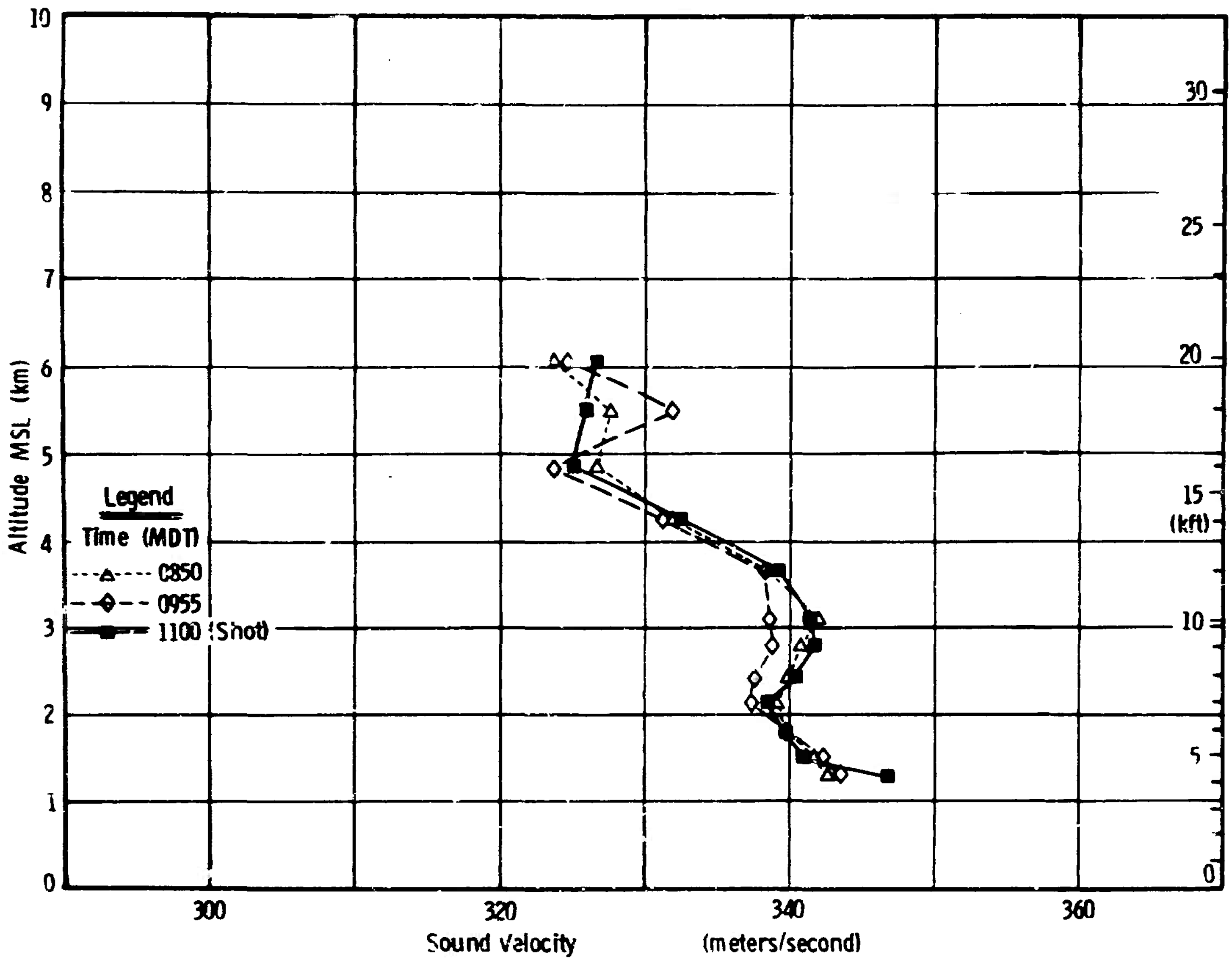

Figure 5. Pre-DICE THROW I Sound Velocities Toward 140° Direction of Tularosa and Alamogordo.

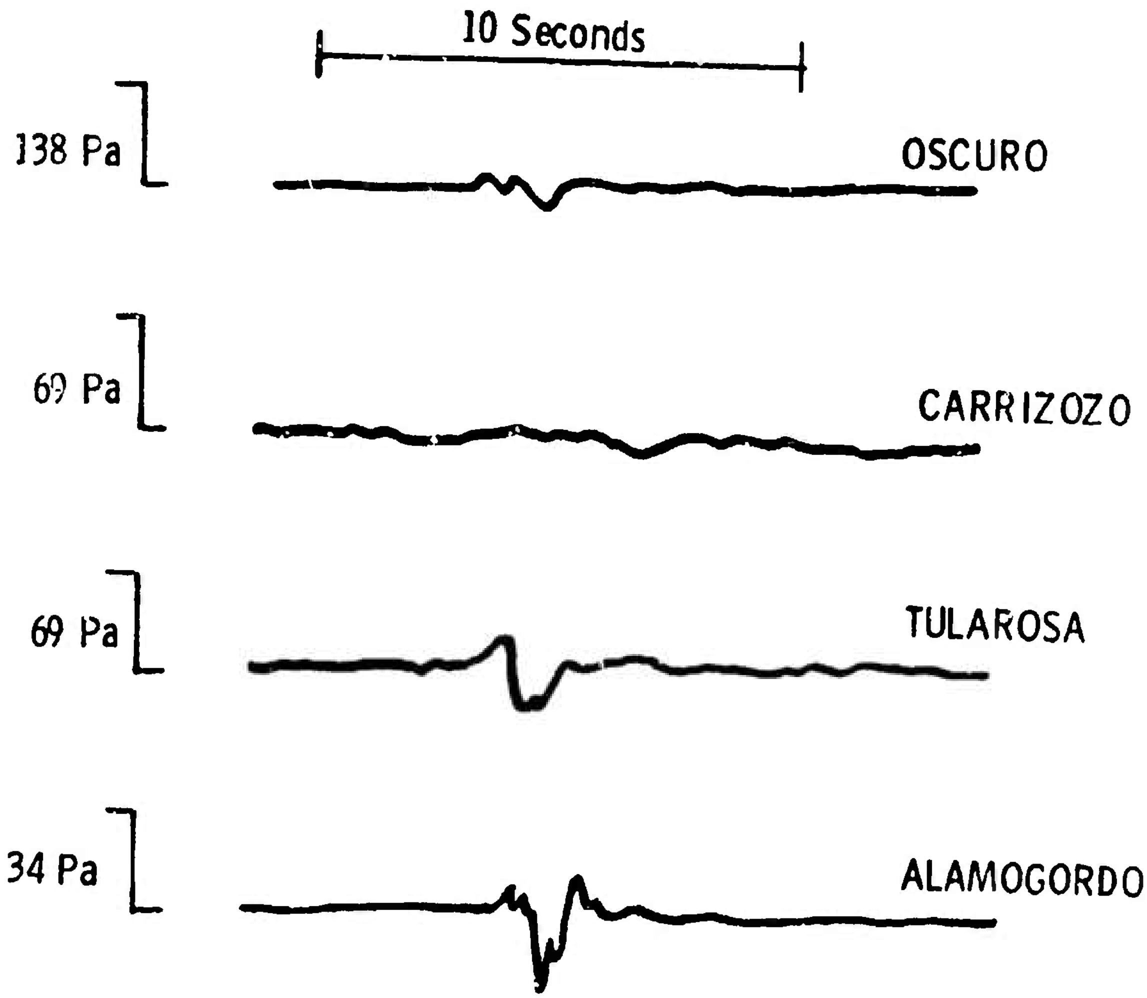

Figure 6. Pre-DICE THROW I Pressure Signatures.

TABLE III. PRE-DICE THROW I

Off-Site Airblast Measurements

Station	Gage	Distance (m)	Arrival Time (sec)	Arrival Velocity (m/s)	Arrival Velocity (ft/sec)	Pressure Amplitude (pascals)	Pressure Amplitude (psi)
Oscuro	TM	31,176	88.33	353	1158	26.3	0.00382
Carrizozo	TM	52,920	157.87	335	1100	10.4	0.00151
	MB		148.5	356	1169	5.8	0.000848
Tularosa	TM	46,080	133.14	346	1136	43.6	0.00633
Alamogordo	TM	66,240	196.90	336	1104	38.2	0.00554

Pre-DICE THROW II:

Distant propagations were again expected and verified to be relatively weak, so that no significant disturbance was created among the WSMR neighbors.

Meteorological observations of rawinsonde ascensions are listed in Table IV, as used in blast prediction calculations. During the final dry run on 9/21/75 a layer of moderate westerly winds at 3.7-4.9 km MSL would have ducted, and possibly focused, relatively strong airblasts toward Oscuro and Carrizozo.

On the test date there was no indication of blast ducting toward either NE or SE directions of concern, after the sun had destroyed a night-time surface temperature inversion. Sound velocities versus height at 1200 MDT are shown in Figures 7 and 8, for dry run and event days, respectively. On shot day a strong sound velocity gradient in both directions was expected to give relatively weak propagations at all off-site airblast measurement sites.

Recorded wave data are listed in Table V. Figure 9 shows the weak waves recorded at Oscuro, with an indication of background wind noise levels. In general, amplitudes over about 10 Pa can be heard, but more than 100 Pa is usually required to get people's attention and start them to complaining. At 400 Pa window breakage becomes likely.

Figures 10 and 11 show recordings at Carrizozo, by microbarograph and the telemetered blast gages, respectively. Wind noise was better filtered by the microbarograph, which has only 30-Hz high frequency response capability, while blast gages respond to about 2 kHz. A discrepancy in timing and general wave appearance cannot be explained; the two sensors were

TABLE IV. PRE-DICE THROW II RAWINSONDE UPPER AIR REPORTS

Temperature (K); Winds (deg./ms^{-1})
Shot Time Surface Pressure: 87.65 kPa

DAY	9/21/75, DRY RUN				9/22/75, LIVE RUN					
TIME (Z)*	1530		1800		1540		1700		1800 (Shot)	
Temperature/Wind	T	W	T	W	T	W	T	W	T	W
ALTITUDE MSL (km)										
Surface 1.341	288.3	350/10.3	290.7	360/10.3	287.3	160/1.5	289.6	CALM	292.2	030/4.6
1.524	286.7	360/12.4	287.9	010/11.3	284.3	045/1.0	287.7	035/4.1	290.4	030/6.7
1.829	283.3	015/15.4	285.2	020/11.8	282.5	030/5.7	284.7	040/7.2	287.4	030/6.2
2.134	283.8	015/11.3	282.3	010/10.8	280.5	025/9.3	283.1	045/8.3	284.3	025/4.6
2.438	283.1	360/6.7	281.4	355/7.7	278.4	040/11.8	280.5	045/8.8	281.1	030/3.6
2.743	281.0	350/10.3	280.6	355/5.1	276.5	045/11.8	278.2	055/8.6	277.7	030/4.1
3.048	278.8	345/9.3	278.8	350/3.1	274.5	080/10.3	276.0	055/8.2	276.3	055/4.[illegible]
3.658	277.5	300/8.8	274.1	265/7.7	272.2	050/8.8	272.4	055/8.8	273.4	055/5.1
4.267	271.8	280/8.2	271.1	285/8.2	271.5	025/5.7	271.8	045/3.2	274.2	015/5.7
4.877	267.1	285/9.3	266.2	275/16.5	267.5	015/5.1	267.9	030/7.2	269.3	010/7.7
5.486	262.3	275/16.0	263.0	290/17.0	263.3	355/8.8	263.4	355/7.2	264.3	350/7.7
6.096	260.7	300/12.9	259.5	300/19.6	259.4	345/9.3	259.1	335/7.2	259.4	340/7.7

*Greenwich Time (Z) - 6 hours = Mountain Daylight Time (MDT)

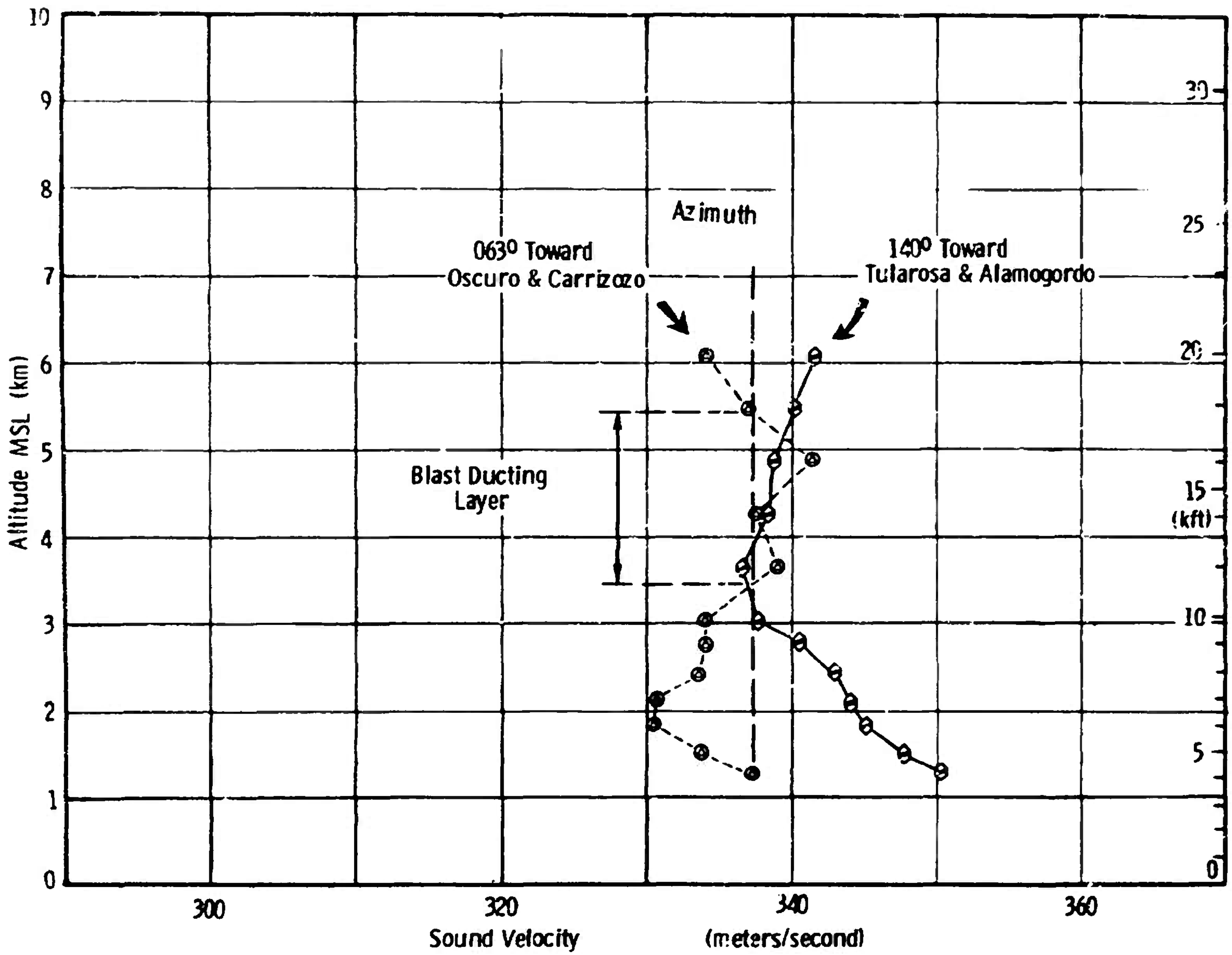

Figure 7. Pre-DICE THROW II Dry Run Sound Velocities at 1200 MDT, 9/21/75.

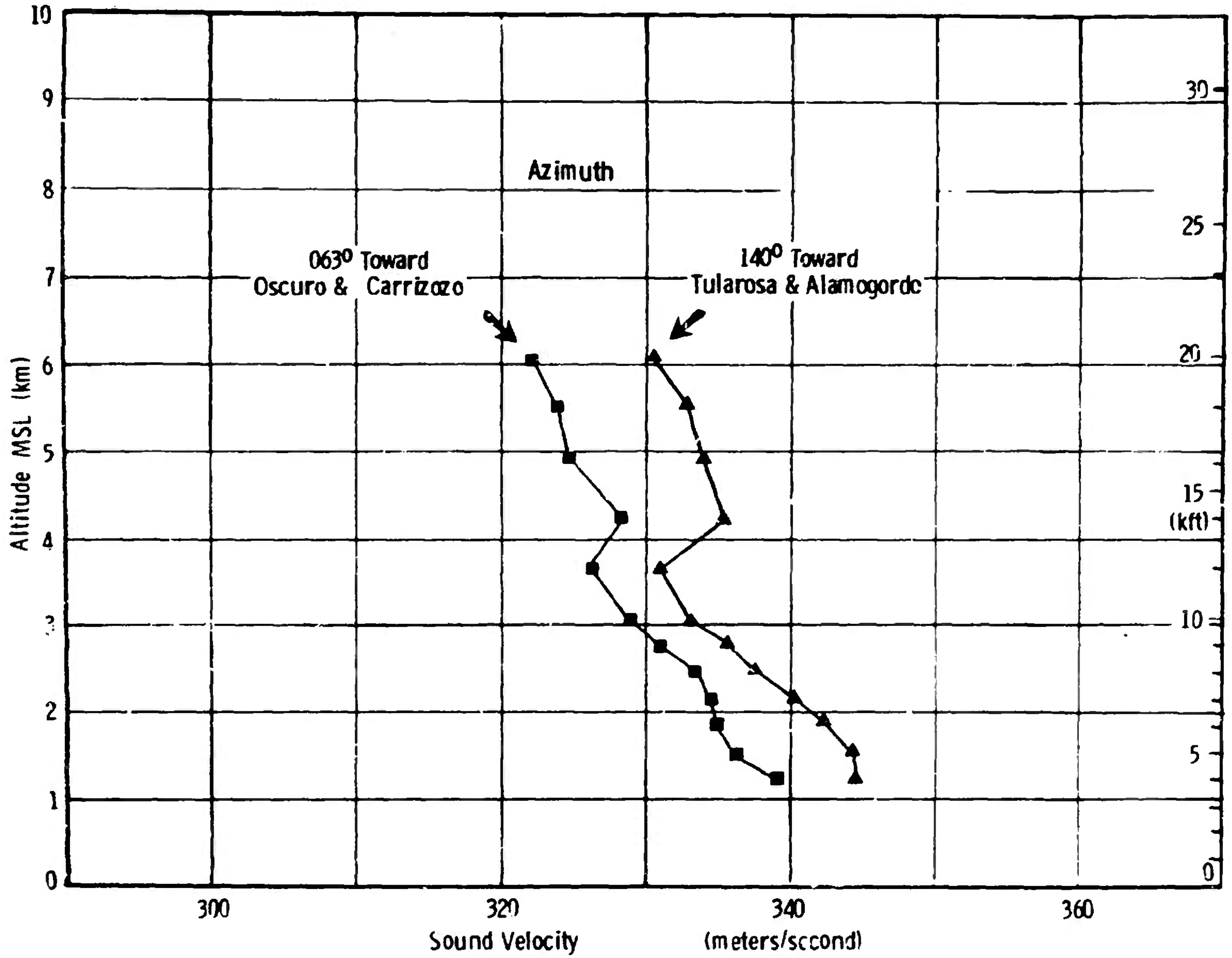

Figure 8. Pre-DICE THROW II Sound Velocities, 1200 MDT, 9/22/75.

TABLE V. PRE-DICE THROW II

Off-Site Airblast Measurements

Station	Gage	Distance (m)	Arrival Time (sec)	Arrival Velocity (m/s)	Arrival Velocity (ft/sec)	Pressure Amplitude (pascals)	Pressure Amplitude (psi)
Oscuro	TM	31,176	93	335	1100	14.96	0.00217
Carrizozo	TM	52,920	165	231	1052	12.69	0.00184
MB			169	313	1027	8.13	0.00118
Tularosa	TM	46,080	145	318	1043	13.17	0.00191
Alamogordo	TM	66,240	Recording failure; Moderate rumbles and echoes.				

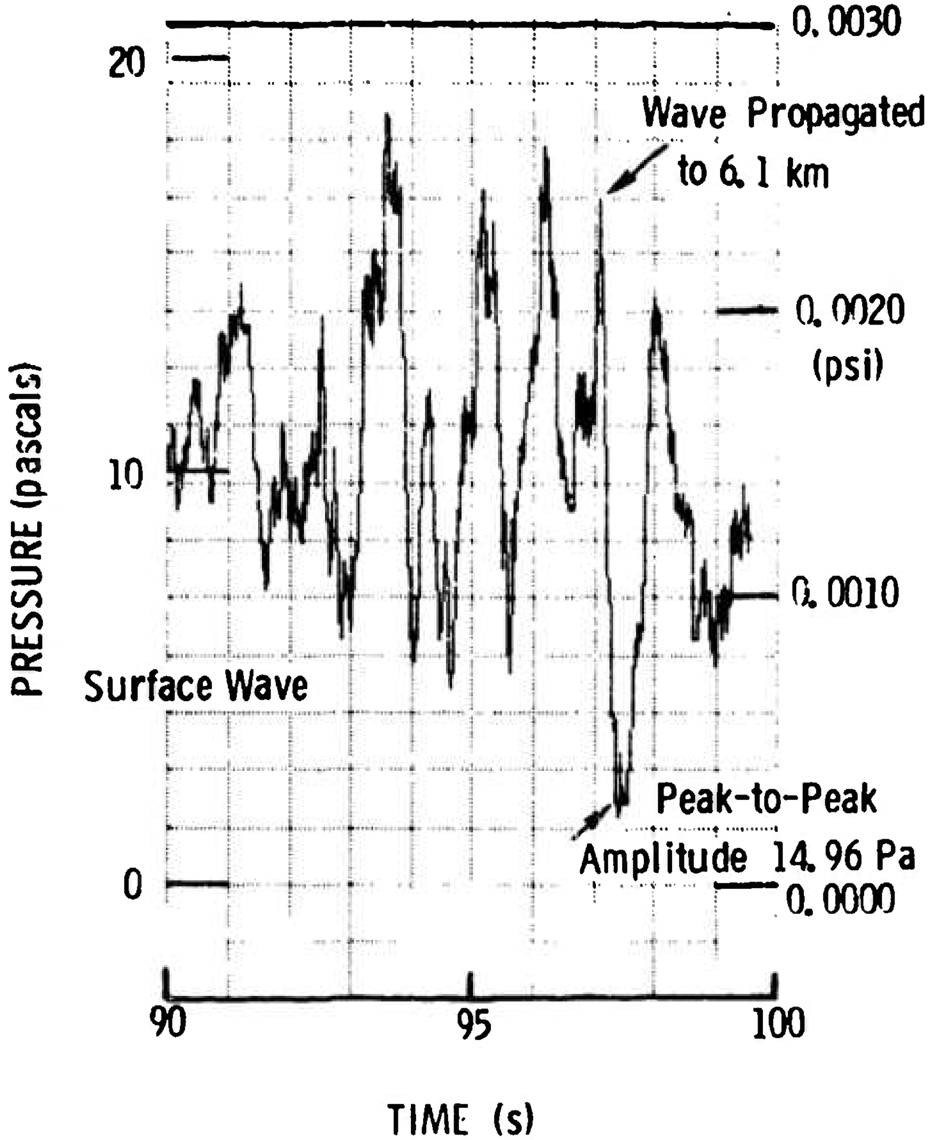

Figure 9. Pressure Gage Record, Pre-DICE THROW II, at Oscuro, New Mexico, 31.1 km Range.

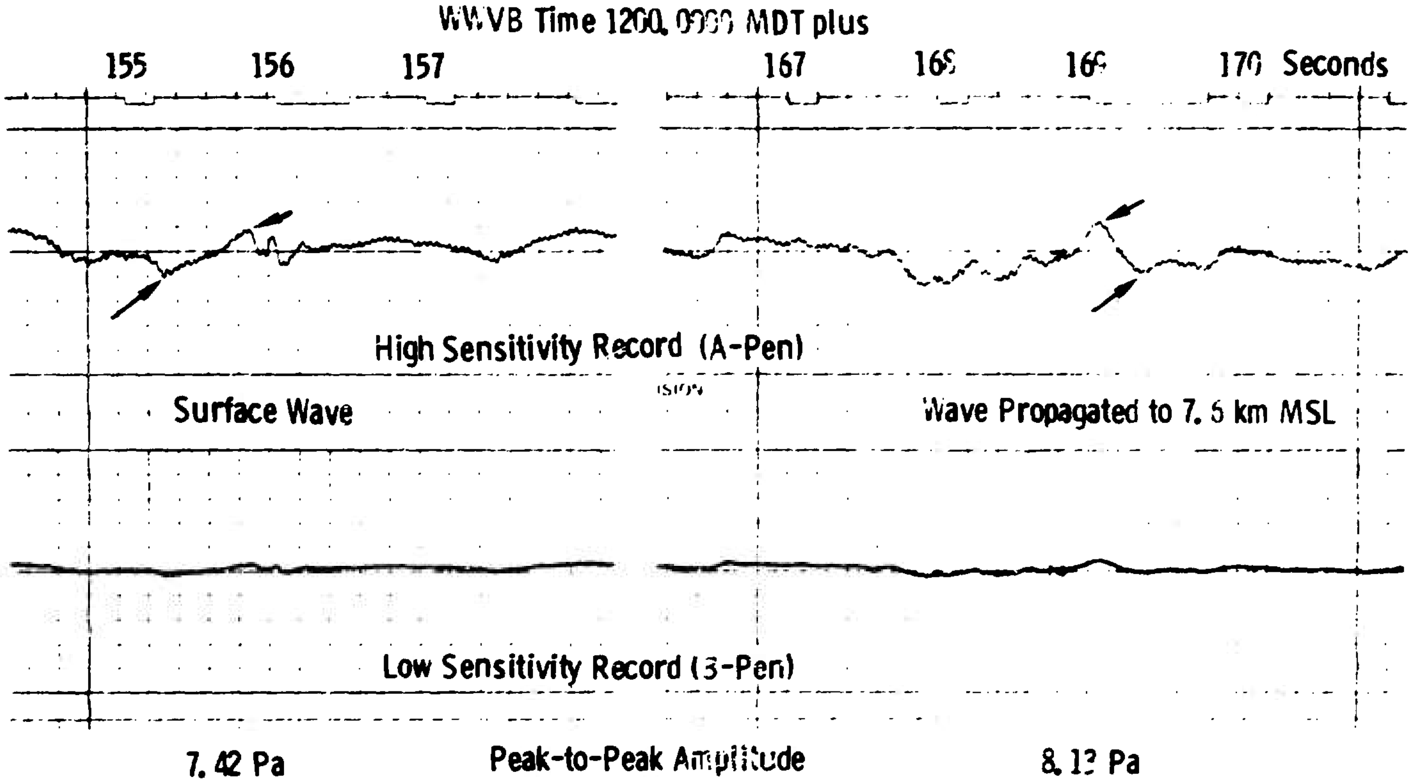

Figure 10. Microbarograph Record, Pre- DICE THROW II at Carrizozo.

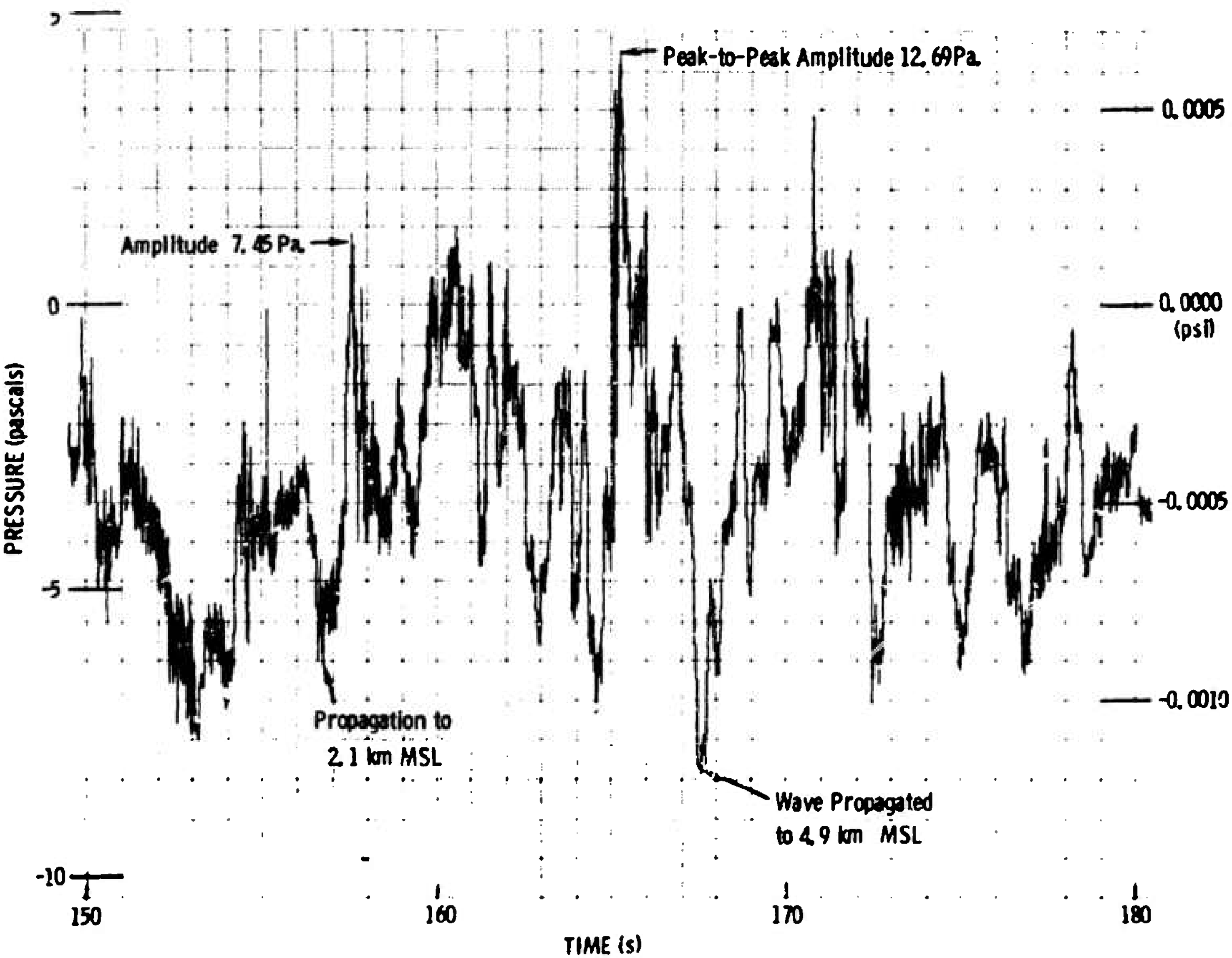

Figure 11. Pressure Gage Record, Pre-DICE THROW II at Carrizozo, New Mexico, 53km Range.

co-located, side-by-side, so there should have been better agreement. The TM timing was from the IRIG standard, while the MB set used a radio receiver on WWVB, world time transmitted from Boulder, Colorado.

There also was trouble with the Alamogordo TM record. A paper record made on-site at blast time showed only an extremely weak, possible signal from Alamogordo, but the channel did appear to have been energized. There was no indication of the easily audible signal that was reported by our technician at the gage site. There was a mix-up in tape channel identifications that we have not been able to correct to allow further playbacks.

On the other hand, ray path calculations have been made from shot time meteorological data that showed arrival times that were consistent within about 1 second for the Oscuro, Tularosa, and Carrizozo MB signals, as reported herein. Ray calculations for Pre-DICE THROW I had also confirmed arrivals from that event where Carrizozo TM and MB records were in disagreement, but the MB operation was suspect in that case. Previous comparison tests between TM and MB systems had not found such troubles.

The Tularosa record is shown in Figure 12, although this was made from a digitized playback of the Alamogordo-labelled tape track. In consequence, because of the uncertainty about which gage calibration was appropriate, reported amplitudes for Tularosa may be low by a factor of two. This would extrapolate from 26 Pa at Tularosa to about 13 Pa at the distance of Alamogordo, and explain the reported easy audibility, where half that amplitude probably would not.

Amplitude and distance data were shown in Figure 1, in comparison with prediction curves for various atmospheric propagation

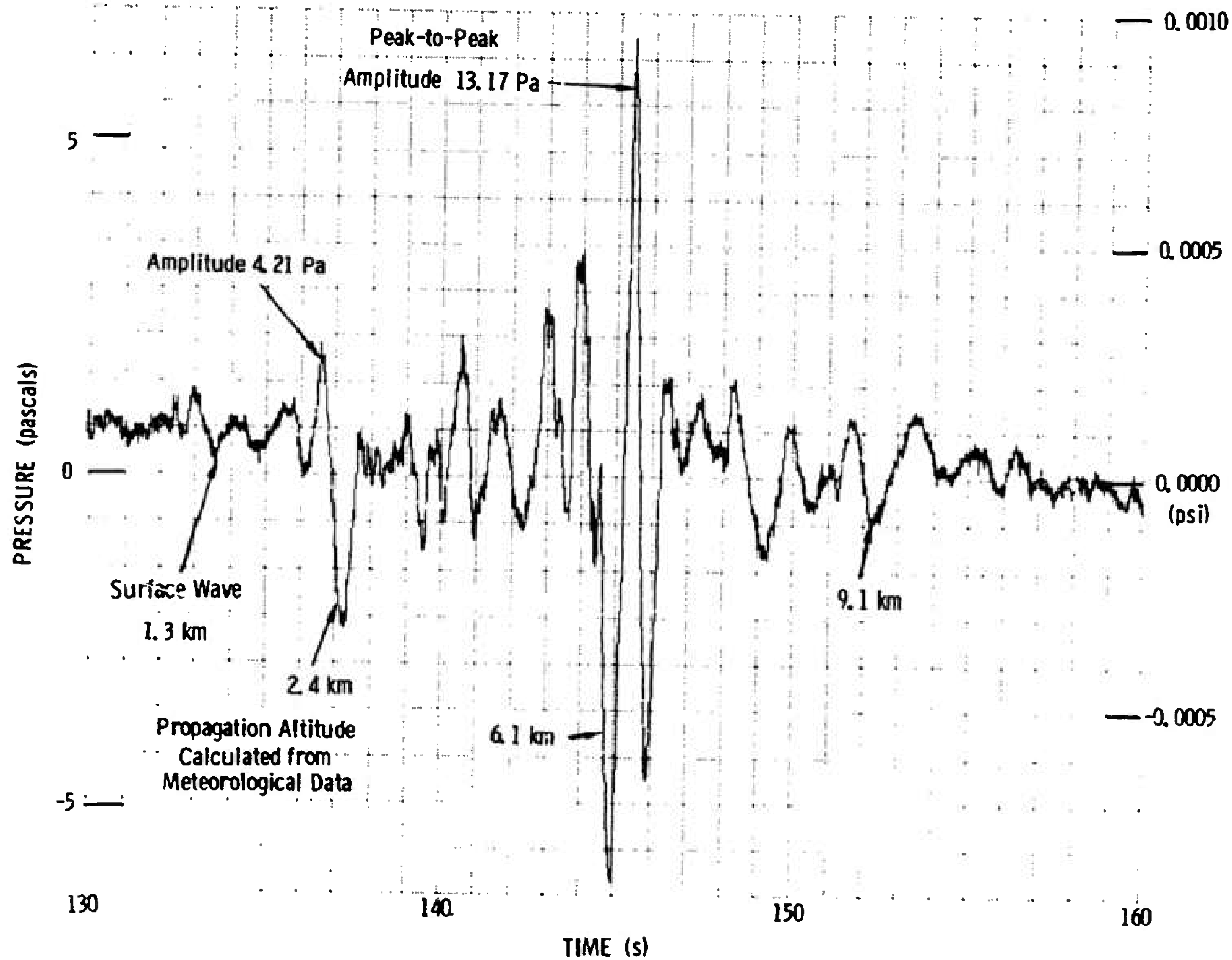

Figure 12. Pressure Gage Record, Pre-DICE THROW II at Tularosa, New Mexico, 46 km Range.

conditions. Clearly, these records show correct magnitudes for gradient propagations, as determined by meteorological input. That plot also showed that the Carrizozo MB amplitude was in better agreement (pressure-distance decay rate) with the Oscuro amplitude, on nearly the same azimuth, than was the Carrizozo TM recording. Greater propagation strength toward the SE direction may be qualitatively explained by the presence of an upper sound velocity inversion at 3.7-4.3 km MSL for the 140° azimuth in Figure 8.

Most of these details are of little practical importance to test operations, as they deal with problems of working in a low signal-to-noise environment. The important conclusion, is, of course, that recorded signals were weak, as predicted from the weather-watch. If this event had been fired just 24 hours earlier, without weather and blast prediction services, amplitudes at Oscuro and Carrizozo could have been as much as 50 to 100 times greater and caused some window breaking and public relations problems.

DICE THROW:

The schedule for weather balloon observing and blast prediction calculation was exercised during the FPFF (full power, full frequency) dry run on 10/4/76. On shot day, 10/6/76, balloon observations were made on schedule with all results shown in Table VI. There was indeed a 2.0-2.5 K surface temperature inversion, that remained from night-time cooling. Predictions on D-2 days for a southeasterly low level (2-3 km) atmospheric circulation did not materialize, because a low pressure wave had developed on an approaching polar front in Colorado. Instead, general northwesterly circulation persisted throughout the entire period from D-3 days. In result, Tularosa and Alamogordo were threatened with relatively strong blast waves, rather than Socorro and Albuquerque.

TABLE VI. DICE THROW RAWINSONDE UPPER AIR REPORTS

Tempèratures (K); Winds (deg/ms^{-1})

Shot Time Surface Pressures: 84.98kPa @ Stallion Site; estimated 85.63kPa @ DICE THROW (1442m MSL)

DAY	10/4/76, DRY RUN				10/6/76, LIVE RUN							
TIME (z)*	1300		1500		1000		1200		1250		1400 (Shot)	
Temperature/Wind	T	W	T	W	T	W	T	W	T	W	T	W
ALTITUDE MSL (km)												
Surface 1.506	281.6	CALM	228.2	330/6.7	284.1	200/3.1	282.8	CALM	282.9	230/5.1	282.9	200/2.1
1.829	283.4	350/8.8	285.7	355/8.8	286.1	235/11.3	283.0	235/7.2	285.4	230/5.1	285.1	230/7.2
2.134	281.4	350/10.3	283.2	005/8.2	286.0	260/10.3	283.2	270/7.7	285.8	270/5.1	285.6	280/6.2
2.438	279.0	340/8.8	280.6	360/7.7	283.2	290/10.3	281.4	305/8.2	283.2	290/8.8	283.6	305/7.7
2.743	276.5	325/6.7	278.3	330/5.7	280.8	295/9.8	279.0	310/9.8	280.8	305/10.8	281.2	310/10.3
3.048	274.3	290/4.6	275.7	310/4.6	278.2	295/9.3	276.4	300/12.4	278.3	320/9.3	278.7	320/10.8
3.658	269.4	250/7.2	271.1	295/6.7	272.8	300/13.4	272.3	305/13.9	274.8	310/8.2	275.2	315/11.3
4.267	266.0	250/10.3	266.4	295/7.2	269.2	315/16.0	270.4	305/15.4	272.3	320/14.9	272.3	310/15.4
4.877	259.5	270/10.8	261.5	300/8.2	269.2	320/16.0	267.0	305/9.8	268.3	305/18.5	268.6	310/19.0
5.486	256.9	290/10.3	256.9	310/8.2	263.7	320/18.0	263.1	310/19.6	263.5	305/19.6	263.9	310/19.0
6.096	251.5	305/8.8	252.0	320/10.3			257.2	315/20.1	258.8	305/20.1	258.6	310/22.1
7.010									254.0	305/21.6	254.1	315/22.7
7.620									249.2	315/24.2	249.1	315/21.6

*Greenwich Time (Z) - 6 hours = Mountain Daylight Time (MDT)

Figure 13 shows the sound velocity versus height structures at shot time toward the 095° azimuth of Carrizozo and 140°, between Tularosa and Alamogordo. There were only minor variations from the H-4 hour sounding and predictions relayed to the Test Group Director during the count-down. The Carrizozo curve showed a strong inversion ducting layer to 2.1 km MSL, but it did not extend above the Oscuro Peaks (2.4-2.7 km MSL), so they provided some protection. The high sound velocity at 5.2 km MSL apparently helped propagate a moderate strength wave into Carrizozo.

Tularosa and Alamogordo were nearly downwind from GZ, and on the 140° azimuth sound velocities increased to a maximum at 5.2 km MSL. There was a strong surface inversion to carry a wave southeast through Mockingbird Gap, as well as a complex ducting structure between 2.7 km and 4.3 km MSL that could cause distant blast focusing. Detailed acoustic ray calculations showed a caustic ring about 10 km short of the distance to Tularosa. Experience has shown that this focal range can only be predicted within several kilometers. Therefore, predictions were made that a few windows could be broken in both Tularosa and Alamogordo, but the probability of dozens being broken was quite small, depending on just where the focus or caustic wave might strike.

Propagation toward Truth or Consequences, NM, shown by Figure 14, was slightly ducted below 2.4 km MSL, but little energy could be trapped by the 0.15 m/s excess sound velocity at that height. This was not of sufficient concern to warrant moving a microbarograph to that community.

Propagation toward 320° azimuth, toward Stallion Site and Socorro, was minimized by a strong gradient of sound velocity with height. The averaged sound velocity gradient from 1.8 km MSL was $-7.6 \times 10^{-3}\ s^{-1}$, compared to the calm standard

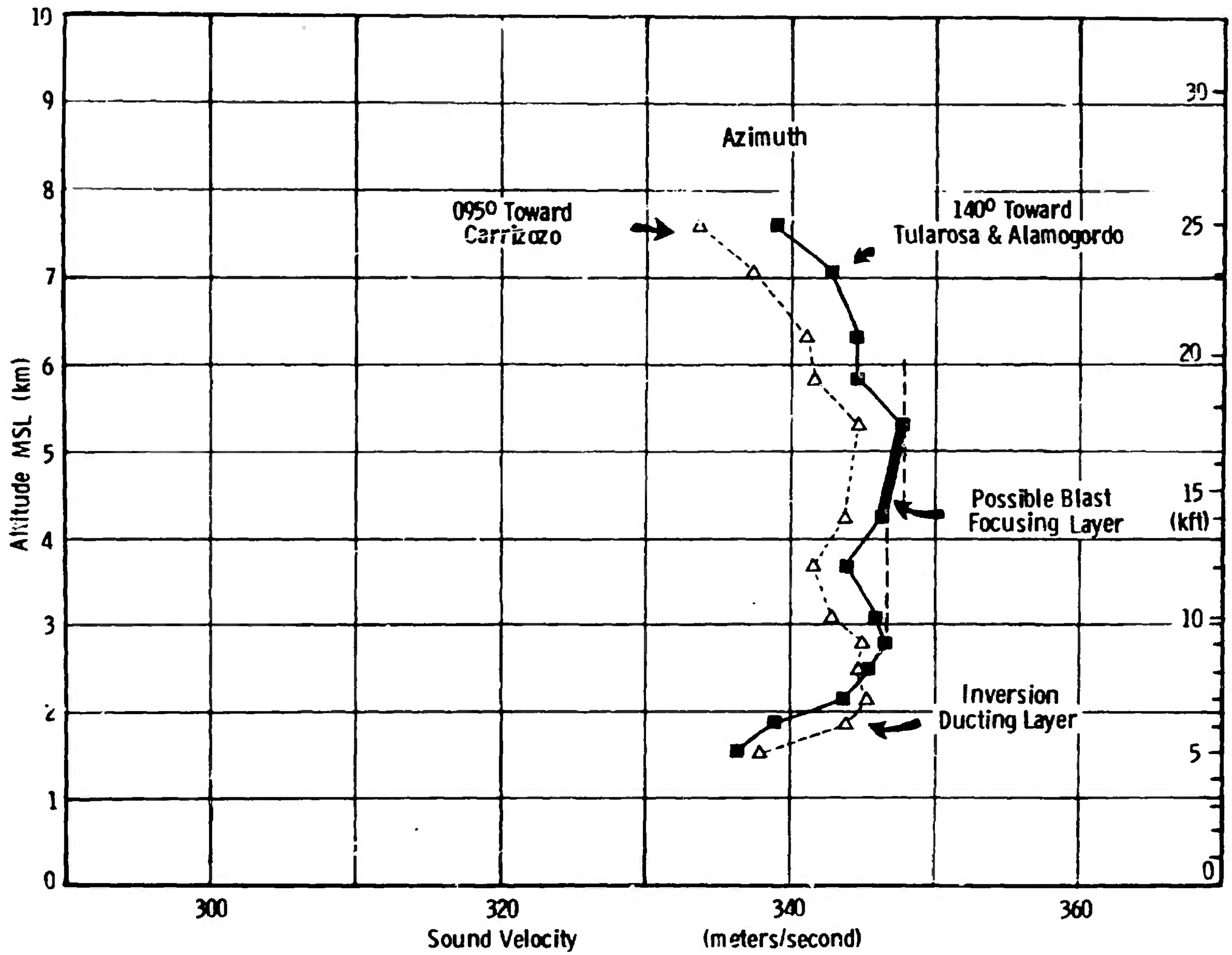

Figure 13. DICE THROW Sound Velocities Toward East Quadrants.

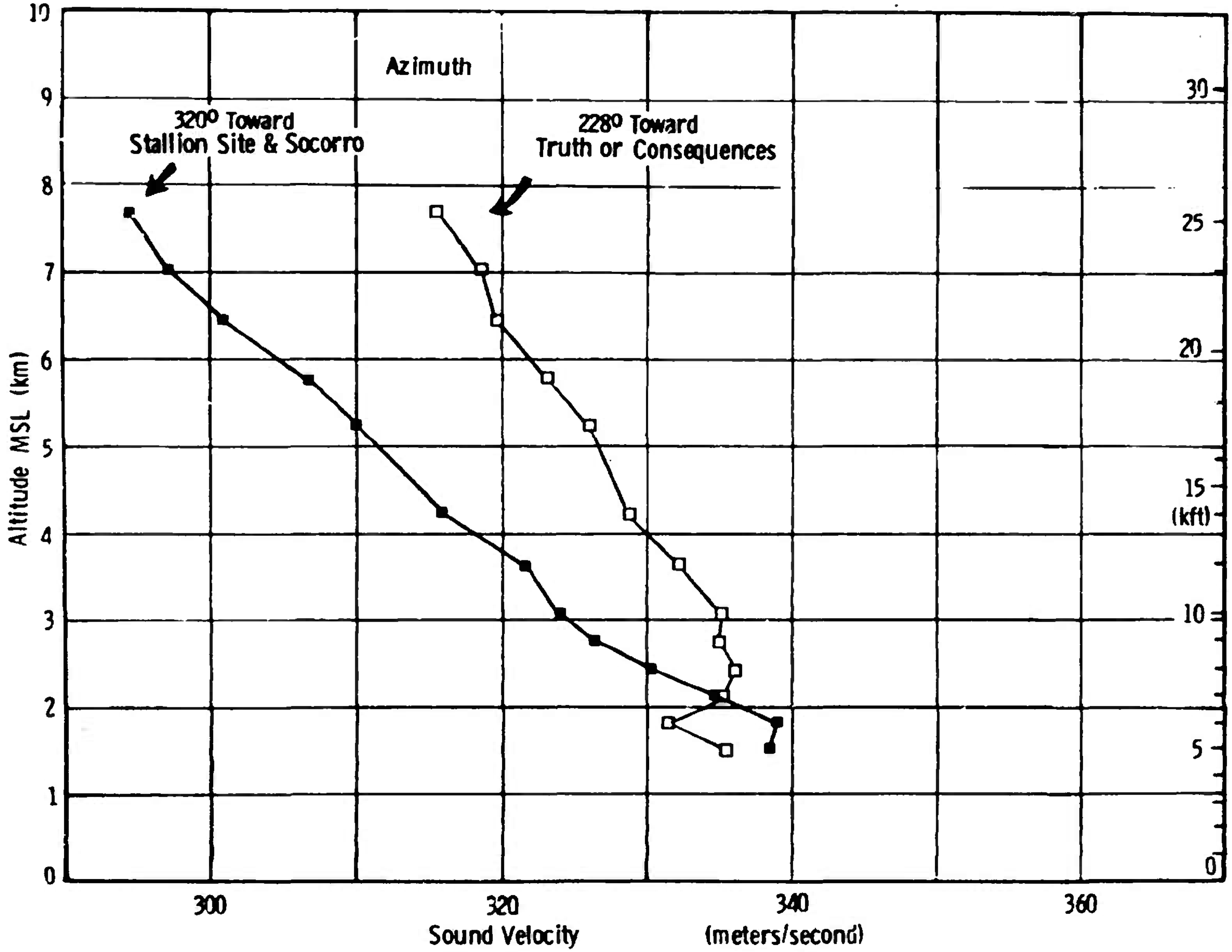

Figure 14. DICE THROW Sound Velocities Toward West Quadrants.

atmosphere gradient of -4×10^{-3} s^{-1} (0.0065 K/m). Thus, minimized propagation was expected for that direction.

Surface weather conditions at Stallion Weather Station (1506 m MSL) were not the same as at DICE THROW GZ (1442 m MSL). This elevation difference was used to estimate GZ ambient air pressure from the Stallion barometer reading given in Table VI.

Reproductions of MB recordings at the five measurement locations are shown in Figures 15-17. Numerical data are listed in Table VII. Each recorder was operated with two pens with set ranges that differed by a factor of four, as shown by Figure 16 and 17. If a signal was weaker than expected it could still be accurately measured from the "High Sensitivity A-Pen". If the signal exceeded expectations it was contained by the scale of the "Low Sensitivity B-Pen". Timing marks were made by a side-marking pen connected to a radio receiver on WWVB.

The Stallion signal consisted of a severely damped explosion waveform, from gradient propagation, followed by two sinusoidal cycles of similar frequency. There were several later cycles of much weaker echo waves that were not reproduced for this report. The 8-Hz oscillations which were superimposed on the fundamental waves probably resulted from weak temperature inversion ducting in the boundary layer which was almost, but not quite, overcome by wind effects, as was shown in Figure 14.

The Socorro record posed a problem with the late arrival time. The first indication of noise came at 159 s, in rough accord with the wave speed determined en route at Stallion. The largest amplitude wave came 50 s later but there was no possible acoustic ray path for this propagation. Ray path analysis has shown this wave probably was a collection of scattered compressions from the proper acoustic wave passing above 9 km MSL.

Figure 15.
Project DICE THROW Microbarograph Records
Shot Time 0800MDT 10/4/76

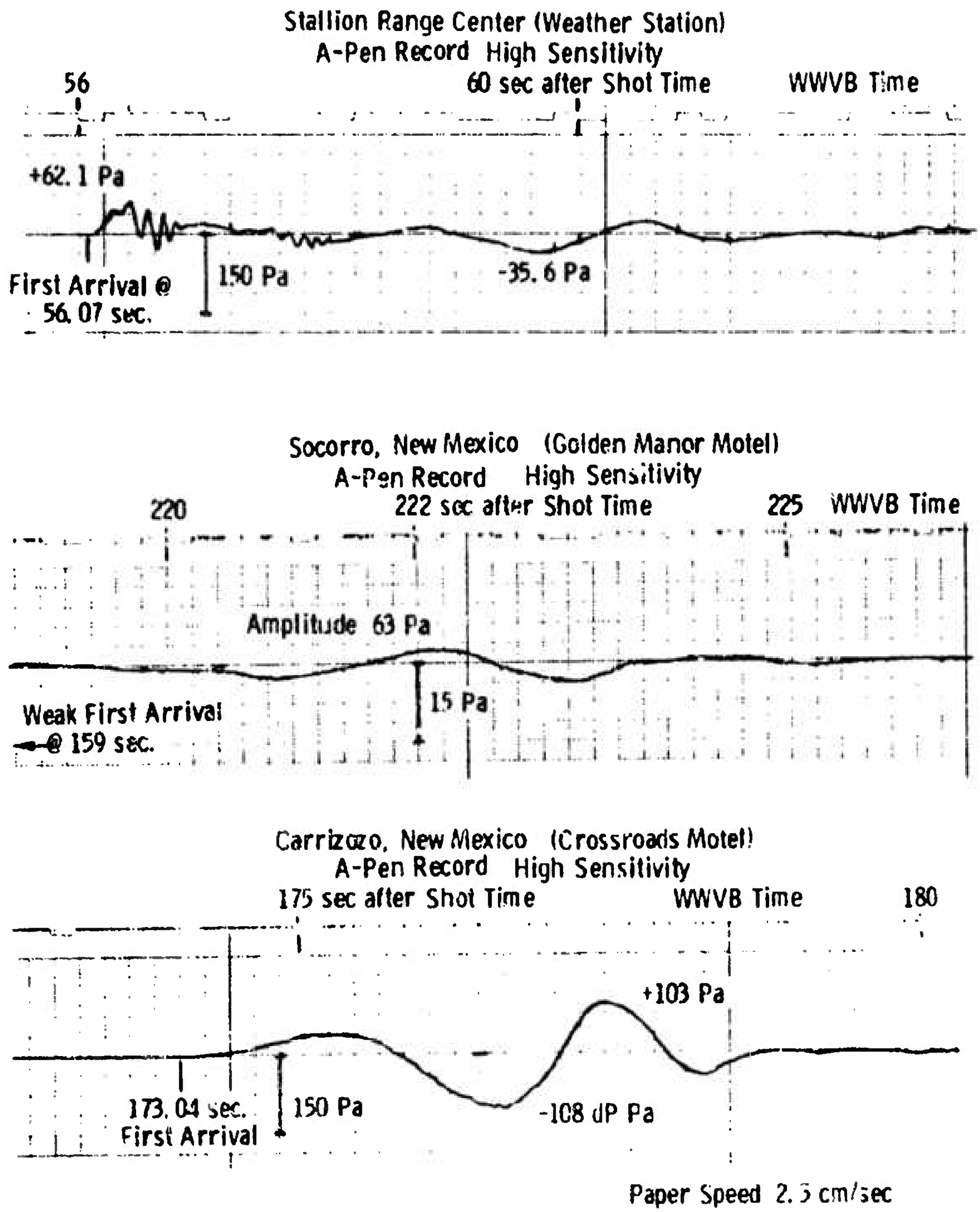

Figure 16.

Project DICE THROW Microbarograph Records

Tularosa, New Mexico (J&J Laundromat)

Shot Time 0800MDT 10/4/76

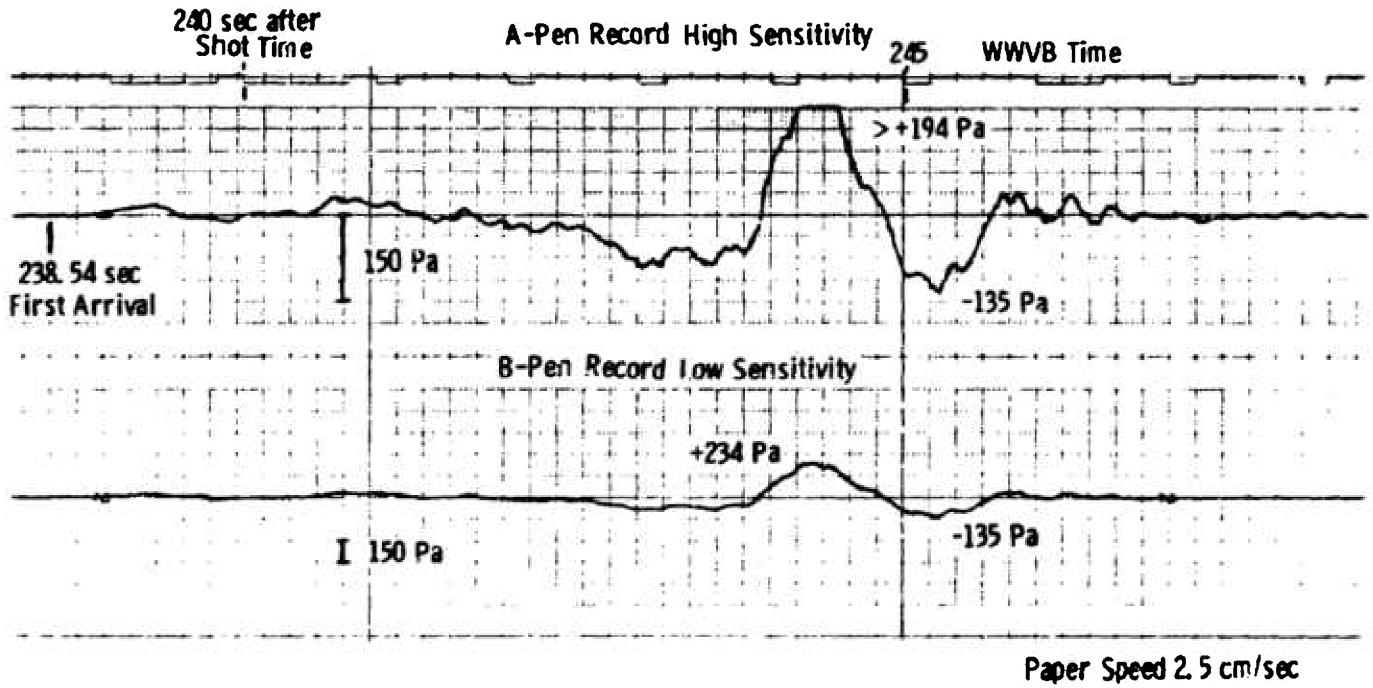

Figure 17.
Project DICE THROW Microbarograph Records
Alamogordo, New Mexico (Sanvis Motel)
Shot Time: 0800MDT, 10/4/76

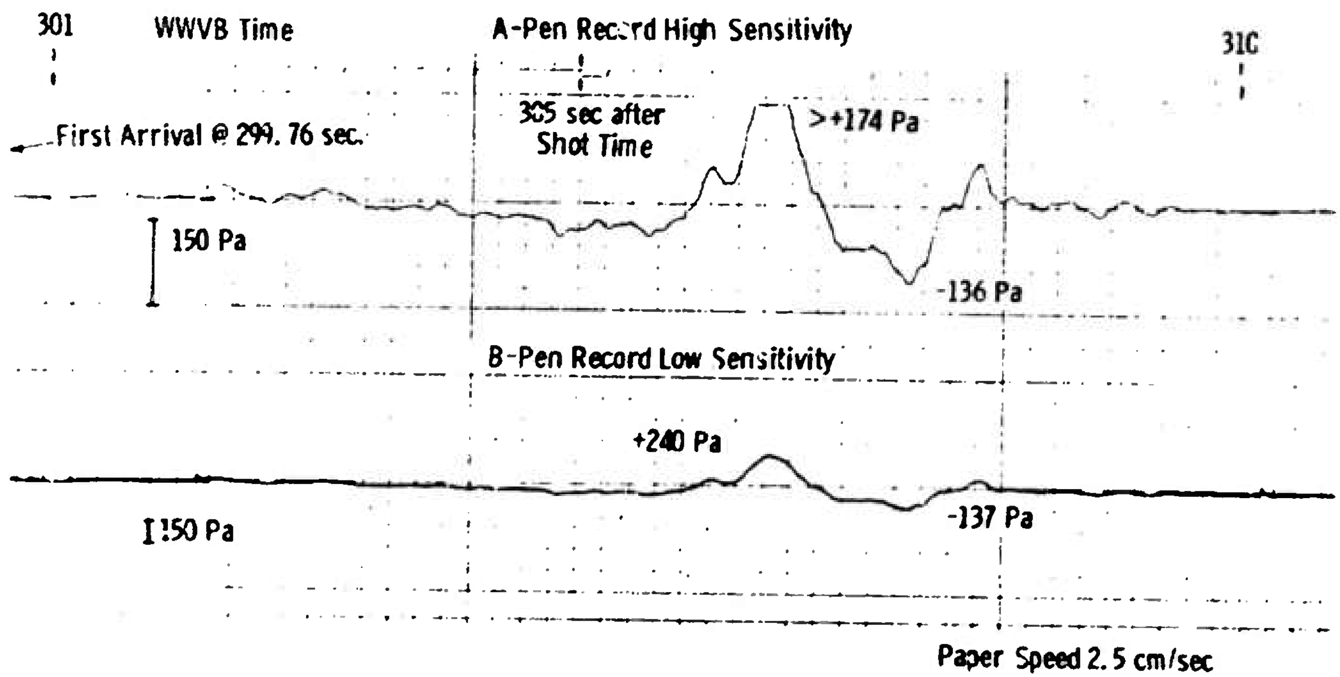

At Carrizozo the record showed two cycles of damped sinusoidal oscillation much as could be expected. Oscuro Peaks blocked any strong inversion propagation indicated by the weather data, but diffraction over Oscuro Peak appears to have been facilitated by high sound velocities up to 5.2 km MSL. Other experience has shown that mountain shielding may attenuate blast amplitudes by about a factor of two at long ranges.

Strong propagations, predicted for Tularosa and Alamogordo, were verified by recordings shown in Figures 16 and 17, respectively. The Tularosa wave went off-scale on the sensitive A-Pen but was contained by the less sensitive B-Pen recording. There does not appear to be any sign of strong magnification with a pressure spike, caused by the complex upper level ducting layer. Thus there probably was no focus or caustic that struck any part of that small town. The recorded signal with 370-Pa amplitude was noisy, easily heard, and approached the 400-Pa rule-of-thumb threshold for window-breaking waves. According to our station operator this blast wave set off a burglar alarm in a building near our sensor. Also, one resident informed him that the blast had caused a crack in his plastered wall, but he probably would not take any claims action.

The Alamogordo recording was also driven off-scale on the sensitive A-Pen, but a complete record was made by the B-Pen. The amplitude of 390 Pa was slightly higher than that recorded at Tularosa. This blast was loud at the station but our operator reported no sounds of breaking glass. A personal report from a Holloman Air Weather Service contact also reported that considerable house rattling was heard indoors but there was no damage, and little disturbance noted by children playing outdoors. This recorded wave amplitude could indeed be expected to break a few windows in so large a population (24,000 people, estimated 460,000 window panes), but no claims reports were received. Also, in the 5-km extent of that community there could have been wave focusing that was not detected by our single microbarograph sensor. This may provide a useful data point near the "threshold" for annoying cosmetic architectural damages. One previous incident in Las Vegas, Nevada, and two incidents in St. George, Utah, from atmospheric nuclear tests in the 1950's, each resulted in one window damage claim from just over 400 Pa recorded amplitudes, but the so-called "threshold" interpretation cannot be taken as well-established from such meager data.

Pressure-time signatures of waves recorded at both Tularosa and Alamogordo indicate that these large amplitudes were probably propagated by an upper level duct between 4.3 km and 5.2 km MSL.

There was a problem with arrival timing and blast wave velocity at Socorro, as shown by results in Table VII. It appeared that waves traveled faster upwind toward Socorro than downwind toward Alamogordo. Explanation may lie in erroneous mapping. If the map distance from GZ to Stallion were reduced by 508 m (2 1/2%), the recorded arrival time would be consistent with the 339 m/s surface velocity of Figure 14. This incremental distance, added to the Alamogordo map distance, would give 342 m/s wave velocity, consistent with maximum propagation speed under the inversion in Figure 13. With such sensitivity to location, surveyed station sites, detailed ray path time calculations, and time correction for strong shock source conditions would be required to reach full internal consistency in results.

Pressure amplitudes shown by the microbarograph records were entered on the pressure-distance graph of Figure 2 for comparison with planning predictions. Amplitudes along the 320° azimuth to Socorro were much below even an average gradient curve. The

TABLE VII. DICE THROW MICROBAROGRAPH AIRBLAST MEASUREMENTS

Station	Azimuth	Distance (km)	Arrival Time (sec)	Arrival Velocity (ms^{-1})	(ft/sec)	Pen	Pressure Amplitude (pascals)	(psi)
Stallion	321°	19.17	56.07	339.3	113	A	97.73	0.014
						B	100.96	0.015
Socorro	320°	55.81	159.00	350.1*	1149	A	First detectable arrival	
			164.35	338.7	1111	A	1.13	0.00016
			197.40	282.7	927	A	First late arrival	
			222.00	251.4	825	A	6.26	0.00091
			222.00	251.4	825	B	6.30	0.00091
Carrizozo-I	095°	60.44	174.04	346.4	1136	A	211.6	0.0307
			174.04	346.4	1136	B	217.9	0.0316
Carrizozo-II			[illegible].04	346.4	1136	A	220.1	0.0319
			174.04	346.4	1136	B	260.2	0.0377
Tularosa	144°	81.50	238.54	341.0	1119	A	First arrival	
			244.30	333.6	1094	A	>329.5	>0.0478
			244.30	333.6	1094	B	369.0	0.0535
Alamogordo	148°	102.51	299.76	341.5	1120	A	First arrival	
			306.43	334.1	1096	A	>309.8	>0.0449
			306.43	334.1	1096	B	377.1	0.0547

*Stallion arrival speed would give 54.09 km range, 1.72 km short of map location.

actual sound velocity gradient toward 320° was indeed stronger than the average gradient encountered in other ducting test environments. The isolated point representing the wave scattered from high altitude down to Socorro also fell well below the gradient curve. Amplitudes from the two MB sets operated at Carrizozo fell almost exactly on the Standard curve, but that is a coincidence of little significance. Lacking the mountain barrier of Oscuro Peaks, appreciably larger amplitudes would have been expected at that station. Both Tularosa and Alamogordo amplitudes were near the upper limit of expectations for inversion propagations but below likely caustic or focus amplitudes. Focus factors at those two stations were about 2.5X and 3.5X above the Standard, and entirely reasonable for the strong propagations indicated by weather data. Both points fell below the window-breaking threshold but with no significant margin of safety. Some windows may have been broken under these conditions. There should not, however, have been any hazard from flying glass, because the breaks would not likely have be more than cracks, with little likelihood of even falling glas

CONCLUSIONS

The Project DICE THROW explosion airblast wave could have broken windows and cracked interior wall plaster to more than 100-km ranges under weather conditions that caused refractive blast focusing. Weather observations showed that there should have been relatively strong propagations toward the southeast and weak propagations toward the northwest. Microbarograph recordings verified these propagation conditions and that wave amplitudes in Tularosa and Alamogordo were large enough to rattle houses, possibly causing some damage. No audible wave was propagated in the opposite direction to the shorter distance of Socorro. Weather observations, blast predictions, and off-site measurements were all performed successfully by, or in support of, this project.

REFERENCES

1. Gould, K. E. and Perry, G. L. E., "Environmental Impact Assessment for the DICE THROW High-Explosive Field Test Program," DASIAC ES 75-1, General Electric-TEMPO, Santa Barbara CA, 7 February 1975 (draft).

2. Strode, J. D., Letter to Distribution, FC-DNA, KAFB-E NM, 17 March 1977.

3. Reed, J. W., "Blast Predictions and Microbarograph Measurements," Project MIXED COMPANY Final Report POR-6603, Sandia Laboratories, KAFB-E NM, October 1973.

4. Reed, J. W., "Distant Airblast Predictions for Explosions," Minutes of the 15th Explosives Safety Seminar, Vol. II, DOD-ESB, Washington, DC, September 1973.

5. Reed, J. W., Pape, B. J., Minor, J. E. and DeHart, R. C., "Evaluation of Window Pane Damage Intensity in San Antonio Resulting from Medina Facility Explosion on November 13, 1963," Annals of the New York Academy of Sciences, 152, Art. 1, October 1968.

6. Needham, C. E., Havens, M. L. and Knauth, C. S., "Nuclear Blast Standard (1 kt)," AFWL-TR-73-55 (Rev.), Air Force Weapons Laboratory, KAFB-W NM, April 1975.

7. Reed, J. W., "Airblast Waves from Contained Underground Explosions," SC-RR-71-0512, Sandia Laboratories, Albuquerque, NM, December 1971.

13. EVENT DICE THROW - INDUSTRIAL EQUIPMENT SURVIVAL/RECOVERY FEASIBILITY PROGRAM

by

Edwin N. York

The Boeing Aerospace Company

[previously published as DNA 4192F]

14. FEDERAL REPUBLIC OF GERMANY STRUCTURES TEST PROGRAM - EVENT DICE THROW

by

James M. Watt, Jr., Major Gerhard Zahlmann,

and Robert A. Cole

U.S. Army Engineer Waterways Experiment Station

[previously published as WES Technical Report N-77-2]

15. AIRCRAFT SHELTER TESTS IN THE DICE THROW EVENT

by

Capt. Harry T. Webster
Air Force Weapons Laboratory,
Civil Engineering Research Division

[also published as AFWL-TR-77-1]

AIRCRAFT SHELTER TESTS IN THE DICE THROW EVENT

INTRODUCTION

In the early 1960 time frame, an intensive effort began within the Air Force to develop a protective arch shelter for tactical aircraft. The prime impetus for shelter development at that time was the need to protect parked aircraft at Southeast Asia (SEA) installations.

Early tests sought to define an optimum configuration of arch structure and protective cover. Later, when the requirement for hardened shelters was defined by O for European theater airbases, the shelter previously designed and deployed in SEA was adapted for construction at NATO installations throughout Europe.

The introduction of newer and larger aircraft such as the F-111 and F-15 necessitated modification of the basic 48 foot arch. Therefore, the Second Generation Shelter was developed to have an elliptical shaped 82 foot span. Later a Third Generation Shelter was also developed from the basic configuration and has a 71 foot span. It should be noted that while the overall shelter geometry was modified to provide larger span arches, the wall material cross-section was not changed from the basic 18-inch thick minimum concrete cover.

Recognizing the liklihood of future requirements to upgrade existing aircraft shelters to defeat a more serious conventional weapons threat, the AFWL initiated two concurrent research efforts during FY74. The efforts were for conceptual design studies directed toward developing an upgraded closure system and an upgraded arch sidewall. These efforts were successfully completed and both upgrades were tested in the DICE THROW event as was the basic 48 foot arch shelter.

During this same time frame, the Boeing Corporation developed a completely new aircraft shelter concept under their IR&D program. AFWL later initiated a contract with Boeing for the design and test plan of a 1/3 size model of this new concept. This model was later tested in the DICE THROW event.

The closest of the four models to be tested in the event was the Hardened Flush Aircraft Shelter (HFAC) developed by the Boeing Corporation (TBC). The shelter was located 90 meters from ground zero (GZ), with an expected incident overpressure level of approximately 265 psi.

The upgraded shelter arch and the upgraded closure were both located 150 meters from GZ with an expected incident overpressure of approximately 65 psi.

The unupgraded or prototype shelter arch was located 180 meters from GZ with an expected incident overpressure of approximately 35 psi.

All four of the test models were located at ranges where preliminary predictions indicated measurable inelastic response of the shelters would occur due to the airblast loads. Complete failure of the structures was not expected or desired.

Shelter B, the Unupgraded arch was a modified 1/3 size model as were the other three aircraft shelter models. Shelter B was 10.4 m in long with a 5.4 m span. The standard USAF aircraft shelter cross-section, consisting of a steel corrugated liner with a minimum 18 inch concrete cover was scaled down by 1/3 and the steel liner was simulated with the use of a concrete T-beam. This was done on all three of the arch structures, as a cost savings. It would have been extremely costly to have had specially fabricated 1/3 size steel corrugated liners. The purpose of testing this model was for a direct comparison with the upgraded arch. The model was also tested to provide correlation between the DICE THROW event and the full size standard aircraft shelter tested in the MIXED COMPANY event (500 ton TNT). The scale models tested in MIXED COMPANY were located at 500 and 600 feet from ground zero side-on to the airblast.

Shelter C, the Upgraded Arch was slightly longer (11.7 m) and wider (7.85 m) than Shelter B. Shelter C had the same basic arch cross-section as Shelter B with the addition of a concrete overlay. The overlay was not bonded to the basic arch. The model overlay was .5 m (20 inches) at the crown and flared to 1.2 m (4 ft) at the foundation. This would scale up to 1.5 m (60 inches) at the crown and 3.6 m (12 ft) at the foundation of a full size shelter. The upgrade was the result of prior conceptual studies, design, and testing. Much of this work was accomplished through AFWL/DE and the Naval Weapons Center at China Lake, California. The goal of the upgrade was increased to survivability of the shelter to conventional weapons, while recognizing that any significant upgrade, if properly designed could also enhance the blast resistance of the structure to a tactical nuclear environment. Several upgrade techniques were developed; the concrete overlay upgrade was chosen for testing in DICE THROW because it seemed the most viable upgrade concept considering available land area and economic conditions in Europe.

Both Shelters B and C were placed side-on to the blast as the worst case condition and for direct comparison with each other, as well as with the shelters tested in MIXED COMPANY.

The actual incident airblast pressure received by Shelters B and C were very close to the predicted incident over pressures of 35 psi and 65 psi incident. The peak reflected pressure on the GZ side of Shelter B was approximately 220 psi, while the corresponding pressure for Shelter C which was at a much higher incident overpressure was only 290 psi. This illustrates the upgraded shelter is obviously more aerodynamically shaped than the unupgraded shelter.

The peak horizontal displacements, derived by integrating velocity gages were in general much higher for Shelter B, than Shelter C. The horizontal displacement of the crown of Shelter B was approximately 170 mm away from GZ. The horizontal displacement of the crown of Shelter C was only about 65 mm away from GZ. Shelter C appeared to be much stiffer than Shelter B from the displacement data.

These same trends were also noted when comparing the strain of the two arches. In general the strains in Shelter C remained below the elastic limit, while those in Shelter B normally exceeded the elastic strength of the reinforced concrete.

Post-test observations of Shelter C showed it to have only minor damage. Minor cracks were noted on the leeward exterior surface of the arch. Minor tensile cracks were also noted on the interior arch surface at the 45 degree point on the windward side of the arch. These cracks were at most 1-2 mm wide running longitudinal with the arch.

Post-test observations of Shelter B indicated considerable inelastic response occurred with resulting large extensive cracking and spalling. The most severely damaged portion of the arch was the stiffener collar, on which the shelter door is normally attached. This collar, or ring inside the arch makes the arch much less flexible at this location. Severe cracking occurred on the collar with some of the crack being over 75 mm wide. Large spalls were noticeable, revealing the reinforcement and several large pieces of the concrete collar had become completely separated and had fallen. Severe longitudinal cracking at the 45 degree point on windward side of the arch was evident. Severe cracking and distress was also evident on the exterior of the arch. The rear wall of the shelter was partially separated from the arch. Severe longitudinal cracking was noticeable on the leeward side of the arch at approximately the 45 degree point. An extremely large circumferential crack was observed immediately in front of the stiffener collar. A somewhat smaller crack was also noticeable immediately behind the collar. It appeared that the middle of the arch between the end wall and the stiffener had deformed relatively more than the remainder of the arch. This again would indicate that the area of the arch adjacent to the collar was much less flexible than the remaining arch.

Shelter A, consisted of a shortened 1/3 size standard (48 ft span) aircraft shelter arch supporting the newly developed hi-threat closure system. Prior aircraft shelter studies and tests (MIXED COMPANY) have shown the present closure to be much less capable of protecting sheltered aircraft than the arch wall. The closure tested in this event was developed as a result of these earlier efforts. It was designed to afford the same protection level to sheltered aircraft as the arch wall.

The closure consists of a massive one-piece reinforced concrete slab with reinforcing webs along the outer edge and at the center line. The closure is designed to roll on roller units located in a foundation trench across the face of the arch. The closure model tested in this event weighed approximately 15 tons. This would scale up to 375 tons for a full size closure.

The closure was located face on to the airblast at a range of approximately 65 psi (.5 MPa) incident overpressure. The maximum peak reflected pressure on the face of the closure occurred on a panel near the bottom rib of the closure. This peak pressure was approximately 520 psi (3.5 MPa).

An acceleration gage at approximately mid-height on the back of the closure registered peak accelerations of approximately 240 g's. Other integrated accelerators and velocity gages recorded peak longitudinal displacements of the closure into the arch wall of about 250-300 mm.

Post-test observation of closure indicated its general response was to move upward with the top of closure moving towards the shelter arch and the bottom of the closure moving away from the arch and coming to rest on the top of the foundation slot. Some permanent inelastic deformation was also noted in the center rib and panels of the closure. Some shear failure was also observed in the closure panels. It also appeared that the front of the arch wall may have lifted and pulled out of the foundation key.

The inelastic response of the closure did not appear to be sufficient to have prevented post-test opening. However, sufficient rigid-body displacement of the closure did occur to prevent it from being opened after the test. No attempt was made to move the closure back into the foundation slot and open it post-test.

The Hardened Flush Aircraft (HFAC) Shelter concept was originally developed by the Boeing Company (TBC) under their IR&D program. AFWL later accepted the concept as having strong potential as an advanced aircraft shelter.

The Boeing HFAC shelter is a compact building design which solves the problem of aircraft access by the use of a roof elevation system and an aircraft elevation system allowing vertical access for the aircraft. This vertical access technique allows vertical columns to be placed such that the 24 m (80 ft) roof span is broken up into three 8 m (26 ft) spans. Consequently, a flat plate roof design is possible.

The HFAC shelter was designed for a composite aircraft and can provide shelter for the following aircraft: F-4, F-15, F-16, F-101, F-105 and the F-111. The shelter also provides space for equipment rooms and personnel living areas.

A 1/3 size model of this system without the aircraft parking platform or the two elevator systems was tested in the DICE THROW event. The model was placed 90 m from GZ, with an expected incident overpressure of 265 psi.

As Shelter D was flush with the ground there was no reflected pressures. The incident overpressure on the structure varied from 270 psi on the GZ side to 250 psi on the other side.

The motion of the movable roof of the shelter was initially downwards followed by an upward rebound. As expected the motions became more severe as one moved further from the vertical columns.

The flexure caused by this movement of the roof was responsible for some cracks on the surface of the roof. These cracks ran perpendicular to the blast and were approximately 2.5 m in length and as wide as 10-15 mm.

Post-test visual observation of this test model indicated it sustained only very minor damage. Damage inside the shelter was limited to minor cracks and one large spall on the fixed cantilever roof. A large steel frame placed in the shelter to support hydraulic jacks for lifting the movable roof was displaced on 6 mm by the shock. The pre- and post-test lifting of the roof required approximately the same force. There were also some external diagonal cracks at the top corners of the walls towards GZ.

In summary, the aircraft shelter experiments in the DICE THROW event were very successful. A data recovery rate of 86% was obtained from the approximately 300 data channels which were installed and recorded by AFWL personnel. The test results validated the upgraded arch and closure concepts and these will be kept ready should the requirement to upgrade existing shelters ever develop. The HFAC shelter's potential as an advanced shelter to protect against much higher threat levels was demonstrated.

This has only been a very preliminary assessment of the test results. One contract is underway and two other contracts are in the process of being negotiated for a detailed analysis of the test results.

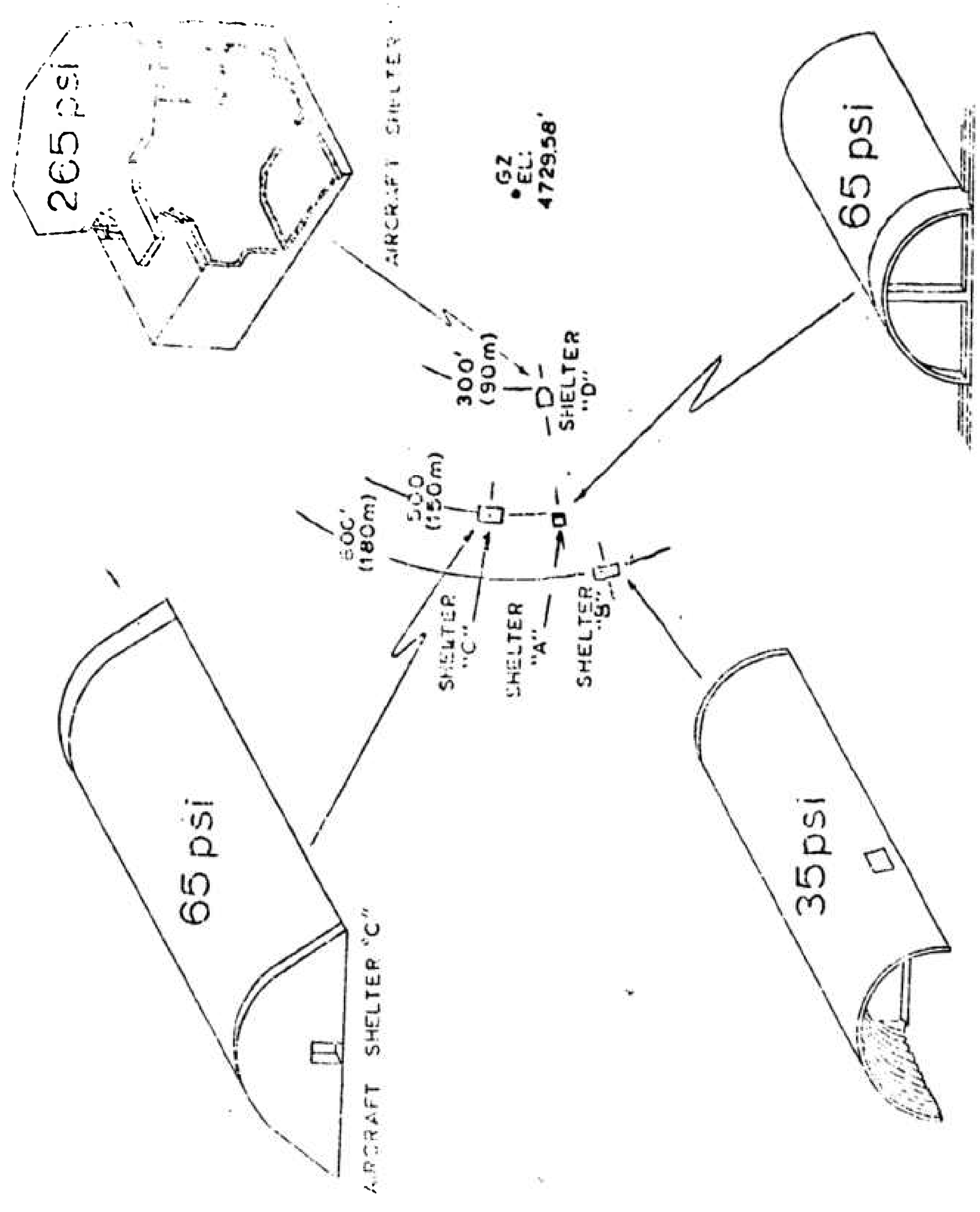

265 psi
AIRCRAFT SHELTER
GZ
EL:
4729.58'
65 psi
AIRCRAFT SHELTER
300' (90m)
SHELTER "D"
500' (150m)
600' (180m)
SHELTER "C"
SHELTER "A"
SHELTER "B"
65 psi
AIRCRAFT SHELTER "C"
35 psi
AIRCRAFT SHELTER "B"

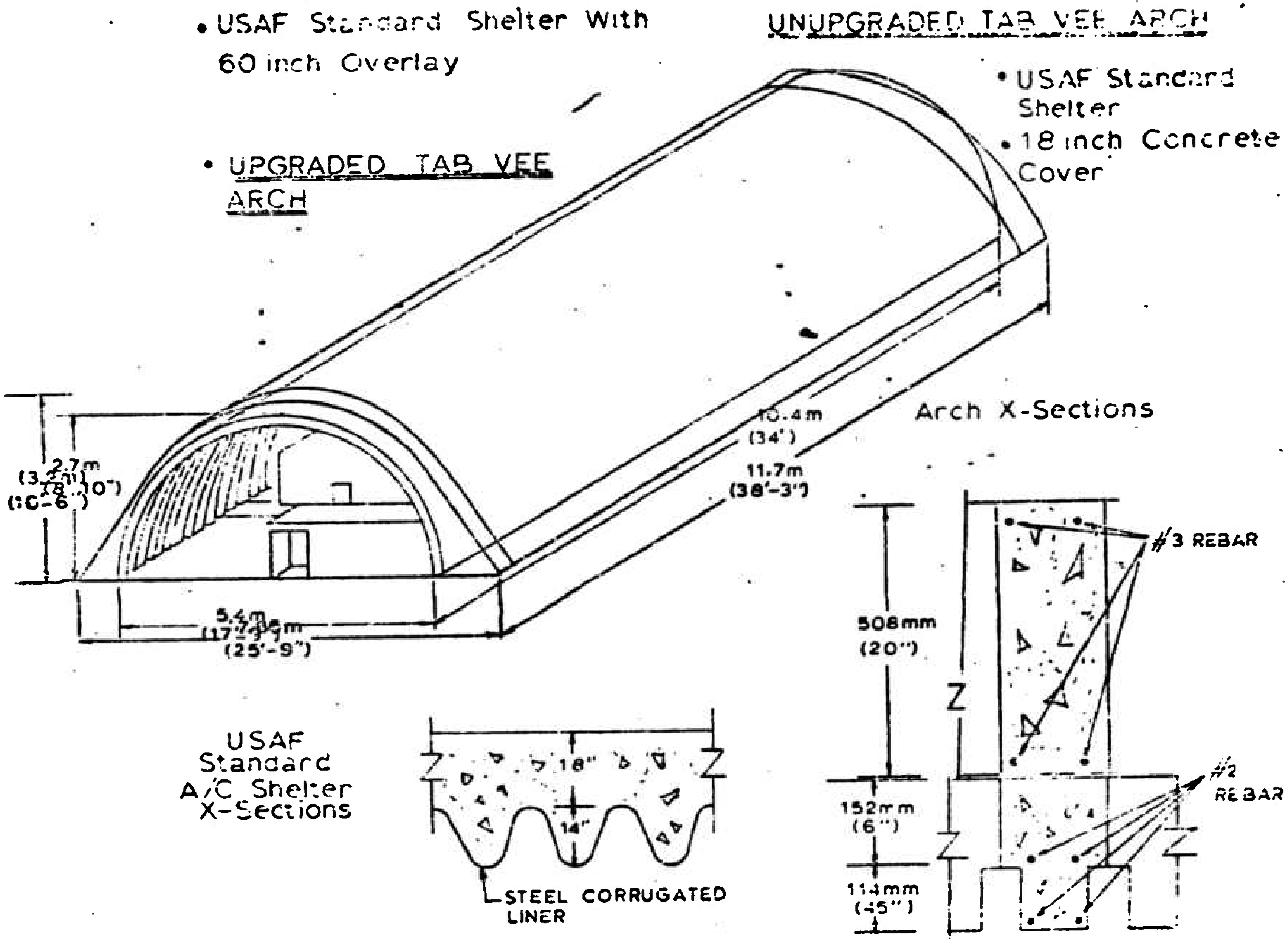

• USAF Standard Shelter With
60 inch Overlay
• UPGRADED TAB VEE
ARCH
UNUPGRADED TAB VEE ARCH
• USAF Standard
Shelter
• 18 inch Concrete
Cover
2.7m
(8'-10")
(10'-6")
5.4m
(17'-9")
7.85m
(25'-9")
10.4m
(34')
11.7m
(38'-3")
Arch X-Sections
#3 REBAR
508mm
(20")
152mm
(6")
114mm
(4.5")
#2
REBAR
USAF
Standard
A/C Shelter
X-Sections
18"
14"
STEEL CORRUGATED
LINER

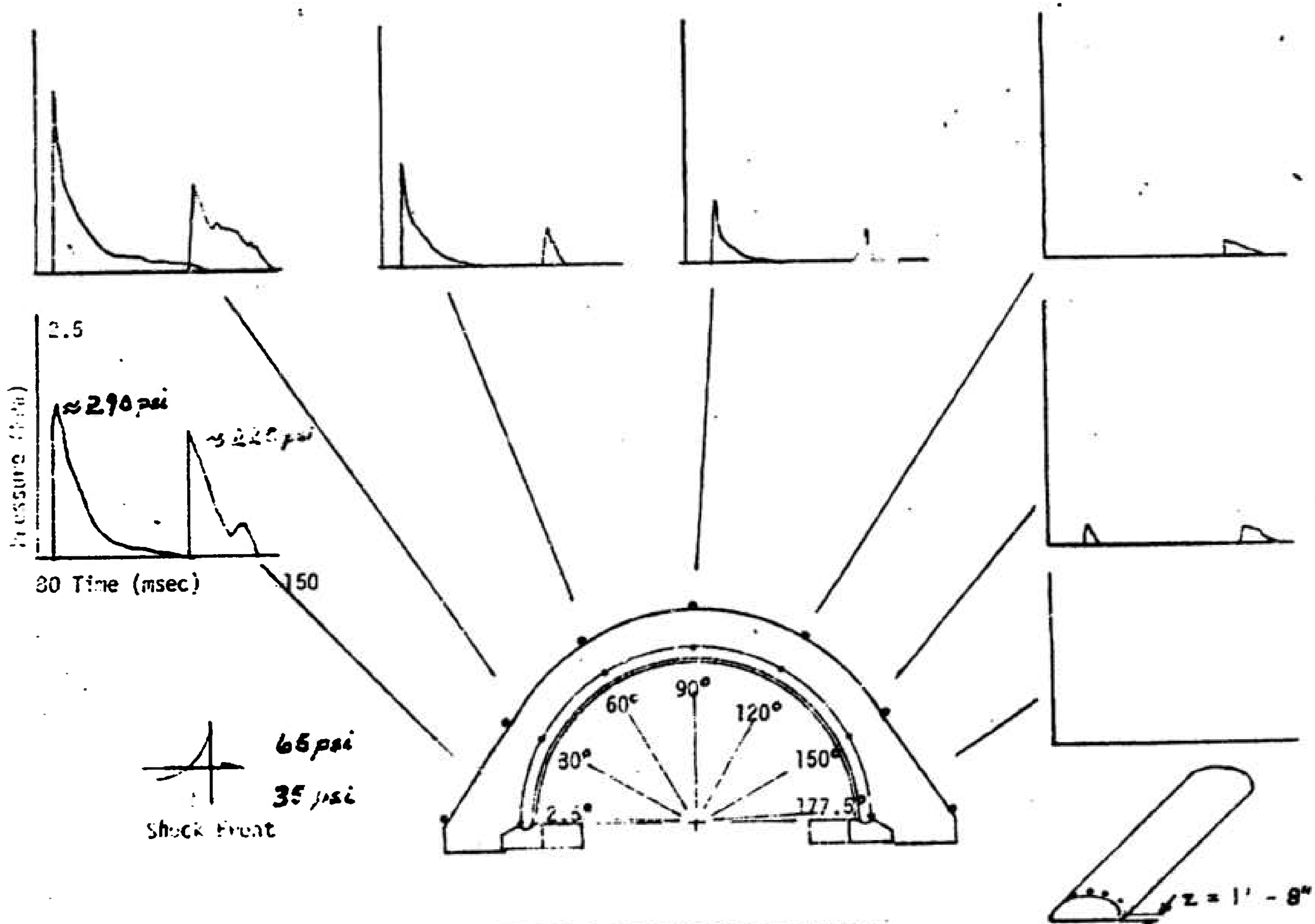

SHELTER B PRESSURE-TIME HISTORIES
SHELTER C PRESSURE-TIME HISTORIES

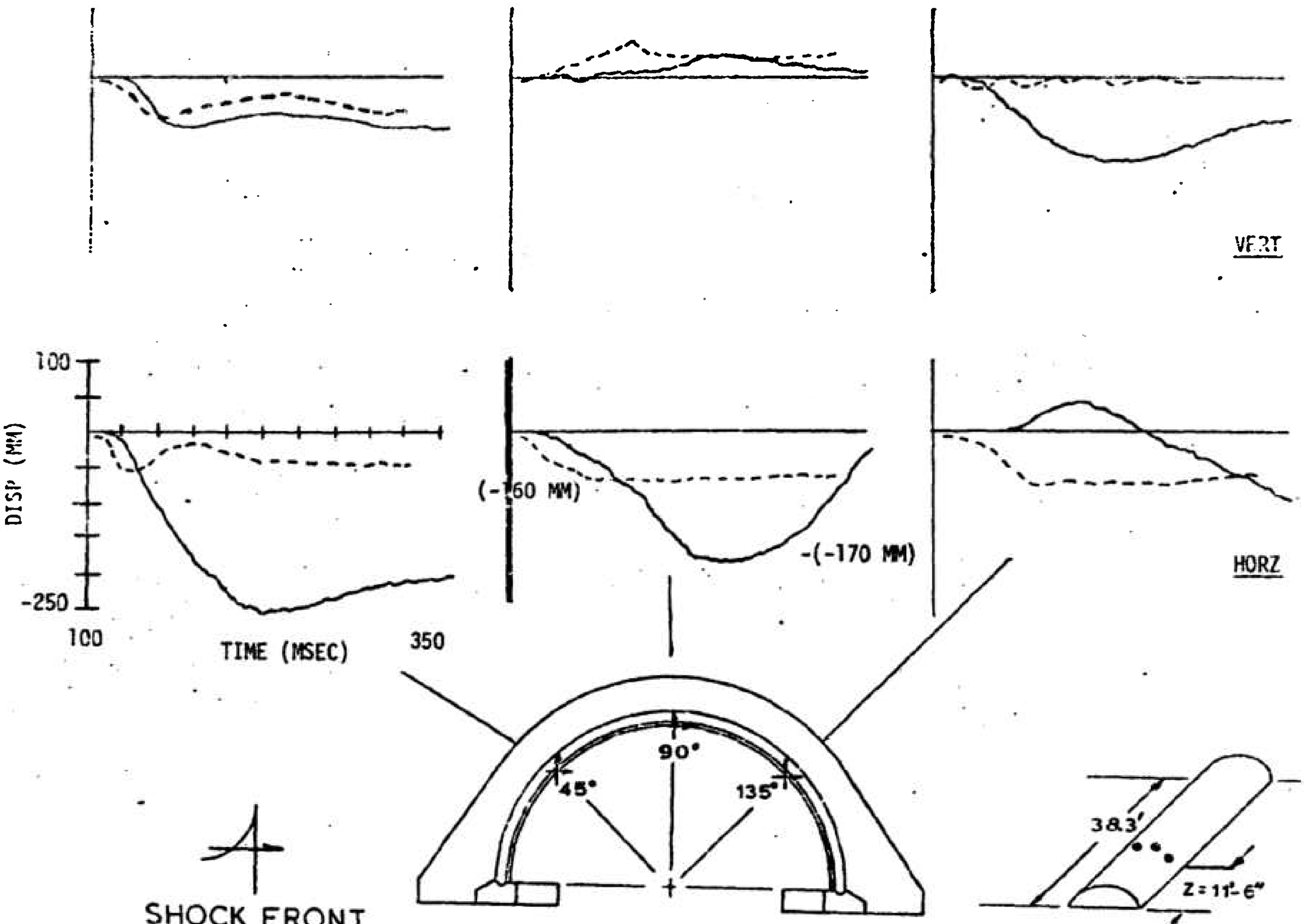

SHELTER C-MOTIONS

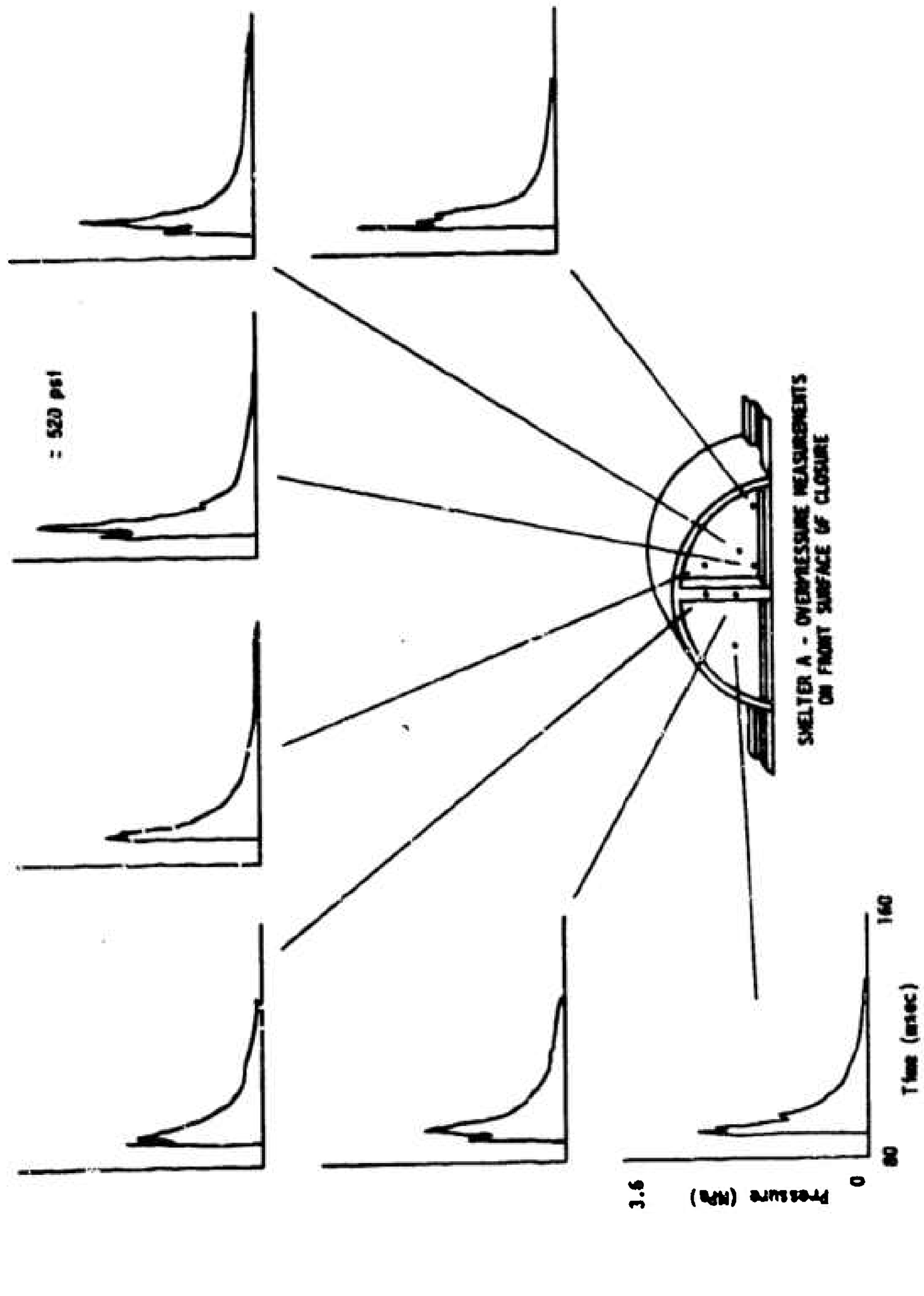

SHELTER A - OVERPRESSURE MEASUREMENTS ON FRONT SURFACE OF CLOSURE

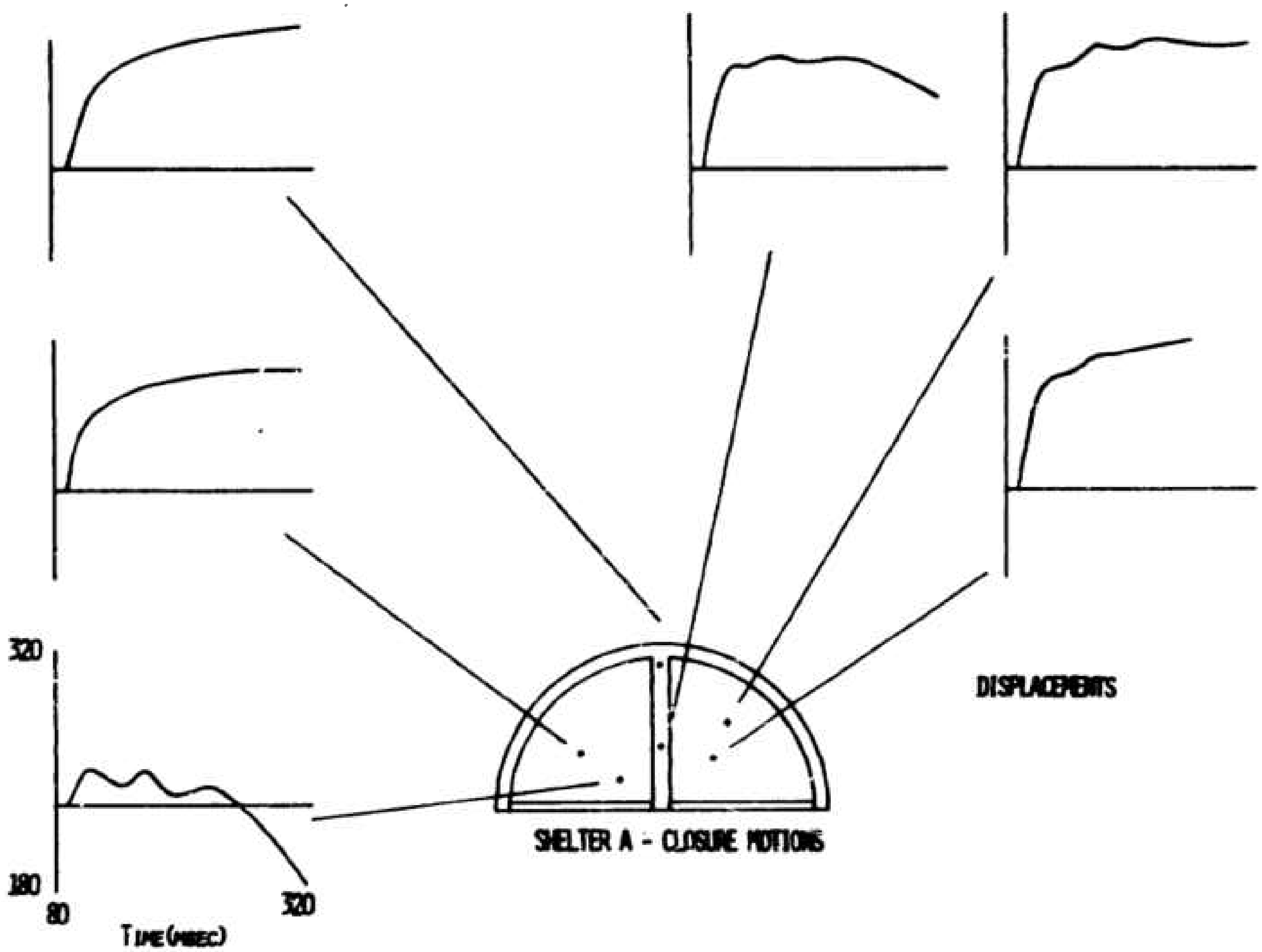
320
180
80
320
TIME (MSEC)
SHELTER A - CLOSURE MOTIONS
DISPLACEMENTS

ADVANCED SHELTER CONCEPT

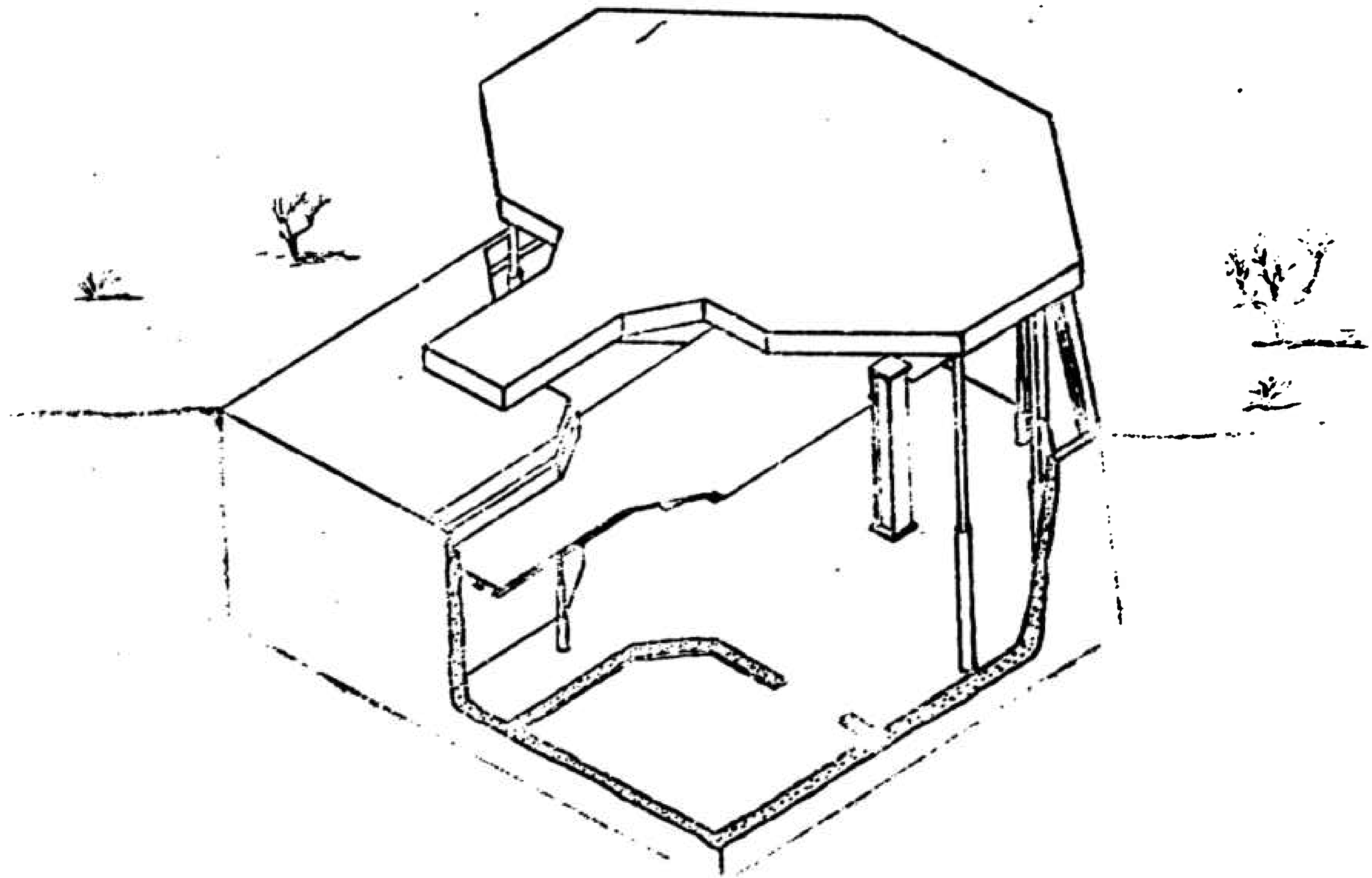

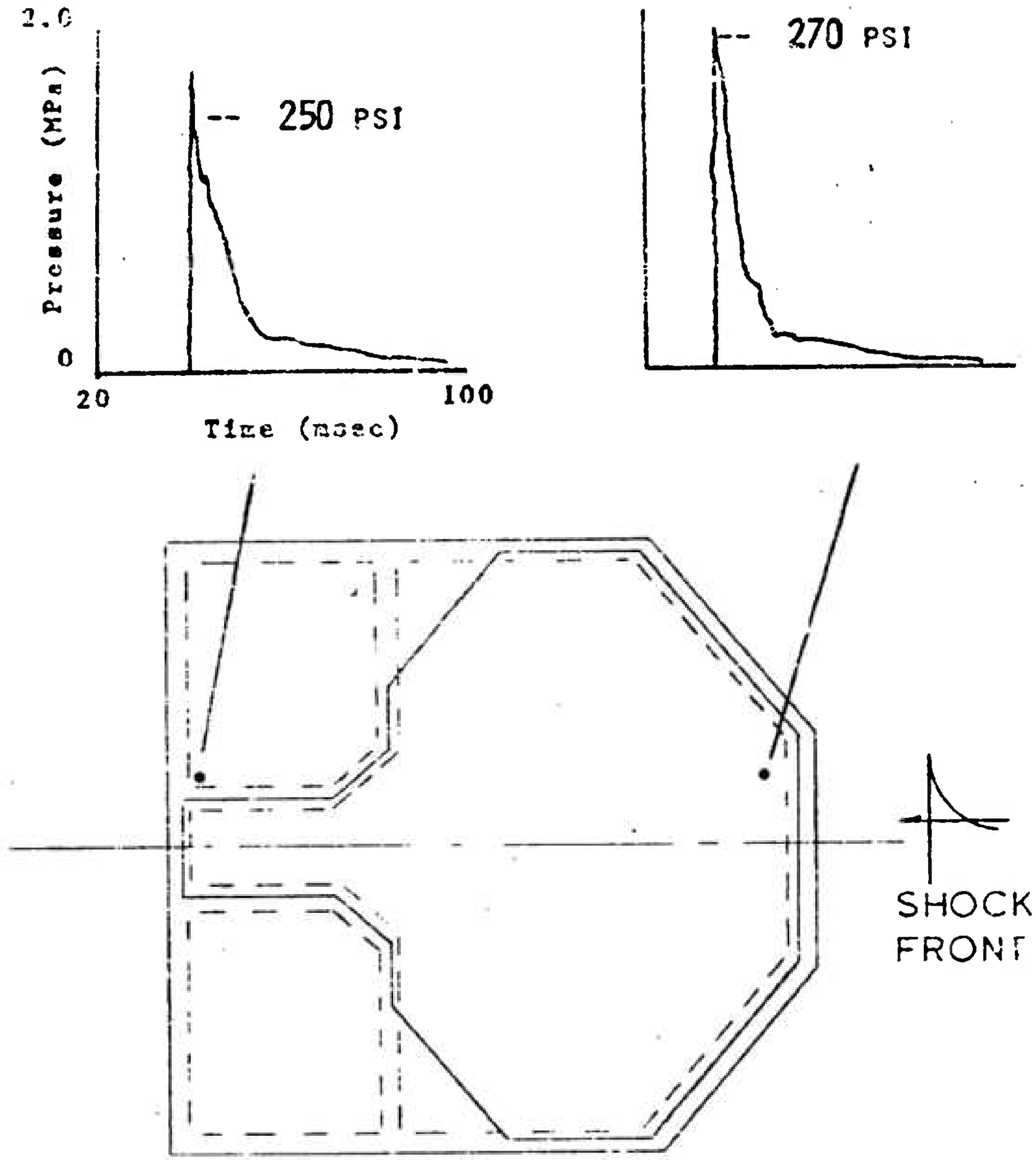

SHELTER D-EXTERNAL PRESSURE LOADING
ON SURFACE OF SHELTER

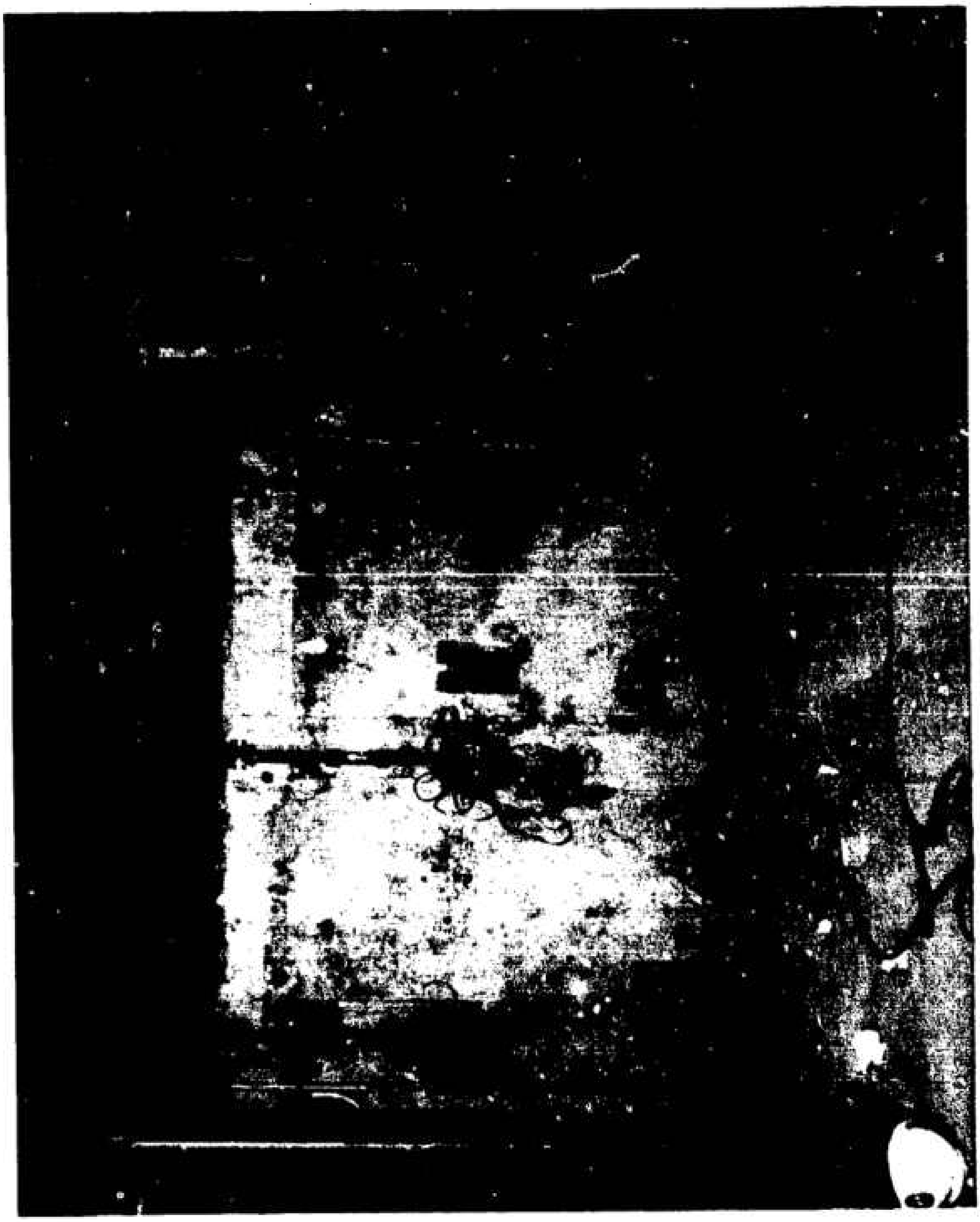

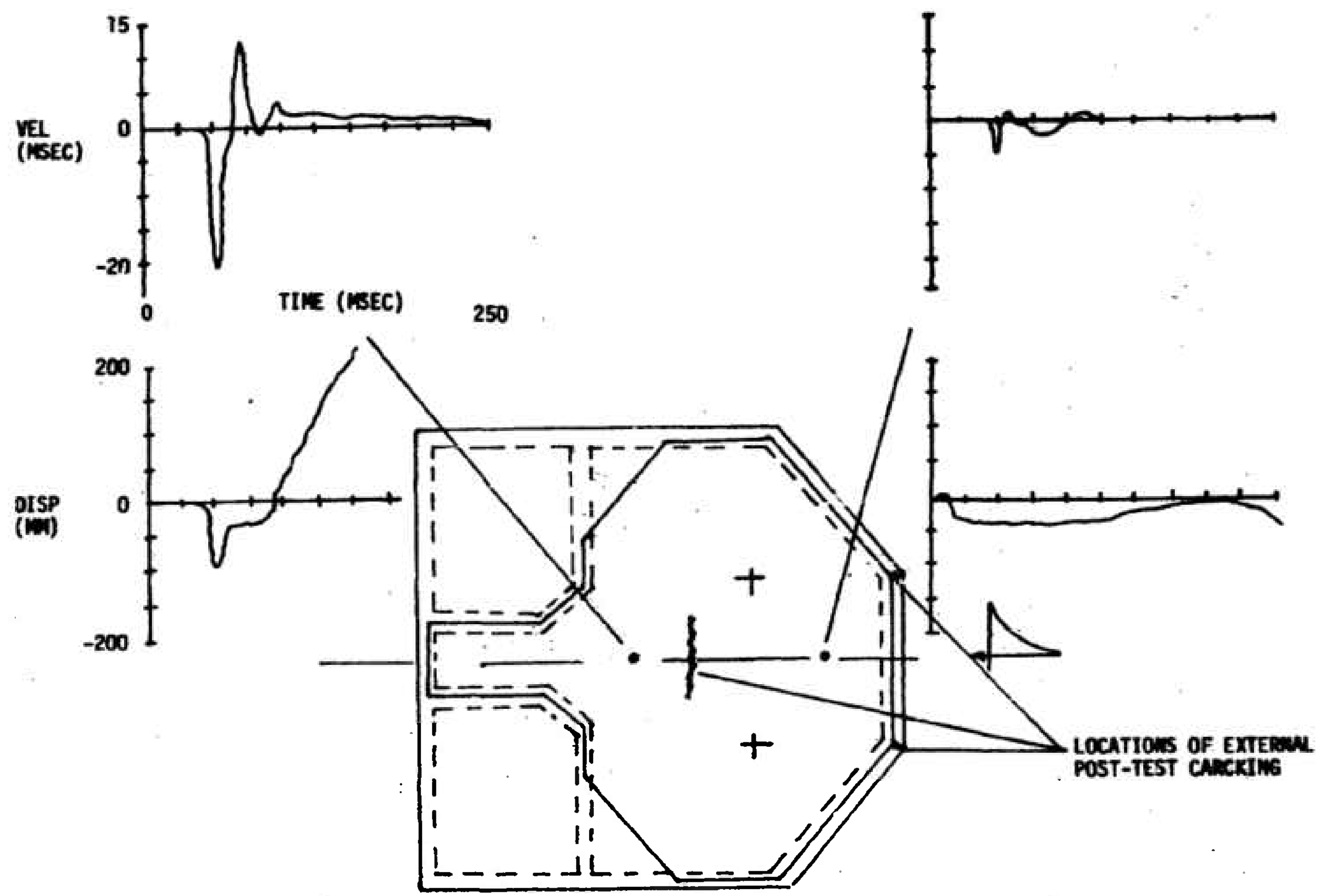

SHELTER D - MOTION OF THE MOVEABLE ROOF

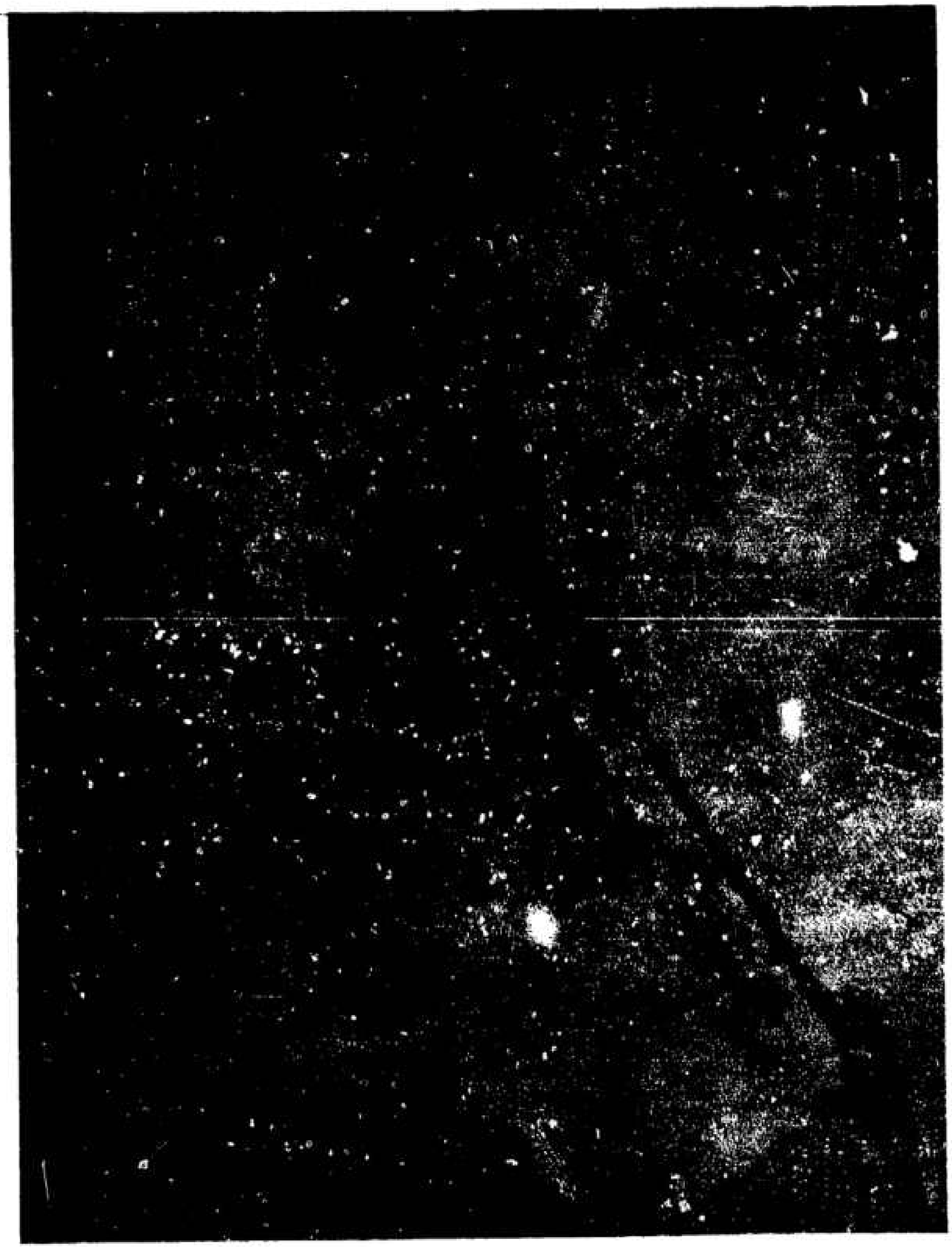

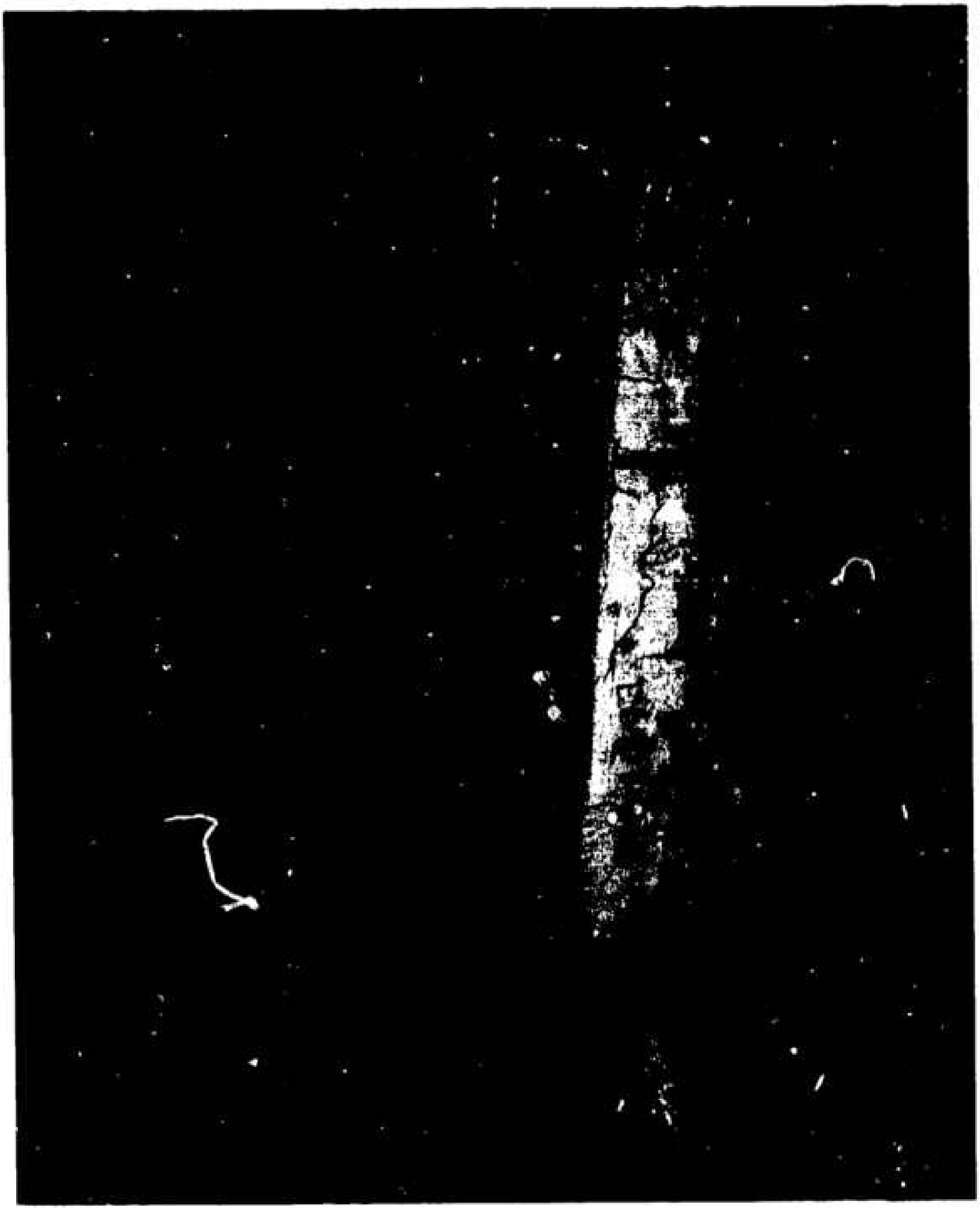

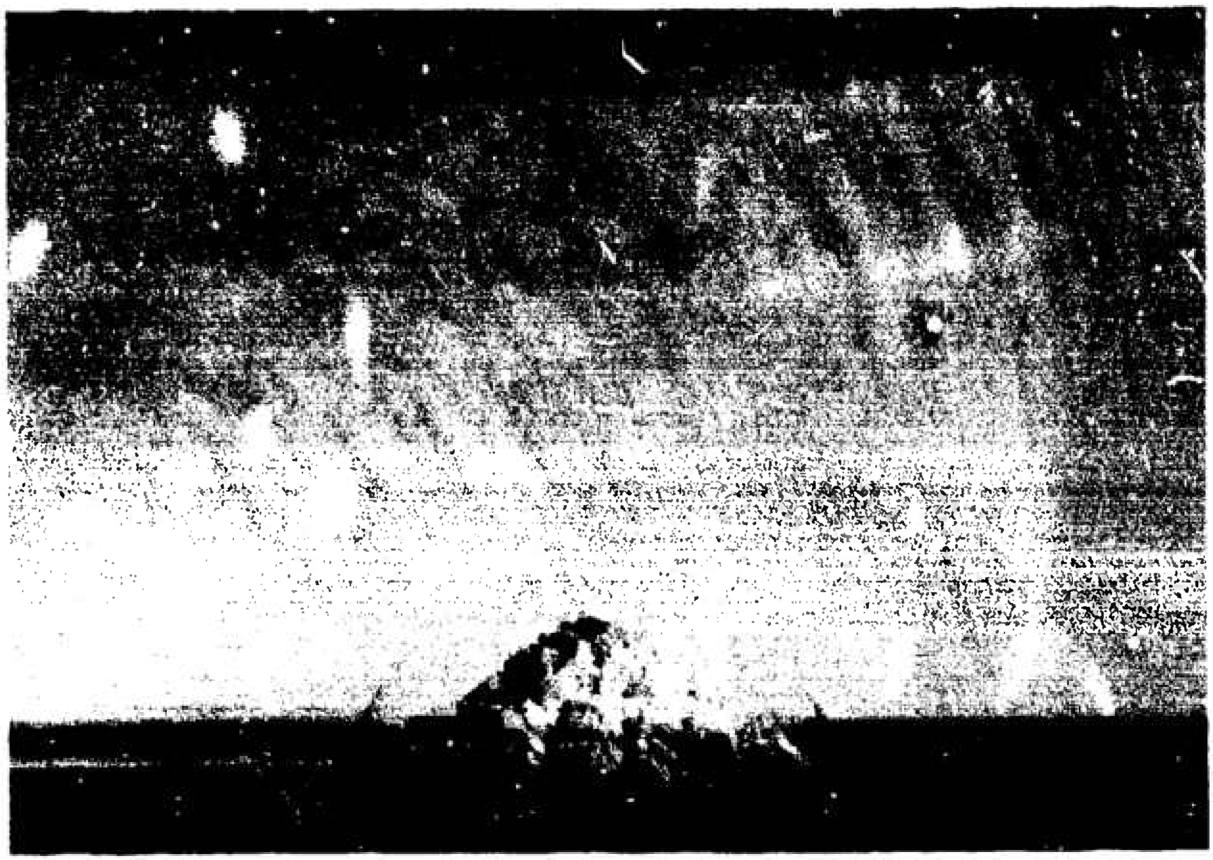

16. GROUP HELMET ARMY PERSONNEL SHELTERS

by

Golden E. Lane, Jr.
Civil Engineering Research Facility

ABSTRACT

The Swedish Government, represented by the Royal Fortification Administration (RFA), fielded an experiment in the DICE THROW Project. The RFA experiment consisted of erecting and exposing two Group Helmet Army personnel shelters to overpressures of 690 and 380 kPa. The University of New Mexico's Civil Engineering Research Facility (CERF) was responsible for construction, instrumentation, monitoring, and reporting of the experiment. The purpose of the experiment was to verify the shelter survivability design overpressure in order to establish a standard personnel shelter design. Each shelter was instrumented with six pressure gages: five inside the shelter and one external to the shelter. Both shelters survived the blast environment with a relatively small amount of damage.

TABLE OF CONTENTS

LIST OF ILLUSTRATIONS

SECTION 1
INTRODUCTION

The Swedish Government, represented by the Royal Fortification Administration (RFA), fielded an experiment in the DICE THROW Project, a 600-ton, high-explosive test conducted at the White Sands Missile Range in New Mexico on October 6, 1976. The RFA experiment consisted of erecting and exposing two *Group Helmet* Army personnel shelters to overpressures of 690 and 380 kPa. The Defense Nuclear Agency's Field Command supported the experiment and the University of New Mexico's Civil Engineering Research Facility (CERF) was responsible for construction, instrumentation, monitoring, and reporting of the experiment.

The purpose of the Swedish experiment in Project DICE THROW was to verify the shelter survivability design overpressure (380 kPa) in order to establish a standard personnel shelter design.

SECTION 2
EXPERIMENTAL PROGRAM

The two test shelters were shipped directly to the White Sands Missile Range from Sweden. Appendix A contains the packing and assembly instructions for the shelters. After the necessary excavation was accomplished, the shelters were assembled according to these instructions by four experimental technicians. A backhoe and front-end loader were used for the excavation and backfilling. Figure 1 shows the layout with respect to ground zero. Figure 2 shows various stages of the shelter erection.

Instrumentation consisted of six Kulite HKS and XTS type diffused silicon, full-bridge, piezoresistive pressure gages for each shelter. Figure 3 shows the location of these gages. The external gages (gage 6) were located on the longitudinal axis of the shelter at the foot of the backfill. Gages 1, 4, and 6 were mounted in concrete cylinders, 305 mm in diameter and 305 mm in height. Gages 2 and 3 were placed on the simulated dummy shown in figure 3. The dummy was constructed with plywood sides and filled with sand to obtain the proper weight. Gage 5 was placed on the lower girder at the back of the shelter. Figure 4 shows the inside of one shelter prior to the test; figure 5 shows the pretest shelter berms.

The gages were connected to a steel junction box located approximately 300 m from the shelters with 4-conductor lead wire buried 1.2 m deep. The junction box was connected to the recording van by 20-pair cables. The recording van was approximately 1800 m from the junction box.

The recording van used for data acquisition was supplied by DNA (Van No. 36040). In the van, the bridge-type pressure gages were excited and conditioned by B&F 1-171 Signal Conditioners. The conditioned signals were amplified with Ray Labs 5503 Amplifiers (dc - 50 kHz). Recording was accomplished on Sangamo Type 4784 32-Track Tape Decks. Wideband FM recording (108 kHz center with ± 40 percent deviation) was used.

Preplacement gage calibration was accomplished at CERF with stimuli provided by a dead weight tester or regulated baffles with calibrated Heise gages. Simple shunt calibration resistors were selected in the field to provide step bridge upsets with known pressure equivalents.

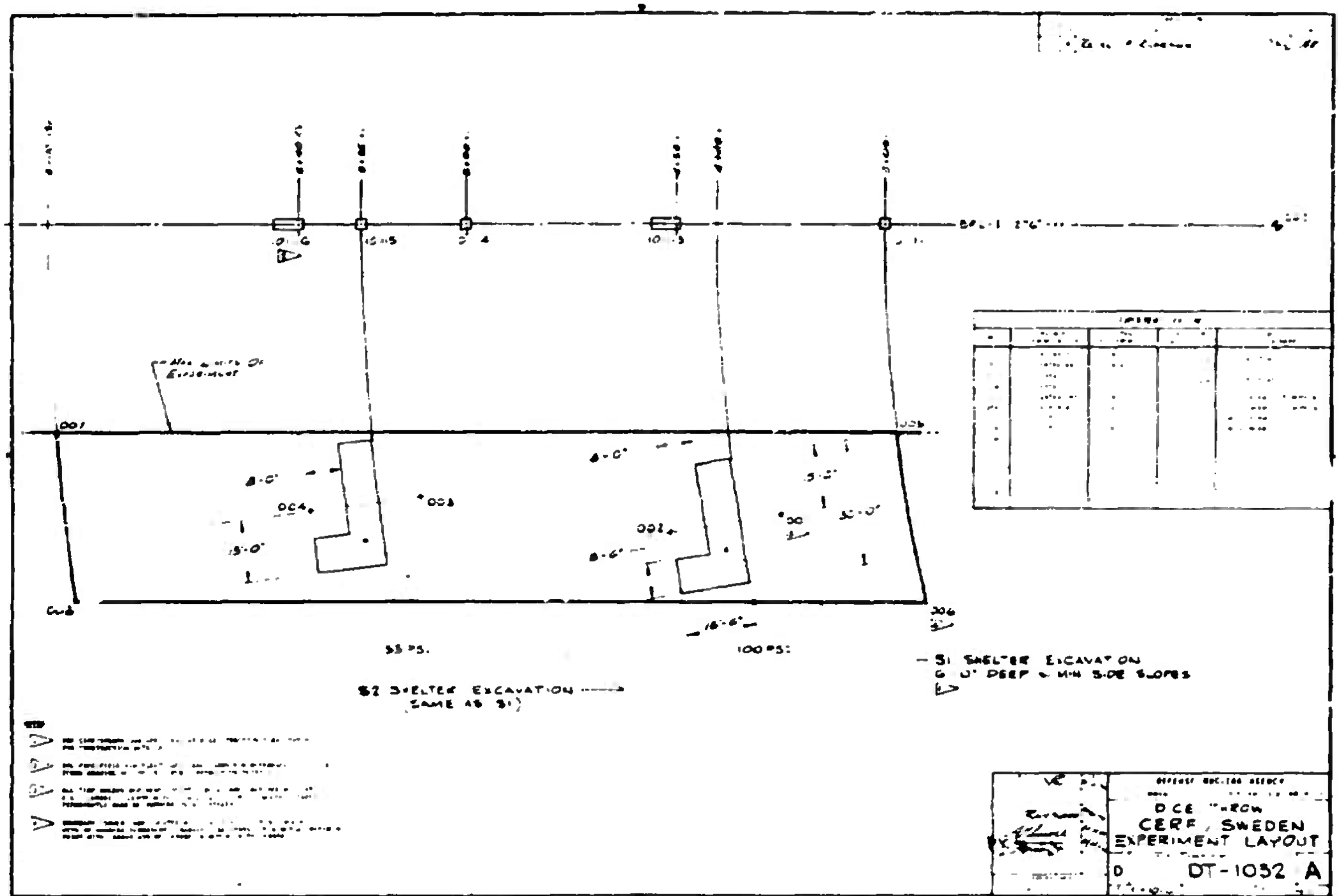

Figure 7. Layout for Swedish Experiment

Figure 2. Shelter Erection (1 of 2)

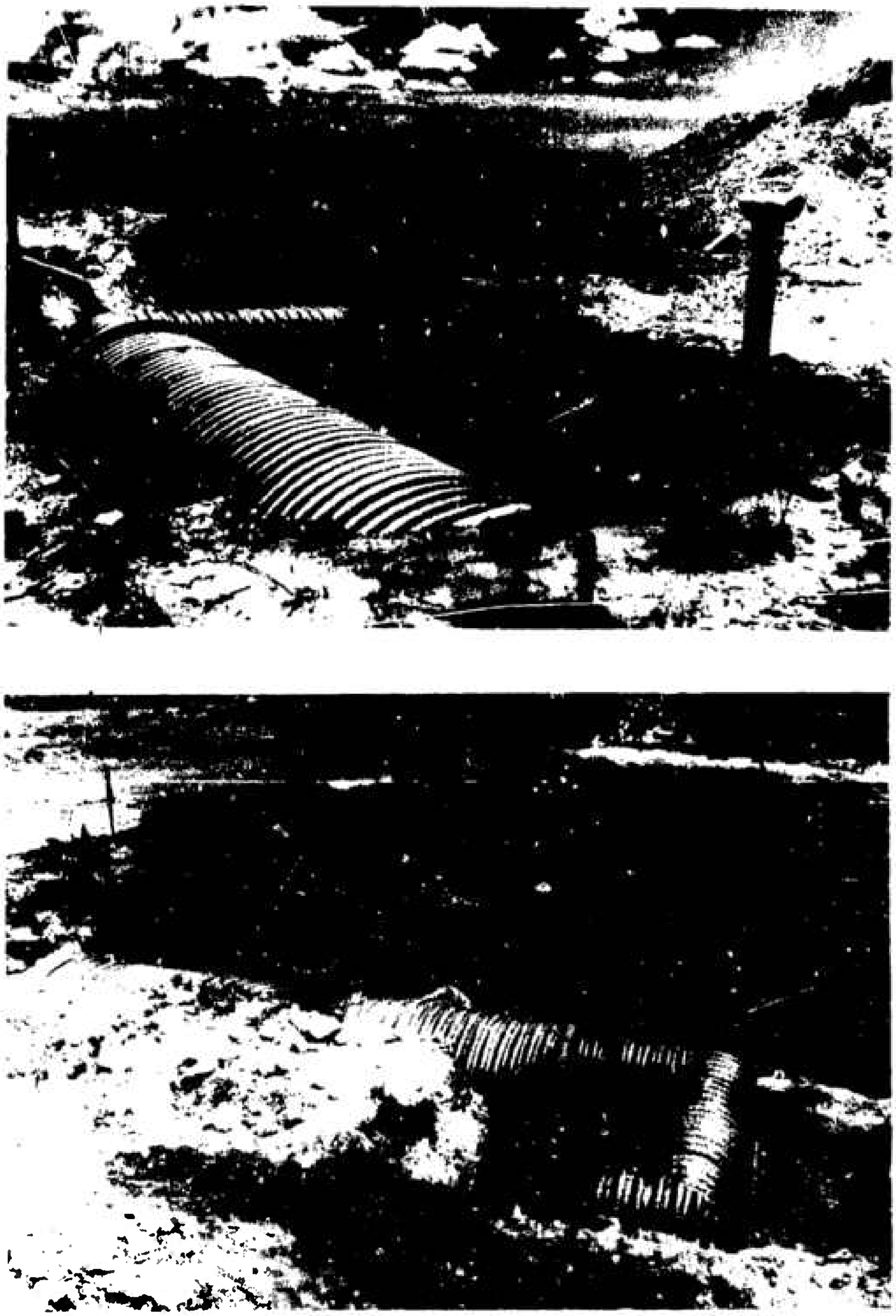

Figure 2. Shelter Erection (2 of 2)

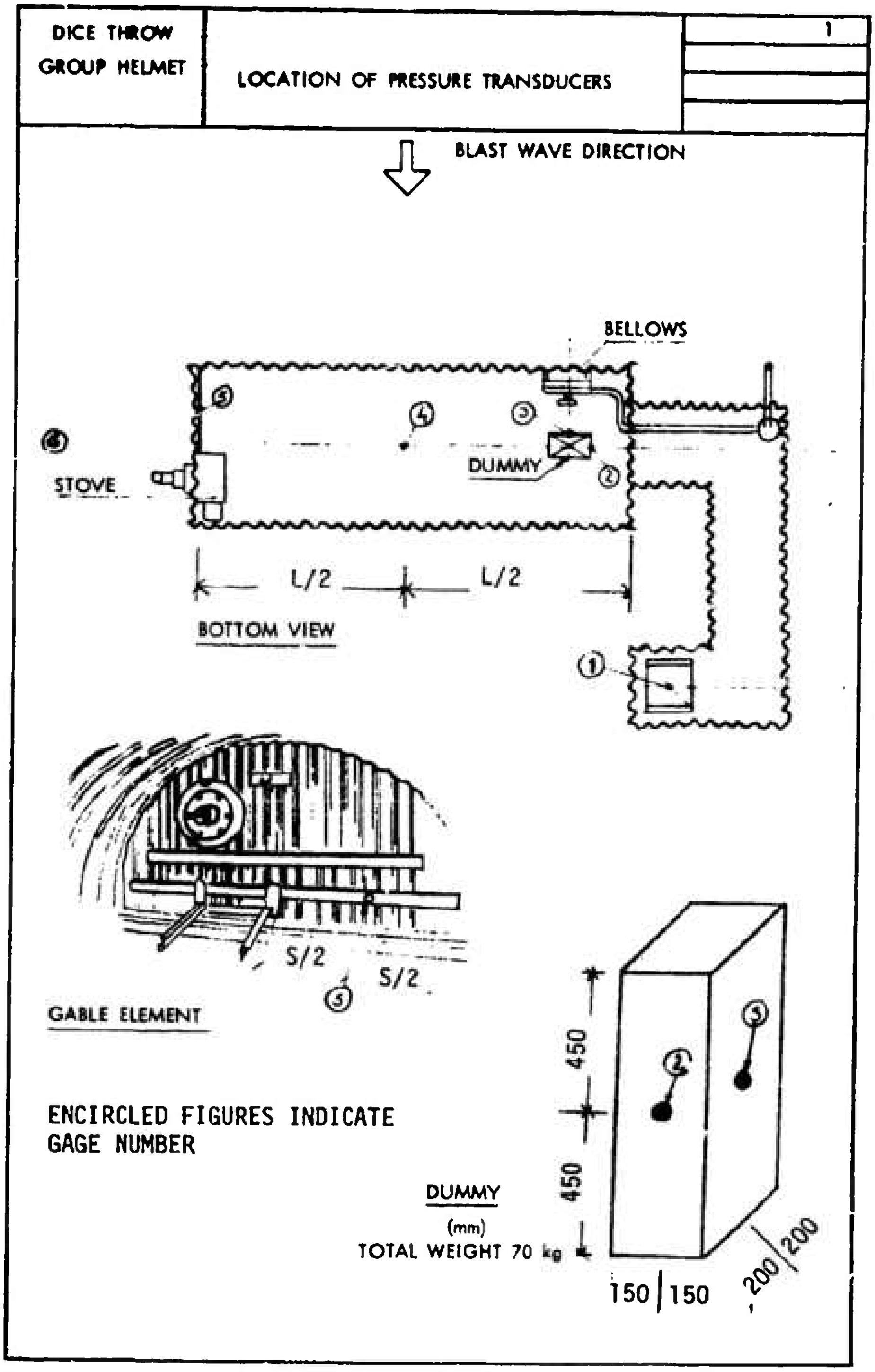

Figure 3. Location of Pressure Gages

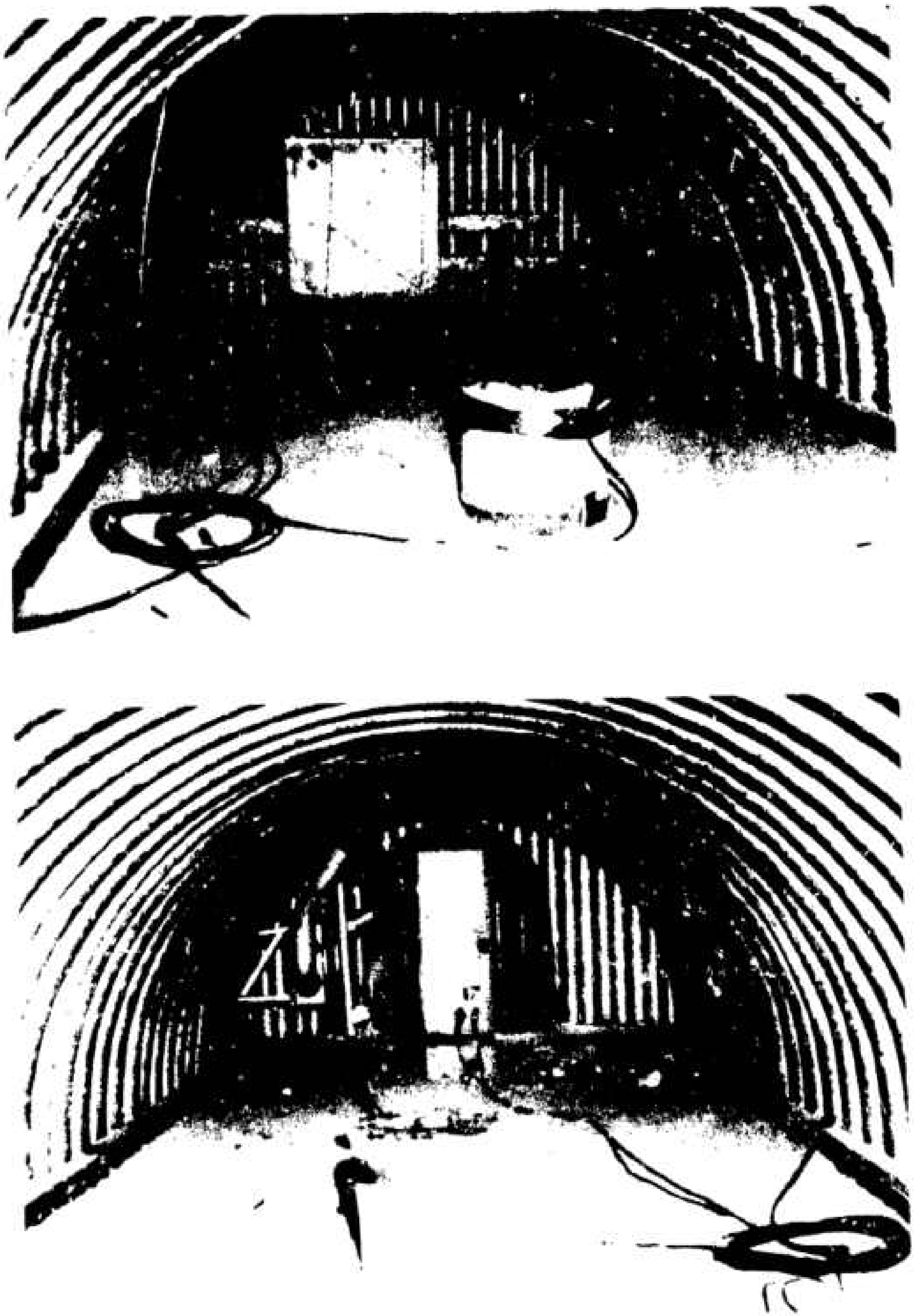

Figure 4. Shelter Before Test

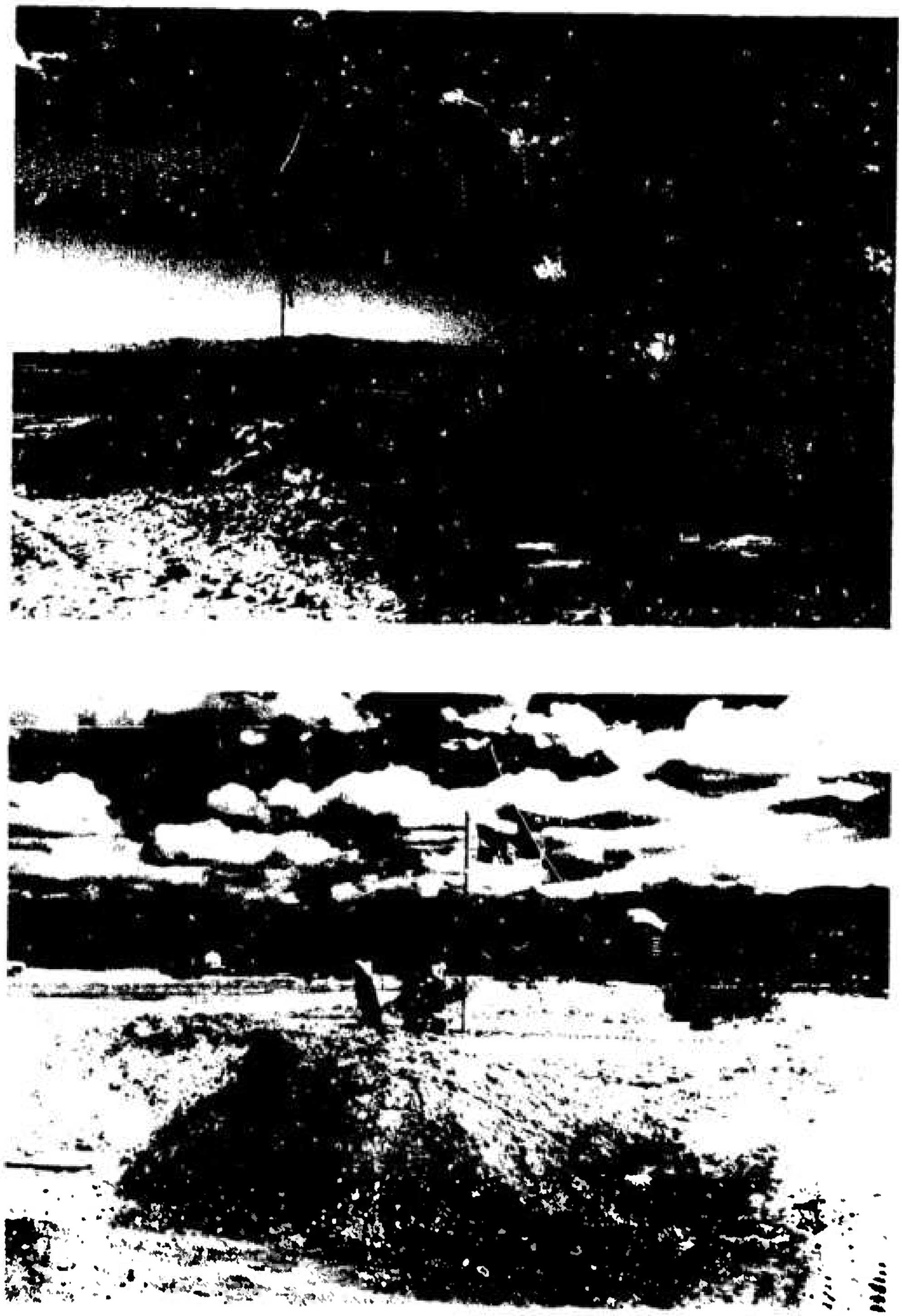

Figure 5. Shelter Berm Before Test

In addition to data, IRIG-B time code and fiducial signals were recorded on each tape deck. During the event, the van was operated remotely from the timing and firing van.

After the event, quick-look data were played back on O-graph paper. Final copy data were prepared at the Air Force Weapons Laboratory data-reduction facility.

A sampling rate of 20,000 points per second and a filter frequency of 5 kHz were used in digitizing the analog data. Each channel was scaled in engineering units and plotted against time.

SECTION 3
TEST RESULTS

The pressure gage data are presented in Appendix B; posttest photographs are presented in Appendix C.

Both shelters survived the blast. The 690-kPa shelter suffered more damage as evidenced by the larger deformation and the greater displacement of the footing members. Also, some of the intake pipe was knocked down during the blast. A comparison of the two sets of posttest photographs shows the relative damage to the two structures.

APPENDIX A

PACKING AND ASSEMBLY INSTRUCTIONS

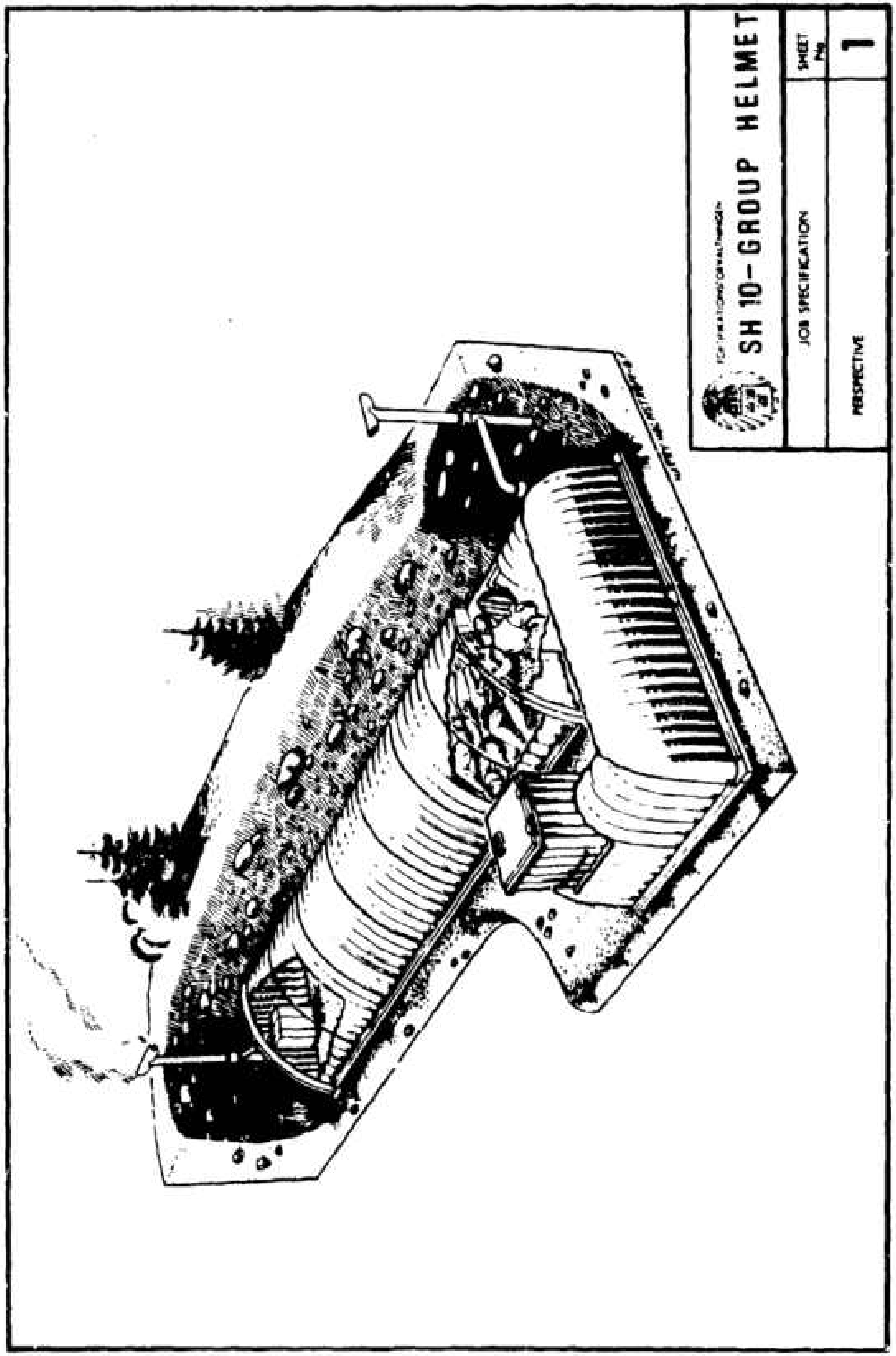
SH 10-GROUP HELMET
JOB SPECIFICATION
PERSPECTIVE
SHEET No
1

INDEX	Sheet No
Perspective	1
Index, General information	2
Foundation	3
List of supplies Compilation	4
Packing plan	5
Excavation Assembling the pad planks	6
Drainage	7
Manual element transport Mounting of details in elements 2 and 8	8
Assembling the shelter elements, bellows, stove box, stove and exhaust pipe	9
Assembling entrance elements 10, 11 and 12 Assembling ventilation pipe	10
Assembling entrance elements 12, 13, 14, 15 and 16 Backfill and cover	11

GENERAL INFORMATION

1. **Purpose.** This description shows the material and work needed to assemble the shelter with ordinary soldiers as labour force.

   The elements and certain accessories and other equipment are delivered on two loading stools, each weighing about one metric ton (cf Sheet 4)

2. **Terms.** The sheets of this description are called SHEETS. The illustrations are called FIGURES.

3. **Grouping.** The sheets of this description are divided (cf the index) in two main groups intended for:
   - general information, reconnoitring, planning and material supply
   - sequential assemblage.

4. **Text** indicating steps in chronological sequence are called STAGES and denoted with sheet number and consecutive order (e.g. 8:1, 8:2, 8:3).

5. **Figures** are denoted in alphabetical order, A, B, C, &c, and the number of the actual sheet (e.g. A15, B15, C15).

6. **Dimensions** are given in millimetres, if not otherwise indicated.

FORTIFIKATIONSFÖRVALTNINGEN

SH 10-GROUP HELMET

JOB SPECIFICATION

INDEX, GENERAL INFORMATION

SHEET No **2**

EXTENSION IN BOTTOM VIEW AND SECTION	DEPTH OF FOUNDATION	

EXTENSION IN BOTTOM VIEW AND SECTION

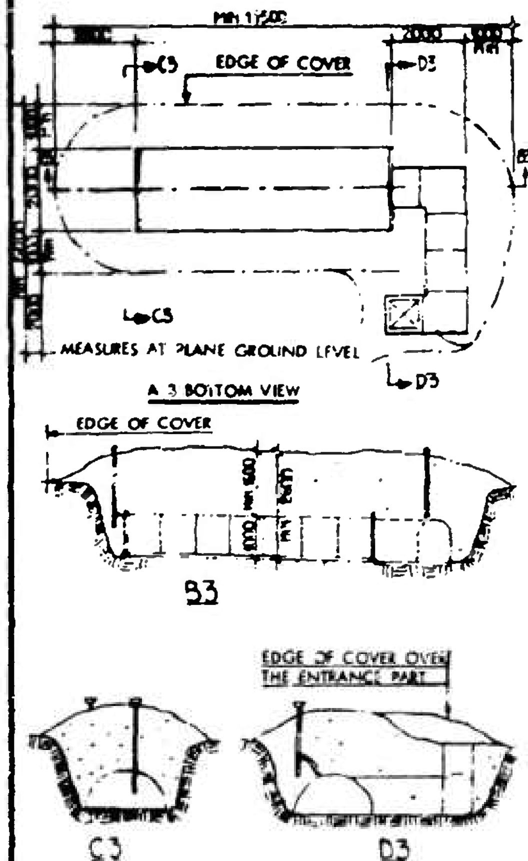

DEPTH OF FOUNDATION

Foundation on a bed of gravel or coarse sand makes special drainage unnecessary.

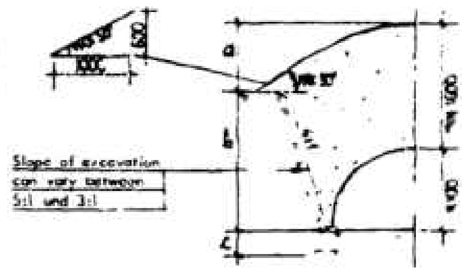

a Final height over surrounding ground.

b Depth of foundation. If this is 1800 mm, there will be balance between excavated masses and rockfill.

c Distance to highest underground water level, minimum 300 mm.

At a slope of excavation of 4:1 the excavated masses amount to 52 m^3 with depth of foundation 1800 mm.

FORTIFIKATIONSFÖRVALTNINGEN

SH 10- GROUP HELMET

JOB SPECIFICATION	SHEET No
FOUNDATION	3

LIST OF SUPPLIES

Number of pieces	Designation	Marking
1	Loading stool No. 1	1
2	Pad planks	2
2	Pad planks	5
1	Stove	
1	Exhaust pipe	
1	Stove box	
1	Entrance element	15
7	Vaulted elements	1, 3-8
2	Gable elements	2, 9
1	Loading stool No. 2	2
4	Pad planks	4
2	" "	1
2	" "	2
2	" "	3
2	" "	6, 7
1	Corner element with blast valve and ventilation pipe	12
1	Corner element	13
1	Entrance element with hatch and cable bushings	16
3	Entrance elements	10, 11, 14
2	Chests	1, 2
1	Branch pipe (ventilation)	
1	Branch pipe (exhaust)	
2	Connector pipes	

Number of pieces	Designation	Marking
	In chest No. 1	
1	Bellows	
1	Bellows bracket	
8	Bolts M8 x 22 with discs	
4	Bolts 5/8"x 35 with nuts	
6	Cotters with sex pins	
4	Plastic covers	
1	Tension spring	
1	Tension spring	
8	Interior ventilation pipes	2-9
2	Exhaust trunks	
	In chest No. 2	
1	Bracket for stove box	
2	Anchor wires for stove box bracket	
1	Bucket with bolts and nuts	
1	Blast valve	
1	Water level	
1	Folding rule	
8	Lifting hooks	
1	Straightening tool	
1	Adjustable wrench	
1	Screw driver	
1	Box wrench, double open 18 + 19 mm	
1	Box wrench, single open 38 mm	
1	Box wrench, single open 29 mm attached to element No. 16	
1	Polygon wrench 21 + 24 mm	
4	Special wrenches 2 + 2	
1	Hexagon spanner (5 mm for blast valve)	

WORK EFFORTS[1]

Work	Man-hours[2] Men only	Men + earth mover	
Preparation	50	50	-
Excavation	150	5	7
Assemblage	25-30	25-30	-
Backfill	50	10	2
Sum	275-300	90-95	9

1) Work for drainage not included
2) Statements are based on experience from work with a 10 men crew

COMPILATION

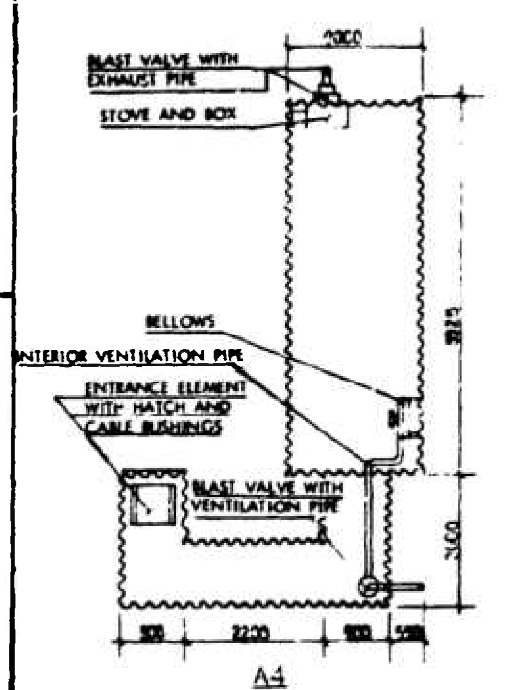

SH 10-GROUP HELMET

JOB SPECIFICATION	SHEET No
LIST OF SUPPLIES, COMPILATION	4

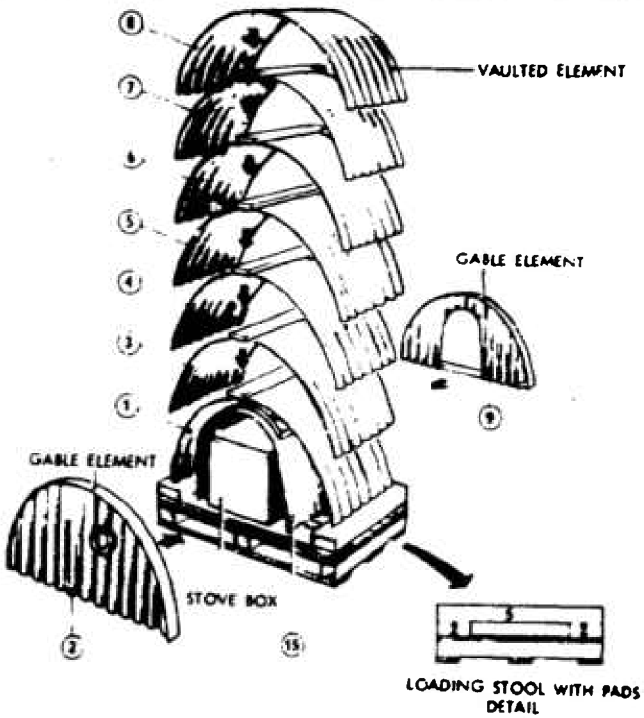

A5 STOOL 1

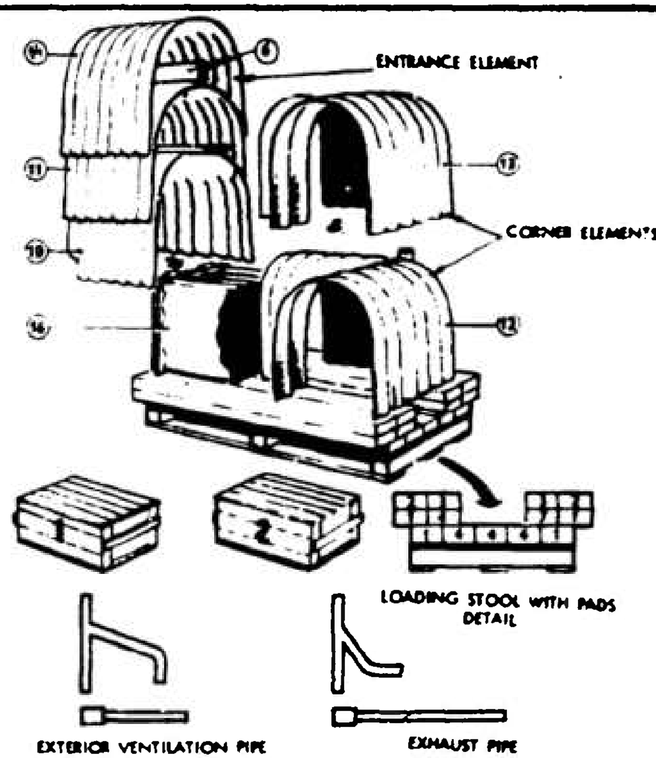

B5 STOOL 2

Loading stool 1, cf Fig A5

5:1 Place pads No. 2 on stool along the longer sides.

5:2 Place pads No. 5 traversing pads No. 2.

5:3 Place stove box and element 15 on the pads.

5:4 Pile the seven vaulted elements on the stool. Note the liners of wooden strips.

5: Place the gable elements 2 and 9 on their respective sides

5:6 Lash the package together on stool.

Loading stool 2, cf Fig B5

5:11 Place pads on stool according to detail in Fig B5.

5:12 Note that pad No. 6 is used as liner between elements 11 and [illegible]

5:13 Place chest No. 1 in element 16

5:14 Place chest No. 2 plus exhaust pipe and exterior ventilat[illegible] pipe in element [illegible]

5:15 Place elements [illegible], 11 and 14 over element 16

5:16 Place element [illegible] on element [illegible]

5:17 Lash the package together on stool

FORTIFIKATIONSFÖRVALTNINGEN

SH 10 – GROUP HELMET

JOB SPECIFICATION	SHEET No
PACKING PLAN	5

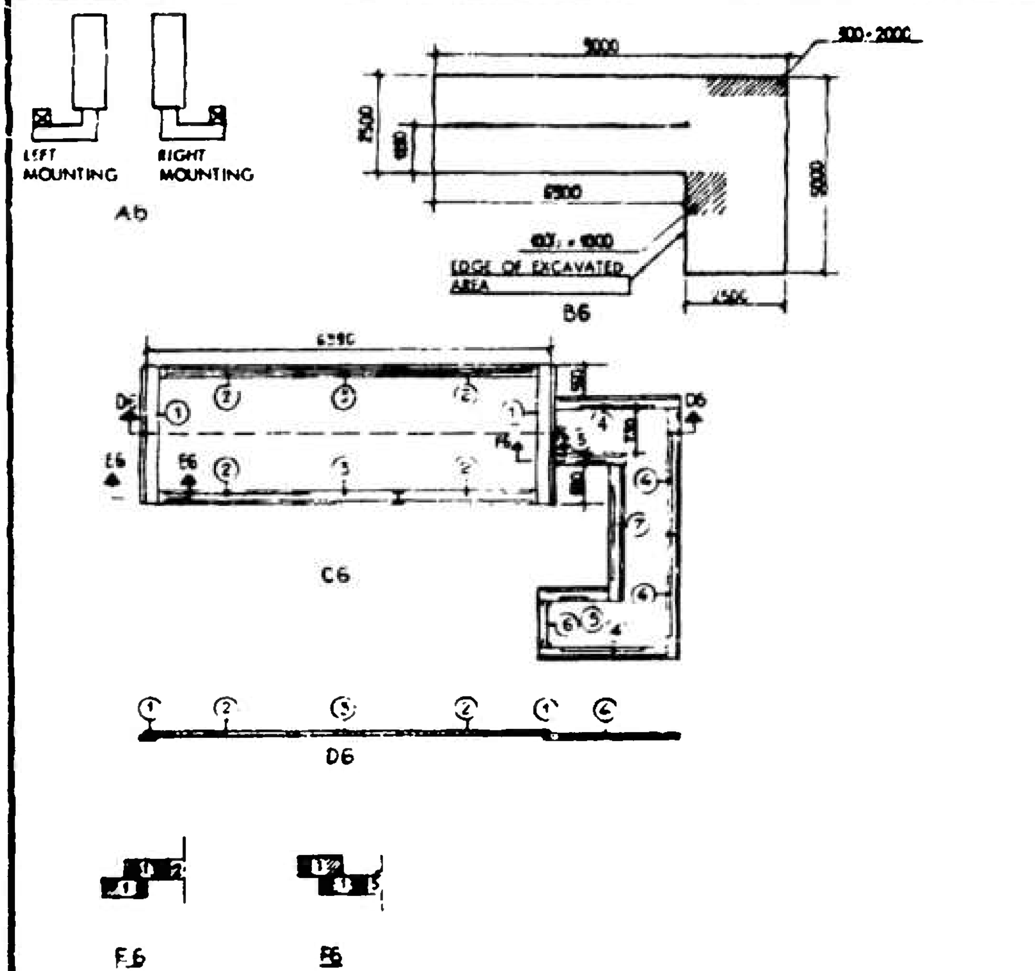

EXCAVATION

6:1 Depth of excavation should be 1800 mm.

6:2 Decide left or right mounting (cf Fig A6).

6:3 At excavation by hand the hatched areas do not need to be taken out.

6:4 If earth mover is used, the last 150 mm at bottom should be hand-excavated anyhow

ASSEMBLAGE OF PADS

6:11 Check the bottom to be in level and horizontal.

6:12 The planks are marked on each side

6:13 Evening under the planks should be made with care. The planks should have a good tread against the ground

6:14 Turn the guide bars of the pads in right direction when laying out the planks, cf Fig C6.

6:15 Pads (2) and (3) under the shelter are placed directly on the ground, cf Figs C6 and D6.

6:16 The pads (1) under the shelter and (4), (5), (6) and (7) under the entrance should be dug down in slots of 75 mm depth. Final placing might be adjusted when assembling the shelter elements, cf Figs C6 and D6.

6:17 Planks (2) should be fitted to planks (1). The fit can be adjusted in the cuts between planks (2) and (3), cf Figs C6 and D6

6:18 The planks should be in level and horizontal. Use the water-level.

FORTIFIKATIONSFÖRVALTNINGEN

SH 10-GROUP HELMET

JOB SPECIFICATION	SHEET No
EXCAVATION ASSEMBLING THE PAD PLANKS	6

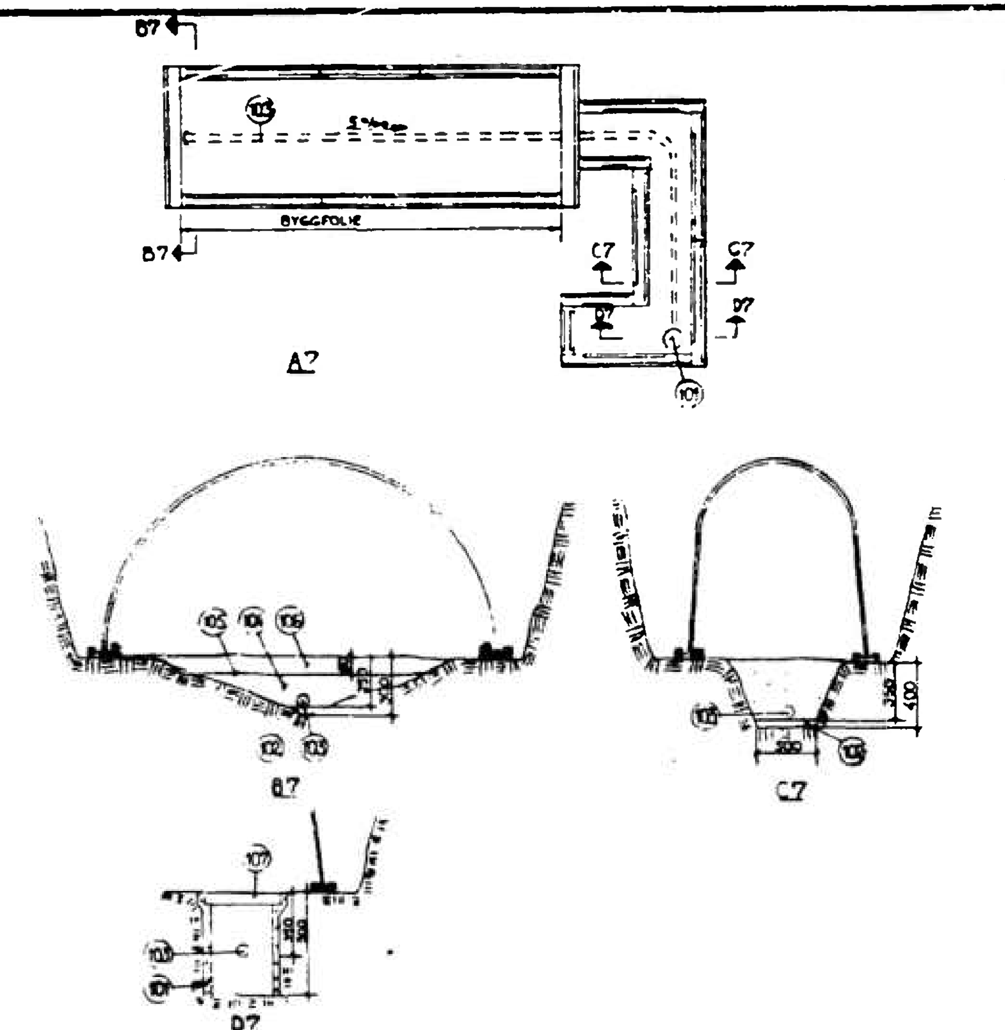

TEXT HERE OMITTED

FORTIFIKATIONSFORVALTNINGEN

SH 10-GROUP HELMET

JOB SPECIFICATION	SHEET No
DRAINAGE	7

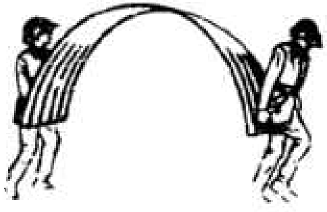

A8

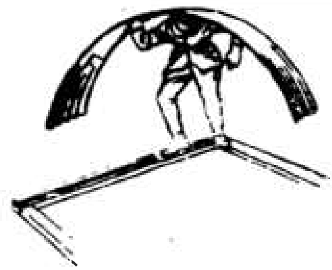

B8

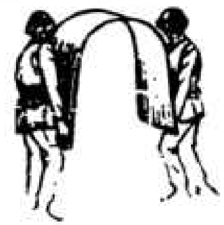

C8

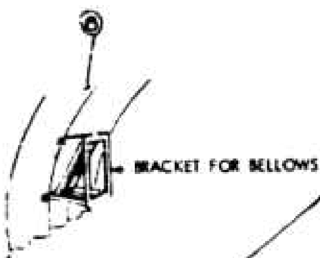

D8

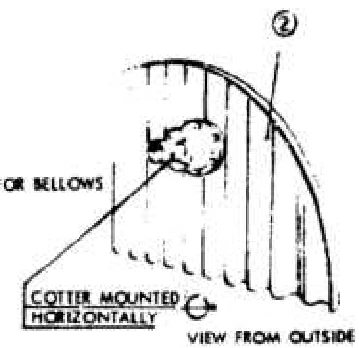

E8

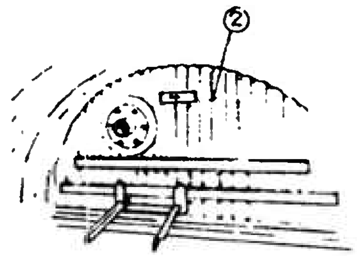

F8

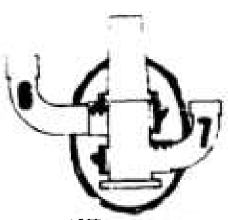

LEFT MOUNTING

G8

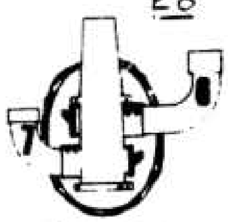

RIGHT MOUNTING

H8

ELEMENT TRANSPORT BY HAND

Example on transport of elements in terrain and on the site of assemblage see Figs A8, B8 and C8.

8:1 Lift hooks should be used for lifting and transport.

ASSEMBLAGE OF DETAILS

8:11 Assemble details in Figs D8, F8 and G9 before the elements are sunk down into the pit.

8:12 Install bellows bracket in element 8, cf Fig D8.

8:13 Install blast valve for exhaust pipe connection in gable element 2 from inside, cf Fig E8.

8:14 Turn the blast valve to get the cotter slot in horizontal position before mounting, cf Fig E8.

8:15 Bolt the blast valve from the outside.

8:16 Protect the blast valve using plastic cover over the outer opening.

8:17 Install the stove box bracket on gable element 2 and check-mount the box for fit to the blast valve, cf Fig F8.

8:18 Mount the ventilation pipes 6 and 7 to the bellows, in left or right-mounting, respectively.

Note: that plastic covers should be used over openings not used cf Figs G8 or H8 (assemblage seen from the rear side of the bellows).

FORTIFIKATIONSFÖRVALTNINGEN

SH 10-GROUP HELMET

JOB SPECIFICATION	SHEET No
MANUAL ELEMENT TRANSPORT MOUNTING OF DETAILS IN ELEMENTS 2 AND 8	8

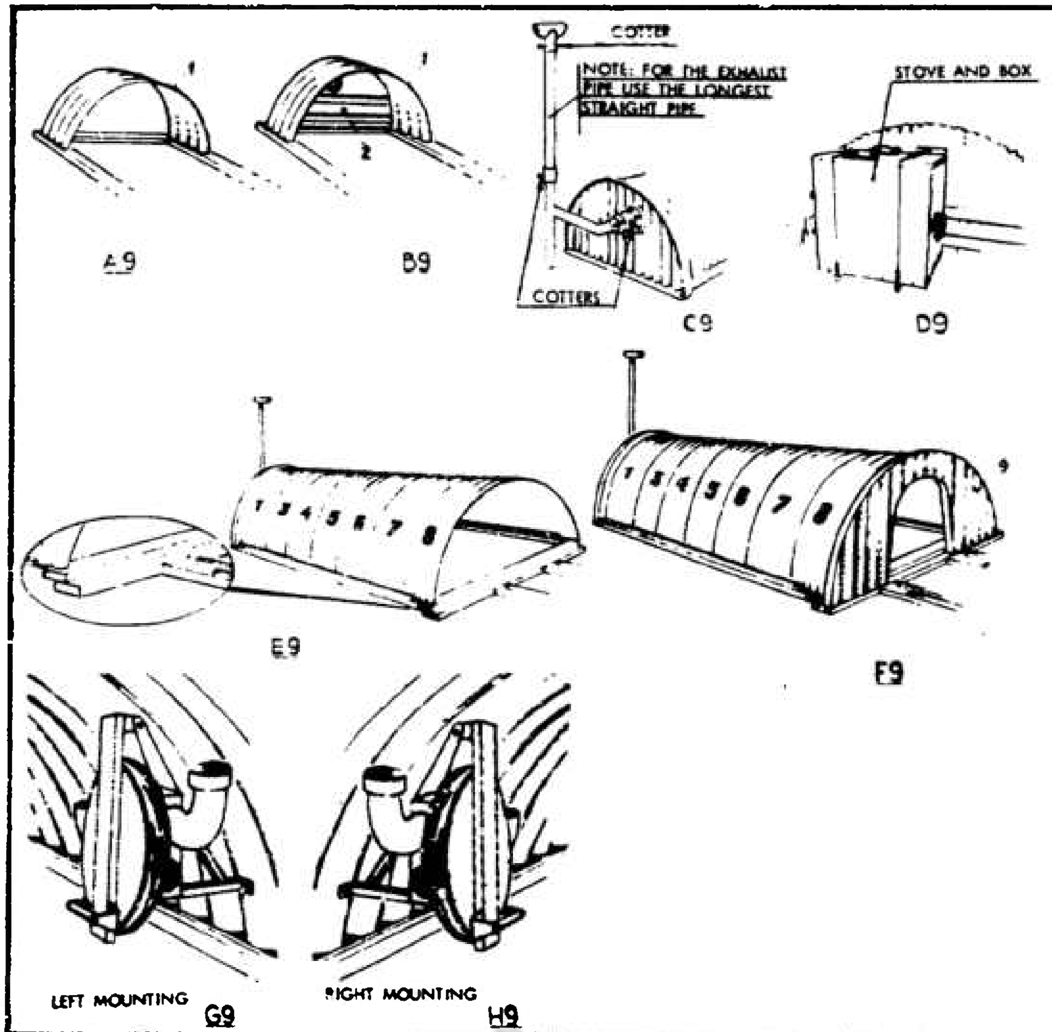

ASSEMBLAGE OF ELEMENTS

9:1 Place element 1 according to Fig A9

9:2 Place element 2 according to Fig B9

9:3 Dig out for the exhaust pipes, Fig C9

9:4 Mount exhaust pipes on the blast valve, Fig C9

9:5 Mount all cotters (3 pieces), of Fig C9

9:6 Mount stove and stove box, Fig D9

9:7 Assemble elements 3 - 8 in sequence, cf E9

9:8 Mount element 9 , Fig F9

The elements should overlap according to marking OVER - UNDER.

In each joint the lowest bolts are first placed on each side. The nut can be half-way drawn. Thereafter the rest of the bolts are placed and the nuts half-way drawn. When the shelter is assembled, all the bolts should be drawn.

9:9 At hand-excavation backfilling could start at this stage, cf Fig F9.

9:10 Mount the bellows and pipe-parts for left or right-mounting at element 8 , see Figs G9 or H9.

FORTIFIKATIONSFÖRVALTNINGEN

SH 10-GROUP HELMET

JOB SPECIFICATION	SHEET No
ASSEMBLING THE SHELTER ELEMENTS, BELLOWS, STOVE BOX, STOVE AND EXHAUST PIPE	9

A 10

B.10

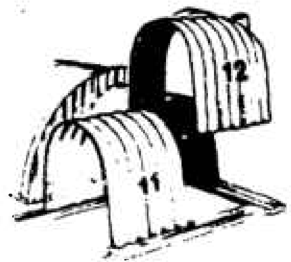

C 10

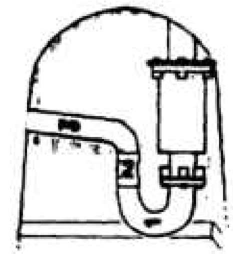

D10

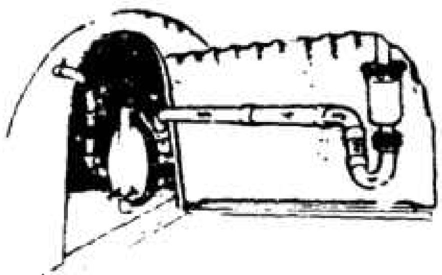

LEFT MOUNTING

E10

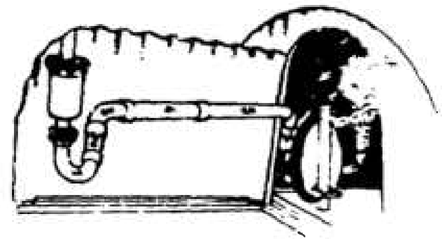

RIGHT MOUNTING

F10

ASSEMBLAGE OF ELEMENTS

10:1 Lift loop and tap is mounted in the roof for suspension of exhaust pipes Nos. 8 and 9, cf Figs E10 or F10.

10:2 Lift loop and tap is bolted in the bore-hole at the cut in element 10 .

10:3 Mount element 10 , Fig A10.

10:4 Mount element 11 , Fig B10.

10:5 Mount element 12 , Fig C10.

10:6 Mount exterior ventilation pipe, Fig B11.

10:7 Turn pipe No. 1 towards the shelter part, Fig D10.

10:8 Assemble remaining ventilation pipes, Figs E10 or F10.

10:9 Ventilation, left mounting, Fig E10.

10:10 Ventilation, right mounting, Fig F10.

FORTIFIKATIONSFÖRVALTNINGEN

SH 10-GROUP HELMET

JOB SPECIFICATION	SHEET No
ASSEMBLING ENTRANCE ELEMENTS 10, 11 AND 12. ASSEMBLING VENTILATION PIPE	10

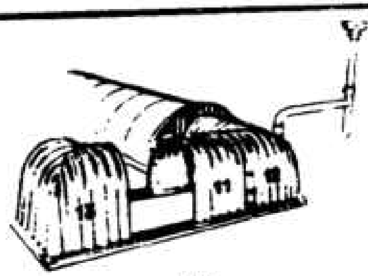

A 11

NOTE: FOR THE EXTERIOR VENTILATION PIPE USE THE SHORTEST CONNECTOR

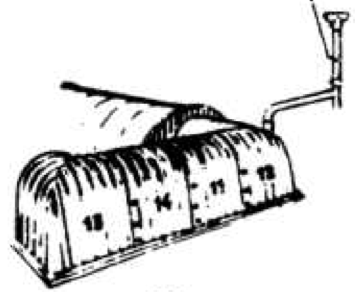

B 11

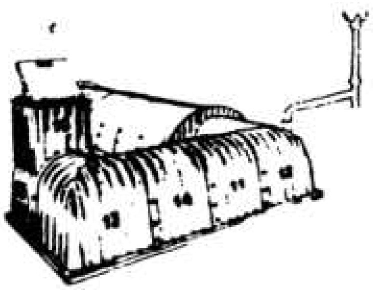

C 11

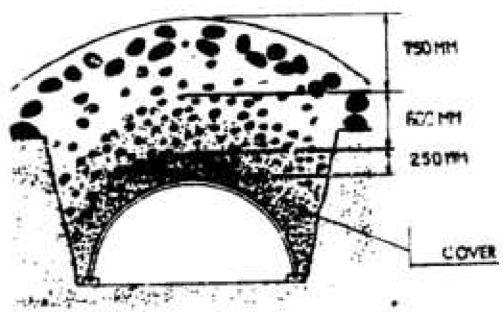

D 11

E 11
DETAIL

ASSEMBLAGE OF ELEMENTS

11:1 Mount element 13, Fig A11.

11:2 Mount element 14, Fig B 11.

11:3 Mount elements 15 and 16, Fig C11.

BACKFILL AND COVER

11:11 Use excavated masses for backfill and cover.

11:12 Try to fill at both sides of the shelter at the same time.

11:13 The cover must not have a steeper slope than 30°.

11:14 Use the bottom of the cowls as aiming points when covering the shelter, cf Fig E 11. The entrance part is covered to corresponding height.

11:15 There must be a 1600 mm cover.

11:16 If necessary, dig 100 mm deep grooves around the upper edge of the entrance element to take care of rain-water.

FORTIFIKATIONSFÖRVALTNINGEN

SH 10-GROUP HELMET

JOB SPECIFICATION	SHEET No
ASSEMBLING ENTRANCE ELEMENTS 12, 13, 14, 15 AND 16. BACKFILL AND COVER	11

APPENDIX B

PRESSURE DATA

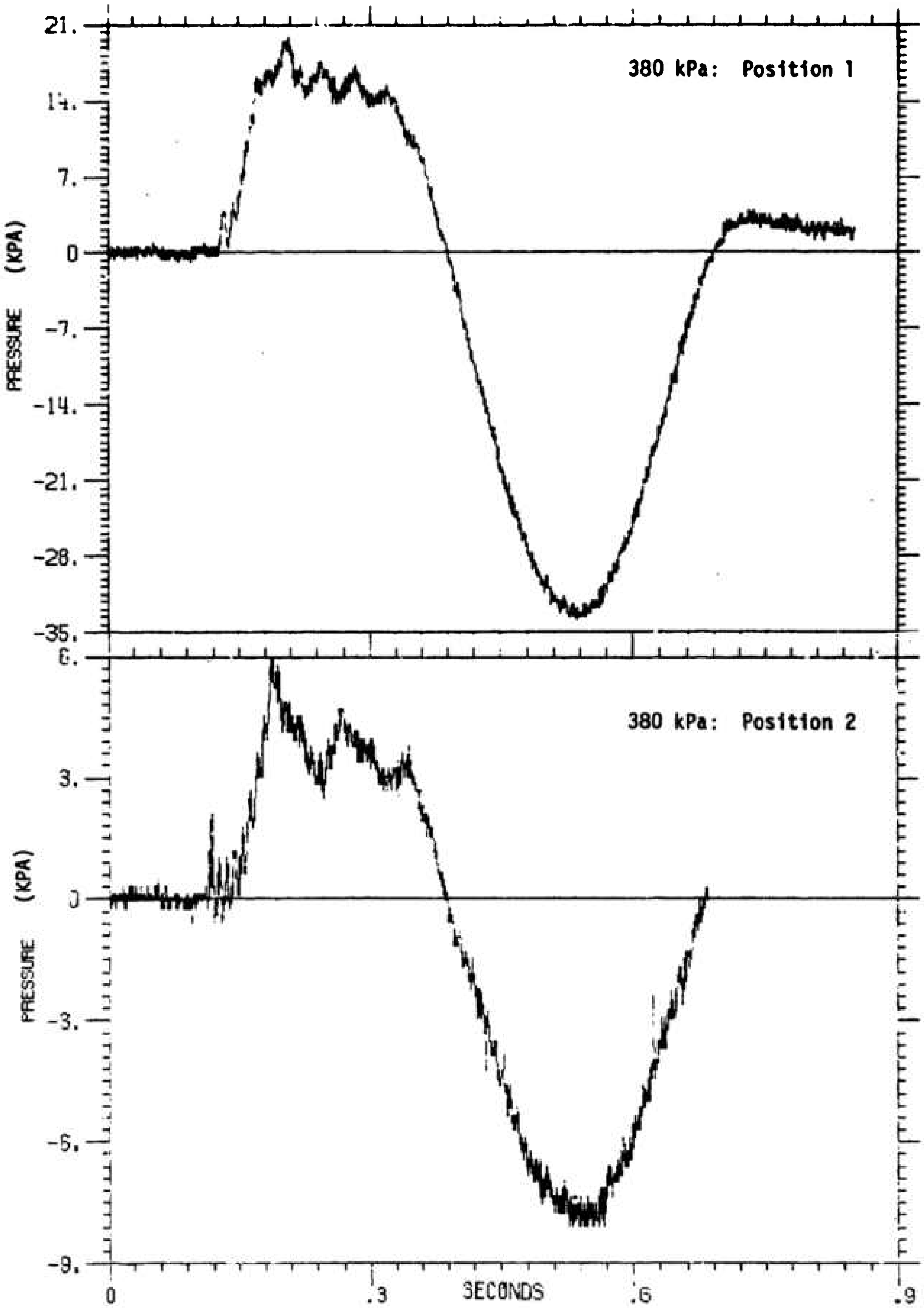

21.
14.
7.
0
-7.
-14.
-21.
-28.
-35.
PRESSURE (KPA)
380 kPa: Position 1
6.
3.
0
-3.
-6.
-9.
PRESSURE (KPA)
380 kPa: Position 2
0
.3
SECONDS
.6
.9

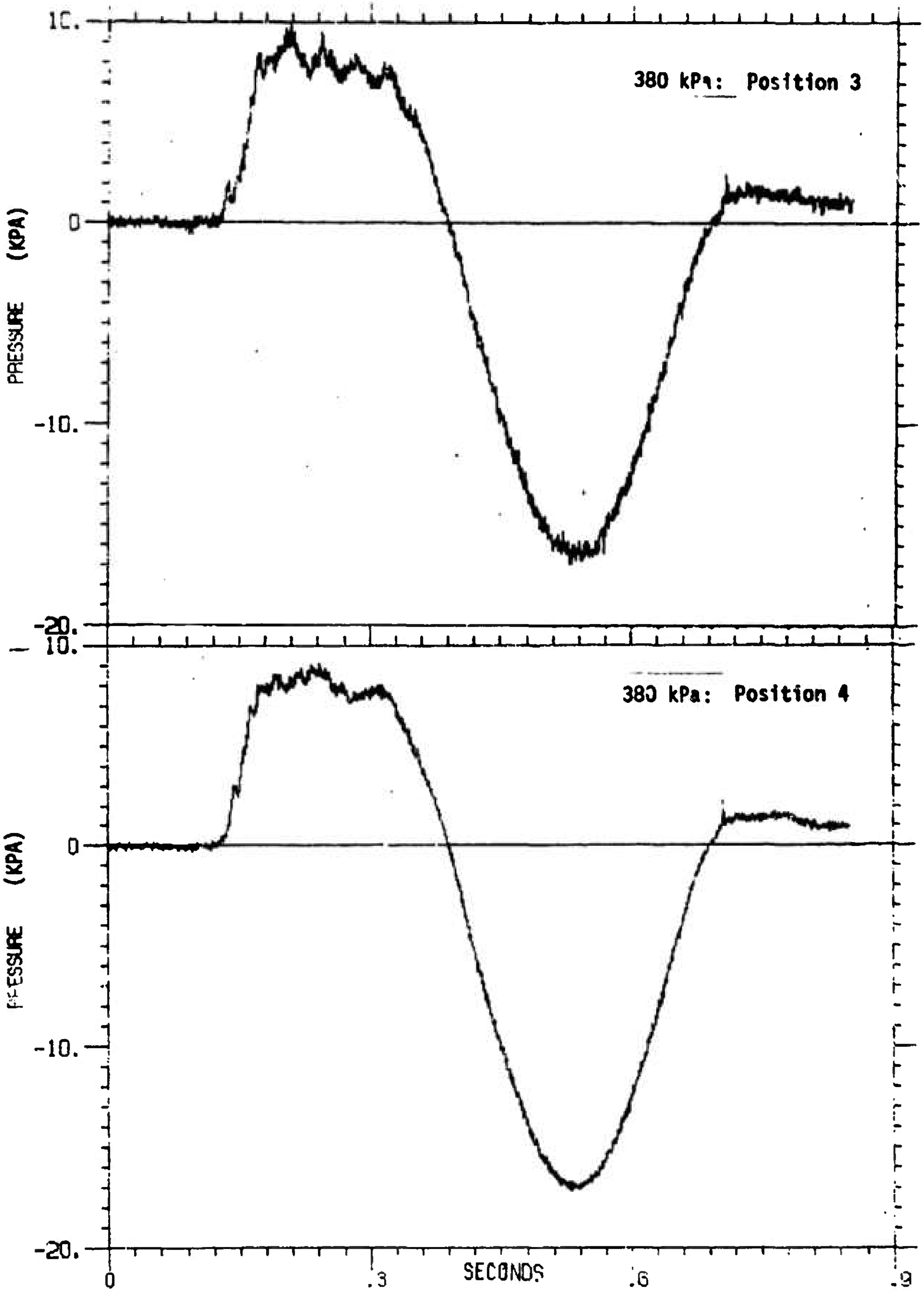
380 kPa: Position 3
380 kPa: Position 4
PRESSURE (KPA)
PRESSURE (KPA)
10.
0
-10.
-20.
10.
0
-10.
-20.
0
.3
SECONDS
.6
.9

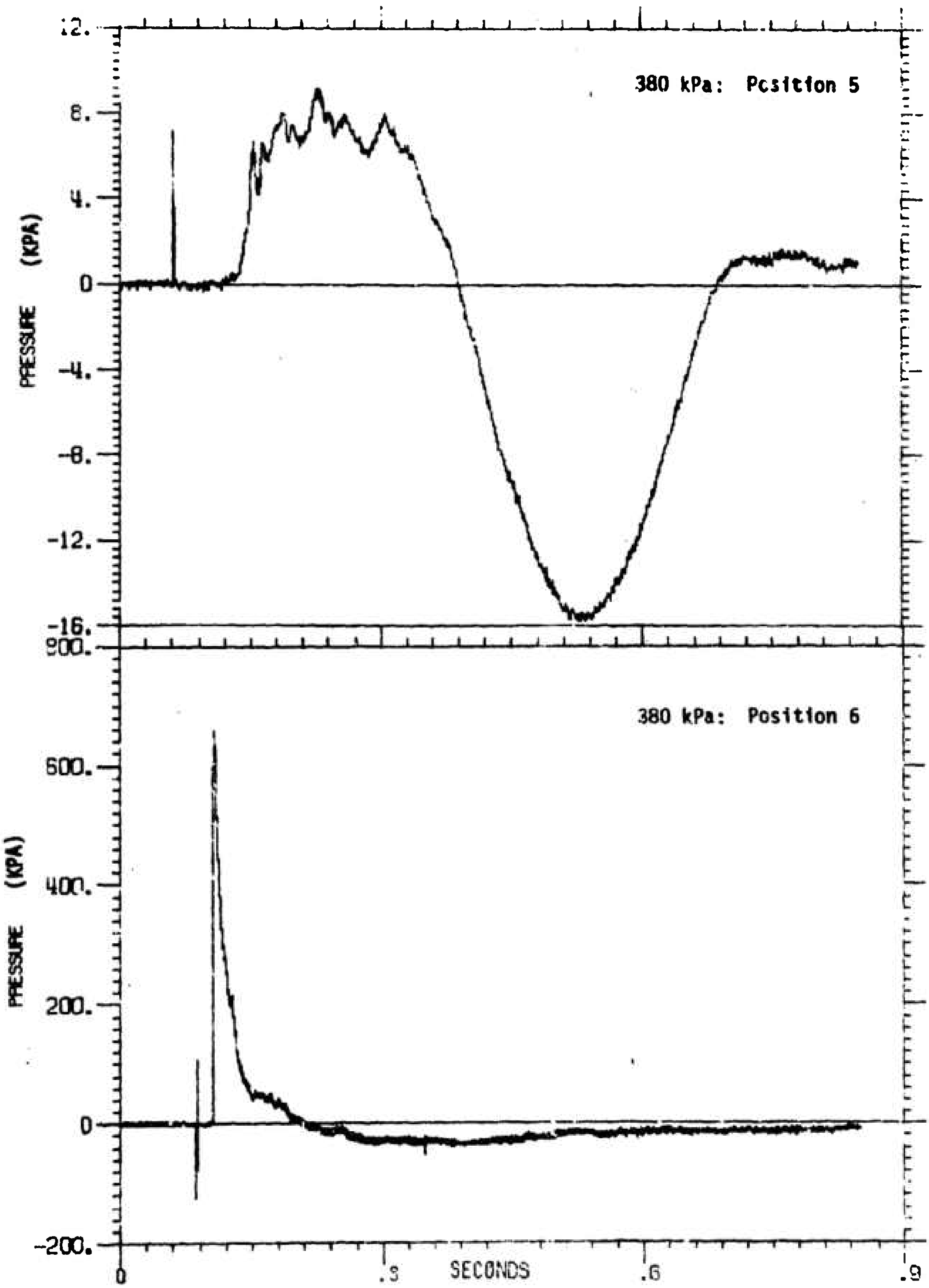
380 kPa: Position 5
380 kPa: Position 6
PRESSURE (KPA)
PRESSURE (KPA)
12.
8.
4.
0
-4.
-8.
-12.
-16.
800.
600.
400.
200.
0
-200.
0
.3
SECONDS
.6
.9

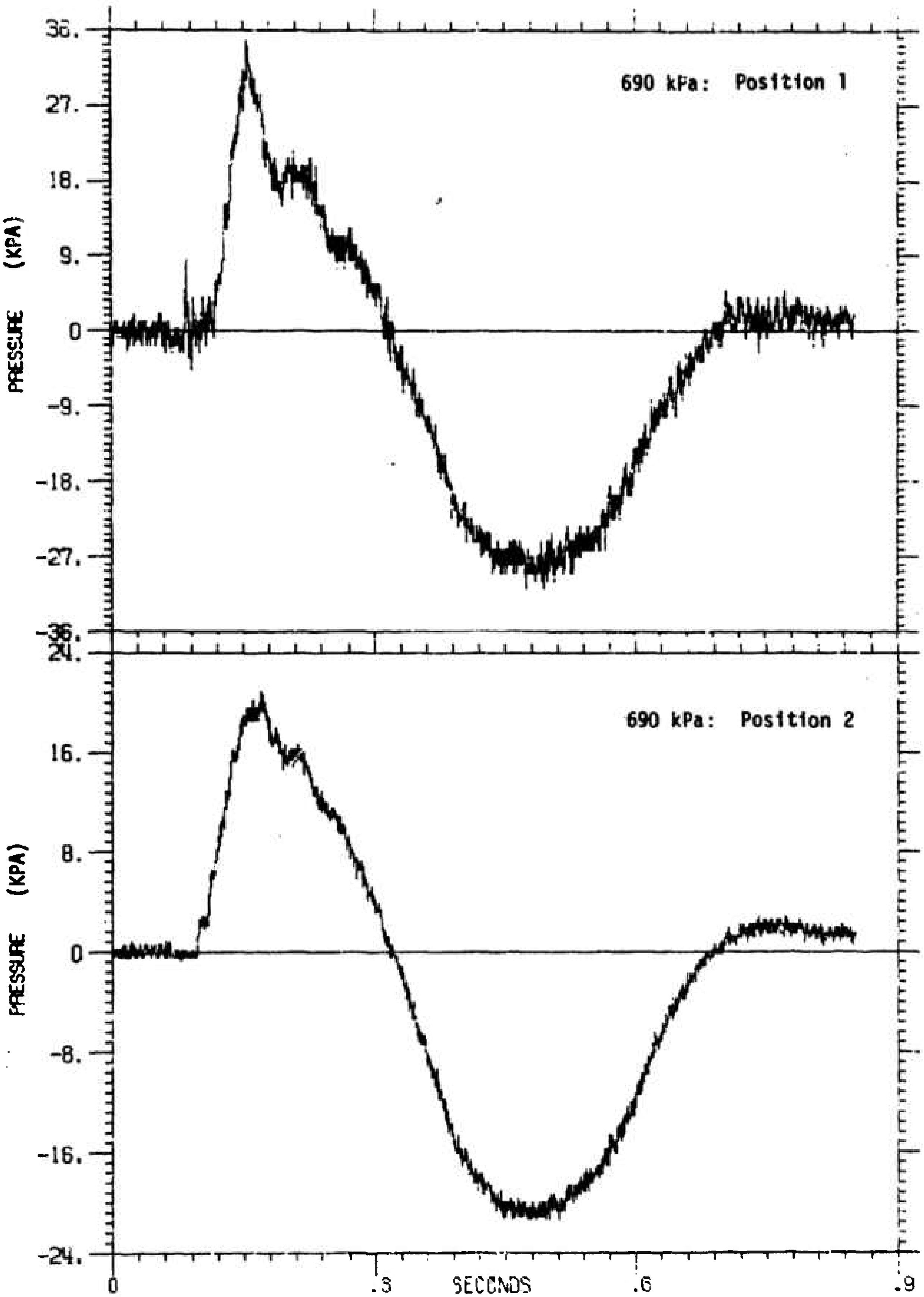

690 kPa: Position 1
690 kPa: Position 2
PRESSURE (KPA)
36.
27.
18.
9.
0
-9.
-18.
-27.
-36.
24.
16.
8.
-8.
-16.
-24.
0
.3
SECONDS
.6
.9

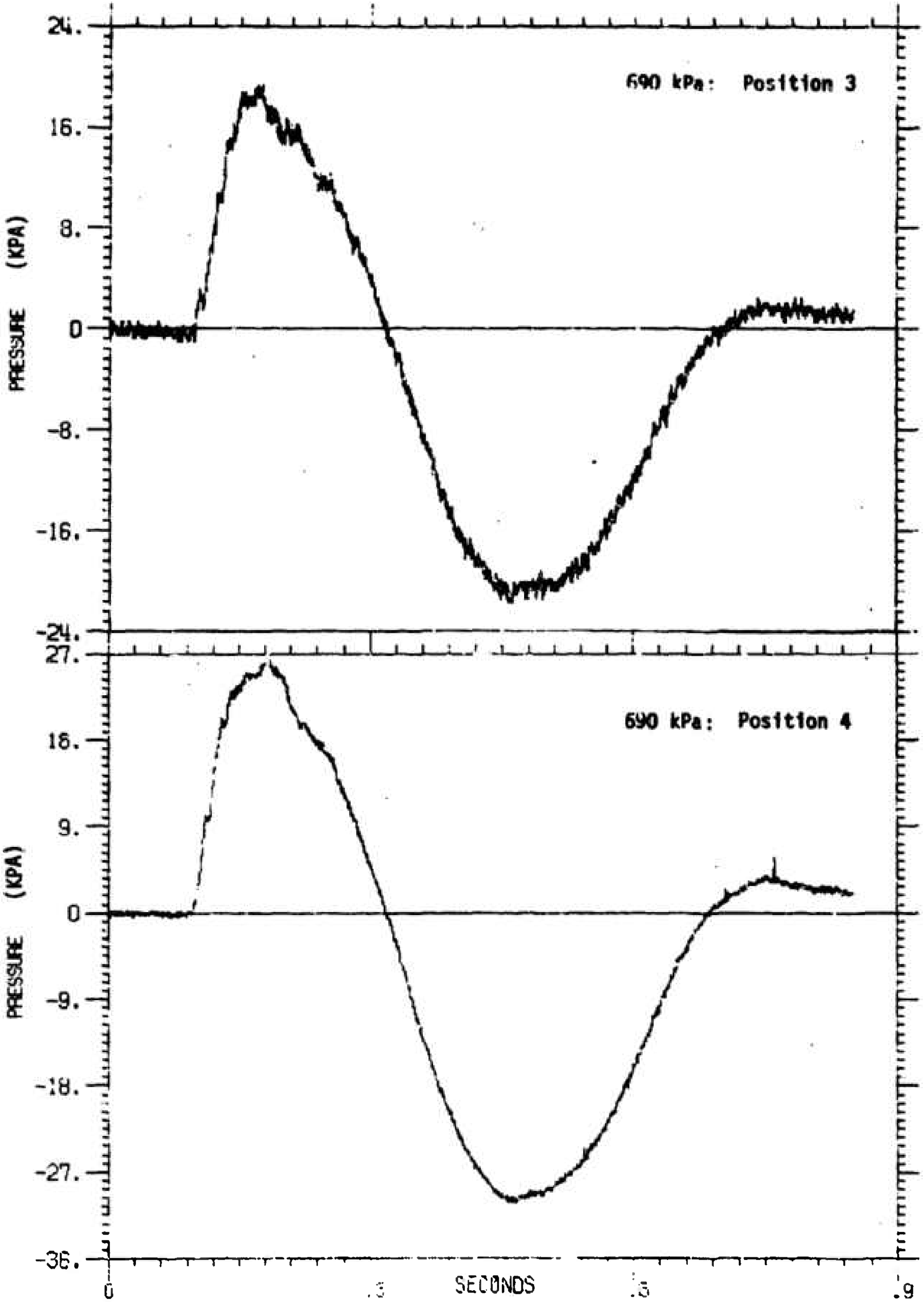
690 kPa: Position 3
690 kPa: Position 4
PRESSURE (KPA)
PRESSURE (KPA)
24.
16.
8.
0
-8.
-16.
-24.
27.
18.
9.
0
-9.
-18.
-27.
-36.
0
.3
SECONDS
.6
.9

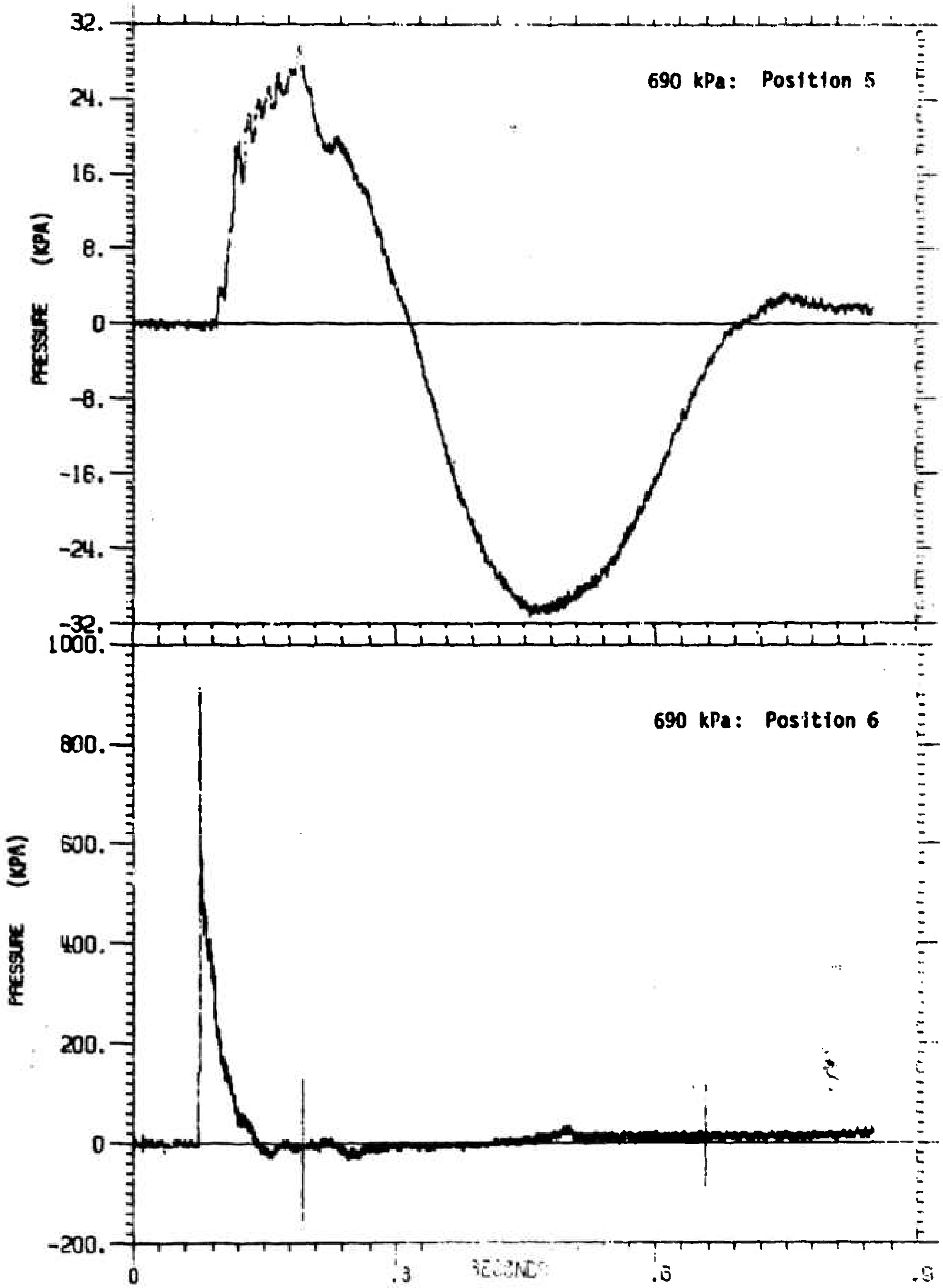

32.
24.
16.
8.
0
-8.
-16.
-24.
-32.
PRESSURE (KPA)
690 kPa: Position 5
1000.
800.
600.
400.
200.
0
-200.
PRESSURE (KPA)
690 kPa: Position 6
0
.3
.6
.9

APPENDIX C

SHELTER DAMAGE

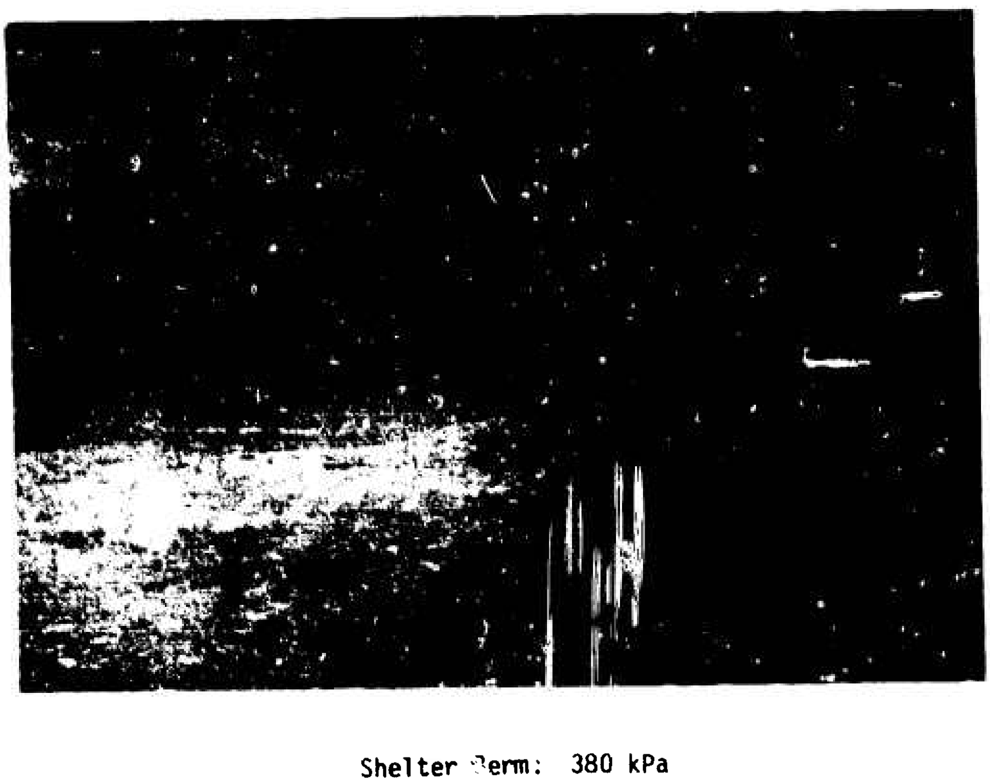

Shelter Berm: 380 kPa

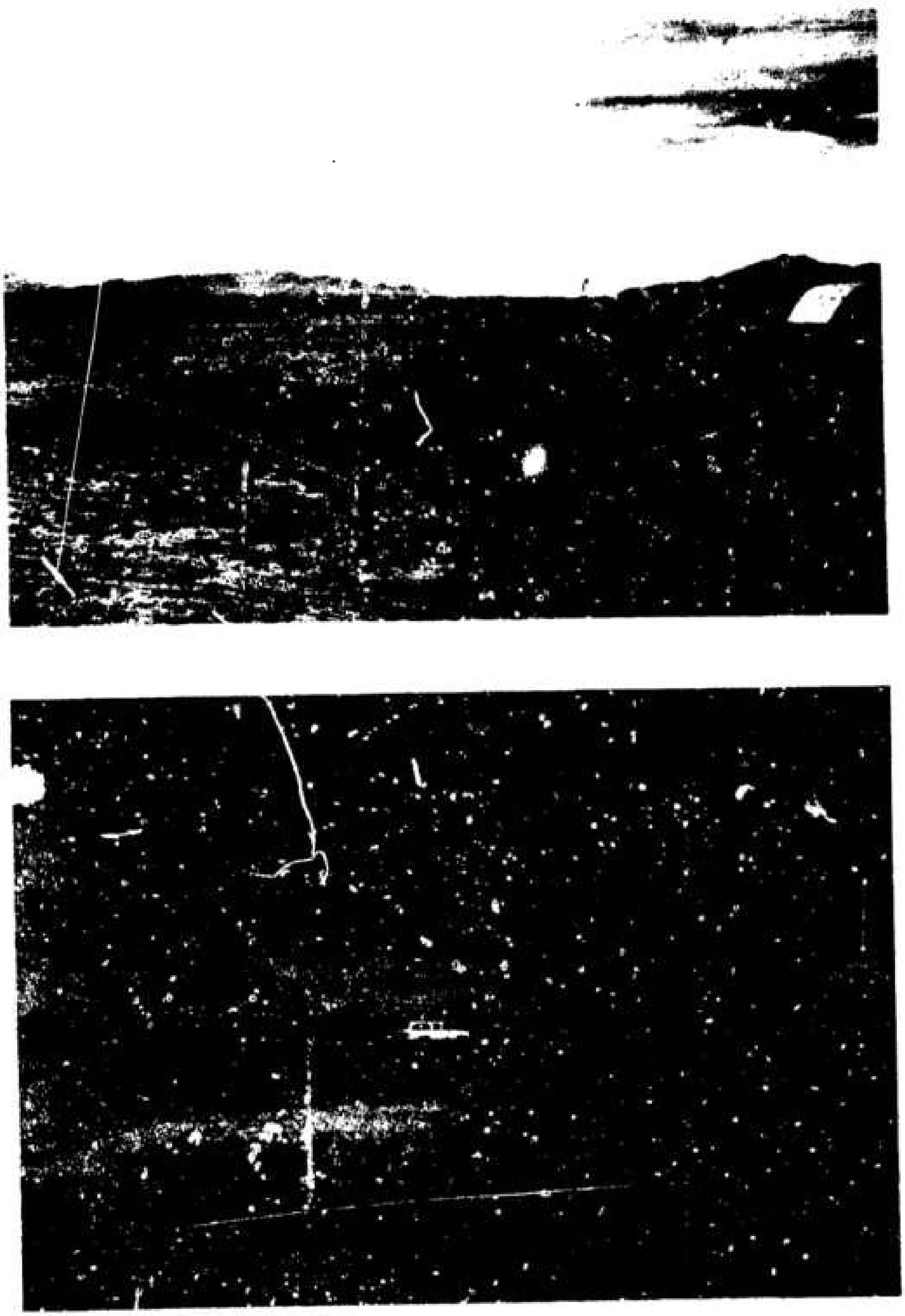

Shelter berm: 690 kPa

Shelter Door: 380 Pa

Shelter Entrance: 380 kPa

Shelter Back: 380 kPa

Shelter Front: 380 kPa

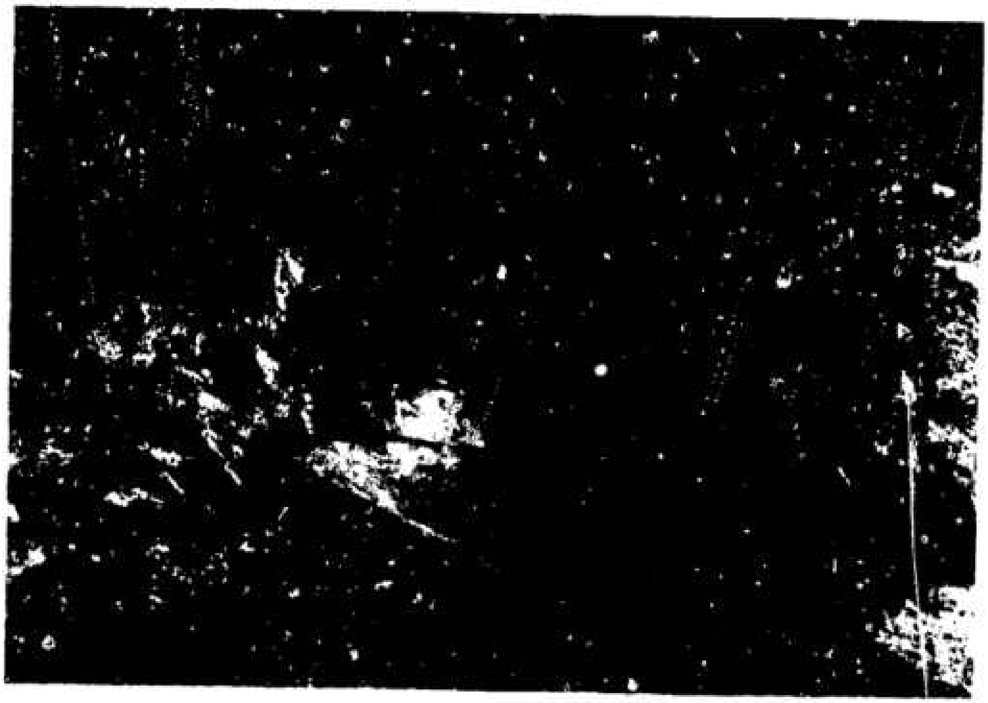

Shelter Door: 690 kPa

Shelter Entrance: 690 kPa

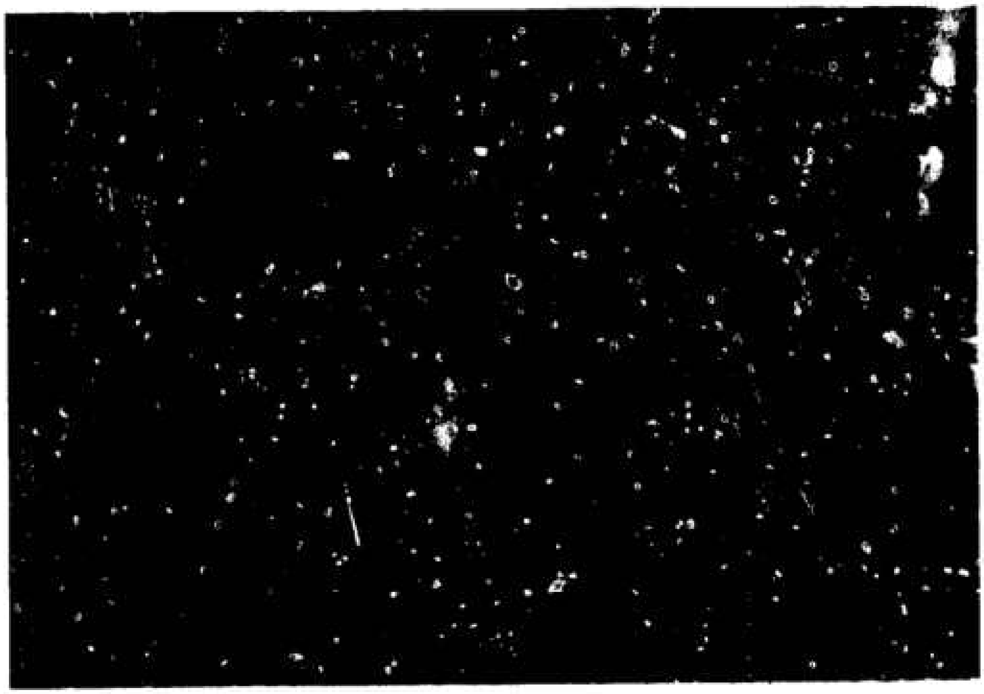

Shelter Intake Pipe: 690 kPa

Shelter Back: 69 kPa

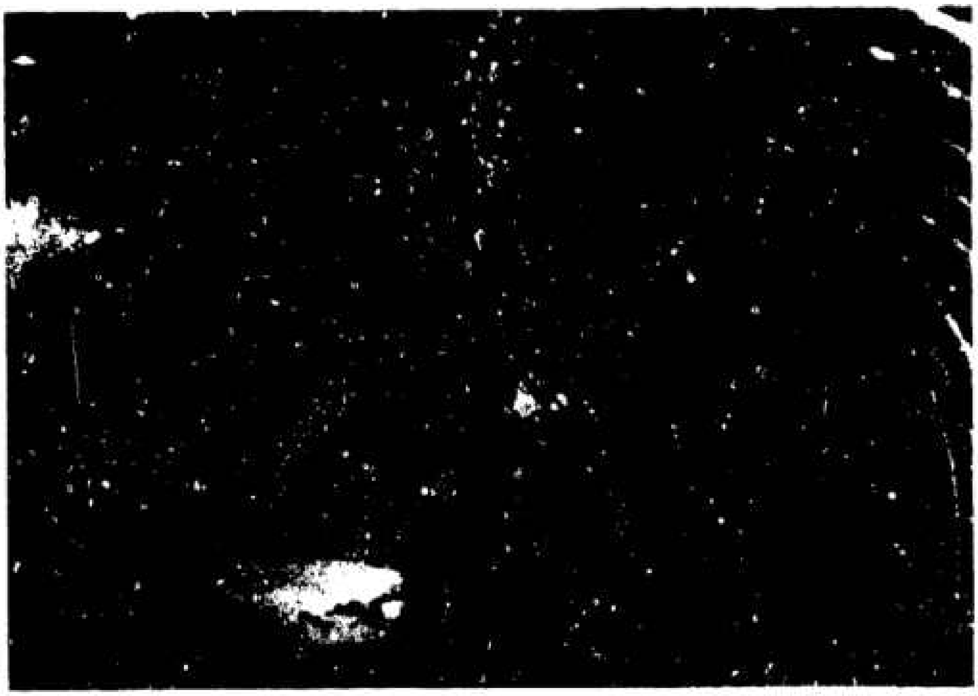

Shelter Front: 690 kPa

Shelter Damage: 690 kPa

Shelter Damage: 690 kPa

Shelter Damage: 690 kPa

17. PROJECT C-4, FREE-FLIGHT MEASUREMENT OF THE DRAG FORCES ON CYLINDERS - EVENT DICE THROW

by

A.W.M. Gibb and D.A. Hill

Defence Research Establishment Suffield

PROJECT C-4 FREE-FLIGHT MEASUREMENT OF THE DRAG FORCES ON CYLINDERS - EVENT DICE THROW

A.W.M. Gibb and D.A. Hill
Defence Research Establishment Suffield
Ralston, Alberta, Canada

ABSTRACT

Results are presented from a Canadian experiment to measure aerodynamic drag on circular cylinders under unsteady flow conditions in a long duration free-field blast wave. These results provided drag loading information required for analysis of the structural response tests on Canadian Navy masts and antennae reported herein. Seven cylinders, distributed at nominal 20, 10, and 7 psi peak overpressure locations and spanning three different diameters (3.5, 9.5, and 18 inches) were studied. The 18-inch diameter cylinder at 20 psi with 48-inch diameter end plates was partially destroyed by a sidewise blast pressure anomaly travelling from east to west. No useful data were obtained for this cylinder, but the remaining six cylinders yielded valid data. A free-flight method, developed in earlier trials (Prairie Flat, Dial Pack, Mixed Company) was employed to measure time-dependent drag pressures. For every cylinder, one velocity transducer was attached to each end of the central shaft to record cylinder velocity vs time, while a high-speed camera recorded displacement vs time. Cylinder acceleration, and hence drag pressure, was obtained from the slope and curvature, respectively, of these curves. Generally good agreement was obtained between results derived from camera and transducer data. Dynamic pressure (needed to extract drag coefficients) was calculated, assuming a Friedlander-type overpressure decay, from ground-level gauge measurements of overpressure-time histories at the 20, 10, and 7 psi peak overpressure locations. Some cylinders were fitted with extended end plates to reduce end effects. Comparison of results for cylinders with and without extended end plates indicated the presence of substantial end effects at critical and supercritical Reynolds numbers. Dust samples were collected at each cylinder location on vertical aluminium channels filled with grease. These samples, combined with camera records, suggest that dust loading was insignificant at the initial cylinder positions 5 or 6 feet above ground. Measured drag coefficients for Mach number <0.4 were in agreement with steady-state values for Reynolds numbers in the range $(4\text{-}30)\times10^5$, but were lower than steady-state values in the range $(30\text{-}40)\times10^5$.

1. INTRODUCTION

One of the Canadian projects in Event Dice Throw was the measurement of aerodynamic drag on right circular cylinders, using the free-flight method. The purpose of the project was to provide blast loading information for the lattice mast[1], polemast[2], and whip antennae[3], which underwent structural response testing during this trial. This project was a continuation of research begun in Operation Prairie Flat and continued in Events Dial Pack[5,6] and Mixed Company[7].

Seven cylinders of circular cross-section were employed. Their basic properties are summarized in Table 1. Two of the diameters employed, 3.5 inches and 9.5 inches, were chosen because they correspond closely to the diameters of the main structural members of the related structures (3.5 inches - whip antenna and lattice mast; 9.5 inches - polemast). The third diameter, 18 inches, was included to support future mast designs. The cylinders were located at the same peak overpressure levels as their related structures (3.5-inch diameter at 10 psi, 9.5-inch diameter at 7 psi). An additional 3.5-inch diameter cylinder was located at 20 psi peak overpressure. The major unresolved problem chosen for study in this test was the influence of end effects on the measured drag coefficient. With this goal in mind, the cylinders of a given diameter were grouped in pairs. In each pair, one cylinder had end plates with the same diameter as the cylinder diameter; the second cylinder had end plates with a diameter which was 3 times the cylinder diameter. The purpose of the extended end plates was to eliminate end effects by cutting off the air flow over the ends of the cylinder.

The methods of data recording were the same as those developed and used in previous trials employing the free-flight method. Velocity transducers were used on all test cylinders to record cylinder velocity as a function of time. In addition, a high-speed camera, operating at approximately 1000 frames/second, was stationed at each cylinder location to record cylinder displacement as a function of time. The slope of the velocity-time curve, and the curvature of the displacement-time curve provided independent measurements of cylinder acceleration, and hence drag force, as a function of time. The camera records also provided secondary information on possible complicating factors such as cylinder rotation and the presence of solids (both fine dust or massive particles) in the blast wave.

All of the measurements reported herein refer to the drag phase of loading on the cylinder. No measurements of loading during the initial shock diffraction phase are reported.

2. APPARATUS

2.1 TEST CYLINDERS AND MOUNTS

Figure 1 indicates the relative position of each cylinder with respect to Ground Zero.

A typical test set-up is shown in Figure 2.

At each location, support for the cylinders was provided by two vertical rectangular plates, made of 0.25-inch steel with their bottom edges fastened firmly to a concrete base. Additional rigidity for these plates was provided by triangular support in the form of two one-inch diameter steel bars welded to the outside of the support plates at an angle of 30 degrees approximately 5 feet above ground level. The lower ends of these bars were set into the concrete base.

The construction of a typical cylinder is illustrated in Figure 3. Each was a right circular cylinder with a solid centre shaft of 0.75 or 1.0-inch diameter which extended 14 inches beyond the ends of the cylinder. Flats were cut in the shaft nine inches from each end of the cylinder, and the cylinder was suspended between the support stand with the flats resting on the tops of the support plates. The purpose of the flats was to prevent the cylinders from rolling off of the supports under the nfluence of small gusts of wind prior to the shot. The coefficient of sliding friction between support plate and cylinder shaft was minimized by application of silicone grease to the top of the support plate.

2.2 VELOCITY TRANSDUCERS

The velocity transducers for measuring cylinder velocity directly as a function of time consisted of seven pairs of Hewlett-Packard Sanborn 7LV9 transducers. On a given cylinder, two transducers were used, one coupled by a mechanical linkage to each end of the cylinder shaft. The transducer signals were recorded separately, on a tape recorder with nominal 4 KHz recording bandwidth. This provided two independent measurements of velocity for each cylinder. A close-up view prior to the shot showing the transducer coil in its gimbal mount, and the mechanical linkage which couples the magnet inside the coil to the end of the cylinder shaft, is presented in Figure 4.

The Sanborn 7LV9 transducers used in this trial had two working lengths (each 9 inches). The overall recording length of approximately 20 inches was sufficient to permit between 80 and 200 miliseconds of cylinder motion to be recorded.

The transducers were calibrated by an electromechanical method which employed a Kistler standard accelerometer and shake table. The calibration error was estimated to be ±3%. In addition, careful inspection of transducer traces indicated possible variations of

±2% in the uniformity of response over any working length. An overall uncertainty of ±5% in the velocity calibration was assumed when analyzing the data.

2.3 CAMERAS

Photosonic framing cameras, operating at nominal speeds of 1000 frames/second were set on camera posts at each cylinder location to record displacement of the cylinders as a function of time. A camera set on its mounting post can be seen in Figure 5. Relevant information on the cameras and their locations is given in Table 2.

The cameras provided internal timing marks which were projected onto the film at 10 millisecond intervals to permit the framing rate to be established and the constancy of the framing rate over the recording interval to be checked. The timing mark generators functioned on all cameras. To signal the time of arrival of the shock front in the film frame, a red ribbon was glued to the back edge of the support plate. Horizontal distance calibration was provided by a photomarker plate with a 12-inch scale marked off in inches. Both of these aids can be seen clearly in Figure 4.

Approximately one week before shot day, Test Command moved the shot time forward from 1300 hours to 0800 hours. This change provided potentially serious problems for the camera recording system. The position of the sun at 0800 hours was such that it came close to shining directly into the camera lenses. The cylinder ends to be photographed were in shadow, and the high background light level caused extremely poor image contrast. Hastily-constructed aluminium foil reflector panels, bolted to each camera post (Fig. 5), provided sufficient reflected light to permit pictures of acceptable contrast to be recorded at shot time by all cameras. However, a slightly denser cloud cover at shot time could have ruined the camera experiment entirely.

2.4 DUST COLLECTORS

Since it was known that dust entrained in the blast wave could significantly alter the measured drag pressure, it was felt to be important to obtain some indication of the contribution of dust loading. A series of simple dust collectors consisting of 6-foot high vertical aluminium channels filled with grease were located at strategic points on the layout (Fig. 6). The results of this experiment are the subject of a separate report.[8]

The ground surrounding the Canadian projects was treated with a sprayed-on plastic coating approximately 1/8-inch thick. Camera records and dust collectors confirmed that the coating was highly effective in suppressing dust. The extent of the treated ground can be clearly seen in Figure 7.

3. DATA ANALYSIS

3.1 GENERAL

The goal of the analysis was to obtain the aerodynamic drag coefficient as a function of time, $C_D(t)$. C_D is defined by the equation[11]

$$P_D(t) = C_D(t)\, q(t) \tag{1}$$

where P_D is drag pressure

C_D is drag coefficient

q is dynamic pressure

and the time-dependence of each quantity is noted explicitly.

The velocity-time data, $v(t)$, and displacement-time data, $x(t)$, were fit by power series in time, as described in Sections 3.2 and 3.3.

Drag pressure is related to the slope of $v(t)$ and curvature of $x(t)$, through the relations

$$\frac{dv(t)}{dt} = a(t), \quad \frac{d^2x(t)}{dt^2} = a(t) \tag{2}$$

and $$P_D(t) = \frac{m}{A}\, a(t) \tag{3}$$

where x is cylinder displacement

v is cylinder velocity

a is cylinder acceleration

m is cylinder mass

A is frontal area of cylinder

t is elasped time after arrival of shock front at cylinder.

For the purposes of this experiment, dynamic pressure, $q(t)$, was replaced in Equation (1) by the closely-related quantity impact pressure, $q_I(t)$, in an attempt to reduce the dependence of $C_D(t)$ on Mach number. The derivation of $q_I(t)$ from measured free-field overpressure-time histories, and the reason for replacing $q(t)$ with $q_I(t)$, are elaborated in Sections 3.4 and 3.5.

3.2 VELOCITY TRANSDUCER DATA

3.2.1 Conversion from Analog to Digital Velocity-Time Signal. The analog signals recorded on magnetic tape during the trial were digitized after the trial at a digitizing rate of 16 KHz using an analog-to-digital converter. A previously-determined calibration factor was applied to each voltage-time record to convert it to a velocity-time record.

After establishing by visual inspection that digital smoothing of the transducer signals would not suppress any significant features in the data, a smoothing was performed by averaging each consecutive interval of 8 points. At the time that the curve fitting was performed, the interval between data points was 0.5 msec.

The characteristic transducer response time (approximately 2 msec) was not fast enough to follow the abrupt change in velocity occurring during the initial diffraction phase of shock loading on the cylinder, which lasts for about 1 millisecond. There was, therefore, little point to analyzing velocity-time data during the initial recovery time of the transducer. For this reason, only data from 3 msec onward were retained for analysis.

3.2.2 Philosophy of Curve-Fitting. A power series in time was chosen to fit the velocity-time data, for three reasons:

(1) Such a series provides a simple analytic expression for acceleration as a function of time, and it is the latter which is required to obtain drag pressure vs time.

(2) A power series in time is linear in the fitting parameters. This fact permits a linear least squares criterion to be used to determine the best-fit function. The theory of linear least squares fitting provides a straightforward prescription for the uncertainties in the fitting parameters, as well as for uncertainties in functions linear in these parameters. This fact permits one to derive the uncertainty in drag pressure in terms of the uncertainties in the original velocity-time data.

(3) Available evidence on the expected shape of $C_D(t)$, and on the known shape of $q_I(t)$ (impact pressure) suggests that, for the Mach and Reynolds number ranges studied in this experiment, the variation of $P_D(t)$ is sufficiently smooth to be well described by a low-order power series in time.

Before a fitted function was accepted as an accurate description of the variation of drag pressure with time, three conditions had to be satisfied:

(1) Reasonable limits on uncertainty in acceleration (low order power series),

(2) Stable first derivative,

(3) Correct physical behaviour at early times (when dynamic pressure is large and decays rapidly) and at later times (when drag pressure is decaying to zero asymptotically).

If the fitting functions failed to meet all of these criteria for a particular data set, then all high-order fits were rejected as unsuitable and a linear fit to drag pressure (quadratic fit to velocity data, cubic fit to displacement data) was chosen. The linear function correctly describes the trend in pressure in that it decreases with time, but is physically unrealistic to the extent that it lacks curvature. It should be considered as a coarse averaging function which contains no information on the detailed shape of drag pressure as a function of time. For this reason, in comparing linear and higher-order fits to drag pressure, only averages over, say, 25 msec intervals should be used.

3.2.3 Effect of Non-Random Fluctuations in Velocity-Time Data. As was the case in all previous trials, non-random fluctuations were evident in all transducer signals. These can be subdivided into two categories:

- pure (damped) sinusoidal oscillations
- irregular fluctuations.

Pure sinusoidal oscillations: Large single-frequency oscillations were observed in the velocity-time spectra from transducers attached to Cylinders, 3, 4, and 5. By inspection of the corresponding camera records, it was established that they were oscillations of the solid centre shaft of the cylinder to which the transducers were attached. An attempt was made to remove this single-frequency component using Fourier analysis. Due to the short length of the v(t) spectrum, the presence of gaps at the beginning and in the middle of the spectrum, and the fact that the oscillation was damped, it proved impossible to apply a sufficiently precise frequency filter which would remove the oscillatory component without simultaneously distorting the shape of the velocity-time trace.

The next approach employed was an attempt to fit the velocity-time spectrum with a function of the form:

$$v(t) = v_1(t) + v_2(t) \tag{4}$$

where

$$v_1(t) = a_1 + a_2 t + a_3 t^2; \quad v_2(t) = a_4 e^{-a_5 t} \sin(2\pi a_6 t + a_7) . \tag{5}$$

This function, which includes an explicit damped sinusoidal term, contained seven fitting parameters (a_1- - - - a_7). A least squares best-fit criterion was adopted, and the best-fit function was found by a parameter search method. It was useful to compare the best-fit coefficients a_1, a_2, a_3 obtained using this function with the best-fit coefficients obtained by a linear least squares procedure using a second order power series only. The results indicate that, at least for a second order polynomial fit to velocity, the two methods give similar answers for the polynomial describing the velocity-time curve. The parameter search method could not be extended to v_1 functions containing powers of t higher than two because of the inordinate demands on computer time.

The results for second order lend credence to the assumption that, when the sinusoidal term is omitted from the fitting functions, oscillations in the data about the mean value are sufficiently rapid that they do not seriously affect the choice of best-fit power series. As explained in Section 3.2.2, a simple power series fitting function was adopted.

Irregular fluctuations: On Cylinders 2, 6, and 7, irregular fluctuations were superimposed on the sinusoidal oscillations. The fluctuations are most likely caused by static friction between the moving magnet and surrounding coil housing at the turning points in the coil motion. In the error analysis, it was assumed that the fluctuations were random.

3.3 CAMERA DATA

3.3.1 Use of Film Reader. Developed films from the high-speed cameras were analyzed with the aid of a precision film reader. Timing marks projected onto the film at 10 millisecond intervals were used to establish the framing rate. A horizontal distance scale in each film frame was provided by a photomarker plate attached to the support plate nearest the camera and marked off over a 12-inch interval in alternate black-and-white 1-inch wide bands. The zero of coordinates was defined for each film frame to be the junction of the photomarker plate with the vertical back edge of the support plate.

For those cameras with 50mm focal length lenses (Table No. 2), non-linearity across the field of view could be neglected. For those cameras with 13mm lenses, a correction had to be applied for non-linearity across the field of view.

The measuring position on the cylinder was defined by the junction of alternate black and white sectors painted onto the end plates. Because the end plate is 9 inches farther from the camera than the photomarker plate, a simple geometrical correction had to be applied to the measured position coordinates.

It was necessary to apply a correction the the measured position coordinates to account for motion of the camera and mounting post under blast loading. The accuracy of position measurement was estimated to be ±.04 inch before any corrections were applied.

3.3.2 Philosophy of Curve-Fitting. The same considerations which governed the fitting of the velocity-time data discussed in Section 3.2 applied to the fitting of the displacement-time record from the high-speed cameras, except that one is interested in the second, rather than the first, derivative, and the record is continuous. In addition, the ability to observe the cylinder end, rather than the end of the cylinder shaft, meant that the oscillations of the cylinder shaft, so prominent in the velocity transducer data, were absent in the camera data.

3.4 FREE-FIELD OVERPRESSURE MEASUREMENTS

Side-on pressure gauges mounted at ground level were used to record overpressure-time histories of strategic points on the Canadian layout. These measurements are the subject of a related report.[9] Four gauges were located in the vicinity of the 20 psi overpressure position, six gauges in the vicinity of the 10 psi overpressure position, and four gauges in the vicinity of the 7 psi overpressure position.

Each overpressure-time curve was assumed to follow the empirical Friedlander decay formula

$$p(t) = p_0 F \tag{6}$$

where

$$F = 1 - \frac{t}{t_+} \; e^{-k\frac{t}{t_+}}$$

with p_0 = peak overpressure (psi)

t_+ = duration of positive overpressure phase

k = Friedlander decay constant (empirically determined).

The positive duration, t_+, was determined by visual inspection of the digitized pressure-time records.

The overpressure impulse, I, defined by

$$I = \int_0^{t_+} p(t)\, dt \tag{7}$$

was obtained by numerical integration of the area under the measured pressure-time record from $t=0$ to $t=t_+$. Integration of Eq. 6 from $t=0$ to $t=t_+$ leads to the equation

$$\frac{I}{p_0 t_+} = \left[\frac{1}{k} - \frac{(1 - e^{-k})}{k^2}\right]. \tag{8}$$

The function on the right is an unique function of the decay constant k only. This function was plotted and the value of k determined graphically for each pressure gauge by calculating the ratio $\frac{I}{p_0 t_+}$ using experimental values of I, p_0, and t_+ determined directly from the measured pressure-time records. Once the parameters I, p_0, t_+ and k were determined for each gauge at a given nominal peak overpressure location, a best value was determined for each parameter by averaging the results from all the gauges at that peak overpressure location. The scatter in the values of the parameters about the mean value was used to provide an estimate of the uncertainty in each parameter.

3.5 IMPACT PRESSURE CALCULATIONS

The dynamic pressure q and impact pressure q_I were assumed to decay as F^2,[10], i.e.,

$$q(t) = q_0 F^2 \tag{9}$$

$$q_I(t) = q_{Io}F^2 \tag{10}$$

where the peak dynamic pressure, q_o, is determined from the Rankine-Hugoniot relations at the shock front to be [10]

$$q_o = \frac{5}{2}\frac{p_o^2}{(p_o + 7p_a)} \tag{11}$$

and the peak impact pressure is determined to be [11]

$$q_{Io} = q_o + \frac{q_o^2}{2.8(p_o + p_a)} \tag{12}$$

where p_o = peak overpressure

p_a = ambient pressure.

It has been the practice in recent years at our Establishment to define drag coefficient in terms of impact pressure, rather than dynamic pressure (see Eq. 1) because drag force for compressible fluids is directly related to impact, rather than dynamic pressure. This practice has been continued in this report. The ratios of impact pressure to dynamic pressure at the 20.1, 9.7 and 6.7 psi peak overpressure locations were 1.103, 1.039, 1.022, respectively, based on Equations 9, 10, 11 and 12.

3.6 CALCULATION OF MACH AND REYNOLDS NUMBERS

Free stream Mach and Reynolds numbers were calculated using standard definitions[11]. Fluid velocity was assumed to decay as $u = u_oF$ (13)

where F is defined in Equation 6,

and u_o was derived in terms of p_o and p_a from the Rankine-Hugoniot relations across the shock front.

The temperature of the flow behind the shock front was approximated by the isentropic relation. The kinematic velocity was described by a power series in temperature, where the coefficients of the series were obtained[4] by fitting a power series to values of kinematic viscosity for air at specific temperatures.

4. RESULTS

4.1 GENERAL

Figures 8 through 18 present results of fits to velocity transducer data and camera data for Cylinders 2 through 7 (except for Cylinder 2 where only transducer data are available). The case of Cylinder 1, which failed to undergo free flight under the influence of a blast anomaly, is discussed below. Figures 19 through 23 present derived drag pressures and drag coefficients for Cylinders 3 through 7 from both camera and transducer data. A summary of results for each cylinder, with qualifying remarks, is presented in Table 3. Tables 4, 5, and 6 have been included because they summarize the variation of dynamic pressure and impact pressure, as well as Mach number and Reynolds number, as a function of time after shock arrival, at the 9.7 and 6.7 psi peak overpressure location for 18-inch, 9.5-inch, and 3.5-inch diameter cylinders.

4.2 VELOCITY TRANSDUCER DATA

The data from east and west ends on a given cylinder were analyzed separately. The best-fit curve is drawn through the velocity-time data as a solid line. The dotted lines in the figures represent ± one root mean square (RMS) deviation in the scatter of data about the best-fit curve. It was assumed for purposes of error analysis, and in the absence of better information, that the RMS deviation had a constant value at all points on the curve. The acceleration curve is the first derivative of the best-fit velocity function. The dotted lines on the acceleration-, drag pressure-, and drag coefficient-time curves, however, respresent ± <u>three</u> standard deviations (99% confidence interval).

Velocity data for Cylinders 3, 4, 6, and 7 were fit by power series with terms up to the fourth power in time (5 parameters). Transducer data for Cylinders 2 and 5 were fit by power series with terms up to the second power in time (3 parameters).

4.3 HIGH-SPEED CAMERA DATA

Cameras recorded the motion of the west cylinder ends only. In the figures, the best-fit power series curve is drawn as a solid line through the displacement-time data. Dotted lines representing ± one RMS deviation, are also drawn, but are not evident on most drawings because the deviation is so small. On the velocity-, acceleration-, drag pressure-, and drag coefficient-time curves, however, the dotted lines represent ± <u>three</u> RMS deviations about the best-fit curve (99% confidence interval). Displacement data for Cylinders 3, 4, 5 and 6 were fit by a power series with terms up to the fifth power in time (6 parameters). Displacement data for Cylinder 7 were fit by a power series with terms up to the third power in time (4 parameters).

4.4 DRAG COEFFICIENT VS REYNOLDS NUMBER - BEFORE CORRECTIONS (FIG. 25)

For a given data record, the drag pressure-time curve was divided by the appropriate impact pressure-time curve (Fig. 24) to obtain drag coefficient as a function of time, $C_D(t)$.

In Figure 26, the resultant $C_D(t)$ curves are plotted as a function of Reynolds number for all cylinders for which the free stream Mach number is less than the critical value Mc = 0.48. For this Mach number range, the dependence of C_D upon Mach number is slight.

The use of impact pressure in place of dynamic pressure probably reduces this dependence even further.

In Figure 26, data which required a linear fit to drag pressure have not been included because a linear fit was felt to provide no detailed information on the <u>shape</u> of the drag pressure-time curve (see Section 3.2). The $C_D(t)$ values are presented as bands of uncertainty for three reasons:

(1) To permit a visual comparison of the relative accuracies of the velocity transducer and high-speed camera techniques.

(2) To emphasize that, for a given data record, the uncertainty in the derived drag coefficients is not constant across the record. The uncertainty is least near the middle of each record.

(3) To show the measure of agreement between drag coefficients obtained using the velocity transducer and high-speed camera technique.

In this Figure, and in the plots of $C_D(t)$ in Figure 19 through 23, no uncertainty in the calculated impact pressure has been included. This has been done so that the ratio of drag coefficients with and without extended end plates could be formed directly to assess the importance of end effects. In such a ratio, impact pressure cancels out, so the uncertainties in Figures 19 through 23 and Figure 26 are the appropriate ones to use for assessing end effects.

Included for completeness in Figure 26 is a solid curve representing drag coefficients measured in a wind tunnel under steady-state flow conditions.[12,13] The extension of the steady-state results to higher Reynolds numbers[14] is represented by the dotted portion of the curve.

4.5 END EFFECTS (FIG. 27)

The flow of air over the ends of finite-length cylinders can produce a measured drag coefficient which is different than the value that would be measured for an infinitely-long cylinder. Since the main structural members of the Canadian Navy masts and antennae tested in Dice Throw had relatively large length/diameter (L/D) ratios, drag coefficients for infinite-length cylinders were the appropriate input to structural response calculations for these structures.

In the present experiment, thin extended end plates were attached to the ends of some cylinders (Figs. 4 and 5) to prevent air flow around the ends of the cylinders, thereby eliminating end effects.

There was, of course, a contribution to the overall drag on the cylinder due to drag on the end plates themselves. However, because the end plates had bevelled knife edges, and the air flow is expected to be parallel to the faces of the end plates, the main contribution to end plate drag was skin friction drag, for which the maximum drag coefficient, according to Hoerner[15], is .008. Using this value for C_D, the fractional contribution by the end plates to the overall measured cylinder drag pressure was assumed to be given by

$$\frac{(C_D A)_{\text{end plate}}}{(C_D A)_{\text{end plate}} + (C_D A)_{\text{cylinder}}}$$

where $A_{\text{end plate}}$ is the total exposed surface area of the two end plates

A_{cylinder} is the frontal area of the cylinder

$(C_D)_{\text{end plate}} = .008$

$(C_D)_{\text{cylinder}} =$ measured value from experiment.

These calculated contributions from the end plates to the measured drag coefficient (approximately 10% for Cylinder 7, 7% for Cylinder 5, and less than 1% for Cylinder 2) were then subtracted from the measured coefficients to produce a set of corrected coefficients appropriate to infinite-length cylinders. It is these coefficients which are plotted in Figure 28.

Since the experiment included pairs of identical cylinders with and without extended end plates, at the same peak overpressure locations, it was possible to measure end effects directly by forming the ratio

$$\frac{C_D \text{ (with extended end plates, corrected for end plate drag)}}{C_D \text{ (without extended end plates)}} .$$

These ratios were formed, using drag coefficients averaged over 25 msec intervals, for Cylinders 6 and 7 (velocity transducer data) and Cylinders 4 and 5 (camera data). The results are plotted in Figure 27 as a function of elapsed time after shock arrival.

For Cylinders 6 and 7, with an L/D ratio of 17, the first two points in Fig. 27

covering 50 msec of motion correspond to Reynolds numbers $(9\text{-}5)\times10^5$, i.e., just above the critical Reynolds number range $(5\text{-}3)\times10^5$. The value of the C_D ratio is slightly less than 1 but consistent with unity. The next three points correspond to Reynolds numbers in the critical range $(5\text{-}3)\times10^5$. For these points, the C_D ratio lies below 1. A slight tendency for the ratio to decrease with time is noted. All points are consistent with the weighted average value of 0.78.

For Cylinders 4 and 5, which have an L/D ratio of 5, all of the data points correspond to Reynolds numbers in the supercritical range $(16\text{-}9)\times10^5$. Initial values of the C_D ratio are substantially greater than 1 and are not consistent with unity within error. Moreover, the ratio increases markedly for later times. The average value for the first 50 msec of motion is 1.43 while for the second 50 msec of motion it is 1.95. The average value for the first 100 msec of motion is 1.58, but not all of the data points agree with this value within error.

Due to the failure of Cylinder 1, the 18-inch diameter cylinder with extended end plates, it was not possible to measure end effects directly using Cylinders 1 and 3. In view of the large end effects observed for Cylinders 4 and 5 in the supercritical Reynolds number range with an L/D ratio of 5, it was felt that substantial end effects could also be expected for the 18-inch diameter Cylinder 3 whose motion spanned a somewhat higher Reynolds [illegible] range and which also had an L/D ratio of 5. Since no direct information was avai[illegible] for Cylinder 3, the average end effect factor of 1.58 measured for Cylinders 4 and 5, was applied to the camera data for Cylinder 3. These corrected data are plotted in Figure 28. It is notable in this Figure that, even after substantial end effect corrections, the two data points at highest Reynolds number (first 50 msec of motion) for the 18-inch diameter cylinder lie well below steady-state values. To obtain agreement with the steady-state values, the measured drag coefficients would have to be multiplied by an approximate factor of 2. If, instead of an average end effect factor, one employed the measured values for each 25 msec interval recorded in Figure 27, the two points at highest Reynolds numbers in Figure 28 would be <u>depressed</u> a further 10%, while the third point would be <u>elevated</u> a further 20% to lie above the steady-state value.

4.6 DUST LOADING

Both the greasy dust collectors described in Section 2.4 and the high-speed camera records provided qualitative information on the amount of dust entrained in the blast wave during the cylinder motion. Both dust collectors (see 7-foot tall dust collector in Figure 6) and camera records confirmed that a significant dust cloud existed only to a height of about three feet above ground, and that relatively little dust existed at the initial cylinder height 5 to 6 feet above ground. One would expect any dust loading to increase the effective drag force on the cylinder, thereby increasing the measured drag coefficient. The insignificance of dust loading is supported by the fact that the measured drag coefficients in Figure 28 were consisted with steady-state values over most of the range of measurement. The plastic coating sprayed onto the ground in the Canadian sector proved highly effective in suppressing dust, as evidenced by the relatively low dust levels in this trial compared to previous trials.

4.7 DRAG COEFFICIENT VS REYNOLDS NUMBER - AFTER CORRECTIONS (FIG. 28)

Figure 28 is a composite semi-log plot showing measured drag coefficients for "infinitely long" smooth cylinders in unsteady flow conditions for Reynolds numbers from $(3\text{-}40)\times10^5$. For the 3.5 inch and 9.5 inch diameter cylinders, data from cylinders with extended end plates were used, after subtracting a correction for end plate drag. For the 18-inch diameter cylinder without extended end plates, the average end effect factor of 1.58 measured for the 9.5-inch diameter cylinder was applied to the 18-inch cylinder results to convert them to values appropriate to a cylinder of infinite length. The error bars on the data points in this Figure include the uncertainties in impact pressure plotted in Figure 24. As in Figure 26, the solid line represents results from wind-tunnel experiments in steady-state flow conditions[12,13]. The extension by other workers of these results to higher Reynolds numbers[14] is represented by the dashed portion of the curve.

4.8 SURFACE ROUGHNESS

All of the cylinders were sanded and polished,after deep scratches were filled in with body-filler compound to ensure that all surface imperfections were less than 1/1000 of the cylinder diameter and that all scratches present were in the direction of air flow over the cylinder. Under these conditions, according to Hoerner[15], the cylinder could be considered aerodynamically smooth and the effect of surface imperfections on the air flow would be negligible.

4.9 DRAG COEFFICIENTS FOR SUPERCRITICAL MACH NUMBERS - CYLINDER 2

For Cylinder 2 at 20.1 psi peak overpressure, the flow Mach number fell from 0.63 to 0.50 during the first 20 msec of motion, and 0.50 to 0.38 during the next 20 msec of motion. During these intervals, Mach number was above $M_{critical} = .48$, so a large drag coefficient was expected. For Cylinder 2, only one transducer record provided useful data and these data contained large irregular fluctuations on the main signal. It was necessary to accept a linear fit to drag pressure to obtain reasonable uncertainty limits; only average drag coefficients over 20 msec intervals were considered meaningful (see Section 3.2.2). The large scatter in results from pressure gauges at the 20 psi peak overpressure location caused a correspondingly large uncertainty in impact pressure which reached 100% after only 60 msec of cylinder motion (Fig. 25). The net result was that only average drag coefficients for 0-40 msec were obtained, and these had large uncertainties associated with them.

The results were:

For 0-20 msec $C_D^{avge} = .76 \pm .20.$

For 20-40 msec $C_D^{avge} = .98 \pm .21.$

4.10 BLAST ANOMALY

High-speed camera records showed that the large end plates on Cylinder 1 distorted and separated from the main body of the cylinder shortly after the cylinder left the support stand. Available evidence suggests that a blast anomaly, in the form of a surface precursor jet moving up the east side of the Canadian sector, was responsible for the failure of Cylinder 1. This anomaly produced a secondary pressure wave which moved diagonally from east to west across the layout behind the main shock front. The dust-raising precursor jet could be clearly seen on overhead photographs of the charge just after detonation. The evidence for the laterally-moving pressure wave follows:

(1) Small secondary pressure peaks were observed[9] on pressure records at the 20 and 10 psi overpressure locations. Correlation of the time of arrival of these secondary pulses with the gauge positions indicated that the pressure wave responsible was moving diagonally from east to west.

(2) All cylinders which translated laterally did so from east to west.

(3) The west support stand for Cylinder 1 had been twisted toward Ground Zero and the stand had been collapsed. The east support stand was somewhat distorted but still upright. The only explanation consistent with these and other pieces of evidence is that the cylinder or cylinder end plates delivered a series of rapid blows to each support plate. The fact that the west support plate collapsed first suggested that it had received the first major blow from the cylinder. This conclusion in turn implied that the cylinder initially had to translate laterally from east to west. An east-west pressure component would have been required to produce this motion.

5. DISCUSSION OF RESULTS

5.1 GENERAL

The principal information gained from the present experiment is (1) the variation of drag coefficient in the range of critical and supercritical Reynolds numbers under unsteady flow conditions of a free-field blast wave, and (2) a measurement of end effects under these same conditions for cylinders with length/diameter ratios of 5 and 17.

All of the measurements recorded in Figures 26, 27, and 28 are for Mach number less than the critical value (Mc=0.41). For M<Mc, C_D is primarily a function of Reynolds number. For M>Mc, C_D depends mainly upon Mach number. As M increases through Mc, an abrupt rise in C_D from 0.3 to approximately 1.2 is observed. This is a result of the fact that, for M=Mc, flow becomes supersonic at some point on the cylinder. The local shock wave which forms causes a buildup in thickness of the boundary layer and a rapid movement of the separation point forward on the cylinder with an attendant rapid rise in drag coefficient.

The principal difference between measurements made in steady and unsteady flow arises from the fact that the unsteady flow is preceded by a shock front which diffracts over the cylinder, sending reflections back and forth several times across the cylinder. The passage of the shock front can "condition" the following air blast flow to produce drag coefficients which are different than one would measure in the steady-flow conditions encountered in wind tunnel tests. The duration of the diffraction phase, τ, is typically 2 msec, so one might expect quasi-steady flow to develop after, perhaps 5τ to 10τ, (10 msec to 20 msec).

5.2 VARIATION OF DRAG COEFFICIENT WITH REYNOLDS NUMBER (FIG. 28)

5.2.1 Cylinder with 3.5-Inch Diameter. The points for Reynolds number in the range $5x10^5$ to $8x10^5$ are in good agreement with steady-state values. The points between $3x10^5$ and $5x10^5$, in the critical range, fall well below steady-state values. This result might be attributable to surface roughness, which tends to move the critical Reynolds region toward lower Reynolds numbers[15]. However, as discussed in Section 4.8, precautions were taken to ensure that the cylinder surface was aerodynamically smooth, so this explanation is an unlikely one. It is more probable that the lack of agreement is caused by the simple fact that the low order power series used to fit the data is not capable of responding to the rapid change in C_D which occurs in this range of Reynolds number.

5.2.2 Cylinder with 9.5-Inch Diameter. Drag coefficients derived for the 9.5-inch diameter cylinder for Reynolds numbers in the range $9x10^5$ to $17x10^5$ are consistent with the steady-state values within error, but tend to lie somewhat higher on average.

5.2.3 Cylinder with 18.0-Inch Diameter. The two C_D values spanning the first 50 msec of motion ($R=42.7\times10^5$ to 29.5×10^5) lie well below steady-state values. The C_D value for the 50-75 msec interval ($R=29.5\times10^5$ to 24.0×10^5) is slightly larger than the steady-state value, but consistent with it within error.

It is possible that the discrepancy between steady and unsteady C_D values observed at highest Reynolds numbers is due to an inadequate end effect correction over this range of Reynolds number. However, to obtain agreement with steady-state values for all three points, it would be necessary to apply an end effect correction which decreased with time after shock arrival. This is contrary to the observed end effect variation for the 9.5-inch diameter cylinder.

If one accepts the data as presented in Figure 28, they suggest that, in the early stage of unsteady flow for Reynolds numbers of order 40×10^5, C_D is lower than the steady-state value. As time progresses, the drag coefficient increases to a value somewhat higher, but consistent with, the steady-state value. The mechanism responsible for the increase in drag coefficient for $R>10^6$ is not completely understood, but Roshko has pointed out[14] the strong similarity in shape of the C_D vs R and 1/S vs R curves, where S is Strouhal number ($S=(fd)/u$ where d is cylinder diameter, u is free-stream velocity, and f is the frequency of vortex shedding at the rear of the cylinder). This similarity suggests that drag coefficient is related to the frequency of vortex shedding. If the initial shock front conditioned the following flow pattern in such a way as to artificially increase the frequency of vortex shedding, it is likely that a decreased drag coefficient would result. One might then expect drag coefficient to increase as quasi-steady flow developed.

5.3 COMPARISON WITH RESULTS OF OTHER WORKERS

A limited number of drag coefficient measurements in unsteady flow are available. These have been carried out primarily at AWRE (UK)[16,17,18] in shock tubes and by DRES in previous free-field blast trials[4,5,6,7]. In several instances, drag coefficients well in excess of steady-state values were observed. In the case of past DRES results, some of this discrepancy can be accounted for by a largely unknown amount of dust loading. Dust loading seems to have been a more serious problem in previous trials than in Dice Throw (see Section 4.6). Some work is underway at DRES to examine the problem of dust loading on circular cylinders using a mathematical model in order to provide some theoretical limits on the potential seriousness of the problem for some representative field conditions.

In the case of at least one set of results from AWRE[17], the high measured drag coefficient of 0.67 for M<Mc may be attributable to the fact that, early in the flow history, the flow Mach number M was >Mc. The authors suggest that the drag coefficient measured for M<Mc may depend upon "conditioning" of the flow while M>Mc. This contention that, in unsteady flow conditions, the measured drag coefficient may depend upon the history of the flow, is carried foward in other work at AWRE[16] by Martin, Mead, and Uppard. In this work, the authors show from shadowgraph records during the shock diffraction phase, that the boundary layer separation point has been moved well forward on the cylinder, and they argue that, because it is unlikely to re-attach downstream during the subsequent flow, an abnormally high drag coefficient is expected (in agreement with observations).

The present data are perhaps notable because they agree with steady-state values over a wide range of Reynolds number. The data for the 18-inch diameter cylinder are new. Until now, no known unsteady flow measurements existed at such high Reynolds number and low Mach number ($M<M_c$ at all times). Dryden and Hill[19] measured C_D for a 12-foot diameter, 120 foot long smoke stack (L/D=10) in a natural wind of about 25-40 mph, which corresponds to Reynolds numbers of 30×10^5 to 50×10^5. These measurements were, however, for extremely low Mach numbers, and were not made in a decaying blast wave which was preceded by a shock front.

5.4 END EFFECTS (FIG. 27)

It has been shown from shadowgraph records that it can take as long as 10 msec for quasi-steady flow to develop over the cylinders after passage of the shock wave. It is somewhat surprising, however, to find that the ratio of C_D's for infinite and finite length cylinders is strongly varying as late as 75 msec into the motion (Fig. 27). Before any conclusions can be drawn, it will be necessary to re-analyze the data to ensure that the observed strong variation in C_D ratio for the 9.5-inch diameter cylinders is not simply an artifact of the data analysis. The average value of the ratio over 100 msec of motion, 1.58, is quite close to the value of 1.67 measured by Dryden and Hill[19] (see Section 5.3) for very low Mach numbers and R in the range 30×10^5 to 50×10^5. This agreement helps to justify the decision to apply the average end effect factor for the 9.5-inch diameter cylinders to the 18-inch diameter cylinder ($R=24 \times 10^5$ to 43×10^5).

The results for the 3.5-inch diameter cylinder are consistent with a value of 1 for the C_D ratio, for Reynolds numbers just above the critical region. This ratio appears to drop below unity by as much as 25% as the critical Reynolds region is entered. The latter must be treated with caution because it is likely that the power series fit to the data is unable to follow the rapid change in C_D in this region, so the results may be somewhat misleading.

5.5 RESULTS FOR SUPERCRITICAL MACH NUMBERS - CYLINDER 2

The initial C_D value of $.76 \pm .20$ measured for Cylinder 2 is more consistent with the results for a finite-length cylinder, with L/D ratio of 17 (C_D=0.9), than for an infinite-length cylinder (C_D=1.3, Gowen and Perkins[13]). Examination of the velocity-time curve in Figure 8 indicates that the initial acceleration values obtained from the fitted curve may well be too low. A more reliable determination of acceleration is not possible, however, given the large fluctuations which are present in the velocity-time data.

6. CONCLUSIONS

1. Aerodynamic drag coefficients measured for "infinite-length" cylinders under unsteady flow conditions in a long-duration (160-300 msec) free-field blast wave were in generally good agreement with steady-state values for Reynolds numbers in the range 5×10^5 to 16×10^5 and Mach numbers <0.41. In the critical Reynolds number range 3×10^5 to 5×10^5, the measured drag coefficients lay well below the steady-state values, but this was felt to be due to the inability of the power series fitting function to respond to the very rapid changes in drag coefficient occurring in this region. In the Reynolds number range 30×10^5 to 40×10^5, measured unsteady flow drag coefficients were approximately 30% lower than steady-state values. Further experiments would be necessary to establish whether this difference is due to an inadequate correction for end effects or due to a real physical effect associated with the diffraction of the shock front across the cylinder.

2. Measurement of drag coefficients for identical cylinders with and without extended end plates permitted the direct measurement of end effects for finite-length cylinders by forming the ratio C_D(infinite)/C_D(finite). For the cylinders with a length/diameter (L/D) ratio of 5, an average C_D ratio of 1.6 was observed over a Reynolds number range of 9×10^5 to 16×10^5($M<0.41$). For the cylinder with L/D of 17, an average C_D ratio of 0.8 was observed for Reynolds numbers in the range 3×10^5 to 8×10^5. The ratio was observed to decrease as Reynolds number dropped from the supercritical to critical range. Further data analysis and experimentation are required to confirm the strong increase in end effect ratio with time after shock arrival which was observed for the cylinder with an L/D ratio of 5.

3. Greasy-stake dust collectors and high-speed camera records confirmed that the plastic coating sprayed onto the ground in the Canadian sector proved highly effective in suppressing dust. It is probable that the dust loading on the cylinders was negligible during the first 100-150 msec of motion over which measurements were taken.

4. Cylinder 1 at the 20.1 psi peak overpressure location failed due to the influence of a ground precursor type of blast anomaly which moved up the east side of the Canadian sector and produced a secondary pressure wave travelling diagonally from east to west across the Canadian layout.

REFERENCES

1. B.G. Laidlaw, "Blast Response of Lattice Mast - Event Dice Throw", Defence Research Establishment Suffield, Ralston, Alberta, Canada, Suffield Technical Paper No. 452, 1977. (See also paper these proceedings.) UNCLASSIFIED

2. C.G. Coffey and G.V. Price, "Blast Response of UHF Polemast Antenna - Event Dice Throw", Defence Research Establishment Suffield, Ralston, Alberta, Canada, Suffield Technical Paper No. 449, 1977. (See also paper these Proceedings.) UNCLASSIFIED

3. G.V. Price and C.G. Coffey, "Blast Response of 35 ft Fibreglass Whip Antenna - Event Dice Throw", Defence Research Establishment Suffield, Ralston, Alberta, Canada, Suffield Technical Paper No. 448, 1977. (See also paper these Proceedings.) UNCLASSIFIED

4. S.B. Mellsen, "Drag Measurement on Cylinders by the Free-Flight Method, Operation Prairie Flat", Defence Research Establishment Suffield, Ralston, Alberta, Canada, Suffield Technical Note No. 249, January 1969. UNCLASSIFIED

5. S.B. Mellsen, "Measurement of Drag on Cylinders by the Free-Flight Method - Event Dial Pack", Defence Research Establishment Suffield, Ralston, Alberta, Canada, Suffield Technical Paper No. 382, December, 1971. UNCLASSIFIED

6. R. Naylor and S.B. Mellsen, "Unsteady Drag from Free-Field Blast Waves", Defence Research Establishment Suffield, Ralston, Alberta, Canada, Suffield Memorandum No. 42/71, January 1973. UNCLASSIFIED

7. S.B. Mellsen, "Measurement of Drag on Cylinders by the Free-Flight Method - Event Mixed Company", Defence Research Establishment Suffield, Ralston, Alberta, Canada, Suffield Technical Paper No. 419, March 1974. UNCLASSIFIED

8. R. Naylor, "Dust Measurements in Event Dice Throw", Defence Research Establishment Suffield, Ralston, Alberta, Canada, Suffield Technical Note No. 398, 1977. UNCLASSIFIED

9. F.H. Winfield, "Event Dice Throw - Canadian Air Blast Measurements", Defence Research Establishment Suffield, Ralston, Alberta, Canada, Suffield Technical Paper No. 451, March 1977. (See also paper these Proceedings.) UNCLASSIFIED

10. S. Glasstone (Editor), "The Effects of Nuclear Weapons", Handbook prepared by U.S. Department of Defense, published by U.S. Atomic Energy Commission, June 1957.

11. G.F. Kinney, "Explosive Shocks in Air", published by the MacMillan Company (New York), 1962.

12. N.K. Delaney and N.E. Sorensen, "Low-Speed Drag of Cylinders of Various Shapes", National Advisory Committee for Aeronautics, NACA Technical Note 3038, November, 1953.

13. F.W. Gowen and E.W. Perkins, "Drag of Circular Cylinders for a Wide Range of Reynolds Numbers and Mach Numbers", National Advisory Committee for Aeronautics, NACA Technical Note No. 2960, June 1953.

14. A. Roshko, "Experiments on the Flow Past a Circular Cylinder at Very High Reynolds Number", Journal of Fluid Mechanics 10, 1961, 345.

15. S.F. Hoerner, "Fluid Dynamic Drag", published by author, 1958.

16. V.C. Martin, K.F. Mead, and J.E. Uppard, "The Drag on a Circular Cylinder in a Shock Wave", Atomic Weapons Research Establishment, Aldermaston, U.K., AWRE Report No. O-34/67, May 1967. UNCLASSIFIED

17. V.J. Bishop, R.D. Rowe, "The Interaction of a Long-Duration Friedlander-Shaped Blast Wave with an Infinitely-Long Right Circular Cylinder", Atomic Weapons Research Establishment, Aldermaston, U.K., AWRE Report No. O-38/67. April 1967. UNCLASSIFIED

18. V.C. Martin, K.F. Mead and J.E. Uppard, "Blast Loading on a Right Circular Cylinder", Atomic Weapons Research Establishment, Aldermaston, U.K., AWRE Report No. O-93/65, November 1965. UNCLASSIFIED

19. H.L. Dryden, G.C. Hill, "Wind Pressure on Circular Cylinders and Chimneys", Bureau of Standards Journal of Research, Washington, 5, 1930, 653.

TABLE NO. 1 SIZE, WEIGHT AND LOCATION OF TEST CYLINDERS

Cylinder Number	Peak Overpressure (psi)	Diameter D (inches)	Length L (inches)	L/D	End Plate Diameter E (inches)	E/D	Total Weight (lb)	Height of Axis Above Ground (feet)	Distance from Ground Zero (feet)
1	20.1	18.0	90.0	5.0	48.0	2.67	266.7	6.0	739
2	20.1	3.5	60.0	17.1	10.5	3.0	63.3	5.0	739
3	9.7	18.0	90.0	5.0	18.0	1.0	162.3	6.0	964
4	6.7	9.5	48.0	5.1	9.5	1.0	37.4	5.0	1139
5	6.7	9.5	48.0	5.1	28.5	3.0	60.0	5.0	1139
6	9.7	3.5	60.0	17.1	3.5	1.0	20.6	5.0	964
7	9.7	3.5	60.0	17.5	17.5	5.0	21.8	5.0	964

TABLE NO. 2 SUMMARY OF CAMERAS USED IN TRIAL

Cylinder Number	Overpressure (psi)	Camera Type	Focal Length of Lens (mm)	F[illegible]ng Rate (frames/sec)	Field of View in Plane of Photomarker Plate	
					Width (inches)	Height (inches)
1	20.1	Photosonic	13	--	85	53
2	20.1	Photosonic	13	1090*	35	22
3	9.7	Photosonic	13	1130	40	25
4	6.7	Photosonic	50	1000	16	10
5	6.7	Photosonic	50	990	16	10
6	9.7	Photosonic	50	941	16	10
7	9.7	Photosonic	50	1090	16	10

* not constant

TABLE NO. 3 SUMMARY OF RESULTS FOR EACH CYLINDER

Cylinder Number	Type of Data*	Useful Data Obtained	Remarks
1	V.T. (East) V.T. (West) Cam. (West)	No No No	- Cylinder failed to undergo free flight due to sidewise blast anomaly at 20 psi peak overpressure location acting on large end plates.
2	V.T. (East)	No	- East magnet broke shortly after shock arrival.
	V.T. (West)	Yes	- Poor signal/noise due to error in circuit controlling sensitivity.
	Cam. (West)	No	- Non-constant film speed; violent displacement of camera post.
3	V.T. (East) V.T. (West)	Yes Yes	- Large amplitude 79 Hz oscillations on signal produced large uncertainties in derived drag pressure.
	Cam. (West)	Yes	- Oscillations absent; smaller uncertainties than for V.T. data.
	Both -	-	- East-West V.T. results consistent over range of measurement. V.T. and Cam. results consistent over entire range of measurement.
4	V.T. (East) V.T. (West)	Yes Yes	- Moderately large 60 Hz oscillations on signals produced increased uncertainties in derived drag pressure.
	Cam. (West)	Yes	- Excellent data; only small corrections for camera motion.
	Both -	-	- East-West V.T. results consistent over range of measurement. V.T. and Cam. data consistent over most of range of measurement.
5	V.T. (East) V.T. (West)	Yes Yes	- Moderately large 60 Hz oscillations on signals; signals terminated prematurely due to contact of cylinder shaft with photomarker plate.
	Cam. (West)	Yes	- Excellent data; only small corrections for camera motion.
	Both -	-	- Linear drag pressure from V.T. data in agreement over most of range with (approximately) linear drag pressure from higher order fit to Cam. data.
6	V.T. (East) V.T. (West)	Yes Yes	- Smaller 59 Hz oscillations with irregular fluctuations superposed.
	Cam. (West)	Yes	- Excellent data; larger corrections for camera motion than for Cyl. 4,5.
	Both -	-	- East-West V.T. results consistent over entire range of measurement. V.T. and Cam. data consistent over most of range of measurement.
7	V.T. (East) V.T. (West)	Yes Yes	- Smaller 59 Hz oscillations with irregular fluctuations superposed. Uncertainties in drag pressure competitive with Cam. data.
	Cam. (West)	Yes	- Large corrections for camera post motion forced linear fit to drag pressure.
	Both -	-	- East-West V.T. results consistent over entire range of measurement. V.T. and Cam. data consistent over most of range of measurement.

* V.T. - Velocity Transducer. Cam. - High-Speed Camera
(East, West) - refers to end of cylinder where measurement recorded.
Both - Comments refer to both V.T. and Cam. data

BEST AVAILABLE COPY

NO 9 18.0 IN DIAM 9.7 PSI 16.0 IN DIAM END PLATES

PEAK OVERPRESSURE 9.7 PSI POSITIVE DURATION 233.0 MSEC

FRIEDLANDER DECAY CONSTANT = 0.85

TIME AFTER SHOCK FRONT ARRIVAL (MSEC)	DRAG PRESSURE PD (PSI)	ABSOLUTE ERROR** (PSI)	RELATIVE ERROR** (PERCENT)	DYNAMIC PRESSURE Q (PSI)	IMPACT PRESSURE QI (PSI)	RATIO (QI/Q)	DRAG COEFFICIENT CD (PD/QI)	ABSOLUTE ERROR**	FLOW MACH NO. M	REYNOLDS NO. R (X10-5)
2.0	0.602	0.163	27.0	2.35	2.45	1.035	0.245	0.066	0.391	42.66
4.0	0.592	0.157	26.5	2.28	2.37	1.039	0.249	0.066	0.386	42.06
6.0	0.582	0.151	25.9	2.21	2.30	1.039	0.252	0.065	0.382	41.46
8.0	0.571	0.146	25.5	2.14	2.22	1.039	0.256	0.065	0.377	40.87
10.0	0.561	0.140	24.9	2.07	2.15	1.035	0.259	0.064	0.372	40.29
12.0	0.550	0.134	24.3	2.01	2.08	1.035	0.263	0.064	0.367	39.70
14.0	0.540	0.129	23.8	1.94	2.02	1.035	0.266	0.063	0.363	39.13
16.0	0.530	0.125	23.2	1.88	1.95	1.035	0.270	0.062	0.358	38.56
18.0	0.519	0.118	22.7	1.82	1.89	1.039	0.273	0.062	0.353	37.99
20.0	0.509	0.112	22.0	1.76	1.83	1.039	0.277	0.061	0.349	37.43
22.0	0.498	0.107	21.4	1.70	1.77	1.039	0.280	0.060	0.344	36.87
24.0	0.488	0.101	20.6	1.65	1.71	1.035	0.284	0.056	0.339	36.32
26.0	0.478	0.096	20.0	1.59	1.65	1.039	0.288	0.057	0.335	35.77
28.0	0.467	0.090	19.2	1.54	1.60	1.039	0.291	0.056	0.330	35.22
30.0	0.457	0.085	16.5	1.49	1.55	1.039	0.294	0.054	0.326	34.69
32.0	0.446	0.080	17.9	1.44	1.49	1.039	0.297	0.053	0.321	34.15
34.0	0.436	0.075	17.2	1.39	1.44	1.039	0.301	0.051	0.317	33.62
36.0	0.426	0.071	16.6	1.34	1.39	1.039	0.304	0.050	0.312	33.10
38.0	0.415	0.066	15.9	1.30	1.35	1.035	0.307	0.048	0.308	32.57
40.0	0.405	0.062	15.3	1.25	1.30	1.039	0.310	0.047	0.304	32.06
42.0	0.394	0.058	14.7	1.21	1.26	1.039	0.312	0.046	0.299	31.55
44.0	0.384	0.055	14.3	1.17	1.21	1.035	0.315	0.045	0.295	31.04
46.0	0.374	0.053	14.1	1.12	1.17	1.039	0.318	0.045	0.291	30.54
48.0	0.363	0.051	14.0	1.09	1.13	1.039	0.320	0.045	0.286	30.04
50.0	0.353	0.050	14.1	1.05	1.09	1.039	0.323	0.045	0.282	29.54
52.0	0.342	0.050	14.6	1.01	1.05	1.035	0.324	0.047	0.278	29.05
54.0	0.332	0.051	15.5	0.97	1.01	1.039	0.326	0.050	0.274	28.57
56.0	0.322	0.052	16.1	0.94	0.97	1.039	0.328	0.053	0.270	28.09
58.0	0.311	0.054	17.3	0.90	0.94	1.035	0.329	0.057	0.265	27.61
60.0	0.301	0.057	18.9	0.87	0.90	1.035	0.330	0.062	0.261	27.14
62.0	0.290	0.060	20.6	0.84	0.87	1.035	0.331	0.068	0.257	26.67
64.0	0.280	0.063	22.5	0.81	0.84	1.039	0.331	0.074	0.253	26.20
66.0	0.270	0.067	24.8	0.78	0.81	1.035	0.332	0.082	0.249	25.74
68.0	0.259	0.071	27.4	0.75	0.78	1.039	0.331	0.090	0.245	25.29
70.0	0.249	0.075	30.1	0.72	0.75	1.039	0.331	0.099	0.241	24.84
72.0	0.238	0.079	33.1	0.69	0.72	1.039	0.329	0.109	0.237	24.39
74.0	0.228	0.083	36.4	0.66	0.69	1.039	0.327	0.119	0.233	23.95
76.0	0.218	0.088	40.5	0.64	0.66	1.035	0.326	0.131	0.229	23.51
78.0	0.207	0.092	44.4	0.61	0.64	1.039	0.322	0.143	0.225	23.07
80.0	0.197	0.093	48.7	0.59	0.61	1.039	0.315	0.155	0.221	22.64
82.0	0.186	0.101	54.3	0.56	0.59	1.035	0.313	0.170	0.218	22.21
84.0	0.176	0.105	59.6	0.54	0.56	1.035	0.305	0.184	0.214	21.79
86.0	0.166	0.110	66.2	0.52	0.54	1.035	0.304	0.201	0.210	21.37
88.0	0.155	0.115	74.1	0.50	0.52	1.035	0.296	0.219	0.206	20.96
90.0	0.145	0.119	82.0	0.48	0.50	1.035	0.266	0.237	0.202	20.55
92.0	0.134	0.124	92.5	0.46	0.48	1.035	0.276	0.257	0.199	20.14
94.0	0.124	0.126	103.2	0.44	0.46	1.035	0.265	0.277	0.195	19.73
96.0	0.114	0.133	116.6	0.42	0.44	1.035	0.256	0.301	0.191	19.34
98.0	0.057	0.061	142.1	0.40	0.42	1.035	0.134	0.191	0.166	18.94
100.0	0.049	0.084	171.4	0.36	0.40	1.035	0.121	0.207	0.184	18.55
102.0	0.041	0.087	212.1	0.37	0.38	1.035	0.106	0.225	0.181	18.16
104.0	0.033	0.090	272.7	0.35	0.36	1.035	0.089	0.243	0.177	17.78
106.0	0.025	0.093	372.0	0.33	0.35	1.035	0.070	0.261	0.171	17.40
108.0	0.017	0.096	564.7	0.32	0.33	1.035	0.050	0.284	0.170	17.02
110.0	0.009	0.099	1100.0	0.30	0.32	1.039	0.027	0.307	0.166	16.65
112.0	0.001	0.103	10300.0	0.29	0.30	1.039	0.003	0.335	0.161	16.28
114.0	-0.667	0.220	-32.9	0.28	0.29	1.039	-2.277	0.751	0.160	15.91
116.0	-0.644	0.199	-30.9	0.26	0.27	1.039	-2.307	0.712	0.156	15.55
118.0	-0.636	0.171	-26.8	0.25	0.26	1.039	-2.392	0.643	0.151	15.19
120.0	-0.665	0.164	-25.4	0.24	0.25	1.039	-2.548	0.648	0.149	14.84

** 3 STANDARD DEVIATIONS

TABLE NO. 4

DRAG COEFFICIENT VS TIME FOR CYLINDER 3 - CAMERA DATA

NO 4 9.5 IN DIAM 6.7 PSI 9.5 IN DIAM END PLATES

PEAK OVERPRESSURE 6.7 PSI POSITIVE DURATION 249.0 MSEC

FRIEDLANDER DECAY CONSTANT = 0.52

TIME AFTER SHOCK FRONT ARRIVAL (MSEC)	DRAG PRESSURE PD (PSI)	ABSOLUTE ERROR** (PSI)	RELATIVE ERROR** (PERCENT)	DYNAMIC PRESSURE Q (PSI)	IMPACT PRESSURE Q1 (PSI)	RATIO (Q1/Q)	DRAG COEFFICIENT CD (PD/Q1)	ABSOLUTE ERROR**	FLOW MACH NO. M	REYNOLDS NO. R (X10-5)
2.0	0.493	0.067	13.4	1.16	1.19	1.022	0.416	0.036	0.296	16.53
4.0	0.482	0.060	12.4	1.14	1.16	1.022	0.413	0.051	0.293	16.34
6.0	0.463	0.032	11.1	1.11	1.13	1.022	0.408	0.043	0.290	16.16
8.0	0.443	0.046	10.3	1.08	1.11	1.022	0.404	0.041	0.287	15.87
10.0	0.434	0.040	9.2	1.05	1.08	1.022	0.400	0.036	0.284	15.79
12.0	0.418	0.034	8.1	1.03	1.05	1.022	0.393	0.032	0.281	15.61
14.0	0.403	0.029	7.1	1.00	1.03	1.022	0.391	0.026	0.278	15.43
16.0	0.388	0.026	6.1	0.98	1.00	1.022	0.386	0.023	0.275	15.23
18.0	0.374	0.020	5.3	0.95	0.97	1.022	0.382	0.020	0.272	15.07
20.0	0.360	0.017	4.7	0.93	0.95	1.022	0.377	0.017	0.269	14.89
22.0	0.346	0.013	3.7	0.90	0.92	1.022	0.372	0.018	0.266	14.71
24.0	0.332	0.011	3.3	0.88	0.90	1.022	0.366	0.012	0.263	14.54
26.0	0.319	0.009	2.8	0.86	0.88	1.022	0.362	0.010	0.261	14.36
28.0	0.306	0.007	2.2	0.84	0.85	1.022	0.355	0.008	0.258	14.19
30.0	0.293	0.006	2.0	0.81	0.83	1.022	0.349	0.007	0.255	14.01
32.0	0.281	0.006	2.1	0.79	0.81	1.022	0.344	0.007	0.252	13.84
34.0	0.268	0.006	2.2	0.77	0.79	1.022	0.337	0.007	0.249	13.67
36.0	0.257	0.007	2.7	0.75	0.77	1.022	0.332	0.009	0.246	13.50
38.0	0.245	0.007	2.8	0.73	0.75	1.022	0.323	0.009	0.243	13.33
40.0	0.234	0.007	2.9	0.71	0.73	1.022	0.319	0.009	0.241	13.16
42.0	0.223	0.008	3.3	0.69	0.71	1.022	0.315	0.011	0.238	12.99
44.0	0.212	0.008	3.7	0.67	0.69	1.022	0.308	0.011	0.235	12.81
46.0	0.202	0.008	3.9	0.65	0.67	1.022	0.299	0.011	0.232	12.64
48.0	0.192	0.008	4.1	0.64	0.65	1.022	0.293	0.012	0.229	12.49
50.0	0.182	0.007	3.8	0.62	0.63	1.022	0.283	0.010	0.227	12.33
52.0	0.173	0.007	4.0	0.60	0.61	1.022	0.279	0.011	0.224	12.17
54.0	0.164	0.006	3.6	0.58	0.60	1.022	0.272	0.009	0.221	12.00
56.0	0.155	0.006	3.8	0.57	0.58	1.022	0.263	0.010	0.219	11.84
58.0	0.147	0.005	3.4	0.55	0.56	1.022	0.259	0.008	0.216	11.68
60.0	0.139	0.005	3.5	0.53	0.55	1.022	0.252	0.009	0.213	11.52
62.0	0.131	0.005	3.8	0.52	0.53	1.022	0.246	0.009	0.210	11.36
64.0	0.123	0.004	3.2	0.50	0.51	1.022	0.236	0.007	0.207	11.20
66.0	0.116	0.004	3.4	0.49	0.50	1.022	0.230	0.007	0.205	11.05
68.0	0.109	0.004	3.6	0.47	0.48	1.022	0.222	0.008	0.202	10.89
70.0	0.102	0.004	3.9	0.46	0.47	1.022	0.215	0.008	0.199	10.73
72.0	0.096	0.005	5.2	0.44	0.45	1.022	0.208	0.010	0.197	10.58
74.0	0.090	0.005	5.5	0.43	0.44	1.022	0.201	0.011	0.194	10.42
76.0	0.084	0.006	7.1	0.42	0.43	1.022	0.194	0.013	0.191	10.27
78.0	0.079	0.006	7.5	0.40	0.41	1.022	0.188	0.014	0.188	10.12
80.0	0.073	0.007	8.5	0.39	0.40	1.022	0.179	0.017	0.186	9.97
82.0	0.069	0.007	10.1	0.38	0.39	1.022	0.173	0.017	0.184	9.82
84.0	0.064	0.007	10.9	0.37	0.38	1.022	0.168	0.018	0.181	9.67
86.0	0.060	0.008	13.3	0.36	0.36	1.022	0.162	0.021	0.178	9.52
88.0	0.056	0.008	14.2	0.34	0.35	1.022	0.157	0.022	0.176	9.37
90.0	0.052	0.008	15.3	0.33	0.34	1.022	0.150	0.023	0.173	9.22
92.0	0.049	0.008	16.3	0.32	0.33	1.022	0.147	0.024	0.171	9.08
94.0	0.046	0.007	15.2	0.31	0.32	1.022	0.142	0.021	0.168	8.93
96.0	0.043	0.007	16.2	0.30	0.31	1.022	0.138	0.022	0.165	8.79
98.0	0.041	0.007	17.0	0.29	0.30	1.022	0.136	0.023	0.163	8.64
100.0	0.038	0.006	15.7	0.28	0.29	1.022	0.130	0.020	0.160	8.50
102.0	0.037	0.006	16.2	0.27	0.28	1.022	0.132	0.021	0.158	8.36
104.0	0.035	0.007	20.0	0.26	0.27	1.022	0.129	0.025	0.155	8.22
106.0	0.034	0.008	23.5	0.25	0.26	1.022	0.130	0.030	0.153	8.07
108.0	0.033	0.010	30.3	0.24	0.25	1.022	0.131	0.039	0.150	7.94
110.0	0.032	0.012	37.5	0.23	0.24	1.022	0.131	[illegible]	0.148	7.80
112.0	0.032	0.015	46.8	0.22	0.23	1.022	0.136	[illegible]	0.145	7.66
114.0	0.032	0.018	56.2	0.22	0.22	1.022	0.142	0.080	0.143	7.52
116.0	0.032	0.022	68.7	0.21	0.21	1.022	0.147	0.101	0.140	7.38
118.0	0.033	0.027	81.8	0.20	0.20	1.022	0.158	0.129	0.138	7.25
120.0	0.033	0.031	93.9	0.19	0.20	1.022	0.164	0.154	0.136	7.11
122.0	0.035	0.037	105.7	0.18	0.19	1.022	0.181	0.192	0.133	6.98
124.0	0.036	0.043	119.4	0.18	0.18	1.022	0.196	0.232	0.131	6.85
126.0	0.038	0.049	128.9	0.17	0.17	1.022	0.213	0.275	0.128	6.71
128.0	0.040	0.056	140.0	0.16	0.17	1.022	0.234	0.328	0.125	6.58
130.0	0.042	0.063	150.0	0.16	0.16	1.022	0.256	0.383	0.124	6.45
132.0	0.045	0.071	157.7	0.15	0.15	1.022	0.288	0.452	0.121	6.32

** 3 STANDARD DEVIATIONS

TABLE NO. 5

DRAG COEFFICIENT VS TIME FOR CYLINDER 4 - CAMERA DATA

NO 6 3.5 IN DIAM 9.7 PSI   5.3 IN DIAM END PLATES

PEAK OVERPRESSURE 9.7 PSI   POSITIVE DURATION 233.0 MSEC

FRIEDLANDER DECAY CONSTANT = 0.83

TIME AFTER SHOCK FRONT ARRIVAL (MSEC)	DRAG PRESSURE PD (PSI)	ABSOLUTE ERROR** (PSI)	RELATIVE ERROR** (PERCENT)	DYNAMIC PRESSURE Q (PSI)	IMPACT PRESSURE QI (PSI)	RATIO (QI/Q)	DRAG COEFFICIENT CD (PD/QI)	ABSOLUTE ERROR**	FLOW MACH NO. M	REYNOLDS NO. R (X10-5)
2.0	1.161	0.241	20.7	2.33	2.49	1.039	0.479	0.098	0.391	8.29
4.0	1.084	0.237	19.0	2.25	2.37	1.039	0.456	0.087	0.386	8.17
6.0	1.012	0.176	17.3	2.21	2.30	1.039	0.439	0.076	0.382	8.06
8.0	0.945	0.148	15.6	2.14	2.22	1.039	0.424	0.066	0.377	7.94
10.0	0.883	0.123	13.9	2.07	2.15	1.039	0.409	0.057	0.372	7.83
12.0	0.826	0.100	12.1	2.01	2.08	1.039	0.393	0.047	0.367	7.72
14.0	0.774	0.080	10.3	1.94	2.02	1.039	0.382	0.039	0.365	7.60
16.0	0.725	0.063	8.6	1.89	1.95	1.039	0.370	0.032	0.358	7.49
18.0	0.681	0.049	7.1	1.82	1.89	1.039	0.359	0.025	0.352	7.38
20.0	0.641	0.038	5.9	1.76	1.83	1.039	0.349	0.020	0.349	7.27
22.0	0.604	0.029	4.8	1.70	1.77	1.039	0.340	0.016	0.344	7.17
24.0	0.571	0.023	4.3	1.65	1.71	1.039	0.332	0.014	0.339	7.06
26.0	0.542	0.026	4.4	1.59	1.65	1.039	0.326	0.014	0.335	6.95
28.0	0.515	0.023	4.8	1.54	1.60	1.039	0.321	0.013	0.330	6.85
30.0	0.492	0.026	5.2	1.49	1.55	1.039	0.317	0.016	0.326	6.74
32.0	0.471	0.030	5.9	1.44	1.49	1.039	0.314	0.018	0.321	6.64
34.0	0.452	0.029	6.4	1.39	1.44	1.039	0.312	0.020	0.317	6.53
36.0	0.436	0.029	6.6	1.34	1.39	1.039	0.311	0.020	0.312	6.43
38.0	0.423	0.029	6.8	1.30	1.35	1.039	0.312	0.021	0.308	6.33
40.0	0.411	0.028	6.8	1.25	1.30	1.039	0.314	0.021	0.304	6.23
42.0	0.401	0.026	6.4	1.21	1.26	1.039	0.316	0.020	0.299	6.13
44.0	0.392	0.026	6.1	1.17	1.21	1.039	0.322	0.019	0.295	6.03
46.0	0.385	0.022	5.7	1.12	1.17	1.039	0.327	0.018	0.291	5.95
48.0	0.379	0.020	5.2	1.09	1.13	1.039	0.334	0.017	0.286	5.86
50.0	0.374	0.018	4.8	1.05	1.09	1.039	0.342	0.016	0.282	5.74
52.0	0.370	0.017	4.5	1.01	1.05	1.039	0.351	0.016	0.278	5.65
54.0	0.366	0.016	4.3	0.97	1.01	1.039	0.360	0.015	0.274	5.55
56.0	0.363	0.017	4.6	0.94	0.97	1.039	0.370	0.017	0.270	5.46
58.0	0.359	0.018	5.0	0.90	0.94	1.039	0.380	0.019	0.265	5.36
60.0	0.356	0.021	5.8	0.87	0.90	1.039	0.391	0.023	0.261	5.27
62.0	0.353	0.023	6.5	0.84	0.87	1.039	0.402	0.026	0.257	5.18
64.0	0.349	0.025	7.1	0.81	0.84	1.039	0.413	0.029	0.253	5.09
66.0	0.345	0.027	7.8	0.78	0.81	1.039	0.424	0.035	0.249	5.00
68.0	0.340	0.028	8.2	0.75	0.78	1.039	0.435	0.033	0.245	4.91
70.0	0.333	0.029	8.7	0.72	0.75	1.039	0.442	0.038	0.241	4.83
72.0	0.326	0.029	8.8	0.69	0.72	1.039	0.450	0.040	0.237	4.74
74.0	0.317	0.029	9.1	0.66	0.69	1.039	0.455	0.041	0.233	4.65
76.0	0.307	0.027	8.7	0.64	0.66	1.039	0.459	0.040	0.229	4.57
78.0	0.293	0.026	8.8	0.61	0.64	1.039	0.459	0.040	0.225	4.48
80.0	0.281	0.024	8.5	0.59	0.63	1.039	0.455	0.038	0.221	4.40
82.0	0.264	0.024	9.0	0.56	0.59	1.039	0.443	0.040	0.218	4.32
84.0	0.246	0.026	10.5	0.54	0.56	1.039	0.432	0.045	0.214	4.23
86.0	0.224	0.032	14.2	0.52	0.54	1.039	0.410	0.058	0.210	4.15
88.0	0.200	0.041	20.5	0.50	0.52	1.039	0.382	0.078	0.206	4.07
90.0	0.173	0.053	30.6	0.48	0.50	1.039	0.344	0.103	0.202	3.99
92.0	0.143	0.068	47.5	0.46	0.48	1.039	0.297	0.141	0.199	3.91
94.0	0.110	0.086	78.1	0.44	0.46	1.039	0.238	0.186	0.195	3.83
96.0	0.075	0.107	140.3	0.42	0.44	1.039	0.165	0.242	0.191	3.76
98.0	0.032	0.130	406.2	0.40	0.42	1.039	0.075	0.307	0.188	3.68
100.0	-0.012	0.156	-1300.0	0.38	0.40	1.039	-0.029	0.383	0.184	3.60

** 3 STANDARD DEVIATIONS

TABLE NO. 6

DRAG COEFFICIENT VS TIME FOR CYLINDER 6 - CAMERA DATA

TABLE NO. 7 SUMMARY OF BEST VALUES FOR DRAG COEFFICIENT*

Cylinder Diameter (inches)	Time After Shock Arrival (msec)	Average Reynolds Number	Average Drag Coefficient
3.5	3-25	7.66	.274±.054**
	25-50	6.34	.255±.042
	50-75	5.14	.251±.049
	75-100	4.08	.282±.065
	100-125	3.13	.382±.148
9.5	3-25	15.5	.508±.106
	25-50	13.3	.482±.085
	50-75	11.3	.455±.106
	75-100	9.4	.401±.160
18.0	3-25	39.4	.420±.121
	25-50	32.6	.449±.099
	50-75	26.5	.625±.137

* Data plotted in Figure 28.

** 3 Standard deviations of uncertainty (99% confidence interval)

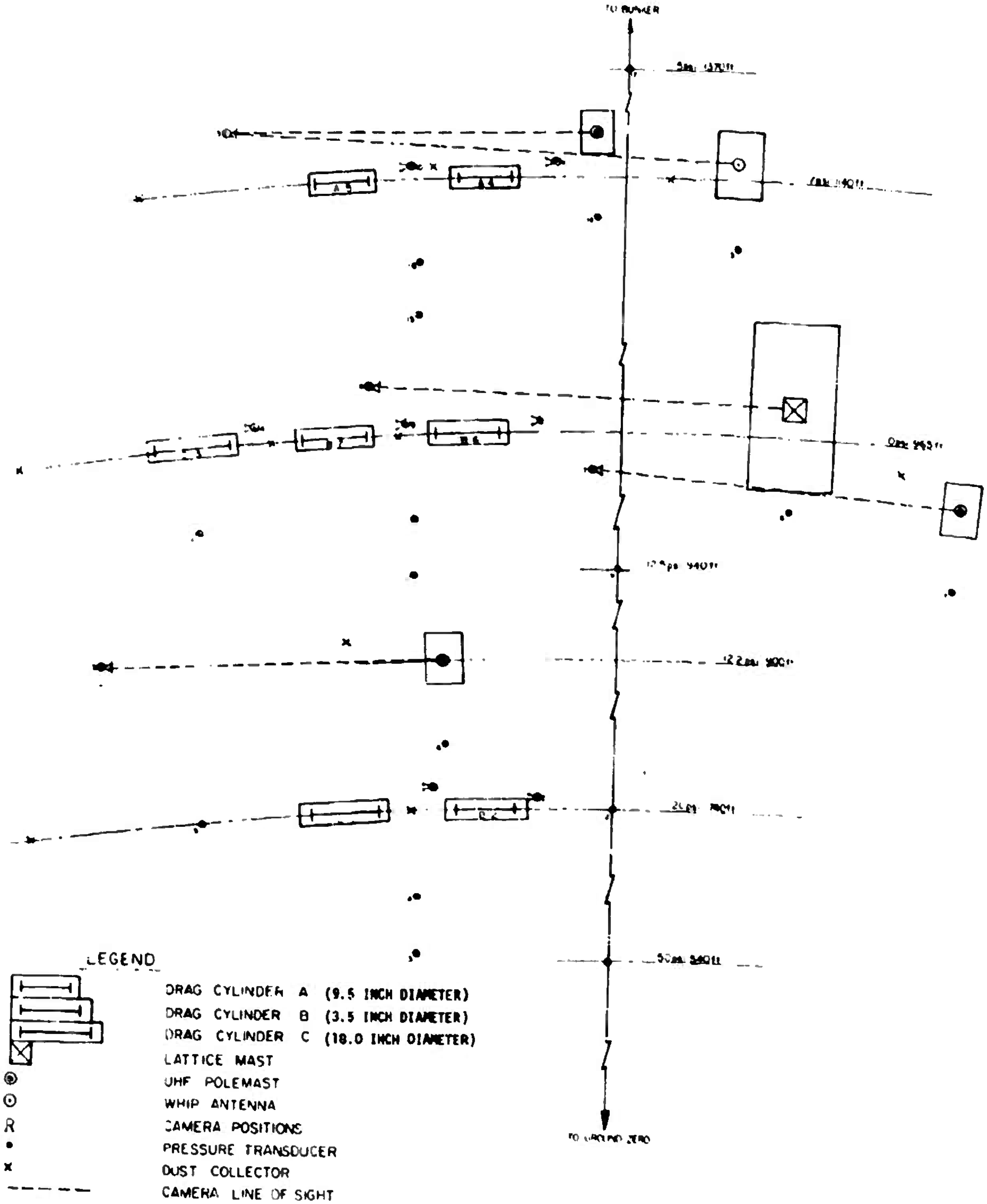

FIG. 1 LAYOUT OF CYLINDER DRAG PROJECT

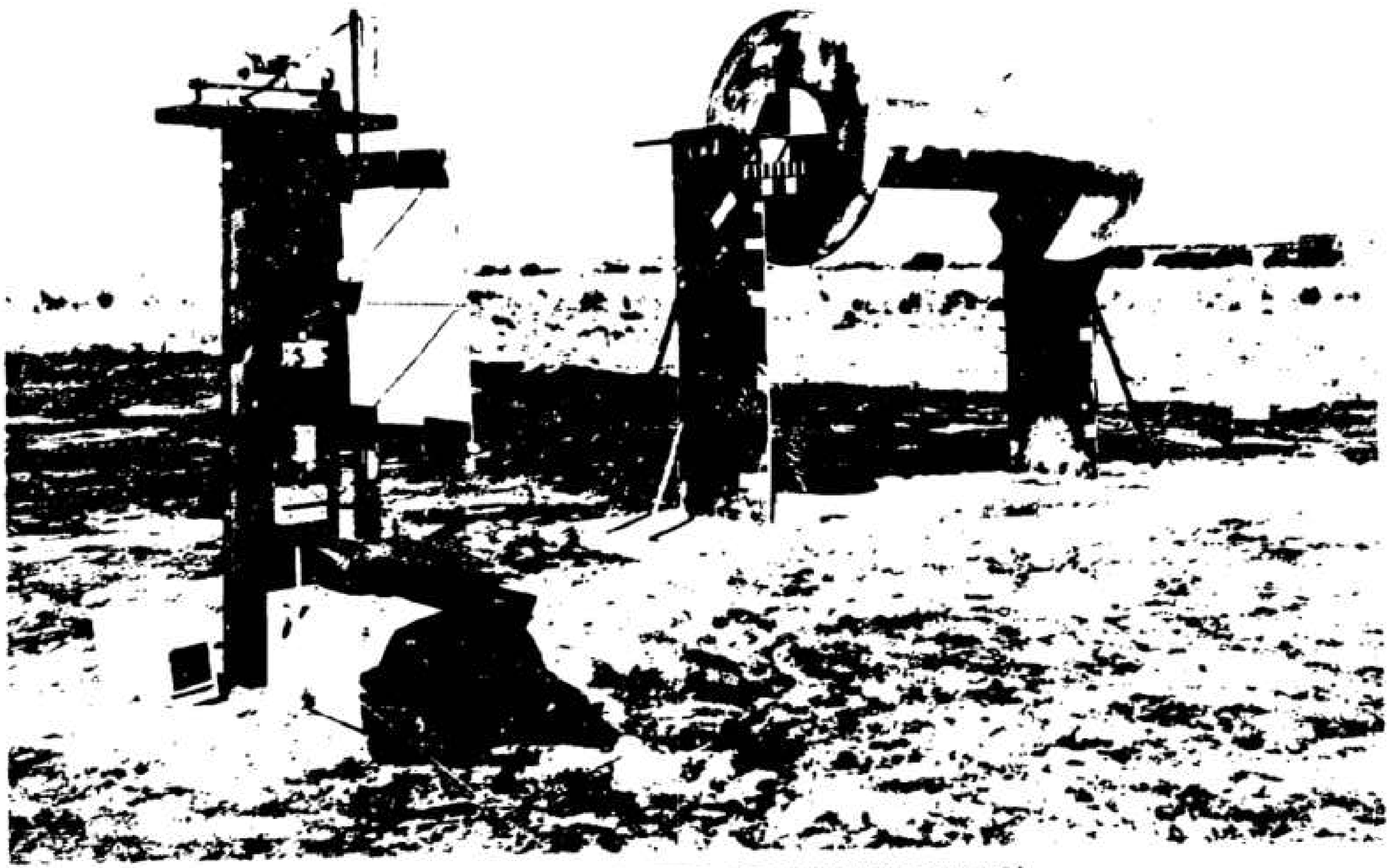

FIG. 2 TYPICAL TEST LOCATION (CYLINDER 1)

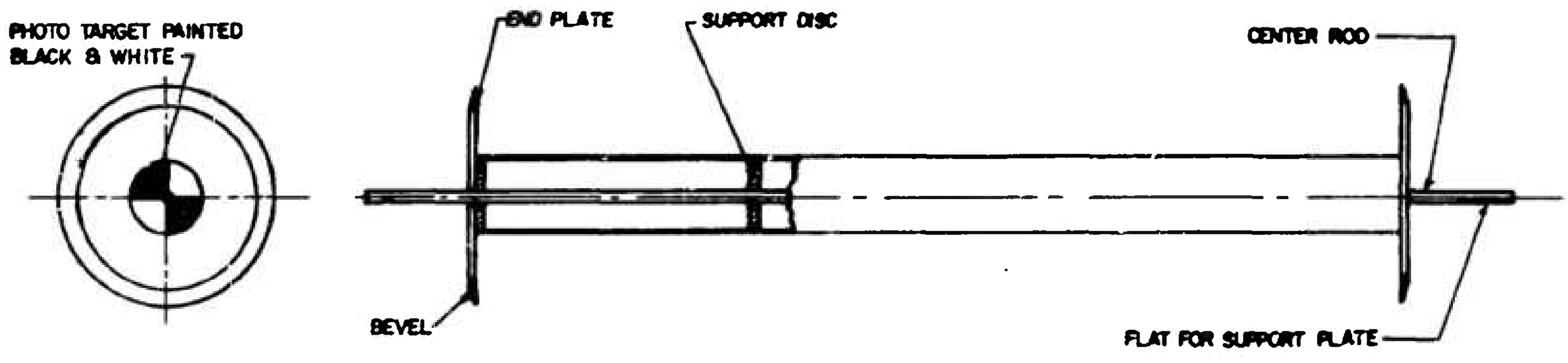

FIG. 3 MECHANICAL DESIGN OF TYPICAL CYLINDER

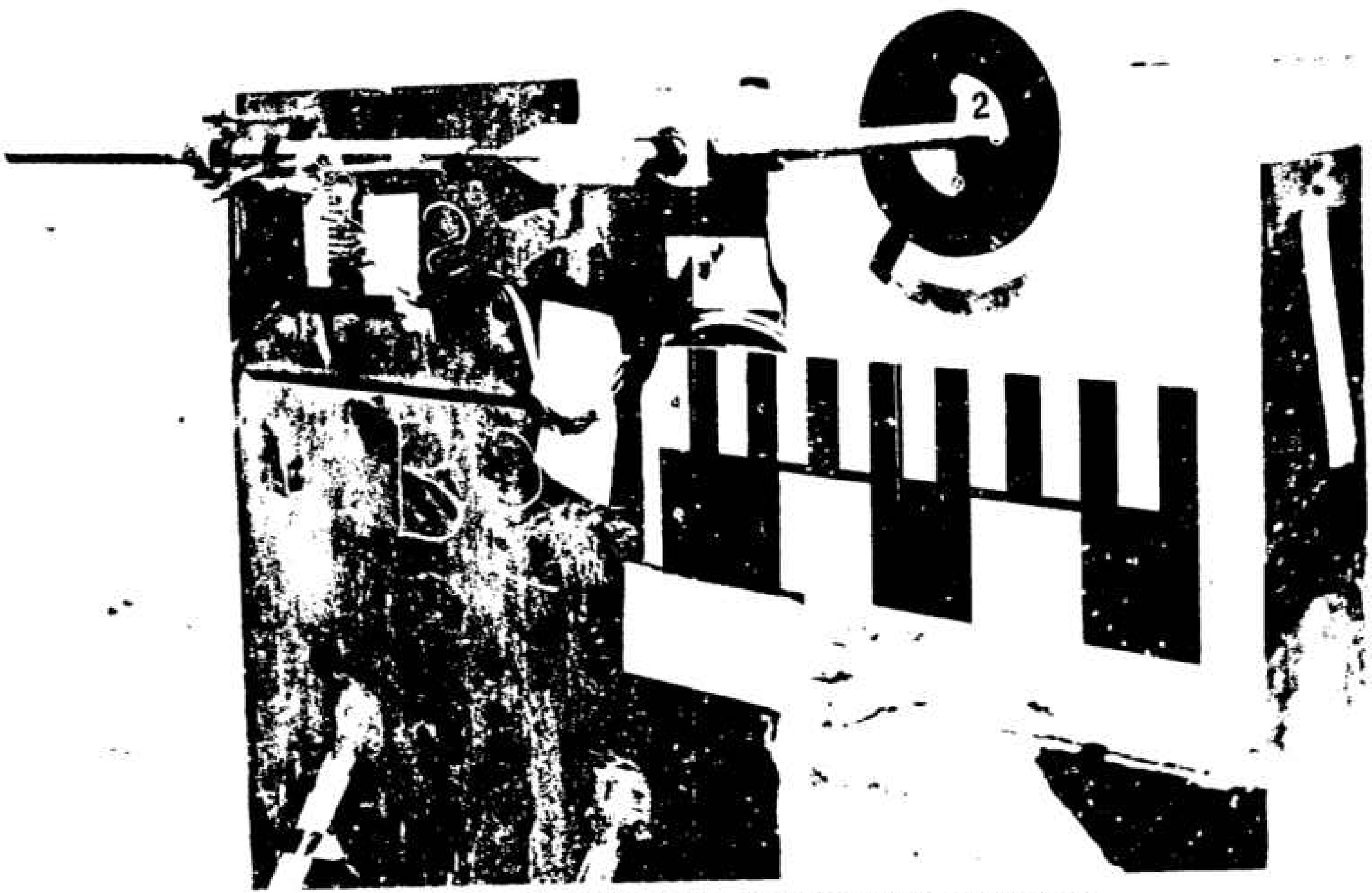

FIG. 4 CLOSE-UP VIEW OF VELOCITY TRANSDUCER ASSEMBLY

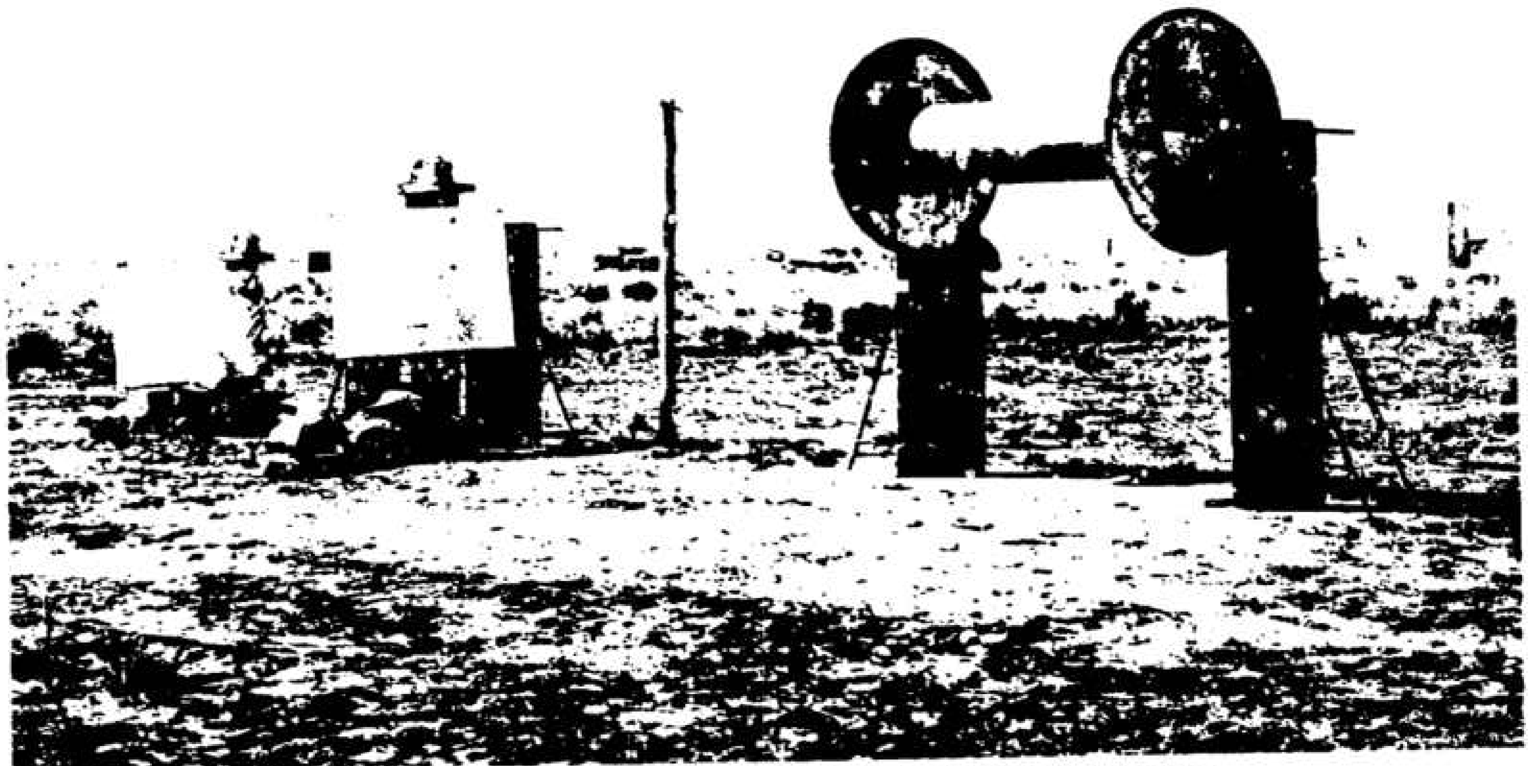

FIG. 5 HIGH-SPEED CAMERA ON POST WITH LIGHT REFLECTOR

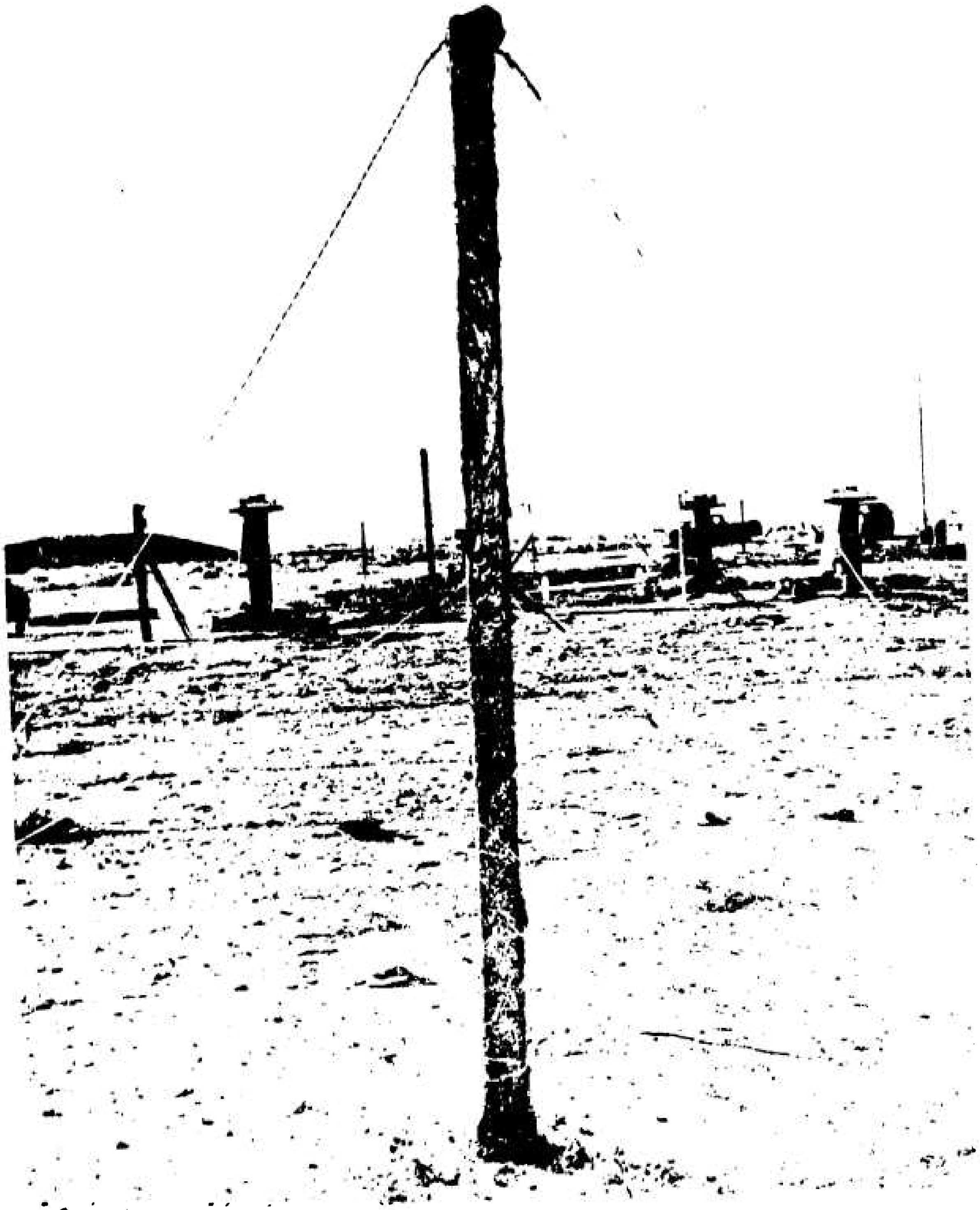

FIG. 6 GREASY STAKE DUST COLLECTOR (POST-SHOT)

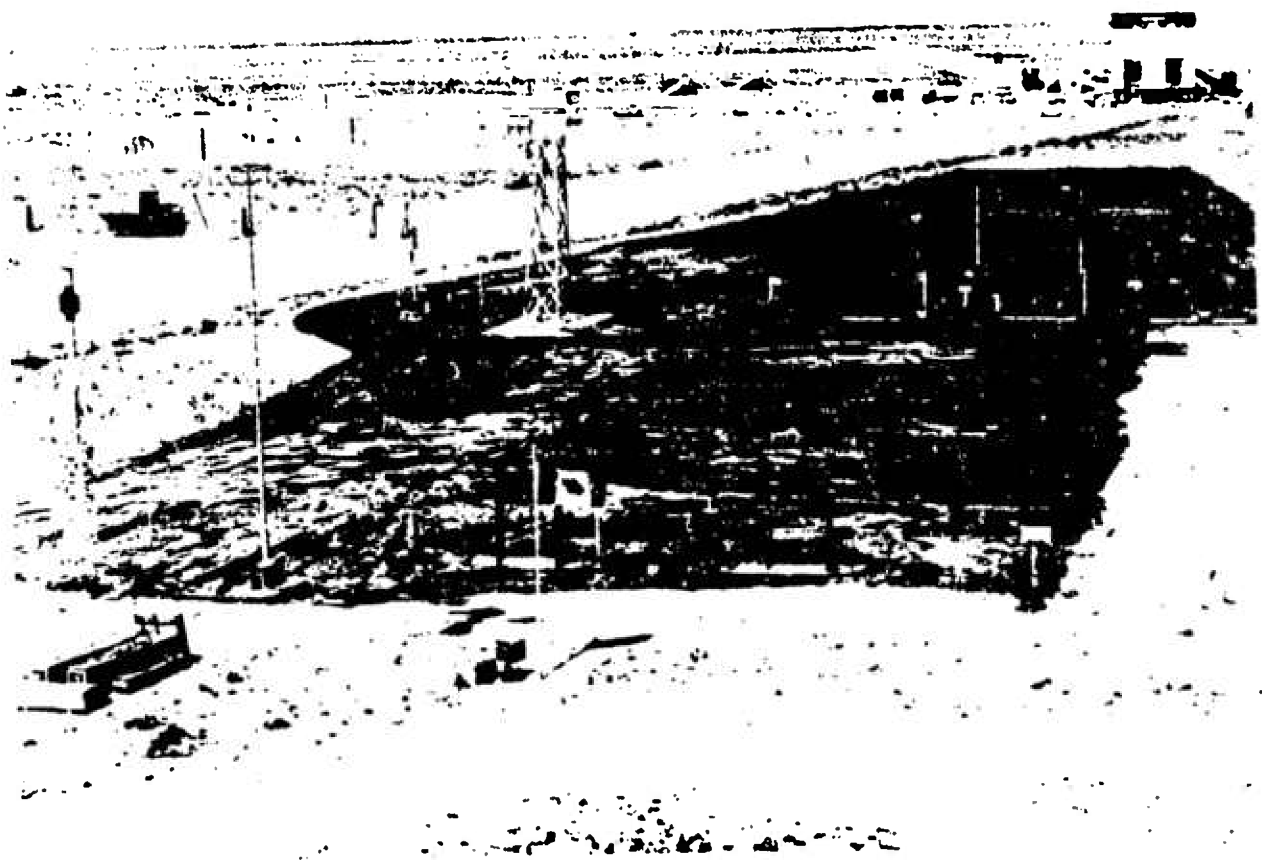

FIG. 7 PRE-SHOT VIEW OF CANADIAN SECTOR SHOWING AREA COVERED BY TREATED GROUND

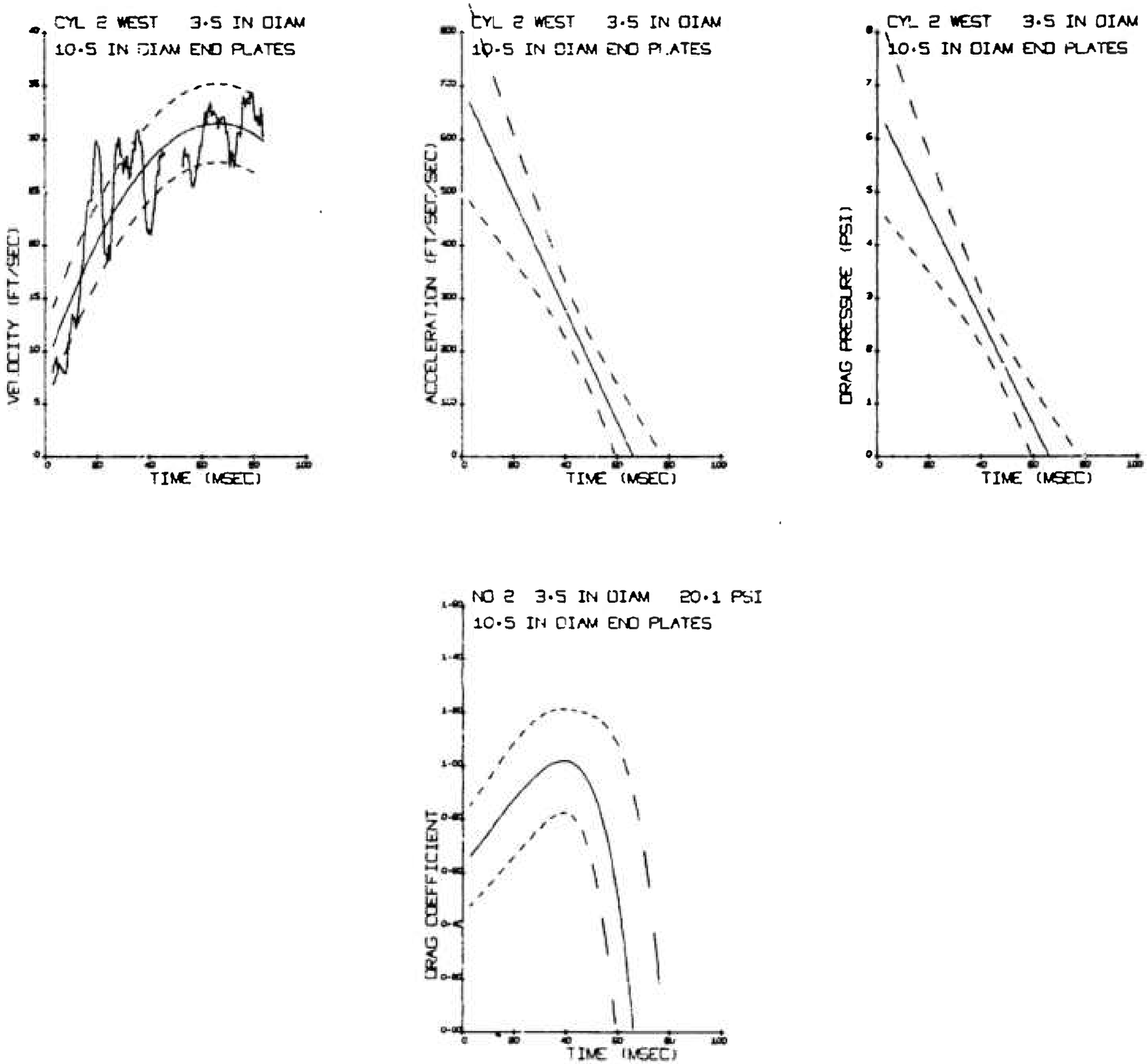

FIG. 8 CYLINDER 2 - VELOCITY TRANSDUCER DATA
(20.1 PSI PEAK OVERPRESSURE)

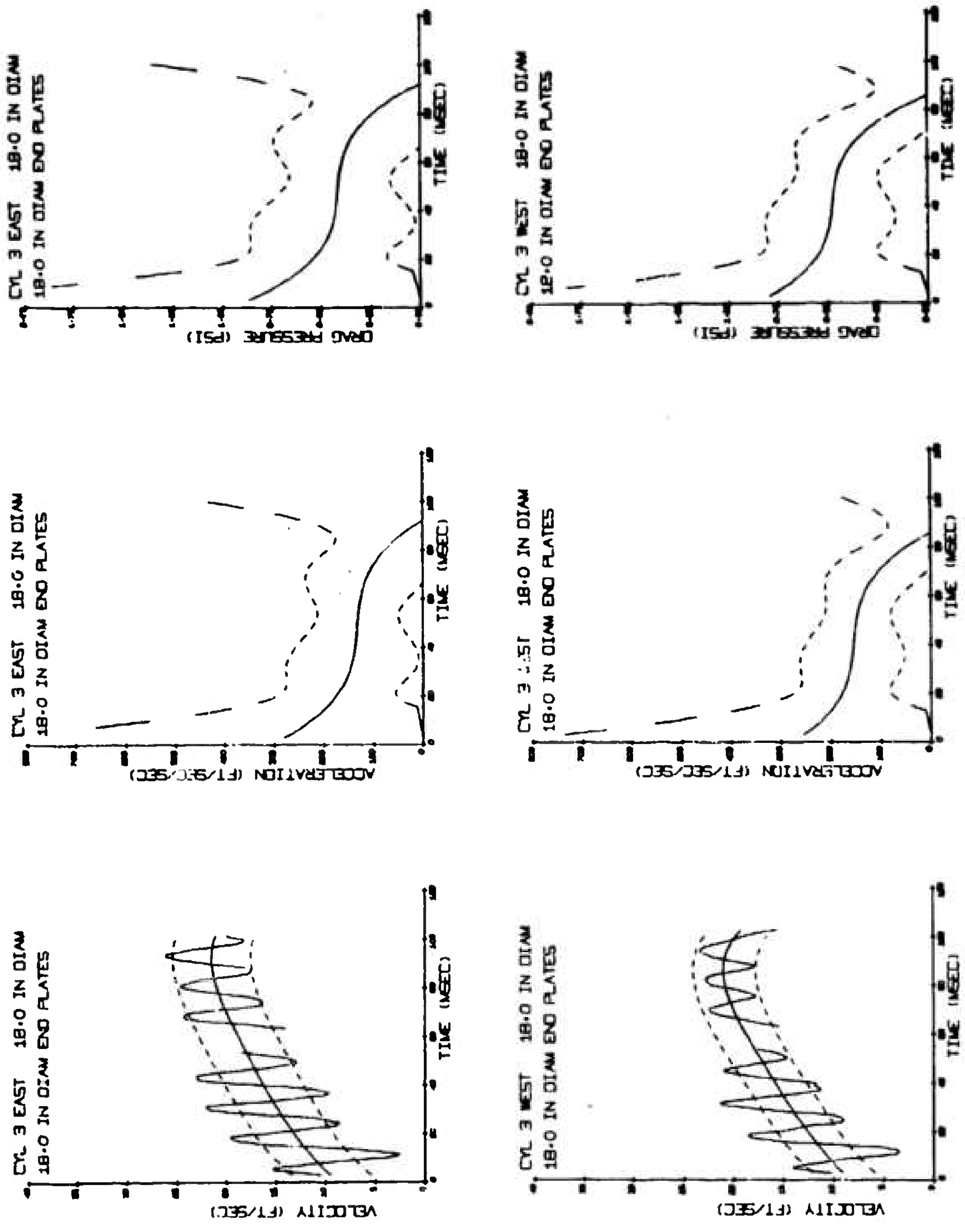

FIG. 9 CYLINDER 3 - VELOCITY TRANSDUCER DATA (9.7 PSI PEAK OVERPRESSURE)

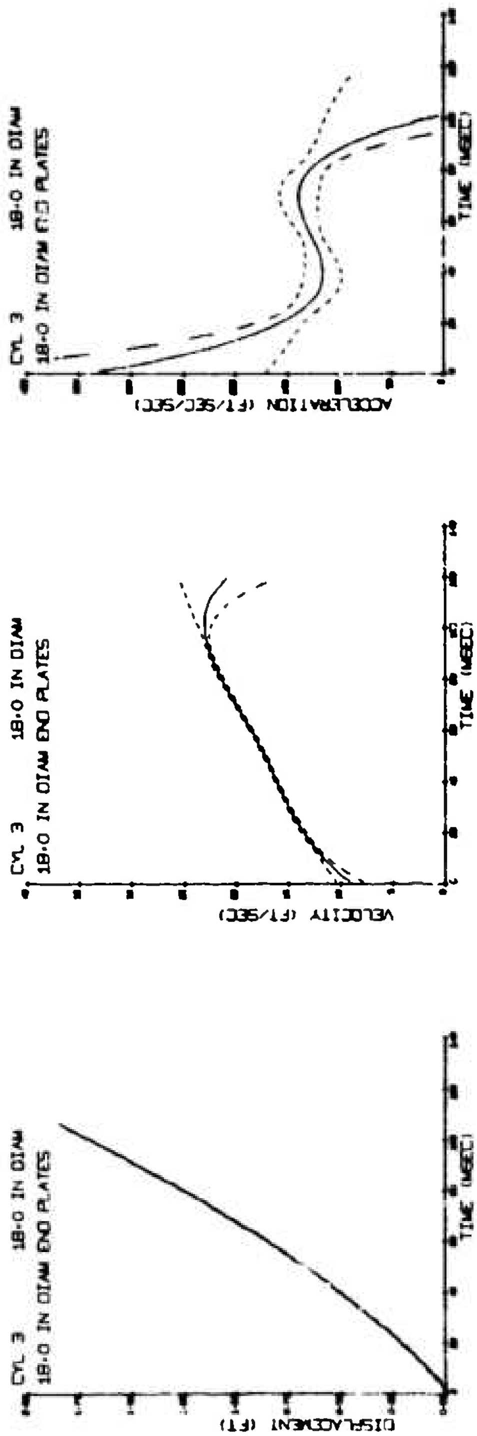

FIG. 10 CYLINDER 3 - HIGH-SPEED CAMERA DATA
(9.7 PSI PEAK OVERPRESSURE)

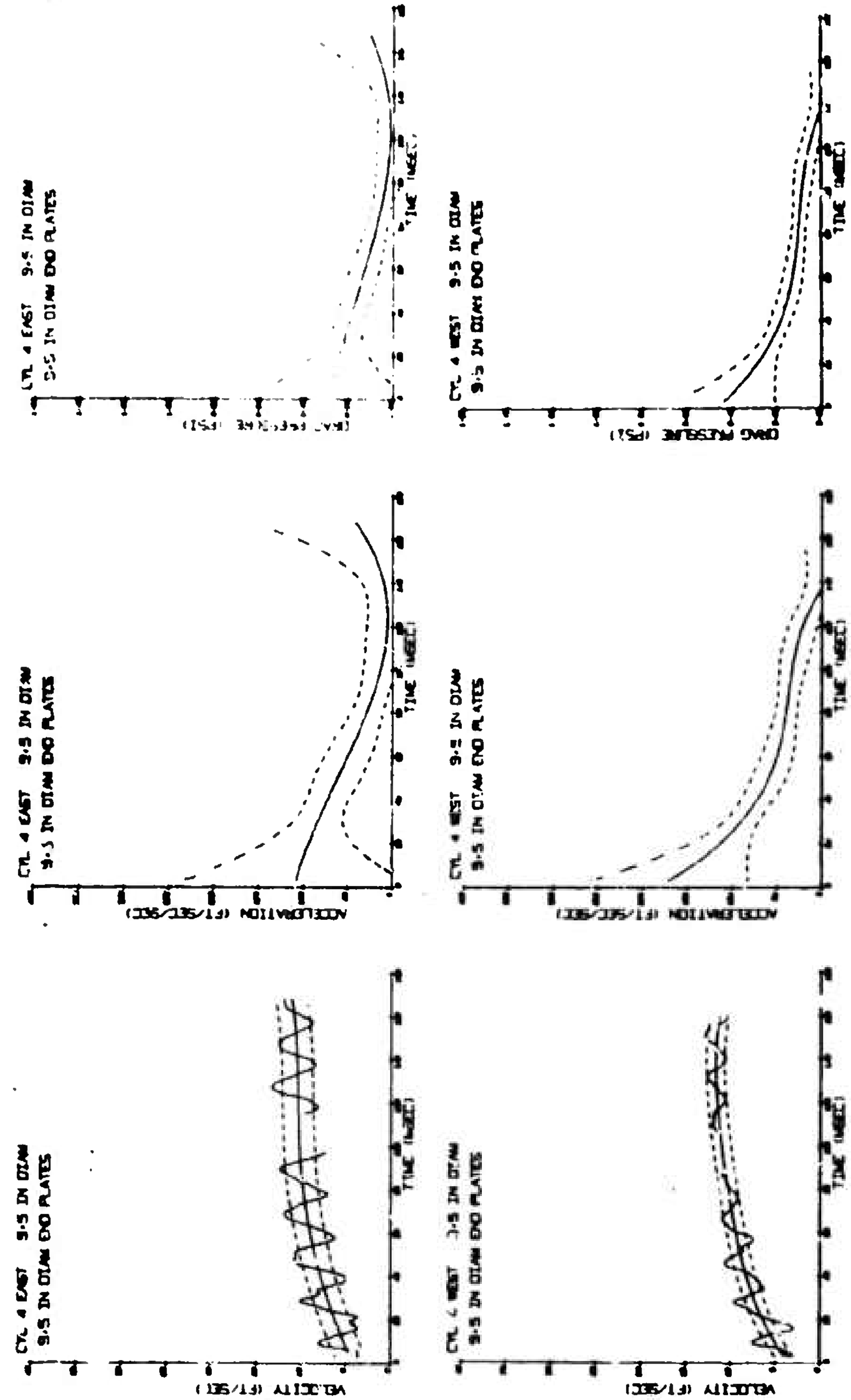

FIG. 11 CYLINDER 4 - VELOCITY TRANSDUCER DATA
(6.7 PSI PEAK OVERPRESSURE)

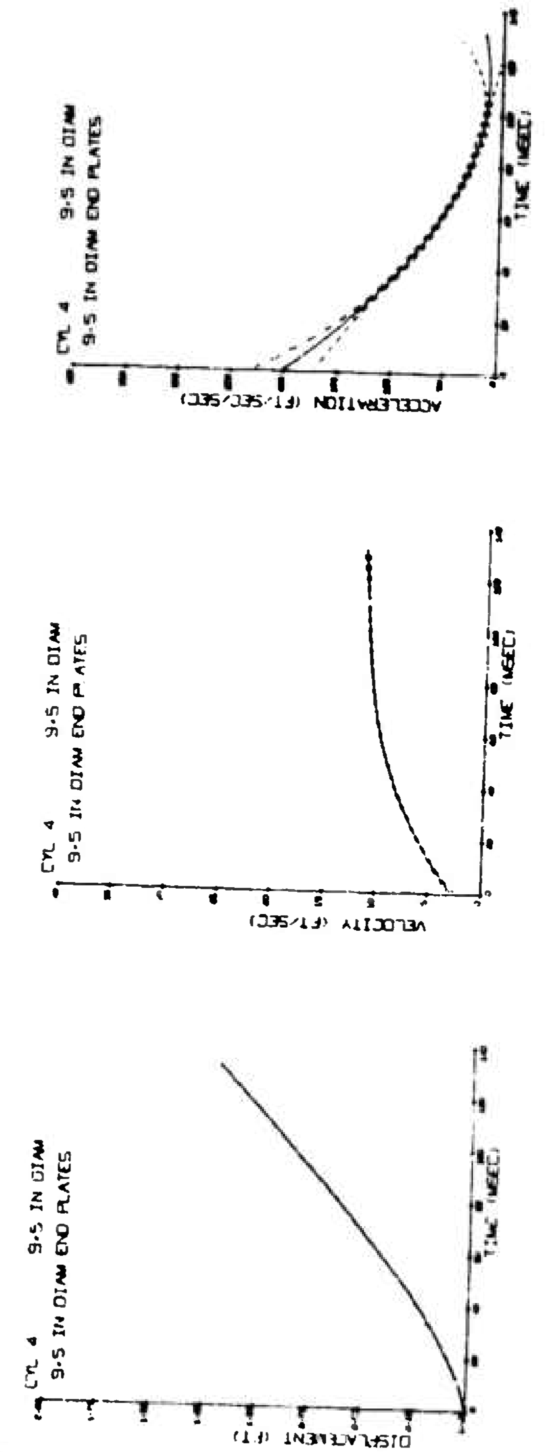

FIG. 12 CYLINDER 4 - HIGH-SPEED CAMERA DATA (6.7 PSI PEAK OVERPRESSURE)

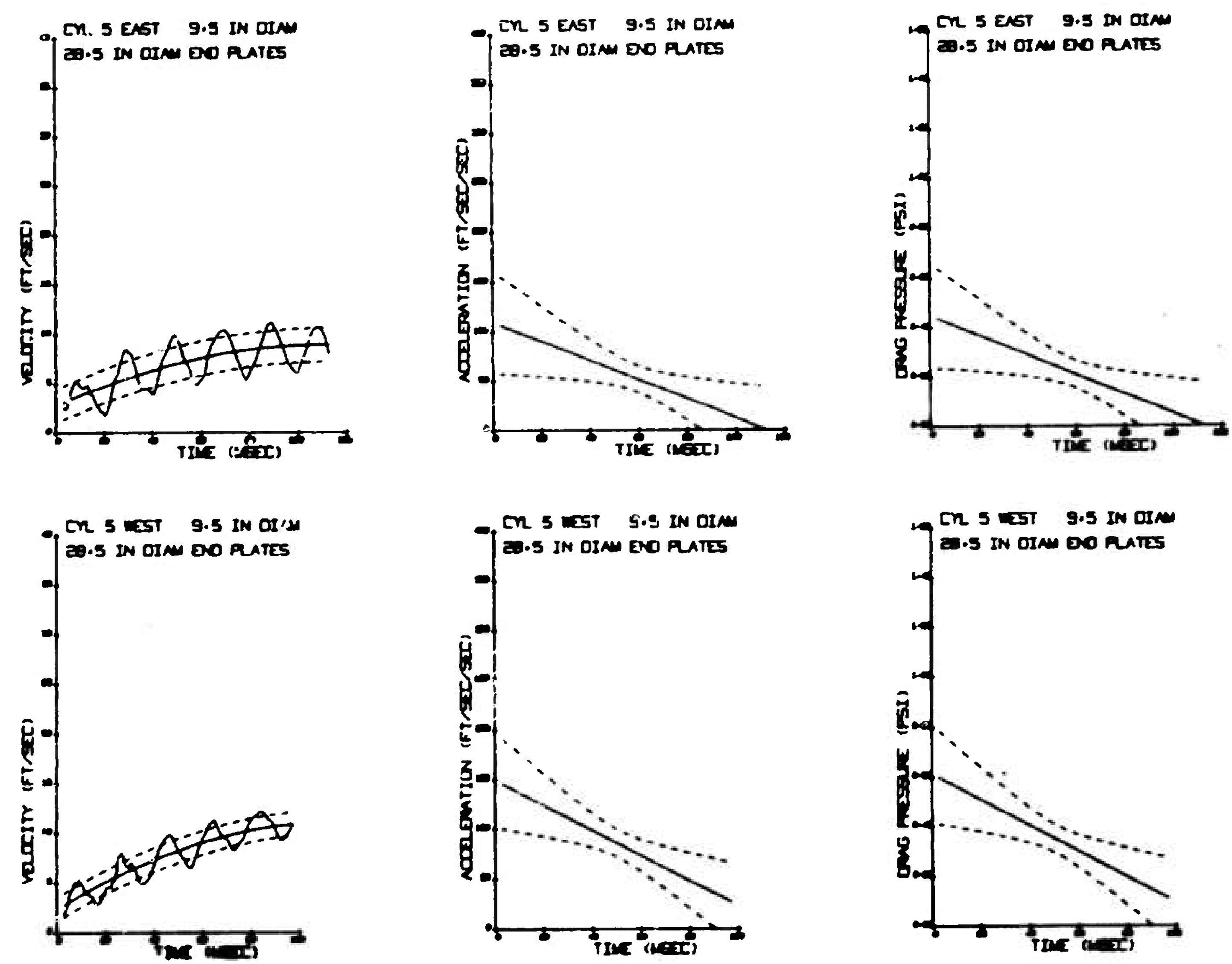

FIG. 13 CYLINDER 5 - VELOCITY TRANSDUCER DATA
(6.7 PSI PEAK OVERPRESSURE)

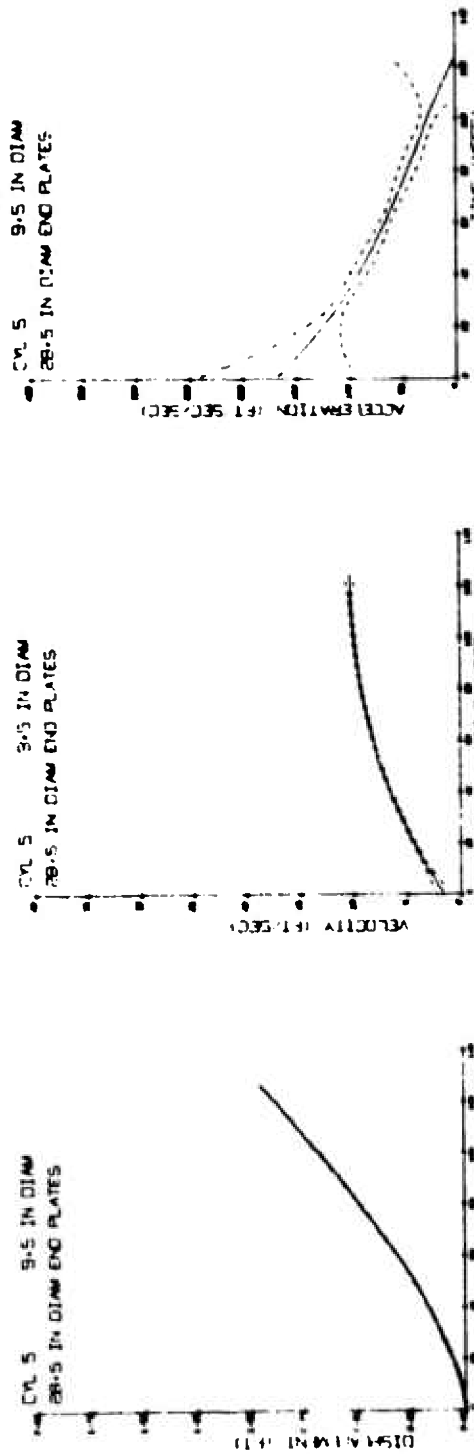

FIG. 14 CYLINDER 5 - HIGH-SPEED CAMERA DATA (6.7 PSI PEAK OVERPRESSURE)

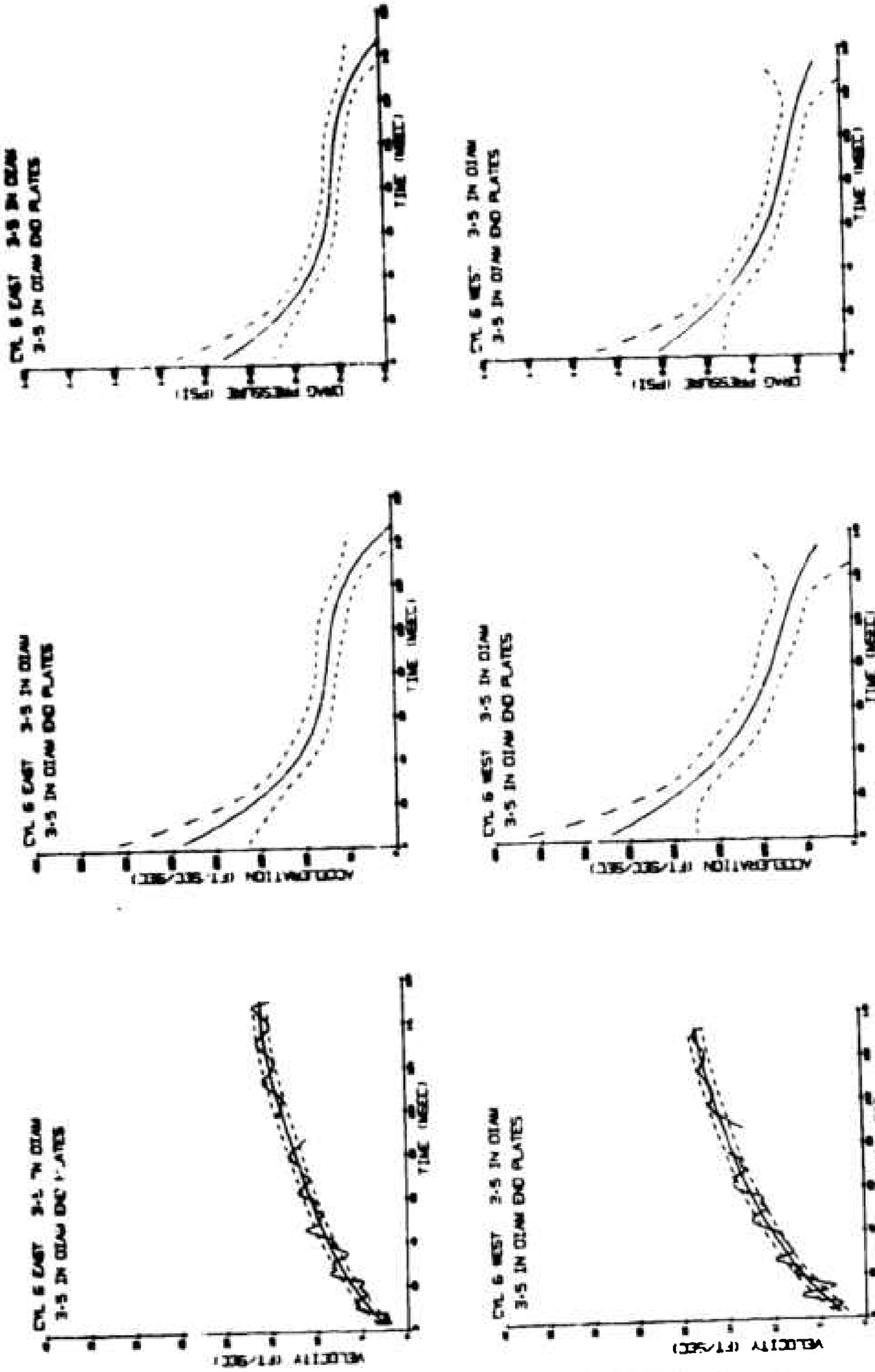

FIG. 15 CYLINDER 6 - VELOCITY TRANSDUCER DATA
(9.7 PSI PEAK OVERPRESSURE)

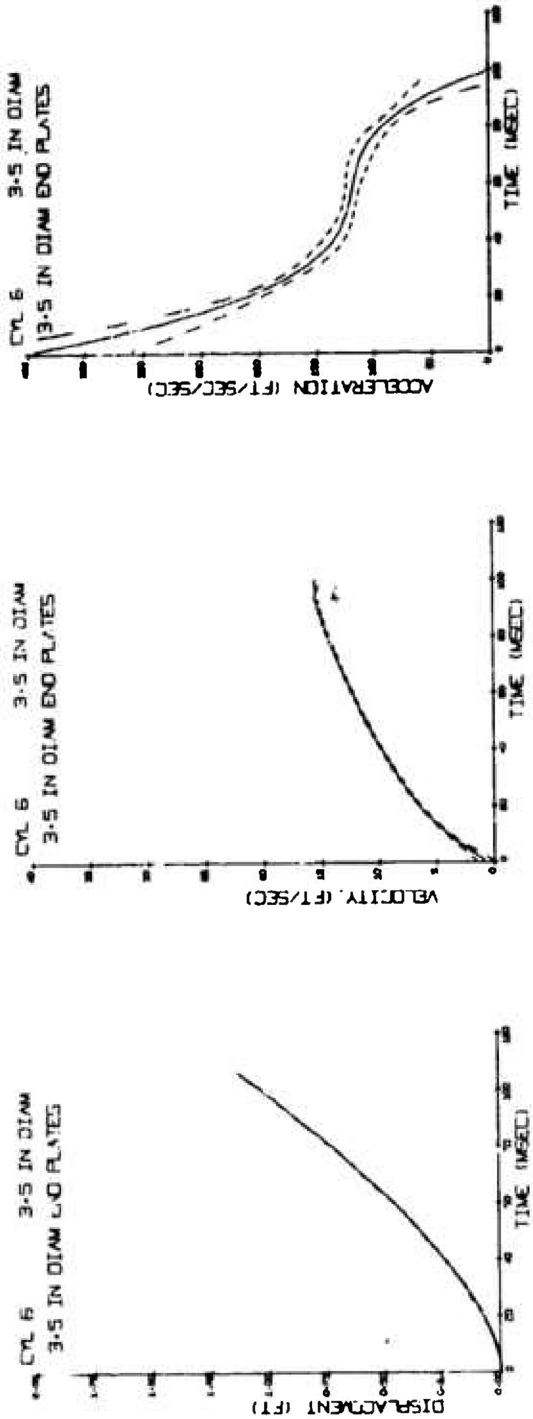

FIG. 16 CYLINDER 6 - HIGH-SPEED CAMERA DATA (9.7 PSI PEAK OVERPRESSURE)

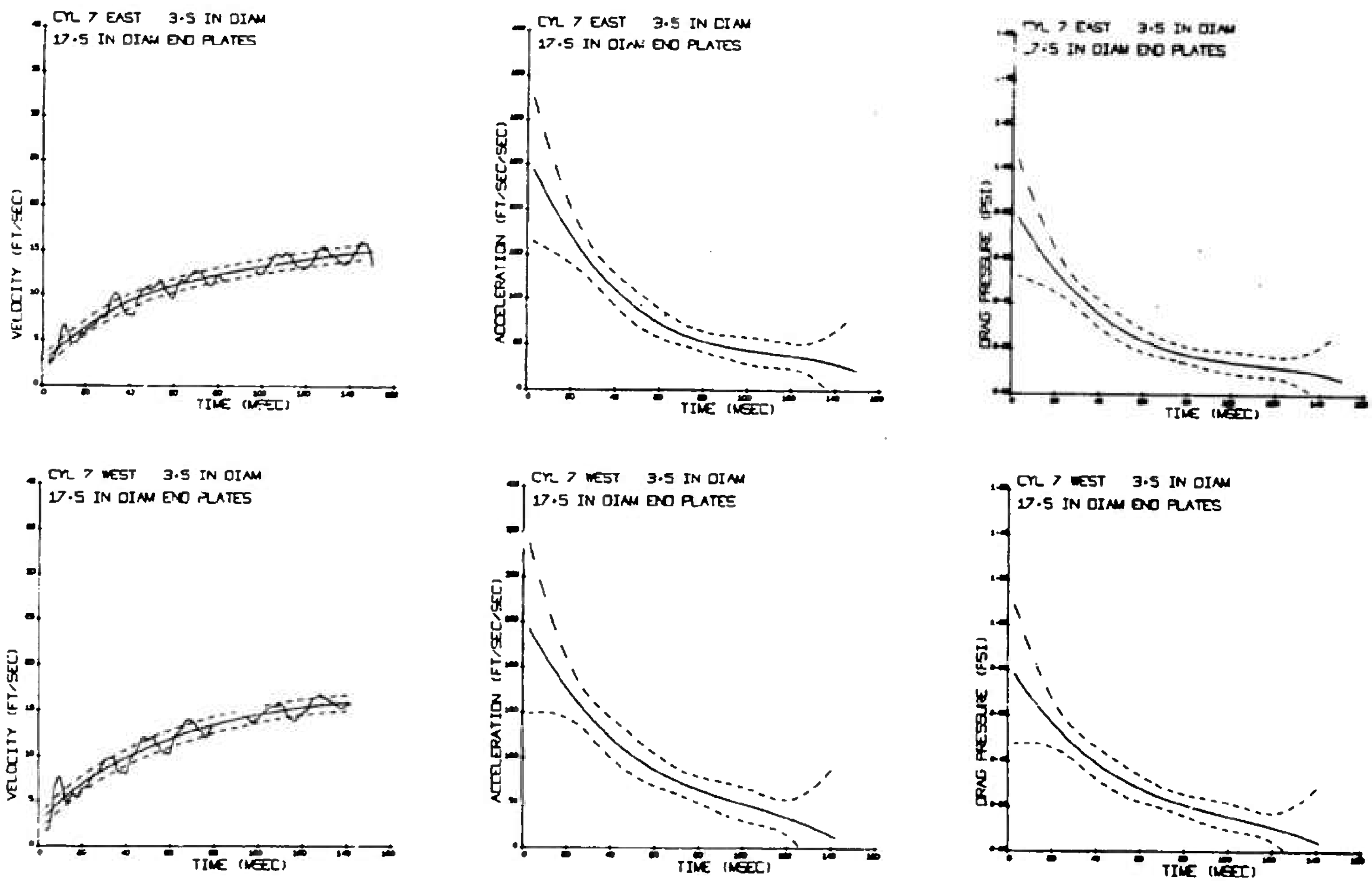

FIG. 17 CYLINDER 7 - VELOCITY TRANSDUCER DATA
(9.7 PSI PEAK OVERPRESSURE)

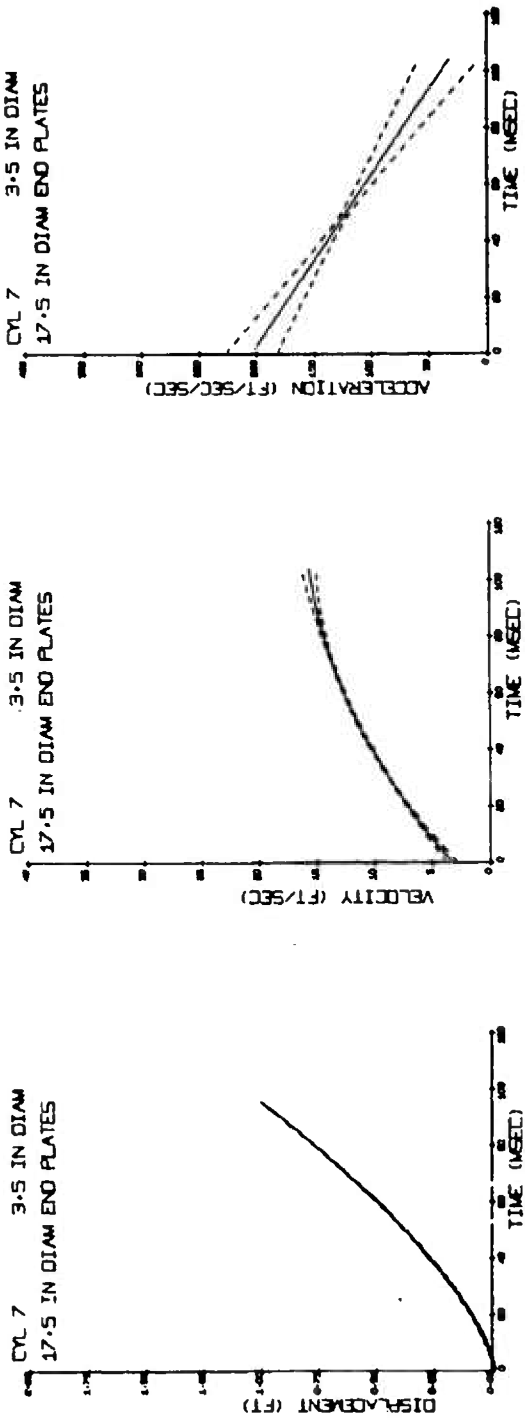

FIG. 18 CYLINDER 7 - HIGH-SPEED CAMERA DATA (9.7 PSI PEAK OVERPRESSURE)

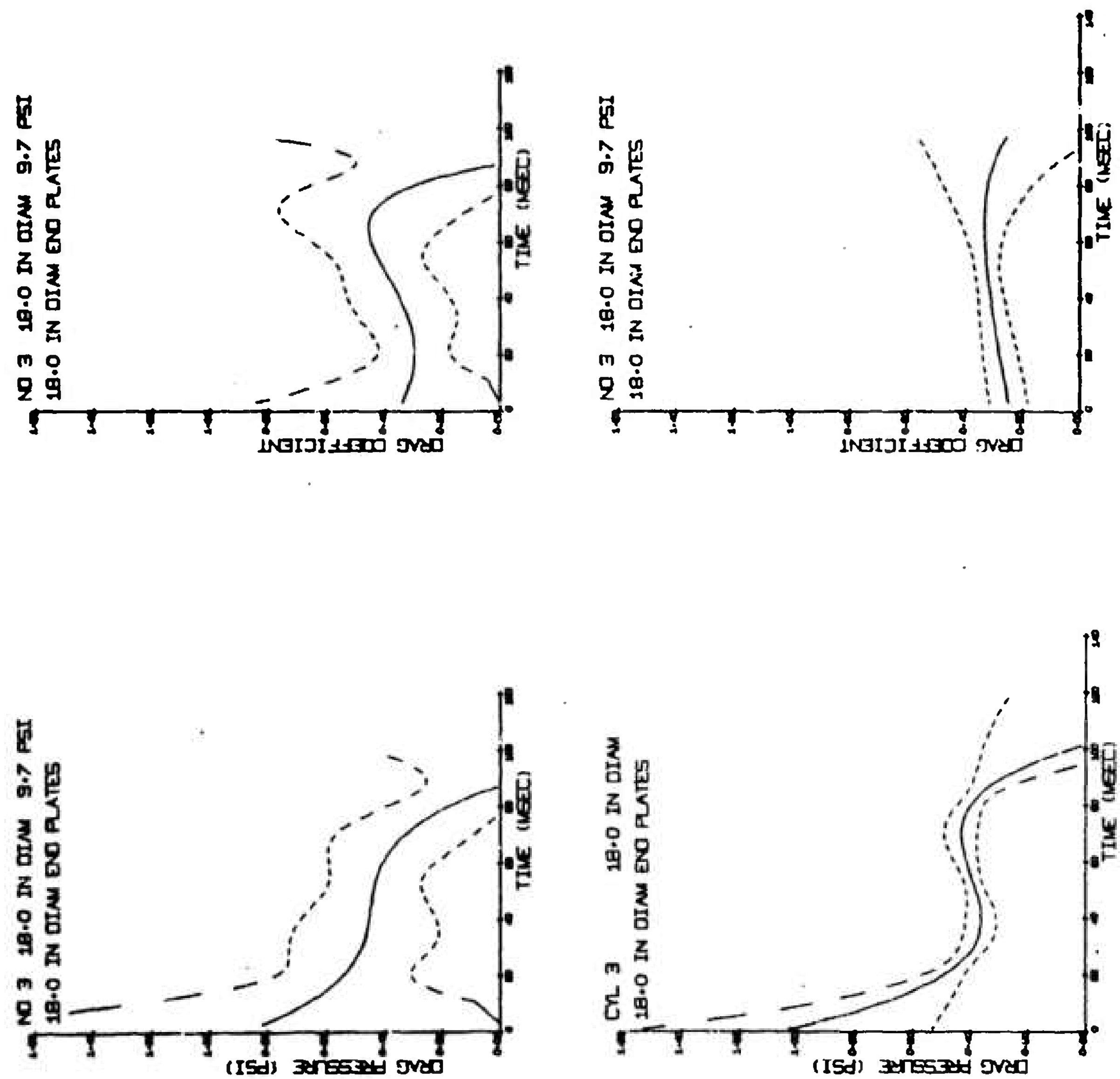

FIG. 19 CYLINDER 3 - DRAG COEFFICIENT VS TIME

Top - Velocity Transducer Data
Bottom - Camera Data

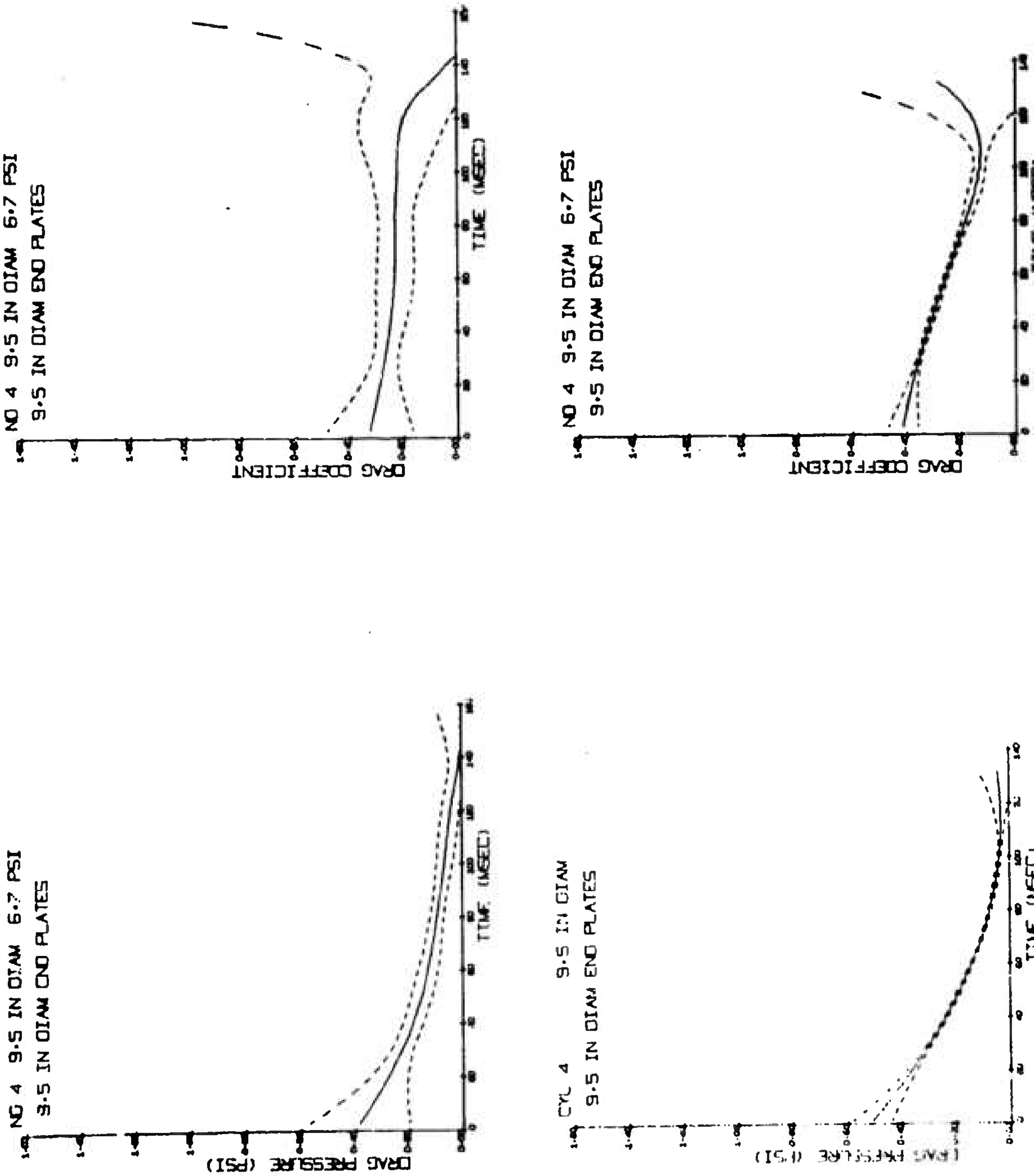

FIG. 20 CYLINDER 4 - DRAG COEFFICIENT VS TIME

Top - Velocity Transducer Data
Bottom - Camera Data

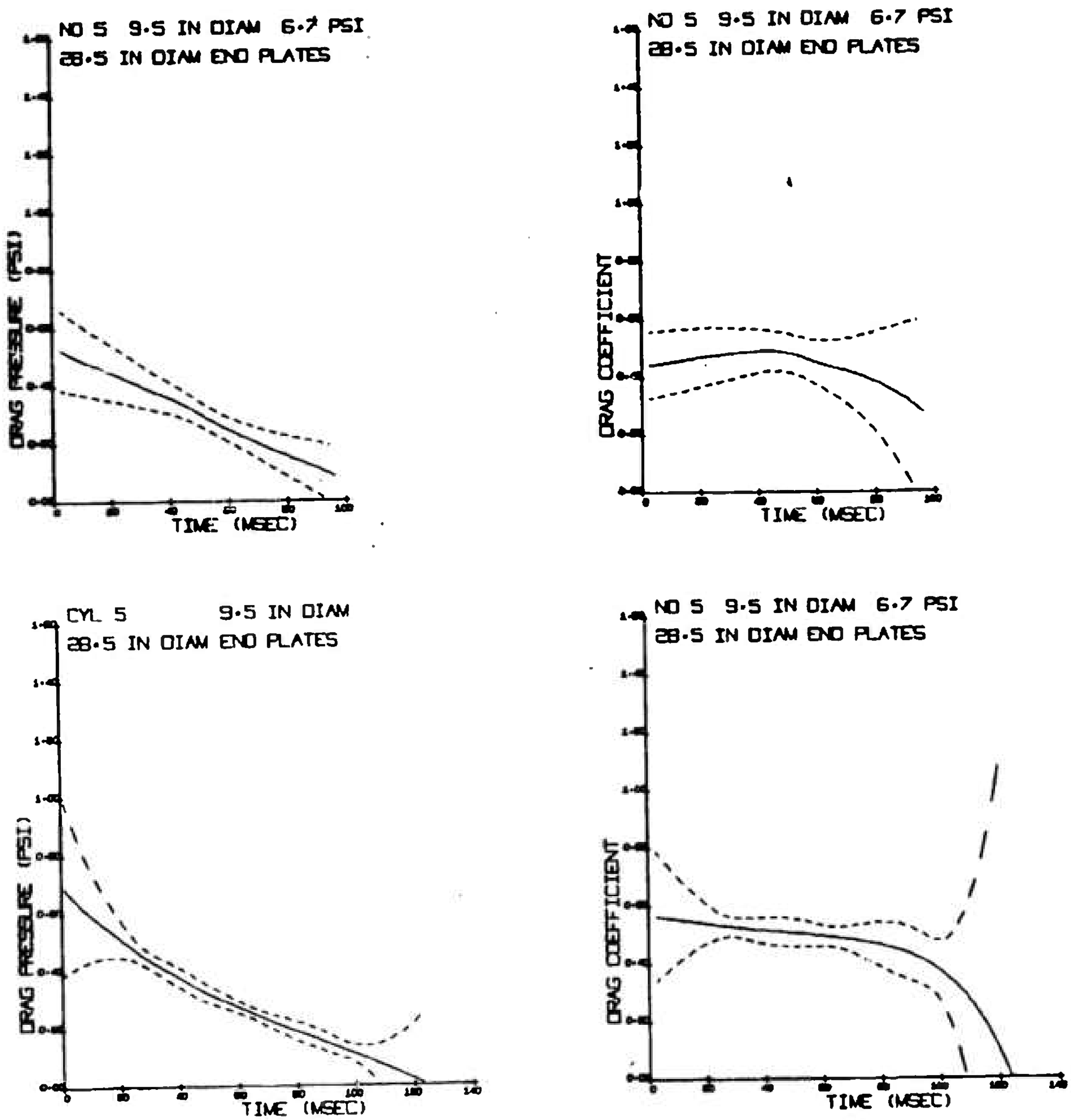

FIG. 21 CYLINDER 5 - DRAG COEFFICIENT VS TIME

Top - Velocity Transducer Data
Bottom - Camera Data

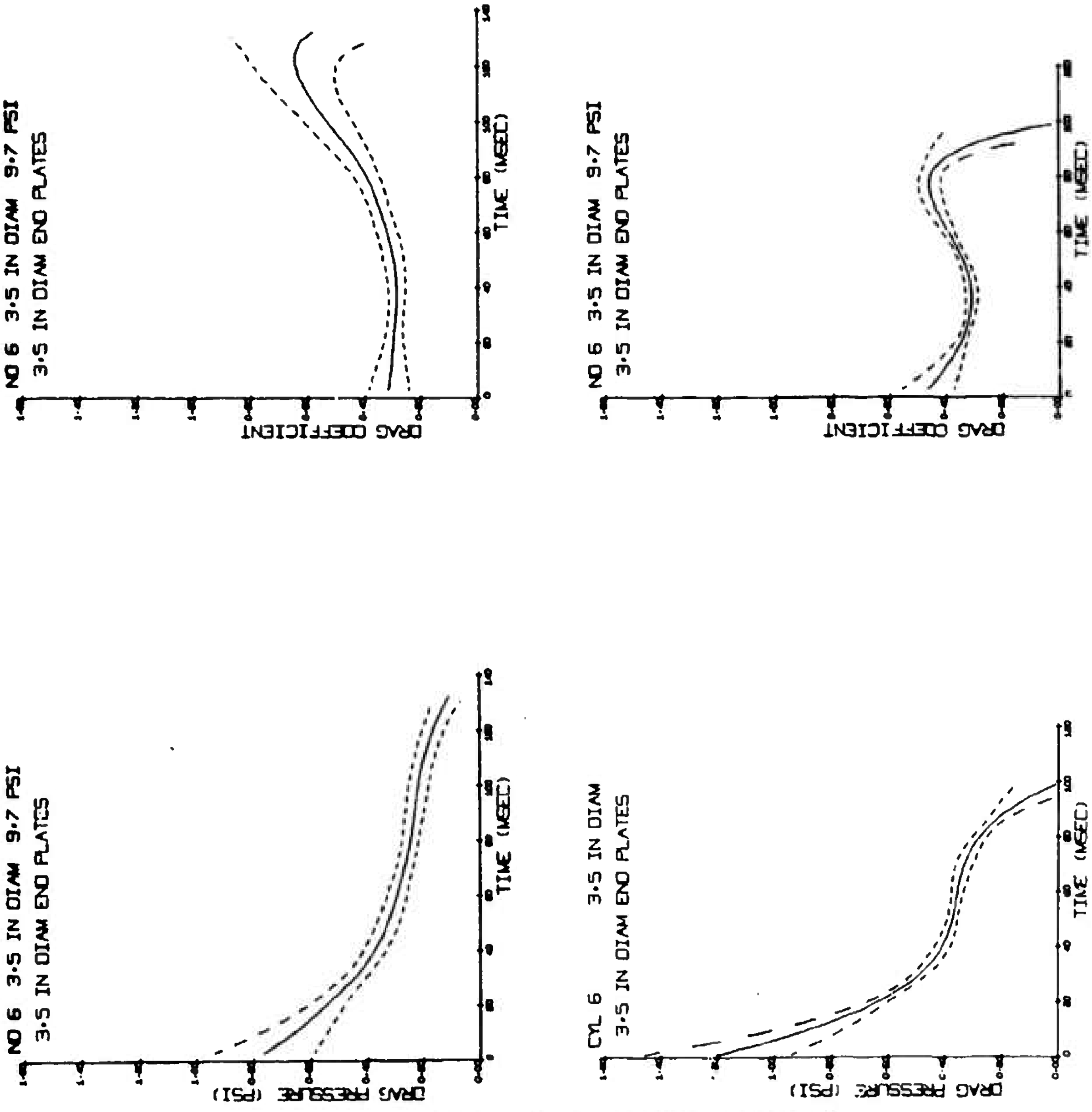

FIG. 22 CYLINDER 6 - DRAG COEFFICIENT VS TIME

Top - Velocity Transducer Data
Bottom - Camera Data

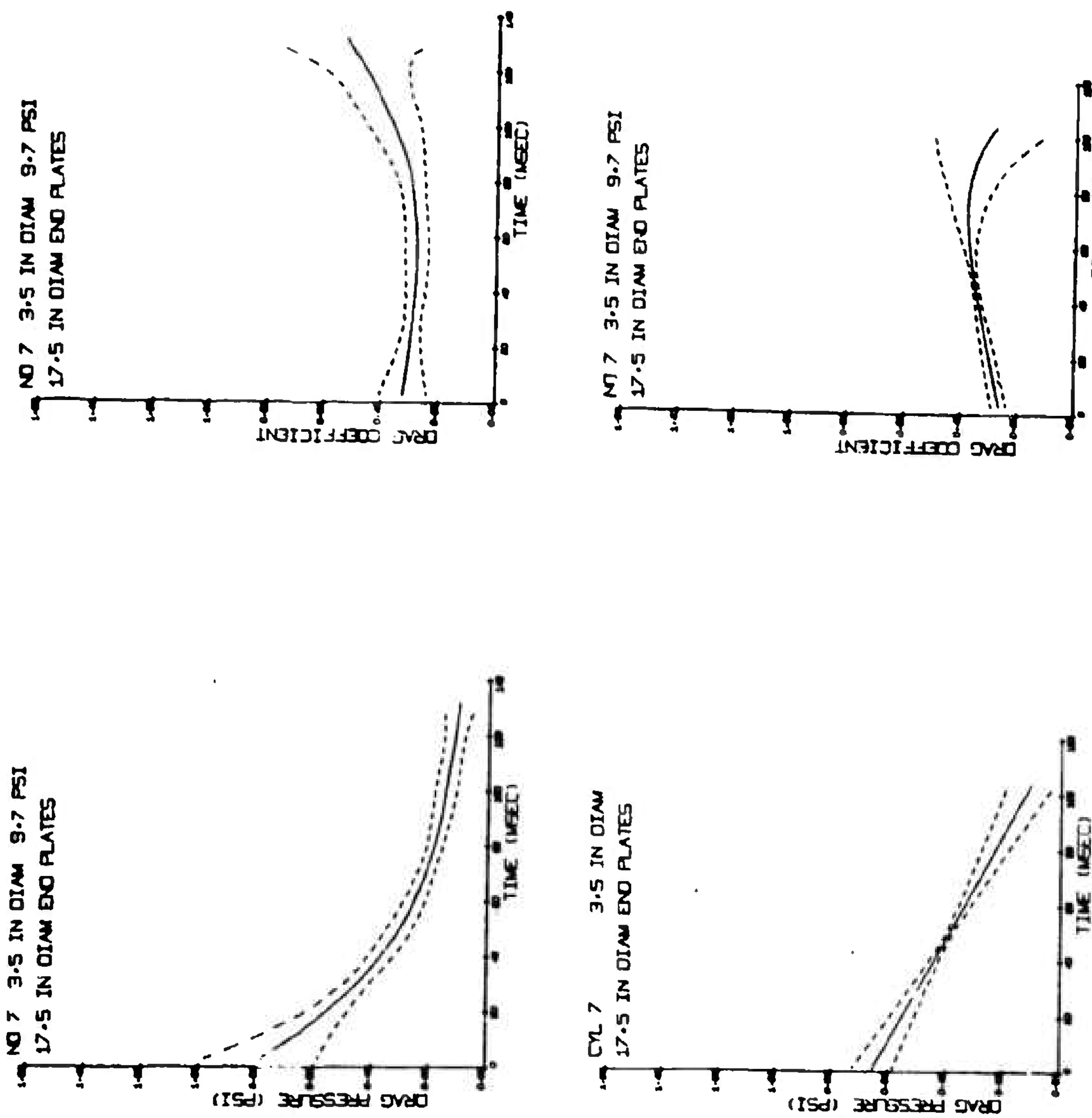

FIG. 23 CYLINDER 7 - DRAG COEFFICIENT VS TIME

Top - Velocity Transducer Data
Bottom - Camera Data

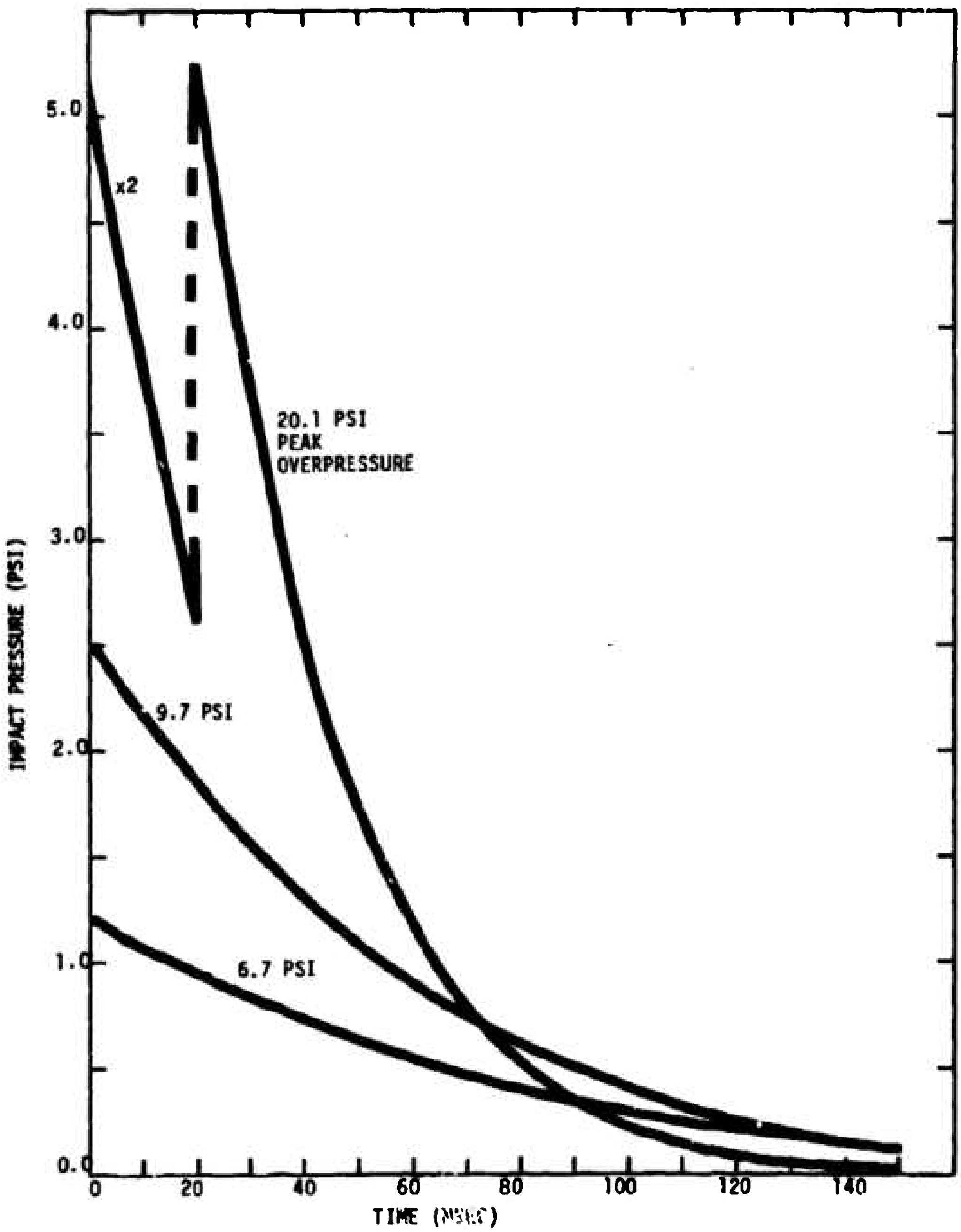

FIG. 24 IMPACT PRESSURES USED IN DATA ANALYSIS

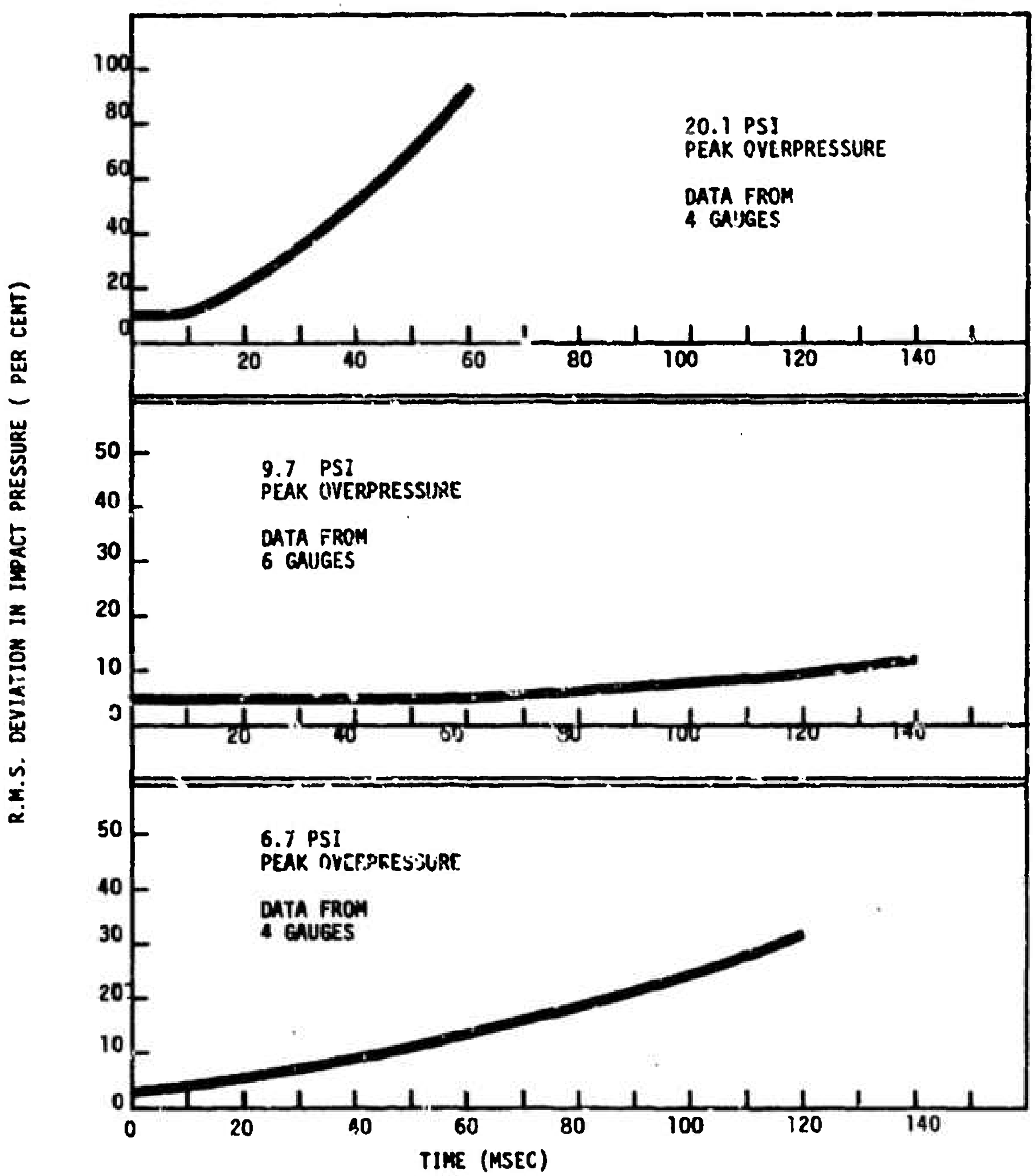

FIG. 25 UNCERTAINTY IN IMPACT PRESSURE VS TIME

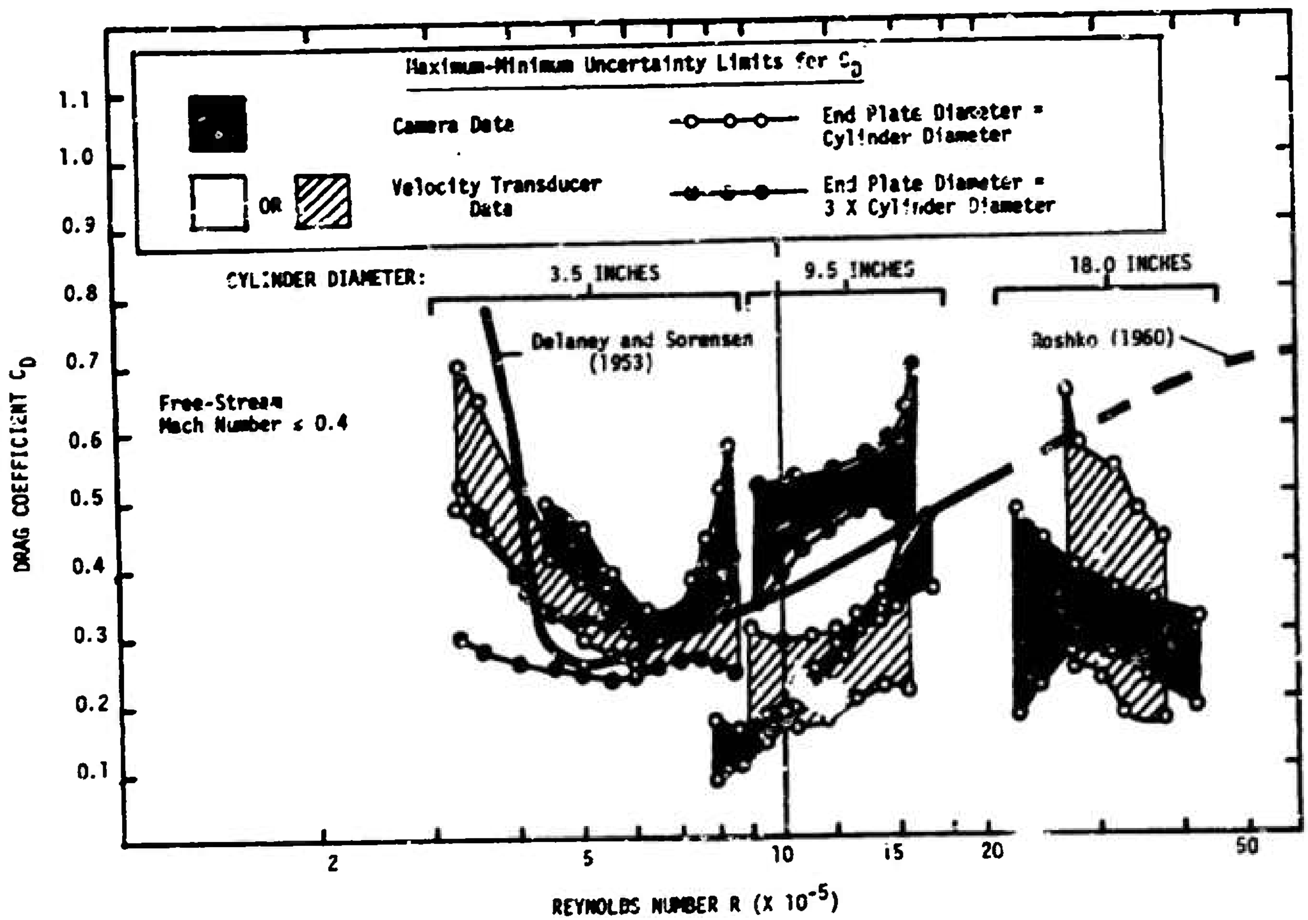

FIG. 26 MEASURED DRAG COEFFICIENT VS REYNOLDS NUMBER - COMPOSITE PLOT FOR ALL CYLINDER DIAMETERS

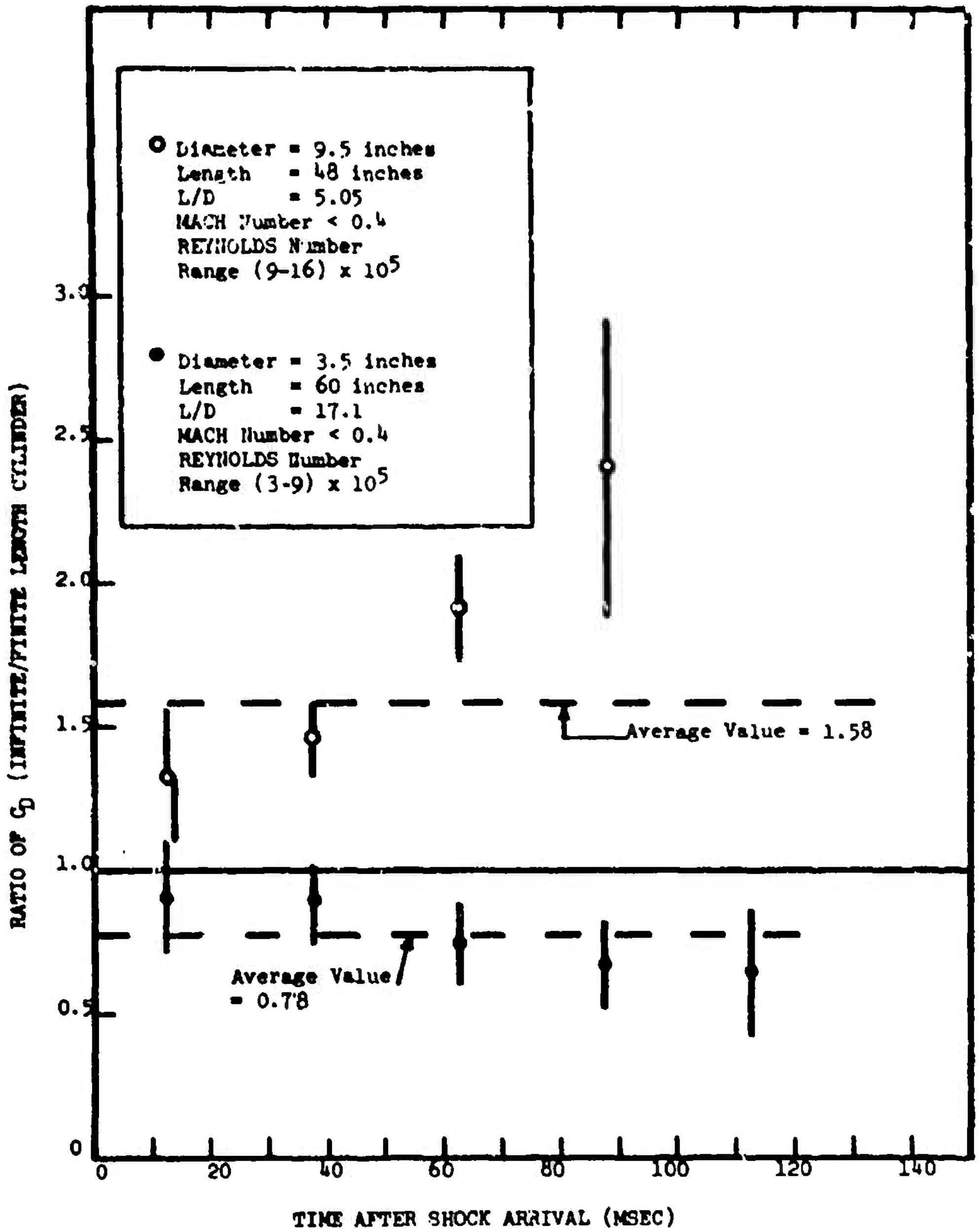

FIG. 27 MEASURED END EFFECTS FOR FINITE-LENGTH CYLINDERS

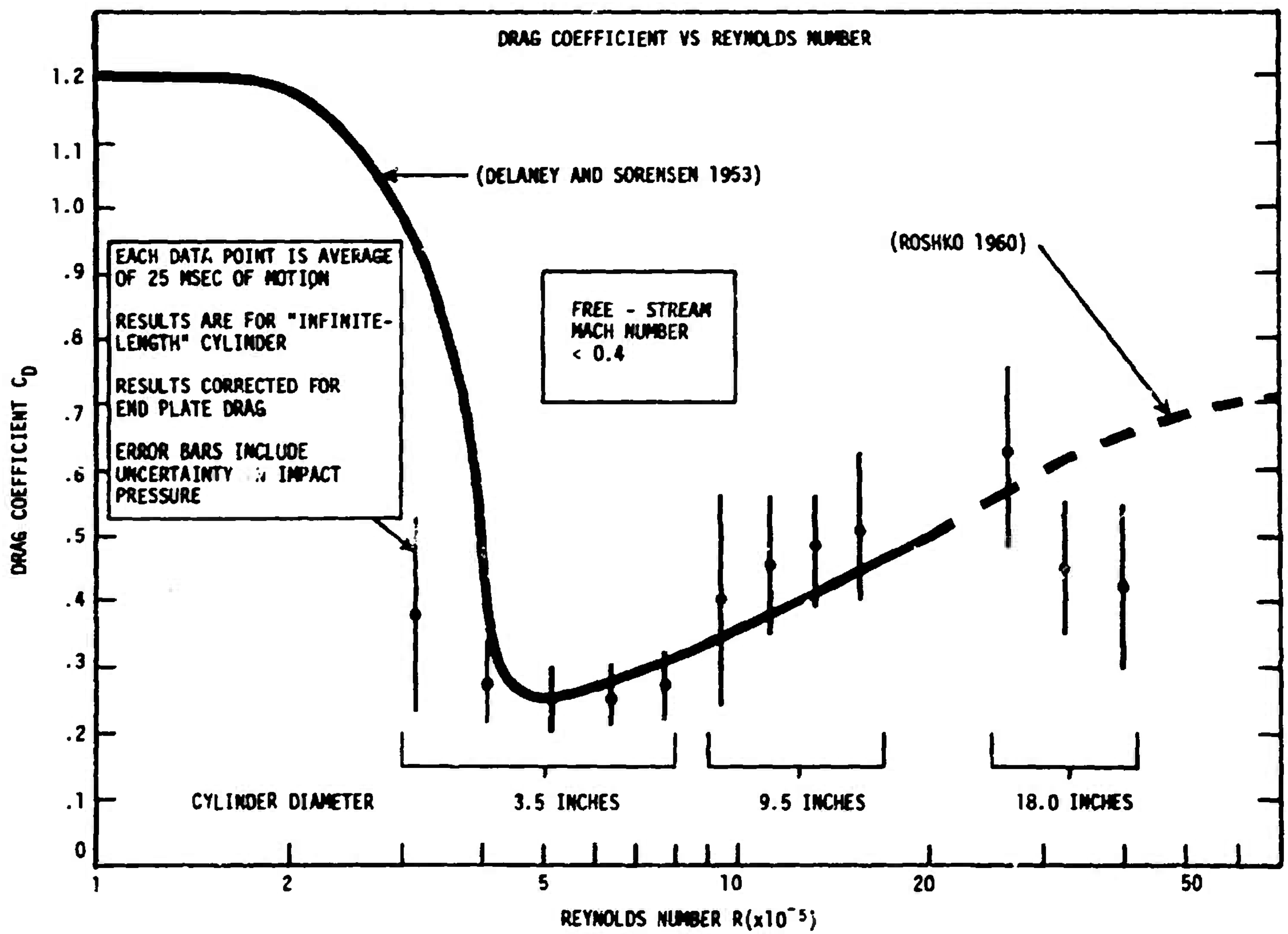

FIG. 28 DRAG COEFFICIENT VS REYNOLDS NUMBER - BEST VALUES (AFTER CORRECTIONS)

18. PROJECT C-2, BLAST RESPONSE OF UHF POLEMAST ANTENNA - EVENT DICE THROW

by

C.G. Coffey and G.V. Price
Defence Research Establishment Suffield

PROJECT C2 BLAST RESPONSE OF UHF POLEMAST ANTENNA - EVENT DICE THROW

C.G. Coffey and G.V. Price

DEFENCE RESEARCH ESTABLISHMENT SUFFIELD
RALSTON, ALBERTA, CANADA

ABSTRACT

The blast response of a 23 ft UHF Polemast Antenna was investigated in a free-field blast trial and in numerical simulation experiments. The antenna satisfactorily withstood the air blast loading at the nominal 7.0 psi peak overpressure location in Event Dice Throw, and the numerical model predictions for the natural frequencies and transient strain were in excellent agreement with the values obtained experimentally.

INTRODUCTION

The Defence Research Establishment Suffield (DRES), in support of the Canadian Forces (Maritime) policy on blast hardening of ships and sub-components, has conducted a series of tests to determine the ability of certain antenna designs to withstand blast overpressures of various intensities. During Event Dice Throw, a 620 ton AN/FO free-field blast trial conducted by the United States Defence Nuclear Agency at the White Sands Missile Range in New Mexico on 6 October, 1976, several antenna designs were tested at various overpressure levels. One of the antennas evaluated in the trial was a 23 ft UHF Polemast Antenna, of the type intended for several classes of ships (IRE-257, DDE-261, DDH-265, and AOR508).

The objectives of this study were to determine the ability of the Polemast Antenna Assembly, complete with attached fibreglass covered radiators, to withstand a blast wave at the 7.0 psi peak overpressure level, and to compare the measured antenna response against theoretical predictions determined by a computer model recently developed at DRES [1]. It is intended that experimental verification of the computer model would lead to a criterion for predicting the blast response of polemast designs in general.

CONSTRUCTION OF THE PROTOTYPE POLEMAST ANTENNA

A prototype Polemast Antenna was constructed at DRES in accordance with drawings supplied by DMCS-6. During the fabrication of the prototype, design modifications were required in order to accommodate the facilities of the DRES Machine Shop. The design modifications are examined in detail in Appendix A. It is anticipated that the suggested design changes will generally make the antenna more cost effective by simplifying the fabrication procedures.

A schematic view of the Polemast Antenna is shown in Figure 1. The structural portion of the antenna is a seamless aluminum tube 9.5" O.D. x .261 " wall x 19'-7" long. The tubing was fabricated by Alcan Canada Products Ltd., and a summary of the physical properties of the tubing is provided in Appendix B. Attached to the aluminum tubing were an Upper and Lower Radiator, a Lower Transformer, a Cross Arm, and an AN/SRD-501 Antenna at the mast head. The Lower Radiator and Transformer were actual test items, while the Upper Radiator and the AN/SRD-501 Antenna were mock-ups constructed to simulate the approximate weight, and projected cross-sectional area of the respective items.

The Prototype Polemast Antenna was mounted vertically in a lattice structure at the nominal 7.0 psi peak overpressure level, 1135 ft from ground zero (GZ). The lattice structure was used in a previous multi-ton trial ("Event Dial Pack" held at DRES in 1970) as a mounting for a GRP Topmast [2]. The lattice structure and mountings for the Polemast are shown in Figure 2. As shown in the figure, the distance between the clamp assemblies attaching the Polemast to the lattice structure was 36 in. The upper clamp assembly was in accordance with drawing DDDS-000143 supplied by DMCS-6 (a change in this design is recommended, as noted in Appendix A). The lower clamp assembly, as shown in Figure 2, was different from that specified in drawing DDDS-000157 supplied by DMCS-6. Changes to this assembly were introduced to expedite assembly in the field (see Figure 2, Section B-B). The modifications to the lower clamp assembly did not in any way affect the structural integrity of the joint.

The lattice structure was mounted on a 12 ft x 6 ft x 2.5 ft heavy reinforced concrete foundation (DRES drawing MES-CDT-100-C2-1). The Polemast and Antenna components were assembled while lying horizontal, and the complete assembly was lifted with a crane over the lattice structure and lowered into place. After the upper and lower clamp assemblies were secured, no further adjustments were required since the upper and lower mounting plates on the lattice structure were normal to the uprights and parallel to the level of the concrete pad. The complete Polemast assembly (excluding the lattice structure) weighed approximately 348 pounds.

This may be compared to the weight of the corresponding Polemast Antenna for ship use, estimated at 463 pounds. The difference in weight is due to the weight of additional clamps and cables used aboard ship which were considered unnecessary for the blast trial.

A photograph of the completed prototype Polemast Antenna installed for the Event Dice Throw field trial is shown in Figure 3. The orientation of the Polemast with respect to the direction of the blast is shown in Figure 1. As indicated in the figure, the fore-aft line of the Polemast was orientated normal to the direction of the blast, thereby resulting in the maximum blast loading on the brackets supporting the Radiators.

INSTRUMENTATION

Five pairs of MICRO-MEASUREMENTS type CEA-13-250UW-120 strain gauges were bonded directly to the aluminum tubing of the prototype Polemast. The strain gauge locations are shown in Figure 1. The gauges which constitute a strain gauge pair were bonded to opposite sides of the aluminum tubing on a line corresponding to the blast direction, thereby measuring the maximum flexural strain at the specified cross-sections. The signals from the strain gauge pairs were conditioned with bridge and balance units, amplified, F.M. multiplexed and then recorded on 14 track magnetic tape with a frequency response of DC to 4 KHz. In this fashion, five channels of experimental data were multiplexed onto one tape channel, a procedure which was required by the large number of DRES data channels and limited number of tape recorders. A block diagram describing the instrumentation is shown in Figure 4, and a photograph of the DRES Instrumentation Bunker in which the data signals were processed and recorded is shown in Figure 5.

In addition to the strain gauge data, the response of the prototype Polemast was recorded on a LOCAM high-speed camera pre-set to run at 500 frames per second. Confirmation of the camera speed was arranged through the use of a time mark generator.

COMPUTER MODEL SIMULATION

A numerical procedure was developed at DRES to predict the elastic response of a variable cross-section cantilever beam when subjected to a transient air blast load [1]. The procedure begins with the Bernoulli-Euler equation of a vibrating beam. The normal modes and natural frequencies of the beam are determined by solving the differential equations for free vibration using successive relaxation, Rayleigh quotient and Gram-Schmidt orthogonalization numerical techniques. The forced vibration solution is obtained using normal mode coordinates and Laplace transforms.

The computer model simulation used in pin-pin-free boundary condition of the form

$$\left.\begin{array}{ll} (1) & \underline{\text{pin}} \text{ at } x=0\text{, zero displacement and moment,} \\ (2) & \underline{\text{pin}} \text{ at } x=3 \text{ ft, zero displacement,} \\ (3) & \underline{\text{free}} \text{ at } x=L\text{, zero moment and shear,} \end{array}\right. \qquad (1)$$

where x is a distance coordinate measured from the base of the antenna, and L is the length of the antenna. In addition, the following values for the drag coefficient C_D were used in computing the aerodynamic drag portion of the blast wave loading on the antenna: [3, 4].

$$C_D = \left\{ \begin{array}{lll} 0.7 & , & M \geq 0.48,\ Re \geq 3\times10^5, \\ 0.6 & , & M < 0.48,\ Re \geq 3\times10^5, \\ 1.2 & , & M < 0.48,\ Re < 3\times10^5. \end{array} \right\} \qquad (2)$$

In the above equation, M is the instantaneous Mach number of the flow incident on the antenna, and Re is the instantaneous Reynolds number (based on local diameter).

The structure of the Polemast Antenna was represented in the computer model in such a way as to simulate the mass and projected (normal to blast direction) cross-sectional area profiles of the prototype. The physical features which describe the prototype Antenna and the corresponding computer simulation of the antenna are respectively outlined in Tables 1 and 2. It should be noted that the computer simulation of the antenna agrees with the actual structure of the prototype in the following critical area: weight distribution, total weight, projected (normal to blast direction) cross-sectional area distribution, and total projected cross-sectional area.

COMPARISON OF THEORETICAL AND EXPERIMENTAL NATURAL FREQUENCIES

TWANG TEST

Prior to the blast trial, a "Twang Test" was performed to obtain free vibration strain data for the prototype Polemast. A static load was applied near the top of the antenna using an anchored wire rope at a pull angle of 30^0 to the horizontal. The load was subsequently released electrically and the strain data for free vibration was recorded. The experiment was performed to determine the natural frequencies of the antenna and to verify the test instrumentation.

A photograph of the Twang Test apparatus is shown in Figure 6. The apparatus consisted of a 1/4 in wire rope attached to a bracket at the top of the Polemast and anchored to a truck, a 6000 lb capacity L.A.B. Corp. Quick Release Hook, a hand-operated mechanical winch to take up slack in the system, a hydraulic (pull) cylinder for fine load adjustments, and a Transducers Inc. strain-type load cell (model ML2-151-1K) with a Budd strain indicator readout (model P-350) to measure the applied load. The applied load was monitored locally with the load cell while the bending strains as measured by the strain gauges bonded to the antenna were recorded remotely in the Instrumentation Bunker.

A comparison of predicted and measured peak bending strains (prior to the electric release of the load on the antenna) is presented in Table 3. The predicted strains were found to be in good agreement with the values obtained experimentally.

The load on the antenna was released electrically and the bending strain data for free vibration were recorded in the Instrumentation Bunker. In this fashion it was possible to establish that the field instrumentation was operational.

A Fourier analysis was subsequently performed for the experimental strain data to determine the natural frequencies of the antenna. The free vibration strain history and corresponding Fourier analysis for gauges 3 and 5 are presented in Figures 7 and 8. The lowest natural frequency is sharply identified as 4.00 cps by the Fourier analysis, while the higher natural frequencies are less distinct or not apparent. The best resolution of the higher natural frequencies occurs for the gauge located closest to the centre of the antenna, gauge 5, and only a weak band of indistinct higher frequencies in the range 19.7 to 32.1 cps is apparent.

The theoretical (numerical simulation) predictions for the three lowest natural frequencies and corresponding normal modes are presented in Figure 9, and a comparison of theoretical and experimental natural frequencies is presented in Table 4. It is apparent from this comparison that the predicted frequencies are in good agreement with the values obtained experimentally.

COMPARISON OF THEORETICAL AND EXPERIMENTAL BENDING STRAIN HISTORIES

EVENT DICE THROW

The theoretical (numerical simulation) model was used to generate two sets of bending strain predictions. The first predictions (set A) were produced using a Friedlander overpressure wave which corresponds to the nominal Defense Nuclear Agency (DNA) pre-trial predictions for peak overpressure (7.0 psi), positive duration (242 msec) and positive phase impulse (600 psi-msec). The second predictions (set B) were produced using a Friedlander overpressure wave which corresponds to the average measured[1] peak overpressure (6.6 psi), positive duration (251 msec) and positive phase impulse (705 psi-msec) of the blast wave itself.

A comparison of the above two overpressure waves is presented in Table 5 and Figure 10. It should be noted that despite the lower peak overpressure in the experimental Friedlander wave, the total impulse associated with the experimental wave is approximately 18% higher than the corresponding impulse of the predicted wave.

A comparison of theoretical (numerical simulation) and experimental (blast trial) strain histories for the two sets (A and B) of bending strain predictions is presented in Figures 11 and 12. The comparison for prediction set B is repeated in Figures 13 to 17 in an enlarged format; in general, the predicted strains are found to be in excellent agreement with the experimental strains.

The strain predictions B are somewhat larger than predictions A, a result due to the larger positive phase impulse over the first quarter period (63 msec) in B compared to A.

The very small bending strains measured by gauge 1 and the corresponding small predicted strain at this location provided experimental verification of the assumed "pin" boundary condition (zero displacement and moment) at the base of the simulated antenna.

As expected, the largest predicted and measured strains occur at gauge 3, located slightly above the upper clamp assembly.

Finally, it is noted that the predicted strains for gauge 5 display excessively strong contributions from the second natural frequency (25.5 cps) and normal mode compared to the measured strain history at this location. Although the measured strain history at this location begins with a superimposed strain component

---

1 The free-field overpressure at the base of the antenna was measured using four Bytrex Model HFH-100 strain-type pressure transducers [3]. The "measured" overpressure wave properties were considered to be the average of the properties determined by the individual pressure transducers.

corresponding to the second natural frequency, the superimposed component rapidly diminishes with time, demonstrating strong selective damping of the second mode compared to the fundamental mode. Since the numerical simulation model has no provisions for damping, the second mode in the strain predictions does not diminish with time. This accounts for the observed differences between the predicted and measured strains at gauge 5. The differences would be reduced significantly if the numerical simulation model was extended to include the effects of damping.

A general evaluation of the ability of the numerical simulation model to predict peak bending strains is presented in Table 6. It is apparent from this table that there is excellent agreement between predicted and experimental peak bending strains, since the average ratio of peak theoretical to experimental bending strain from all five gauge pairs is 1.19 for predictions A and 1.25 for predictions B.

SUPPLEMENTAL EXPERIMENTS

SIMPLIFIED ANTENNA SIMULATION

A third set of strain predictions (set C) was produced to determine the effect of the mass of the antenna assemblies (Lower and Upper Radiator, SRD-501 Antenna) on the transient response of the Polemast in general. The structure of the simulated antenna in this case was assumed to be the same as the structure described in Table 2, with the exception of the interior diameter profile (ID) which was changed to 8.978 in at all positions along the antenna. This change was equivalent to neglecting the mass of the antenna assemblies and including only the uniform mass distribution of the aluminum tubing. In all other regards, this simulation experiment was identical to the previous prediction experiment A.

A comparison of strain prediction set C against the measured natural frequencies and bending strains is presented in Figure 18 and Table 7. It is apparent from this comparison that the natural frequencies and bending strains C are considerably poorer than the corresponding predictions A which were obtained using a more realistic simulated mass profile. This demonstrates the critical importance of having the computer mass profile simulation agree with the actual structure of the antenna.

VOLTAGE STANDING WAVE RATIO TEST

Tests were performed before and after the blast trial to determine the effect of the blast wave on the Voltage Standing Wave Ratio (VSWR) of the fibreglass covered Radiator. Only the Lower Radiator was evaluated, since the Upper Radiator was a mock-up unit. The pre-trial and post-trial VSWR tests were conducted by the DMCS-6 Project Officer on 30 September and 6 October, 1976 [4]. Additional information relating to the VSWR measurement techniques and equipment may be obtained from the DMCS-6 Project Officer.

The pre-shot and post-shot VSWR test results are shown in Figure 19. Calculations for the VSWR versus frequency are shown in Figure 20. It should be noted that the pre-shot VSWR test was performed without the Screen (Drawing Number 000-000145) while the post-shot test was performed with the Screen in place. However, the presence or absence of the Screen was found to have no influence on the VSWR test, since a further post-shot VSWR test without the Screen produced results imperceptibly different from the post-shot VSWR test with the Screen in place.

It is apparent from the VSWR measurements and comparisons in Figures 19 and

20 that the blast wave caused no immediate deterioration in the electrical performance of the Lower Radiator. In addition, a visual inspection of the Lower Radiator indicated no evidence of physical damage arising from the blast wave.

CROSS-ARM DEFLECTION TEST

At the request of the Polemast design authority, a simple bending test was conducted on the Cross-Arm Assembly (Drawing DODS-OC0146) located at the Mast Head. The test was performed to determine the load versus deflection on one of the four arms, the yield point of the arm, and the corresponding arm safety factor.

The apparatus consisted of a 1/2 in wire rope attached to one of the four arms (the attachment point was a hole in the web on the arm, 16 in from the mast centreline) and anchored to a bolt in the concrete base (loading was normal to the arm), a turnbuckle to apply the load, and a Transducer Inc. strain-type load cell (model BTC-FM52-CD-10K) with a Budd strain indicator readout (model P-350) to measure the applied load.

The results from this test are presented in Table 8. In the first loading application, the cross-arm demonstrated a linear load-deflection behavior up to 3500 lb, and the arm retained a permanent deflection of 1/4 in on release of the load. A similar linear relationship (up to 3500 lb) was apparent in a second loading application, and increasing the load to 6000 lb resulted in a permanent deflection of 7/8 in on release of the load. No other deformation of the assembly was apparent.

It was concluded that the cross-arm yield point is in the vicinity of 3000 lb (vertical load) and the arm is capable of withstanding a vertical load of 6000 lb with only a small amount of permanent deformation.

CONCLUSIONS

The blast response of a 23 ft UHF Polemast Antenna was investigated in a free-field blast trial and in numerical simulation experiments. The Polemast Antenna, complete with fibreglass covered radiators, satisfactorily withstood the air blast loading at the nominal 7.0 psi peak overpressure location in Event Dice Throw. The corresponding antenna response was modelled numerically, and the computed natural frequencies and transient strains were in excellent agreement with the values obtained experimentally. Subject to an accurate numerical simulation of the antenna's mass and projected (normal to blast direction) cross-sectional area profiles, the computer model is recommended as a design tool in the development of polemast designs in general.

REFERENCES

1. G.V. Price, "Numerical Simulation of The Air Blast Response of Tapered Cantilever Beams", Defence Research Establishment Suffield, Ralston, Alberta. Suffield Technical Paper No. 447. 1977. UNCLASSIFIED.

2. C.G. Coffey, "Blast Response of the GRP Topmast (U)". Suffield Memorandum No. 10/71. 13 pp. 1971. UNCLASSIFIED.

3. R. Naylor and S.B. Mellsen, "Unsteady Drag From Free-Field Blast Waves (U)". Defence Research Establishment Suffield, Ralston, Alberta. Suffield Memorandum No. 42/71. 22 pp. 1973. UNCLASSIFIED.

4. B.R. Long, B.G. Laidlaw and R.J. Smith, "The Analysis of Shipboard Lattice Antenna Motor Under Air Blast and Underwater Shock Loading, Part III - Final Report (U)". Defence Research Establishment Suffield, Ralston, Alberta. Suffield Technical Paper No. 431. 37 pp. 1975. UNCLASSIFIED.

5. F.H. Winfield, "Event Dice Throw - Canadian Air Blast Measurements (U)". Suffield Memorandum No. . pp. 1977. UNCLASSIFIED.

6. C.G. McIntyre, "Trip Report of P. Sparrow, Private Communication to C.G. Coffey. File No. 10011-3656356 (DMCS-6). Received 2 November 1976.

7. C.G. Coffey, "Private communication to R. McInnis", NDHQ/DMCS-6. DRES File No. 3611F-8. 18 June 1976.

8. Department of Supply and Services Contract No. CAL75-5942/1. 13 April 1976.

9. Alcan Products Ltd. Release Note and Certificate to Wilkinson Co. Ltd. Calgary. 6 August 1976.

10. R.M. Hardy and Associates Metal Test Report L76-1645. Private Communication to G.V. Price. 25 August 1976.

x[1] (ft)	ID[2] (in)	OD[2] (in)	OD[3] (in)	Weight (lb)
0	8.978	9.500	9.500	
				26.8
3	8.978	9.500	9.500	
				26.8
6	8.978	9.500	9.500	
				26.8+24.0[4]
9	8.978	9.500	22.81[4]	
				26.8+24.0[4]
12	8.978	9.500	9.500	
				26.8
15	8.978	9.500		
			22.81[5]	26.8+37.0[5]
18	8.978	9.500		
				13.4
21	SRD-501 Antenna (19.58 to 22.83 ft)	SRD-501 Antenna (19.58 to 22.83 ft)	25.75[6]	89.0[6]
				<u>348</u> Total

[1] Distance from the base of the antenna.

[2] This profile corresponds to the extruded aluminum tubing.

[3] This profile corresponds to the complete antenna (tubing plus antenna assemblies).

[4] Lower Radiator.

[5] Upper Radiator.

[6] SRD-501 Antenna.

$E = 10 \times 10^6$ psi

$\rho = 0.003044$ slugs/in^3

<u>TABLE 1</u>: Physical features of the prototype Polemast Antenna.

x[1] (ft)	ID[2] (in)	OD[2] (in)	OD[3] (in)	Weight (lb)
0[7]	8.978	9.500	9.500	
				26.8
3[7]	8.978	9.500	9.500	
				26.8
6	8.978	9.500	9.500	
				50.8[4]
9	7.950	9.500	17.22[4]	
				50.8[4]
12	8.978	9.500	9.500	
				35.9[5]
15	8.600	9.500	13.36[5]	
				45.1[5]
18	8.600	9.500	13.36[5]	
				52.4[6]
21	8.290	9.500	10.08[6]	
				59.6[6]
24[7]	8.290	9.500	10.08[6]	
				348 Total

[1] Distance from the base of the antenna.

[2] This profile is calculated to establish the correct mass distribution, assuming a fixed OD equal to that of the seamless extruded aluminum tubing which constitutes the primary structural portion of the antenna.

[3] This profile is calculated to establish the correct projected (normal to blast direction) cross-sectional area distribution.

[4] Includes a contribution from the Lower Radiator.

[5] Includes a contribution from the Upper Radiator.

[6] Includes a contribution from the SRD-501 Antenna.

[7] Boundary conditions: pin at x=0 ft, pin at x=3 ft, free at x=24 ft.

$E = 10\times10^6$ psi
$\rho = 0.003044$ slugs/in^3
$\Delta x = 3$ ft
$N = 8$
$L = 24$ ft

TABLE 2: Physical features of the computer simulation of the prototype Polemast Antenna. The calculated profiles in this table are dependent on the distance between data points (Δx).

Gauge	Bending Strain (μin/in)[1] Cable Load is 808 lb		
	Predicted	Measured[2]	Pred./Meas.
1	68	43	1.58
2	408	328	1.24
3	817	771	1.06
4	743	767	0.97
5	371	400	0.93
			Avg. 1.16

[1] The cable load of 808 lb was applied to the antenna at a pull angle of 30° to the horizontal. The corresponding horizontal component of the load was 700 lb. This loading was reached in three approximately equal stages. The horizontal deflection at the top of the mock-up SRD-501 Antenna corresponding to the 808 lb cable load was 3.5 in (measured using a transit, 5% reading uncertainty).

[2] The bending strains were recorded in the Instrumentation Bunker using the same procedures to be followed in the blast trial itself.

TABLE 3: Twang Test bending strains prior to the electric release of the load.

Mode	Natural Frequencies (cps)		
	Theoretical	Experimental	Theo./Exp.
1	4.62	4.00	1.16
2	25.5	24.1 [1]	1.06
3	72.4	—	—

[1] This value represents an average of indistinct frequencies which appear in band over the range 19.7 to 32.1 cps.

TABLE 4: A comparison of theoretical (numerical simulation) and experimental (Twang Test) natural frequencies for the Polemast Antenna.

Symbol	Description	Set A	Set B
P_A (psi)	atmospheric pressure	12.58	12.42
T_A (°F)	atmospheric temperature	54.0	48.0
p_o (psi)	peak overpressure	7.0	6.6
t_d (msec)	positive phase duration	242	251
I_D (psi-msec)	positive phase impulse	600	705
κ (computed)[2]	Friedlander decay constant	1.127[2]	0.505[2]
Δt (msec)	time step in the numerical integration[1]	1.00	1.00

[1] The numerical simulation of the time response is formed using only the lowest 3 natural frequencies and corresponding normal modes.

[2] The decay constant is computed based on the condition that the Friedlander wave be characterized by the specified values of p_o, t_d and I_D.

TABLE 5: Air blast data used in the theoretical (numerical simulation) model to generate prediction sets A and B.

Gauge	Peak Bending Strains (μin/in)				
	Experimental	Predictions A		Predictions B	
		Theoretical	Theo./Exp.	Theoretical	Theo./Exp.
1	132	208	1.58	222	1.68
2	973	1248	1.28	1333	1.37
3	2010	2414	1.20	2582	1.28
4	1917	2008	1.05	2160	1.13
5	927	774	0.83	737	0.80
			Avg 1.19		Avg 1.25

TABLE 6: Comparison of peak theoretical and experimental bending strains (first quarter cycle only).

Mode	Natural Frequencies (cps)		
	Predictions C	Experimental [1]	Pred/.Exp.
1	5.03	4.00	1.26
2	30.2	24.1	1.25
3	79.7	—	—

[1] Twang Test data reported in Table 4.

Gauge	Peak Bending Strain (μin/in)		
	Predictions C	Experimental [2]	Pred./Exp.
1	295	132	2.23
2	1769	973	1.82
3	3445	2010	1.71
4	2985	1917	1.56
5	1399	927	1.51
			Avg 1.77

[2] Blast trial data reported in Table 6.

TABLE 7: Comparison of strain prediction set C against the measured natural frequencies and bending strains.

First Loading		Second Loading	
Load[1] (lb)	Deflection[2] (in)	Load[1] (lb)	Deflection[2] (in)
100	0	100	0
1000	1/4	1000	1/4
2000	1/2	2000	1/2
3000	3/4	3000	3/4
4000	1-1/16	4000	7/8
100	1/4	5000	1-5/16
		6000	1-5/8
		100	7/8

[1] The load was measured by a load cell and is accurate to 0.1%.

[2] The deflection was measured by hanging a weight from the cross-arm and measuring the vertical displacement of the weight at ground level (measurement uncertainty is of the order of 1/16 in).

TABLE 8: Cross-arm deflection test.

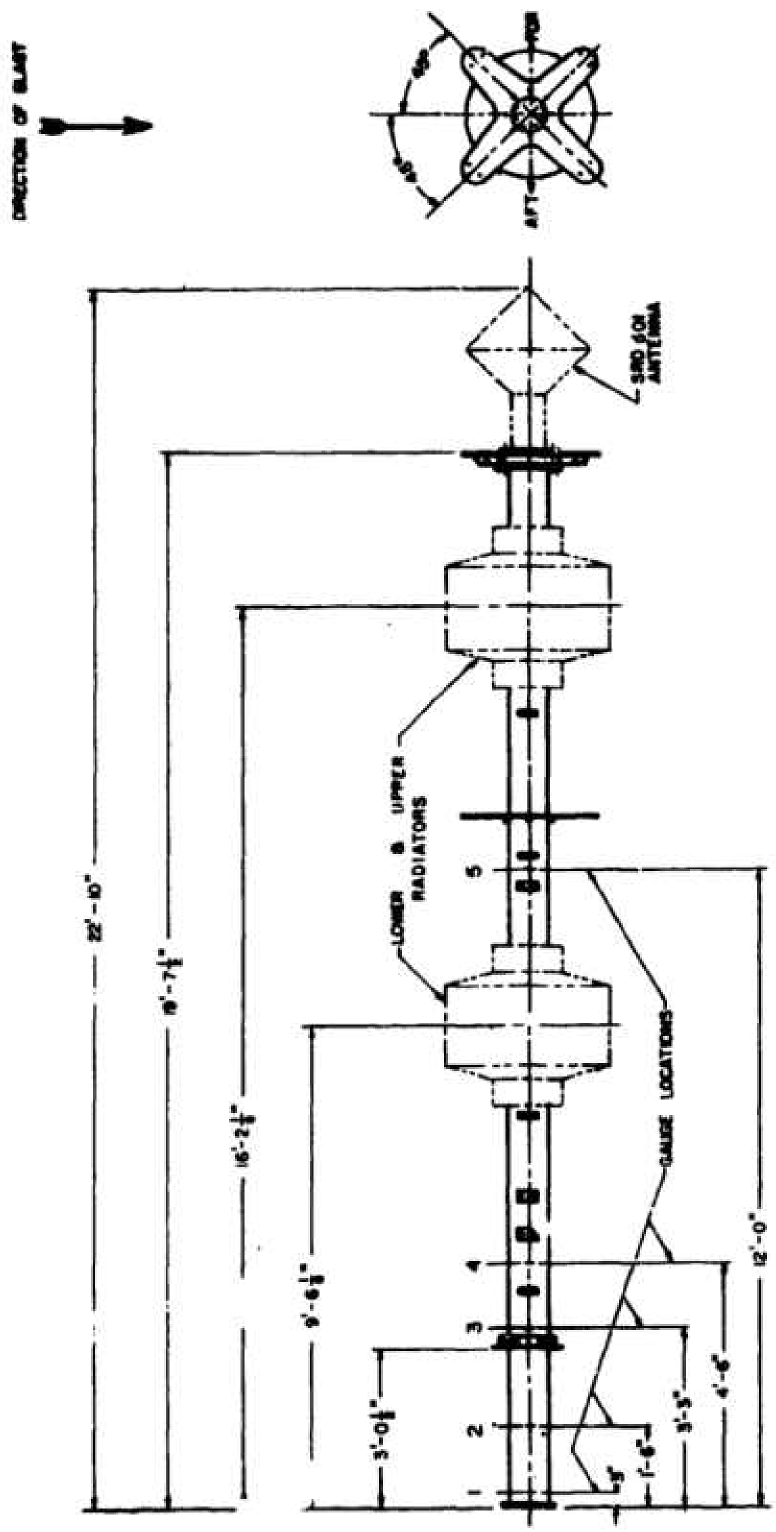

FIG. 1 SCHEMATIC OF THE PROTOTYPE POLEMAST ANTENNA, INCLUDING THE LOCATIONS OF THE STRAIN GAUGES

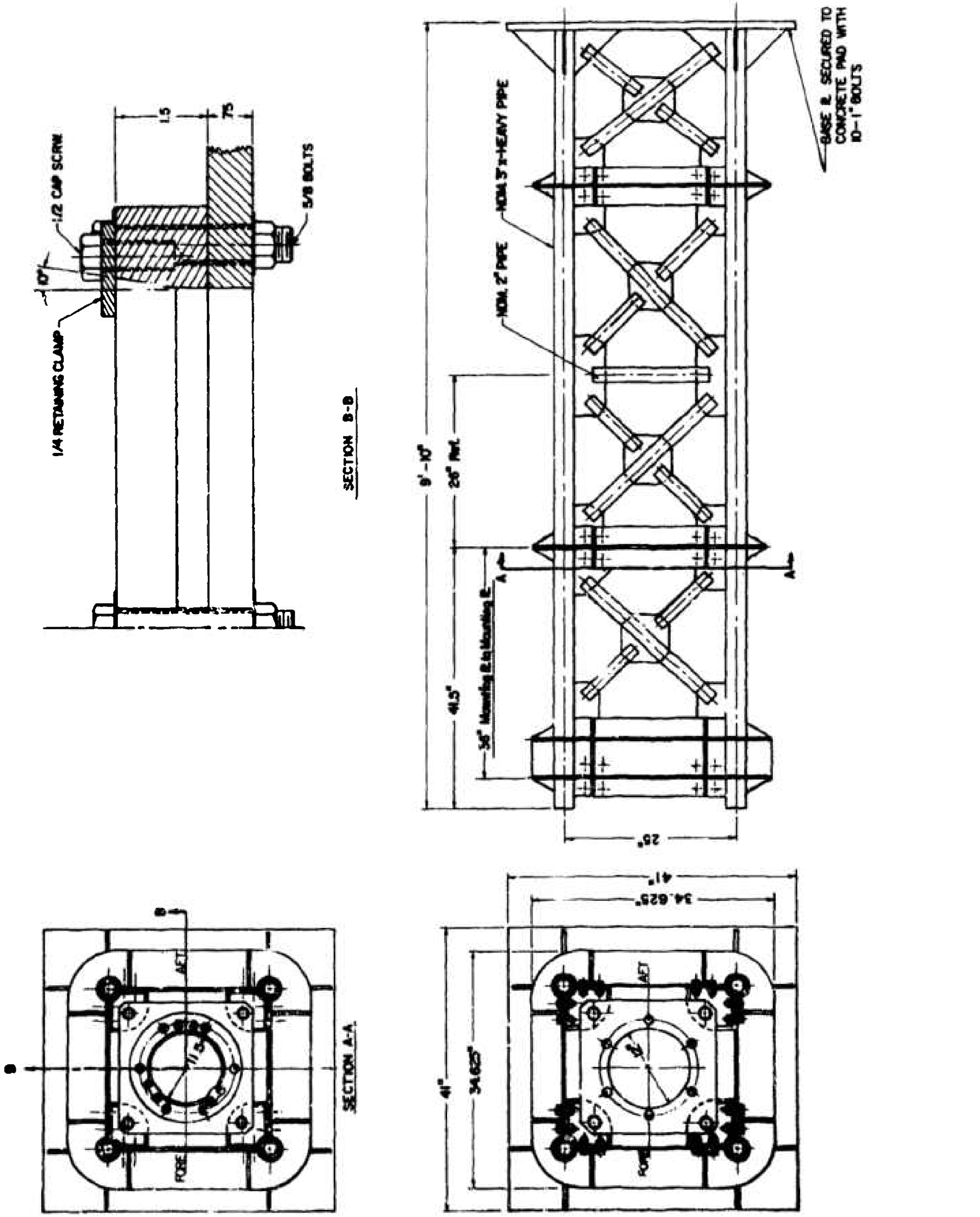

FIG. 2 SCHEMATIC OF THE LATTICE STRUCTURE MOUNTING FOR THE PROTOTYPE POLEMAST ANTENNA

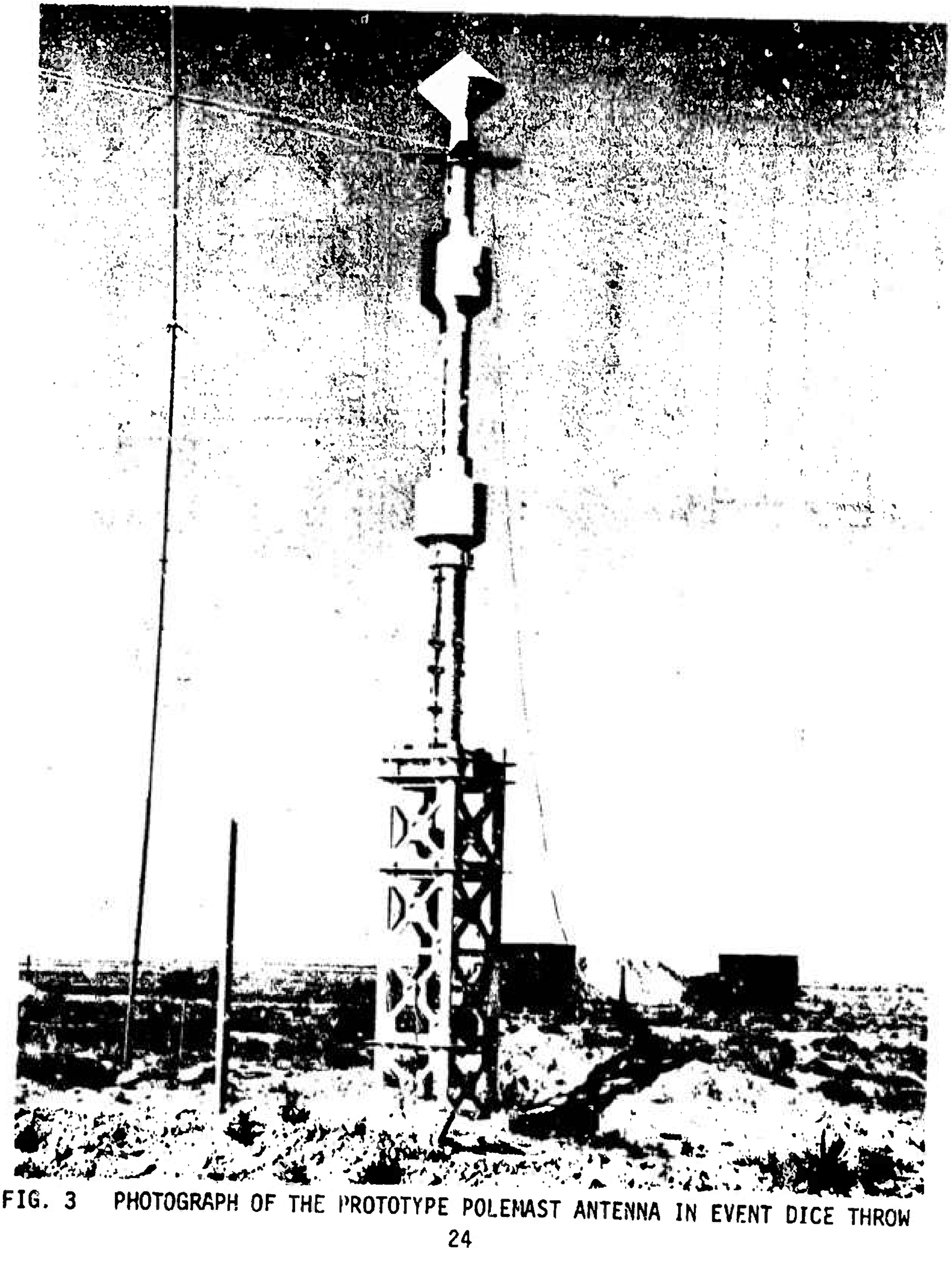

FIG. 3 PHOTOGRAPH OF THE PROTOTYPE POLEMAST ANTENNA IN EVENT DICE THROW

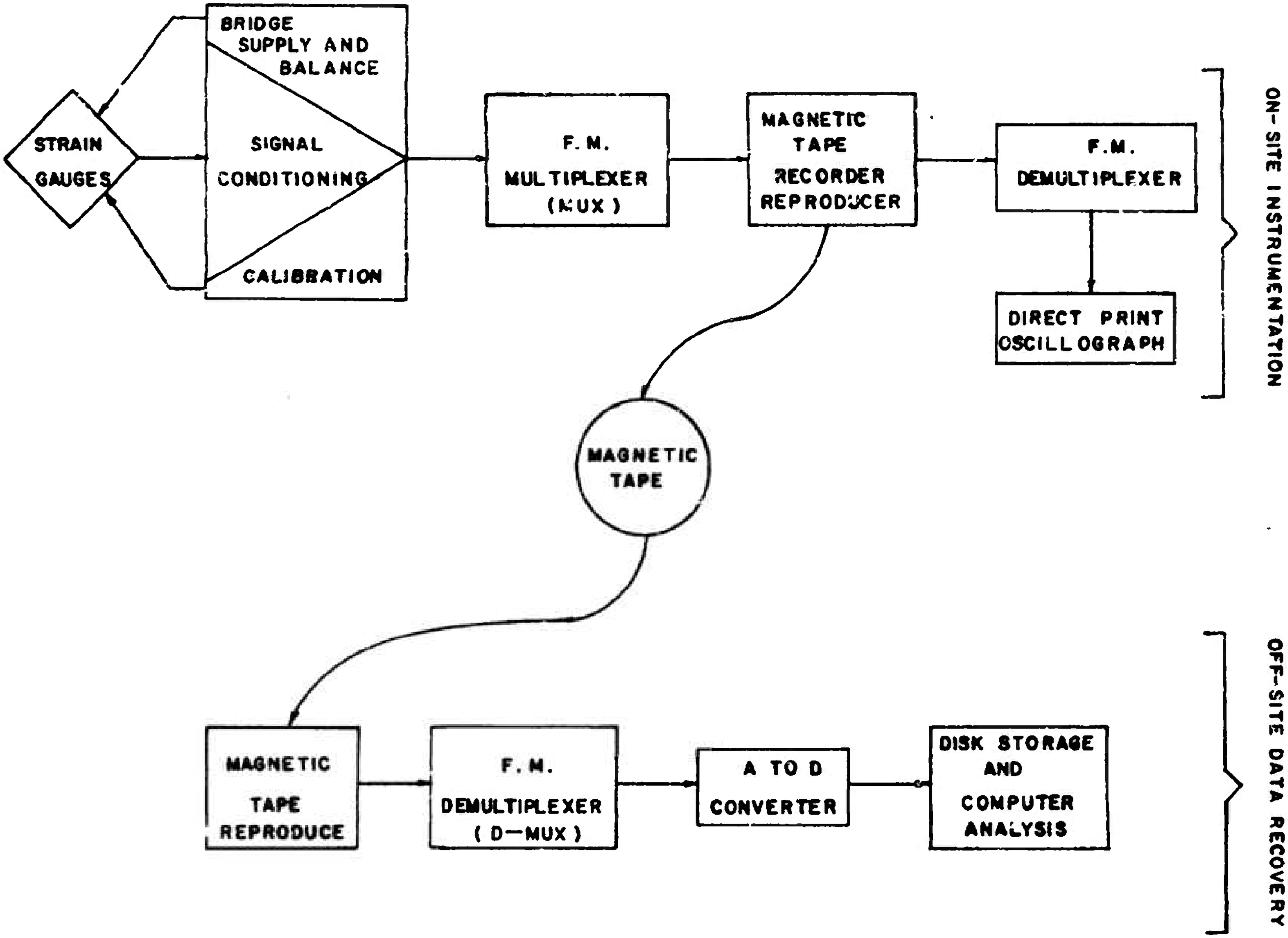

FIG. 4 SCHEMATIC DIAGRAM OF THE STRAIN GAUGE INSTRUMENTATION IN EVENT DICE THROW

FIG. 5 DRES INSTRUMENTATION BUNKER IN EVENT DICE THROW

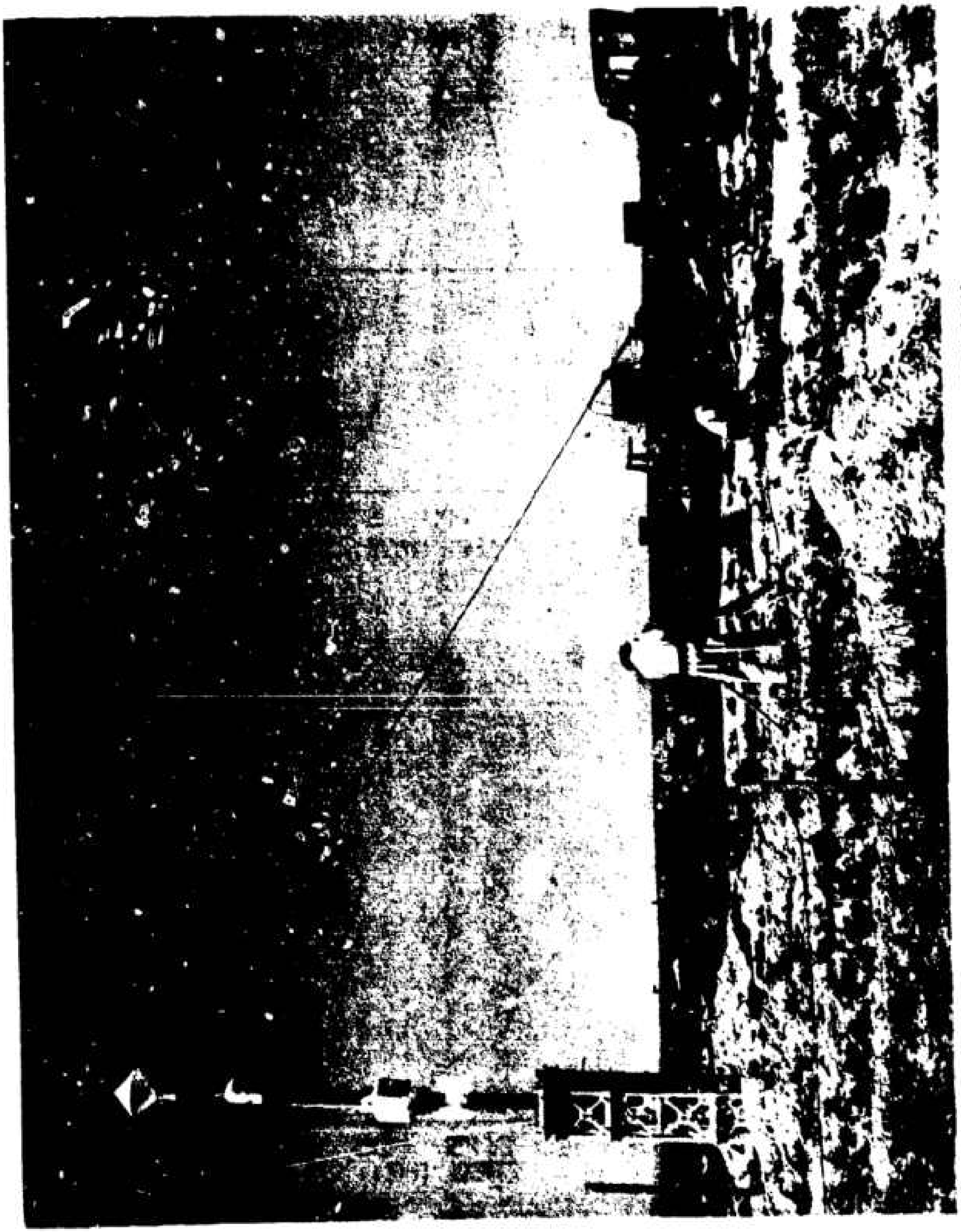

FIG. 6 PHOTOGRAPH OF THE TWANG TEST APPARATUS

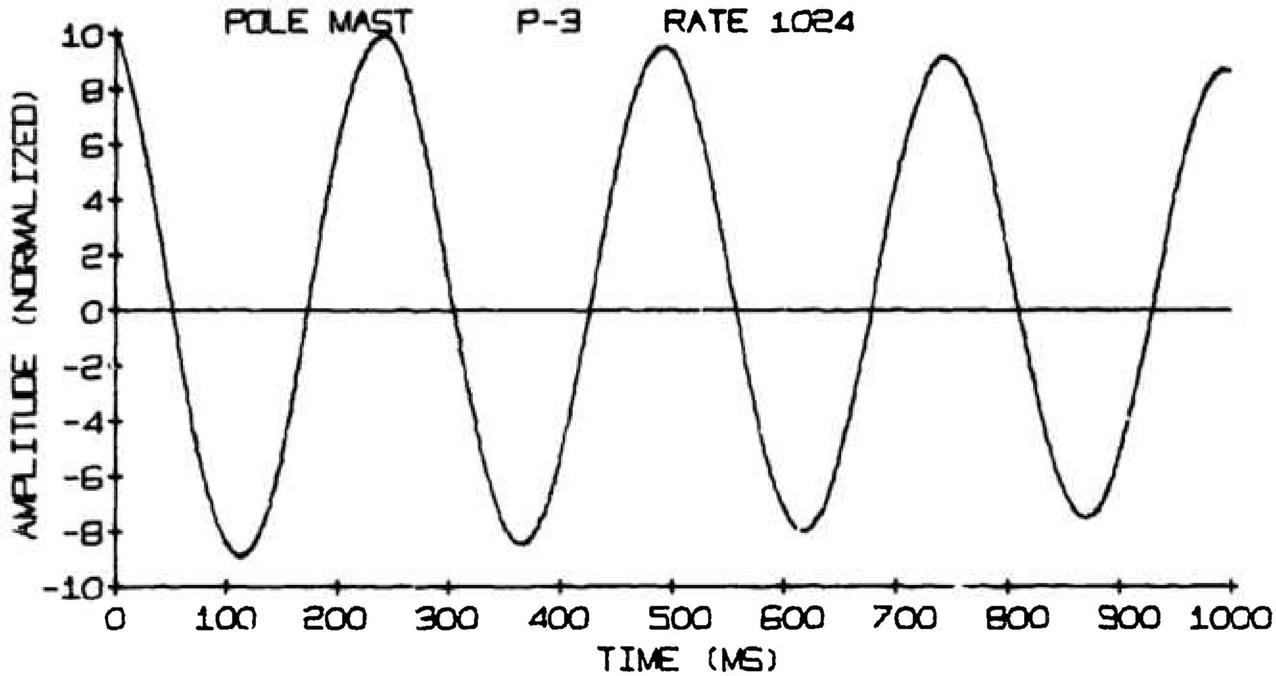

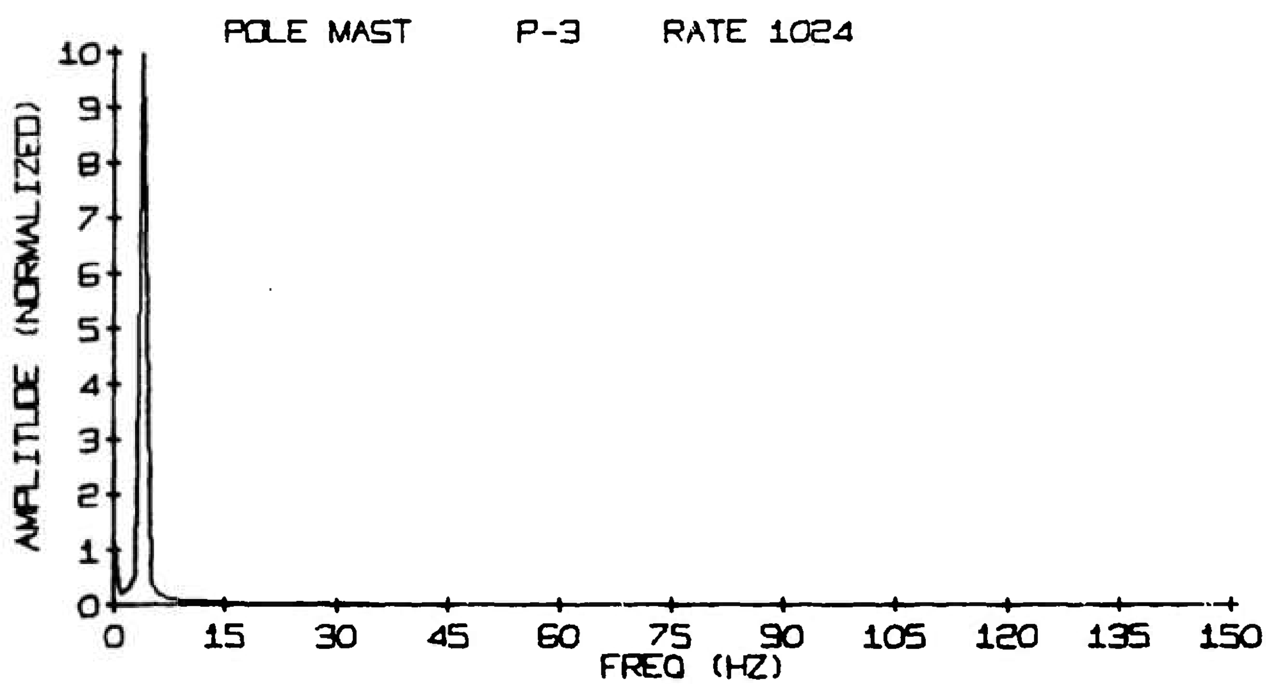

FIG. 7 TWANG TEST BENDING STRAIN HISTORY AND CORRESPONDING FOURIER ANALYSIS FOR GAUGE 3

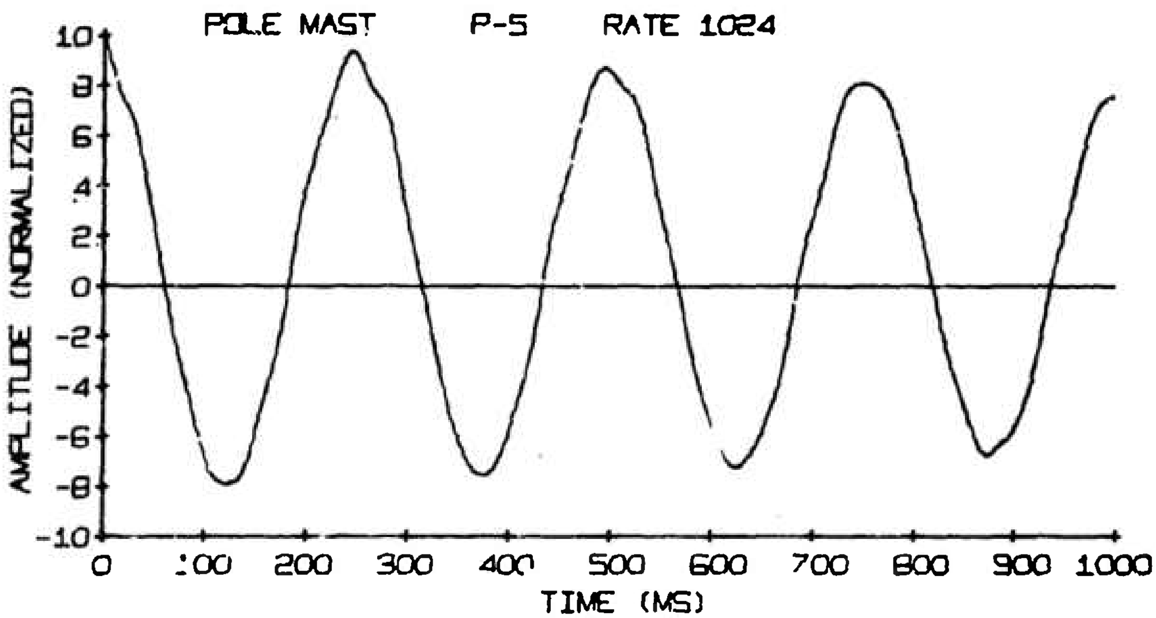

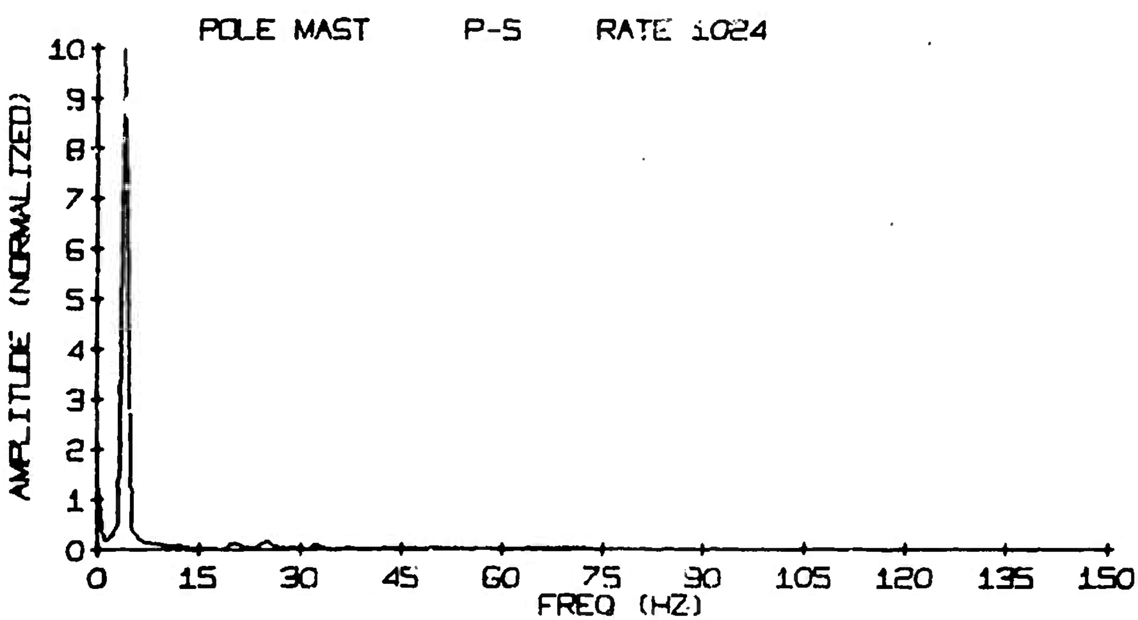

FIG. 8 TWANG TEST BENDING STRAIN HISTORY AND CORRESPONDING FOURIER ANALYSIS FOR GAUGE 5

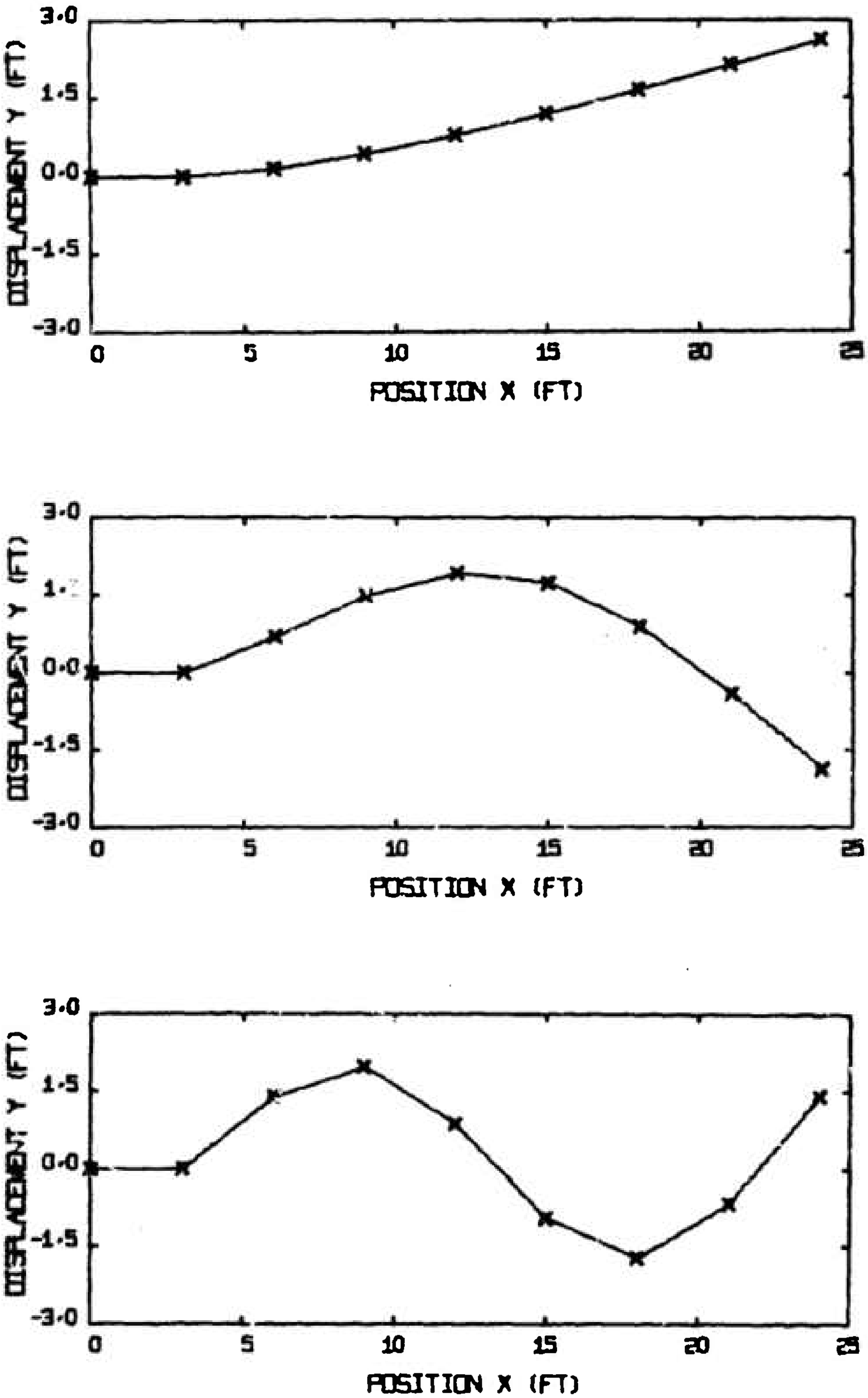

FIG. 9 THEORETICAL (NUMERICAL SIMULATION) PREDICTIONS FOR THE THREE LOWEST NATURAL FREQUENCIES AND CORRESPONDING NORMAL MODES FOR THE POLEMAST ANTENNA

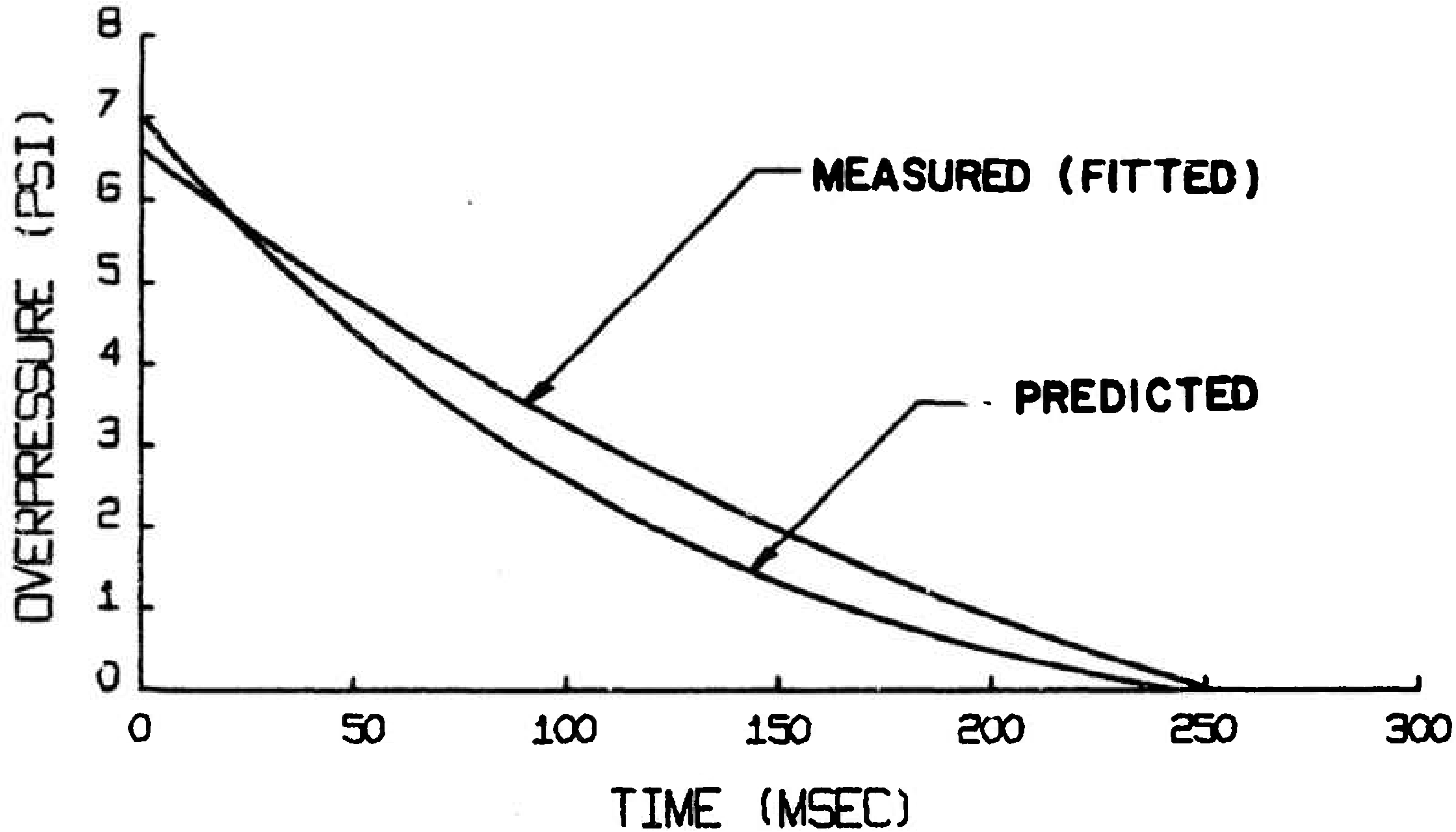

NOMINAL VS. EXPERIMENTAL OVERPRESSURE

FIG. 10 COMPARISON OF THE FRIEDLANDER WAVE WHICH CORRESPONDS TO THE PRE-TRIAL DNA OVERPRESSURE PREDICTIONS AGAINST THE FRIEDLANDER WAVE WHICH CORRESPONDS TO AVERAGE EXPERIMENTAL OVERPRESSURE MEASUREMENTS

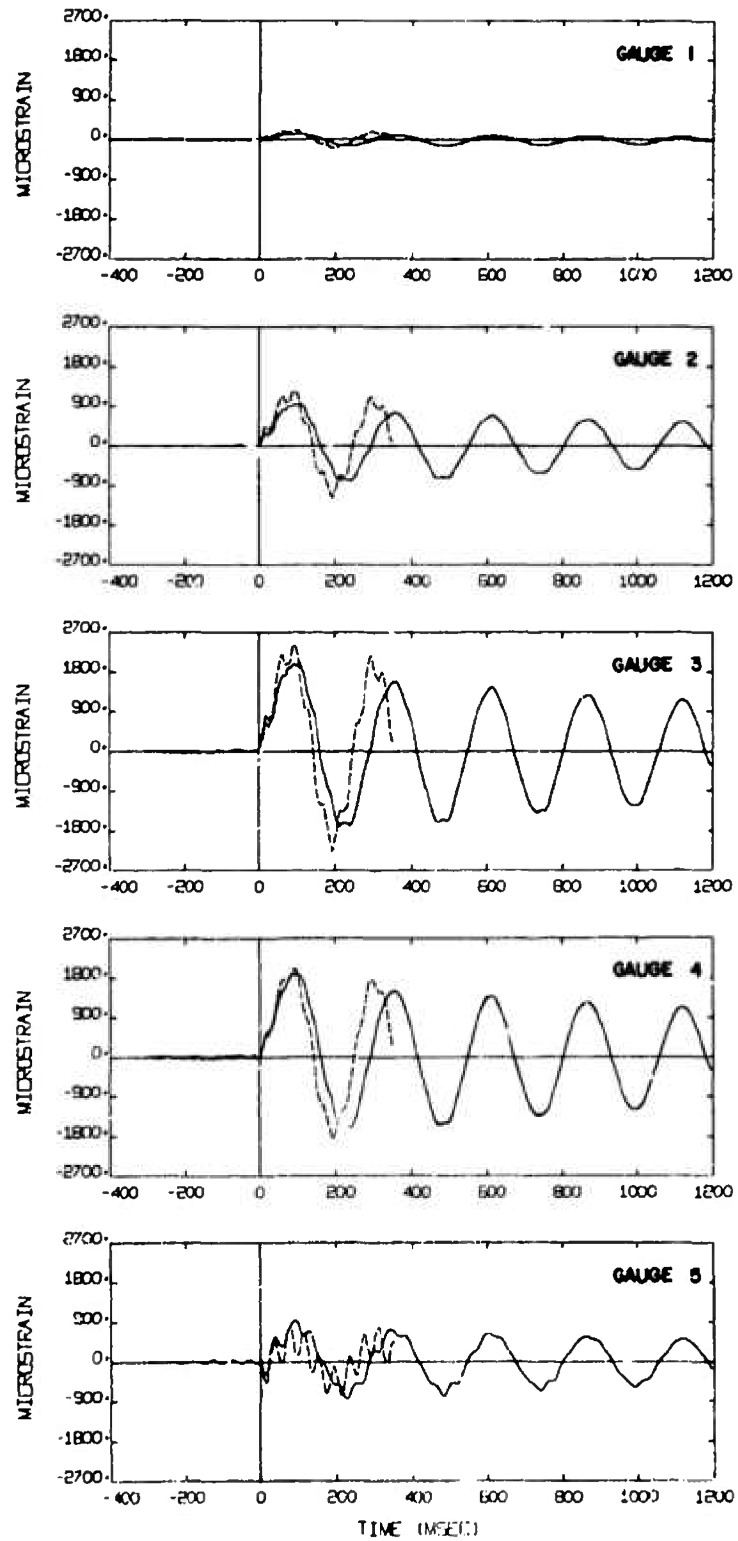

FIG. 11 COMPARISON OF BENDING STRAIN PREDICTIONS A (DASHED LINES) AGAINST THE MEASURED STRAINS (SOLID LINES) AT GAUGE LOCATIONS 1 TO 5

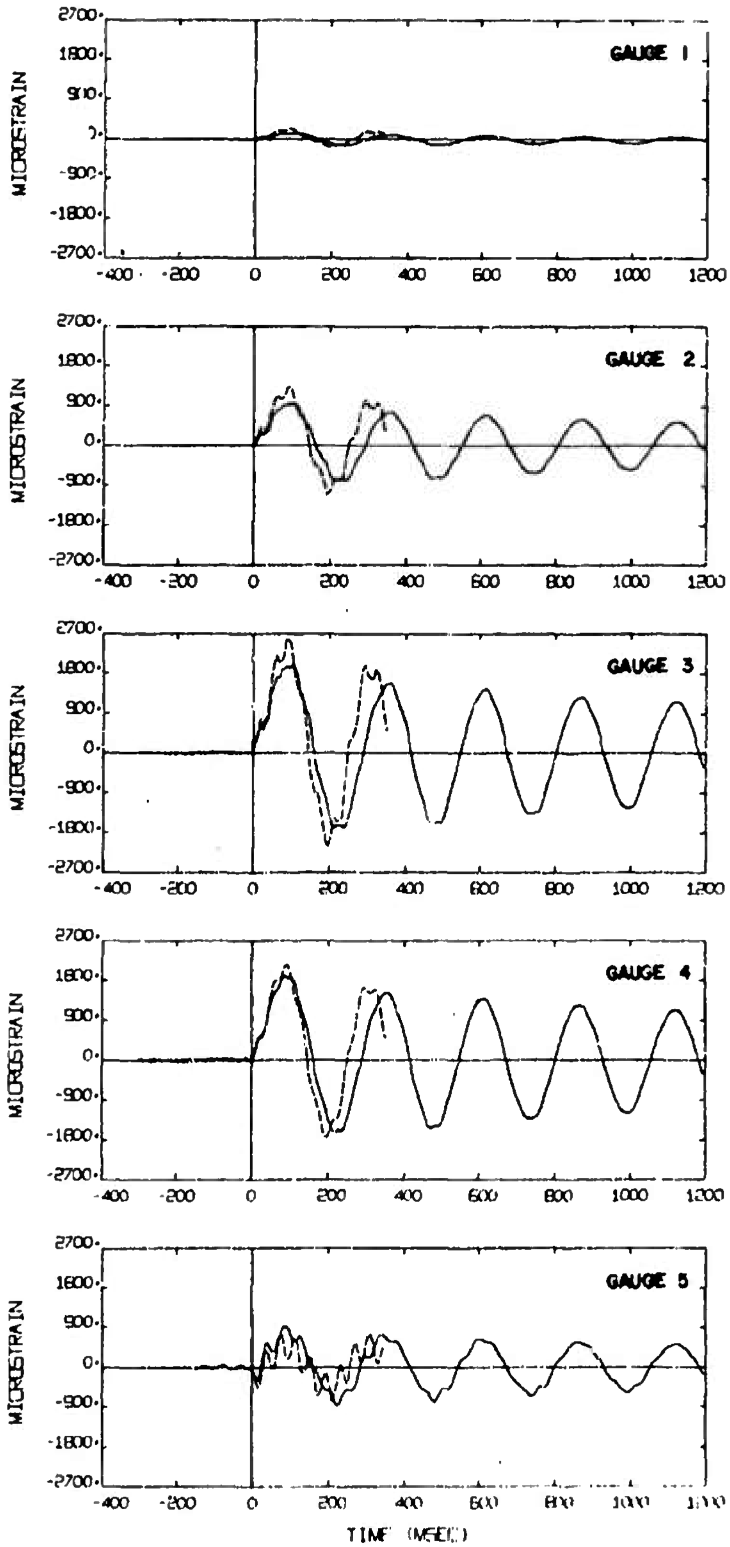

FIG. 12 COMPARISON OF BENDING STRAIN PREDICTIONS B (DASHED LINES) AGAINST THE MEASURED STRAINS (SOLID LINES) AT GAUGE LOCATIONS 1 TO 5

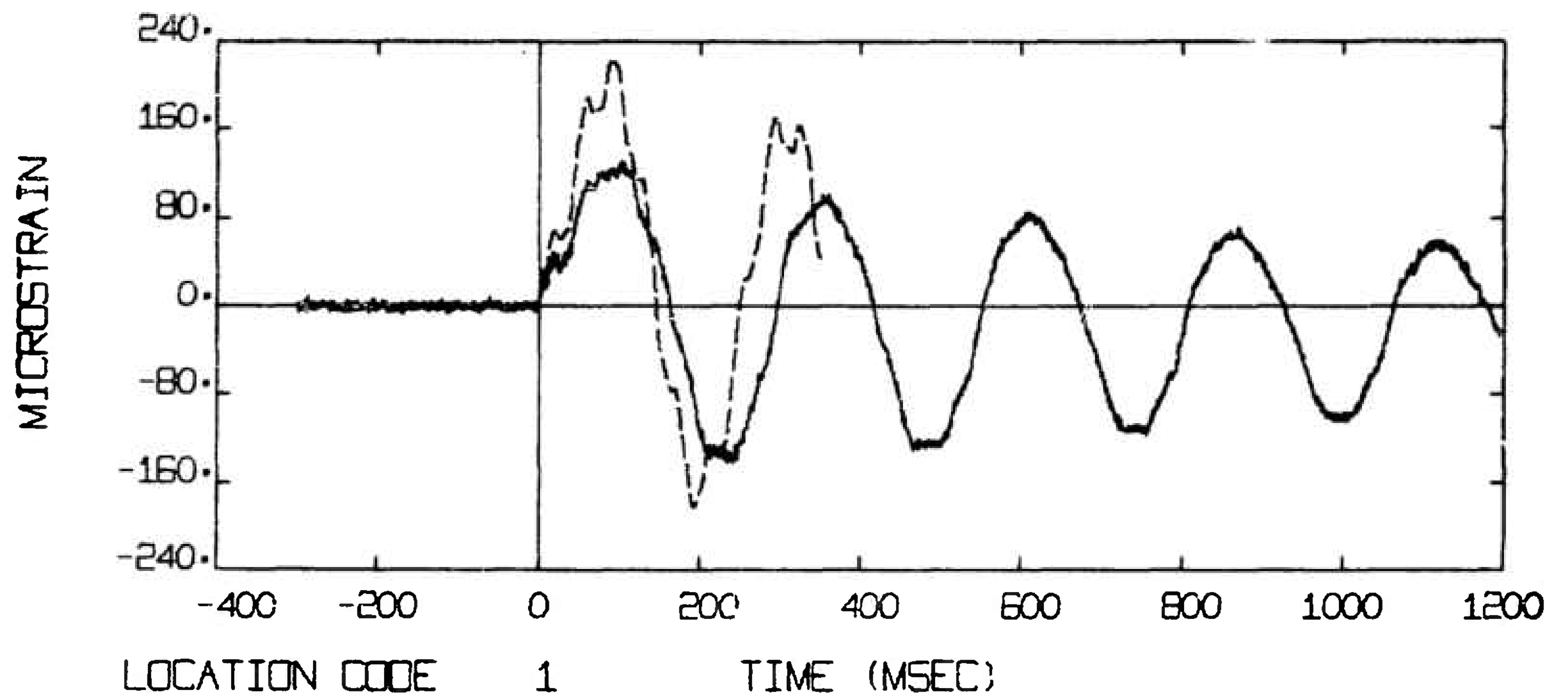

FIG. 13 COMPARISON OF BENDING STRAIN PREDICTIONS B(DASHED LINES) AGAINST THE MEASURED STRAINS (SOLID LINES) AT GAUGE LOCATION 1

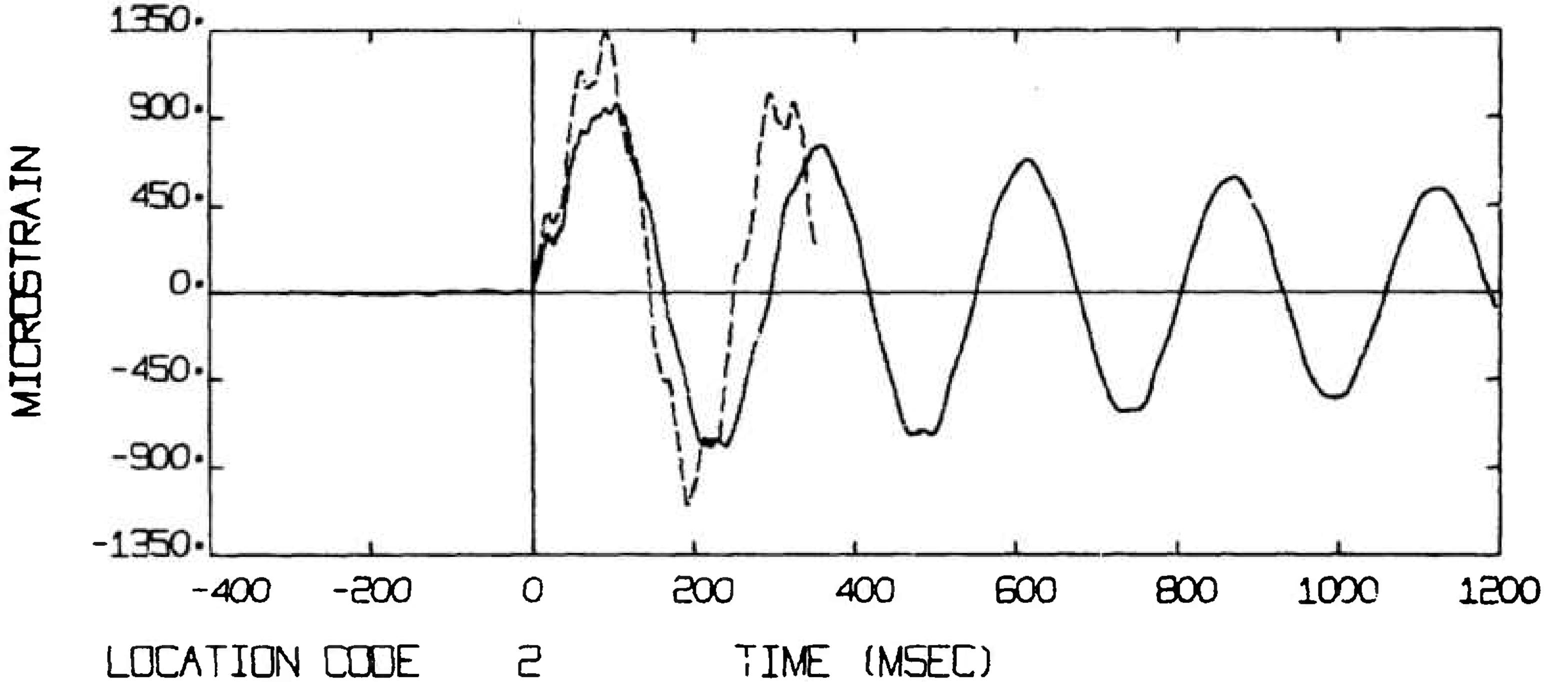

FIG. 14 COMPARISON OF BENDING STRAIN PREDICTIONS B (DASHED LINES) AGAINST THE MEASURED STRAINS (SOLID LINES) AT GAUGE LOCATION 2

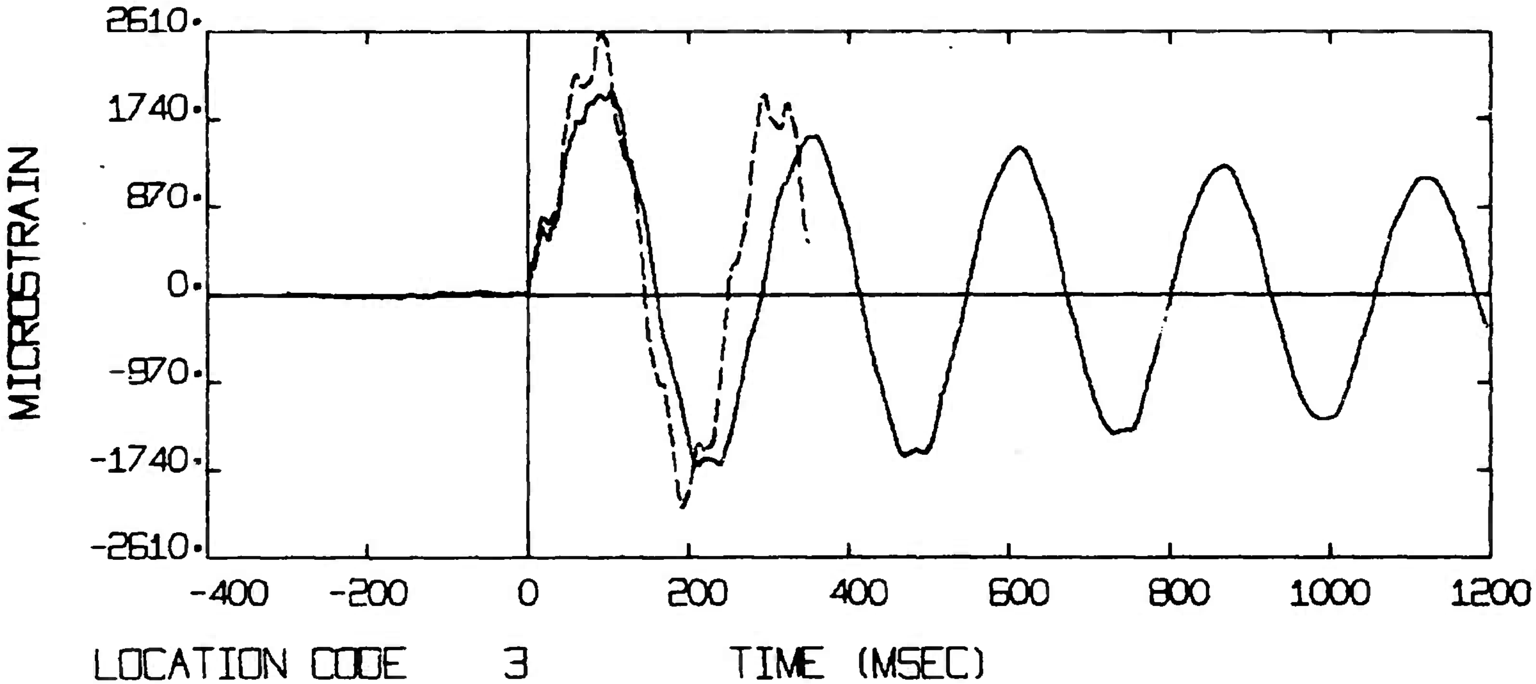

FIG. 15 COMPARISON OF BENDING STRAIN PREDICTIONS B (DASHED LINES) AGAINST THE MEASURED STRAINS (SOLID LINES) AT GAUGE LOCATION 3

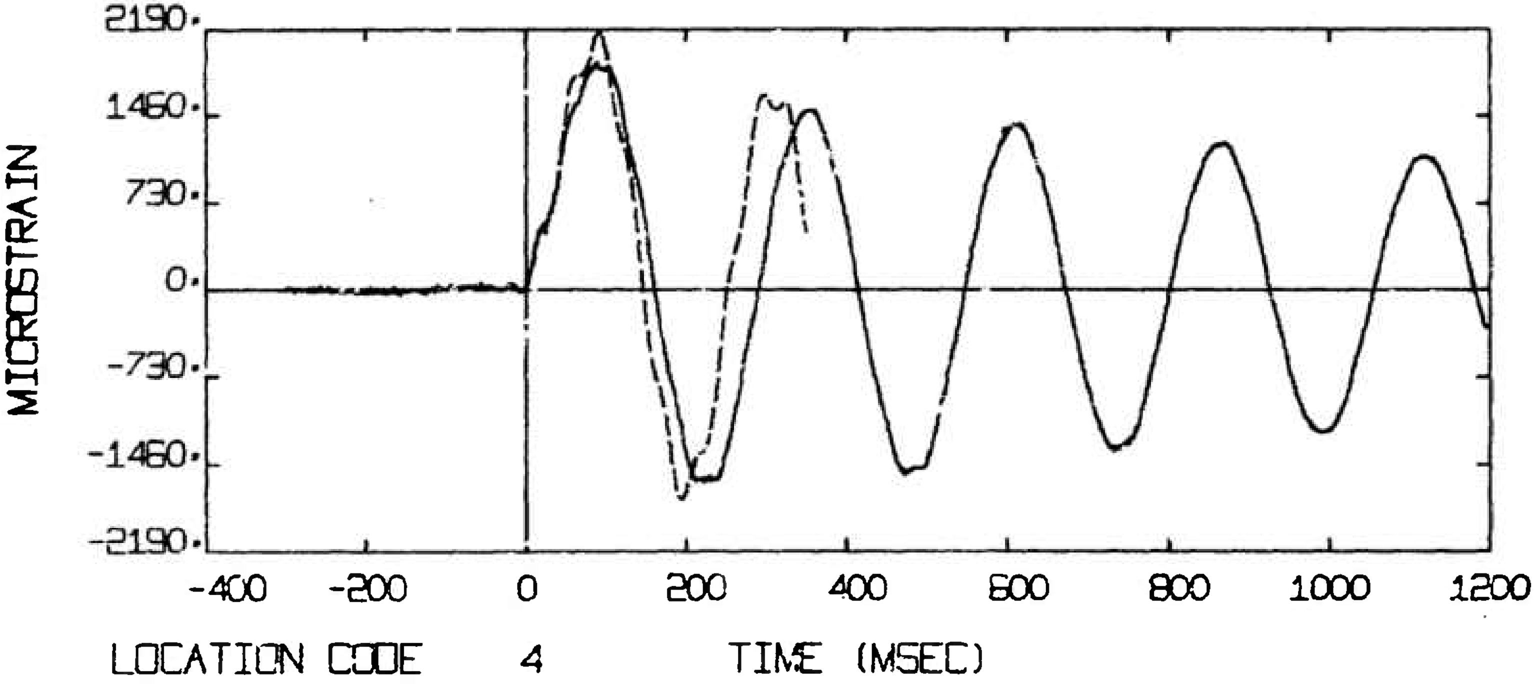

FIG. 16 COMPARISON OF BENDING STRAIN PREDICTIONS B (DASHED LINES) AGAINST THE MEASURED STRAINS (SOLID LINES) AT GAUGE LOCATION 4

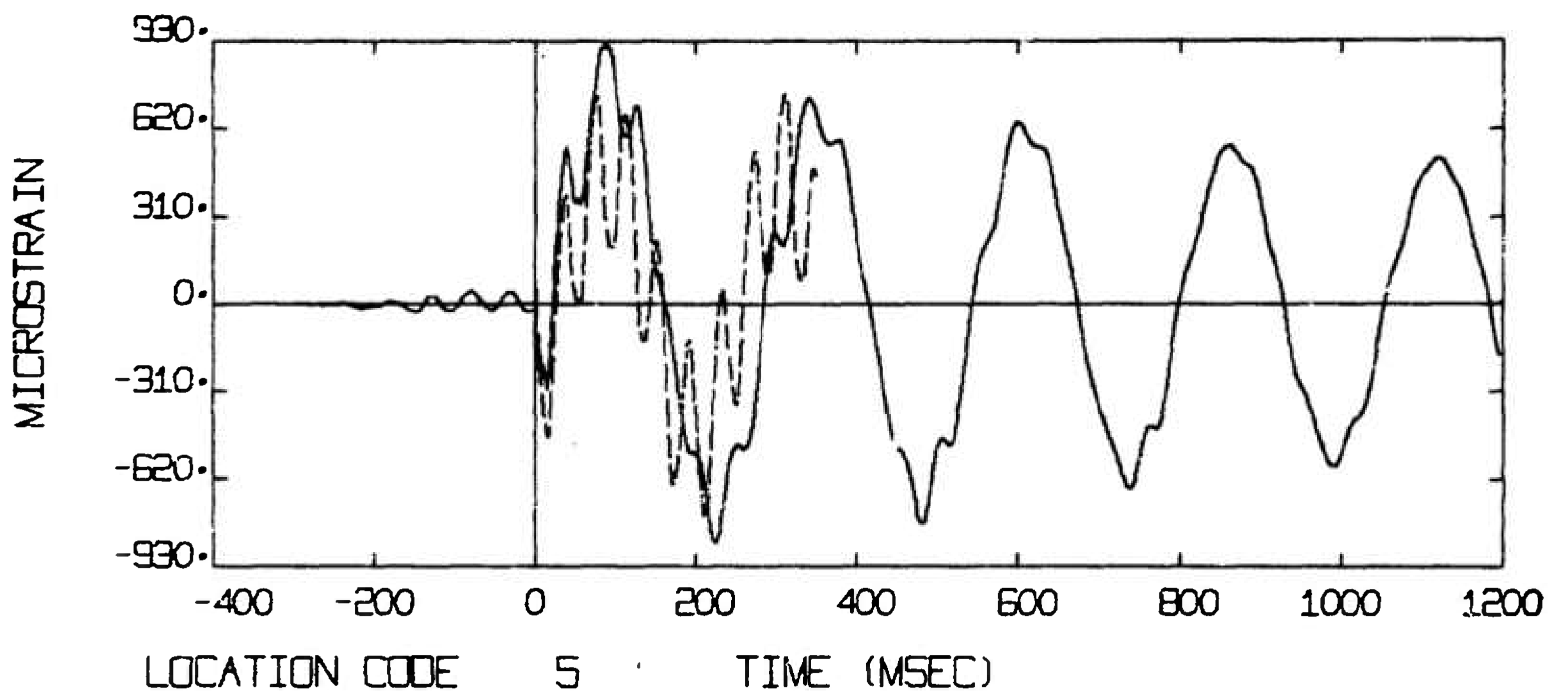

FIG: 17 COMPARISON OF BENDING STRAIN PREDICTIONS B (DASHED LINES) AGAINST THE MEASURED STRAINS (SOLID LINES) AT GAUGE LOCATION 5

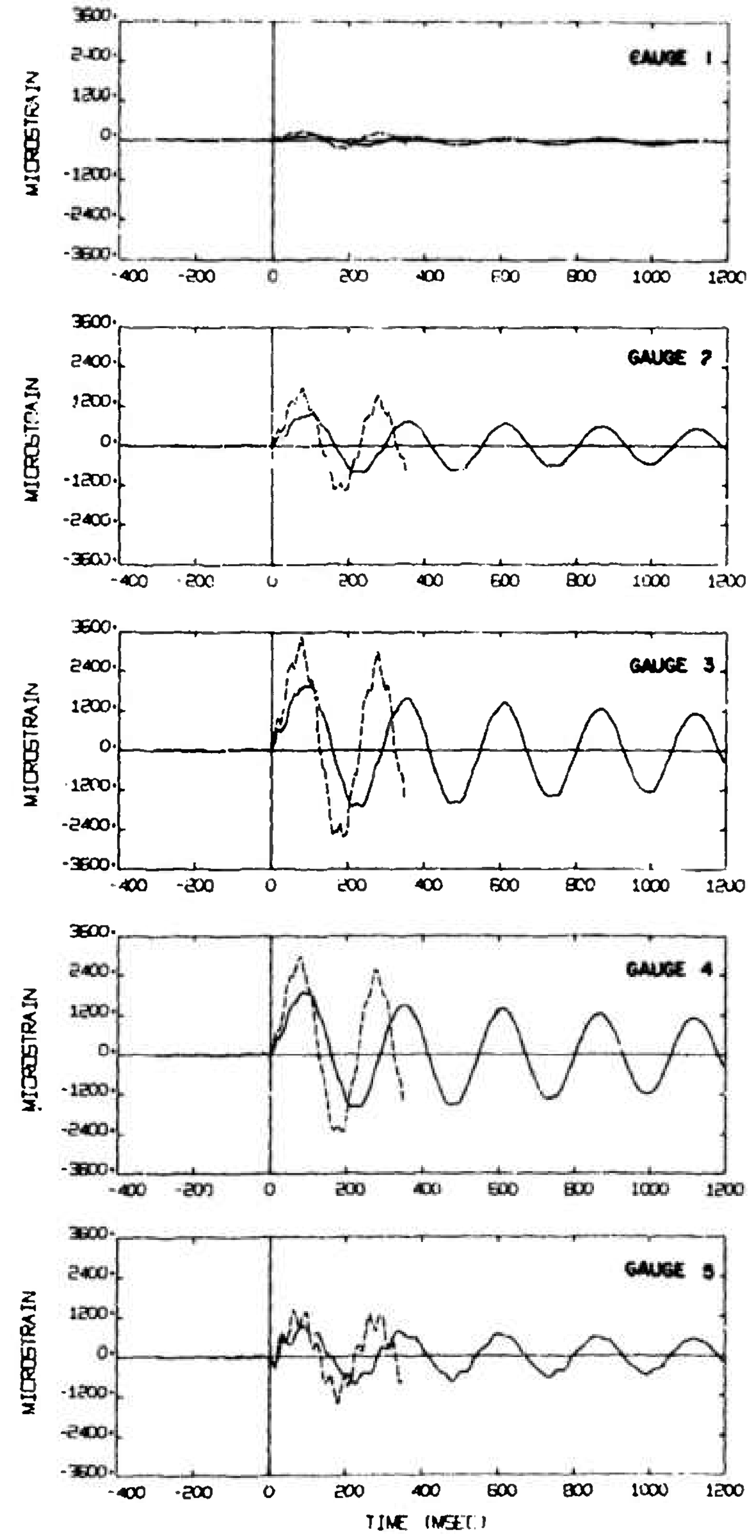

FIG. 18 COMPARISON OF BENDING STRAIN PREDICTIONS C (DASHED LINES) AGAINST THE MEASURED STRAINS (SOLID LINES) AT GAUGE LOCATIONS 1 TO 5

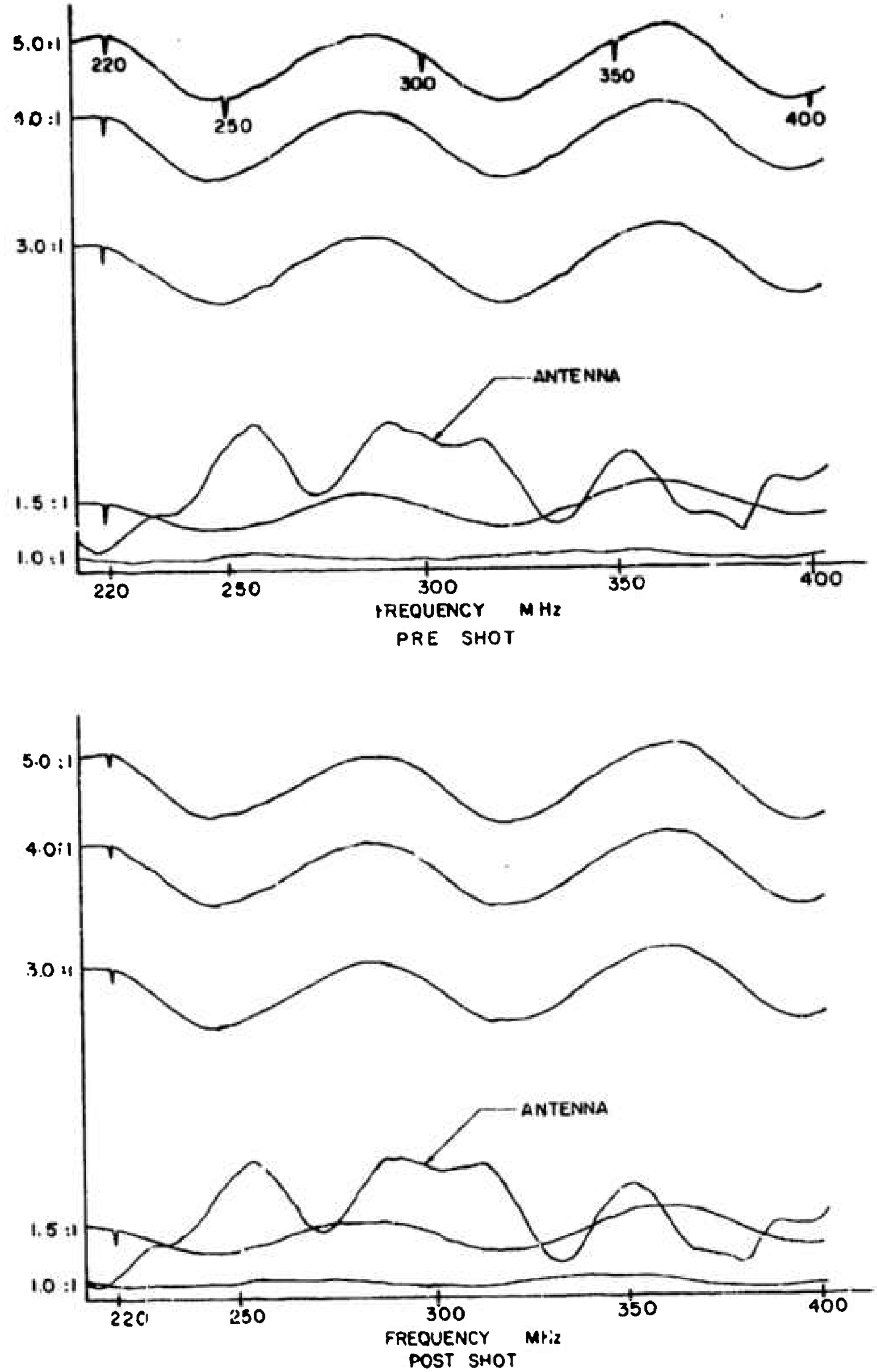

FIG. 19 PRE-TRIAL AND POST-TRIAL VSWR TEST RESULTS

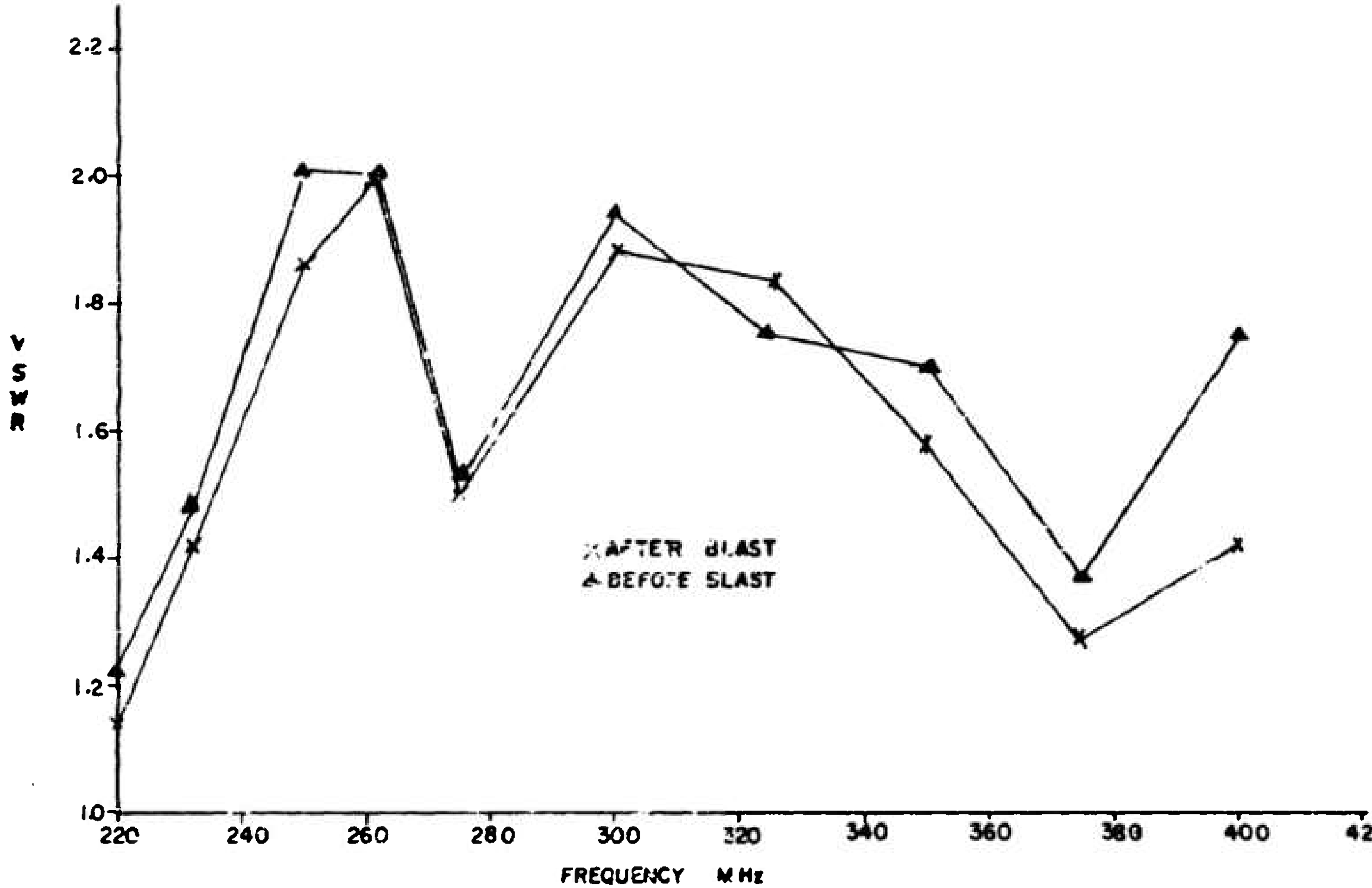

FIG. 20 PRE-TRIAL AND POST-TRIAL CALCULATED VALUES OF THE VSWR VERSUS FREQUENCY

APPENDIX A

PROTOTYPE UHF POLEMAST ANTENNA DESIGN MODIFICATIONS

During the fabrication of the prototype Polemast at DRES, design modifications were required in order to accommodate the facilities of the Machine Shop (the DRES Machine Shop is considered to be well equipped). It is anticipated that the suggested design changes will generally make the item more cost effective and open to a greater number of fabricators during the tendering for the lot production.

The design modifications are summarized below in tabular form. A justification for the individual modifications is considered immediately following the table.

Description	Drawing No.	Modification
(a) Top Inside Flange Ring	DDDS-000147	- see Figure A1
(b) Polemast Weldment Assembly	DDDS-000159	- material change - delete machining on the OD and ID of the mast
(c) Screen	DDD-000145	- delete welding and assemble by riveting - replace round bar stock with square
(d) Clamp Assembly	DDD-000143	- see the footnote
(e) Tolerance	———	- see the footnote

TABLE A1: UHF Polemast Antenna design modifications.

(a) Welding the bottom face of the flange as shown in the drawing to the inside diameter of the tube was not possible. In addition, to ensure a flat surface without machining the top face of the flange, it was necessary to design a mounting as shown in Figure A1.

(b) The original material specification was 6061-T6 aluminum with a 1/4 in wall and a 9-1/2 in outside diameter (OD). Based on the recommendation of an Alcan representative and a preliminary stress analysis [5], the material was changed to

PRECEDING PAGE BLANK

6351-T6 aluminum. A 9-1/2 in OD by 1/4 in wall extrusion was not available in Canada. The closest acceptable substitute was a 9-1/2 in Od by 0.261 in wall extrusion die.

Machining, as specified on the drawing was deleted since a lathe of sufficient size was not available. This should be considered a permanent modification since the dimensions of the top clamp can accommodate the tolerance of seamless extruded tubing as specified by the Aluminum Association, and the bottom and top rings can be machined to suit the tube.

It should be noted that tube ovality was removed both when determining the diameter by the use of "C" clamps and when fitting the bottom ring to the tube. Heat distortion in welding the ring to the tube produced a 0.020 in ovality in the ring. This did not cause a problem with assembly. Complete circumferential seating was achieved when the Polemast was mounted into the lower clamp.

(c) Welding, as specified in the drawing, was unacceptable due to heat distortion. Substituting a heavier gauge material did not resolve the welding heat distortion problem. Following are the design modifications which resolved the problem: (i) replace 20 gauge material with 14 gauge; (ii) replace round stock with 1/4 in square stock (cold rolled steel was used in place of 6061-T6 AL as the AL was not available in time for the trial); and (iii) welding was replaced with riveting, using 1/8 in diameter by 7/16 in long 16 ST AL rivets on a 1/2 in pitch. All surfaces were zinc chromated before assembly.

(d) Clamp Assembly was fabricated according to the drawing. However, due to the large heat distortion caused by welding (approximately 1/16 in on the 9-1/2 in diameter and 3/32 in curvature on the flange), the following design modifications are recommended: 3/8 in thick material should be used for the collar, and 3/4 in plate should be used for the flange (machined perpendicular to the 9-1/2 in diameter after welding).

(e) Based on modification (b) described above, items such as the Clamp Assembly, Top Inside Flange Ring, and Bottom Ring could have looser tolerances to accommodate the tube as supplied. The following information was determined for a random sample of aluminum tubes taken from the 25 20-ft (nomonal) lengths (measurements at 32^{0}F): minimum OD - 9.507 in, maximum OD - 9.548 in, minimum wall thickness - 0.248 in, maximum wall thickness OD - 0.271 in. It is noted that the above dimensions are will within the allowable specifications for seamless extruded tubing, as specified by the Aluminum Association.

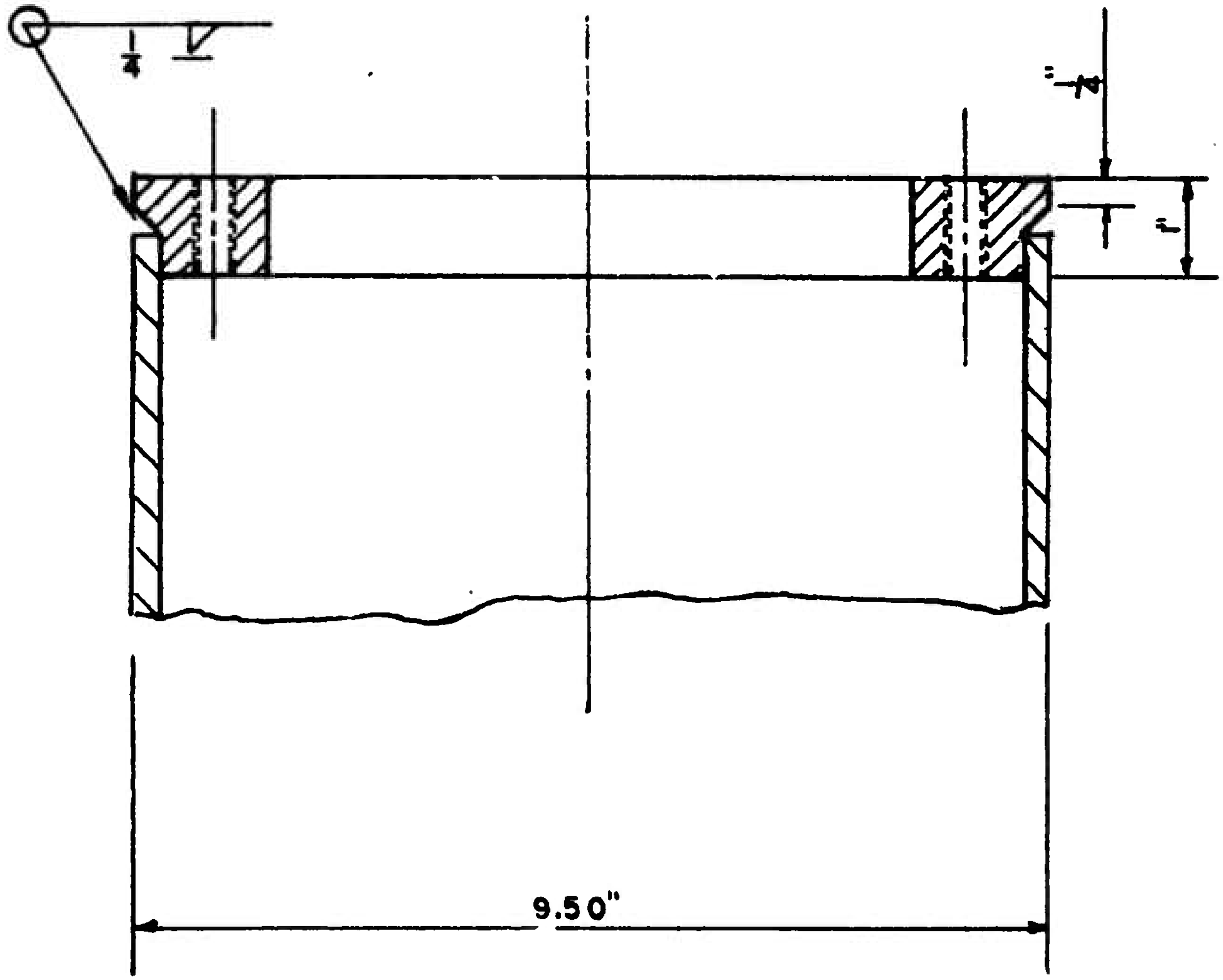

FIG. A1 MODIFIED TOP INSIDE FLANGE RING USED ON THE PROTOTYPE UHF POLEMAST ANTENNA

APPENDIX B

PHYSICAL PROPERTIES OF THE POLEMAST ANTENNA ALUMINUM TUBING

The structural portion of the prototype Polemast Antenna is a seamless aluminum tube of length 19 ft 7.5 in. This tubing was fabricated by Alcan Canada Products Ltd. according to Department of Supply and Services Contract No. CAL75-5942/1 [6]. Following is a summary of the physical and chemical properties of the aluminum tubing, as provided by an Alcan "Release Note and Certificate" [7]:

Material: 6351-T6 aluminum extruded seamless tubing with a 0.261 in wall and 9.5 in outside diameter, supplied in nominal 20-ft lengths. Total weight of the 25 pieces supplied was 4430 lb.

Alcan Order Number: 11-76-02595.

Consignee: Wilkinson Co. Ltd., Calgary, Alberta.

Identification: 12-47-209.

Tensile Strength (psi): 49,300.

Yield Stress (psi): 45,000 (0.2% offset).

Elongation (%): 14.

Gauge (in): 2.

Chemical Compositions Limits (% weight):

	Al	Cu	Fe	Mg	Mn	Ni	Si	Ti	Zn	Cr	Zr	Other Each	Other Total	Fe + Si
Max.		.10	.50	.8	.8		1.3	.20	.20			.05	.15	
Min.				.40	.40		[illegible]							

In order to obtain confirmation of the tensile properties of the aluminum tubing in the prototype Polemast, four test specimens were machined from the 4.5 in surplus piece which was removed to bring the tube to its design length. The specimens were fabricated according to ASTM standard A370-71 for round tension test specimens. The tests were performed and certified by R.M. Hardy and Associates Ltd., Metalurgical Division, Calgary. Tensile properties of the specimens are outlined below in tabular form [8]. It may be concluded from this table that the aluminum tubing meets or exceeds the manufacturer's specifications for tensile properties of 6351-T6 aluminum.

Specimen deminsions:

Specimens were cut parallel to the longitudinal axis of the tube.

Gauge length: 0.750 in

Gauge diameter: 0.160 in

Specimen overall length: 4.5 in

Grip section diameter: .25 in

Grip section thread: 20 threads/in

Stress (psi)	Specimen Number				
	1	2	3	4	Average
Ultimate	51,650	51,083	51,243	50,845	51,205
Yield [1]	48,058	46,851	47,263	47,263	47,358

[1] 0.2% offset

TABLE B1: Tensile tests on 6451-T6 aluminum tubing.

19. BLAST RESPONSE OF LATTICE MAST - EVENT DICE THROW

by

B.G. Laidlaw

Defence Research Establishment Suffield

ABSTRACT

Some experimental results are presented for the response of a 30 feet high lattice mast structure to air blast loading in the 600 ton AN/FO (ammonium nitrate - fuel oil) explosion known as Event Dice Throw which was held in October, 1976 at the White Sands Missile Range, New Mexico, U.S.A. The tubular seamless steel mast, with an eccentric side antenna responded in the elastic range under a free-field overpressure of 10 psi. No permanent deformations of the structure were observed. Analysis of the data generated has shown that there is a good agreement between measured results (both static and dynamic) and results predicted using a design procedure and associated computer code developed by Martec Limited, Ocean Science and Engineering Consultants, Halifax, Nova Scotia, Canada, thereby validating the procedures. Previously established analysis procedures developed by Defence Research Establishment Suffield, Alberta, Canada, (DRES) also produced an acceptable correlation between theoretical and experimental strains. In both cases the DRES computer code TDCCP (Transient Drag on Circular Cylinders and Plates) was used and has been shown to provide very reasonable air blast loading for the theoretical analysis.

1. INTRODUCTION

1.1 OBJECTIVES

The purposes of this work are to determine the blast resistance of a lattice antenna mast which has been constructed in accordance with a computerized design procedure developed by Martec Limited (formerly Can Plan Oceanology Ltd.) and to compare the theoretical predictions with the experimental results thereby validating this procedure and hence finalizing the development of an engineering design standard for lattice antenna mast structures presently used on Canadian naval ships.

1.2 BACKGROUND

This report represents the culmination of the studies carried out by Mechanics Research Incorporated (MRI), Royal Military College of Canada, Defence Research Establishment Suffield (DRES) and Martec Limited on the design and testing of shipboard lattice antenna masts currently used by the Maritime Branch of the Canadian Forces. The overall aim of the project was to develop a computer based design/analysis standard for such structures which would yield a more efficient design in a shorter time in comparison to the older manual procedures.

Three simulated model lattice antenna masts were analytically designed by Mechanics Research Incorporated and exposed to air blast loading in Operation Prairie Flat. The results of this study are presented in Reference 1. Royal Military College of Canada meanwhile was considering the preliminary design phase of the problem. The experimental results obtained in Event Dial Pack were reported and compared with those obtained in Operation Prairie Flat in Reference 2. Standard finite element techniques were used to calculate the dynamic response of the structures and it was found that calculated stresses were generally about two-thirds as large as those obtained experimentally (Reference 3), a discrepancy attributed to inadequate definition of the structural loading as used in the transient response analysis. A final report outlining a systematic air blast analysis procedure along with analytical procedures to be considered for prediction of response due to underwater shock concluded the DRES program (Reference 4) at the end of 1974.

A further contract for development of an engineering design standard was let to Can Plan Oceanology who created a design standard (Reference 5) and designed a model mast (Reference 6) to be exposed to a 10 psi overpressure air blast loading in Event Dice Throw.

This report presents some of the results obtained from Event Dice Throw and compares the experimental results with both the theoretical values provided by Martec Limited (formerly Can Plan) and the theoretical values provided by Beta Machinery Analysis Ltd. who utilized the former DRES analysis techniques. Transient drag loading functions for both programs were generated using the DRES program TDCCP (Transient Drag on Circular Cylinders and Plates).

2. DESCRIPTION OF THE TEST STRUCTURE

A photograph of the 30 foot mast is shown in Figure 1. The mast was mounted on a 27' x 15' x 5.5' reinforced concrete base and was constructed of seamless tubular steel pipe with nominal pipe diameters ranging from 2 to 3 1/2 inches. The structure weighed about 7000 lbs. The cylinder members terminating at a joint are slit at the ends and gusset plates connecting adjacent members are inserted. All connections are welded. The front of the mast faced the point of blast origin since this orientation was assumed to yield maximum response to blast.

On previous tests, modeling the antenna was a very difficult task due to the complex interaction, shading and solidity effects created by the closely spaced cylindrical members. To eliminate this problem a flat plate for which the drag loading is well known was used to simulate the antenna component.

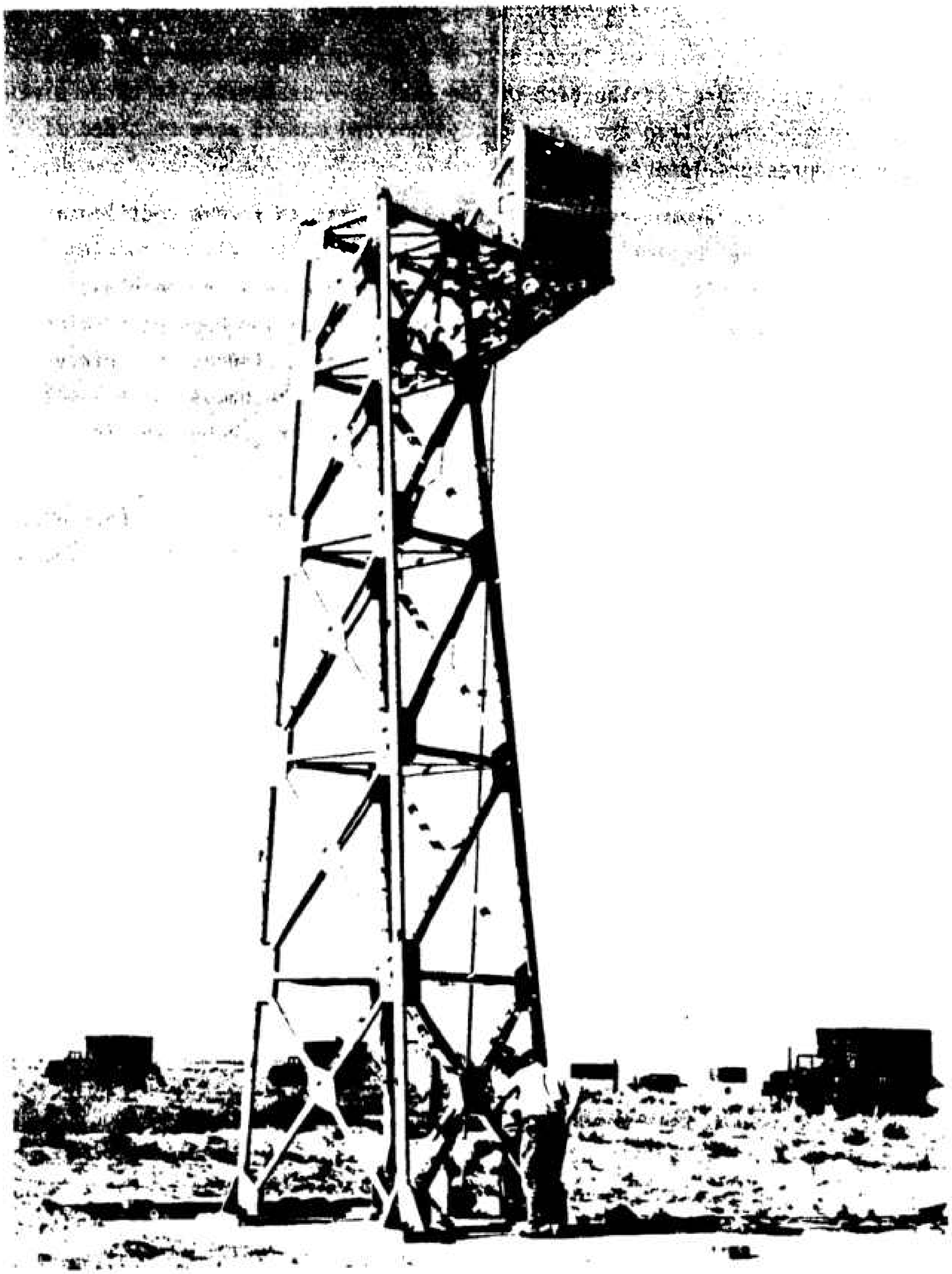

Figure 1. 30 Foot Lattice Mast

3. EXPERIMENTAL PROCEDURE

The 30 foot mast was located at a free-field overpressure of 10 psi. Free-field overpressures at the base of the mast were measured with three piezoelectric transducers. Drag pressures on cylindrical models were recorded at the same overpressure location.

Three accelerometers were placed on the mast to record rectilinear accelerations in the vertical and horizontal directions as well as rocking acceleration in the blast direction. The motion of the mast in the blast direction was recorded using a high speed camera. Axial and bending strains were recorded for members on the mast, mast support and antenna; the thirty-eight positions are shown in Figure 2. The bending strain gauges were located on tubular members a few inches from joint gussets, recording bending in directions both parallel and perpendicular to the blast travel.

All data signals were conditioned and then recorded on 14 track Ampex tape recorders. Combined bridge supply and signal conditioning amplifiers were used on all strain gauges and accelerometers. All pressure, acceleration and strain data were multiplexed in groups of five and recorded on tape channels using a constant frequency bandwidth division system which limited frequency response to 4000 Hz.

A static free vibration test (S/FV) was performed on the mast prior to the blast test to check out the instrumentation mounted on the mast and the associated recording channels, to check the linearity of the mast response, to compare the measured experimental strains with the theoretical predictions for a static load in order to confirm the validity of the mathematical mast model, and to record the natural frequencies of the mast. To perform these tests, a static load was applied at the top of the mast acting at 26.2° to the horizontal. This load was released suddenly by an electrical release system. Strain gauge outputs were recorded for 22 of the 38 positions.

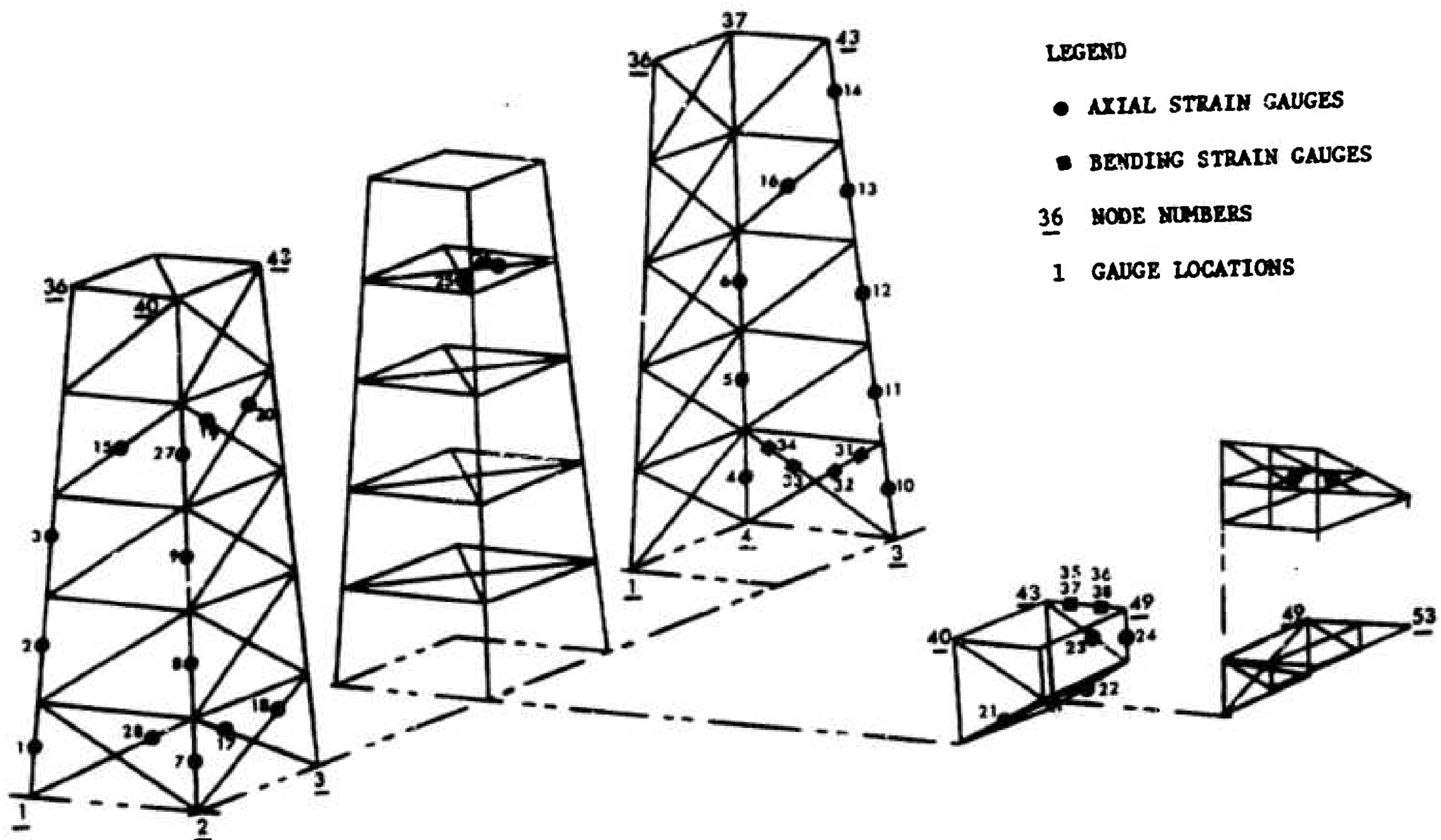

Figure 2. Location of Strain Gauge Instrumentation

4.0 RESULTS

Only a few representative results of this project are presented. A more comprehensive report on all the experimental data and their correlation to the theoretical model is now in the draft stages.

4.1 S/FV TEST

Records obtained from the free vibration portion of the test were used to determine the modal frequencies of the structure. This was done by digitizing the records and calculating Fourier amplitude spectra using a standard FFT (Fast Fourier Transform) computer code. The experimental results are listed in Tables 1 and 2 with those predicted by Martec Ltd. (Reference 7) and Beta Machinery Analysis Ltd. (Reference 8). There is a reasonably good agreement between the theoretical and experimental static strains.

The incident free-field pressure seen by the mast was 10.1 psi and had a positive duration of 230 msec. Two of the three accelerometers functioned indicating very small displacements. The camera coverage of the mast was much better than in previous tests due to a lower density of dust. The largest displacement observed was no more than a few inches.

4.2 MEASURED TRANSIENT STRAINS

All test data were demultiplexed and read directly from the magnetic tape into the DRES IBM 1130 digital computer using a Miniverter analogue-to-digital converter operating at a rate of 1600 samples per second. The maximum values for axial and bending strains recorded are listed in Table 3 as well as the theoretical predictions.

Predicted and measured strains at four positions are compared in Figure 3.

Table 1. Predicted and Observed Natural Frequencies of Mast

Mode	Martec Frequency Hz [7]	Beta Frequency Hz [8]	Experimental Frequency Hz
1	8.7	8.8	--
2	9.9	10.2	10
3	21.8	21.5	23
4	28.4	29.6	31
5	37.6	--	--
6	--	--	44
7	--	50.9	48
8	--	57.7	55
9	--	--	60
10	--	68.0	68

Table 2. Measured and Predicted Peak Static Strains for S/FV Test

Gauge Location Code	Martec Predicted [7] μ-ε*	Beta Predicted [8] μ-ε	Measured μ-ε
1	-74.4	-72	--
2	-75.3	-73	-76
3	-55.3	-54	-53
4	62.7	62	59
5	62.8	62	66
6	44.7	44	50
7	-57.2	-56	-54
8	-62.8	-61	-40(?)
9	-54.3	-53	-57.2
10	54.0	53	56
11	57.3	57	50
12	48.6	48	59
13	41.7	41	40
14	16.5	16	--
15	-3.2	-3	-3
16	0.8	1	-6
17	-13.1	-13	-14
18	11.5	12	10
19	-20.6	-20	-19
20	16.8	17	17
27	-49.3	-47	-57
28	-33.1	-32	-31

* *Microstrain*

Table 3. Measured and Predicted Peak Transient Strains

Gauge Location No.	Type	Predicted [7] μ-ε	Predicted [8] μ-ε	Measured μ-ε
1	Membrane	565	578	530
2	"	469	489	461
3	"	270	304	310
4	"	-568	-585	-594
5	"	-461	-490	-486
6	"	-280	-319	-285
7	"	521	557	412
8	"	472	495	486
9	"	320	354	338
10	"	-512	-542	-490
11	"	-470	-491	-441
12	"	-320	-357	-322
13	"	-223	-207	-234
14	"	-87	-86	-80
15	"	459	500	440
16	"	-506	-481	-479
17	"	325	310	301
18	"	-320	-312	-306
19	"	406	425	366
20	"	-400	-420	-363
21	"	357	387	329
22	"	-407	-374	-330
23	"	211	164	153
24	"	-239	-172	-169
25	"	191	169	164
26	"	-202	174	-163
27	"	221	216	207
28	"	452	450	428
29	"	-96	--	-85
30	"	-103	--	-125
31	Bending	-130	--	-165
32	"	193	--	433
33	"	128	--	209
34	"	-182	--	-185
35	"	-47	--	-72
36	"	-29	--	-48
37	"	63	--	53
38	"	79	--	-112

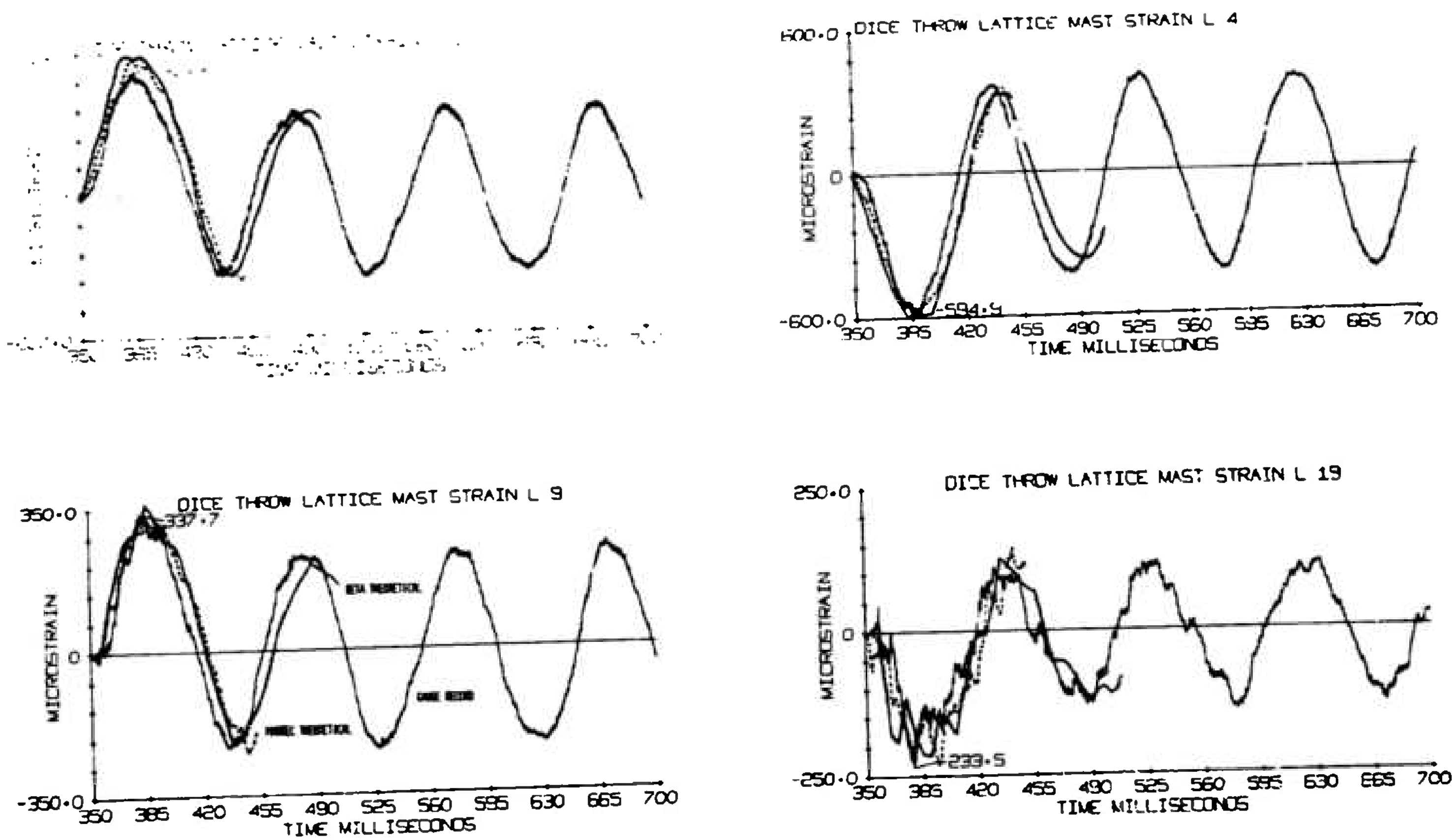

FIGURE 3. COMPARISON OF MEASURED [illegible] AND THEORETICAL PREDICTED STRAINS

5. DISCUSSION AND CONCLUSION

The computer code Transient Drag on Circular Cylinders and Plates (TDCCP) was used to calculate the transient drag pressures required for input for both theoretical programs. This program was developed at DRES and takes into consideration the cumulative results of the DRES drag program conducted on circular cylinders, known loading functions for plates and correction factors to account for shading, solidity, and plate cylinder interaction, again based upon past DRES experiments in these areas of study.

The agreement between calculated and measured results is very satisfactory with the exception of bending stresses. These were not dealt with at all by Beta Machinery Analysis Ltd. and the Martec Ltd. predictions are not as reliable as their other results. However, the magnitude of the bending stresses indicate they cannot be ignored. This is one area which requires further study.

In both theoretical approaches the predicted axial strains were slightly conservative which is good from a design stand point.

Effectively, this concludes the study on lattice mast structures as the results of this study validate TDCCP, the analytical procedures previously developed by DRES and the design procedure and associated computer code developed by Martec Ltd. The result is a computerized engineering design standard that can be used by the Maritime Branch of the Canadian Forces to effectively design lattice-type masts.

REFERENCES

1. R. Geminder and R.W. Hicks, "Analytical and Empirical Study of Shipboard Antenna Masts Subjected to a Blast Environment", Volumes I and II, Mechanics Research Inc., Los Angeles, California, November 1969.

2. D.S. Walkinshaw, B.G. Laidlaw and B.R. Long, "Shipboard Lattice Antenna Masts Under Blast Loading, Part I, Strains in Model Masts in Operation Prairie Flat and Event Dial Pack", Defence Research Establishment Suffield, Ralston, Alberta, Canada, Suffield Technical Paper No. 402, May 1973. UNCLASSIFIED.

3. B.R. Long and B.G. Laidlaw, "Shipboard Lattice Antenna Masts Under Blast Loading, Part II: Comparisons of Experimental Results with Theoretical Predictions by Computer Programs", Defence Research Establishment Suffield, Ralston, Alberta, Canada, Suffield Technical Paper No. 418, September 1973. UNCLASSIFIED.

4. B.R. Long, B.G. Laidlaw and R.J. Smith, "The Analysis of Shipboard Lattice Antenna Masts Under Air Blast and Underwater Shock Loading, Part III, Final Report", Defence Research Establishment Suffield, Ralston, Alberta, Canada, Suffield Technical Paper No. 431, June 1975. UNCLASSIFIED.

5. "Engineering Standard for the Design of Lattice Masts of Warships", Can Plan Oceanology Limited, Halifax, Nova Scotia, Canada, October 1975.

6. "Book of Design Calculations", Can Plan Oceanology Limited, Halifax, Nova Scotia, Canada, October 1975.

7. "Validation of Lattice Mast Design Procedure: Comparison of Predicted and Measured Responses of a Model Mast Tested at Event Dice Throw", Martec Limited, Halifax, Nova Scotia, Canada, March 1977.

8. "Report on Dynamic Analysis of Antenna Mast Structure for Defence Research Establishment Suffield", Beta Machinery Analysis Ltd., Calgary, Alberta, Canada, March 1977.

20. BLAST RESPONSE OF 35-FT FIBERGLASS WHIP ANTENNA - EVENT DICE THROW

by

G.V. Price and C.G. Coffey

Defence Research Establishment Suffield

PROJECT C3 BLAST RESPONSE OF 35 FT FIBREGLASS WHIP ANTENNA - EVENT DICE THROW

G.V. Price and C.G. Coffey

DEFENCE RESEARCH ESTABLISHMENT SUFFIELD
RALSTON ALBERTA

ABSTRACT

The blast response of 35 ft fibreglass Whip Antennas was investigated in a free-field blast trial and in numerical simulation experiments. The antennas satisfactorily withstood the air blast loading at nominal 7.0, 10.0 and 12.2 psi peak overpressure locations in Event Dice Throw. The numerical model predictions for the natural frequencies are in excellent agreement with results obtained experimentally, however the corresponding predictions for the transient strain using pre-trial drag coefficients were approximately double the values obtained experimentally. Subsequent revised numerical predictions for the transient strains using experimental drag coefficients obtained independently in the blast trial itself have produced results in more reasonable agreement with the experimental transient strains.

INTRODUCTION

The Defence Research Establishment Suffield (DRES), in support of the Canadian Forces (Maritime) policy on blast hardening of ships and components, has conducted a series of tests to determine the ability of certain antenna designs to withstand blast overpressures of various intensities. During Event Dice Throw, a 620-ton AN/FO free-field blast trial conducted by the United States Defense Nuclear Agency at the White Sands Missile Range in New Mexico on October 6, 1976, several antenna design were tested at various overpressure levels. One of the antenna designs evaluated in the trial was a 35 ft fibreglass Whip Antenna.

The objectives of this study were to determine the ability of three 35 ft fibreglass Whip Antennas to withstand the effects of blast waves at the nominal 7.0, 10.0 and 12.2 psi peak overpressure levels respectively, and to compare the measured response of the antennas against theoretical predictions determined by a computer model recently depeloped at DRES [1]. It was intended that experimental verification of the computer model would lead to a criterion for predicting the blast response of whip antenna designs in general.

INSTALLATION AND INSTRUMENTATION OF THE WHIP ANTENNAS

The Whip Antenna design evaluated in the study was Model AS5085-SR manufactured by Valcom Ltd., Guelph, Ontario. A schematic of the antenna is shown in Figure 1. According to the manufacturer [2], the main shaft of the antenna was composed of alternate fibreglass layers at 90^{0} and 0^{0} angles relative to the axis of the antenna. The volume ratio of longitudinal to circumferential fibres was approximately 2:1 throughout the antenna except in the region of the base of the antenna. The lower three feet of the shaft was increased in size by additional circumferential wrappings up to 3/4 in thick (the additional wrappings at the base added no additional flexural strength to the antenna). The antenna was fabricated in two pieces which joined together through an embedded brass coupling located approximately 18 ft from the base (see Figure 1). Additional physical characteristics of the antenna, as supplied by the manufacturer, are presented in Table 1.

Three Whip Antennas were installed for the Event Dice Throw field trial. The antennas were located at the nominal 7.0, 10.0 and 12.2 psi peak overpressure locations (1135, 940 and 875 ft respectively from ground zero). For discussion purposes, the antennas will be referred to by the nominal peak overpressure locations at which they were installed. Each antenna was mounted on a 24 in x 30 in x 21.5 in steel box (DRES drawing MES-CDT-100-C3-2) of a type used in a previous multi-ton field trial ("Event Dial Pack" held at DRES in 1970) as a mounting for a GRP Whip Antenna [3]. The steel box assemblies were subsequently bolted to 5 ft x 8 ft x 2 ft heavy reinforced concrete foundations (DRES drawing MES-CDT-100-C3-1). A photograph of the three Whip Antennas installed for the Event Dice Throw field trial is shown in Figure 2.

Five pairs of MICRO-MEASUREMENTS type EA-41-10CBE-120 strain gauges were bonded directly to the outer surface of the nominal 7.0 psi Whip Antenna. The gauge locations are shown in Figure 1. In addition, two strain gauge pairs were bonded to the outer surface of the nominal 10.0 and 12.2 psi Whip Antennas. The locations of the nine strain gauge pairs are summarized in Table 2. The gauges which constitute a strain gauge pair were bonded to opposite sides of the antennas on a line corresponding to the blast direction, thereby measuring the maximum flexural strain at the specified cross-sections.

The signals from the strain gauge pairs were conditioned with bridge and balance units, amplified, F.M. multiplexed and then recorded on 14-track magnetic tape with a frequency response of DC to 4 KHz. In this fashion, five channels of experimental data were multiplexed onto one tape channel, a procedure which was required by the large number of DRES data channels and limited number of tape recorders. A block diagram describing the instrumentation is shown in Figure 3, and a photograph of the DRES Instrumentation Bunker in which the data signals were processed and recorded is shown in Figure 4.

In addition to the strain gauge data, the response of the 7.0, 10.0 and 12.2 psi Whip Antennas was recorded respectively on a LOCAM high-speed camera at 500 frames per second, a FASTAIR high-speed camera at 320 frames per second and a FASTAIR high-speed camera at 600 frames per second. A time mark generator was used to confirm the above film speeds.

COMPUTER MODEL SIMULATION

A numerical procedure was developed at DRES to predict the elastic response of a variable cross-section cantilever beam when subjected to a transient air blast load [1]. The procedure begins with the Bernoulli-Euler equation of a vibrating beam. The normal modes and natural frequencies of the beam are determined by solving the differential equations for free vibration using successive relaxation, Rayleigh quotient and Gram-Schmidt orthogonalization numerical techniques. The forced vibration solution is obtained using normal mode coordinates and Laplace transforms.

The computer model simulation used a clamped-free boundary condition of the form

(a) clamp at x-0, zero displacement and slope,
(b) free at x=L, zero moment and shear, (1)

where x is a distance coordinate measured from the base of the antenna and L is the length of the antenna. In addition, the following values for the drag coefficient C_D were used in computing the aerodynamic drag portion of the blast wave loading on the antenna in the first set of simulation experiments:

$$C_D = \begin{cases} 0.7 \ , & M \geq 0.48,\ Re \geq 3\times10^5, \\ 0.6 \ , & M < 0.48,\ Re \geq 3\times10^5, \\ 1.2 \ , & M < 0.48,\ Re < 3\times10^5. \end{cases} \qquad (2)$$

In the above equation, M is the instantaneous Mach number of the flow incident on the antenna, and Re is the instantaneous Reynolds number (based on local diameter). A revised set of drag coefficients (based on independent drag experiments in Event Throw itself) were used in a subsequent simulation experiment, to be considered in detail in a later section.

The structure of the Whip Antenna was represented in the computer model in such a way as to simulate the mass and projected (normal to blast direction) cross-sectional area profiles of the antenna. Three different mass/projected cross-sectional area profiles were considered. The first profile (simulation A) corresponded to physical data supplied by the manufacturer (Table 1; [2]). The second profile (simulation B) corresponded to antenna wall thicknesses measured from x-ray examination of the nominal 7.0 psi Whip Antenna (radiography examination by R.M. Hardy and Associates [4]). The final profile (simulation C) corresponded to micrometer measurements of test samples cut out of the antenna to determine the wall thicknesses for the nominal 7.0 psi Whip Antenna. With these measurements, adjustment to the profiles near the base and in the vicinity of the junction between lower and upper portions of the antenna were made to account for the additional mass (measured) and stiffening in the indicated regions. In addition, the third simulation used a mass-weighted average value for Young's Modulus based on tensile tests performed by R.M. Hardy and Associates (Figure 5; [5]). In summary, simulations A and B were based on antenna features which were known or measured prior to the blast trial, while simulation C was based on antenna properties which were obtained in destructive tests and measurements of the nominal 7.0 psi Whip Antenna following the blast trial.

A comparison of the three simulations for the mass/projected cross-sectional area profiles of the nominal 7.0 psi Whip Antenna is presented in Table 3. Simulation A (manufacturer's data) is found to differ significantly from simulation B and C (measured data) above the lower 3 ft portion of the antenna. The differences in the profiles will result in differences in the corresponding strain predictions, a point which will be examined in more detail in Section 5.

COMPARISON OF THEORETICAL AND EXPERIMENTAL NATURAL FREQUENCIES: TWANG TEST

Prior to the blast trial, a "Twang Test" was performed to obtain free vibration strain data for the Whip Antennas. A static load was applied near the top of each antenna using an anchored nylon rope at a pull angle of 30^o to the horizontal. The load was subsequently released electrically and the strain data for free vibration was recorded. The experiment was performed to determine the natural frequencies of the antennas and to verify the test instrumentation.

A photograph of the Twang Test apparatus is shown in Figure 6. The apparatus consisted of a 1/4 in nylon rope attached to a bracket at the 30 ft location on each of the antennas and anchored to a truck, a 6000 lb capacity L.A.B. Corp. Quick Release Hook, a hand-operated mechanical winch to take up slack in the system, and a Transducers Inc. strain-type load cell (model ML2-151-1K) with a Budd Strain indicator readout (model P-350) to measure the applied load. The applied loads were monitored locally with the load cell while the bending strains as measured by the strain gauges bonded to the antenna were recorded remotely in the Instrumentation Bunker.

The loads on the antennas were released electrically and the bending strain data for free vibration ("Twang Test") were recorded in the Instrumentation Bunker. In this fashion it was possible to establish that the test instrumentation was operational.

A Fourier analysis was subsequently performed for the experimental strain data to determine the natural frequencies of each antenna. The free vibration strain history and corresponding Fourier analysis for gauges 2 and 5 are presented in Figures 7 and 8. As shown, the lowest natural frequency for the 7.0 psi Whip Antenna is sharply identified as 1.27 cps by the Fourier analysis, while the higher natural frequencies are less distinct. The best resolution of the higher natural frequencies occurs for the gauge located in the upper region of the antenna, gauge 5. The three lowest natural frequencies of the three antennas, as determined from a Fourier analysis of the Twang Test strain measurements, are presented in Table 4. The observed differences between the experimental natural frequencies of the three antennas are due to differences in antenna construction. In particular, the 10.0 and 12.2 psi antennas were 15 inches longer than the 7.0 psi antenna [6].

The theoretical (numerical simulation) predictions for the three lowest natural frequencies and corresponding normal modes for simulation A of the 7.0 psi Whip Antenna are presented in Figure 9. Normal modes of a similar general shape were obtained for simulations B and C. A comparison of the natural frequencies for simulations A, B and C of the 7.0 psi Whip Antenna against the experimental values obtained from the Twang Test is presented in Table 5. It is apparent from this comparison that the predicted frequencies are in excellent agreement with the values obtained experimentally.

COMPARISON OF THEORETICAL AND EXPERIMENTAL BENDING STRAIN HISTORIES: EVENT DICE THROW

The numerical simulation model was used to generate bending strain predictions corresponding to two types of Friedlander overpressure waves. The two sets of overpressures respectively correspond to Defense Nuclear Agengy (DNA) pre-trial predictions (blast data A) and average measured[1] blast wave properties (blast data B) at the nominal 7.0, 10.0 and 12.2 psi peak over pressure locations.

A comparison of the two sets of Friedlander overpressure waves is presented in Table 6 and Figure 10. It should be noted that despite the lower peak overpressure in the experimental Friedlander waves, the total inpulse associated with the experimental waves is 18 to 49% higher than the corresponding impulse of the 7.0, 10.0 and 12.2 psi predicted waves.

PREDICTIONS BASED ON PRE-TRIAL DRAG COEFFICIENTS

Three sets of bending strain predictions were calculated using the pre-trial drag coefficients summarized in equation (2). The discussion which follows considers only the predictions for the 7.0 psi Whip Antenna, since the trends apparent in this set of results are representative of the results obtained with the other antennas. A summary of the essential features of the three prediction experiments is presented in Table 7.

The first set of predictions (predictions 1) used physical data supplied by the contractor (simulation A) together with pre-trial blast data provided by DNA (blast data A). This set of predictions is therefore based on pre-trial physical and blast data supplied by external agencies.

A comparison of predicted against experimental strain histories for the 7.0 psi Whip Antenna is presented in Figure 11, and an evaluation of the ability of the model to predict peak bending strains is given in Table 8. Although certain gauge locations display reasonably good agreement between predicted and experimental strains, most gauges indicate considerably larger predicted strains compared to the experimental results. This is apparent from the large value for the average ratio of peak theoretical to experimental strains (1.62; see Table 8). In addition, the ratio of peak theoretical to experimental strains fluctuates considerably from gauge

---

[1] The free-field overpressure at the base of the three antennas measured using ten Bytrex Model HFH-100 strain-type pressure transducers [7]. The "measured" overpressure wave properties were considered to be the average of the properties determined by the individual pressure transducers.

to gauge, indicating that the mass profile simulation does not accurately follow the mass distribution trends in the antenna itself.

The second set of predictions (predictions 2) used physical data corresponding to x-ray measurements at DRES (simulation B) together with pre-trial blast data provided by DNA (blast data A). As in the previous prediction experiment, this calculation is based on pre-trial data since non-destructive techniques were used to determine the antenna properties.

A comparison of the corresponding predicted strains against the experimental results is provided in Figure 12 and Table 8. It is noted that the predictions are in poorer agreement with the experimental results than in the first prediction set, a result which was not anticipated since more accurate simulation data was used to describe the antenna structure in this case compared to the former. It is therefore apparent that the earlier prediction set 1 involved compensating errors in that an erroneous simulated mass profile produced errors which compensated for an unknown factor which is causing the strain predictions to be much larger than the experimental values would indicate.

The third set of predictions (predictions 3) used experimentally determined physical and blast data as input to the numerical prediction model. This represents the best available input data to the numerical prediction model, and should therefore produce the best strain predictions. The mass profile in the calculation corresponds to measurements obtained from post-trial destructive tests performed on the 7.0 psi Whip Antenna (simulation C), and the air blast data corresponds to average measured blast wave properties (blast data B).

A comparison of the corresponding predicted strains against the experimental results is presented in Figure 13 and Table 8. Similar to the previous prediction experiments, the predictions are considerably larger than the experimental results. However, the ratio of peak theoretical to experimental strains fluctuates considerably less from gauge to gauge compared to the earlier predictions, indicating that the mass profile simulation more accurately follows the actual mass distribution trends in the antenna itself. In addition, it should be noted that this prediction is based on blast data which has an 18 to 49% larger positive phase impulse than in the earlier prediction experiments. The earlier prediction sets 1 and 2 therefore had compensating errors, since artificially low pre-trial DNA blast data compensated for an unknown factor which is causing the strain predictions to be much larger than the experimental values would indicate.

At this point, the only remaining area to be evaluated in assessing the cause of the poor performance of the numerical prediction model lies with the empirical drag coefficients. This will be considered in detail in the following section.

PREDICTIONS BASED ON DICE THROW DRAG COEFFICIENTS

An aerodynamic drag project was independently undertaken in the Event Dice Throw field trial [8]. The drag forces on cylinders of various diameters were determined using free-flight measurement techniques, and preliminary drag coefficient results, as shown in Figure 14, are now available in the low Reynolds number regime, applicable to the Whip Antenna study.

It is apparent from these preliminary results that the drag coefficients at low Reynolds number in Event Dice Throw are much smaller than anticipated from earlier field trials. Based on the preliminary results presented in Figure 14, a drag coefficient profile appropriate to the low Reynolds number regime in Event Dice Throw is of the form

$$C_D = \left\{ \begin{array}{ll} 0.3 \;, & M<0.48,\ Re \geq 4\times10^5, \\ 0.6 \;, & M<0.48,\ Re<4\times10^5. \end{array} \right\} \quad (3)$$

It should be noted that this profile is based on preliminary drag measurements, and the reader is referred to the final drag study report [8] for more details and revised C_D profiles.

A final set of strain predictions was produced using the drag coefficient profile specified by equation (3). The predictions were computed using experimentally determined physical and blast data (mass profile simulation C, blast data B) as input to the numerical prediction model (see Table 7). A comparison of the corresponding predicted strains against the experimental results is presented in Figures, 15, 16, and 17, and Table 8. The comparisons for the 7.0 psi Whip Antenna are repeated in Figures 18 to 22 in an enlarged format.

In general, the predicted strains are found to be in reasonable agreement with the experimental strains. The average ratio of peak theoretical to experimental bending strains is 1.27, a value significantly less than the results from the previous prediction experiments. The best agreement between the predicted and experimental strains occurs with gauges 4 and 5, located in the upper portion of the 7.0 psi Whip Antenna.

The poorest agreement in this prediction experiment is obtained for gauge 6, located in the lower portion of the 10.0 psi Whip Antenna (see Figures 1 and 16). This result is in part a consequence of using a mass profile simulation based on the 7.0 psi antenna (simulation C) in generating the time response of the 10.0 psi antenna. As noted earlier, the three antennas differ in construction [6], and measured mass profile data was not available for the 10.0 and 12.2 psi antennas.

Due to strain gauge failure early in the time response, experimental verification of strain predictions from three of the four strain gauge pairs on the 10.0 and 12.2 psi Whip Antennas is not available.

CONCLUSIONS

The blast response of 35 ft fibreglass Whip Antennas was investigated in a free-field blast trial and in numerical simulation experiments. The antennas satisfactorily withstood the air blast loading at nominal 7.0, 10.0 and 12.2 psi peak overpressure locations in Event Dice Throw. The corresponding antenna response was modelled numerically, and predictions of natural frequencies and transient bending strains were generated for various antenna mass profile simulations and air blast loadings.

The predicted natural frequencies were in excellent agreement with experimental results and the transient strain predictions using experimental drag coefficients obtained independently in the blast trial itself were in reasonable agreement with the experimental transient strains.

Accuracy of the transient strain predictions was found to depend significantly on the following three conditions:

(a) the computer simulation must agree with the mass profile and physical properties of the actual antenna,

(b) the computer simulation must agree with the air blast properties of the actual blast wave (peak overpressure, positive phase duration, and particularly the positive phase impulse),

(c) the computer simulation must agree with the aerodynamic drag coefficient (C_D) relevant to the antenna geometry and blast wave in question.

Conditions (a) and (b) are generally known with some degree of certainty prior to a blast trial (if necessary, destructive material tests may be carried out on a duplicate antenna to establish the correct mass profile and physical properties for the numerical simulation). However, there appears to be some doubt regarding correct drag coefficient relationship for air blast waves (as function of Reynolds number, Mach number, and blast wave properties) particularly in the low Reynolds number regime which applies to whip antennas. Evidence of drag coefficient uncertainty was apparent in this study through the large differences in transient strain predictions obtained using pre-trial C_D profiles and profiles of C_D determined from the blast trial itself. Reducing the uncertainty in C_D at low Reynolds and Mach numbers represents an area requiring further investigation.

Subject to an accuract simulation of the antenna mass profile, blast wave properties, and drag coefficient profiles, the computer model is recommended as a design tool in the development of whip antennas in general.

REFERENCES

1. G.V. Price, "Numerical Simulation of The Air Blast Response of Tapered Cantilever Beams (U)". Defence Research Establishment Suffield, Ralston Alberta Suffield Technical Paper No. 447. 1977. UNCLASSIFIED.

2. S.B. Clarke, "Private Communication to G.V. Price", April 23, 1976.

3. L.W. Tamke and B.R. Long, "Evaluation of GRP Whip Antenna - Event Dial Pack (U)". Event Dial Pack Symposium Report, Vol. 1. Defence Research Establishment Board of Canada, pp. 263-274. 1971.

4. R.D. Vergetti, "Private Communication to G.V. Prive Regarding a Radiographic Inspection on April 21, 1976 by D.R. Shannon. File No. CXR76-824. May 4, 1976.

5. R.M. Hardy and Associates Metal Test Report, Lab Order No. 6103-1795, "Private Communication to G.V. Price". December 8, 1976.

6. G.V. Price, "Private Communication to R. McInnis, DMCS-6, DRES File No. 3611F-8(MCS). May 27, 1976.

7. F.H. Winfield, "Event Dice Throw - Canadian Air Blast Measurements (U)". Defence Research Establishment Suffield, Ralston, Alberta. Suffield Technical Paper No. 451. 1977. UNCLASSIFIED.

8. A.W.M. Gibb and D.A. Hill, "Free-Flight Measurement of The Drag Forces On Cylinders in Event Dice Throw (U)". Defence Research Establishment Suffield, Ralston, Alberta. Suffield Technical Paper No. 453. 1977. UNCLASSIFIED.

x[1] (ft)	OD[2] (in)	ID[3] (in)
2	6.5	4.4
6	5.0	4.1
10	4.5	3.7
14	4.15	3.4
18	3.9	3.0
22	3.0	2.6
26	2.4	2.1
20	2.1	1.8
34	1.9	1.5

[1] Distance from the base of the antenna.

[2] Outside diameter.

[3] Inside diameter.

$E = 3.9 \times 10^6$ psi

$\rho = 0.002298$ slugs/in^3

Table 1: Physical features of the Valcom AS5085-SR fibreglass Whip Antenna, as supplied by the manufacturer [2].

Gauge	Antenna (nominal)	x (ft)
1	7.0 psi	3.5
2	7.0 psi	10.5
3	7.0 psi	17.0
4	7.0 psi	18.4
5	7.0 psi	24.0
6	10.0 psi	10.5
7	10.0 psi	24.0
8	12.2 psi	10.5
9	12.2 psi	24.0

Table 2: Strain gauge locations for the three Whip Antennas.

x (in)	Simulation A			Simulation B			Simulation C		
	ID (in)	OD (in)	Wt (lb)	ID (in)	OD (in)	Wt (lb)	ID (in)	OD (in)	Wt (lb)
0.0	4.400[1]	6.500[1]		5.537[1]	6.457[1]		5.540[1]	9.640[2]	
			48.41			22.63			84.54
41.9	4.283	5.942		4.411	5.199		4.167	4.965	
			30.03			15.89			15.90
83.7	4.002	4.878		3.845	4.503		3.845	4.535	
			17.30			11.73			12.15
125.6	3.655	4.459		3.678	4.205		3.640	4.177	
			14.74			9.93			10.04
167.4	3.403	4.154		3.381	3.929		3.341	3.901	
			14.37			8.96			12.81
209.2	3.056	3.935		3.224	3.709		2.551[2]	3.609	
			11.33			6.67			10.72
251.1	2.707	3.241		2.619	2.997		2.659	3.067	
			5.90			4.37			4.65
292.9	2.298	2.638		2.280	2.582		2.251	2.562	
			3.57			3.22			3.54
334.8	1.957	2.257		2.047	2.319		2.021	2.346	
			3.05			2.49			2.91
376.6	1.695	2.030		1.851	2.071		1.825	2.075	
			3.17			1.82			2.06
418.5	1.500[1]	1.900[1]		1.777[1]	1.947[1]		1.741[1]	1.937[1]	
			Total: 151.87			Total: 87.71			Total: 159.32
	$E = 3.9 \times 10^6$ psi [2]			$E = 3.9 \times 10^6$ psi [2]			$E = 4.27 \times 10^6$ psi [5]		
	$\rho = 0.002298$ slugs/in^3, $\Delta x = 41.8$ in, $N = 10$, $L = 418.5$ (34.88 ft)								

[1] Extrapolated.

[2] Calculated based on the measured mass distribution; calculation depends on Δx.

Table 3: Physical features of the three computer simulations of the 7.0 psi fibreglass Whip Antenna.

Mode	Natural Frequencies (cps)		
	7.0 psi	10.0 psi	12.2 psi
1	1.27	1.03	1.02
2	4.20	3.46	3.52
3	9.50	8.25	7.75

Table 4: Natural frequencies of the three Whip Antennas as determined from a Fourier analysis of the Twang Test strain measurements.

Mode	Natural Frequencies (cps)						
	Experimental	Simulation A		Simulation B		Simulation C	
		Theoretical	Theo./Exp.	Theoretical	Theo./Exp.	Theoretical	Theo./Exp.
1	1.27	1.47	1.16	1.33	1.05	1.34	1.06
2	4.20	4.09	0.97	4.08	0.97	4.06	0.97
3	9.50	9.55	1.01	9.47	1.00	10.16	1.07
			Avg. 1.05		Avg. 1.01		Avg. 1.03

Table 5: Comparison of theoretical (numerical simulations A, B and C) and experimental (Twang Test) natural frequencies for the 7.0 psi Whip Antenna.

Symbol	Units	Description	Blast Data A			Blast Data B		
			7.0	10.0	12.2	7.0	10.0	12.2
P_A	psi	atmospheric pressure	12.58	12.58	12.58	12.42	12.42	12.42
T_A	°F	atmospheric temperature	54	54	54	48	48	48
p_o	psi	peak overpressure	7.0	10.0	12.2	6.6	9.9	12.0
t_d	msec	positive phase duration	242	189	172	250	231	254
I_D	psi/msec	positive phase impulse	600	695	750	707	863	1119
κ[1]	--	Friedlander decay constant	1.137	1.002	1.104	0.482	0.911	1.009

[1] The decay constant is computed based on the condition that the Friedlander wave is to be characterized by the specified values of p_o, t_d and I_d.

Table 6: Air blast data corresponding to the pre-trial DNA predictions (blast data A) and the average measured blast wave properties (blast data B).

Transient Strains Prediction Set	Mass Profile Simulation [1]	Air Blast Data [2]	Drag Coefficient Equation No.
1	A	A	2
2	B	A	2
3	C	B	2
4	C	B	3

[1] See Table 3.

[2] See Table 6.

Table 7: Summary of the four numerical prediction experiments for transient bending strains.

Gauge	Peak Bending Strains (μin/in)								
	Experimental	Predictions 1		Predictions 2		Predictions 3		Predictions 4	
		Theoretical	Theo./Exp.	Theoretical	Theo./Exp.	Theoretical	Theo./Exp.	Theoretical	Theo./Exp
1	2009	2050	1.02	4601	2.29	5371	2.67	2768	1.38
2	2381	3443	1.45	6300	2.65	6656	2.80	3438	1.44
3	1335	3112	2.33	5773	4.32	3579	2.68	1838	1.38
4	2376	3578	1.51	6263	2.64	4066	1.71	2090	0.88
5	3713	7171	1.93	7712	2.08	7334	1.98	3777	1.02
6	3902	5756	1.48	10574	2.71	11584	2.97	5993	1.54
7	-- [1]	12491	--	13137	--	13128	--	6784	--
8	-- [1]	7609	--	13748	--	17150	--	8998	--
9	-- [1]	16510	--	17136	--	19411	--	10099	--
			Avg. 1.62		Avg. 2.78		Avg. 2.47		Avg. 1.27

[1] Strain gauge failure.

Table 8: Comparison of peak theoretical and experimental bending strains (first quarter cycle only).

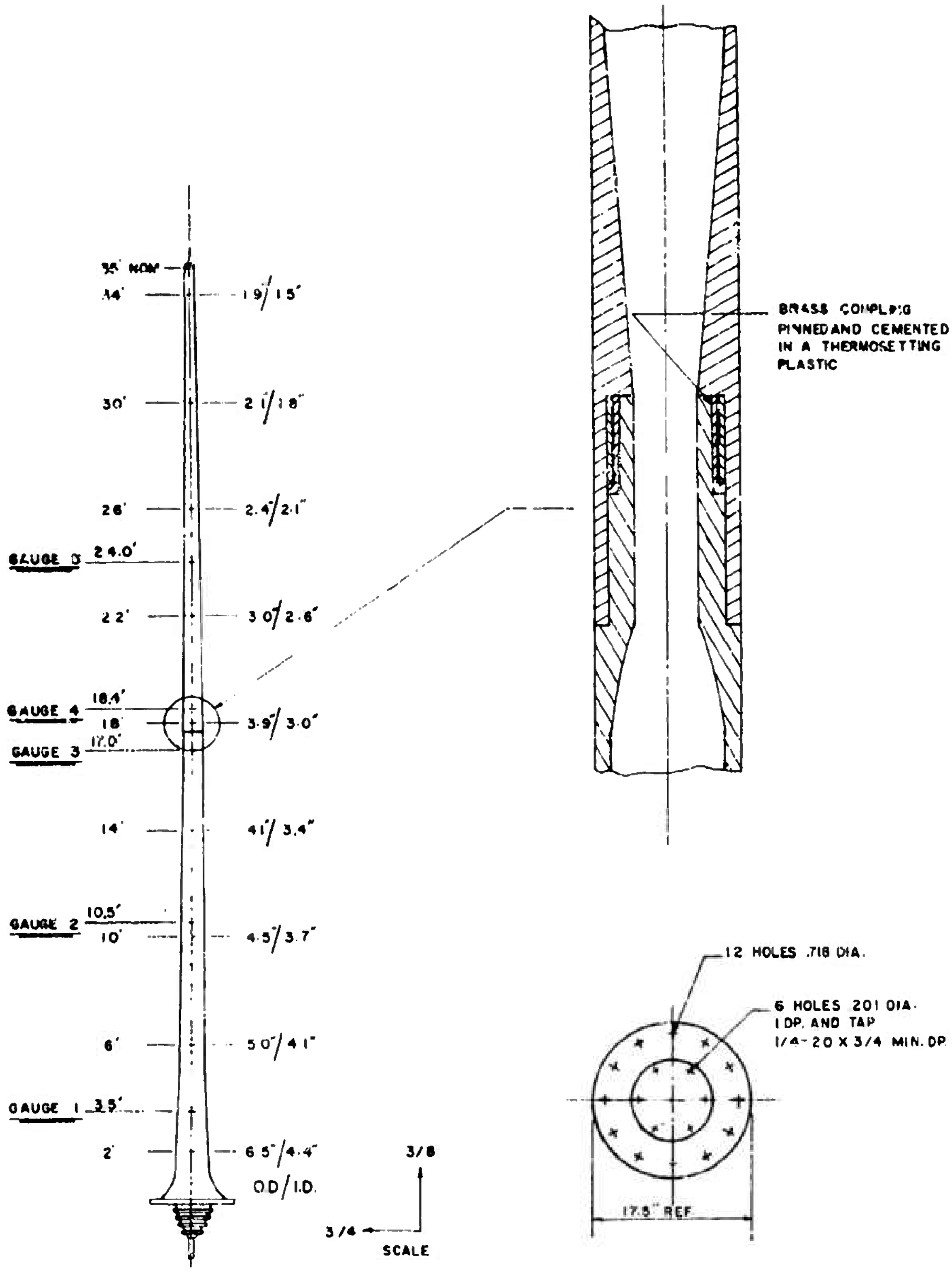

FIG. 1 SCHEMATIC OF THE NOMINAL 7.0 PSI 35 FT FIBREGLASS WHIP ANTENNA, INCLUDING THE LOCATIONS OF THE STRAIN GAUGES.

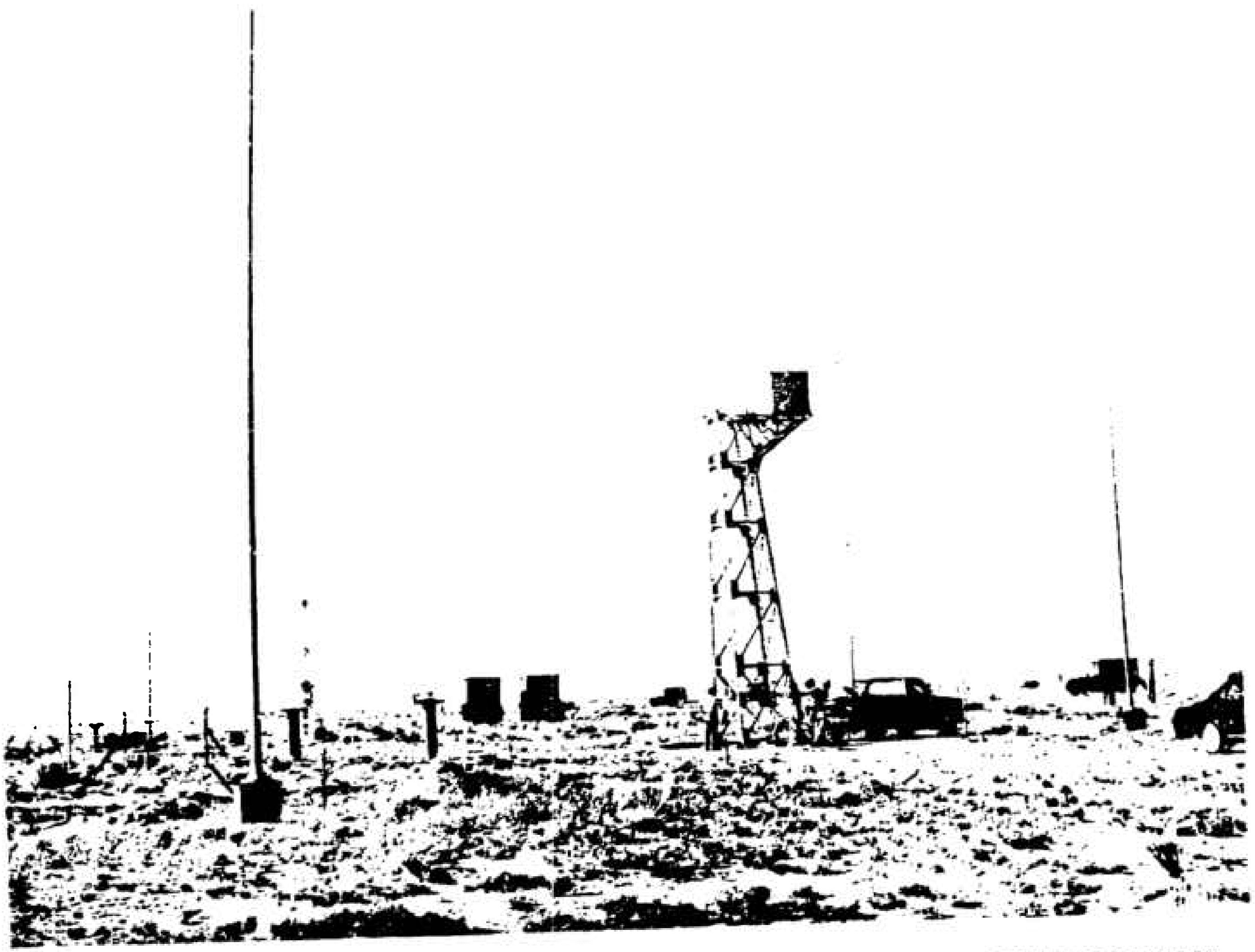

FIG. 2 PHOTOGRAPH OF THE THREE 35 FT FIBREGLASS WHIP ANTENNAS IN EVENT DICE THROW.

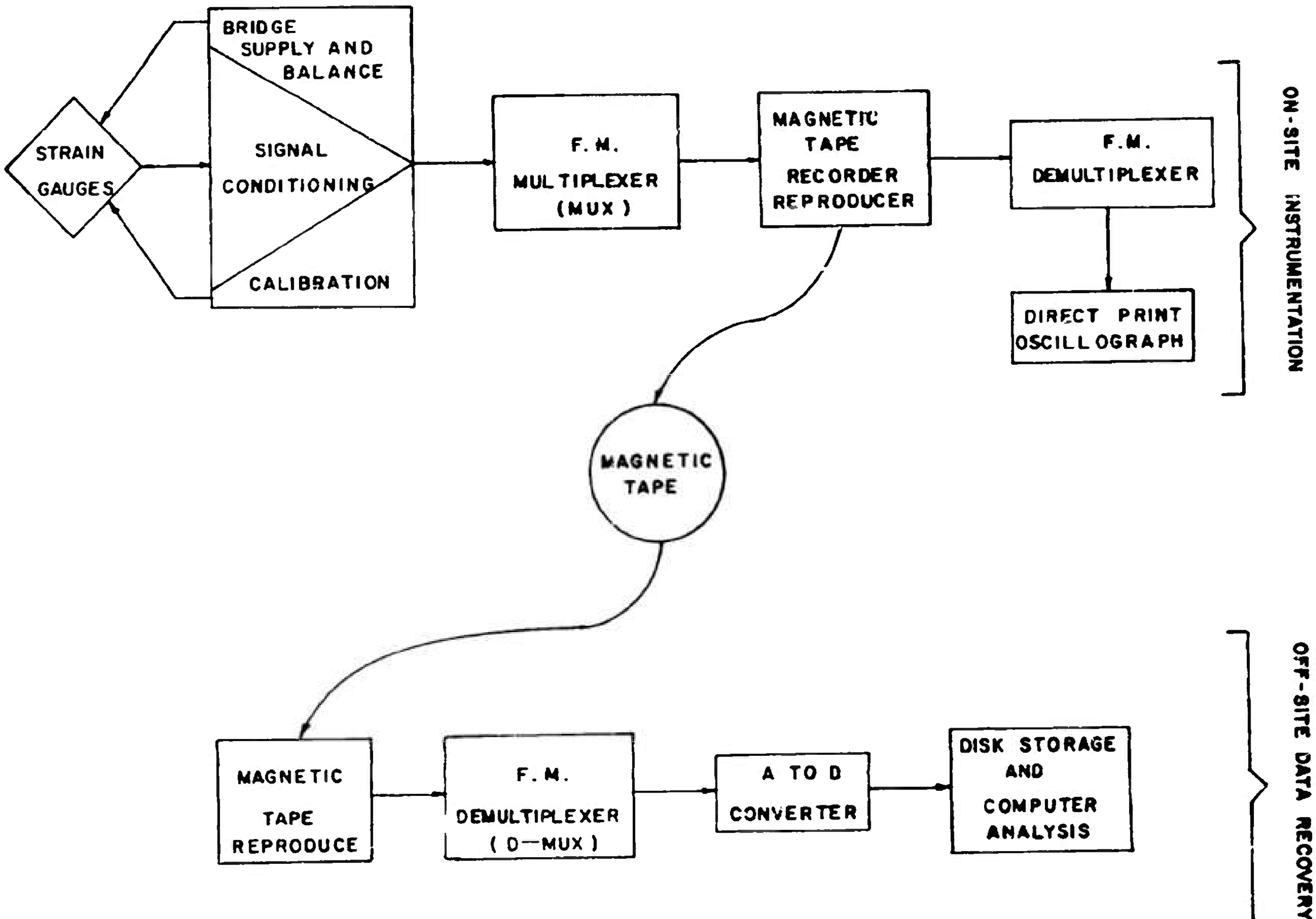

FIG. 3 SCHEMATIC DIAGRAM OF THE STRAIN GAUGE INSTRUMENTATION IN EVENT DICE THROW.

FIG. 4 DRES INSTRUMENTATION BUNKER IN EVENT DICE THROW.

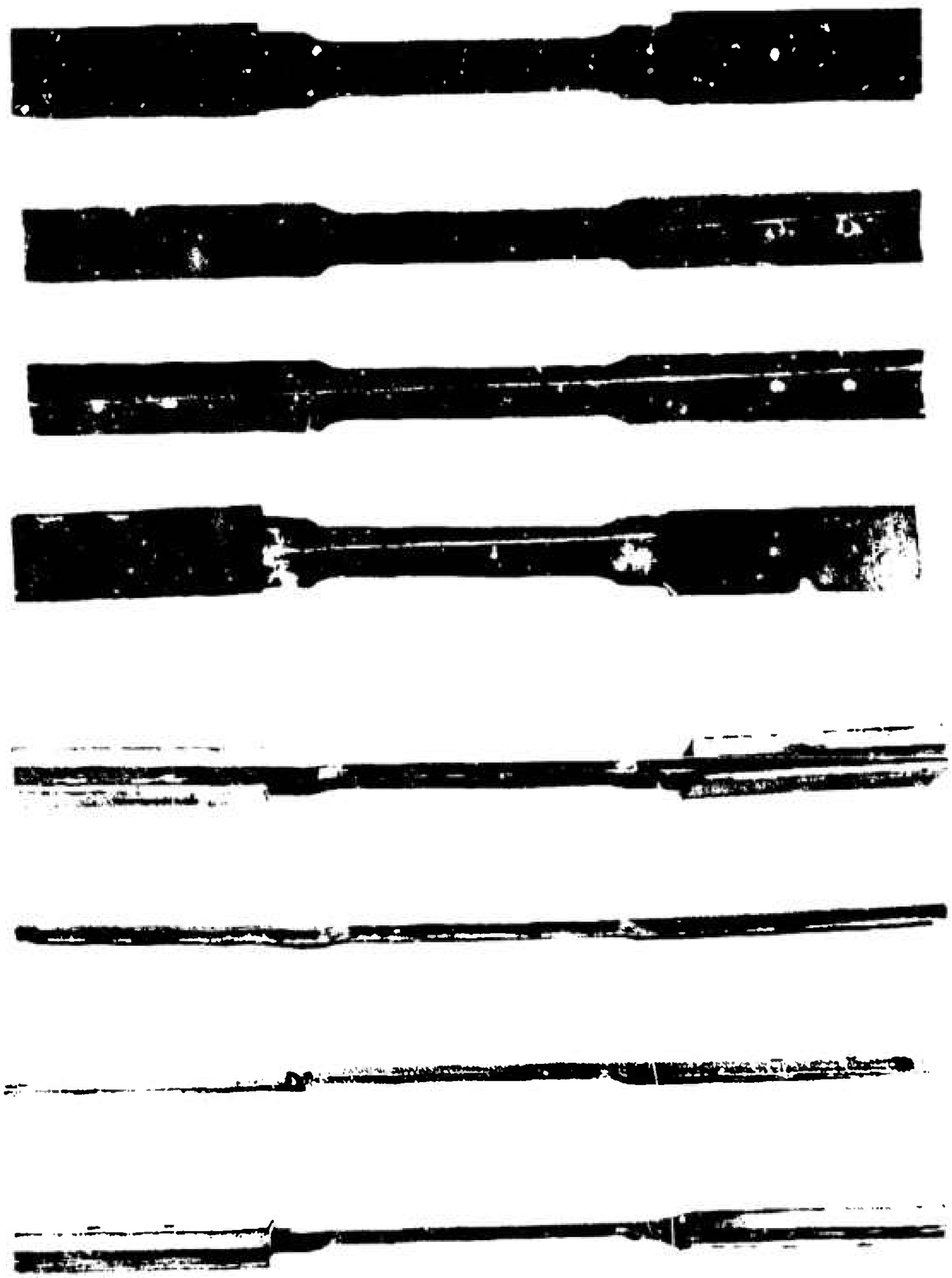

FIG. 5 TENSILE SPECIMENS, R.M. HARDY MATERIAL TESTS [5].

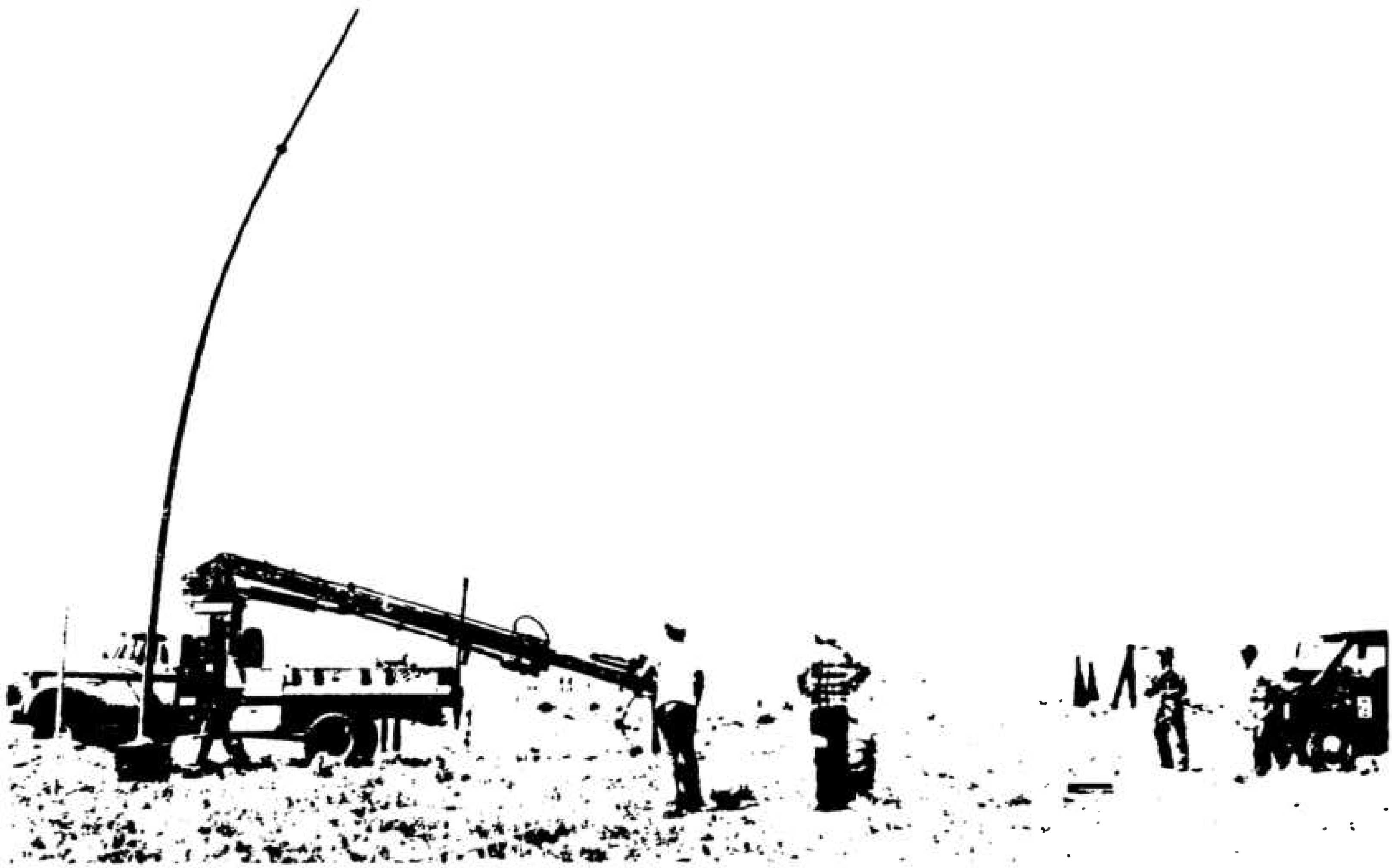

FIG. 6 PHOTOGRAPH OF THE TWANG TEST APPARATUS.

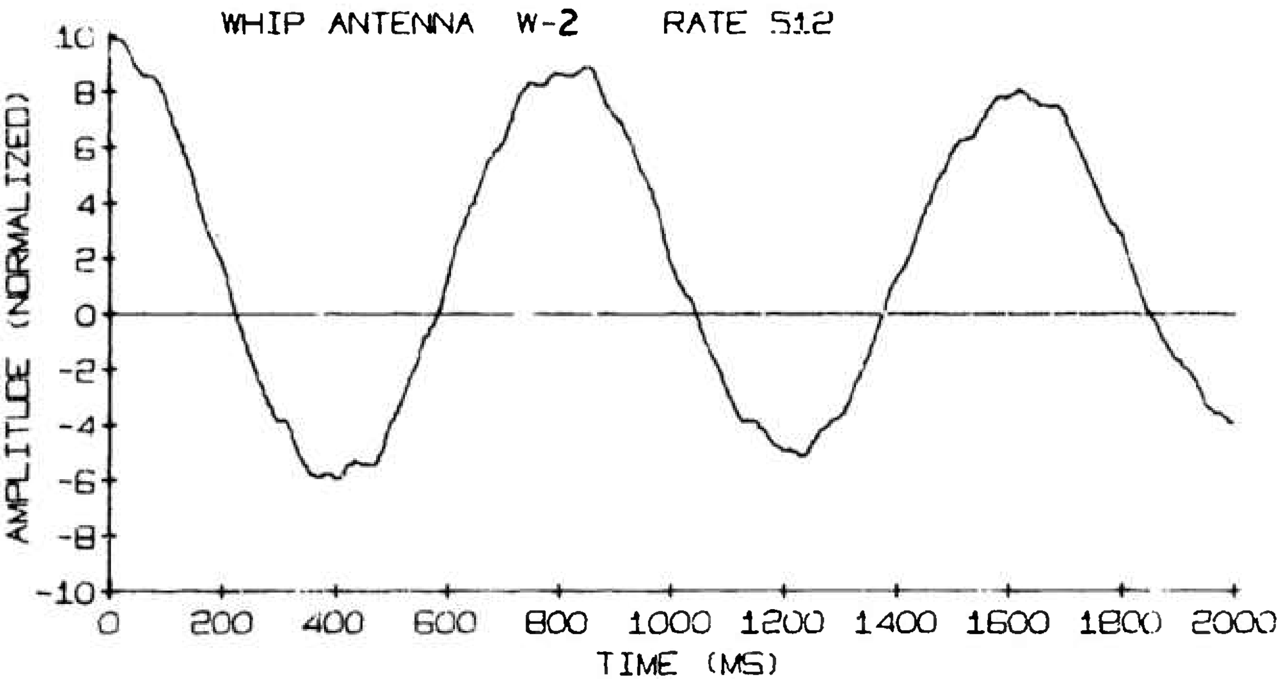

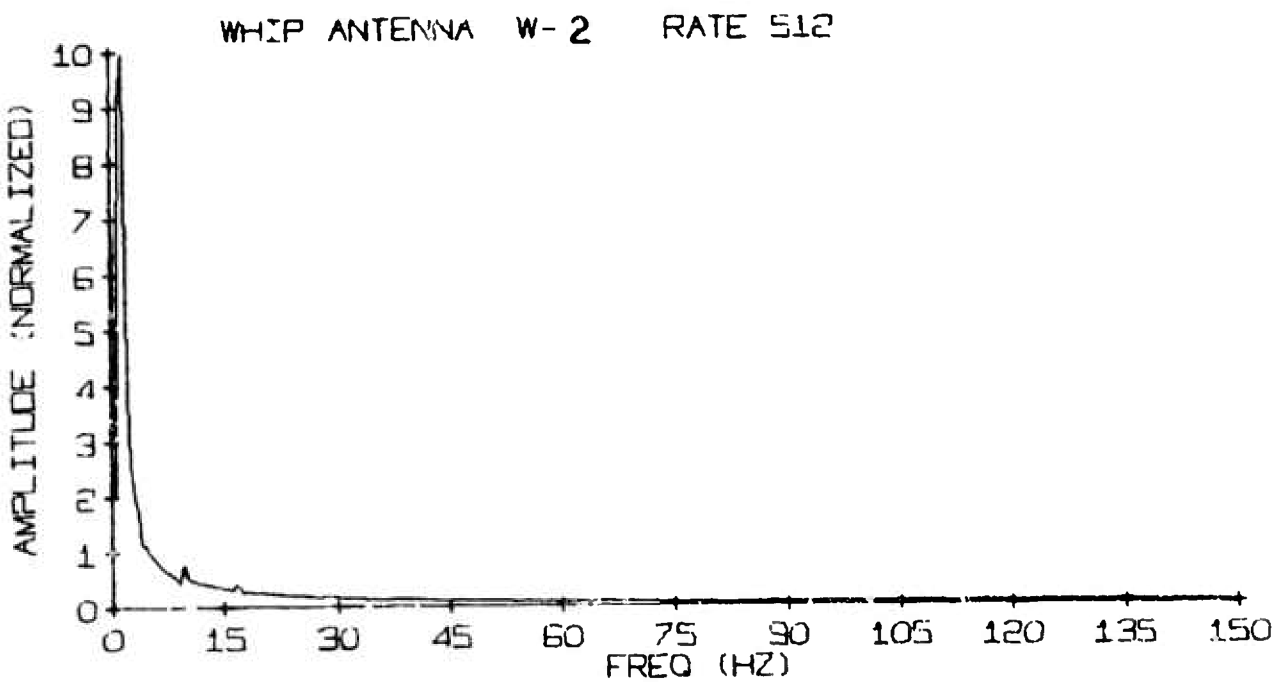

FIG. 7 TWAN' .EST BENDING STRAIN HISTORY AND CORRESPONDING FOURIER ANALYSIS FOR GAUGE 2.

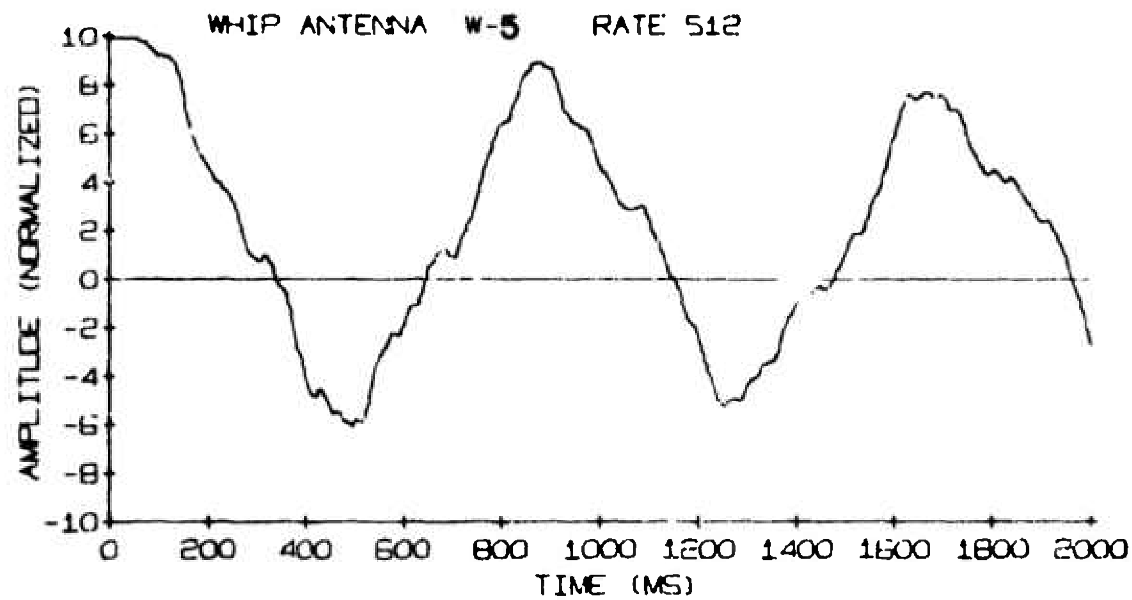

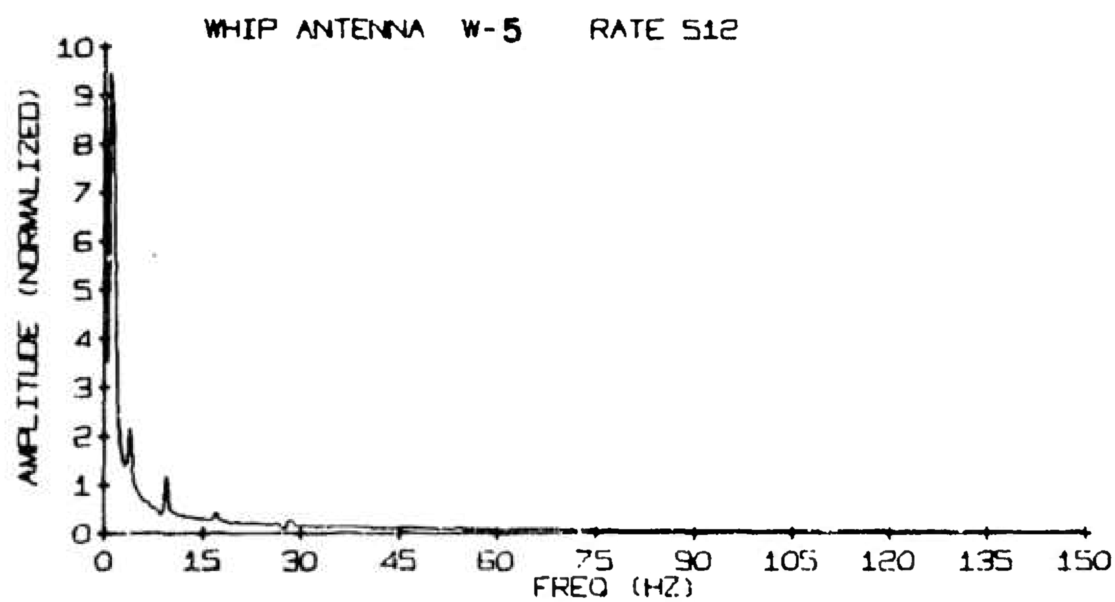

FIG. 8 TWANG TEST BENDING STRAIN HISTORY AND CORRESPONDING FOURIER ANALYSIS FOR GAUGE 5.

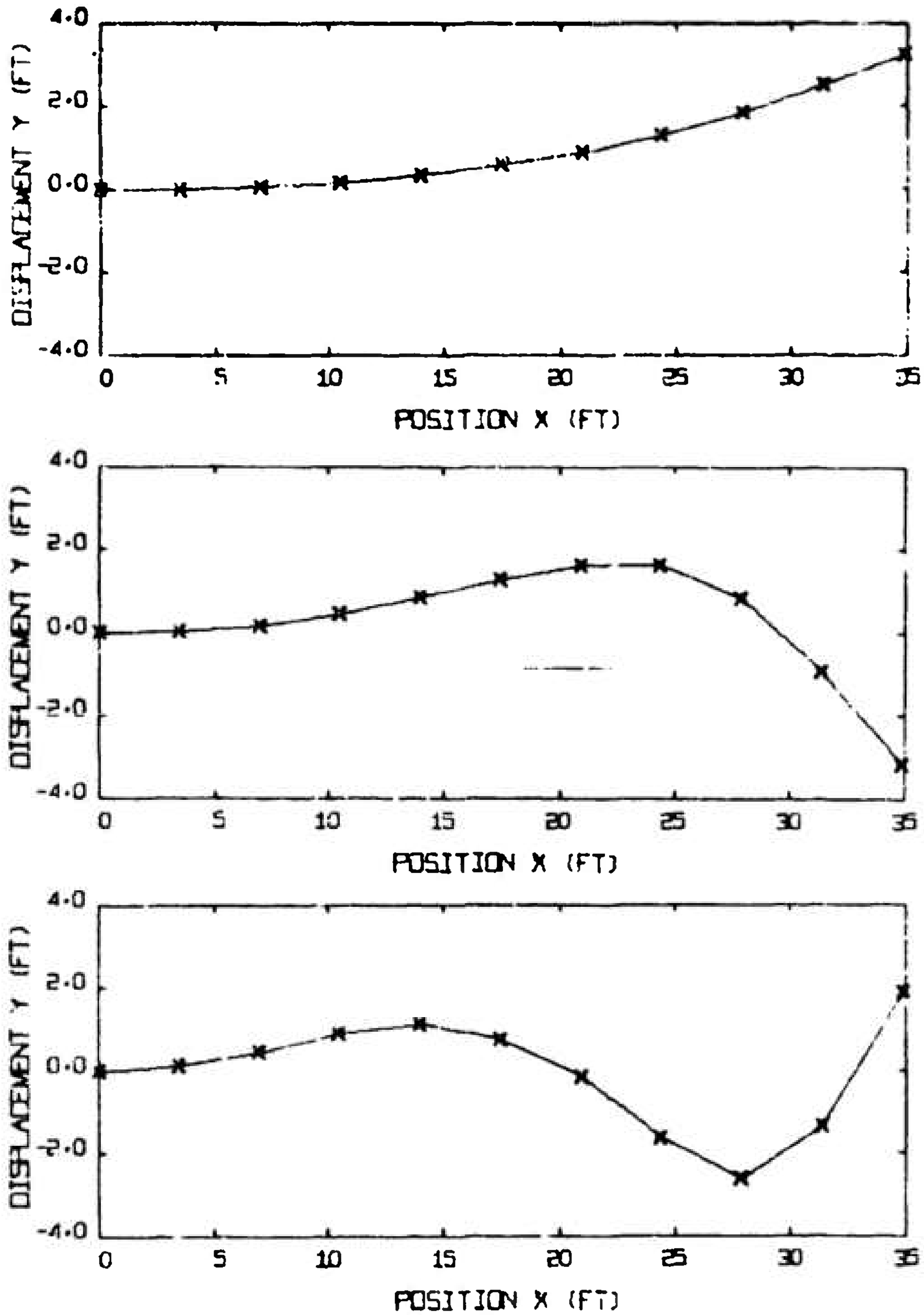

FIG. 9 THEORETICAL (NUMERICAL SIMULATION) PREDICTIONS FOR THE THREE LOWEST NATURAL FREQUENCIES AND CORRESPONDING NORMAL MODES FOR SIMULATION A OF THE 7.0 PSI WHIP ANTENNA.

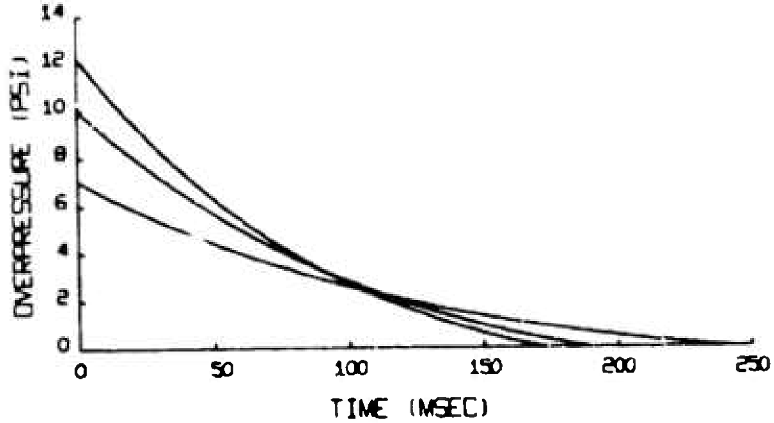

(a) WHIP ANTENNA - NOMINAL OVERPRESSURE

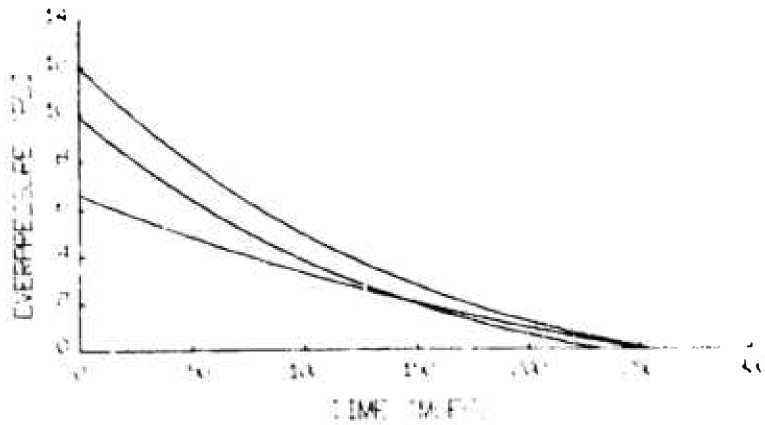

(b) WHIP ANTENNA - EXPERIMENTAL OVERPRESSURE

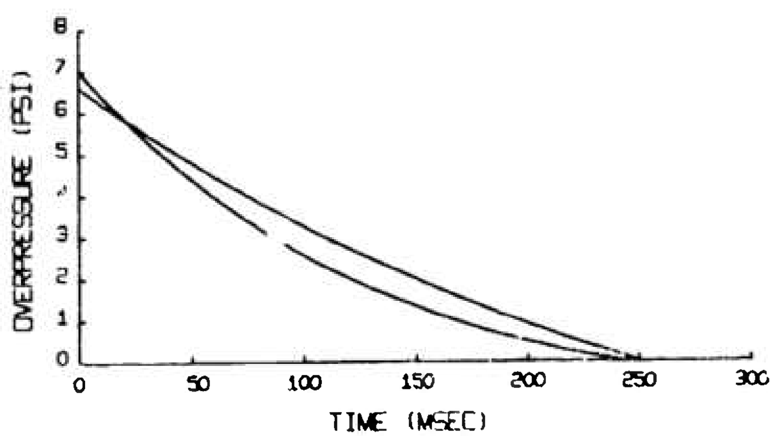

(c) NOMINAL VS. EXPERIMENTAL OVERPRESSURE

FIG. 10 FRIEDLANDER OVERPRESSURE WAVES AT THE NOMINAL 7.0, 10.0, AND 12.2 PSI PEAK OVERPRESSURE LOCATIONS WHICH CORRESPOND TO (A) PRE-TRIAL DNA PREDICTIONS (BLAST DATA A), (B) AVERAGE MEASURED BLAST WAVE PROPERTIES (BLAST DATA B), AND (C) COMPARISON OF THE DNA PREDICTION AGAINST THE MEASURED WAVE AT THE 7.0 PSI LOCATION.

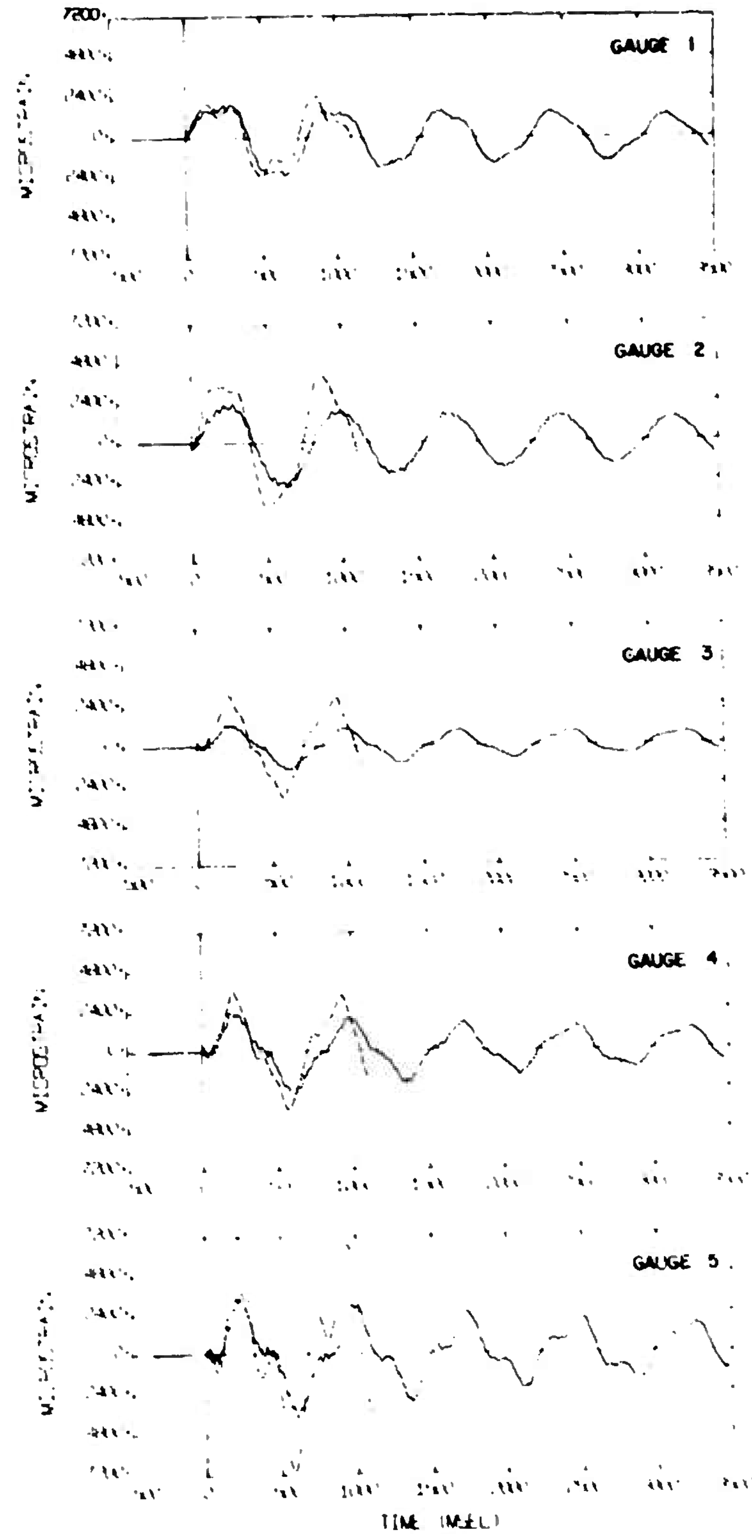

FIG. 11 COMPARISON OF BENDING STRAIN PREDICTIONS SET 1 (DASHED LINES) AGAINST THE MEASURED STRAINS (SOLID LINES) FOR THE 7.0 PSI WHIP ANTENNA AT GAUGE LOCATIONS 1 TO 5.

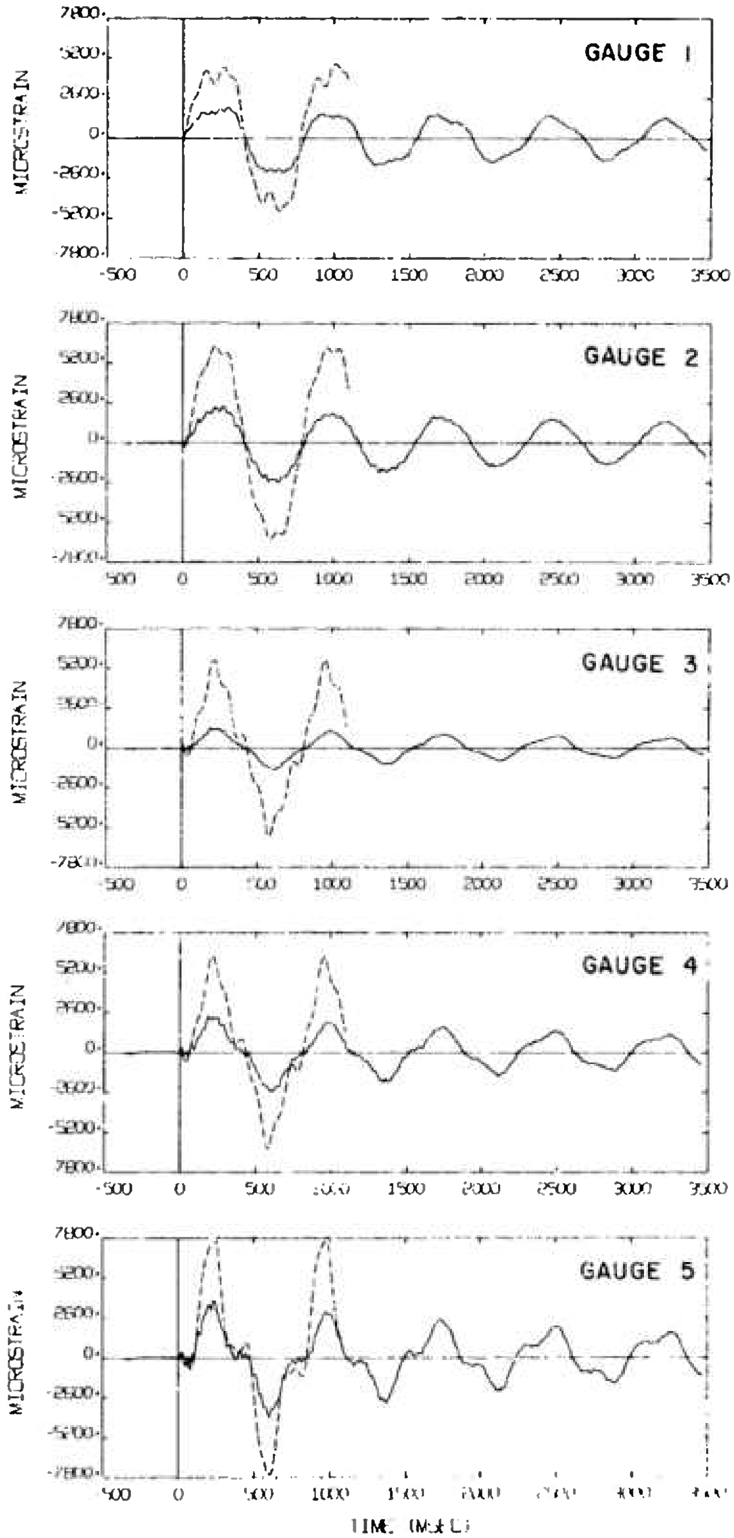

FIG. 12 COMPARISON OF BENDING STRAIN PREDICTIONS SET 2 (DASHED LINES) AGAINST THE MEASURED STRAINS (SOLID LINES) FOR THE 7.0 PSI WHIP ANTENNA AT GAUGE LOCATIONS 1 TO 5.

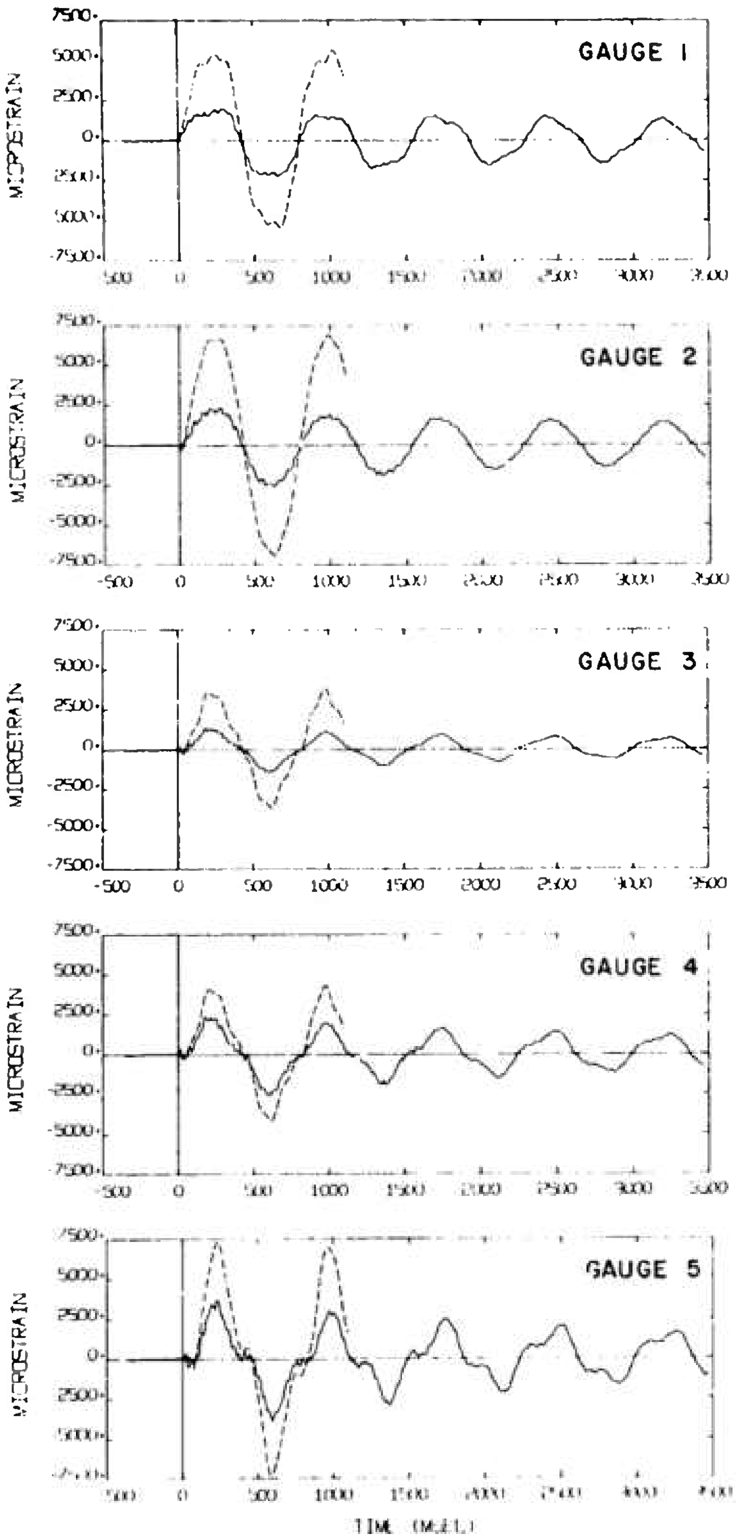

FIG. 13 COMPARISON OF BENDING STRAIN PREDICTIONS SET 3 (DASHED LINES) AGAINST THE MEASURED STRAINS (SOLID LINES) FOR THE 7.0 PSI WHIP ANTENNA AT GAUGE LOCATIONS 1 TO 5.

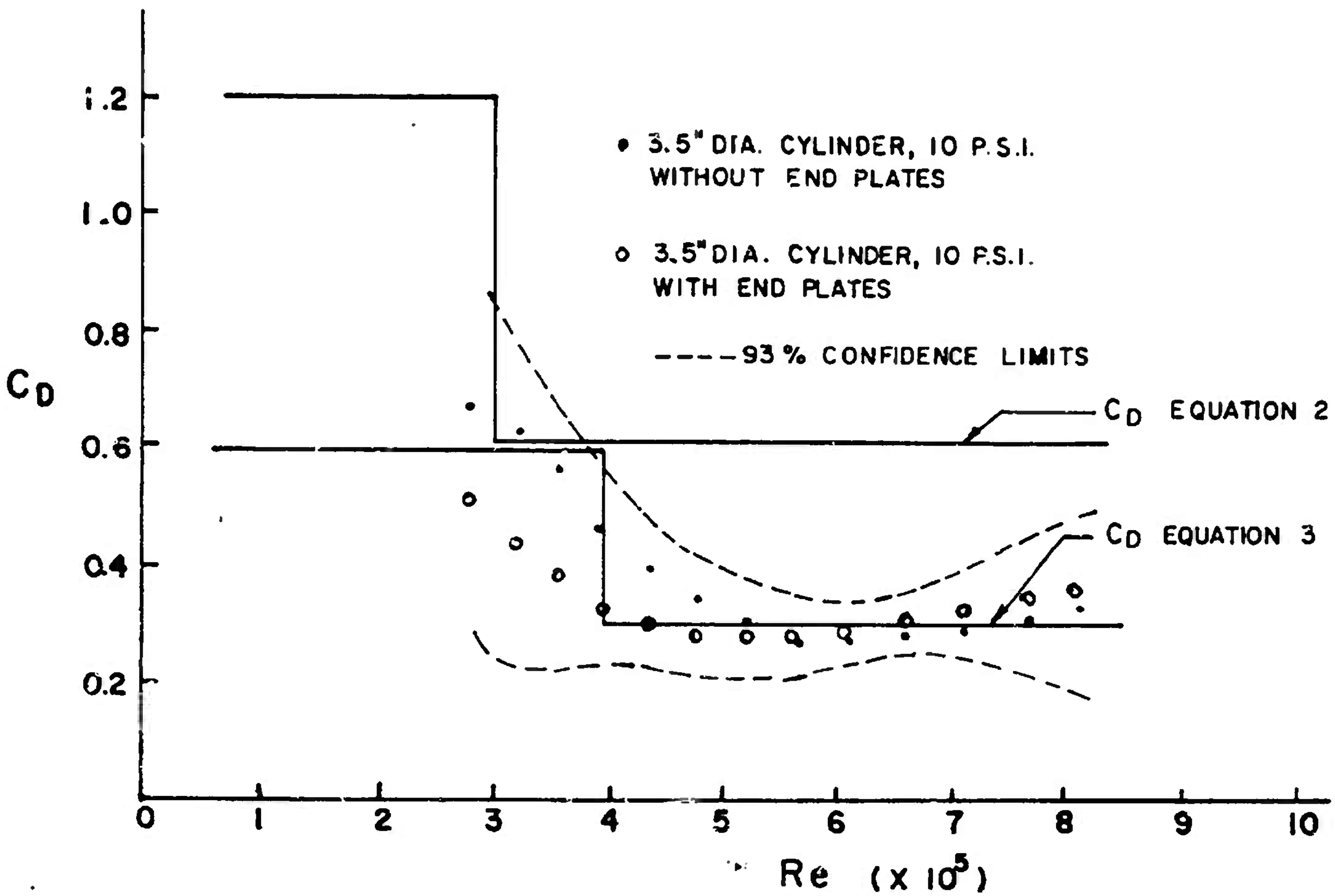

FIG. 14 PRELIMINARY DRAG COEFFICIENT PROFILES DETERMINED FROM THE DICE THROW DRAG EXPERIMENT [8].

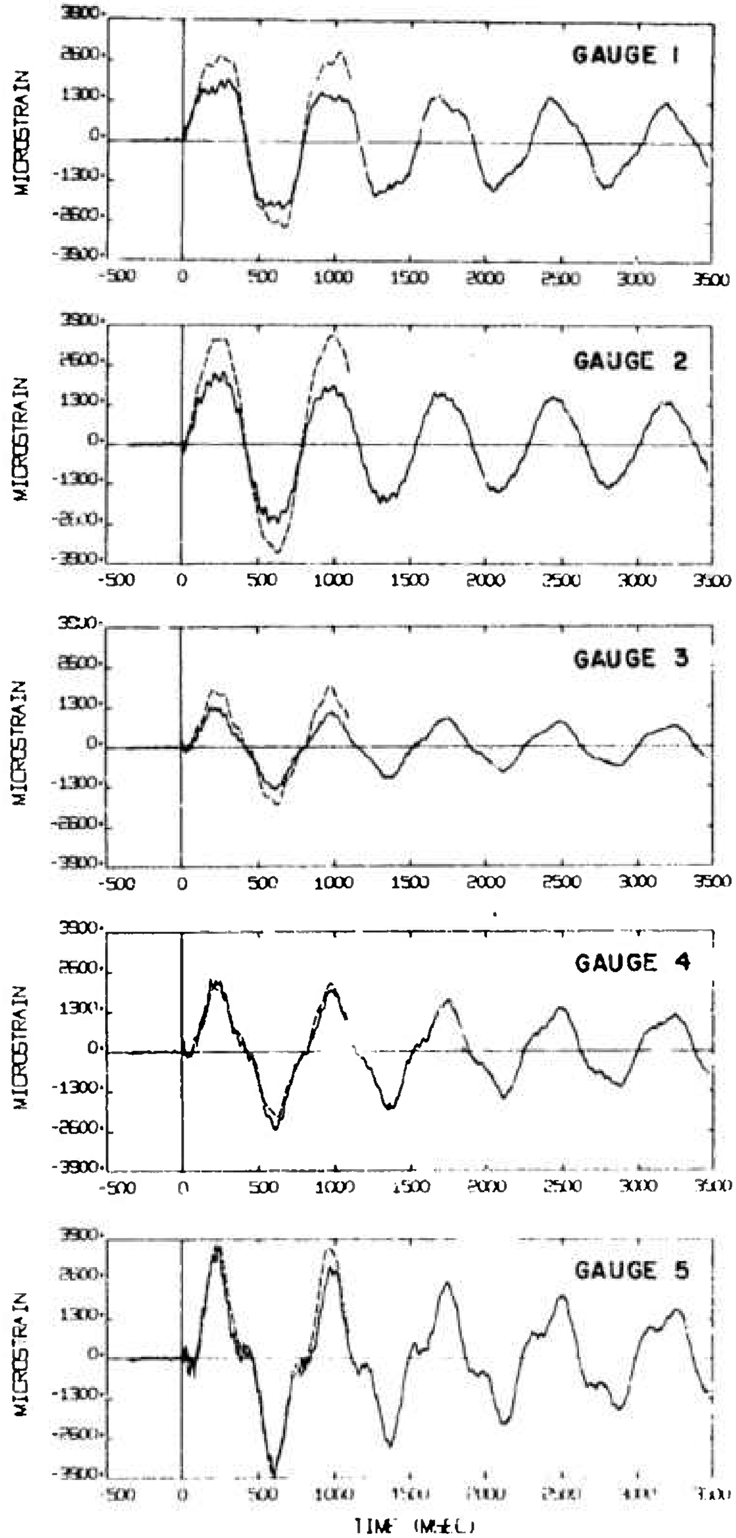

FIG. 15 COMPARISON OF BENDING STRAIN PREDICTIONS SET 4 (DASHED LINES) AGAINST THE MEASURED STRAINS (SOLID LINES) FOR THE 7.0 PSI WHIP ANTENNA AT GAUGE LOCATIONS 1 TO 5.

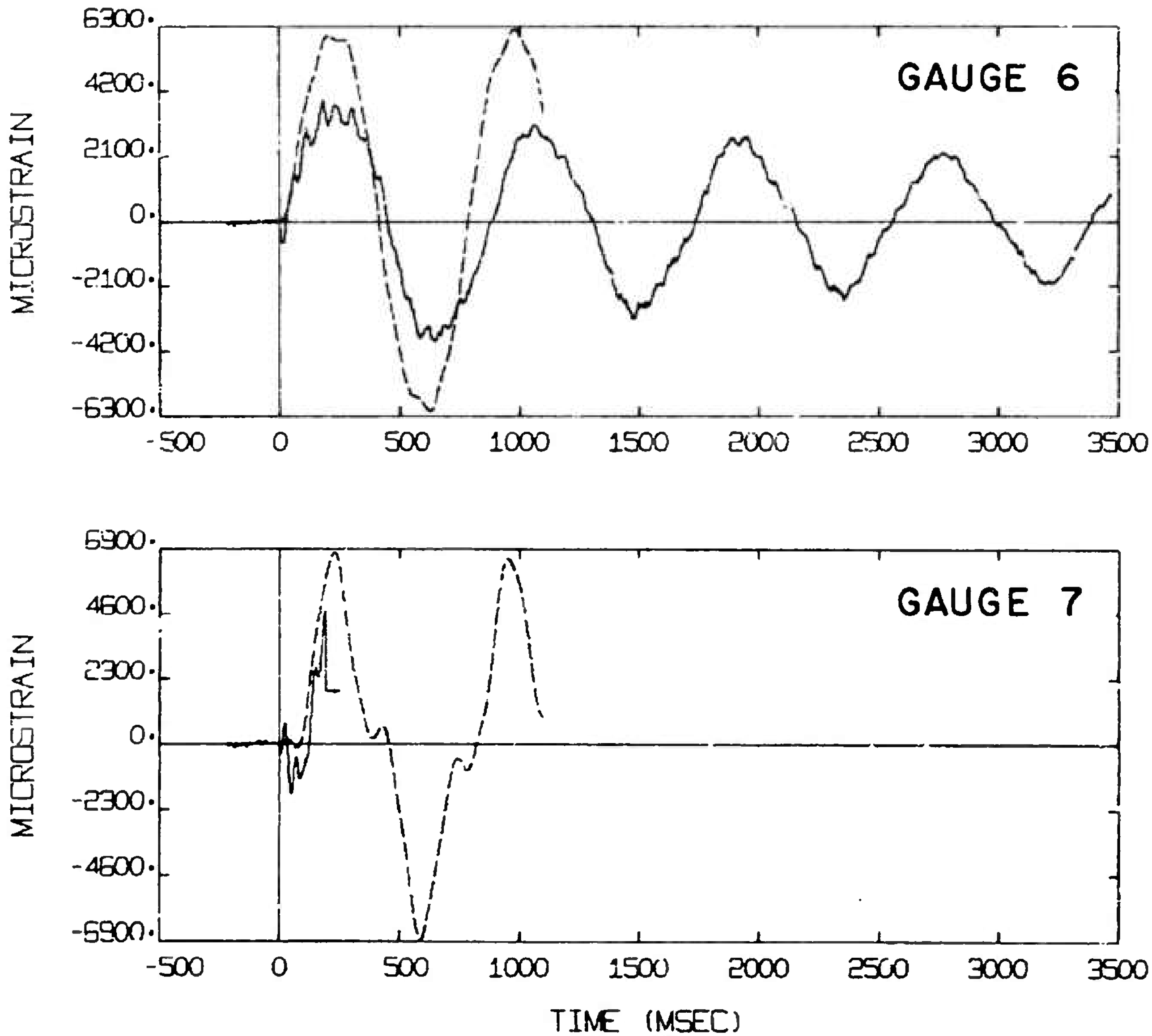

FIG. 16 COMPARISON OF BENDING STRAIN PREDICTIONS SET 4 (DASHED LINES) AGAINST THE MEASURED STRAINS (SOLID LINES) FOR THE 10.0 PSI WHIP ANTENNA AT GAUGE LOCATIONS 6 AND 7.

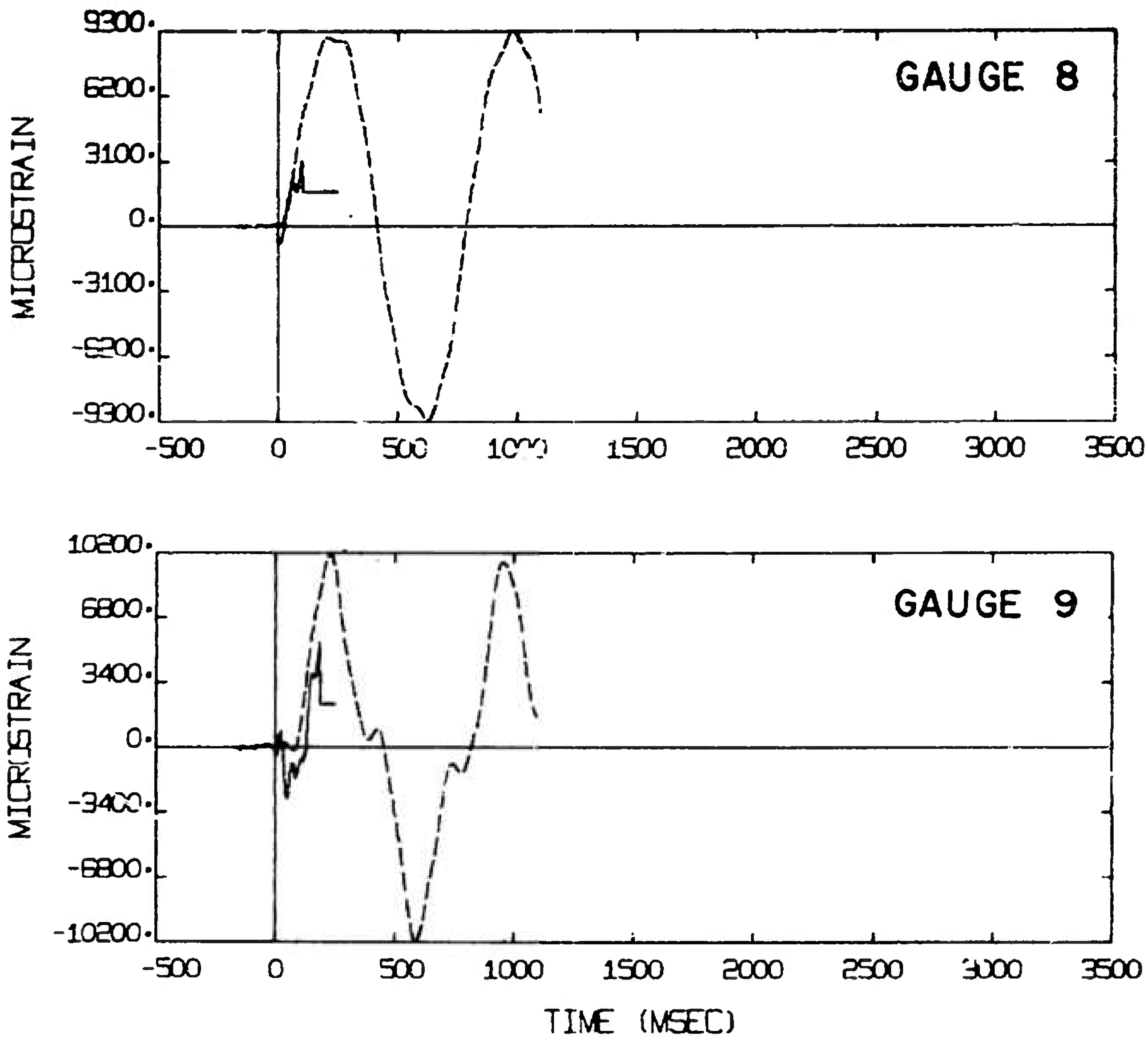

FIG. 17 COMPARISON OF BENDING STRAIN PREDICTIONS SET 4 (DASHED LINES) AGAINST THE MEASURED STRAINS (SOLID LINES) FOR THE 10.0 PSI WHIP ANTENNA AT GAUGE LOCATIONS 8 AND 9.

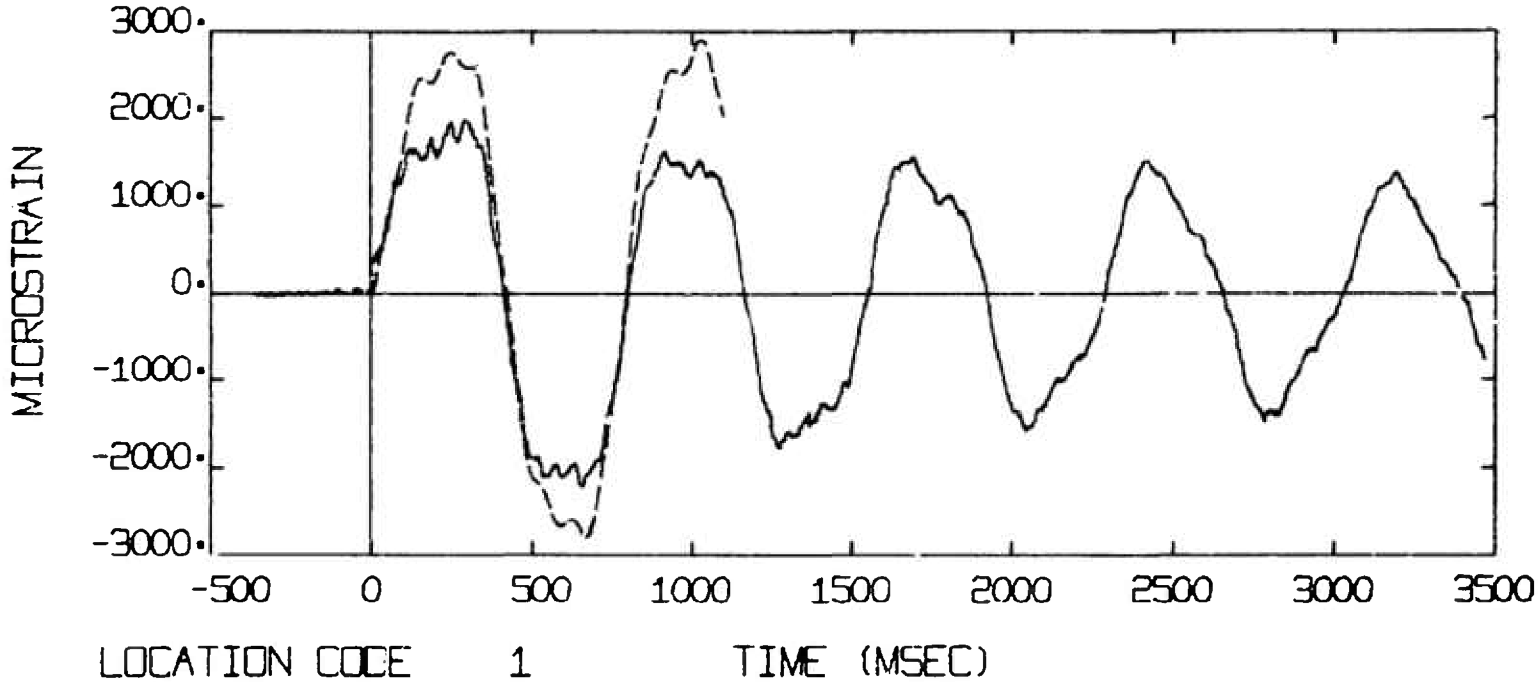

FIG. 18 COMPARISON OF BENDING STRAIN PREDICTIONS SET 4 (DASHED LINES) AGAINST THE MEASURED STRAINS (SOLID LINES) FOR THE 7.0 PSI WHIP ANTENNA AT GAUGE LOCATION 1.

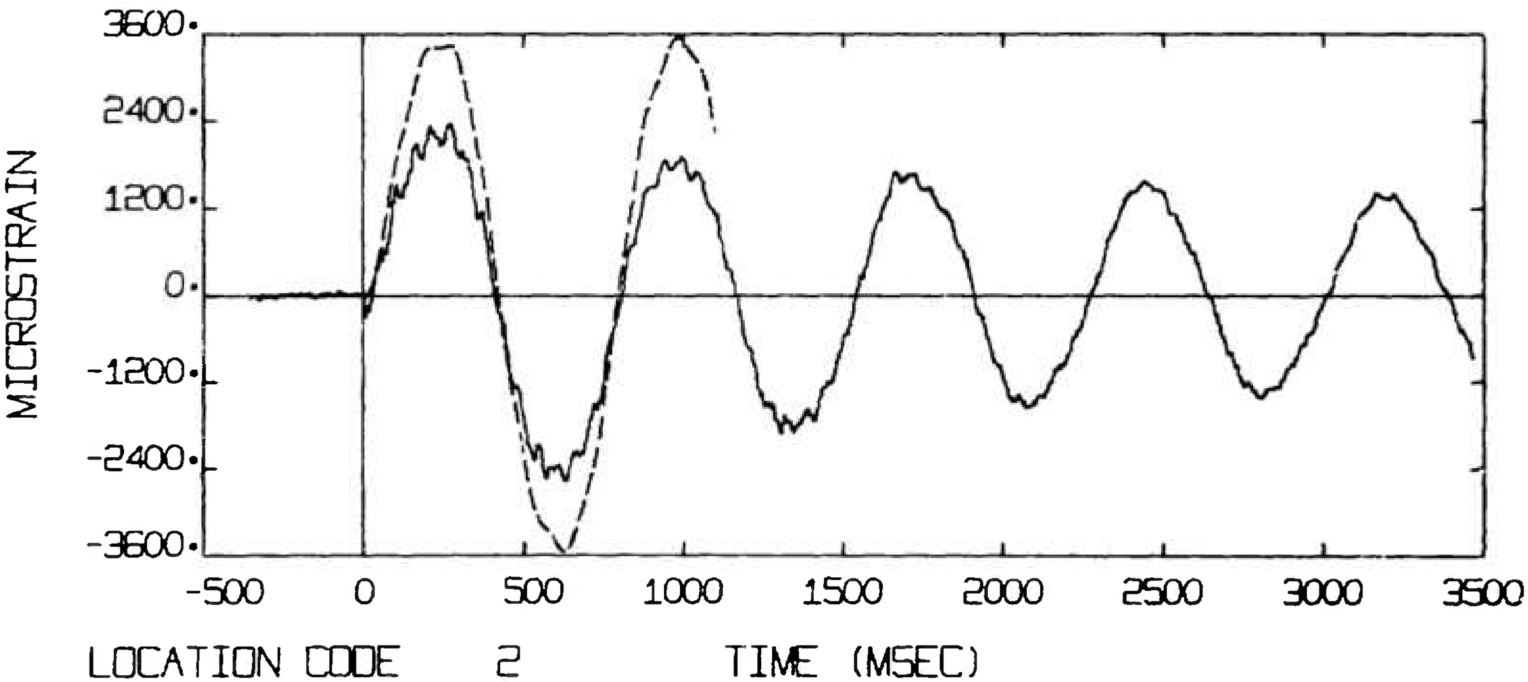

FIG. 19 COMPARISON OF BENDING STRAIN PREDICTIONS SET 4 (DASHED LINES) AGAINST THE MEASURED STRAINS (SOLID LINES) FOR THE 7.0 PSI WHIP ANTENNA AT GAUGE LOCATION 2.

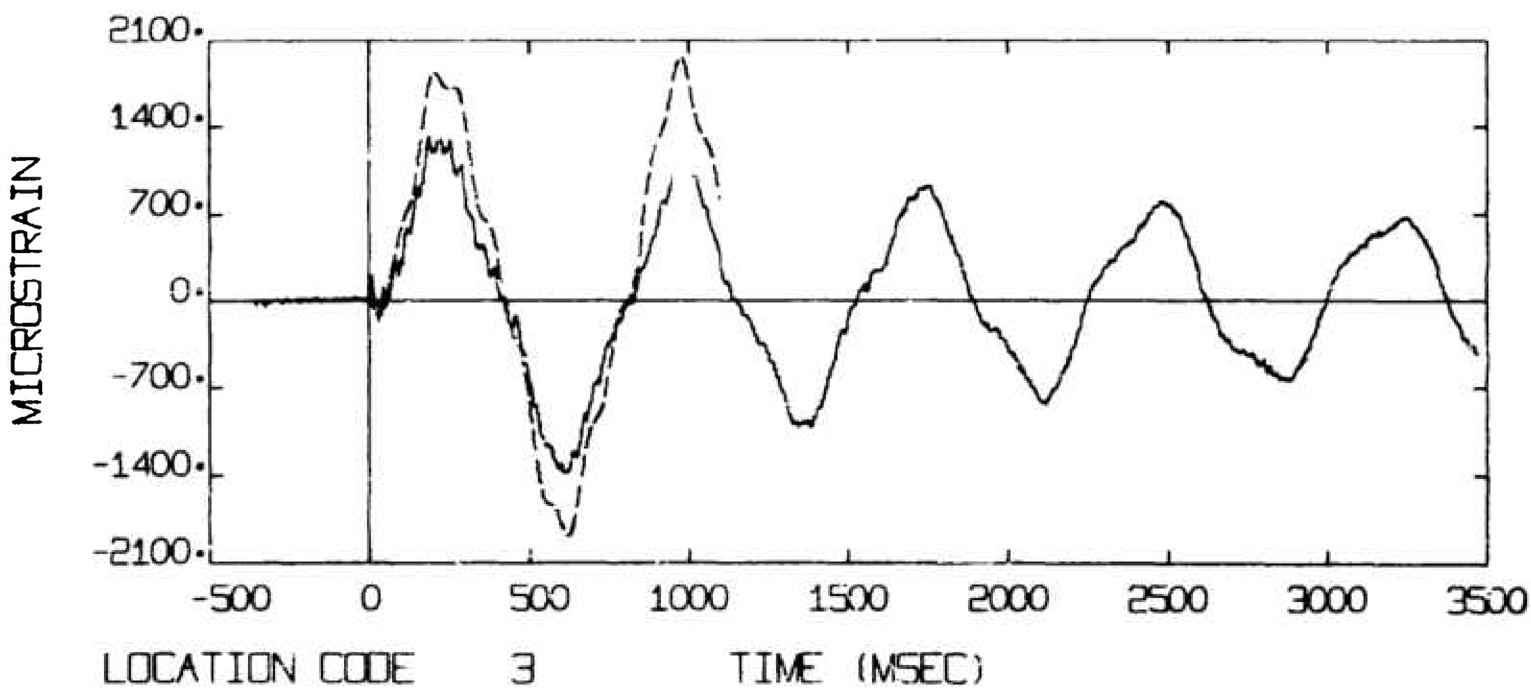

FIG. 20 COMPARISON OF BENDING STRAIN PREDICTIONS SET 4 (DASHED LINES) AGAINST THE MEASURED STRAINS (SOLID LINES) FOR THE 7.0 PSI WHIP ANTENNA AT GAUGE LOCATION 3.

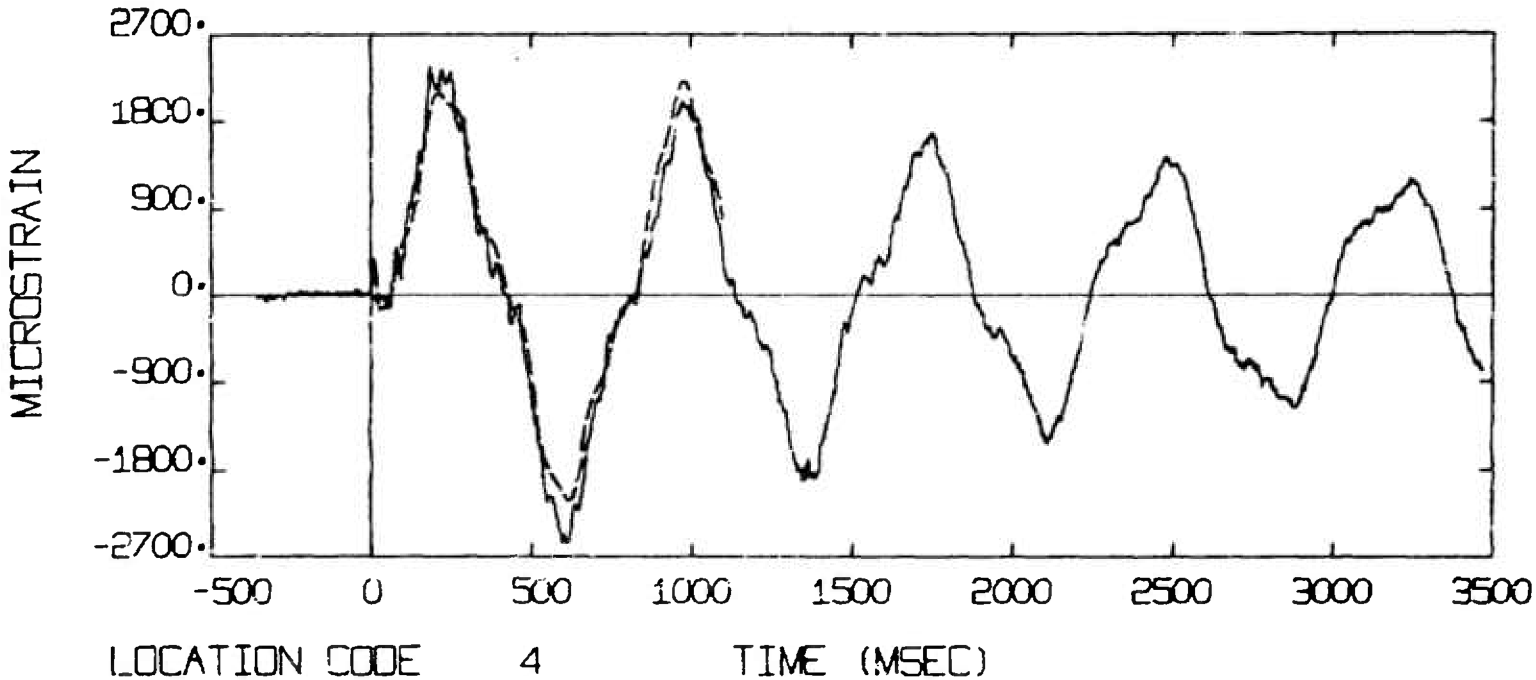

FIG. 21 COMPARISON OF BENDING STRAIN PREDICTIONS SET 4 (DASHED LINES) AGAINST THE MEASURED STRAINS (SOLID LINES) FOR THE 7.0 PSI WHIP ANTENNA AT GAUGE LOCATION 4.

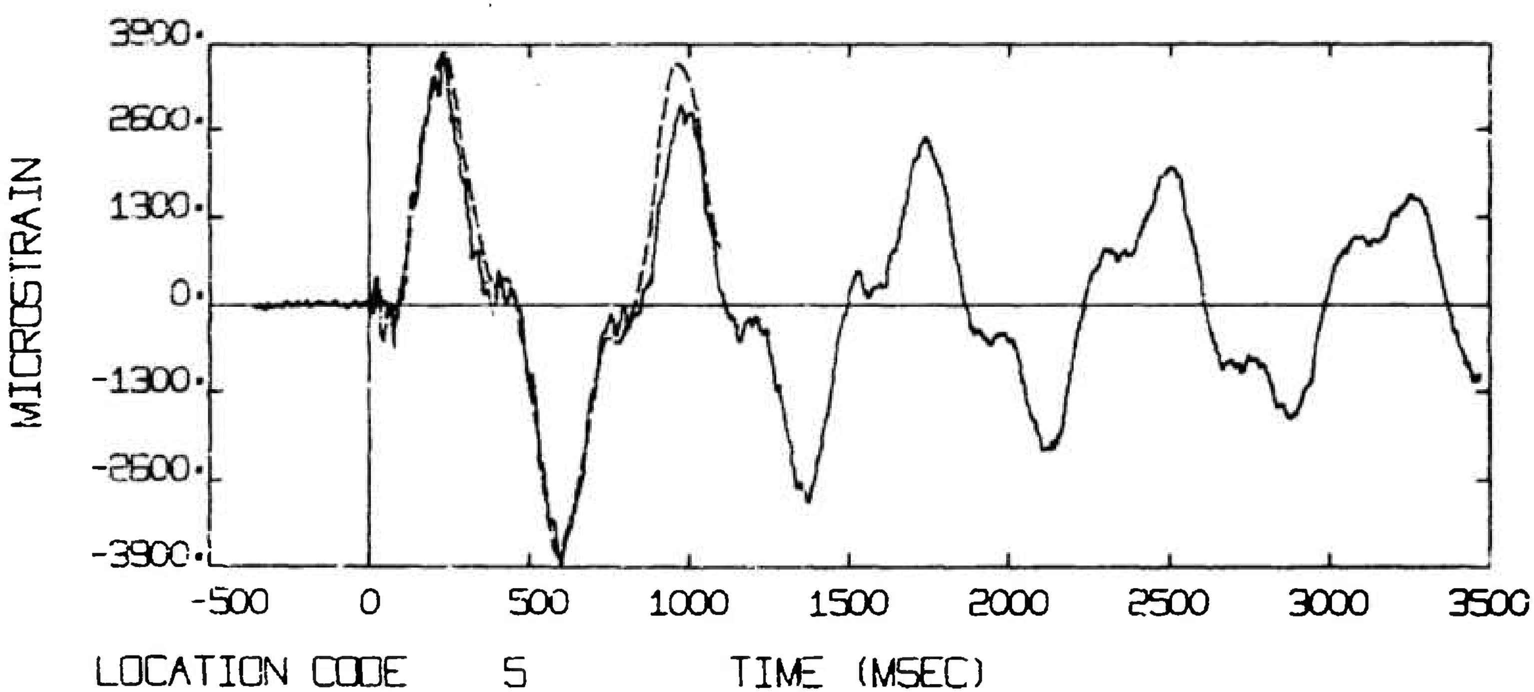

FIG. 22 COMPARISON OF BENDING STRAIN PREDICTIONS SET 4 (DASHED LINES) AGAINST THE MEASURED STRAINS (SOLID LINES) FOR THE 7.0 PSI WHIP ANTENNA AT GAUGE LOCATION 5.

21. PROJECT C-5, CANADIAN AIR BLAST MEASUREMENTS - EVENT DICE THROW

by

F.H. Winfield

Defence Research Establishment Suffield

3. PROJECT C5 CANADIAN AIR BLAST MEASUREMENTS - EVENT DICE THROW

F.H. Winfield
Defence Research Establishment Suffield
Ralston, Alberta, Canada

ABSTRACT

Results are presented for air blast measurements made in the Canadian sector in Event Dice Throw. These measurements were made in support of other Canadian projects whose objectives were the study of aerodynamic drag on circular cylinders and the determination of the structural response of Canadian Navy masts and antennae. A total of seventeen strain-type pressure gauges, mounted six inches above ground level and located at strategic points between the 50 psi and 5 psi peak overpressure locations, recorded overpressure-time histories. The measured values for peak overpressure impulse, and positive duration were quite close to the predicted values; the overpressure-time records showed classic waveforms. An anomaly which developed to the east of the Canadian sector produced a weak shock wave which traversed diagonally across the layout behind the main shock front.

INTRODUCTION

Canadian participation in Event Dice Throw was comprised of five projects. Projects C1, C2 and C3 involved the measurement of structural response of a lattice mast, UHF polemast and three whip antennae, respectively. Project C4 involved the measurement of aerodynamic drag on cylinders due to the passage of the blast wave and Project C5 involved measurement of the blast environment to which Projects C1, C2, C3 and C4 were exposed. The layout of projects and associated pressure transducers is shown in Figure 1.

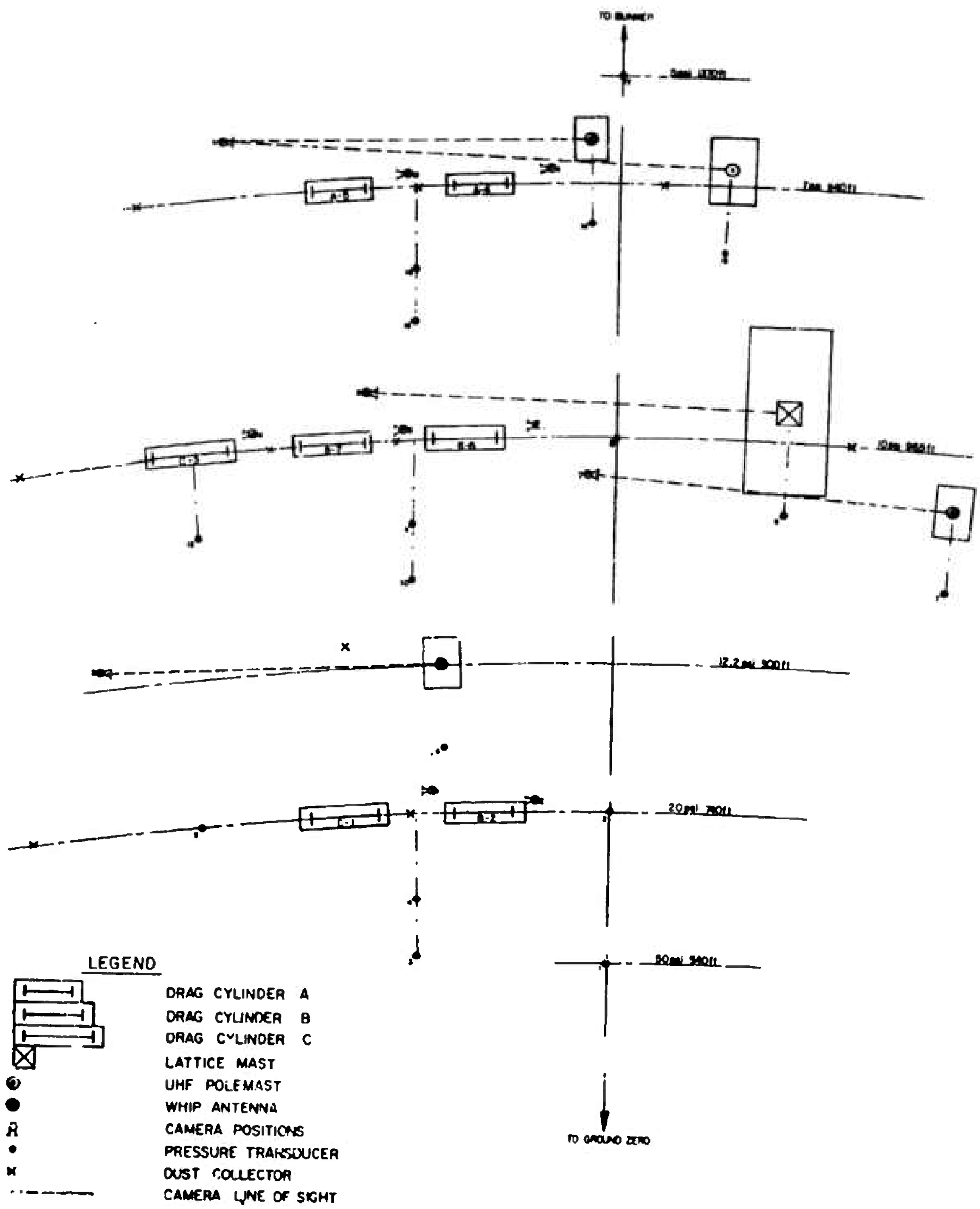

FIG. 1 LAYOUT OF PROJECTS IN CANADIAN SECTOR

INSTRUMENTATION

A total of 17 Bytrex model HFH-100 strain type pressure transducers was used in this event. Each transducer was mounted in an airfoil type stand so that the transducer was 6 inches above the surface of the ground. Fifteen of them were installed ahead of, or adjacent to, the structural response targets and the aerodynamic drag experiments to define the blast environment to which they were exposed and one transducer was installed at each of the 50 psi and 5 psi locations to extend the range over which pressure versus distance data would be obtained for this type of charge.

At the 20 psi, 10 psi and 7 psi levels, transducers were set out so that two transducers were on a radial line through ground zero. The time of arrival of the shock wave at the successive gauges would be used to calculate the shock front velocity from which peak overpressure could be calculated for comparison with the results obtained from individual transducers.

RESULTS AND DISCUSSION

All instrumentation functioned correctly and good quality records were obtained. The records from all the transducers are included in Appendix A.

The increase in overpressure seen on most of the records, at times varying from 20 msecs to 80 msecs after arrival of the shock front, was caused by a jet which developed to the east of the Canadian layout and produced a weak shock wave which moved diagonally across the layout behind the main shock front at these distances from ground zero.

The results obtained from the pressure-time records are presented in Table 1. Peak overpressure was obtained directly from the records, while time of arrival, positive duration and overpressure impulse were obtained by digitizing the records and using numerical integration techniques, (Ref. 1). Pressure-distance data and its relationship with the pre-test predictions (Ref. 2) are shown in Figure 2 as well as given in Table 1.

1. Anderson, J.H.B. and Fenrick, W.J., "Canadian Air Blast Measurements on Event Dial Pack" Suffield Technical Note No. 296, 1972.
2. "Airblast Predictions for Dice Throw", Defense Nuclear Agency, Field Command, 9 March, 1976.

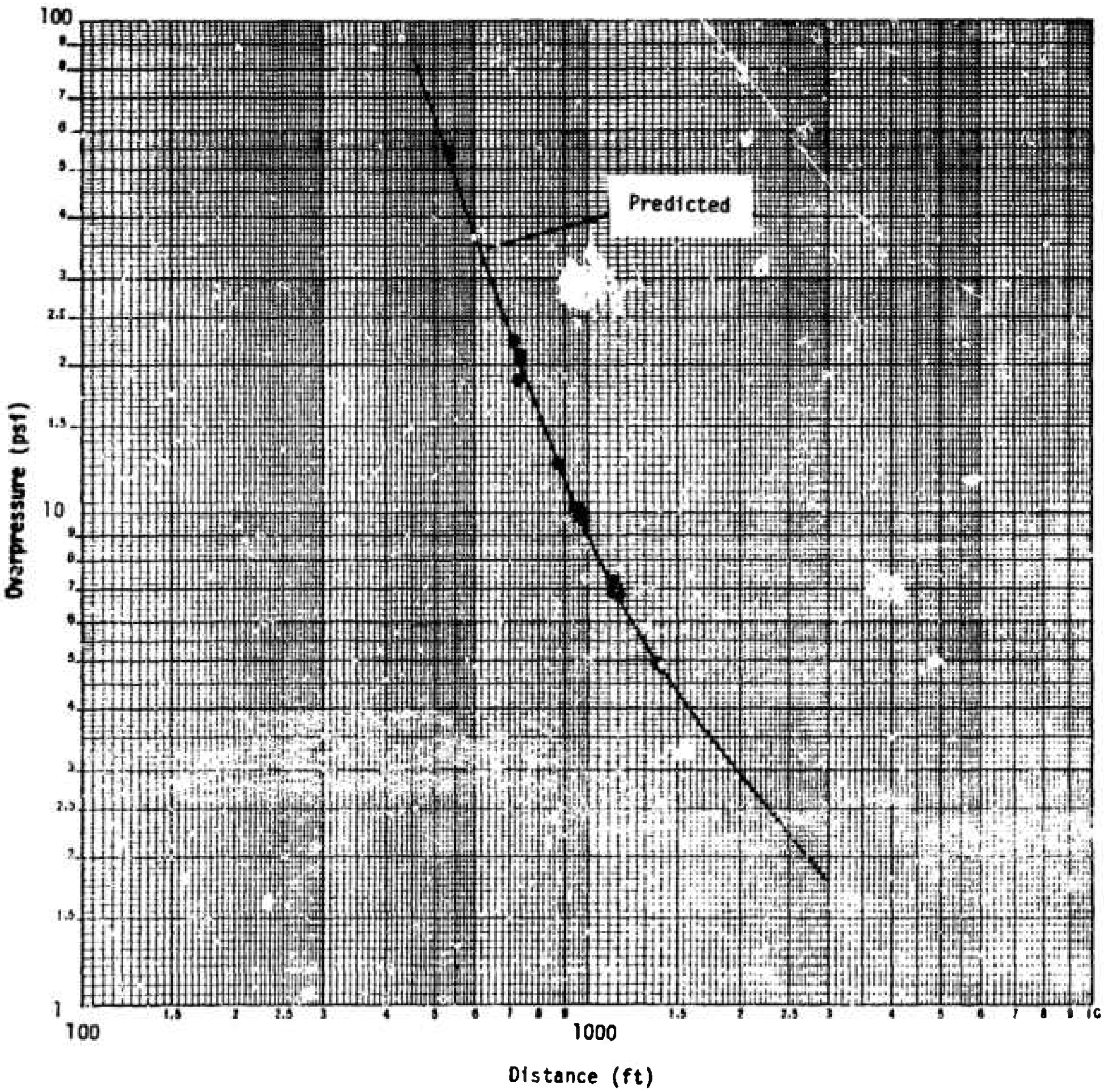

FIG. 2 COMPARISON OF PREDICTED AND MEASURED OVERPRESSURES

TABLE 1. SUMMARY OF RESULTS FROM PRESSURE-TIME TRANSDUCERS

Gauge Number (See Fig.2)	Location (See Fig.2)	Project Number	Distance from GZ (ft)	Predicted Overpressure (psi)	Shock Wave Time of Arrival (ms)	Positive Duration (ms)	Positive Overpressure Impulse (psi-ms)	Peak Overpressure (psi)	Overpressure from Velocity Pairs (psi)
1	pressure-distance	[illegible]	538.9	53	107.8	162.0	1325.5	54.7	
2	drag cylinder #2	C4	735.0	20.3	206	127.1	723.3	20.6	
3	drag cylinders #1&2	C4	713.9	21.8	193.8	168.2	1045.7	22.2	21.5
4	drag cylinders #1&2	C4	724.8	21.0	199.3	286.9	1609.9	21.5	
5	drag cylinder #1	C4	735.0	20.3	202.6	160.0	785.5	18.5	
6	whip antenna	C3	875.3	12.5	293.6	250.4	1130.6	12.5	
7	whip antenna	[illegible]	940.4	10.4	337.6	238.5	903.8	10.4	
8	lattice mast	[illegible]	949.8	10.7	344.2	229.3	829.1	10.5	
9	drag cylinder #6	C4	964.5	10.0	354.5	225.8	834.7	9.3	
10	drag cylinders #6&7	C4	940.0	10.4	337.5	144.4	479.5	10.0	10.1
11	drag cylinders #6&7	[illegible]	950.1	10.7	344.6	227.8	862.0	10.1	
12	drag cylinder #3	C4	953.2	10.6	347.3	230.0	846.9	9.8	
13	whip antenna	C3	1125.4	7.3	471.9	216.1	694.2	7.0	
14	UHF polemast	C2	1135.1	7.1	479.5	212.1	584.5	6.7	
15	drag cylinders #4&5	C4	1115.1	7.5	465.0	303.9	881.3	7.2	7.3
16	drag cylinders #4&5	C4	1125.0	7.3	472.4	242.0	700.0	6.9	
17	pressure-distance	C5	1369.4	5.0	661.1	298.4	619.2	4.9	

CONCLUSION

The results obtained from the air blast measurements carried out on Event Dice Throw to define the blast environment in the vicinity of the structural response and aerodynamic drag projects were close to those predicted. Pressure-distance data for a hemispherically capped, cylindrical 628-ton AN/FO charge were obtained between the 50 psi and 5 psi levels.

APPENDIX A

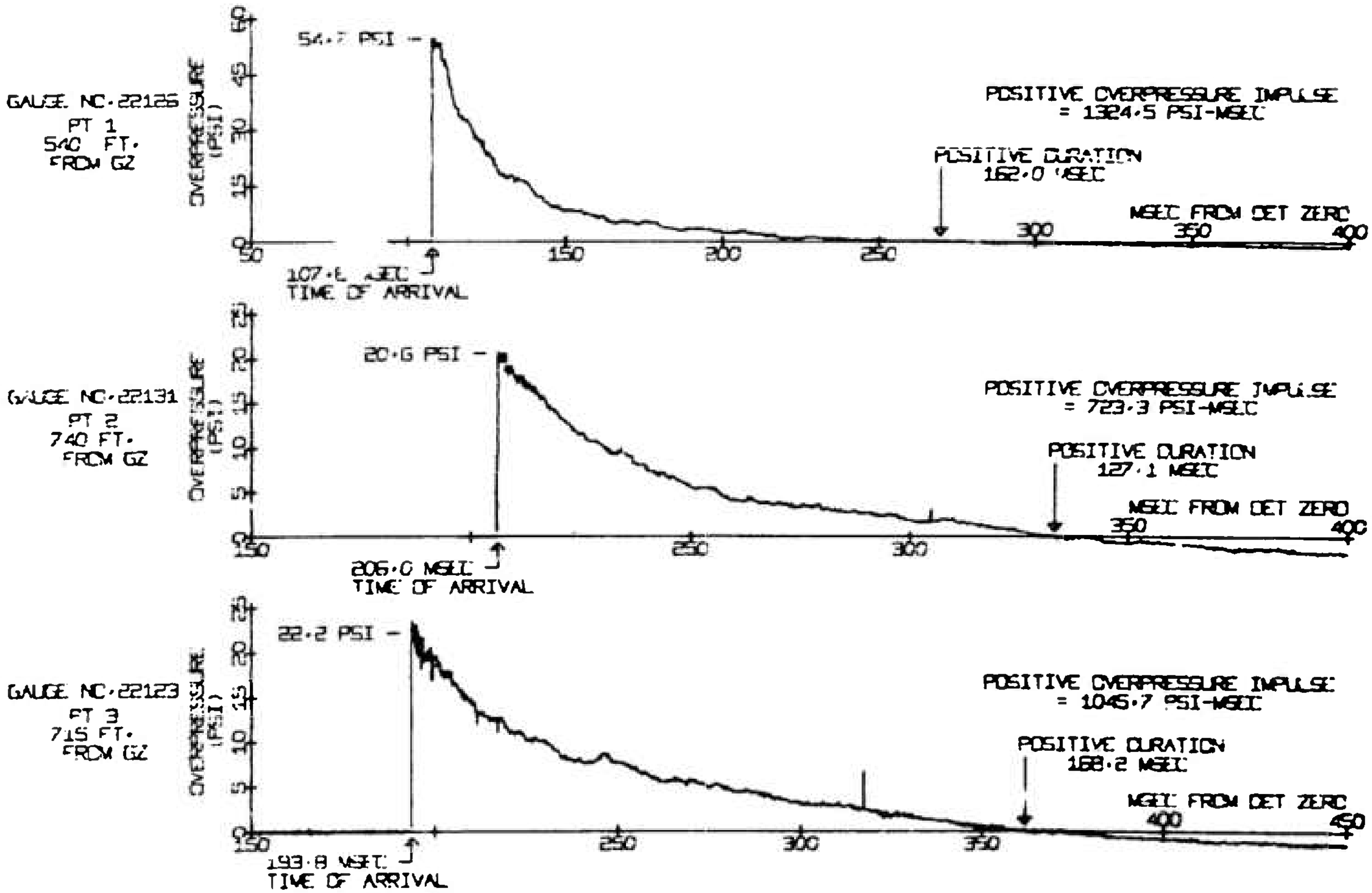

EVENT DICE THROW
PRESSURE TIME RECORDS

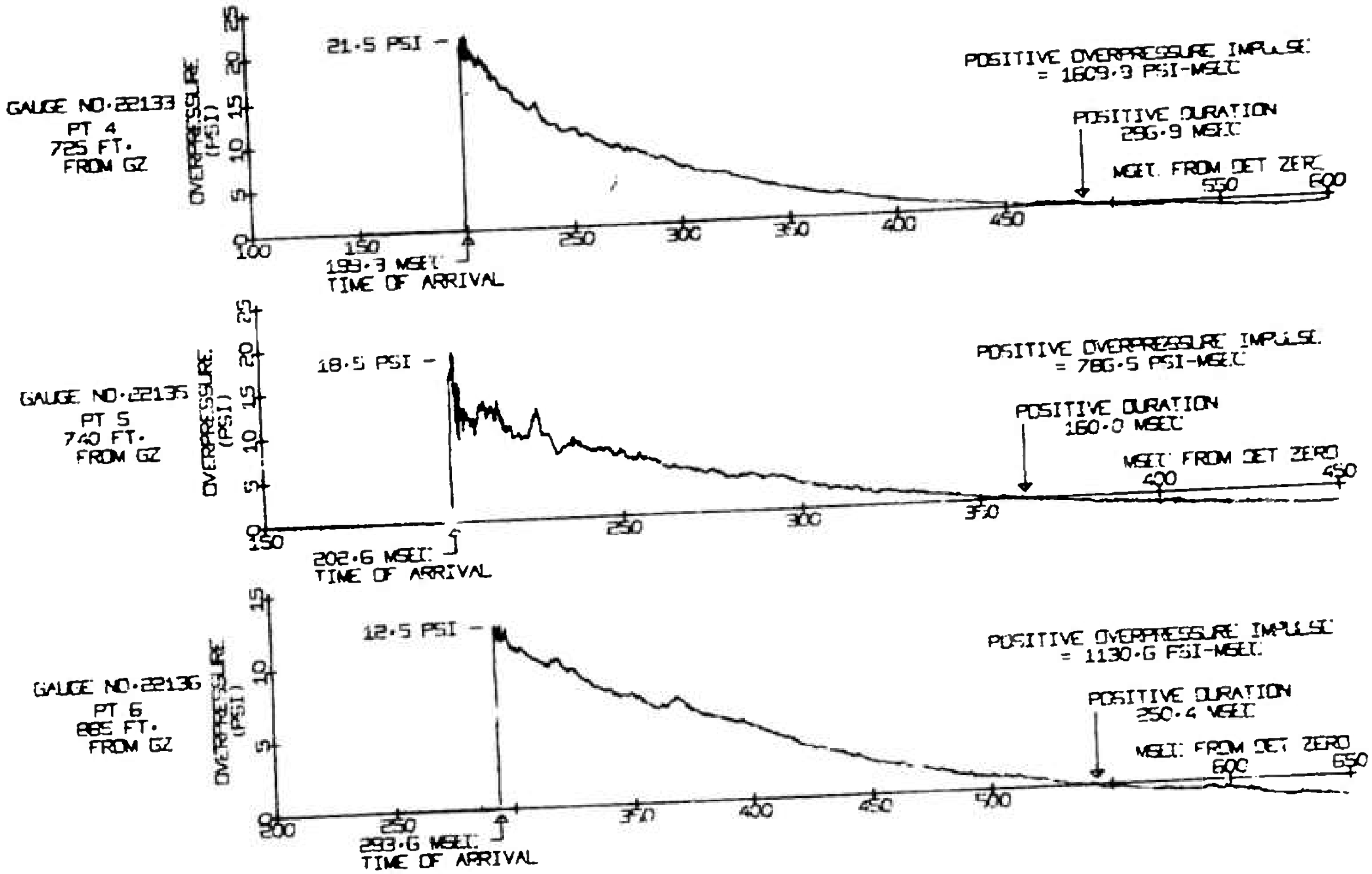

EVENT DICE THROW
PRESSURE TIME RECORDS

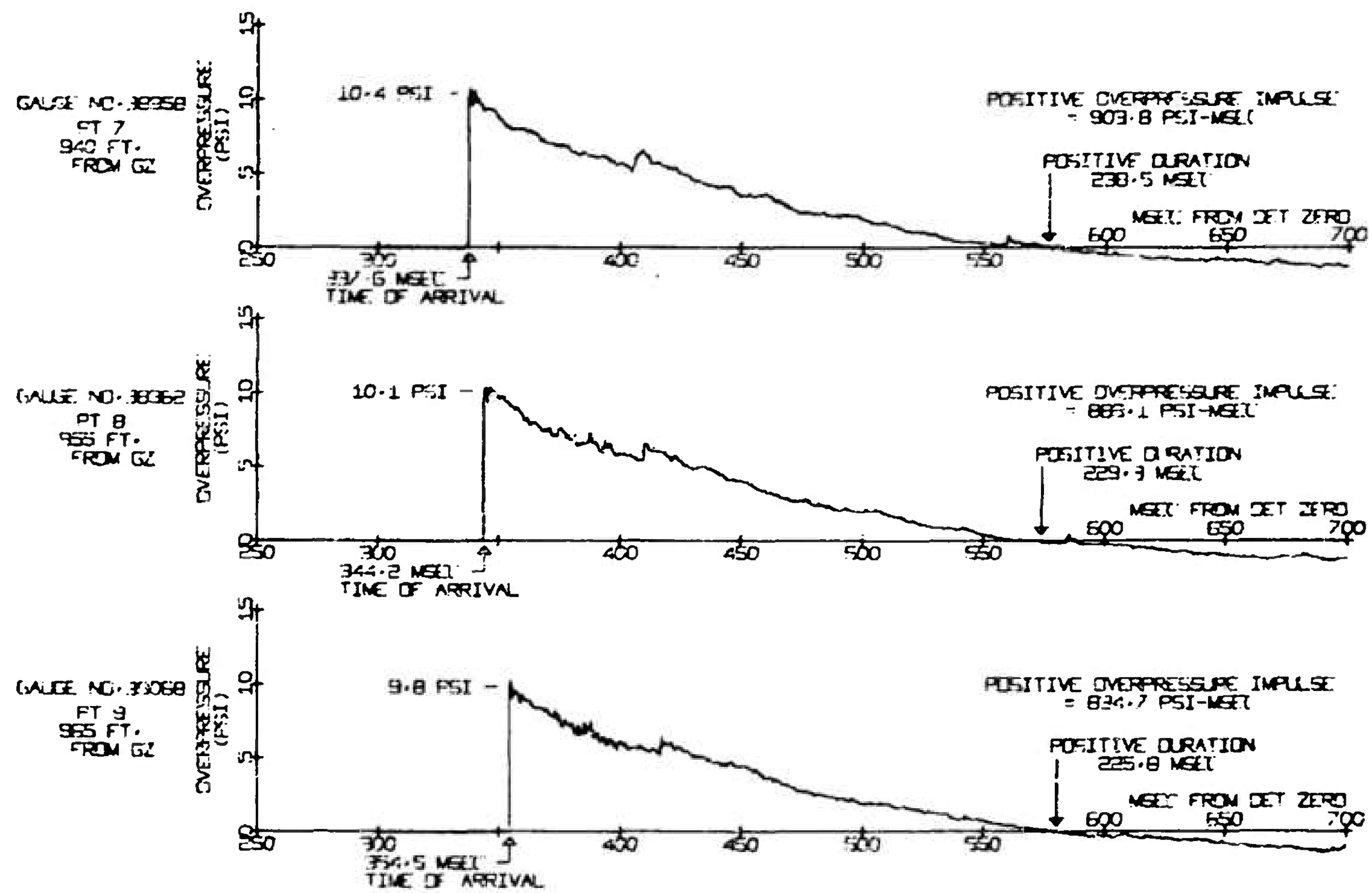

EVENT DICE THROW
PRESSURE TIME RECORDS

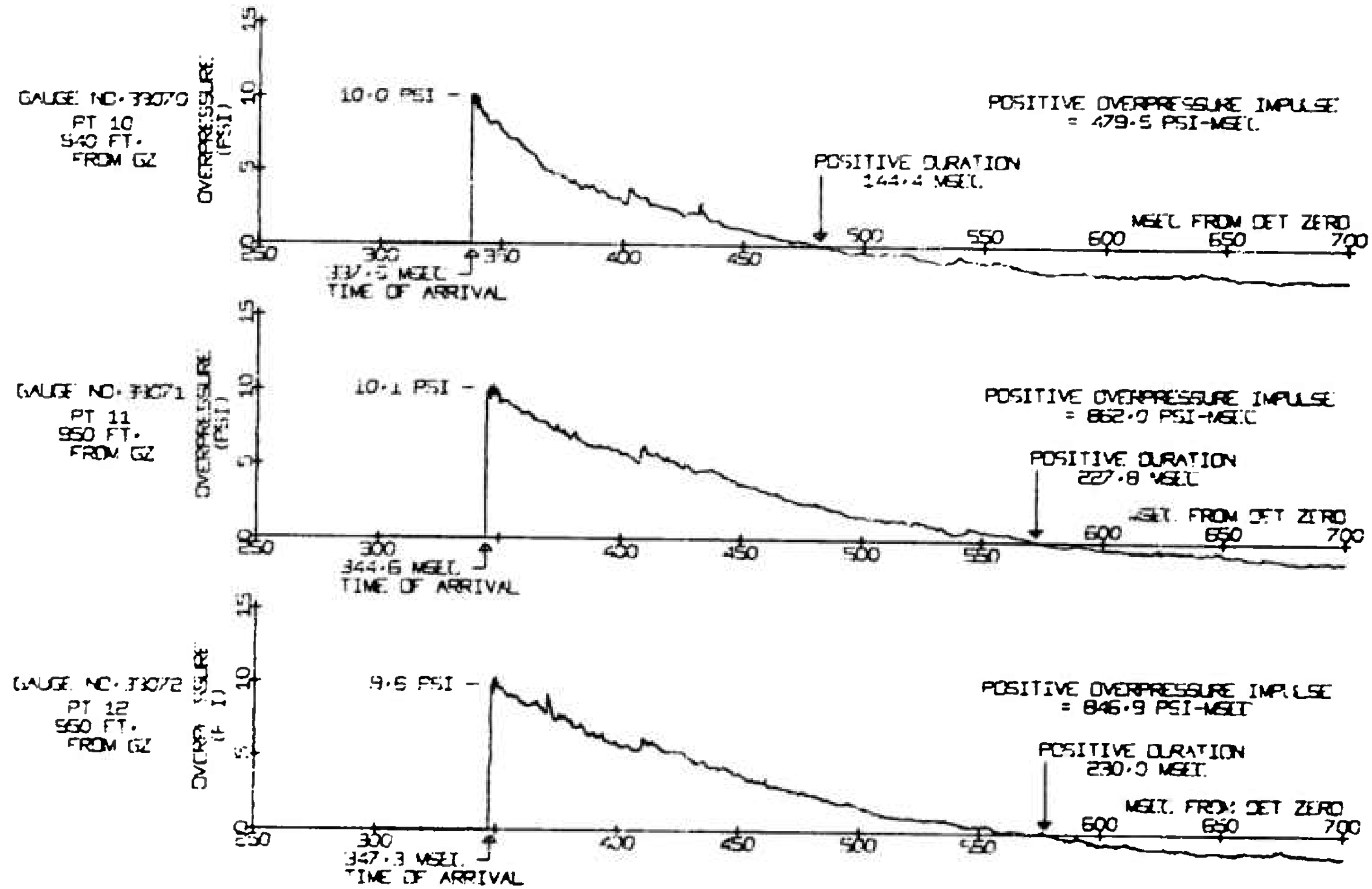

EVENT DICE THROW
PRESSURE TIME RECORDS

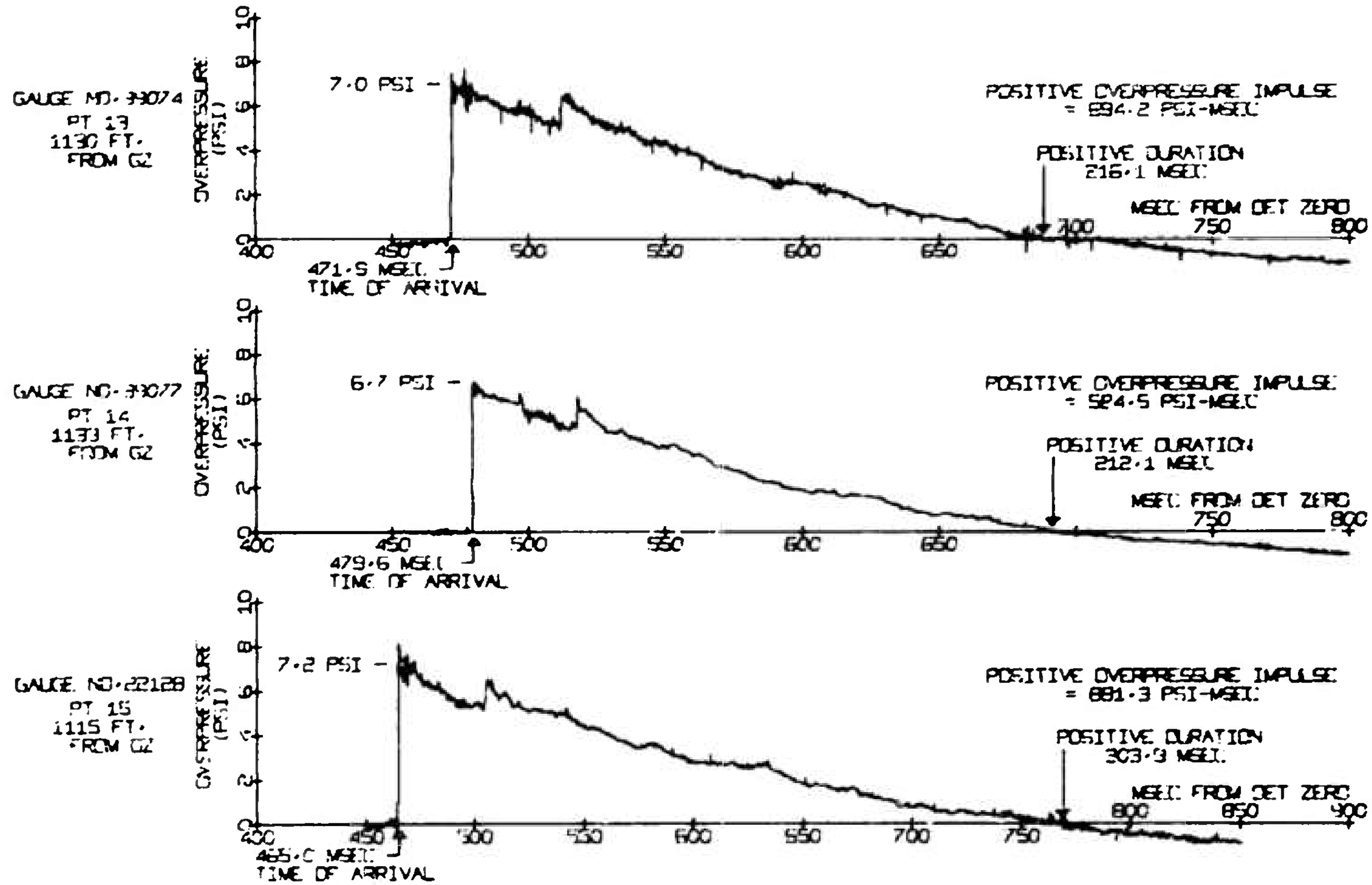

EVENT DICE THROW
PRESSURE TIME RECORDS

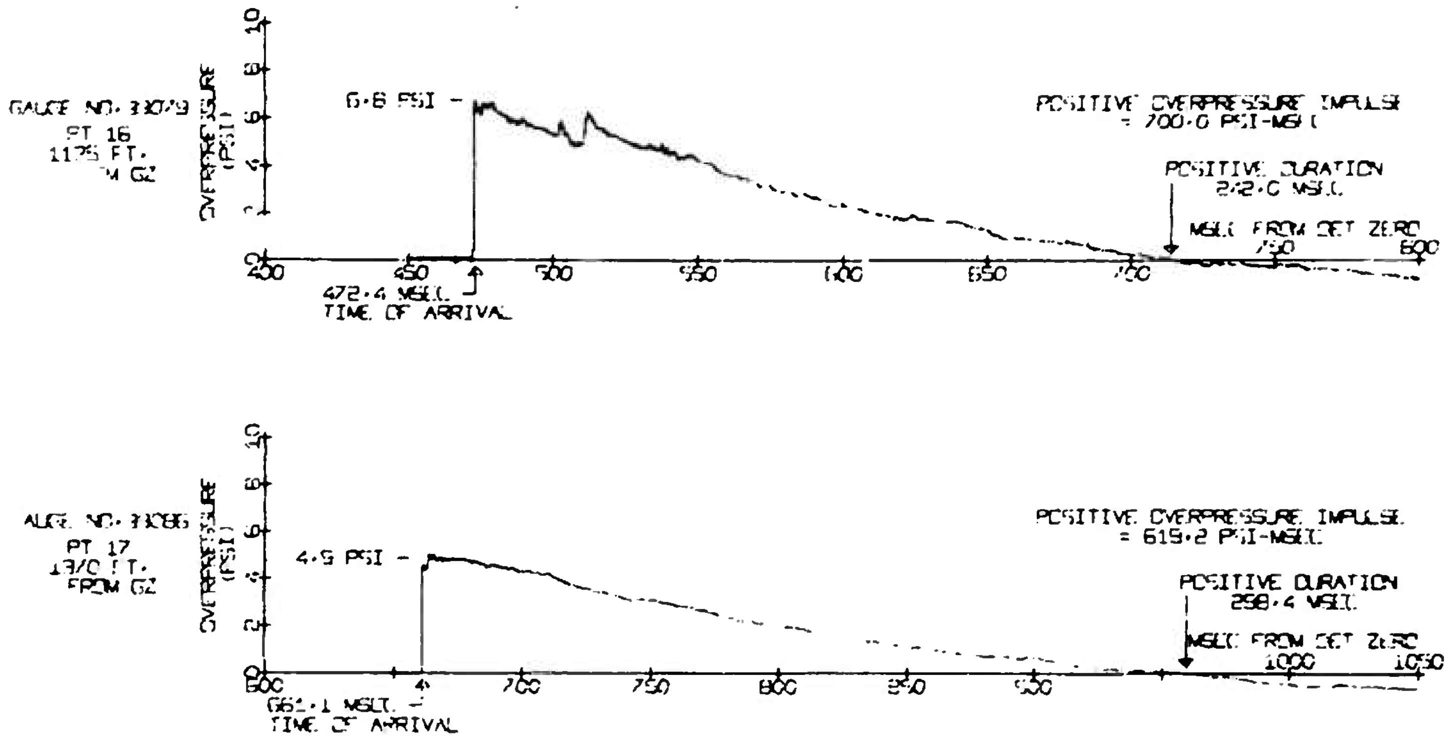

EVENT DICE THROW
PRESSURE TIME RECORDS

22. UHF/SHF TRANSMISSION EXPERIMENT

by

Alan A. Burns

SRI International

UHF/SHF TRANSMISSION EXPERIMENT

ABSTRACT

A UHF/SHF transmission experiment was fielded to measure the effects on signal propagation of the dust cloud lofted by the DICE THROW detonation. CW signals at eight frequencies between about 400 MHz and 10 GHz were transmitted along six paths penetrating the space above and near ground zero, although not all frequencies were used on each path. All the signals were derived from a common source, and, because a phase reference from the transmitter was supplied to the receiving system along a path skirting the detonation, phase as well as amplitude perturbations could be measured. Special photographic coverage designed to record the evolution of the dust cloud from several vantage points supplemented and supported the RF measurements.

Amplitude fluctuations were as great as 20 dB peak-to-peak at 400 MHz, and exceeded 50 dB at 10 GHz in some instances. A measured phase change of about 4 radians at 400 MHz on a path passing directly above ground zero corresponded to an integrated dust density, or dust content, of about 120 gm/cm^2; a uniform dust density of 4×10^{-3} gm/cm^3 over a 300-m dust cloud diameter would result in a 100-gm/cm^2 dust content. However, the possibility that diffraction distorted the phase measurements means that one should be cautious about associating phase shift with integrated dust density. Some decorrelation occurred between the fluctuations of signals spaced about 35 MHz apart, around 400 MHz.

Extensive dust clouds can be lofted by surface and near surface nuclear detonations. Such clouds may seriously affect communications and radar systems, particularly at shorter wavelengths, especially millimeter wavelengths. Experiments such as the one described here serve to quantify the effects of dust clouds on RF propagation.

I INTRODUCTION

SRI fielded a UHF/SHF transmission experiment, sponsored by the Atmospheric Effects Division of the Defense Nuclear Agency under Contract DNA001-75-C-0206, to measure the effects of dust and debris on signals passing through the cloud lofted by the DICE THROW main event. Since the explosion apparently lofted about 3 to 5 kt of soil, it simulated in at least one way a much larger nuclear detonation than its 500-ton TNT equivalent. Measurement of dust-induced perturbations and degradations of UHF and microwave signal propagation constituted the overall objective of this experiment.

An important specific objective of the transmission experiment was to provide inputs for developers of codes for predicting the effects and characteristics of dust clouds. Codes such as HULL, DUSTY, DICE, VORDUM, SCOUR, etc., are the only means of generalizing or extrapolating from one situation to another (e.g., HE to nuclear). Comparison between code predictions and experimental data for the DICE THROW test leads either to more confidence in the code predictions or to improvement of the codes themselves. The groundwork for comparisons between theory and experiment was begun prior to the DICE THROW test. This experiment was the first to measure amplitude and phase perturbations due to a dust cloud from an explosion.

Another objective was to establish an effects threshold. It is assumed that the nuclear situation will be far worse.

PRECEDING PAGE BLANK

The matter present in the dust cloud increases the refractive index of the medium, which causes a retardation of the phase of an RF signal passing through the cloud. This localized phase retardation, in turn, can give rise to refractive (focussing) and diffractive (scattering) effects that can seriously disrupt a communications (or radar) signal through effects such as fading and bandwidth reduction. Because the dust particles are also lossy, significant absorption of RF energy by the dust cloud can also occur. Scattering of RF energy out of the beam is a further source of attenuation. Other objectives of the experiment were to determine the relative magnitudes of the two components of attenuation and the phase shift and to establish their wavelength dependencies.

When all of the dust particles are much smaller than the wavelengths, the phase shift and absorption can be theoretically related in a very straightforward way to the integrated dust density through the cloud. Thus, in the absence of significant distortion due to diffractive effects, an average value for the dust density as a function of time can be computed. Such diagnostic measurements of dust density comprised another experimental objective.

These measurements have important implications for communications and radar systems. The much larger dust clouds following nuclear detonations may seriously disrupt SHF and EHF systems for prolonged periods of time. Even in the UHF range, a dust cloud could disturb a low-margin system. Thus it is important to quantify the effects of dust clouds on RF propagation in order to properly take them into account.

II EXPERIMENT DESCRIPTION

Figure 1 shows the layout of the UHF/SHF transmission experiment. A hardened main transmitting system was placed atop on earthen mound 630 m from ground zero. Its signals were received at three antenna locations about 4 km on the other side of ground zero. Path 1 went directly through ground zero, 11 m above the surface. The main

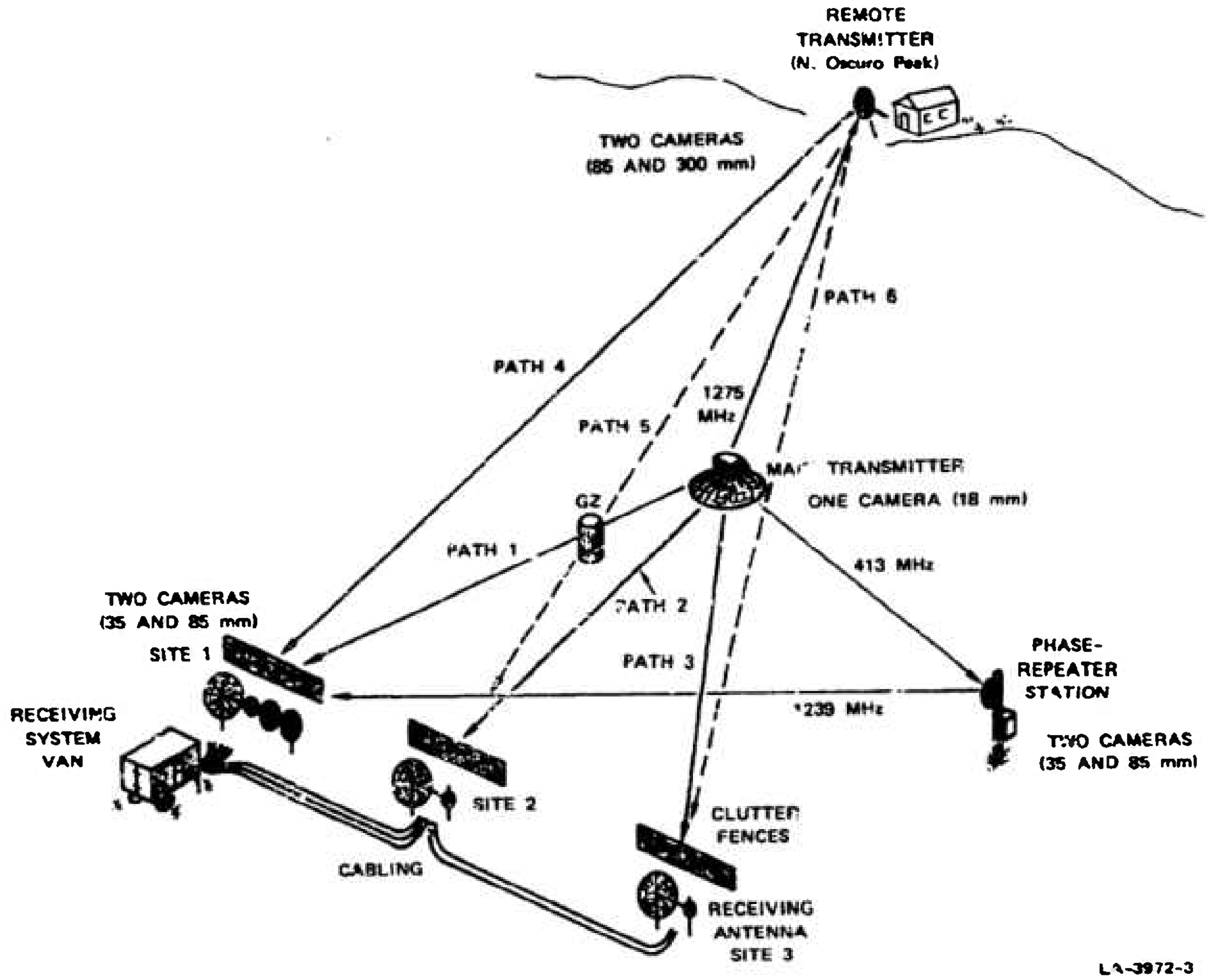

FIGURE 1 EXPERIMENTAL LAYOUT OF DICE THROW TRANSMISSION EXPERIMENT

transmitter location was a compromise between equipment survivability and the desire to reduce the Fresnel zone at ground zero, thus increasing the lateral spatial resolution of the experiment. A "phase repeater" system relayed a signal from the main transmitter around the region disturbed by the dust cloud to serve as the phase reference signal at the receiver. "Clutter fences" were constructed to help suppress ground-reflected multipath signals.

A remote transmitter was located on N. Oscuro Peak directly in line with the receiving system, ground zero, and the main transmitter (Figure 2). This transmitter was phase locked to the main transmitter and it radiated signals along paths passing about 190 m above ground zero to the receiving antennas. Figure 3 shows the penetration points of the signal paths in a vertical plane through ground zero and perpendicular to paths 1 and 4. Table 1 lists the WSMR coordinates of the various UHF/SHF transmission experiment sites.

Table 1

WSMR COORDINATES OF DICE THROW MICROWAVE TRANSMISSION EXPERIMENT SITE LOCATIONS

Site	WSMR Coordinates (ft)		
	E	N	H
Main Transmitter	444,781	651,329	4756
Remote Transmitter (North Oscuro Peak)	488,230	376,969	7938
Phase Repeater	444,300	643,600	4720
Receiving Site 1 (Main)	431,805	643,672	4689
Receiving Site 2 (Outrigger 1)	432,556	643,028	4689
Receiving Site 3 (Outrigger 2)	432,079	640,811	4687

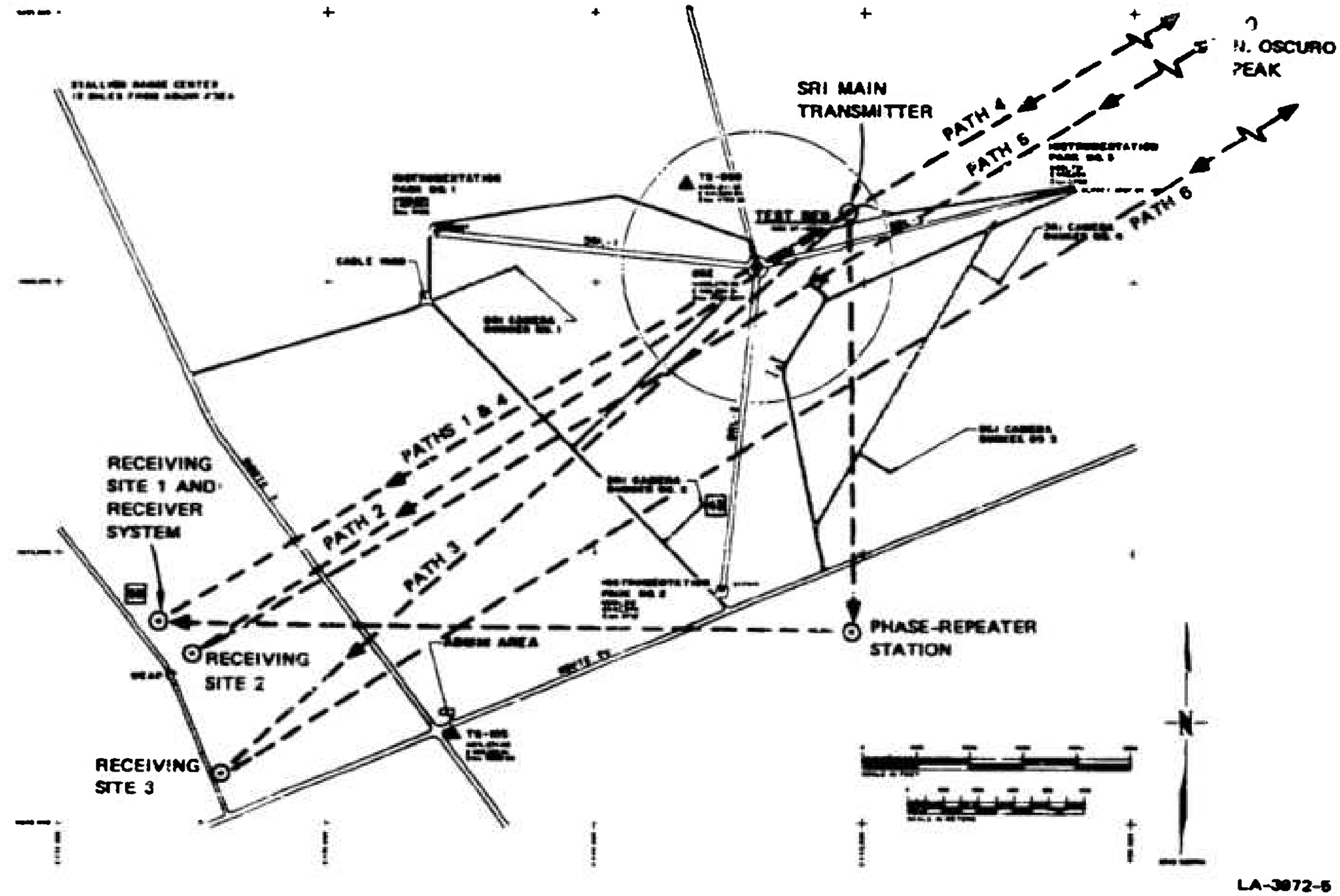

FIGURE 2 DICE THROW SITE LAYOUT WITH MICROWAVE TRANSMISSION EXPERIMENT SITE LOCATIONS

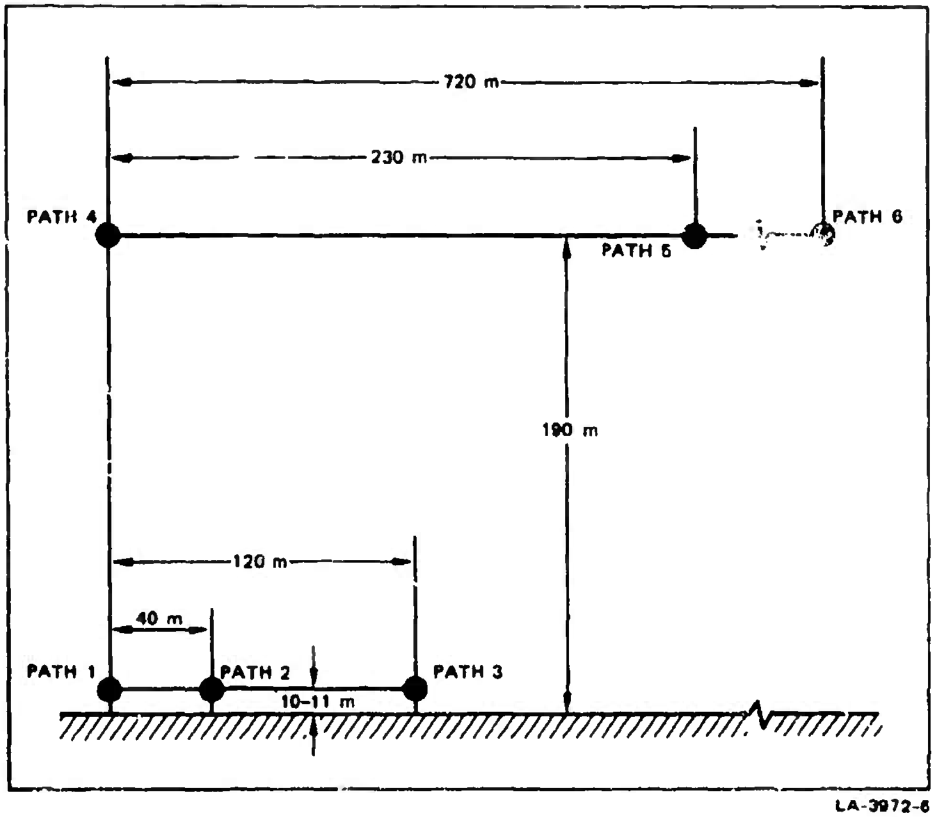

FIGURE 3 LINE-OF-SIGHT PENETRATION POINTS IN VERTICAL PLANE THROUGH GROUND ZERO AND PERPENDICULAR TO PATHS 1 AND 4

Fourteen different combinations of signal paths and frequencies were used (Table 2). The 424.5-MHz signal from N. Oscuro Peak was received at all three receiving antenna locations but recorded on a time-shared basis with a 2-s commutation cycle (1 s, Path 4; 0.5 s, Path 5; 0.5 s, Path 6). Although Path 6 passed quite far away from ground zero, it was believed that there was a reasonable chance that the cloud might drift into that path at later times.

Slow-rate framing cameras were installed to record the evolution of the dust cloud in support of the transmission experiment. The SRI camera locations are shown in Figure 1, and Table 3 lists their operating characteristics.

Table 2

MEASUREMENT FREQUENCIES

Path	Frequency (MHz)
1	[illegible].608, 413.028, 447.447
	1273.503
	2891.196
	10188.024
2	413.028
	10188.024
3	413.028
	10188.024
4	424.501
	8914.521
5	424.501
6	424.501

All of the transmissions were CW signals derived from a single reference. Power levels ranged from less than 1 mW to about 10 mW, resulting in signal-to-noise ratios ranging from 35 to 55 dB in the 500-Hz receiver bandwidths. The quadrature components of the complex envelopes of the received signals were obtained by means of a pair of synchronous demodulators in each of the receiver channels.

The primary data acquisition system consisted of a 500-sample-per-second-per-channel analog-to-digital conversion system and a pair of digital tape recorders under the control of an HP-2100 minicomputer. Each of the tape recorders operated independently of the other so as to provide redundancy in case of recorder failure. A separate analog recorder was used as well as an overall backup system.

Prior to T - 10 min the main transmitter and phase repeater were connected to dummy loads. They were switched automatically to their

Table 3

AUTOMAX 35-mm FRAMING CAMERA DATA

No.	Location	Focal Length (mm)	Field of View (°V x °H)	Framing Rate (per second)
1	R1	35	30 x 38	5, then 1
2	R1	85	12 x 17	5, then 1
3	MT	18	53 x 70	2
4	PR	35	30 x 38	2
5	PR	85	12 x 17	2
6	NOP	85	12 x 17	5, then 1
7	NOP	300	3.6 x 4.8	5, then 1

R1--Receiver Site 1
MT--Main Transmitter
PR--Phase Repeater
NOP--North Oscuro Peak

antennas at T - 10 min by means of appropriate signals from the timing and firing (T&F) system. The N. Oscuro Peak transmitter was operated manually. The cameras were turned on at T - 1 min either by T&F signals or manually, depending on their locations. System tests and calibrations were carried out before and after the detonation.

III RESULTS

Figures 4 and 5 present the principal raw amplitude and phase data from Path 1 up to T + 15.5 s. A large number of 360-degree phase wrap-ups occurred on all but the UHF signals, where a peak phase change of about 4 radians occurred. Because only one sample in 1000 is plotted here, phase discontinuities at ±180° are not well resolved; this effect is more noticeable at the higher frequencies where larger and more rapid phase shifts occurred. The 379- and 447-MHz perturbations were somewhat different from the 413-MHz perturbation, which indicates that the coherent bandwidth at 400 MHz was not much greater than 70 MHz.

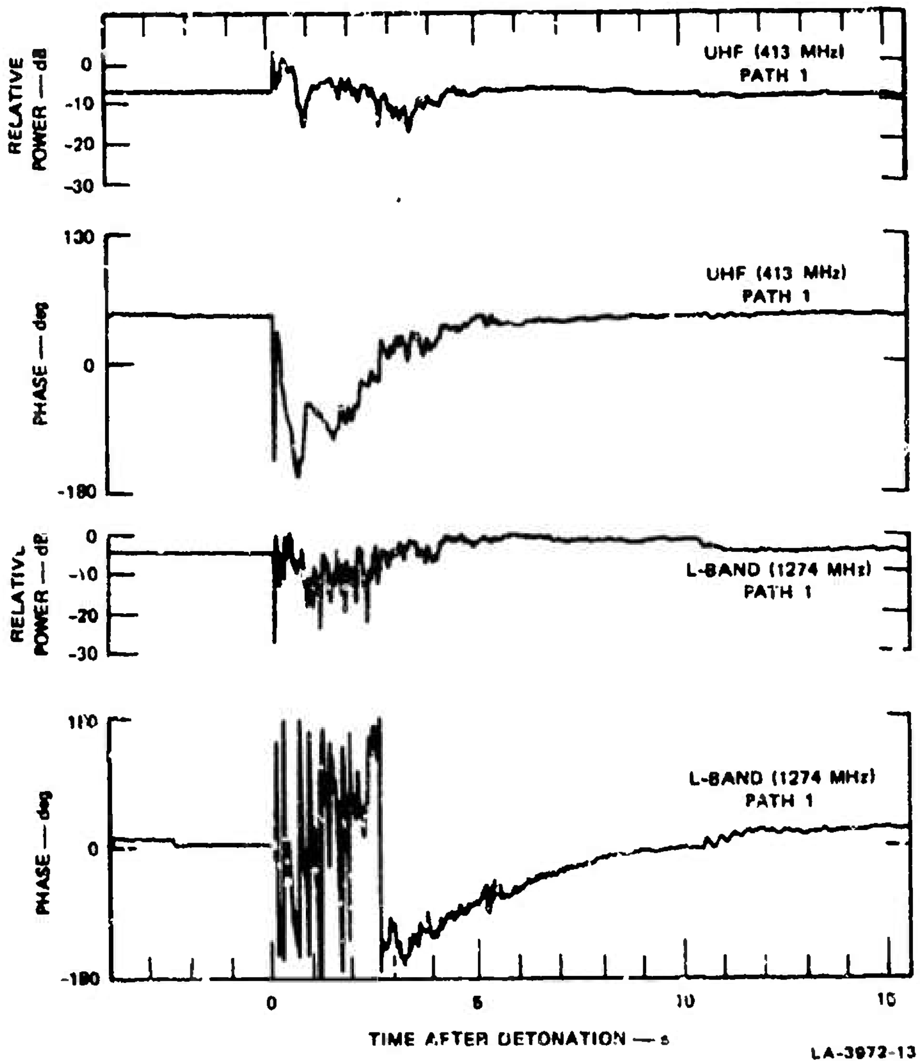

FIGURE 4 PATH 1 UHF AND L-BAND AMPLITUDES AND PHASES

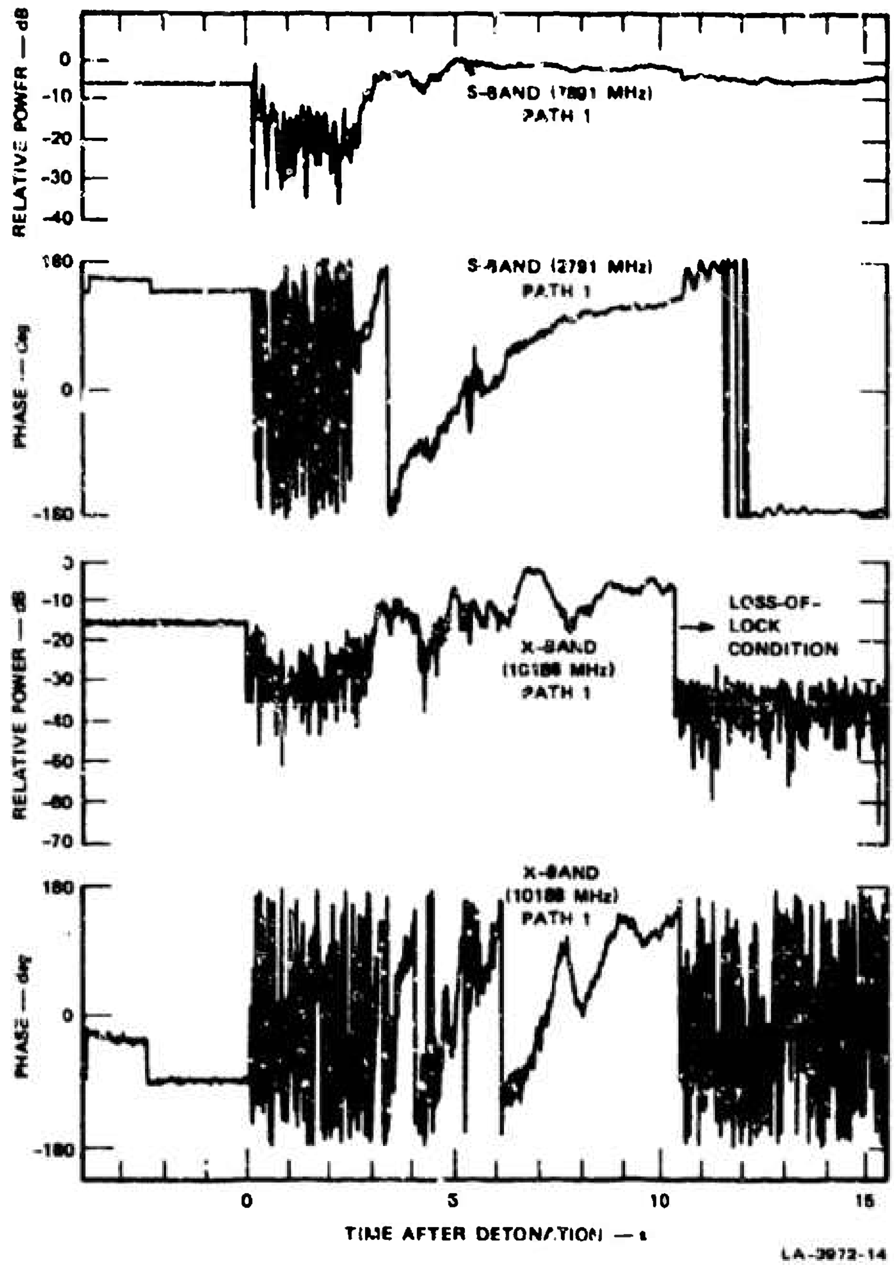

FIGURE 5 PATH 1 S- AND X-BAND AMPLITUDES AND PHASES

Although the strongest perturbations died down by about T + 6 s, dust effects on the phase shifts persisted until about T + 26 s before suddenly ceasing (Figure 6). At T + 10.4 s the arrival of the shock wave at the receiving site shook the phase-reference receiving antenna enough to cause the three phase-locked oscillators in the 10.2-GHz receiving systems to lose lock. The effects of the oscillating antenna may be seen in all of the lower-frequency records (the peak antenna displacement was about 5 mm).

Figures 7 and 8 show similar plots of the raw amplitude and phase of the UHF and X-band signals for Paths 2 and 3. Again, the strongest perturbations of the UHF signal died out by about T + 5 or 6 s. At X-band, however, the strongest perturbations seem to be progressively more delayed in time as the offsets of the paths from ground zero increase. This effect is probably due to scattering from the larger crater ejecta particles that follow ballistic trajectories. While larger particles are more effective scatterers at short wavelengths, they only slightly affect the UHF signals.

Sudden cessations of phase effects similar to that at T + 26 s noted for Path 1 also occurred on Paths 2 and 3, but at T + 22 and T + 16 s, respectively. These times are consistent with the rapid right-to-left lateral motion of the dust cloud as seen from the receiving sites, and imply a 10-to-12-m/s surface wind velocity. This value agrees very well with the 11.5-m/s velocity of the cloud base determined from the photographic data, and is substantially larger than the 1.5-m/s surface wind velocity reported at Stallion Range Center. The rapid lateral motion of the cloud was probably the most important factor that limited the duration of signal perturbations.

Because of its rapid lateral motion, only a small part of the cloud interdicted Path 4. Figure 9 shows four views of the cloud, two at T + 20 s and two at T + 30 s, in relation to the signal paths. The only part of the cloud affecting Path 4 was the single convective cell protruding from the south side of the cloud. Figure 10 presents the X-band amplitude and phase for Path 4. Signal perturbations associated with

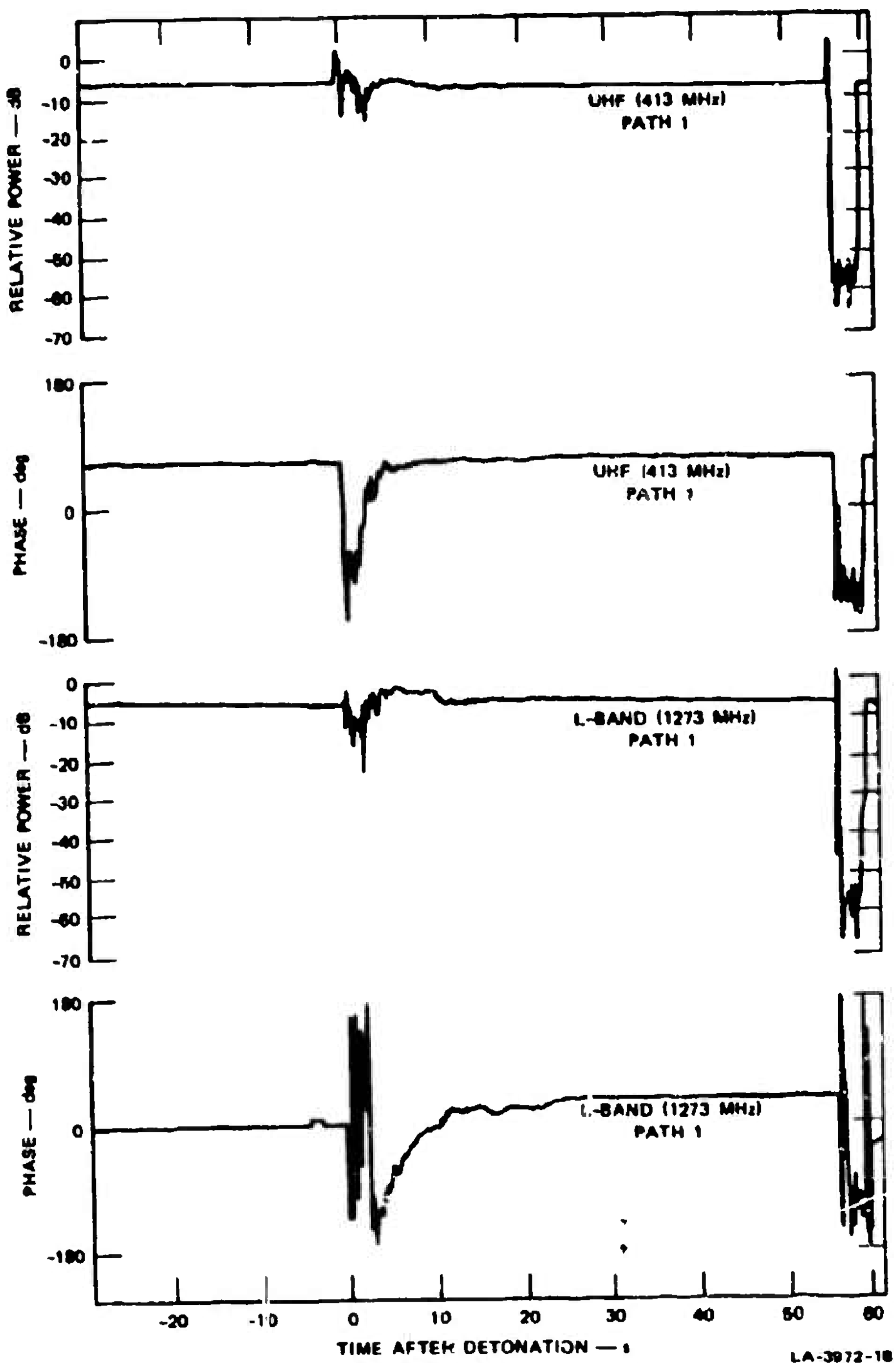

FIGURE 6 PATH 1 UHF AND L-BAND AMPLITUDES AND PHASES

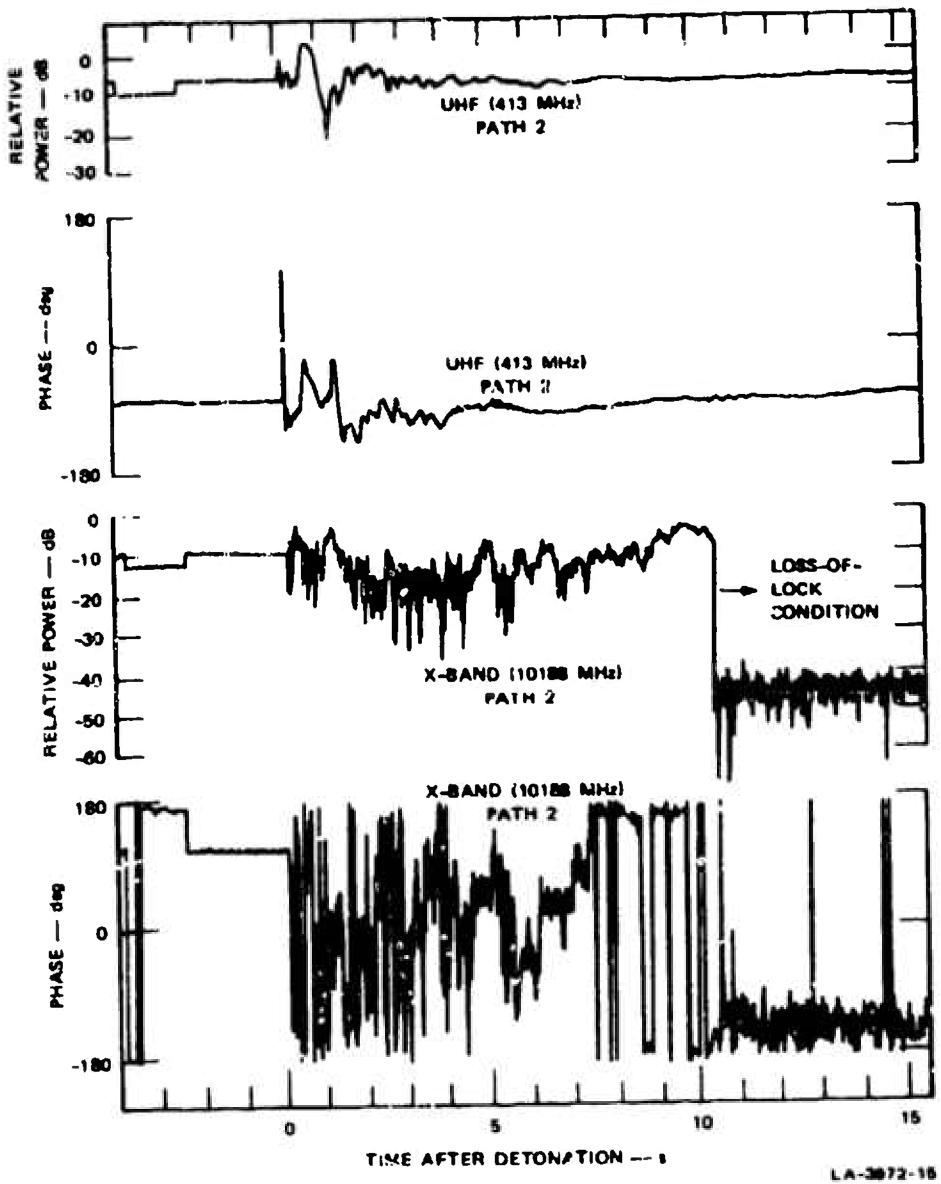

FIGURE 7 PATH 2 UHF AND X-BAND AMPLITUDES AND PHASES

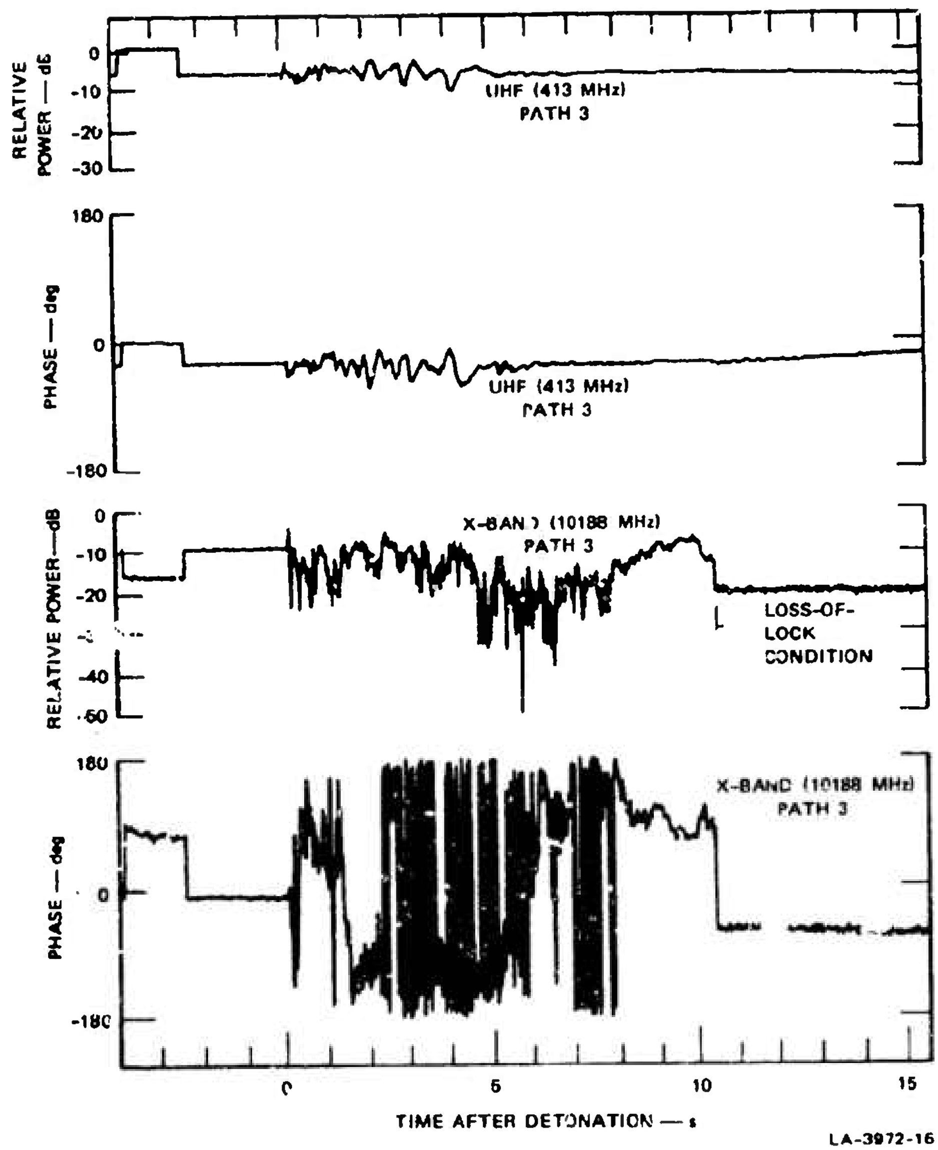

FIGURE 8 PATH 3 UHF AND X-BAND AMPLITUDES AND PHASES

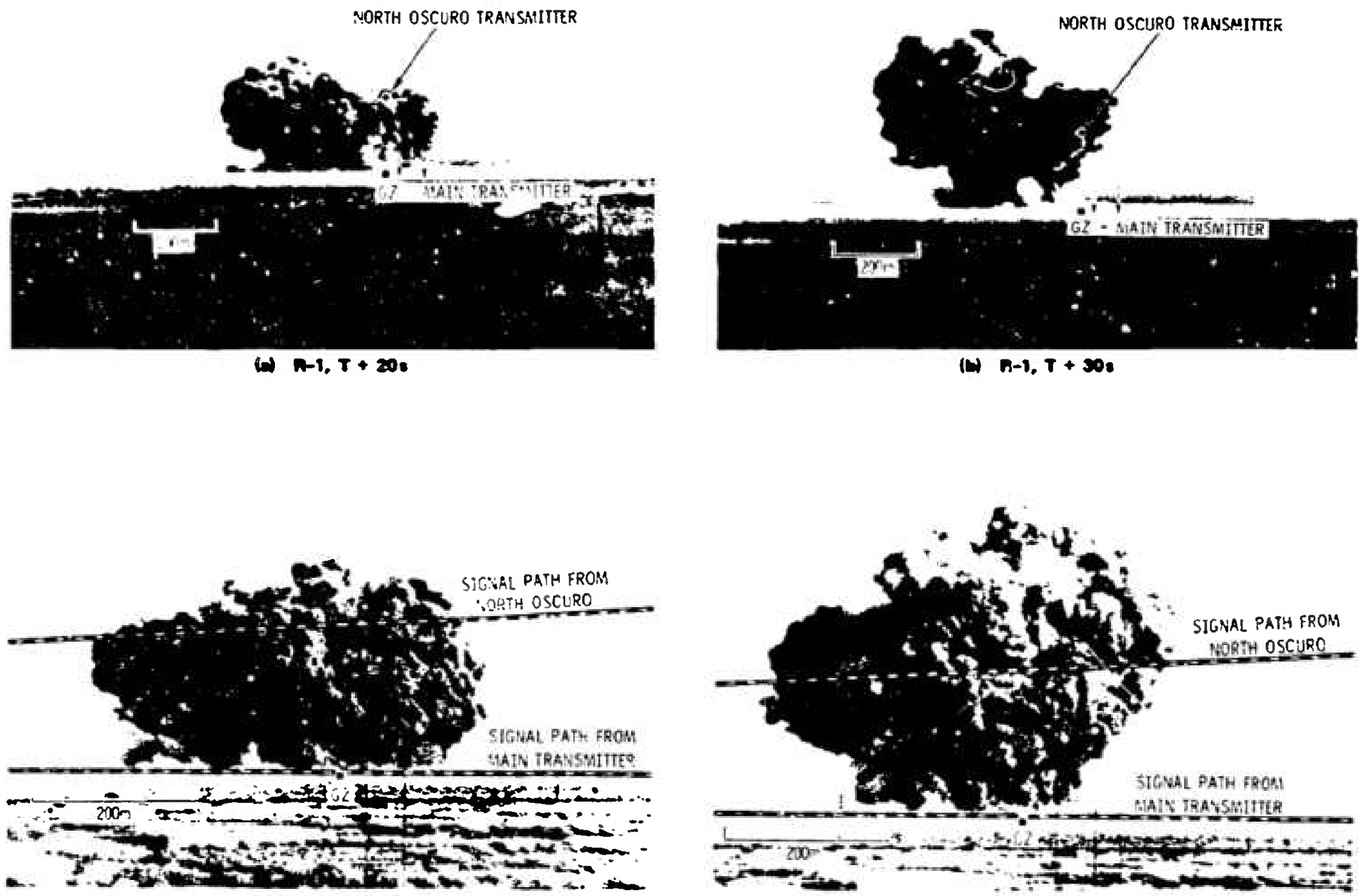

(a) R-1, T + 20s
(b) R-1, T + 30s
(c) PR, T + 20s
(d) PR, T + 30s

LA-3072-31

FIGURE 9 DUST CLOUD VIEWS AT T + 20 AND T + 30 s AS SEEN FROM RECEIVER AND PHASE REPEATER SITES

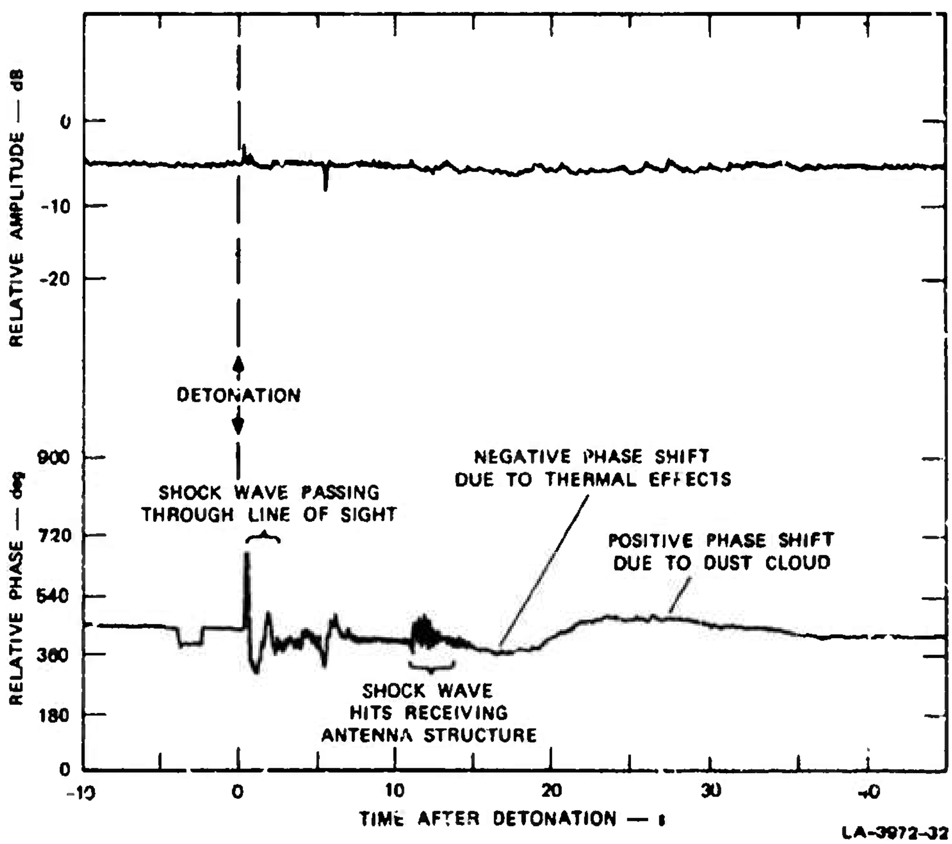

FIGURE 10 PATH 4 AMPLITUDE AND PHASE vs. TIME AT 8.9 GHz

the passage of the primary and reflected shock waves through the line of sight can be seen prior to the occultation by the dust cloud between T + 17 and T + 36 s. Just before occultation a negative phase shift occurred, which was apparently caused by a thermally enhanced low-density air bubble surrounding the dust cloud. Weak amplitude fluctuations superimposed on a small decline in general signal strength also occurred during the occultation. The wavelength-scaled UHF phase effects were in very close agreement with the X-band effects.

Part of this effort was to determine the dielectric properties of the dust cloud. Toward that end several samples of powdered material were collected from the crater and rim and analyzed in the laboratory.

The samples, which were named "sand," "caliche A," and "caliche B" on the basis of their appearance, are thought to be reasonably representative of the material comprising the dust cloud. Table 4 summarizes the results of the laboratory measurements for two of the samples. The solid particle density was obtained using Avogadro's method, and the average dielectric properties of the individual grains comprising the particles were computed using two "mixing laws"--the Rayleigh and the Lichtenecker formulas. It was found that the dielectric content decreased slowly as the frequency increased, and that the loss tangent could be characterized by two terms. The first term, which exhibited an inverse frequency dependence, is due to the electrical conductivity (σ) of the grains, while the constant second term ($\tan \delta_o$) is a "molecular loss" term. (As expected, both terms were very sensitive functions of the moisture content of the samples, which was determined by drying the samples in a vacuum.)

The theoretical dielectric properties of the low-density dust cloud could then be computed from the average properties of the grains. Figure 11 shows the refractivity--defined as $N = (n - 1) \times 10^6$, where n is the refractive index--as a function of dust cloud mass density for two of the samples. For reference, the typical range of the ambient atmospheric surface refractivity was included in Figure 11. Figure 12 shows the ratio of theoretical signal attenuation in decibels per radian of phase retardation suffered by a signal passing through dust clouds composed of the three sample materials. The increase in the ratio at low frequencies is due to the conductivity term.

The results shown in Figure 11 can be used to infer dust densities in the cloud. In the absence of distortions due to effects such as diffraction, the phase shift is proportional to the integrated refractivity and hence to the integrated dust density along a line of sight. Figure 13 shows the UHF and X-band phases with the 360° ambiguities removed. Only the 413-MHz results can be used for this purpose because the X-band perturbations were so severe that there was a complete loss of the coherent signal component. And even the UHF curve should be used with caution because the substantial accompanying amplitude fluctuations

Table 4

INFERRED AVERAGE DIELECTRIC CONSTANT, MOLECULAR
LOSS TANGENT, AND CONDUCTIVITY FOR SOLID PARTICLES

Sample	Solid Particle Density (gm/cm^3)	Moisture Content (percent)	f (GHz)	Rayleigh			Lichtenecker		
				ϵ_r	tan δ_o	σ mho/m	ϵ_r	tan δ_o	σ mho/m
Sand	2.56	2.74	1	6.6	0.051	4.9	6.0	0.042	4.0
			10	4.8	0.043	4.1	4.7		
Caliche A	2.64	12.73	1	14.7	0.11	14.2	9.5	0.052	6.7
			10	7.9	0.072	9.3	6.8		

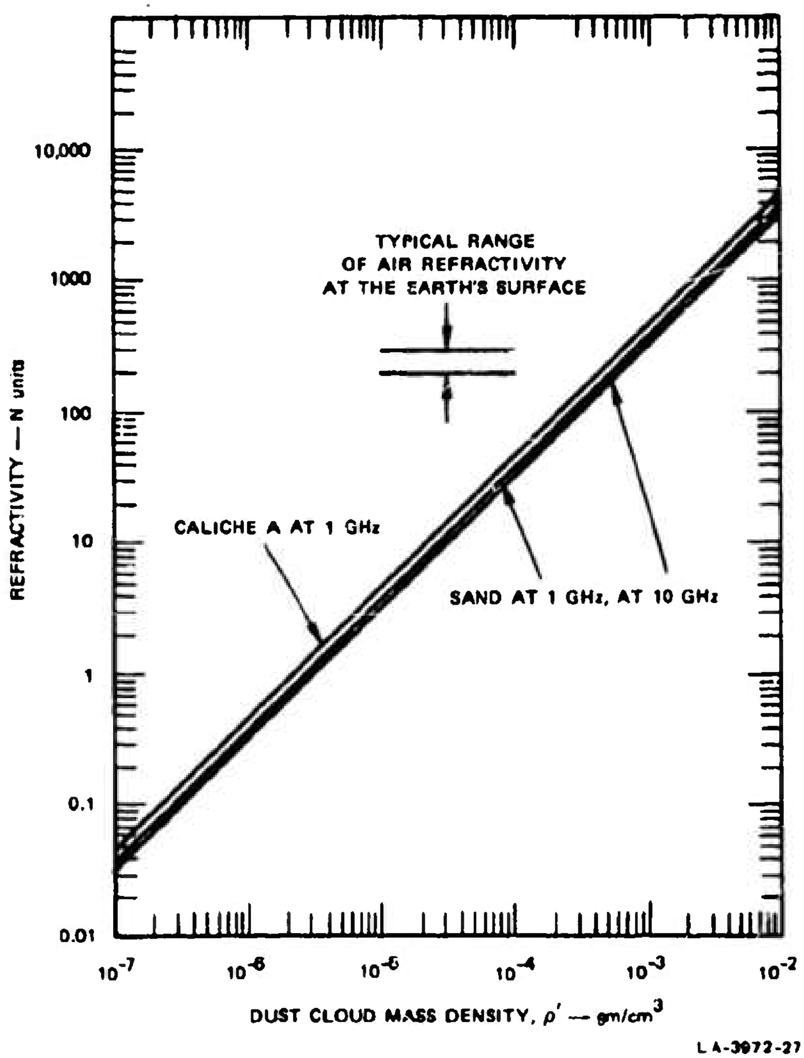

FIGURE 11 REFRACTIVITY vs. MASS LOADING

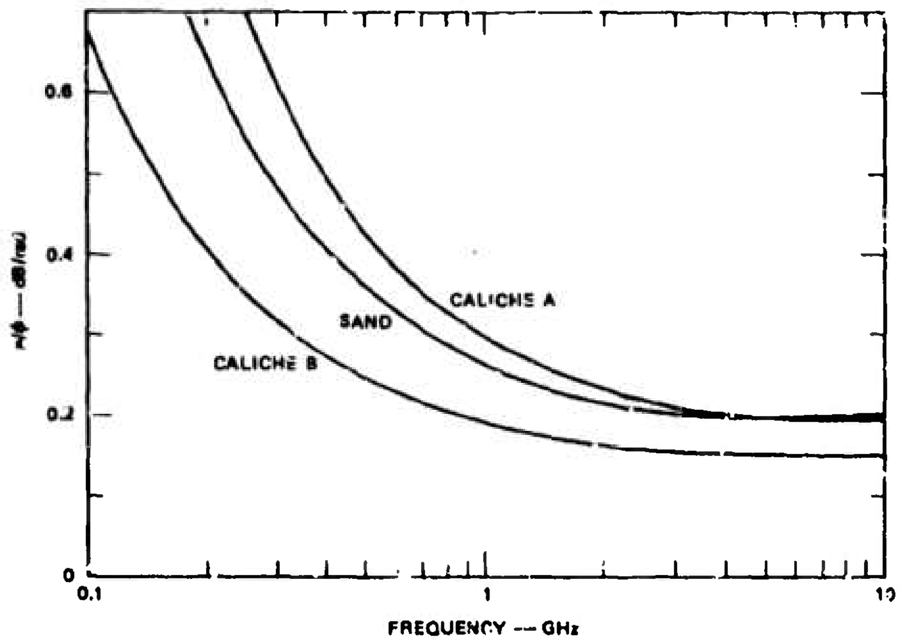

LA-3072-28

FIGURE 12 ATTENUATION PER RADIAN OF EXCESS PHASE SHIFT vs. FREQUENCY

(see Figure 4) indicate that substantial diffraction was present. But if we assume that the 4-radian peak phase shift at 413 MHz is a reasonably accurate number, an integrated dust density of about 115 gm/cm^2 follows, which implies a 3.7×10^{-3} gm/cm^3 average dust density over the 315-m path length through the cloud. Diffraction calculations using simple models for the dust cloud give results for both Paths 1 and 2 consistent with average dust densities on the order of 10^{-2} gm/cm^3, and indicate that the Path 1 results may be reasonably accurate.

Diffraction was not a factor in the Path 4 occultation described above (Figures 9 and 10). The peak phase shift at X-band of about 1.8 radians at T + 23 s corresponds to an integrated dust density of 1.9 gm/cm^2. Since the path length through the small part of the cloud that interdicted Path 4 was about 300 m, the average dust density in that part of the cloud then was 6.5×10^{-5} gm/cm^3. Substantially greater effects would have been observed had the cloud risen vertically.

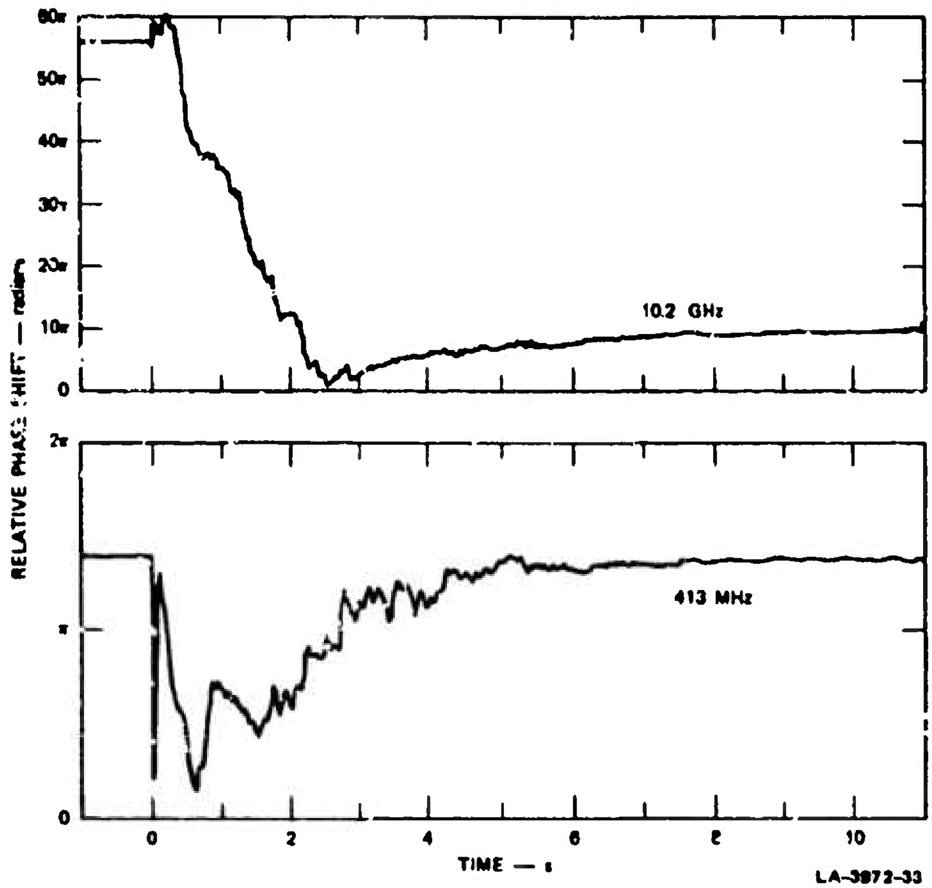

FIGURE 13 PATH 1 PHASE SHIFT vs. TIME

The measured Path 1 UHF phase shift can also be used to estimate the theoretical attenuation due to absorption for the higher-frequency signals on that path. This is accomplished by scaling the phase shift directly according to frequency and then applying the results shown in Figure 12. Figure 14 shows the comparisons between the measured signal strengths and the absorptions computed according to the method above. The theoretical absorption curves have been placed to match the eventually measured signal levels after the dust cloud blew away. The reason that the pre-detonation signal strengths are lower than the eventual level is

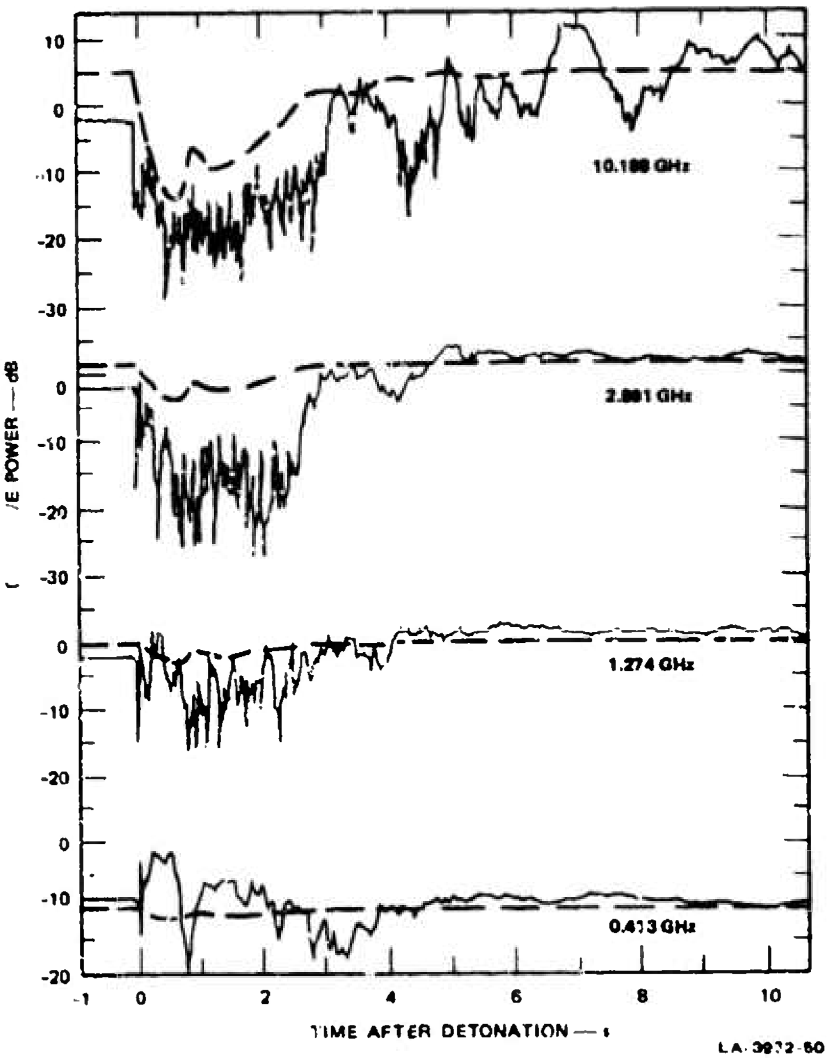

FIGURE 14 COMPUTED ATTENUATION (dashed curves) COMPARED TO MEASURED SIGNAL-STRENGTH FLUCTUATIONS -- PATH 1

that the explosive charge partly obstructed Signal Path 1; this effect is greater at the higher frequencies.

The peak calculated absorptions ranged from 1.5 dB at UHF to nearly 20 dB at X-band. Scattering losses presumably accounted for the remainder of the observed average declines in signal strength. That the scattering loss at 10.2 GHz appears to be smaller than at 2.9 GHz is anomalous. A possible explanation is that focusing is more effective at higher frequencies and partly makes up for the increased attenuation.

IV CONCLUSION

The UHF/SHF Transmission Experiment was successful in collecting good quality data during the DICE THROW HE event. Although the arrival of the shock wave at the receiver site caused the loss of three of the twelve measurement channels from T + 10.5 s until T + 60 s, little data was actually lost. Data from other transmissions along the same signal paths were initially unaffected by the shock wave. And because the dust cloud moved unexpectedly rapidly away from the signal paths, the strongest effects were essentially over by the time the outage occurred.

Extensive photographic coverage of the dust cloud was also accomplished. This specialized coverage supported the microwave transmission experiment by providing photographs of the dust cloud at relatively slow rates for an extended period of time along, and at right angles to, the signal paths.

Very large amplitude fluctuations and fades occurred at early times (before T + 5 s) on the low-altitude signal paths. Fluctuations ranged from 20 dB peak-to-peak at 400 MHz, to more than 50 dB at 10.2 GHz. Although diffraction phenomena were very important o the observed amplitude fluctuations, extinction due to absorption and scattering also contributed to signal strength declines. A peak phase shift of about 4 radians was seen at 413 MHz, which corresponds to an integrated dust density of 120 gm/cm^2, if diffraction effects are neglected. This in turn corresponds to a uniform dust density of 4×10^{-3} gm/cm^3 spread over a 300-m path through the cloud.

It had originally been anticipated that phase perturbations would dominate the results. Such phase perturbations could have severe impacts on certain types of communications systems, particularly on systems having wide bandwidths or using phase-lock techniques. But the large amount of amplitude fluctuation seen even at UHF suggests that unsophisticated systems may be adversely affected by dust-laden environments. Thus, the possibility of encountering larger perturbations spread over a greater area (after a nuclear detonation or a series of nuclear detonations) than the already significant perturbations measured for the limited area, 500-ton DICE THROW event could strongly influence systems design and configuration choices. It is anticipated that the results from this type of experiment will strengthen the nuclear predictive codes.

At 300 MHz the calculated attenuation/excess phase shift from the measured properties of the samples ranged from 0.3 to 0.6 dB per radian. Thus, even at UHF an extensive dust cloud or dust-laden region following a series of nuclear surface bursts could seriously affect a system having a low signal-to-noise margin. Several decibels of attenuation could occur for many tens of minutes or for several hours, depending on wind-drift rates.

Absorption becomes more severe as the frequency increases. At 10 GHz, for example, a dust cloud could be responsible for several tens of decibels of attenuation. Millimeter waves could be even more severely affected. Even a modest dust cloud could darken the 30-GHz atmospheric window from absorption alone. Extinction of signals by scattering would further increase attenuation and exacerbate the situation.

Fading due to diffraction may be superimposed on the general level of attenuation by a dust cloud. This possibility must be considered as well during systems evaluations.

23. DICE THROW DUST CLOUD CALCULATIONS

by

Major Gary P. Ganong, Susan E. Check,

and Charles E. Needham

Air Force Weapons Laboratory

ABSTRACT

The Air Force Weapons Laboratory was requested by RAAE of Headquarters Defense Nuclear Agency (DNA) to make cloud rise calculations for Dice Throw. Both preshot and postshot calculations were done.

The preshot calculations predicted the dust cloud rise and growth and aided Stanford Research Institute (SRI) in designing microwave transmission experiments for Dice Throw (Ref 1).

Postshot calculations were done to help explain the results of the test. They included the effects of the dust clouds on microwave phase shift and attenuation. The ambient shear winds present at the test site on the morning of the event were later included in the calculations.

INTRODUCTION

The dust cloud rise calculations were done in four steps.

1. A calculation of the air blast environment out to one second after detonation was done using the HULL hydrodynamics code (Ref 2). This calculation used 3 materials with high explosive burn. The rezone technique used to retain high resolution of the air blast in the grid resulted in coarse zoning in the fireball region (Ref 3).

2. An additional HULL calculation was begun from the air blast calculation. It was started at a time when the charge had expanded sufficiently to define the air shock but the zoning in the fireball region was still fine enough to define cloud rise. This calculation was run to 180 seconds and defined air velocities, densities, and temperatures as function of time and space.

3. Using DUSTY, AFWL's dust cloud code, the trajectories of 2000 discrete representative particles were computed. Each particle was assigned a radius depending on the predicted particle size range. The particle radii were assumed to range from .0025 and 100 cm. Drag and gravity forces were included in these trajectory calculations.

4. The total mass ejected was divided among the representative particles according to an assumed particle size distribution. This size distribution, along with the particles positions in the air and on the ground determine the mass aloft, the cloud density, and the number densities, and were used to calculate radio transmission effects.

CALCULATIONS

Preshot calculations did not agree well with the observed Dice Throw dust cloud for two reasons; poor initial conditions and inadequate hydrodynamic definition in the fireball region.

The assumed initial conditions were based on photographs of Pre-Dice Throw II-2 (Ref 1), which had a similar charge composition and configuration (hemispherically capped cylinder). Ejecta and the early time dust cloud from Dice Throw was quite different from that of Pre-Dice Throw II-2. Probably the absence of a water table at Dice Throw changed the ejecta pattern and size distribution.

Since the HULL computational mesh expanded to contain the blast waves, the preshot calculations suffered from inadequate zoning. By one minute after detonation, the dust cloud occupied only a few of the 16800 zones in the calculation.

To correct this deficiency in the preshot calculations, a new rezone technique was developed and incorporated into the HULL. With this method, 25% of the total number of zones were in the fireball area, and were allowed to expand at a slower rate than those in the shock region. The resolution of air blast was diminished while cloud definition was increased. Figures 1 and 2 compare the grids used in the two HULL calculations. For clarity, in both cases, only every fourth zone boundary from the HULL calculation is shown.

Ideally, a calculation should be run with constant fine zoning throughout the HULL grid which would result in good definition in both the fireball and shock regions. This would require a very large number of zones and would be costly to run.

Initial calculations were done using a cratering and ejecta model developed for nuclear cases. The calculated cloud did not agree with the observed Dice Throw dust cloud. In the absence of a good cratering model, the initial conditions for ejecta were based on photographs of Dice Throw taken by SRI (Ref 4) at early times. The photograph of the dust cloud at 1 second (Fig 3) indicates a relatively stationary dust dome atop a slightly rounded dust platform in contact with the ground. Figure 4 illustrates the DUSTY model for the initial dust cloud. At one second the dust particle velocities were assumed to be zero because of the relatively stationary appearance of the overall cloud. These initial zero velocities had no effect on the hydrodynamic flow fields and in the first cycle particle motion was initiated.

The dust cloud and stem which evolved from these initial conditions (Fig 5) gives good qualitative agreement with the photographic data but exhibits smaller dimensions than the observed cloud.

In calculating the mass loading of the dust cloud it is necessary to assume a dust particle size distribution. Two distributions were used in the postshot calculations: a Dice Throw distribution and a hard rock distribution (Fig 6).

The Dice Throw particle size distribution was obtained from in-situ measurements taken at the test site (Ref 5).

The hard rock distribution has a large portion of its mass in cobbles and boulders. It illustrates a possible distribution if the soil clumps, agglomerates, or otherwise is not reduced to in-situ size by the cratering process.

The assumption was made that there were ten kilotons of ejecta in the cloud initially (A cylinder of ambient soil density of the cloud's radius and less than 2 cm in depth would contain more than ten kilotons of mass). Using the two particle size distributions and computed particle trajectories, the mass aloft versus time was calculated (Fig 7).

The hard rock cloud loses most of its mass quickly as the large particles fall out. Once the cobbles and boulders have fallen out, the cloud density for the hard rock particle size distribution is two orders of magnitude lower than for the Dice Throw distribution.

In calculating particle size distributions, it is often assumed that the size distribution is inversely proportional to the particle radius raised to some power. For hard rock the initial power of the cloud is 3.5, and for Dice Throw distribution it is 4.8. As the larger particles fall out, the size distribution power increases. Figure 8 compares size distribution power versus time for the two soil types.

Finally the SRI scattering and absorption models were applied to determine the phase shift and attenuation of microwave transmissions along the various paths in the SRI experiments (Ref 1 & 6). The computed phase shift is proportional to the cloud mass density. Because both soil distributions had the same, initial mass loading and density, the initial phase shift of 4.2 radians for the Dice Throw distribution (Fig 9) and 5 radians for the hard rock distribution (Fig 10) are nearly equal. The fact that the initial calculated phase shifts are close to the 4 radian phase shift measured by SRI (Ref 6) implies that the initial mass aloft of ten kilotons in the calculations was approximately correct.

Initial calculations of attenuation were based on scattering only (Ref 1) and exhibited poor agreement with the experimental data. However, when an absorption term (Ref 6) was added to the calculation, the results agreed much more closely with experimental data.

The attenuation for the Dice Throw distribution is due entirely to absorption (Ref 6). At the 10GHz frequency, absorption accounts for almost all of the measured attenuation (Fig 11). At the 416 MHz frequency, absorption accounts for only 20% of the measured attenuation (Fig 12).

The attenuation for the hard rock distribution is due equally to scattering and absorption. At the 10 GHz frequency, the hard rock distribution predicts six more times more attenuation than measured (Fig 13). At 416 MHz, the same assumed distribtuion predicts approximately the measured value for attenuation (Fig 14).

From this information we conclude that the actual particle size distribution for Dice Throw is either between or some combination of these two distributions.

Analyses of these sorts appear to offer a method for deriving the size distribution for ejecta while it is still aloft. This information is essential to accurate nuclear cloud calculations.

None of these calculations took into account the effects of ambient shear winds. Later calculations were done with shear winds, as measured from SRI's photographs, included. Figures 15 and 16 are photographs of the dust cloud taken at 35.9 and 45.9 seconds by SRI from North Oscuro Peak. Figure 17 shows a calculation of particle positions and their images, including wind shears at 40 seconds. It can be seen that the calculated cloud cloud closely resembles the actual dust cloud.

Similarly, Figures 18 and 19 compare a photograph of the dust cloud at 77.9 seconds and the calculated cloud at 80 seconds.

Even though the calculations are 2-dimensional, the shear winds are perpendicular to the line of view, they give a good representation of the actual cloud. The next step would be to perform the phase shift and attenuation calculations with ambient shear winds.

CONCLUSION

It is evident from comparisons of these calculations to experimental data that the dust clouds calculated by the HULL and DUSTY codes can be used to predict dust clouds from high explosive and nuclear bursts. With the addition of a measured dust particle size distribution, the accur   of the calculations will be greatly improved. Until such data is available, these codes along with anticipated particle distributions give AFWL the capability of doing dust cloud rise and microwave transmission calculations.

References

1. Bollen, R. L., Chestnut, W. G., Hatfield, V. E., Smith, C., "Predictions of Effects Upon Microwave Links Following the Dice Throw Detonation," Preliminary Draft, Stanford Research Institute, September 1976.

2. Fry, M. A., et al. "The Hull Hydrodynamics Computer Code," AFWL-TR-76-183, Air Force Weapons Laboratory, September 1976.

3. Needham, C. E., "Dice Throw Project Officer Report Theoretical Air Blast Calculations," Air Force Weapons Laboratory, June 1977.

4. Chestnut, W. G., Durfey, G. K., Hodges, J. C., Burns, A. A., "Dice Throw Photographic Notes," Stanford Research Institute, January 1977.

5. Melzer, S., Henny, R., Private communication.

6. Burns, A. A., "UHF/SHF Properties of Dust from the Dice Throw HE Test," Stanford Research Institute, Feb 1977.

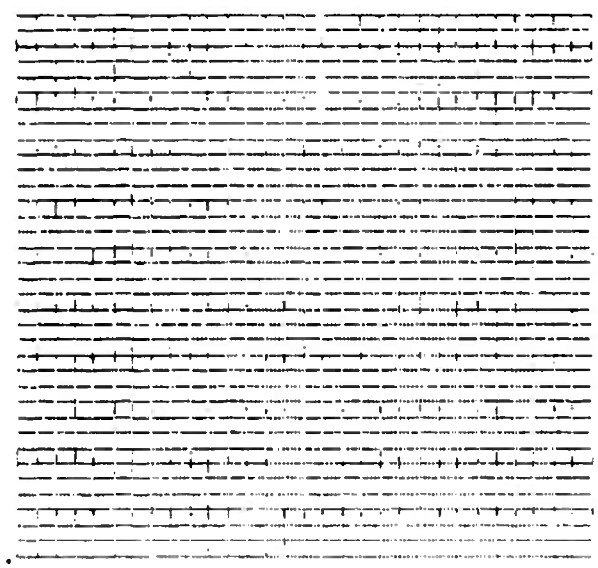

FIGURE 1. HULL COMPUTATIONAL MESH
FROM OLD REZONE PROCEDURE

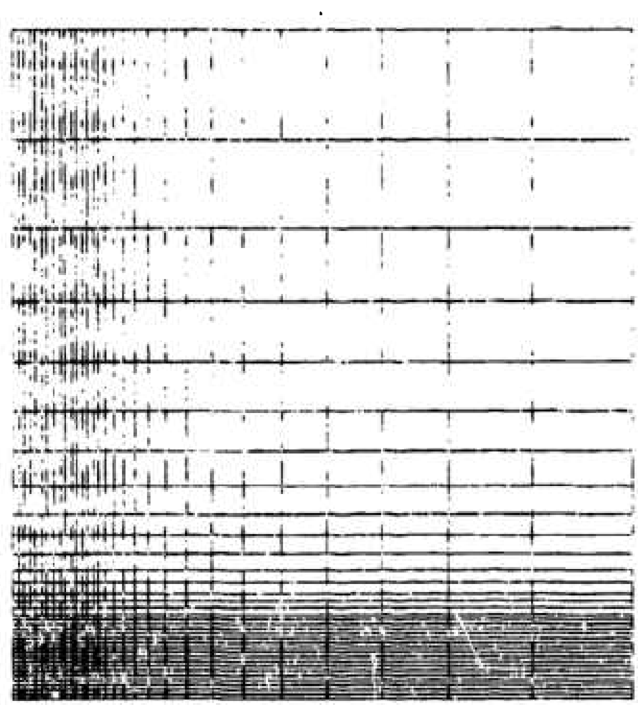

FIGURE 2. HULL COMPUTATIONAL MESH
FROM NEW REZONE PROCEDURE

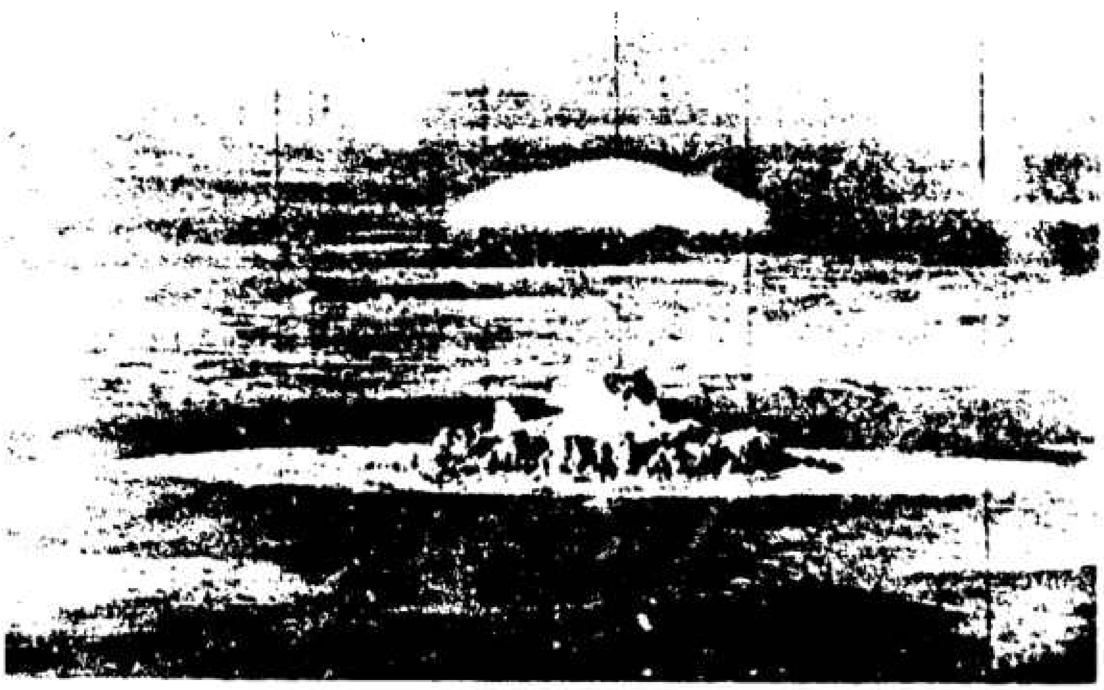

FIGURE 3: DUST CLOUD AS VIEWED FROM NORTH OSCURO PEAK AT ONE SECOND

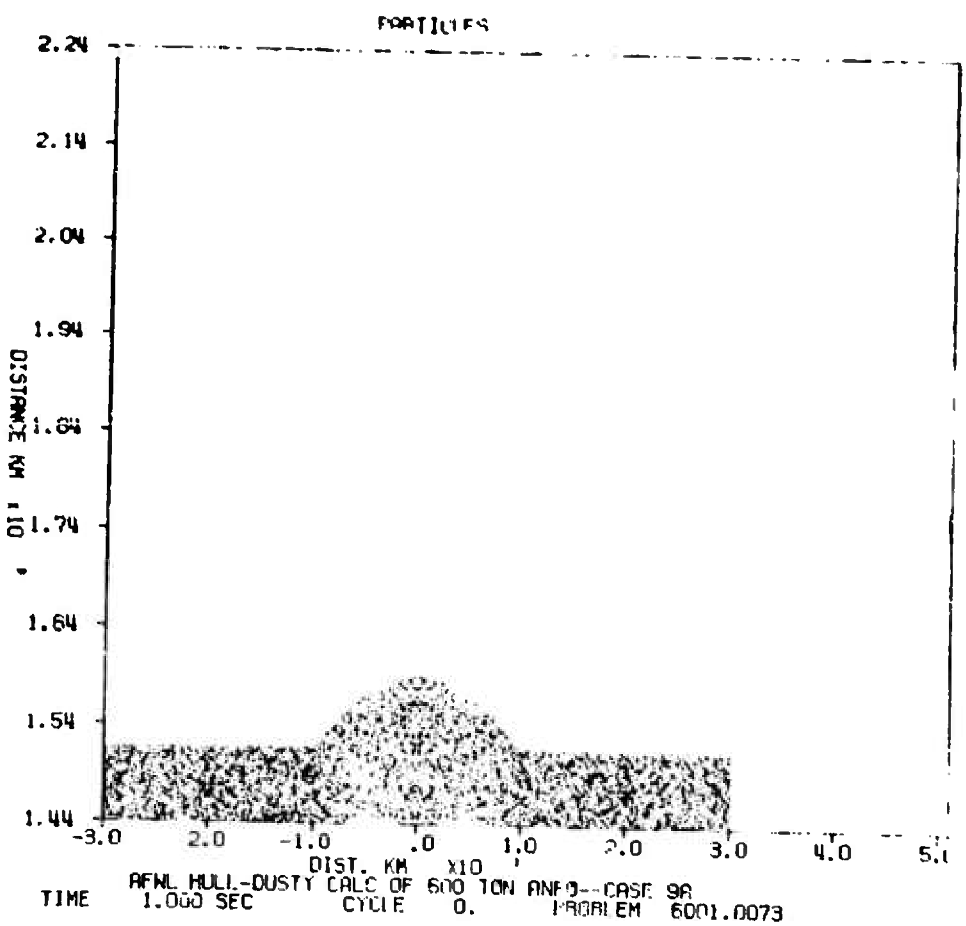

FIGURE 4. DUSTY MODEL FOR DUST CLOUD AT ONE SECOND

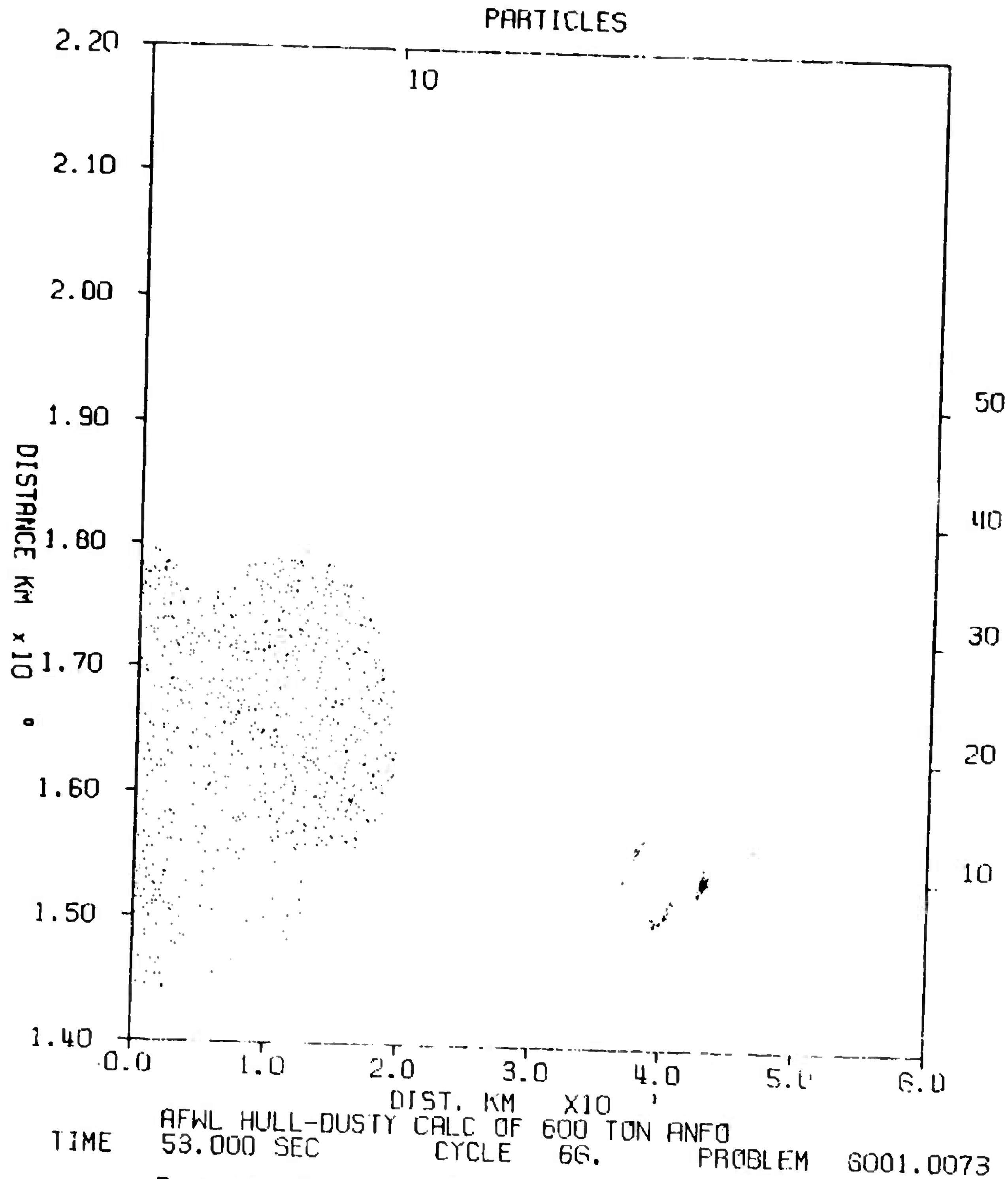

Figure 5: Calculated Dust Cloud At 53 Seconds

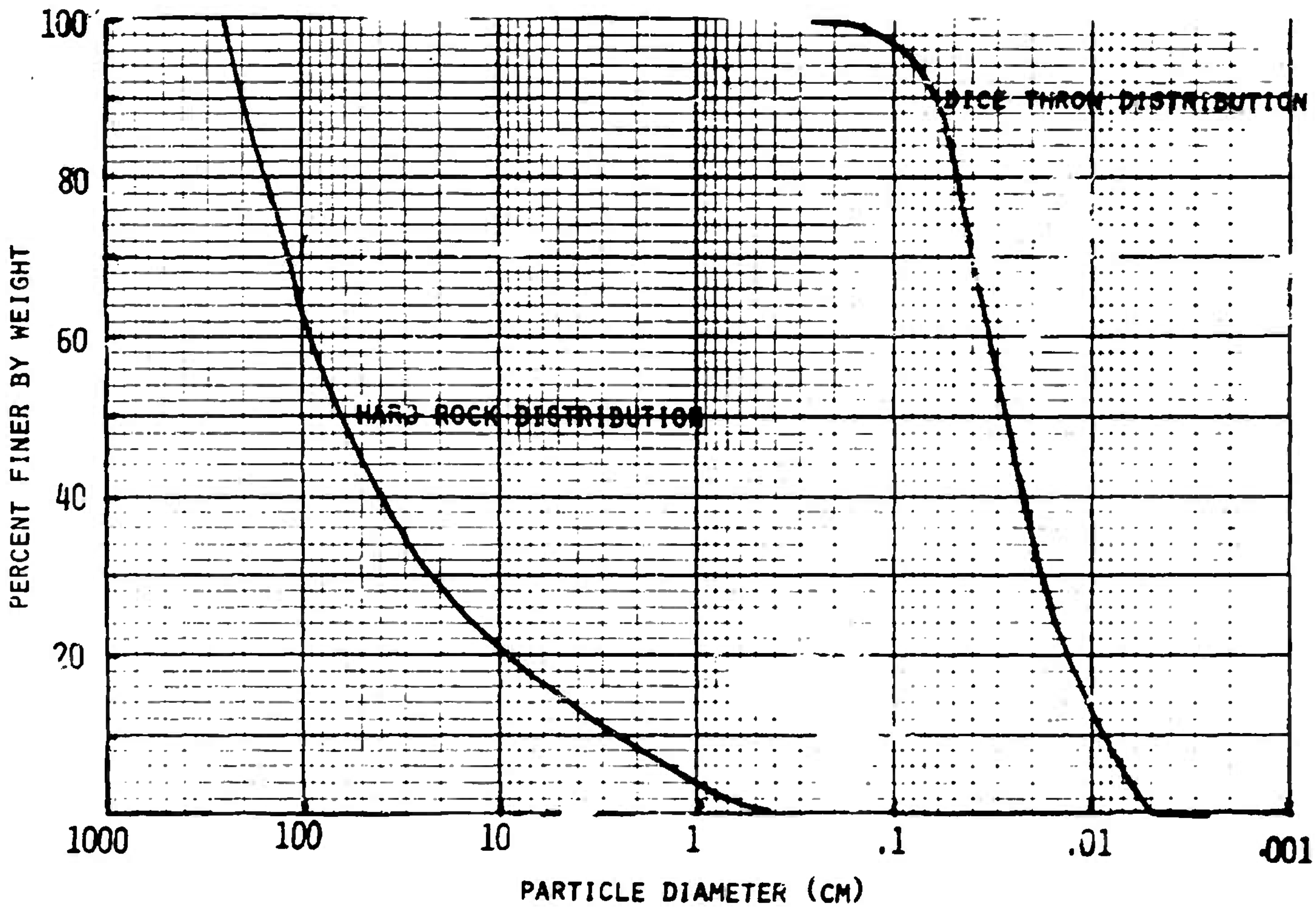

FIGURE 6. DICE THROW AND HARD ROCK PARTICLE DISTRIBUTIONS

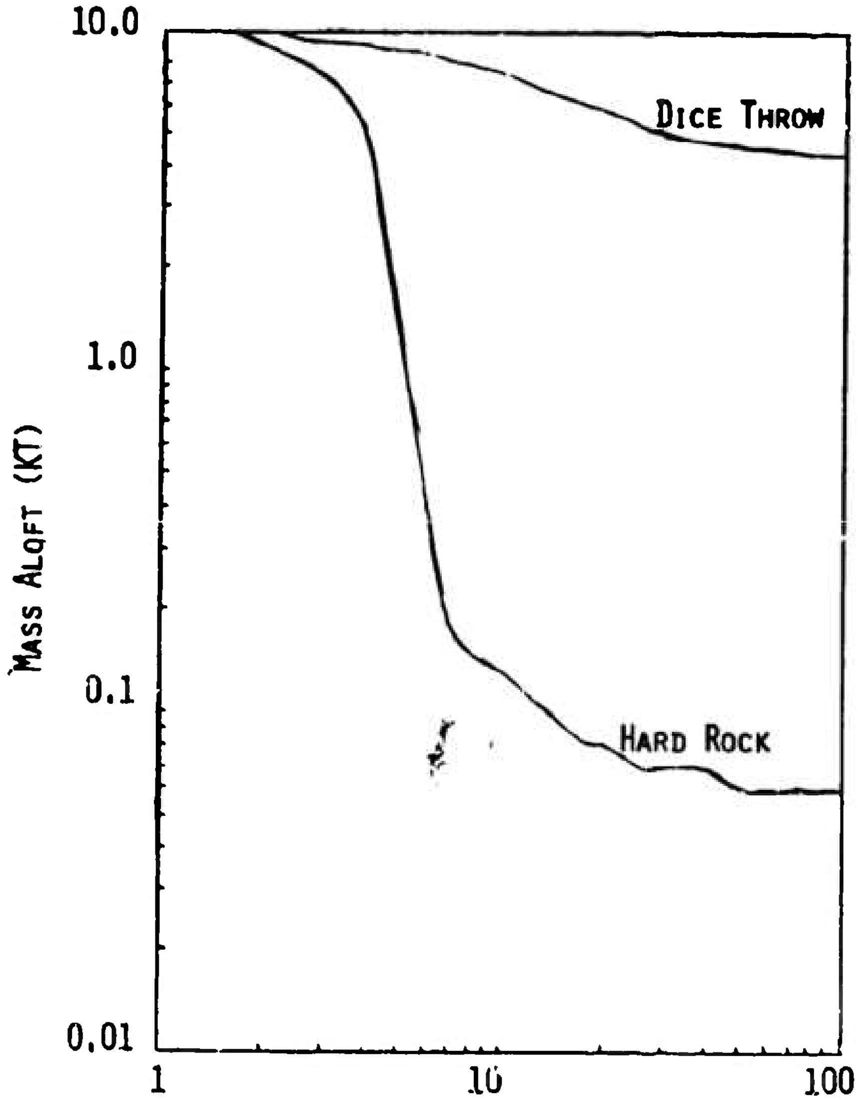

FIGURE 7. MASS OF DUST ALOFT VERSUS TIME FOR DICE THROW AND HARD ROCK PARTICLE SIZE DISTRIBUTIONS

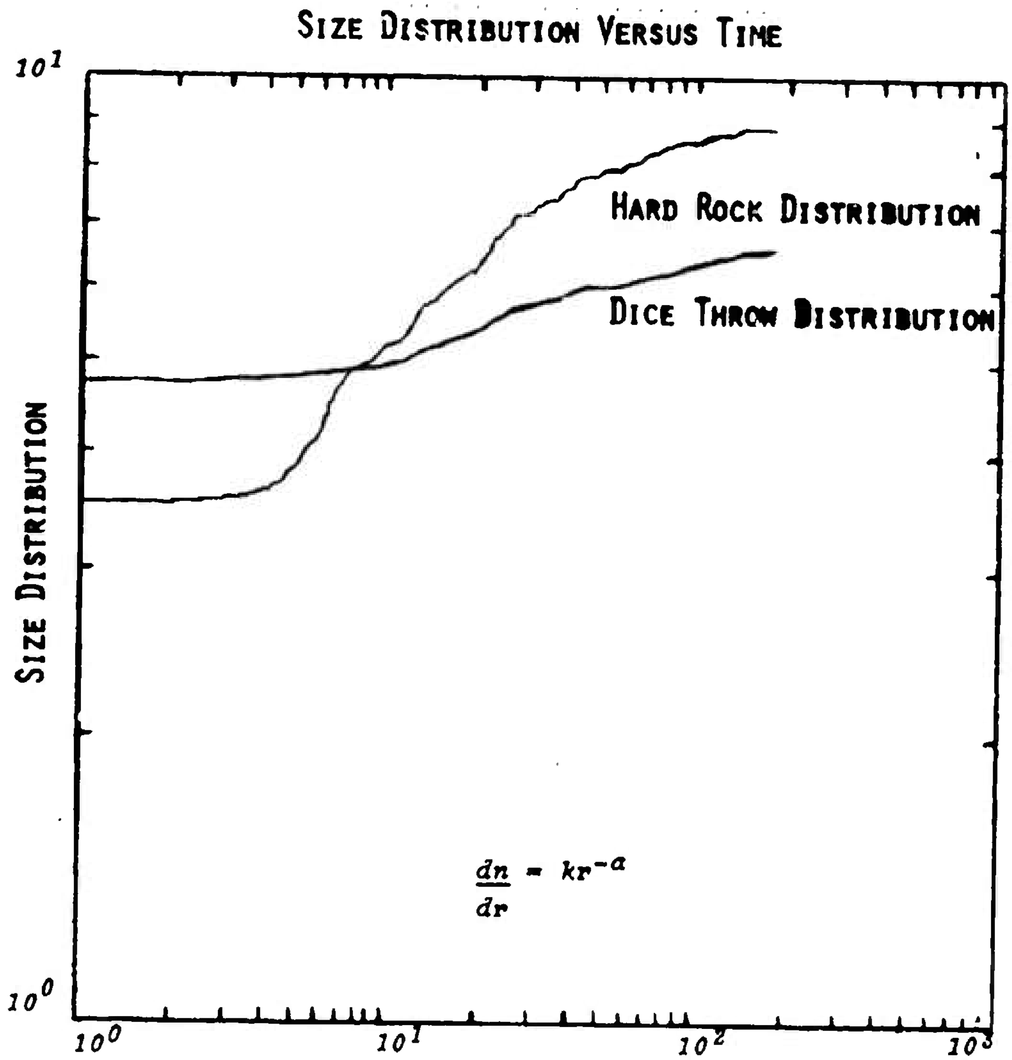

ANFO Dust Cloud Case By

FIGURE 8. PARTICLE SIZE DISTRIBUTION POWER (a) VERSUS TIME FOR DICE THROW AND HARD ROCK PARTICLE SIZE DISTRIBUTIONS

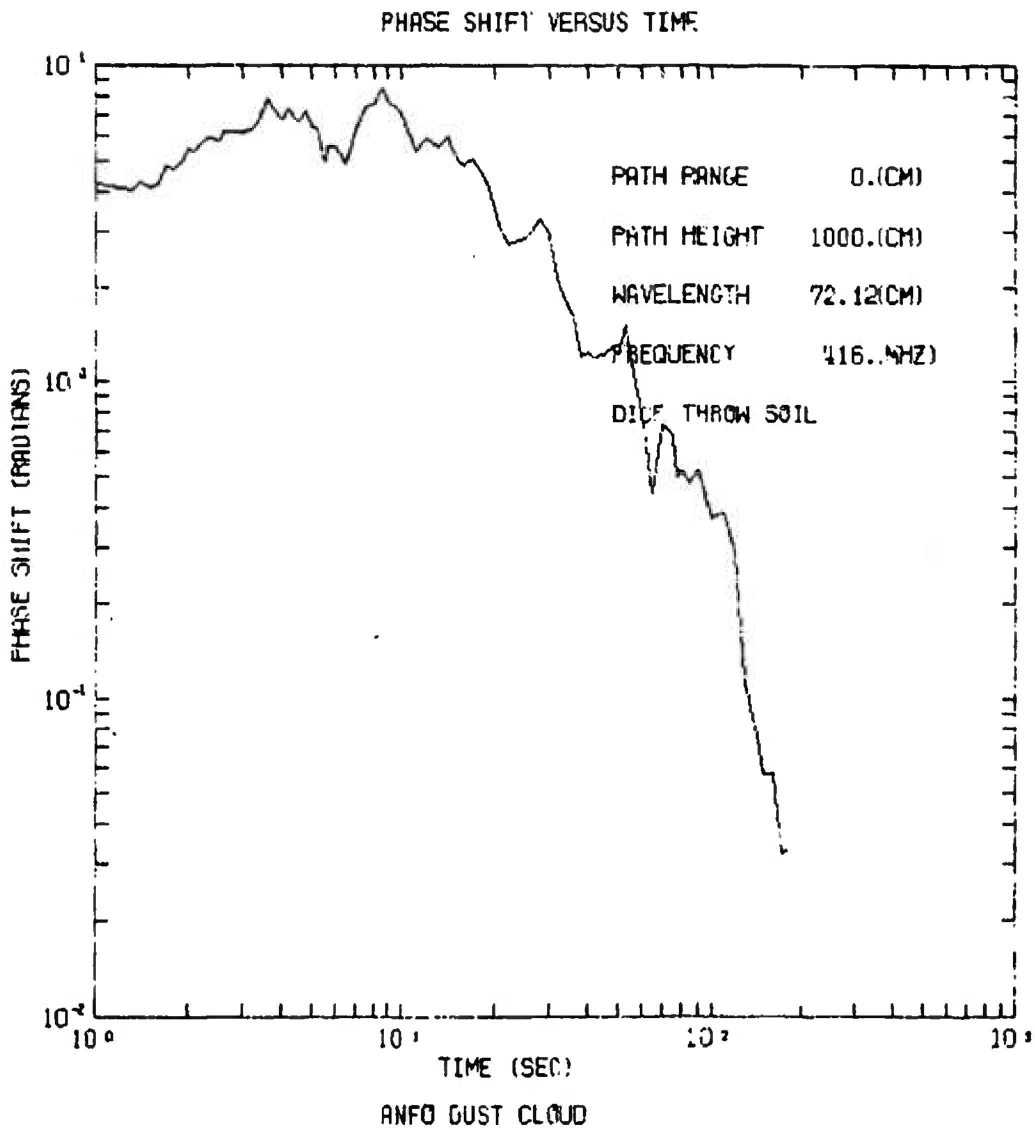

FIGURE 9. PHASE SHIFT VERSUS TIME, PATH 1,
DICE THROW PARTICLE SIZE DISTRIBUTION

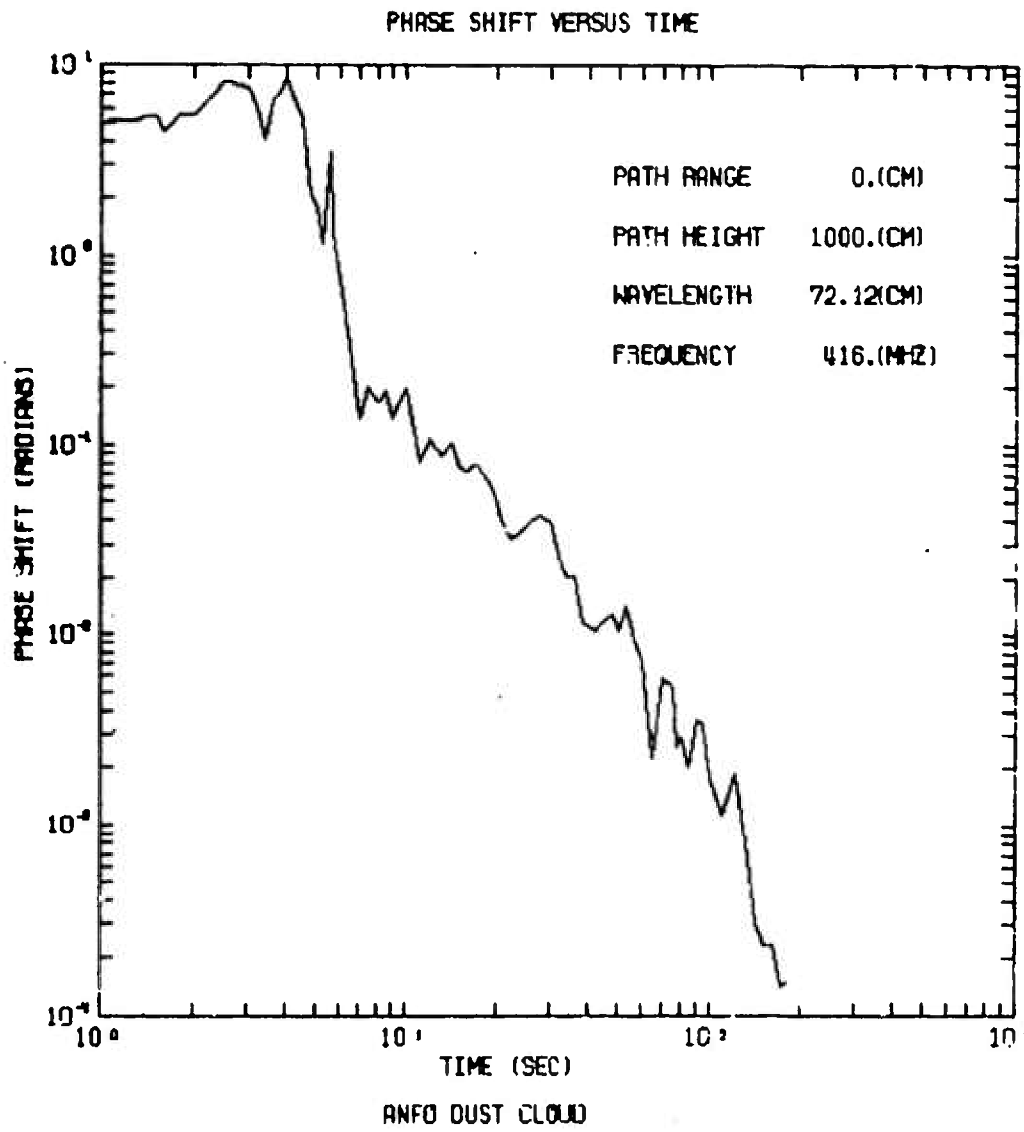

FIGURE 10 , PHASE SHIFT VERSUS TIME, PATH 1
HARD ROCK PARTICLE SIZE DISTRIBUTION

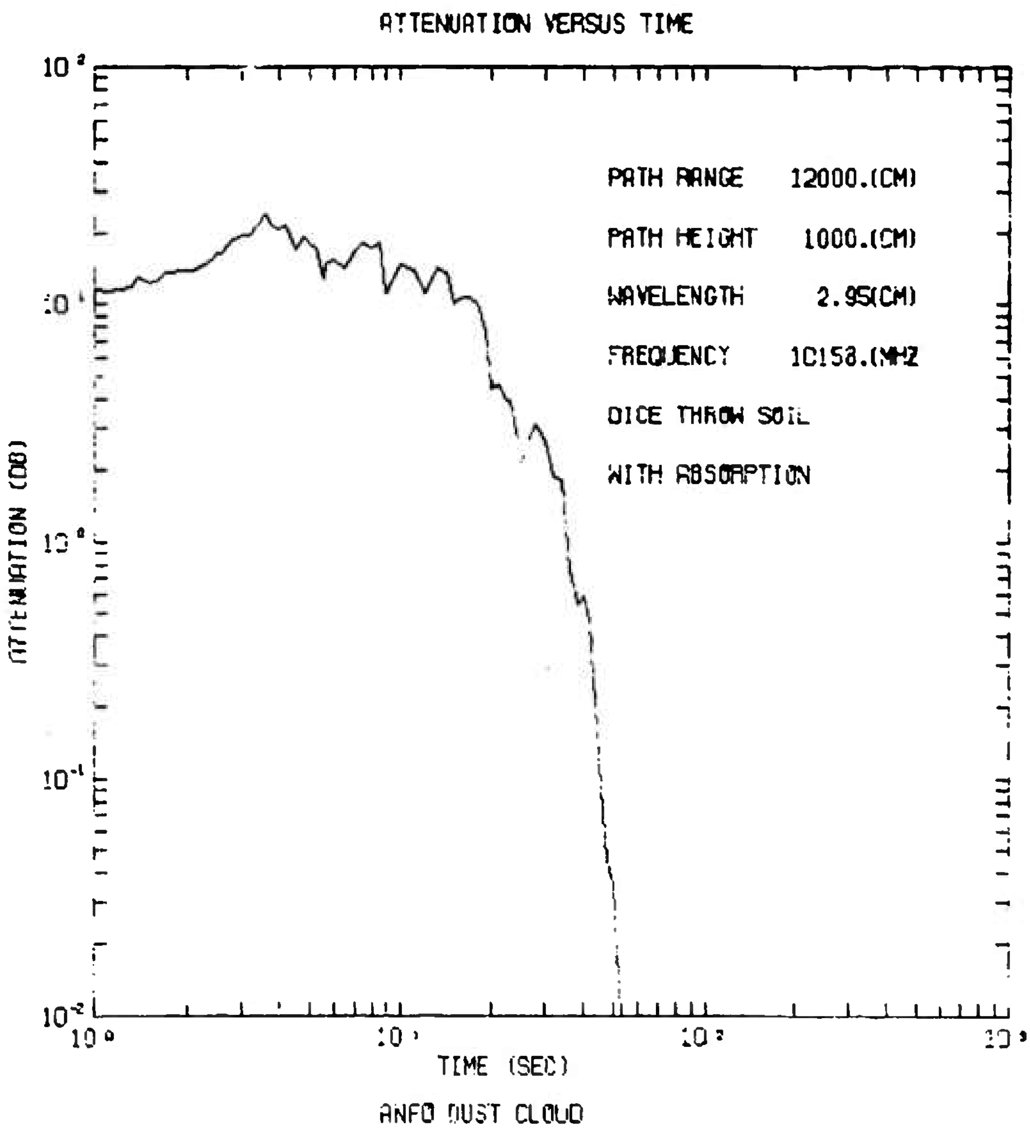

FIGURE 11. ATTENUATION VERSUS TIME, PATH 1,
DICE THROW PARTICLE SIZE DISTRIBUTION

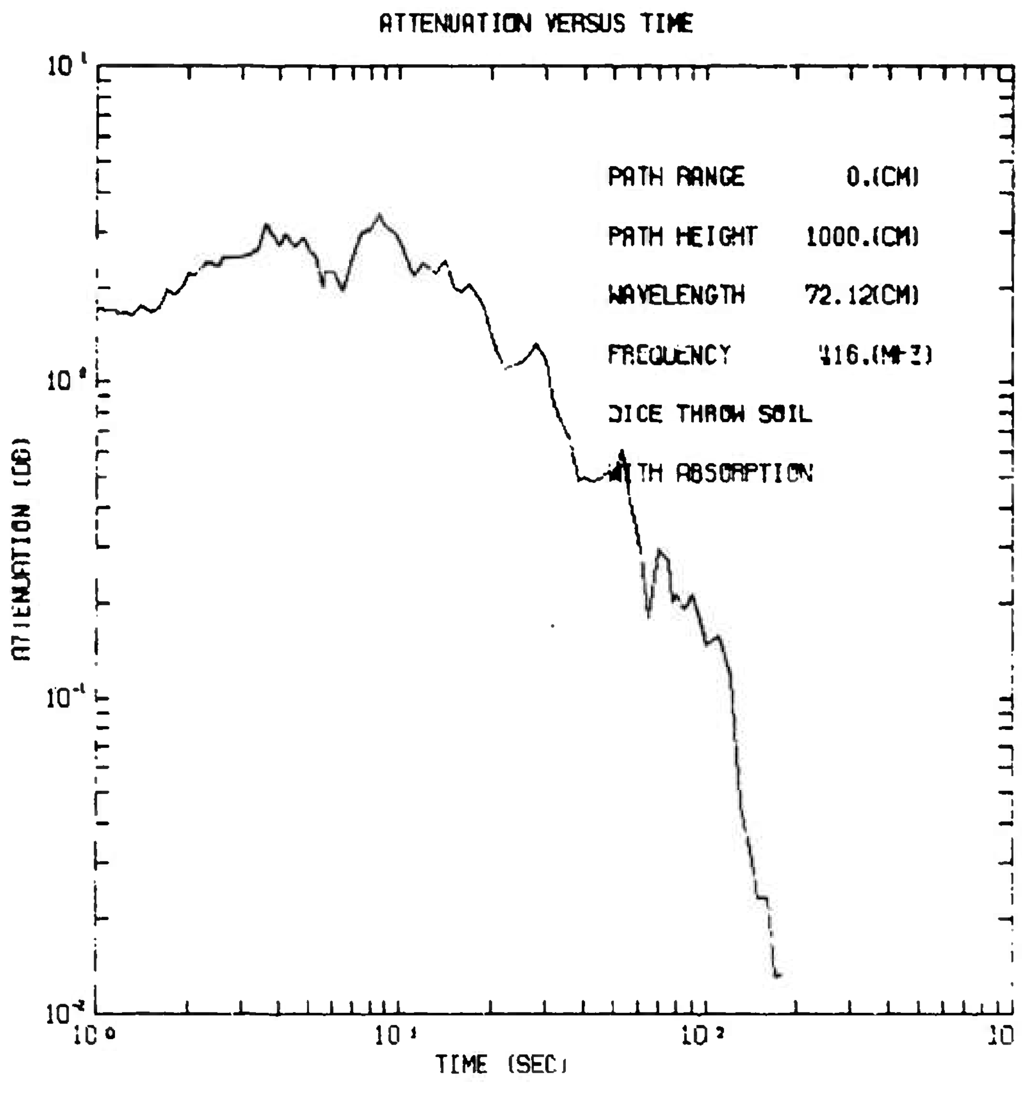

FIGURE 12. ATTENUATION VERSUS TIME, PATH 1, DICE THROW PARTICLE SIZE DISTRIBUTION

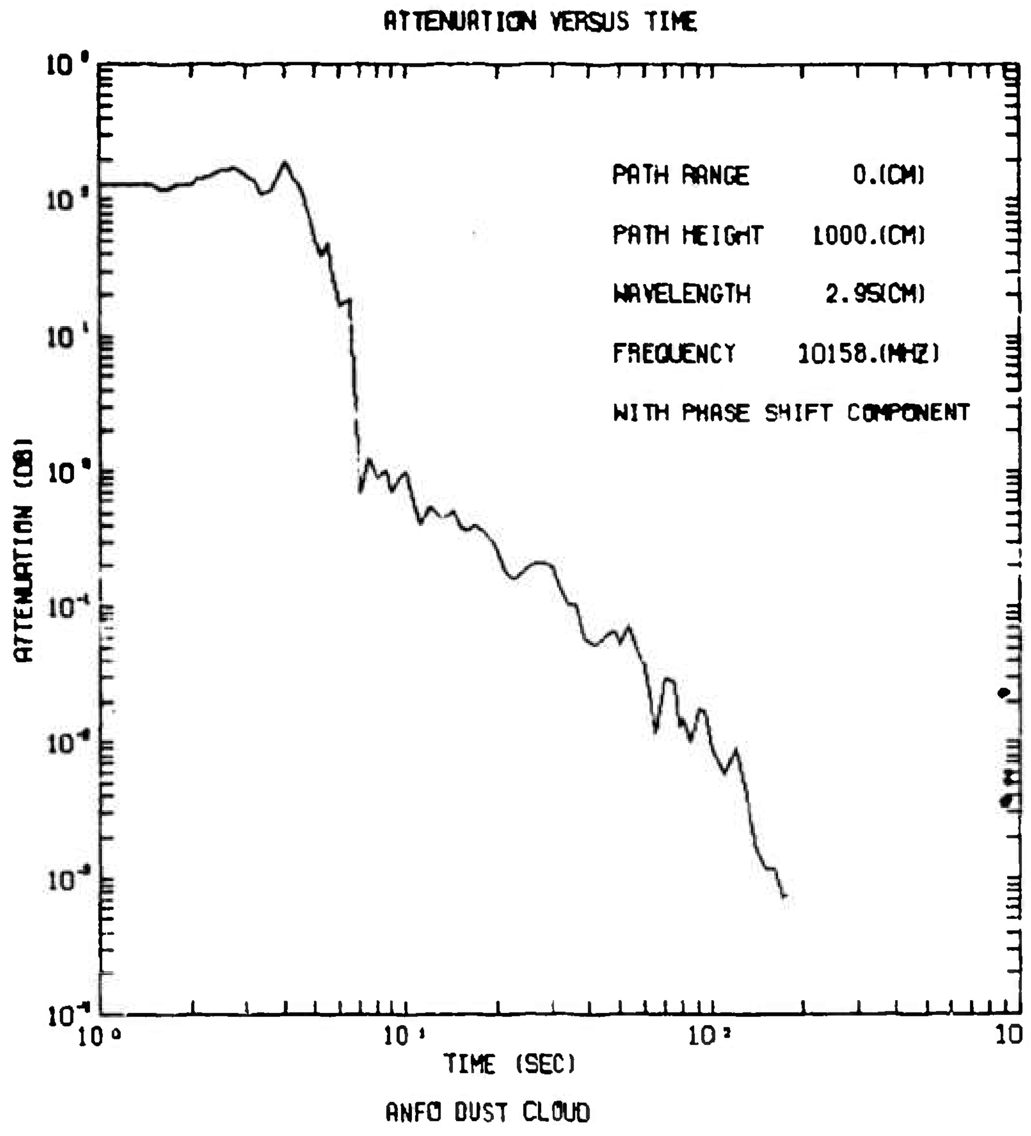

FIGURE 13. ATTENUATION VERSUS TIME, PATH 1, HARD ROCK PARTICLE SIZE DISTRIBUTION

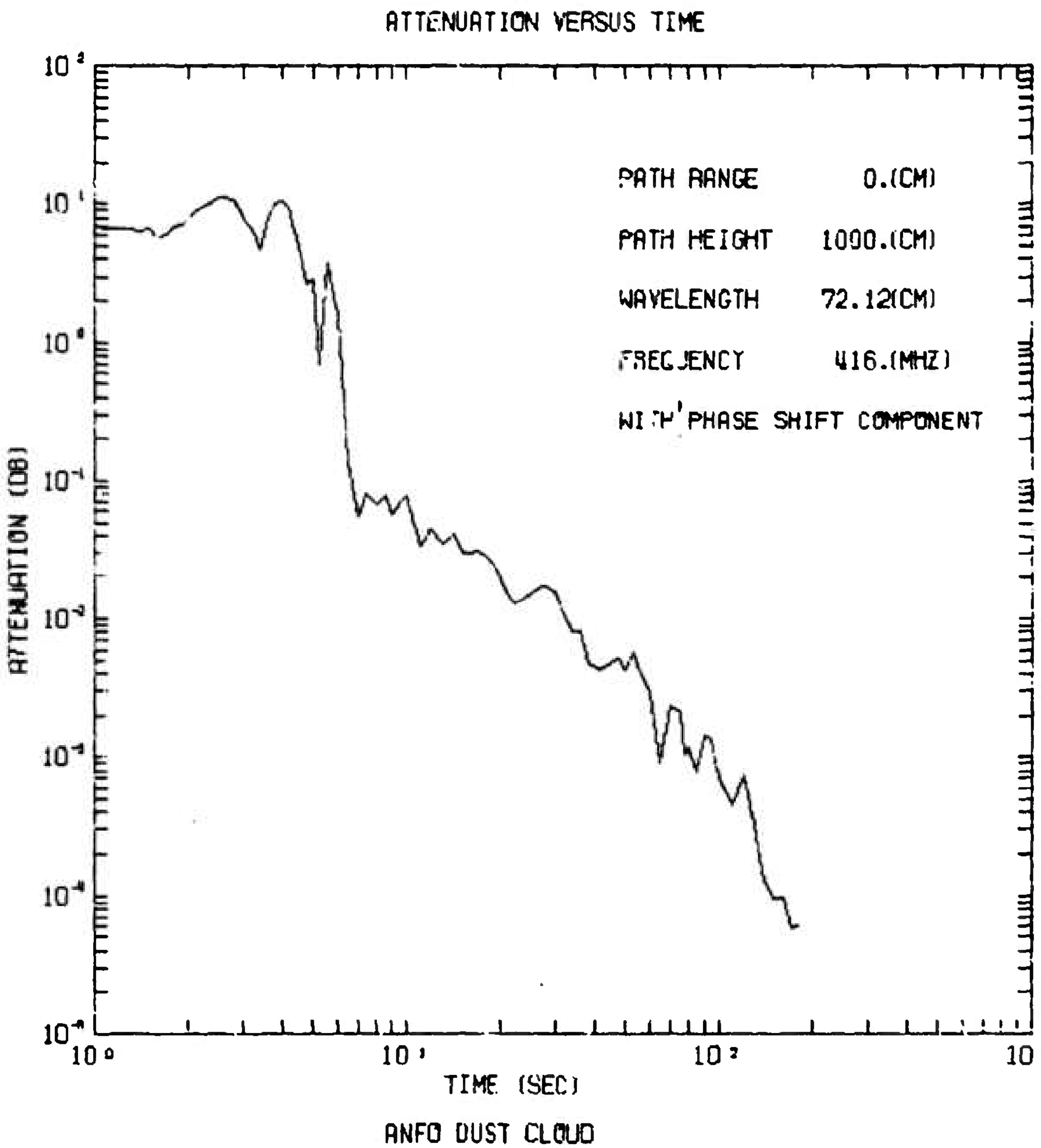

FIGURE 14. ATTENUATION VERSUS TIME, PATH 1, HARD ROCK PARTICLE SIZE DISTRIBUTION

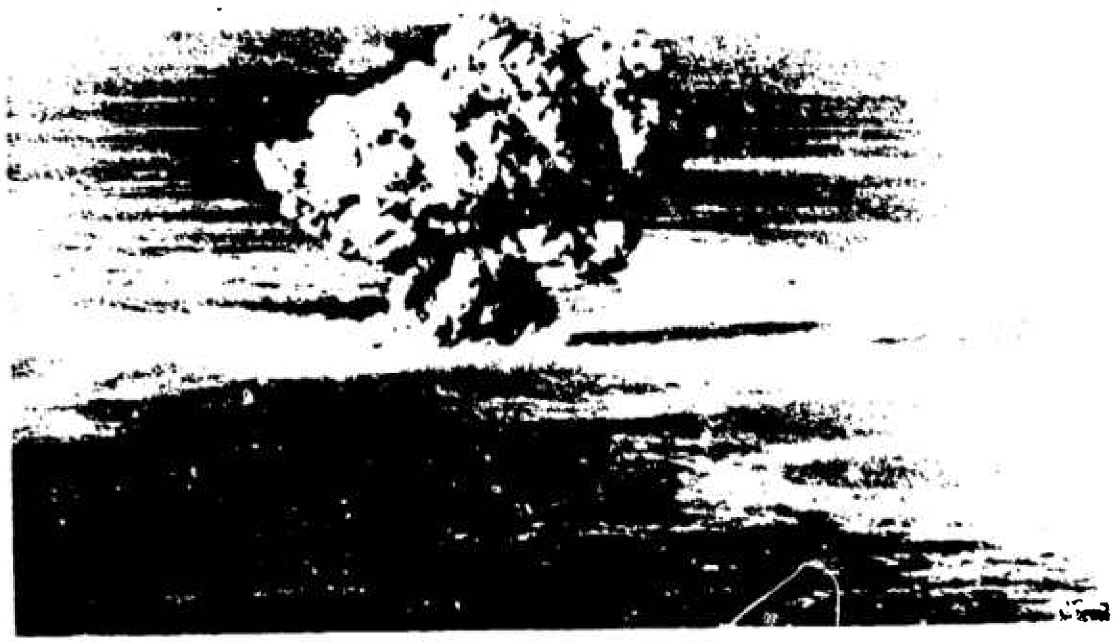

Figure 15. SRI Photograph of Dust Cloud From North Oscuro Peak at 35.4 Sec

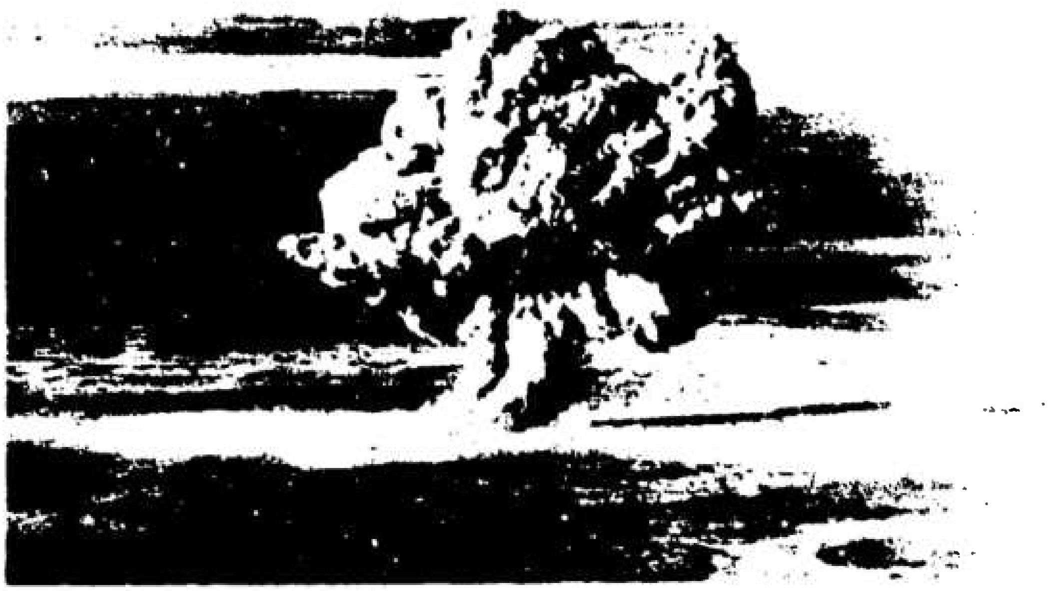

FIGURE 16. SRI PHOTOGRAPH OF DUST CLOUD FROM NORTH OSCURO PEAK AT 45.9 SEC

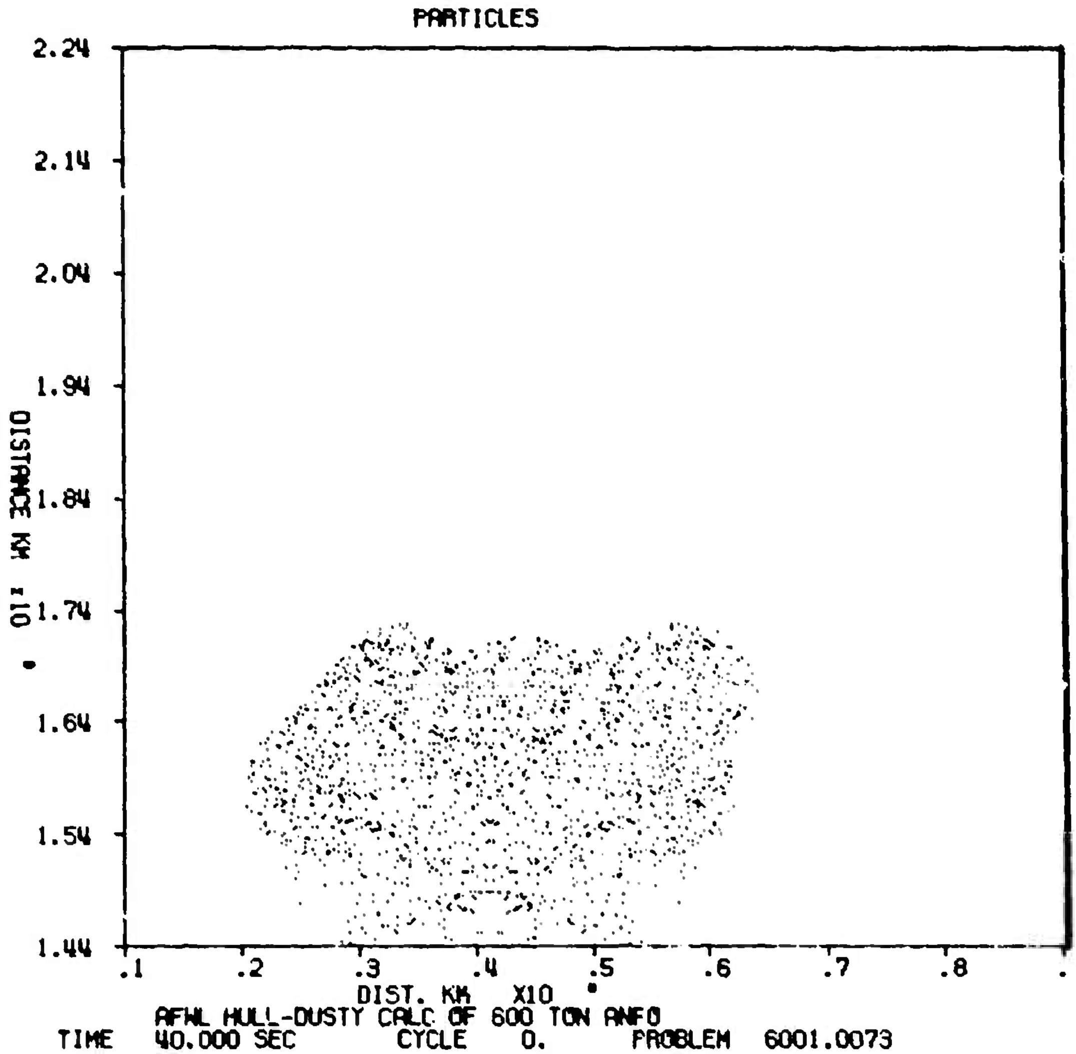

FIGURE 17. REPRESENTATIVE DUST PARTICLES WITH WIND SHEAR AT 40 SEC

FIGURE 18. SRI PHOTOGRAPH OF DUST CLOUD FROM NORTH OSCURO PEAK AT 77.9 SEC

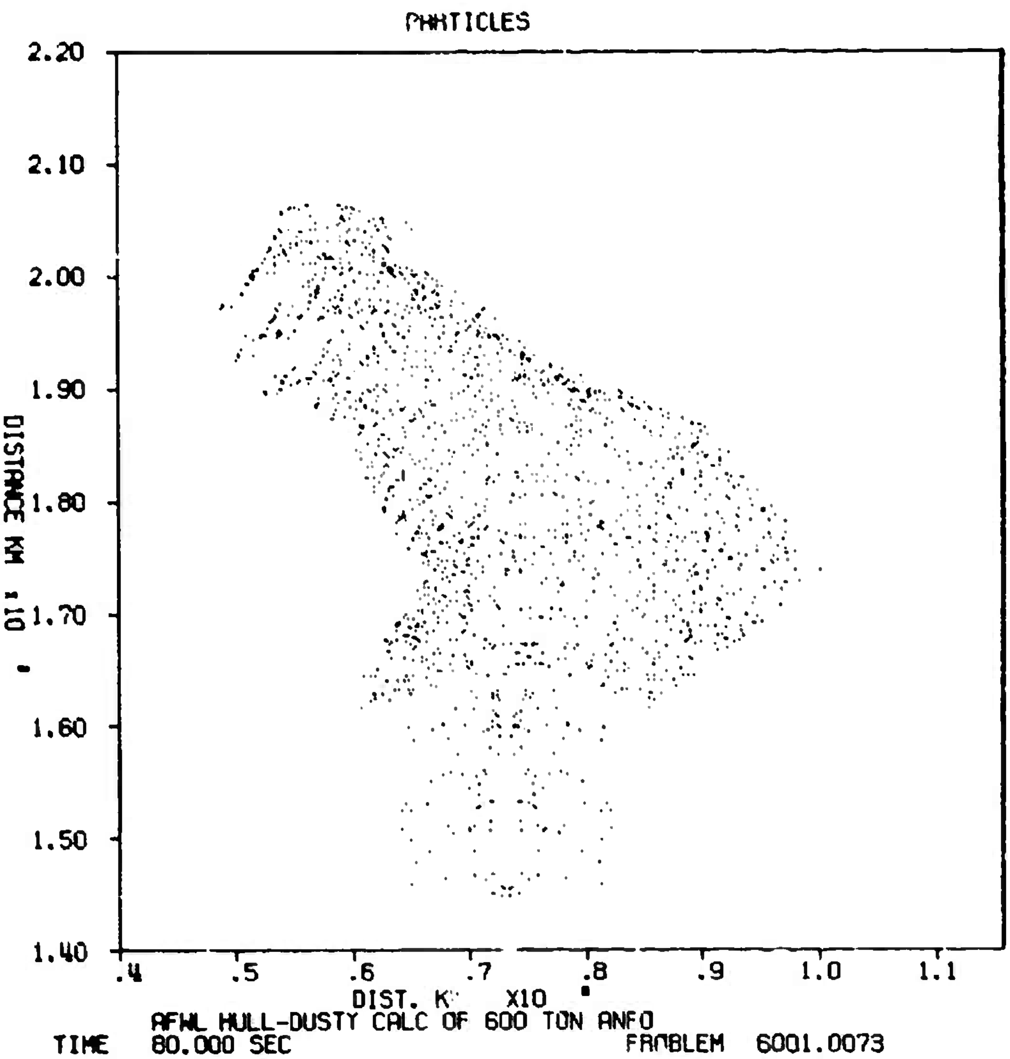

FIGURE 19. REPRESENTATIVE DUST PARTICLES WITH WIND SHEAR

24. DICE THROW SEISMIC MEASUREMENTS

by

Laurence S. Melzer

Air Force Weapons Laboratory

DICE THROW SEISMIC MEASUREMENTS

Laurence S. Melzer

Air Force Weapons Laboratory

Kirtland AFB NM 87117

ABSTRACT

Strong motion and far-field seismic measurements were fielded on the DICE THROW event at ground ranges varying from 380 meters (1,250') to 18,800 meters (62,000')*. The far-field motions in this desert alluvial environment were similar in character to the Pre DICE THROW II test events located in the adjacent Tularosa Basin, the Watching Hill test events (Distant Plain 6, Dial Pack, Prairie Flat) at the Defense Research Establishment at Suffield, Canada, and the Trinity nuclear explosion located 4 km to the east of the DICE THROW ground zero. The far-field motions can be characterized by the predominance of a slow traveling and anomalously large amplitude wave which has now been identified as the theoretically predicted fundamental Rayleigh mode. The anomalously low frequency motions observed near the ground zero on the Pre DICE THROW II events (dubbed the X-wave) originally believed to be correlatable with the above Rayleigh wave is now attributed to the failure and liquefaction of the sands located at a depth of 4.3 to 9.5 meters beneath ground zero. This motion, like the fundamental Rayleigh motion further out, is a 2-hertz oscillatory waveform.

*This effort sponsored by the Air Force Office of Scientific Research.

DICE THROW SEISMIC MEASUREMENTS

Laurence S. Melzer

BACKGROUND

For several years, the AFWL has been involved in programs to monitor explosion phenomena in the earth. This interest stems from concerns over resistance of US land-based strategic missile forces to earth shock. Historically, the primary emphasis has been placed in ground ranges associated with overpressure in the range of hundreds of psi; however, recently, new techniques of analysis and prediction of far-field seismic motions have offered some promise of use in our closer-in, strategically important ground shock regimes.

The Air Force has recently considered the deployment of a land-based ICBM system which would augment/replace MINUTEMAN, and this system would likely be deployed in western desert alluvial environments such as the Tularosa Basin and the Jornada del Muerto Valley, sites for the Pre DICE THROW and DICE THROW tests, respectively. Therefore, it is of interest to gain insight into the mechanisms of wave propagation in these desert alluvial environments.

For the above-stated reasons, the Air Force Office of Scientific Research sponsored the AFWL's participation in the DICE THROW series of tests.

EXPERIMENT DESCRIPTION

The seismic instrumentation for the DICE THROW event consisted of measurements at 17 ground stations as shown in Figure 1. The five close-in (or strong-motion) stations to the west of GZ were recorded by the AFWL, the two far-field stations to the north recorded by Southern Methodist University (SMU), and the ten stations to the east and south were recorded by the Environmental Institute of Michigan (ERIM). All gages at each station provided

DICE THROW SEISMIC STATION LOCATIONS

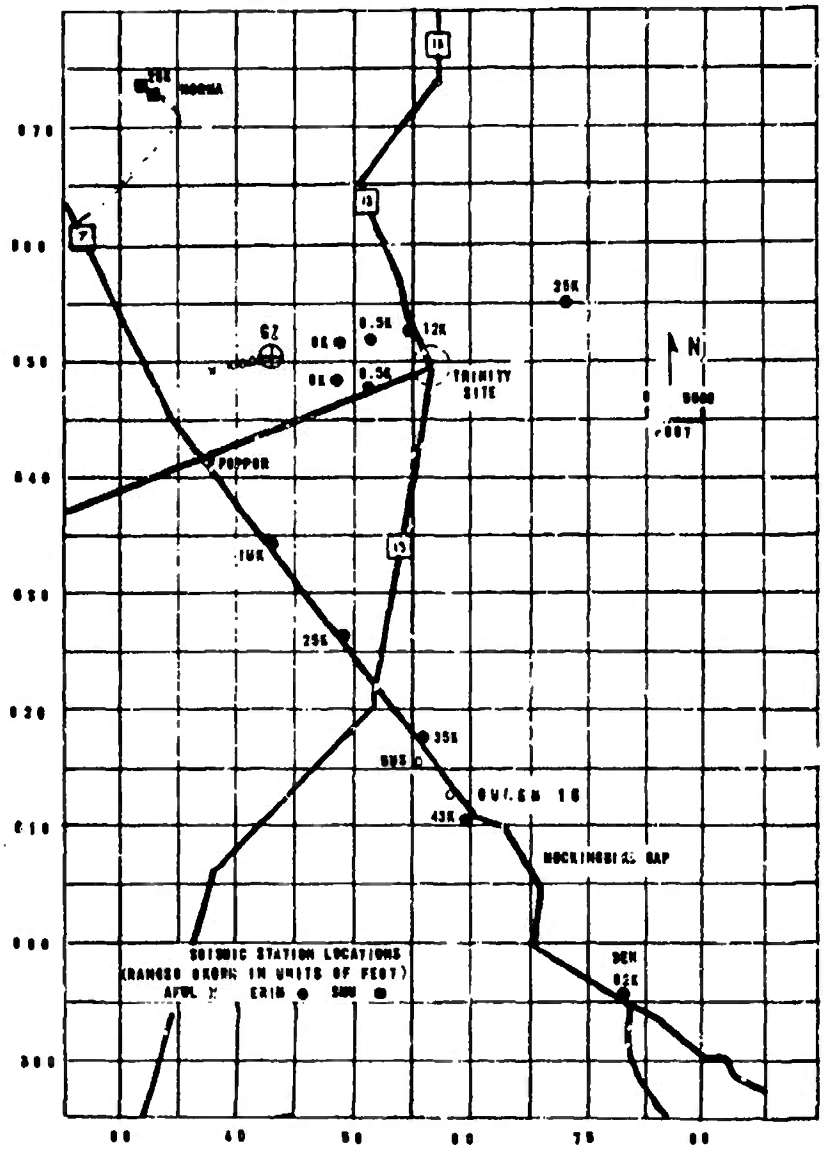

Figure 1

useable data. The layout was designed in a manner similar to the seismic project design for the Pre DICE THROW II experiments (ref 1).

RESULTS

A. Pre DICE THROW II Summary:

A typical far-field seismometer record from the Pre DICE THROW II events is shown in Figure 2. The typical first arrivals at these ranges are always the refracted P-waves followed soon thereafter by a series of oscillations characteristic of the surface Rayleigh wave. Next, and finally, is the local airslap motion due to the passage of the airblast immediately over the station. These Pre DICE THROW events are atypical in that two strong Rayleigh-type oscillatory wave packets or groups are present, and even stranger is the fact that the second is inversely dispersed (higher frequency motion occurring earlier in the wave group).

Detailed analysis of the Pre DICE THROW results has been accomplished. Theoretical Rayleigh wave dispersion curves have been calculated using the method of Haskell (ref 2). The required input for the calculations consists of a P- and S-wave velocity profile which was obtained by refraction seismic profiling techniques conducted by ERIM. Results are shown in Figure 3, along with the profile used in the dispersion curve calculations. (Note that the frequency of motion is centered around 2-hertz.) These results indicate both wave groups can be explained by conventional wave equation solutions for surface wave (Rayleigh) motions. These surface motions become apparent at ground ranges of several hundred meters from bursts of these yields.

Parallel analysis which was performed on the Pre DICE THROW II waveforms offered a contrary explanation for the origin of the second wave group.

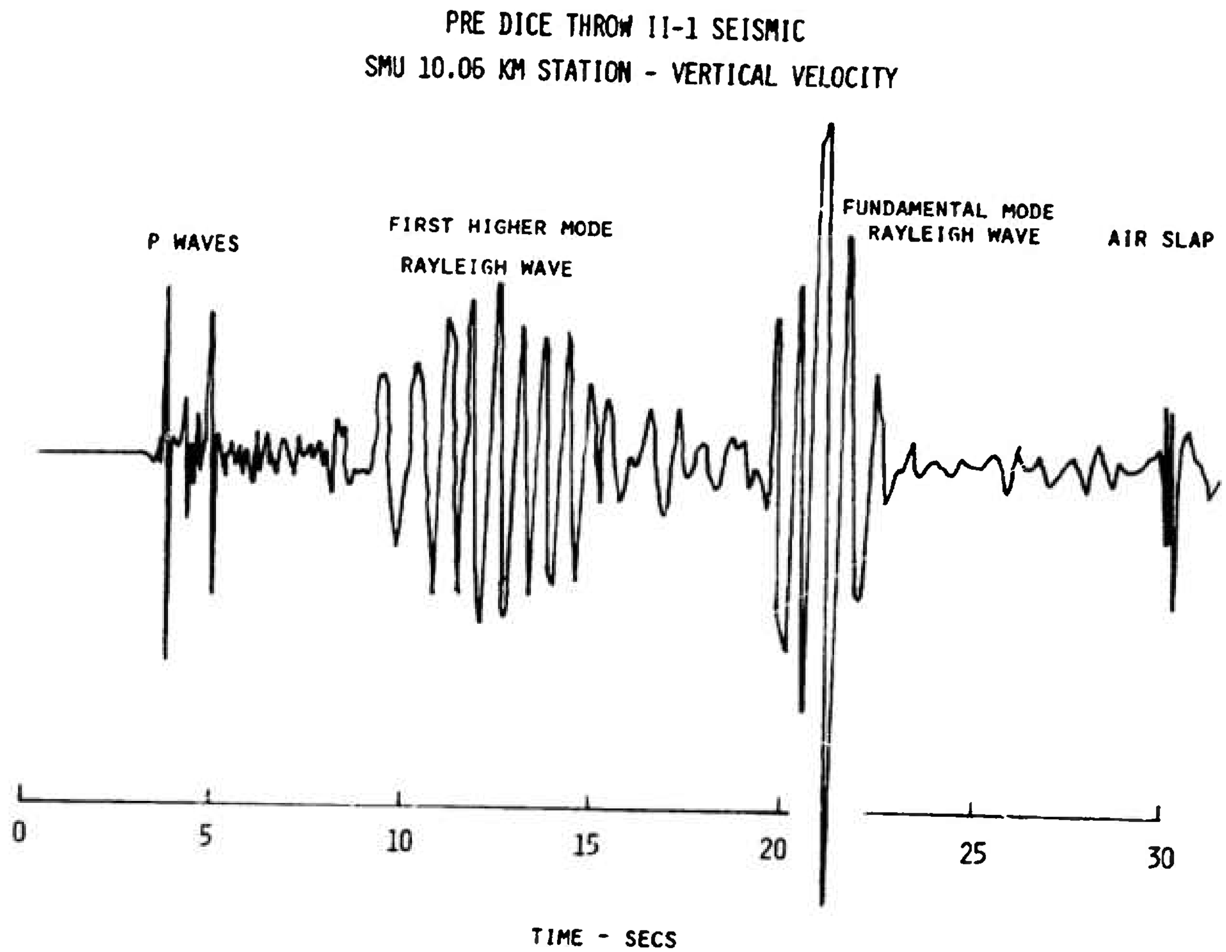
PRE DICE THROW II-1 SEISMIC
SMU 10.06 KM STATION - VERTICAL VELOCITY
P WAVES
FIRST HIGHER MODE
RAYLEIGH WAVE
FUNDAMENTAL MODE
RAYLEIGH WAVE
AIR SLAP
0
5
10
15
20
25
30
TIME - SECS

Figure 2.

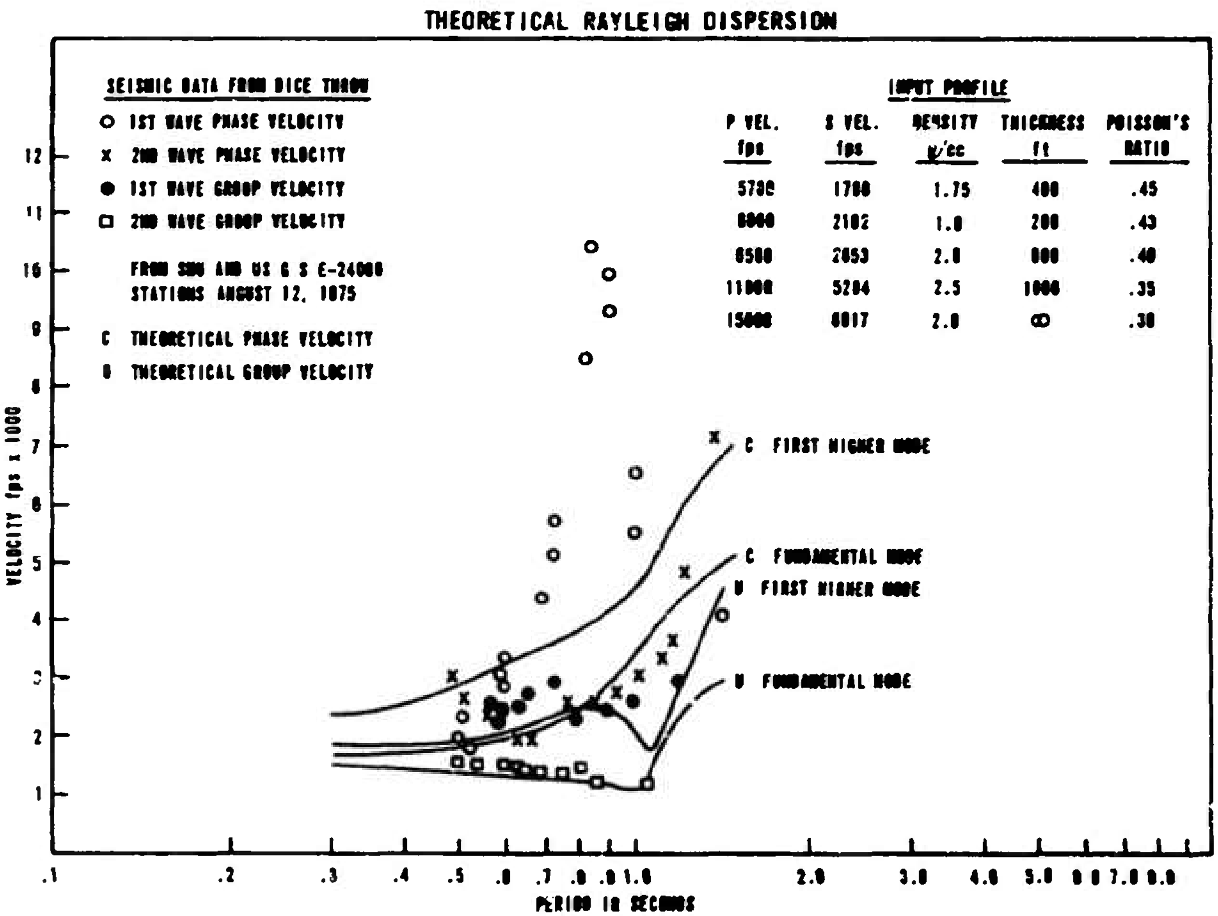

THEORETICAL RAYLEIGH DISPERSION
SEISMIC DATA FROM DICE THROW
1ST WAVE PHASE VELOCITY
2ND WAVE PHASE VELOCITY
1ST WAVE GROUP VELOCITY
2ND WAVE GROUP VELOCITY
STATIONS AUGUST 12,
C THEORETICAL PHASE VELOCITY
THEORETICAL GROUP VELOCITY
INPUT PROFILE
P VEL. fps
S VEL. fps
DENSITY g/cc
THICKNESS ft
POISSON'S RATIO
1.75
.45
2102
.43
.40
2.5
.35
.30
C FIRST HIGHER MODE
C FUNDAMENTAL MODE
U FIRST HIGHER MODE
U FUNDAMENTAL MODE
VELOCITY fps x 1000
PERIOD IN SECONDS

Figure 3.

Analysis of records obtained near the crater region identified a 2-hertz oscillatory wave which apparently originated within the crater region. Figure 4 shows this low frequency motion at the 49-meter range. Note here that the motion is stronger on the horizontal gages than on the vertical, implying an upstream (rather than below) source of motion. Note also that the 6.1 meter depth measurements appear to be leading (in phase) the motions nearer the surface. These observations, coupled with the fact that the crater shape was atypically "flatbottomed," lead us to believe now that a sand layer, forming the floor of the crater, liquefied, and the low frequency motion is a manifestation of the "fluid slosh."

Further correlation performed on the near-crater results (Figure 5) indicates that this low frequency crater region motion is traceable to ranges in excess of 300 meters. This confuses the Rayleigh wave explanation offered earlier because it can be shown that Rayleigh wave motion does not propagate purely horizontally from the crater region.

B. DICE THROW Summary:

The DICE THROW experiment offered a unique opportunity to resolve the apparent contradiction of the Pre DICE THROW wave motions. The shallow geologies at the Pre DICE THROW and DICE THROW sites (Figure 6) are significantly different (wet versus dry) while the deep geologies (Figure 7) are generally quite similar.

There would be every reason to believe that the far-field seismic motions from DICE THROW would be similar to Pre DICE THROW II if the Rayleigh wave explanation was accurate. On the other hand, if the far-field motion was in some way related to the mechanics of motion near the crater region, there would be no reason to believe far-field measurements would be similar.

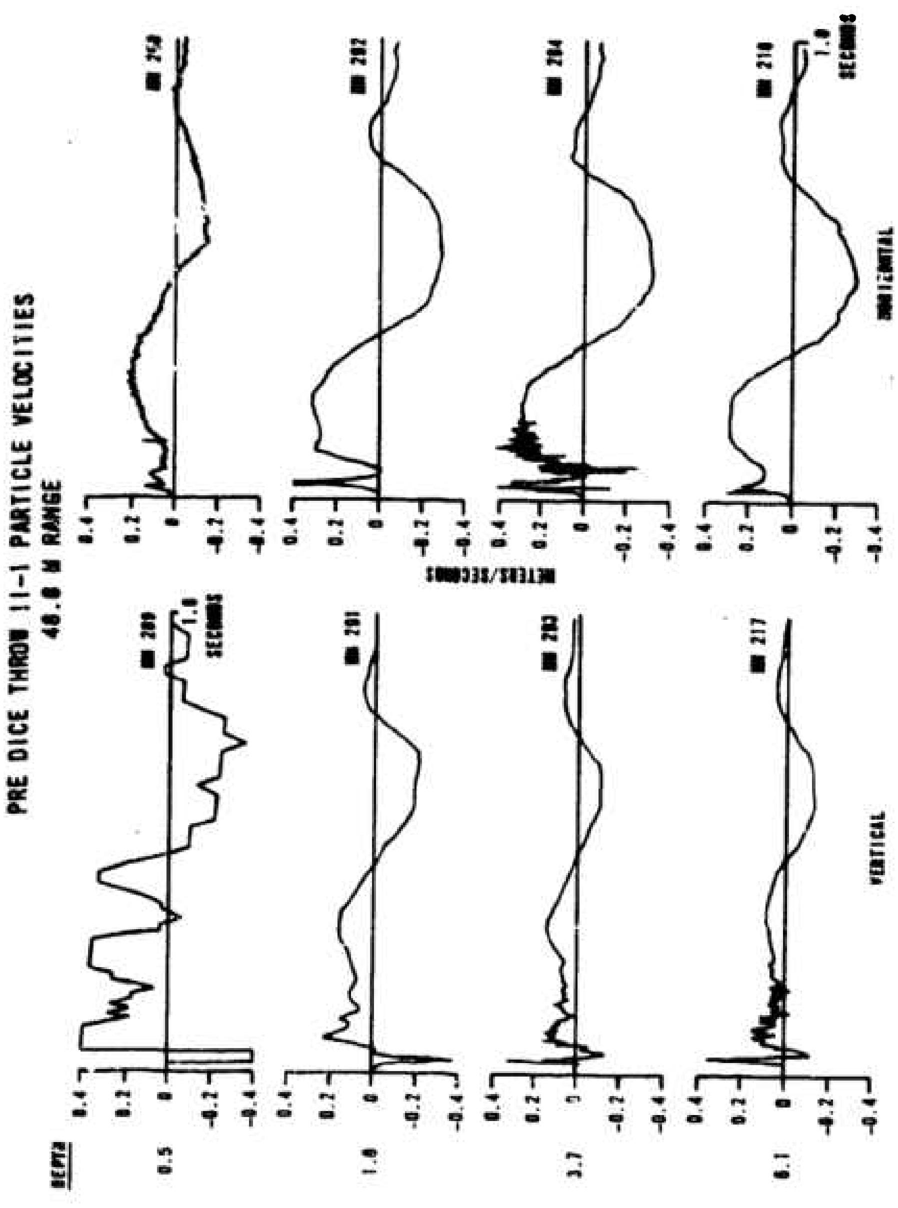
PRE DICE THROW II-1 PARTICLE VELOCITIES
40.0 M RANGE
DEPTH
VERTICAL
HORIZONTAL
METERS/SECONDS
SECONDS

Figure 4.

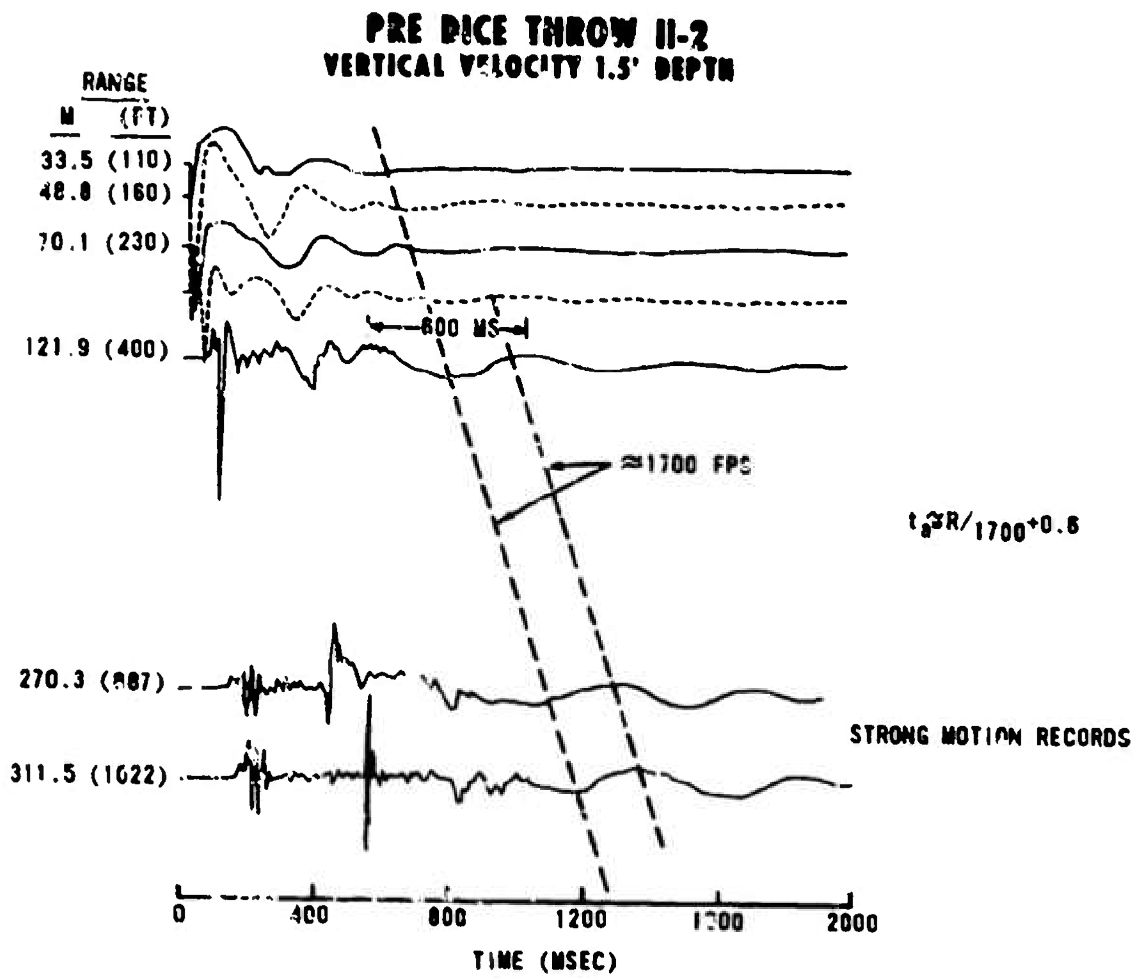
PRE DICE THROW II-2
VERTICAL VELOCITY 1.5' DEPTH
RANGE
M (FT)
33.5 (110)
48.8 (160)
70.1 (230)
121.9 (400)
600 MS
≈1700 FPS
$t_a \approx R/_{1700}+0.6$
270.3 (887)
311.5 (1022)
STRONG MOTION RECORDS
0
400
800
1200
2000
TIME (MSEC)

Figure 5

SHALLOW GEOLOGIC PROFILES

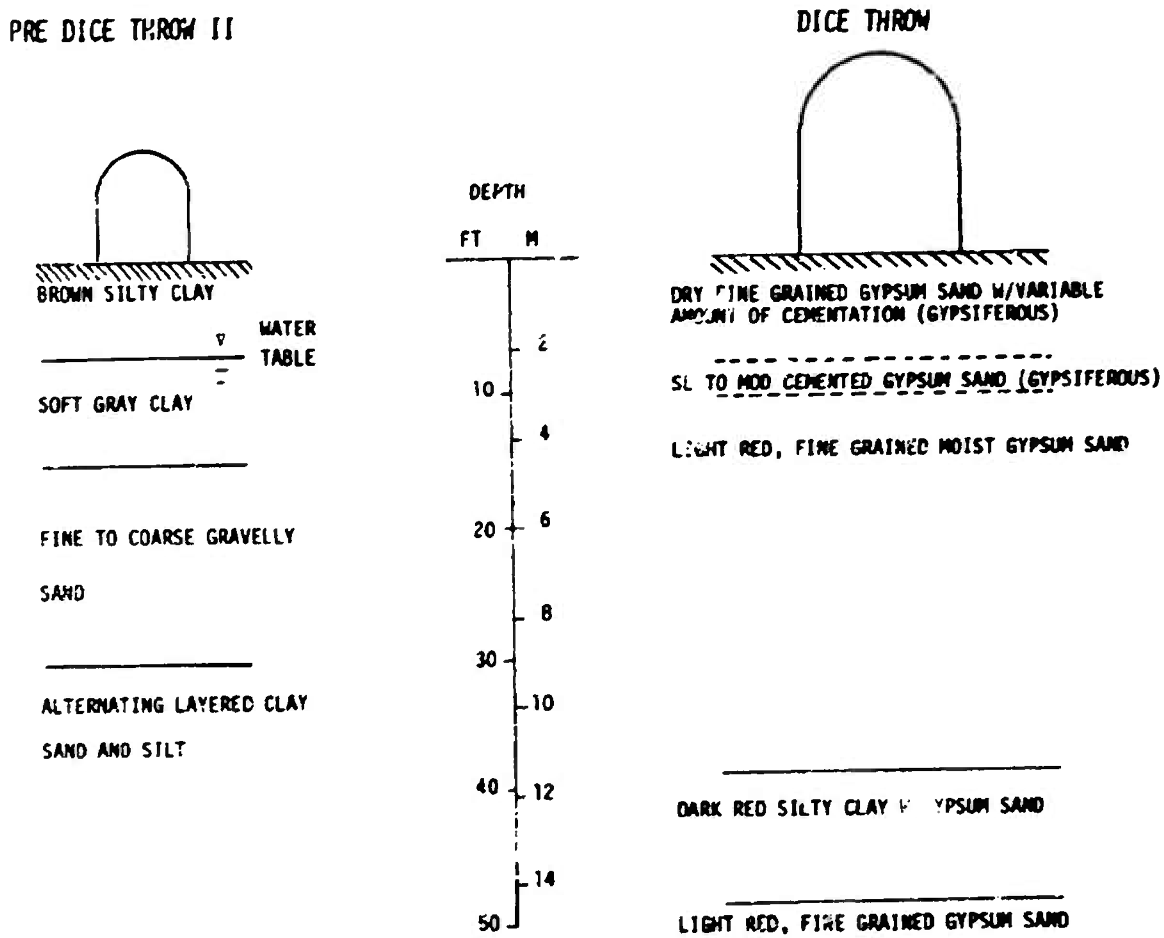

Figure 6.

DEEP GEOLOGIC PROFILES

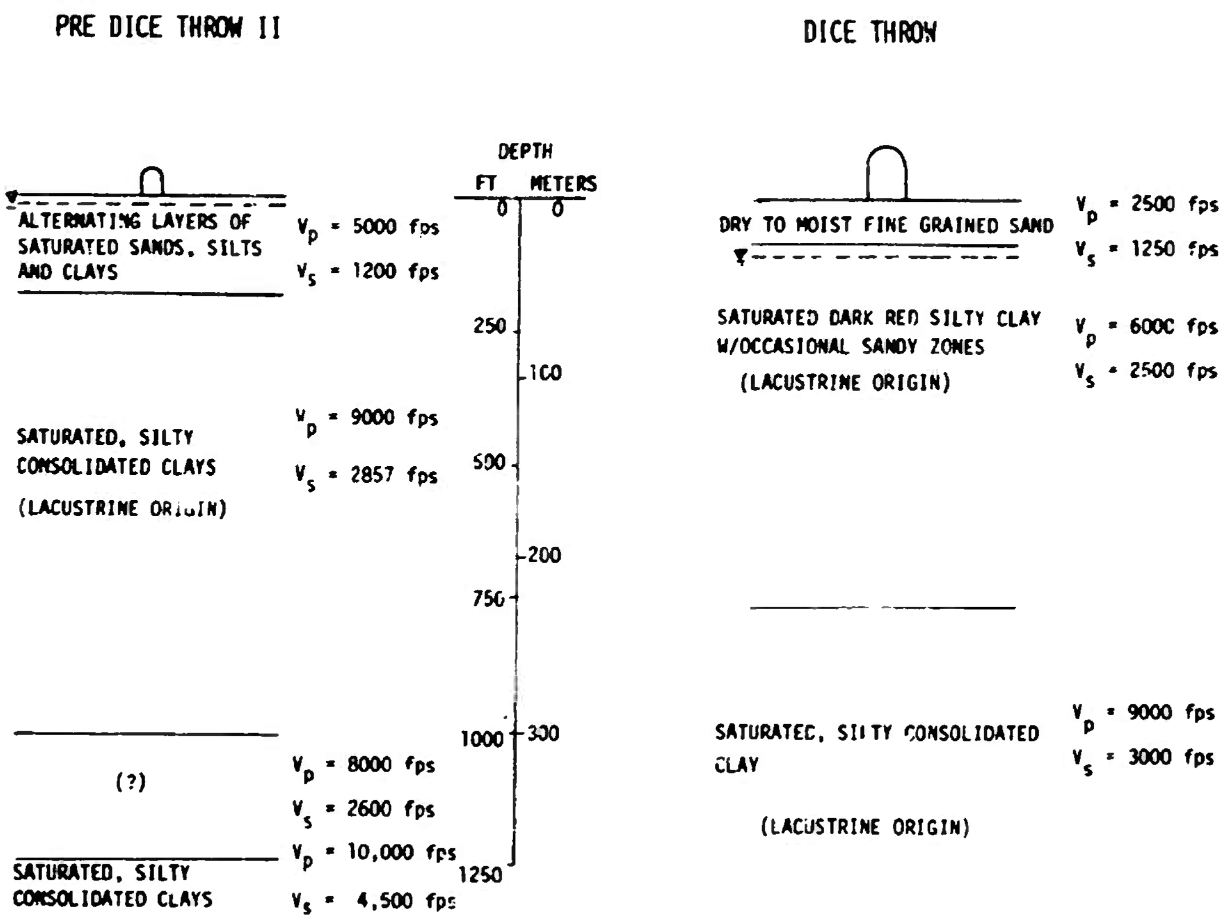

Figure 7.

A typical DICE THROW seismometer is shown in Figure 8. Note the similar wave types. On the other hand, note the comparison in Figure 9 of close-in gages which show significant differences in type and frequency of motion. Therefore, it is concluded, Rayleigh wave theory must explain the far-field motion.

C. Correlation to Other Events:

Ground zero for the DICE THROW event was located about three miles from the site of the Trinity test of July 1945. Don Leet (ref 3) reported wave motion at 8 kilometers from DICE THROW. Leet called the first wave packet the "Hydrodynamic" wave because of its prograde particle motion and identified the slower wave as the Rayleigh wave. This slower wave is now identified as the fundamental Rayleigh mode, while the first is the first higher Rayleigh mode.

Similar waveforms have also been observed on tests conducted at the Watching Hill Test Site on the Defense Research Establishment at Suffield, Canada (ref 3). The deep geology there is similar in origin and properties, so it would seem likely that theoretical Rayleigh wave dispersion curve calculations there would offer like explanations as to the origin of observed seismic motions.

SUMMARY

Seismic motions from the DICE THROW test series were successfully measured. Theoretical Rayleigh wave dispersion curve calculations were performed that agree convincingly with recorded motions. Two wave groups of Rayleigh surface waves are present in these typical alluvial geologies with water tables less than 50 meters in depth. This first occurring wave

DICE THROW SEISMIC

SMU 7.5 KM STATION - VERTICAL VELOCITY

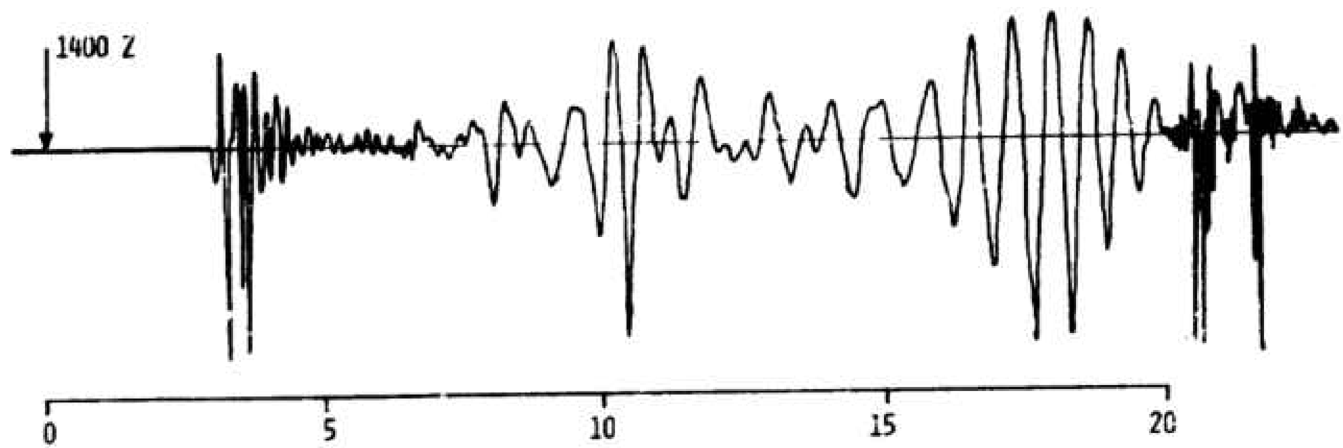

Figure 8.

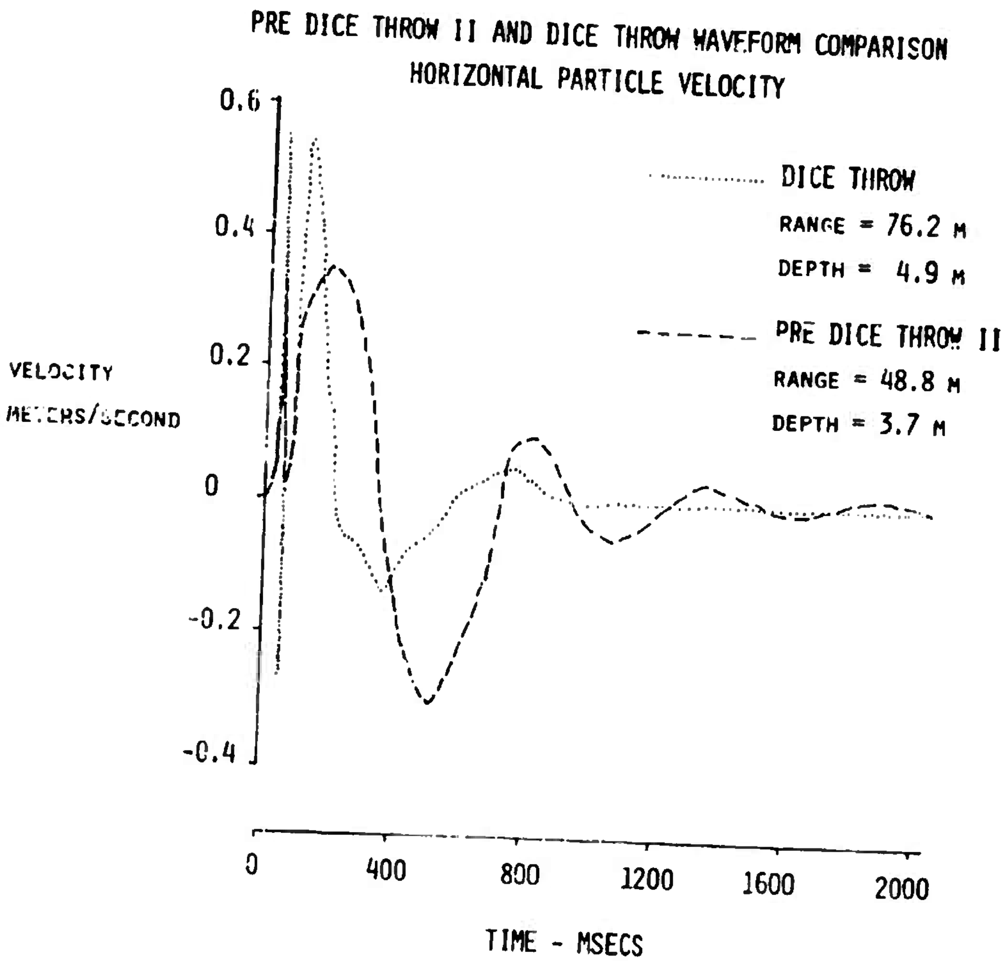
PRE DICE THROW II AND DICE THROW WAVEFORM COMPARISON
HORIZONTAL PARTICLE VELOCITY
0.6
0.4
0.2
0
-0.2
-0.4
VELOCITY
METERS/SECOND
DICE THROW
RANGE = 76.2 M
DEPTH = 4.9 M
PRE DICE THROW II
RANGE = 48.8 M
DEPTH = 3.7 M
0
400
800
1200
1600
2000
TIME - MSECS

Figure 9

group has prograde motion and travels at a group velocity of 1,000 meters per second. The second wave group is inversely dispersed, has retrograde motion, and travels at a group velocity of 500 meters per second. The second wave group agrees well with the calculated fundamental Rayleigh mode while the first occurring agrees with the first higher mode.

Motions near the crater region from the DICE THROW and Pre DICE THROW series are considerably different. The 2-hertz oscillatory signal on the Pre DICE THROW events was not observed on the DICE THROW tests. The flat-bottomed crater and the 2-hertz signal observed on the Pre DICE THROW events are believed to be caused by the liquefaction of the saturated sand immediately beneath the crater.

REFERENCES

1. Hoffman, J.P. and Harding, S.T., Strong Ground Motion in the Tularosa Basin, New Mexico, USGS Open File Rpt 77-143, 1977.

2. Harkrider, D.G., Surface Waves in Multilayered Elastic Media, Part II, Bull. Seism. Soc. Am., 60, 1937-1987, 1970.

3. Leet, L.D., Earth Motion from the Atomic Bomb Test, American Scientist, 34, 198-211, 1946.

4. Hadala, P.F., Effect of Constitutive Properties of Earth Media on Outrunning Ground Shock from Large Explosions, Waterways Experiment Station, TR S-73-6, August 1973.

25. ARMY PERSONNEL SHELTERS - DNA PROJECT NO. 329

by

William L. Huff
U.S. Army Engineer Waterways Experiment Station

ARMY PERSONNEL SHELTERS
DNA PROJECT NO. 329

INTRODUCTION

BACKGROUND

The U. S. Army Engineer Waterways Experiment Station (WES) is conducting research for the Department of the Army to determine the response of tactical protective structures to the effects of nuclear and conventional weapons. Three different buried combat services support shelters and a fighting bunker shell were subjected to the blast and shock effects of the DICE THROW Main Event and follow-on small high-explosive (HE) tests.

OBJECTIVES

The primary objectives of this project were to determine the responses of candidate Army tactical protective structures to the effects of the DICE THROW Main Event, to describe the internal environment of the structures during loading, and to verify design and analytical procedures. Secondary objectives were to determine the responses of the buried metal-framed fabric-covered shelters when subjected to the effects of localized HE loadings simulating the blast effects of conventional weapons.

SCOPE

Four buried metal-framed fabric-covered shelters and two corrugated metal fighting bunker shells were tested. Two of the buried fabric-covered shelters and the two bunker shells were instrumented with 41 channels to obtain pressure, acceleration, velocity, and strain data. Passive instrumentation was used to measure the responses of the remaining two fabric-covered shelters. The airblast loadings were obtained from data collected by the U. S. Army Ballistic Research Laboratory (BRL).

Follow-on tests using 7.26-kg (16-pound) spheres of TNT to simulate the blast effects of conventional weapons were conducted on two of the fabric-covered shelters that were not damaged during the main event.

One of these shelters was instrumented and the other was not. Twenty-five channels of data were recorded.

TEST PROCEDURES

STRUCTURE LAYOUT AND INSTALLATION

Structure layout is shown in Figure 1. Pits were dug with a backhoe 2.1 metres (7 feet) deep and 1.2 metres (4 feet) wider and longer than the shelters. The pits were graded by backfilling with 0.3 to 0.4 metre (12 to 16 inches) of hand-tamped soil. Backfill was placed around the shelters with a small backhoe without any additional compaction. Care was taken to ensure that no large chunks of soil were placed directly against the shelters. The shelters were covered with 1.2 metres (4 feet) of soil, and the two fighting bunkers were covered with 0.6 metre (2 feet) of soil. The instrumented structures (PS1a and b and PS2a and b) were located near the BRL airblast gage line 1 to obtain accurate airblast loadings.

STRUCTURE DESCRIPTION

A comparison of the three fabric-covered shelters (PS1, PS3, and PS4) is presented in Table 1 and Figure 2.

<u>Structures PS1a and b</u>. These identical shelters were placed at different ranges from ground zero (GZ) to gather data on varying degrees of structural damage with range. A conceptual drawing is shown in Figure 3, and construction drawings are shown in Figure 4. Each shelter was composed of semielliptical metal frames covered with a flexible fabric that supported the soil.

The shelter itself was composed of 4 steel elements: interior frames, end frames, longitudinal braces, and pipe connectors; and a flexible fabric cover. The end and interior frames were fabricated from steel tubing formed into an elliptical arch. A straight section of tubing was welded to each of the two sides at the bottom of the arch. End frames were braced vertically and horizontally to provide support for the fabric covering at the end of the shelter. Four longitudinal braces held the frames in place while the shelter was being covered with soil and prevented the shelter from collapsing like an accordion. The flexible fabric cover was a 2-ply, neoprene-coated nylon fabric designated as U. S. Army standard landing mat T-17 membrane.

The 0.6-metre- (2-foot) square vertical entranceway led into a 0.6-metre- (2-foot) wide by 1.8-metre- (6-foot) high by 3-metre- (10-foot) long horizontal corridor connected to the main shelter. The assembled shelter and entranceway are shown in Figure 5. The T-17 membrane was draped over the shelter and allowed to fold on the ground approximately 0.46 metre (18 inches) away from the sides of the shelter (Figure 6). The fabric was wired to the end frames of the shelter to hold it in place during backfilling. Backfill placement and an interior view of the shelter are shown in Figures 7 and 8, respectively.

Structure PS3. This shelter was an enlarged version of Structures PS1a and b. The construction drawing and the assembled shelter are shown in Figures 9 and 10, respectively. The entranceway was a vertical shaft 0.6 metre (2 feet) square and fabricated from 2.54-cm- (1-inch) diameter standard pipe at one end of the structure. An interior view of the completed shelter is shown in Figure 11.

Structure PS4. This shelter consisted of the British Mark II steel-framed structure covered with the T-17 membrane. Construction drawings for the shelter are shown in Figure 12. This shelter was tested in previous nuclear weapons airblast simulation events. The shelter consisted of three simple steel structural members: pickets, arches, and spacers; and a flexible fabric cover. Spacers were used to provide lateral support for the picket-arch frame and acted with the arches to support the earth cover. The framework was covered with the T-17 membrane held in place by the earth backfill. Attachment of the fabric to the shelter is shown in Figure 13, and an interior view of the completed shelter is shown in Figure 14.

Structures PS2a and b. Structures PS2a and b were identical corrugated metal fighting bunker shells located at two overpressure ranges from GZ. These bunker shells were designed at WES in response to requirements during the Vietnam conflict.

Construction drawings are shown in Figure 15. The bunker shells were made of four quarter-circular sections of 1.2-metre (4-foot) radius that, when connected, were 4.3 metres (7 feet 9 inches) square at the base and 0.9 metre (3 feet) high at the crown (Figure 16). When placed over an unlined hole 1.5 metres (5 feet) in diameter and 1.2 metres (4 feet) deep, the bunker shells had a vertical clearance of 2.1 metres (7 feet) at the crown and approximately 1.8 metres (6 feet) at the extreme perimeter of the pit. Also, a firing shelf with a minimum width of 0.4 metre (1 foot 4 inches) was provided at each firing port. The firing or observation ports were 0.6-metre- (24-inch) wide by 0.4-metre- (16-inch) high apertures in each side of the bunker shell. Flat, trapezoidal, corrugated steel sheets were bolted to the sides of the bunker shells over each aperture. The two nonparallel sides of the aperture beam were supported by sandbags. Soil cover on the bunker shells, including the aperture beams, provided protection from conventional weapons effects. For DICE THROW, the bunker shells were covered with 0.6 metre (2 feet) of soil. A completed bunker shell is shown in Figure 17.

MEASUREMENTS AND DATA REDUCTION

Forty-one data channels consisting of pressure, strain, velocity, and acceleration were recorded during the main event on Structures PS1a, PS1b, PS2a, and PS2b. Passive instrumentation was used for Structures PS3 and PS4, and general comparisons of damage levels were made with Structure PS1a. The instrumentation layouts (Figure 18) were identical for Structures PS1a and b. With the exception of the accelerometers located in the floor of Structure PS2b, the instrumentation layouts (Figure 19) were identical for both of the corrugated metal fighting bunker shells.

Photographs of the damage to the structures were taken. Preshot and postshot measurements were made at selected points inside all structures to determine permanent displacements.

All electronic data were recorded in analog form on magnetic tape and were subsequently reduced to digitized magnetic tape form at WES at a digitizing rate of 50 kHz. Data reduction and plotting of the final filtered data were done at WES using standard WES data reduction codes.

FIELD TEST RESULTS AND DISCUSSION

TEST DATA

Two of the 41 channels of data recorded during the main event were lost due to defective relays at the time of the test. Analog records of the remaining 39 data channels are presented in Appendix A. Gage identification is explained in the following example:

```
PS2a    -   2  A  V
 |          |  |  |___ Gage Orientation
Structure   |  |______ Gage Type
 Number     |_________ Gage Location
```

Gage locations and types are shown in Figures 18 and 19. Airblast loadings obtained from BRL data are shown in Table 2.

DAMAGE SURVEY

The fabrics and main frames of Structures PS1a, PS1b, and PS3 were not damaged during the main event. A postshot view of the interior of Structure PS1a is shown in Figure 20. All three shelters were driven into the ground 5.1 to 7.6 cm (2 to 3 inches), and the sag in the fabric was increased approximately 2.5 cm (1 inch) by the explosion effects. Figure 21 shows the penetration of an arch frame base that was originally buried flush with the earth floor. The sides of the entranceways into Structures PS1a and b were bent at midheight and are shown in Figure 22 after all soil was removed. The vertical shaft entranceway to Structure PS3 was undamaged.

Structure PS4 was unsafe to enter after the test. When the shelter was excavated, all of the pickets were found to have 5.1 to 7.6 cm (2 to 3 inches) of permanent deflection at midheight (Figure 23), and the ends of the arch ribs were bent inward about 2.5 cm (1 inch). The entire shelter was driven into the ground approximately 15.2 cm (6 inches).

A large amount of dust was found inside the shelters after the test, illustrating the need for some type of closure and covering on the earth floor of the shelter.

Little structural damage occurred to the two fighting bunker shells, PS2a and b. The firing port beam facing GZ on Structure PS2a, which was located at the 137.9-kPa (20-psi) range, buckled and was folded down into the firing port (Figure 24). The remaining firing ports were blocked by sandbags knocked from the roof by the airblast. There was no other damage. Structure PS2b, which was located at the 68.9-kPa (10-psi) range, received no structural damage. The firing ports were only partially blocked by falling sandbags (Figure 25).

STRUCTURE RESPONSE

The pressure increases in Structures PS1a and b reached a peak of approximately 62.1 kPa (9 psi) with a rise time of 14 msec (Figure 26). This pressure history is sufficient to cause eardrum injury to personnel in the shelter. Possible personnel injuries could occur from objects inside the shelter entrained in the blast flow. Measured accelerations on the floors of the shelters were well below levels that would cause injuries to standing or sitting personnel in the shelter.

Strain and velocity measurements for Shelters PS1a and b are shown in Figures 27 and 28, respectively. Peak strains exceeded the elastic limit; however, there were no signs of permanent deformation. Integrated velocity records show a transient displacement of about 12.7 cm (5 inches) and a permanent displacement of 7.6 cm (3 inches), which was about the same amount that the shelters were driven into the ground.

Recorded pressures inside the two fighting bunker shells, Structures PS2a and b, were about the same as the free-field blast pressures at the same range. Typical strains measured were 0.007 to 0.008 mm/cm (700 to 800 μin./in.) or about one-half the yield strain of the steel. Velocity records were integrated to obtain deflections at the crowns. The integrated records showed the bunker shells to have moved upward approximately 2.5 cm (1 inch) during the passage of the airblast and then returned to their original position. Pressure, strain, and velocity measurements for Structure PS2a are shown in Figure 29.

FOLLOW-ON TESTS

TEST PLAN

Originally, HE follow-on tests were to be conducted on the three fabric-covered shelters located at the 206.7-kPa (30-psi) overpressure range. However, Structure PS4 was excluded because of the extent of damage received in the main event. The other two shelters were subjected to the detonation of 7.26-kg (16-pound) spheres of TNT placed at the locations shown in Figure 30. The 7.26-kg (16-pound) TNT spherical charges produce approximately the same blast effect as a 155-mm artillery round. The instrumentation used for the main event in Structure PS1a was also used during the follow-on tests. Twenty-five channels of data were recorded.

STRUCTURE RESPONSE

Structure PS1a was not damaged from the effects of the detonation of the TNT charges with centers of gravity located above the crown of the structure and on the surface of a 1.2-metre- (4-foot) thick soil cover or buried at middepth and 3 metres (10 feet) from the side of the shelter. When this charge was located at middepth and 3 metres (10 feet) from the endwall, the endwall was bowed in approximately 5 cm (2 inches) at its center. The fabric cover was not damaged. With the soil cover depth reduced to 0.9 metre (3 feet) and the TNT charge detonated half buried over the shelter crown, the fabric cover ruptured (Figure 31). Instrumentation mounts located on the frame directly beneath the charge appeared to have caused the fabric cover to tear. The steel frame was not damaged structurally (Figure 32). The third frame from the left end in Figure 32 was bent while attempting to lift the shelter from the pit before all of the soil backfill was excavated. Data indicate that the shelter frame directly under the TNT charge was stressed to about 1-1/2 times yield, and that there was a pressure buildup inside the shelter of about 6.9 kPa (1 psi).

Structure PS3 was not damaged when the charges were placed over the shelter crown with 1.2 metres (4 feet) of soil cover or at the shelter middepth and 3 metres (10 feet) from the side. The charge at the shelter middepth and 3 metres (10 feet) from the rear endwall pushed the center of the endwall inward about 5 cm (2 inches) (Figure 33). With the soil cover reduced to 0.9 metre (3 feet) and the TNT charge detonated half buried over the crown of the shelter, the frame directly beneath the charge was bent as shown in Figure 34. The crown was deformed approximately 15.2 cm (6 inches) and is compared in Figure 35 with an undeformed frame. The deformed framework for the entire shelter is shown in Figure 36.

CONCLUSIONS

Based on the results of the main event, the following conclusions were drawn for the buried combat services support shelters:

1. Structures PS1a, PS3, and PS4 will survive the ground shock and airblast at the 206.7 kPa (30-psi) overpressure range.

2. Structures PS1 and PS3 are stronger than Structure PS4.

3. Accelerations inside the shelters at the 206.7-kPa (30-psi) range are not sufficient to cause personnel injury.

4. Simple blast closures should be provided to reduce the effects of airblast, dust, and debris on personnel.

5. The shelters should be constructed with some type of flooring to minimize dust.

From the follow-on HE tests, it can be concluded that Structures PS1 and PS3 with 1.2 metres (4 feet) of soil cover can survive a direct hit by a point-detonating 155-mm artillery round or a delay-fuzed round landing within 3 metres (10 feet) of the shelters.

The fighting bunker shells, Structures PS2a and b, will survive the effects of long-duration airblast loadings. The blast pressure buildup inside the bunker shells is about the same as that of open field fortifications.

TABLE 1 COMPARISON OF METAL-FRAMED FABRIC-COVERED SHELTERS

Item	Structure: PS1 Small Elliptical	PS3 Large Elliptical	PS4 Rectangular
Height, m (ft)	1.80 (5.90)	1.96 (6.44)	1.83 (6)
Width, m (ft)[a]	1.40 (4.60)	1.73 (5.67)	1.68 (5.5)
Length, m (ft)	3.05 (10)	3.05 (10)	2.90 (9.5)
Floor area, m^2 (ft^2)	3.34 (36)	4.37 (47)	6.32 (68)
Shelter volume, m^3 (ft^3)	6.51 (230)	8.78 (310)	9.63 (340)
Shipping volume, m^3 (ft^3)[b]	0.82 (29)	1.42 (50)	0.68 (24)
Shipping weight, kg (lb)[b]	227.27 (500)	318.18 (700)	215.91 (475)

[a]At widest point.

[b]Does not include entrance tunnel.

TABLE 2 FREE-FIELD TRANSIENT OVERPRESSURE DATA

Structure	Range from GZ m (ft)	Peak Pressure kPa (psi)	Time of Arrival msec	Positive Phase Duration msec	Impulse kPa-msec (psi-msec)
PS1a, PS3, PS4	198.12 (650)	215 (31.2)	156	122	6930 (1005)
PS1b, PS2a	228.60 (750)	137 (19.9)	210	140	5655 (820)
PS2b	304.80 (1000)	60 (8.7)	376	203	5468 (793)

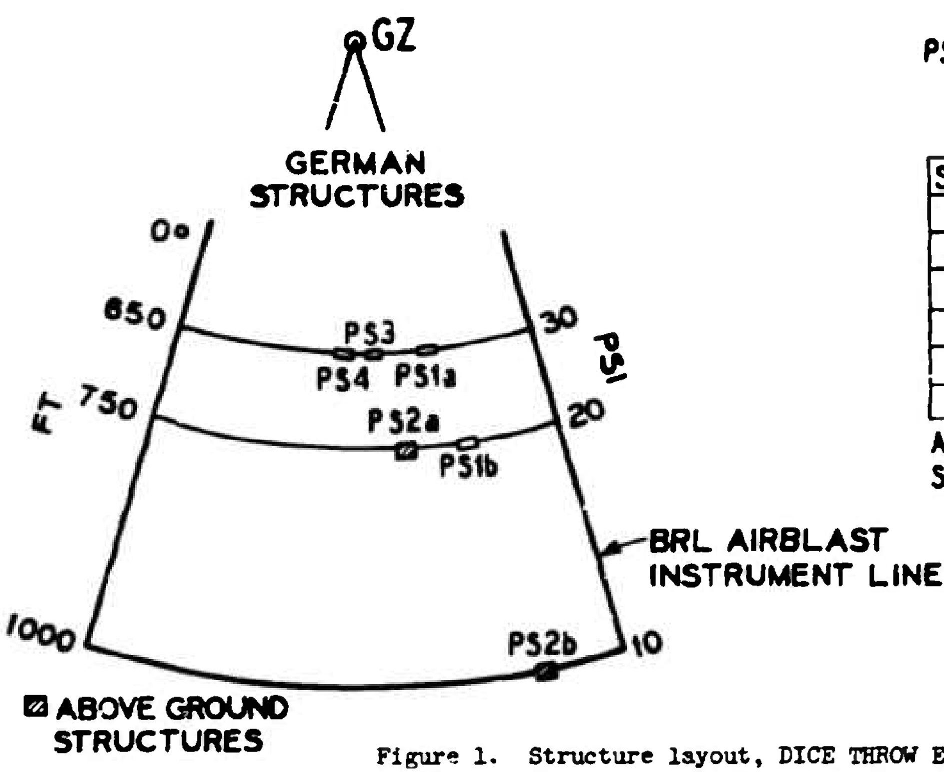

LEGEND

PS1a & PS1b – BURIED FABRIC-COVERED ELLIPTICAL SHELTERS

PS2a & PS2b – CORRUGATED METAL FIGHTIN HOLE

PS3 – BURIED FABRIC COVERED ELLIPTICAL SHELTER, LARGE SIZE

PS4 – BURIED MEXE SHELTER

STRUCTURE LOCATION

STRUCTURE	AZIMUTH	RANGE
PS1a	50°	650'
PS1b	52.5°	750'
PS2a	47.5°	750'
PS2b	55°	1000'
PS3	45°	650'
PS4	42.5	650'

ALL RANGE DISTANCES ARE TO THE STRUCTURE CENTERLINE

Figure 1. Structure layout, DICE THROW Event.
Note: to convert feet to metres, multiply by 0.3048. To convert pounds (force) per square inch to kilopascals, multiply by 6.894.

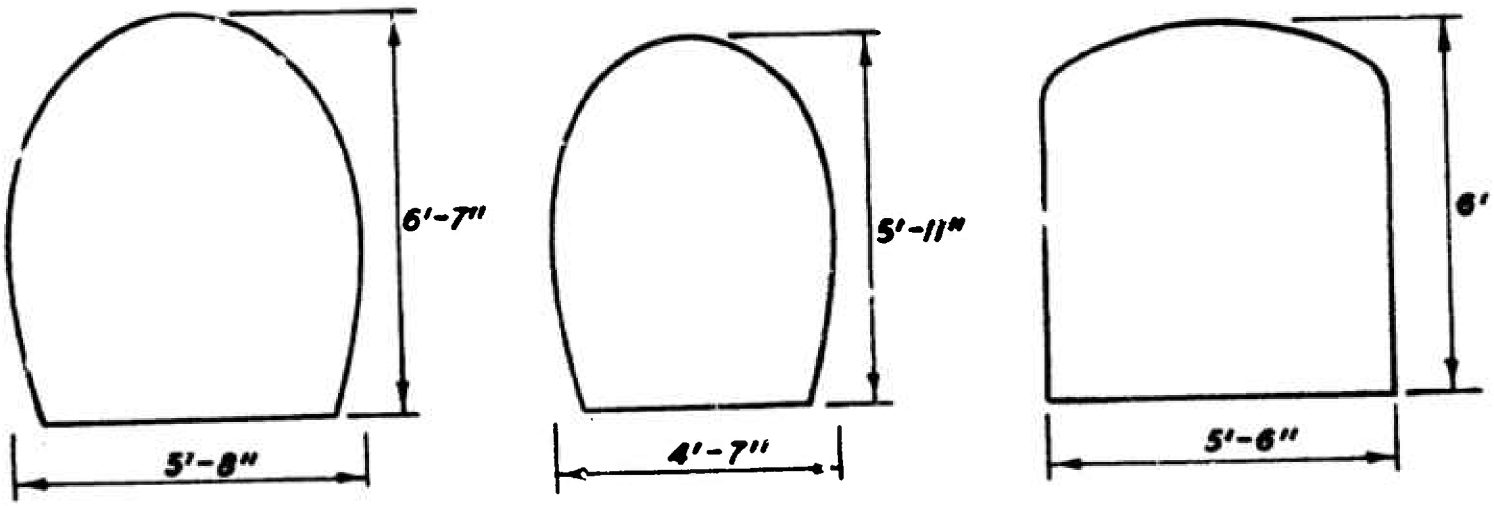

Figure 2. Dimensions of fabric-covered shelters.
Note: To convert inches to metres, multiply by 0.0254.

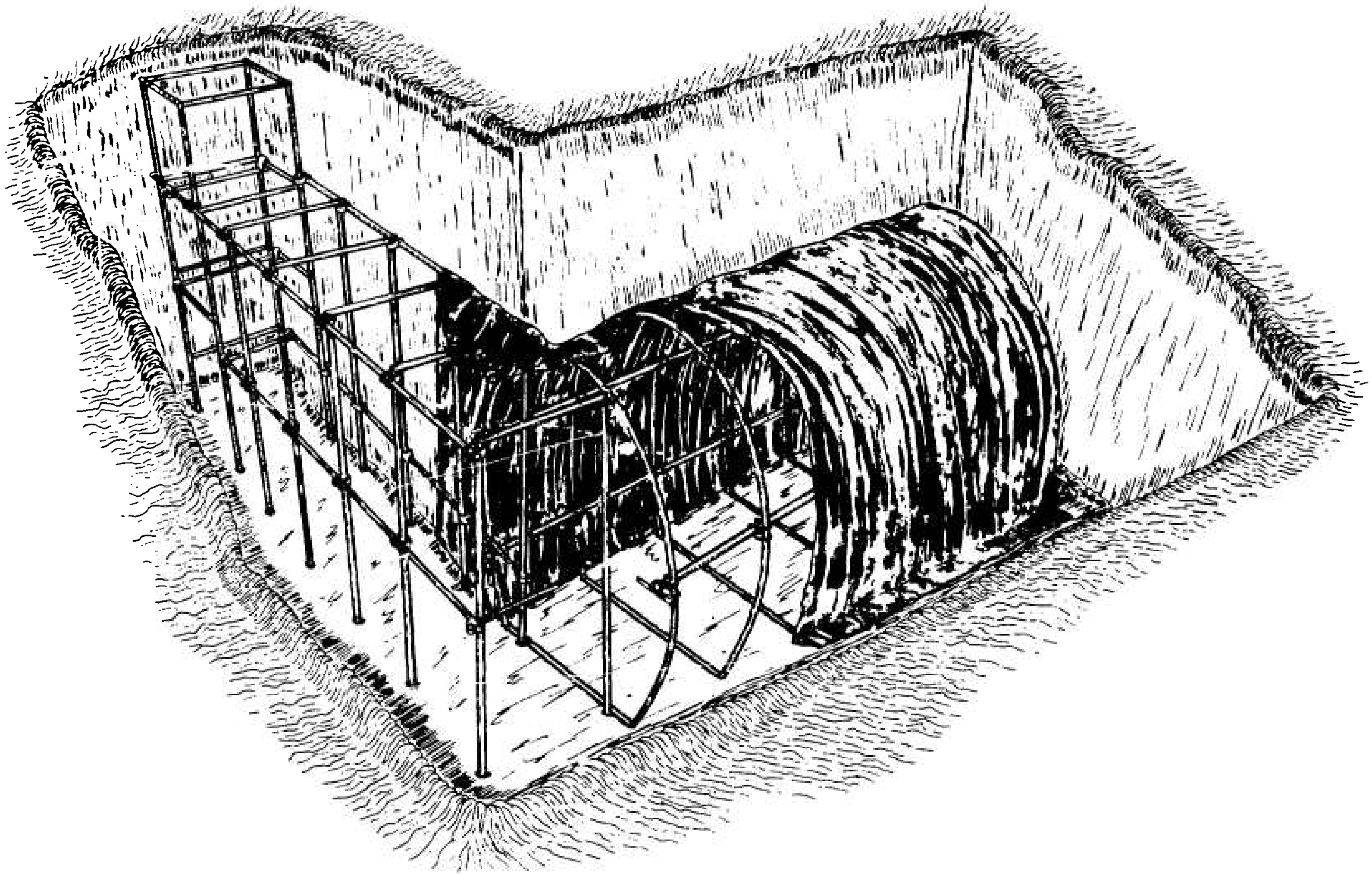

Figure 3. Conceptual drawing for Structures PS1a and b.

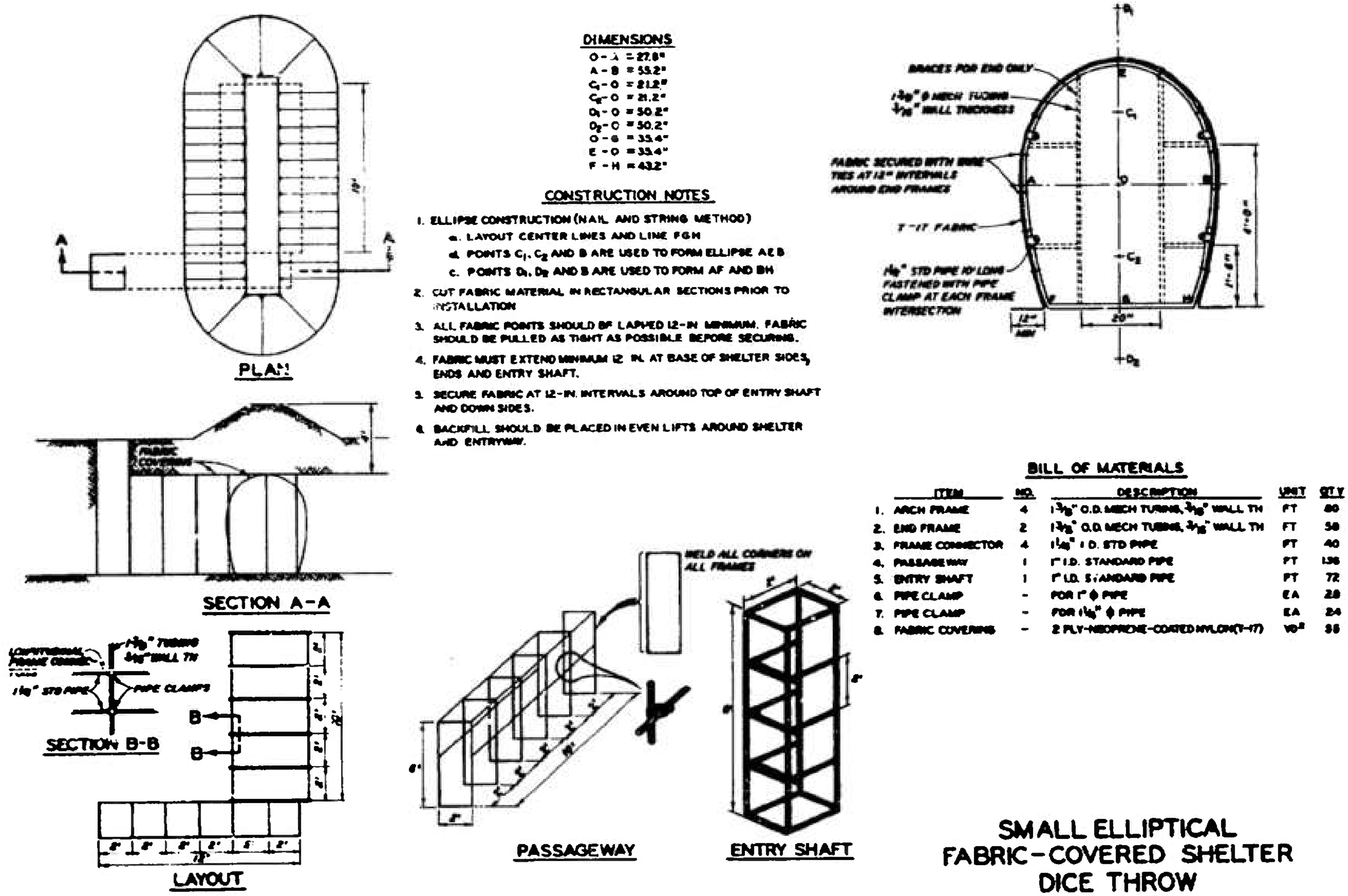

Figure 4. Construction drawings for Structures PS1a and b.

Figure 5. Assembled framework for Structure PS1a.

Figure 6. Structure PS1a with fabric cover.

Figure 7. Placement of backfill.

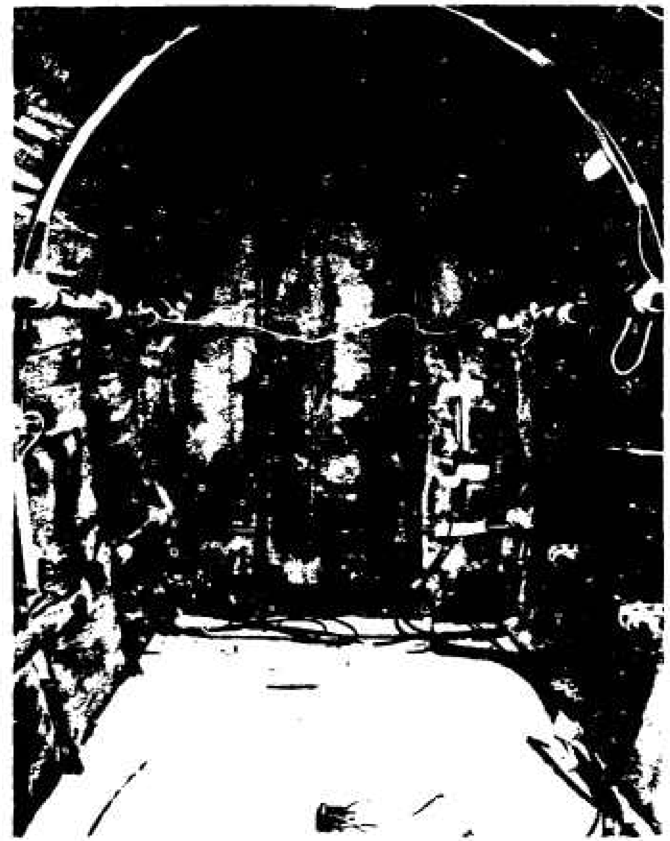

Figure 8. Interior of Structure PS1a.

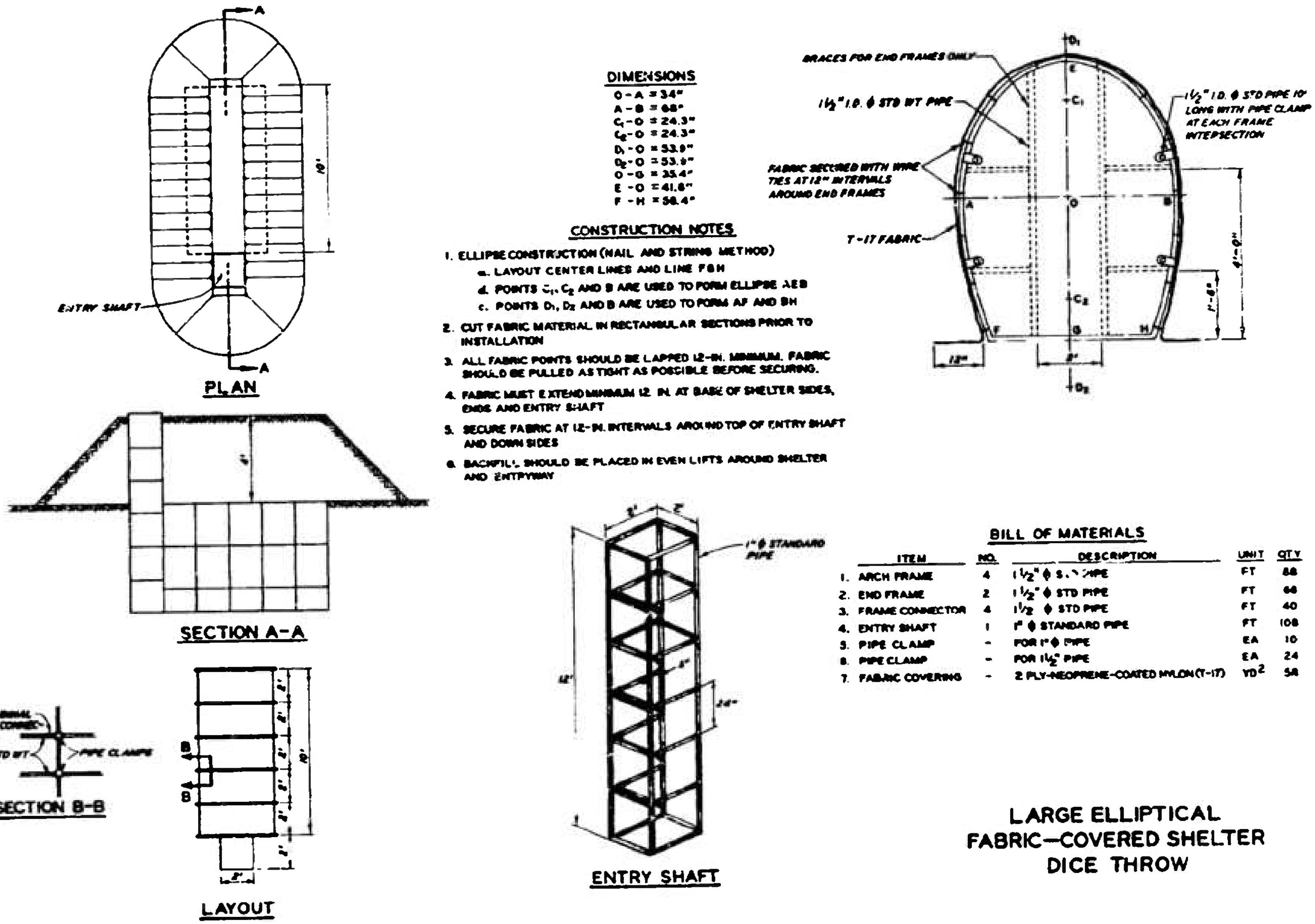

Figure 9. Construction drawing for Structure PS3.

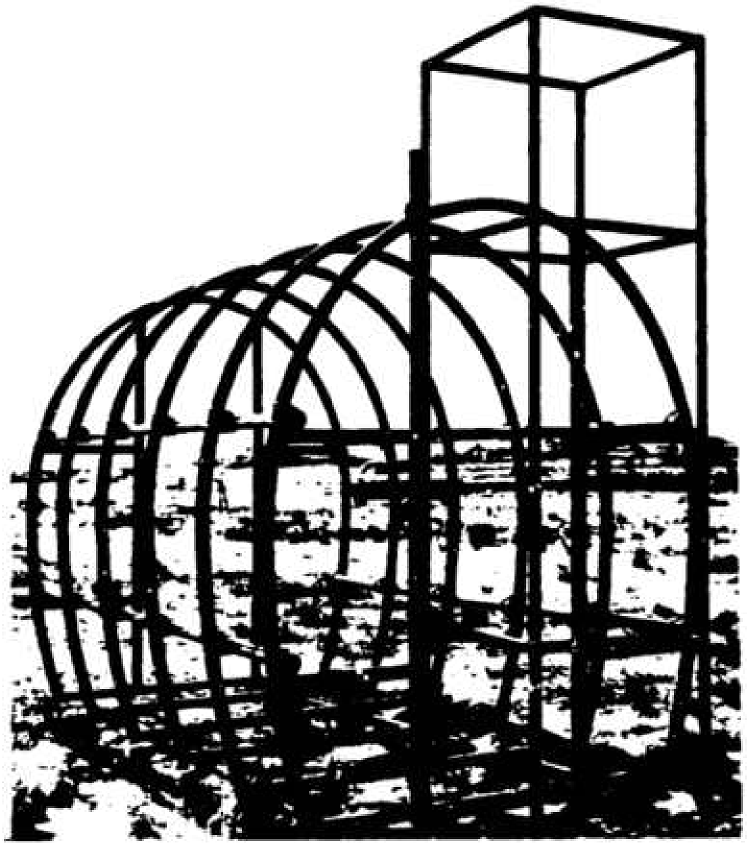

Figure 10. Assembled frame of Structure PS3.

Figure 11. Interior view of Structure PS3.

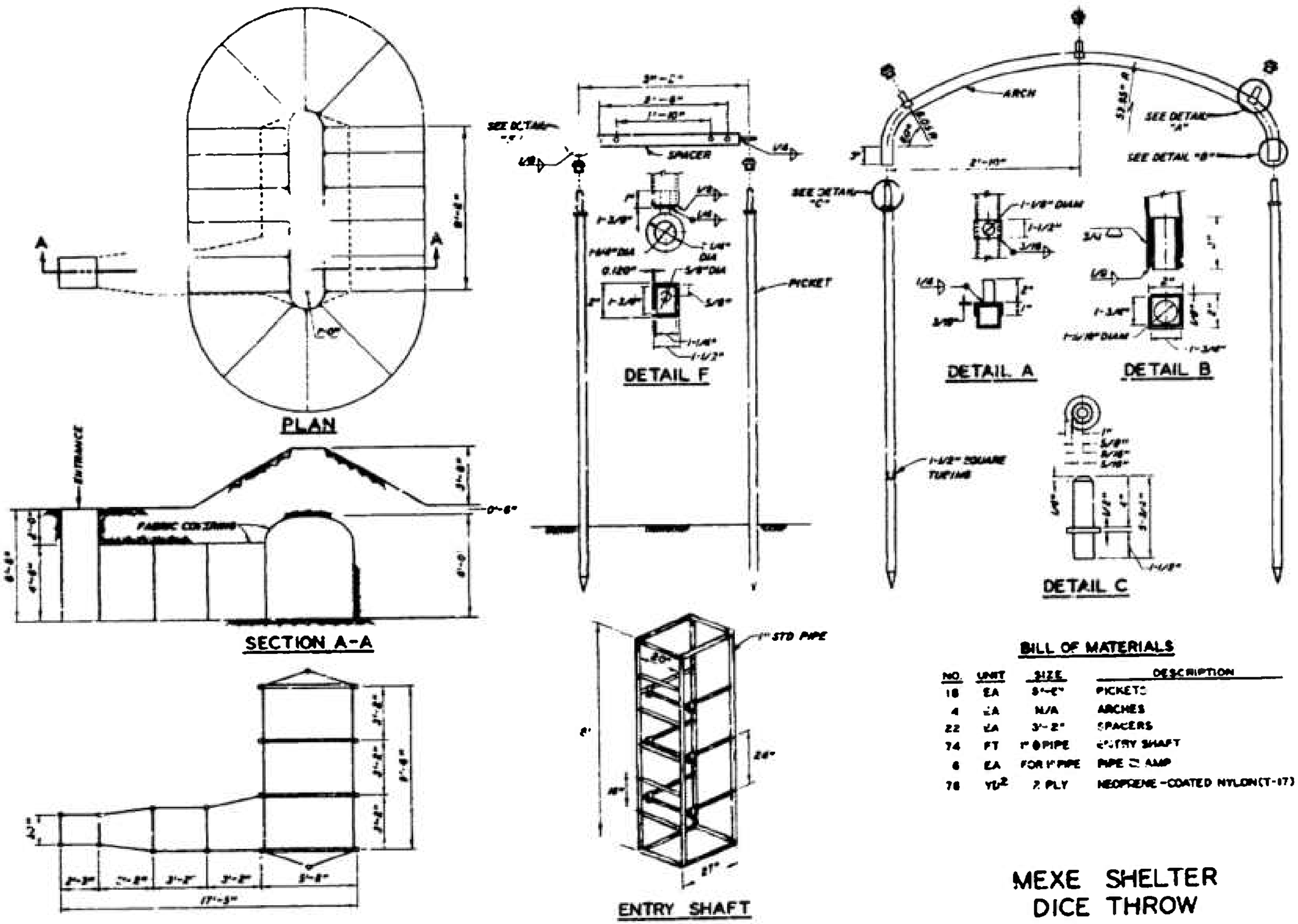

Figure 12. Construction drawing for Structure PS4.
Note: 60 degrees = π/3 radian.

Figure 13. Attachment of fabric to Structure PS4.

Figure 14. Interior view of Structure PS4.

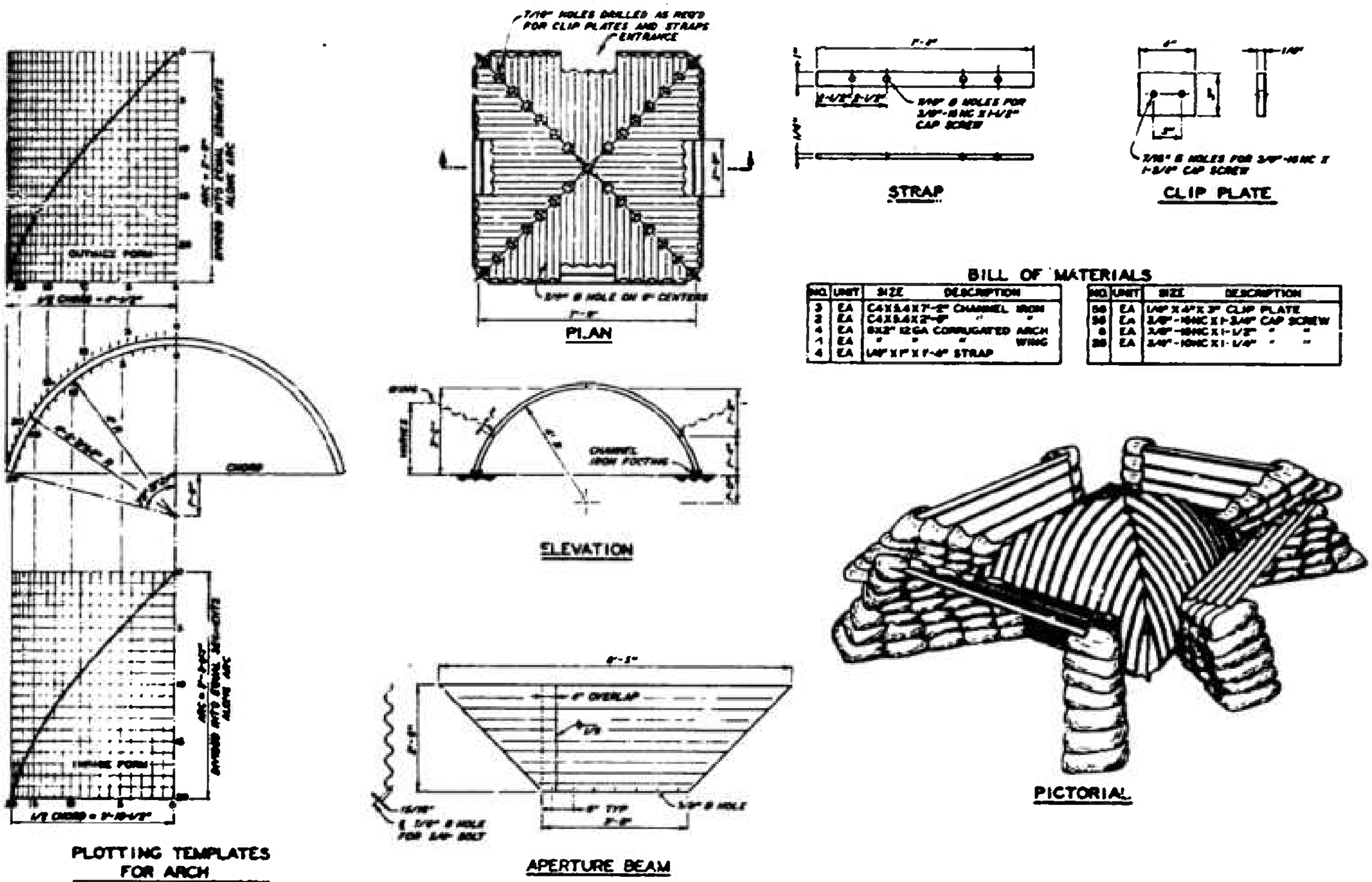

BILL OF MATERIALS

NO.	UNIT	SIZE	DESCRIPTION
3	EA	C4X5.4X7'-2"	CHANNEL IRON
2	EA	C4X5.4X2'-6"	" "
4	EA	8X2" 12GA	CORRUGATED ARCH
4	EA	" "	" WING
4	EA	1/4" X 1" X 1'-4"	STRAP

NO.	UNIT	SIZE	DESCRIPTION
56	EA	1/4" X 4" X 3"	CLIP PLATE
56	EA	3/8"-16NC X 1-3/4"	CAP SCREW
8	EA	3/8"-16NC X 1-1/2"	" "
28	EA	3/8"-16NC X 1-1/4"	" "

Figure 15. Construction drawing for Structures PS2a and b.

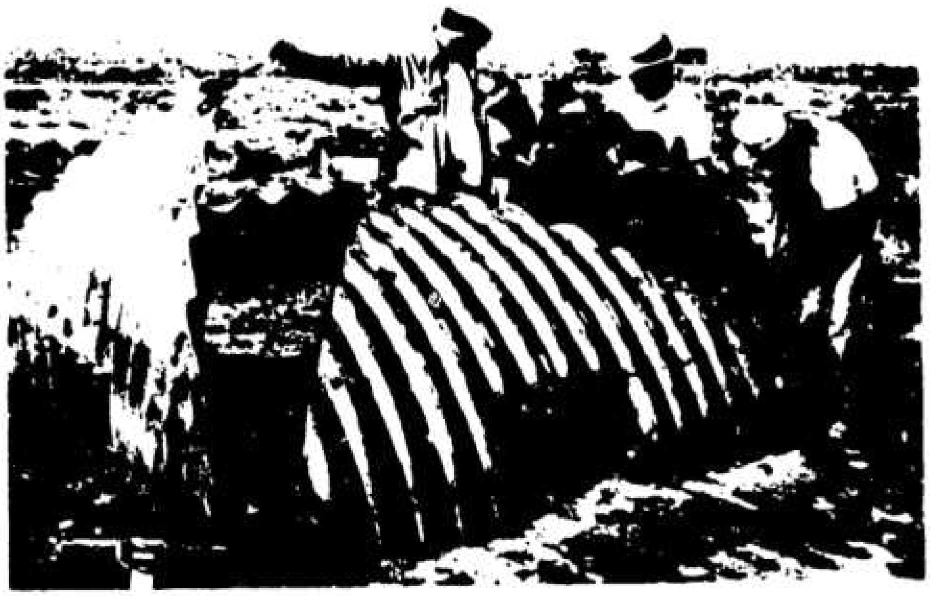

a. Quarter panel assembly.

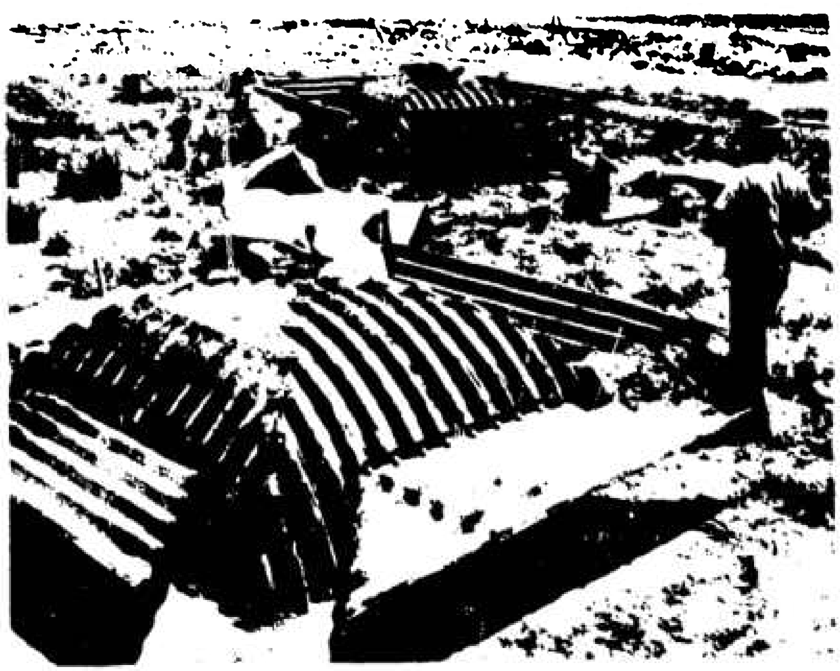

b. Completed bunker.

Figure 16. Assembly of Structures PS2a and b.

Figure 17. Structure PS2a completed.

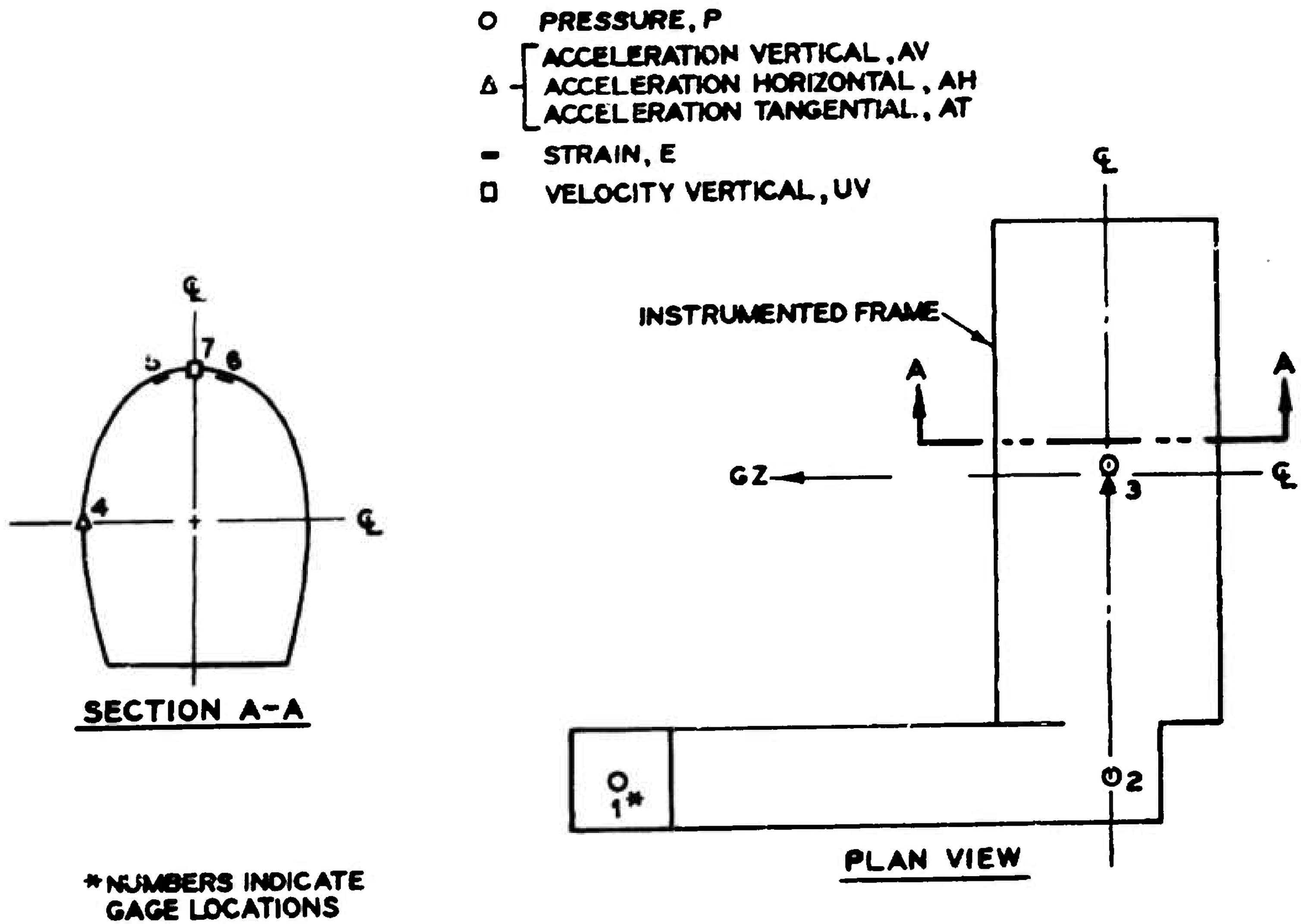

Figure 18. Instrumentation layout for Structures PS1a and b.

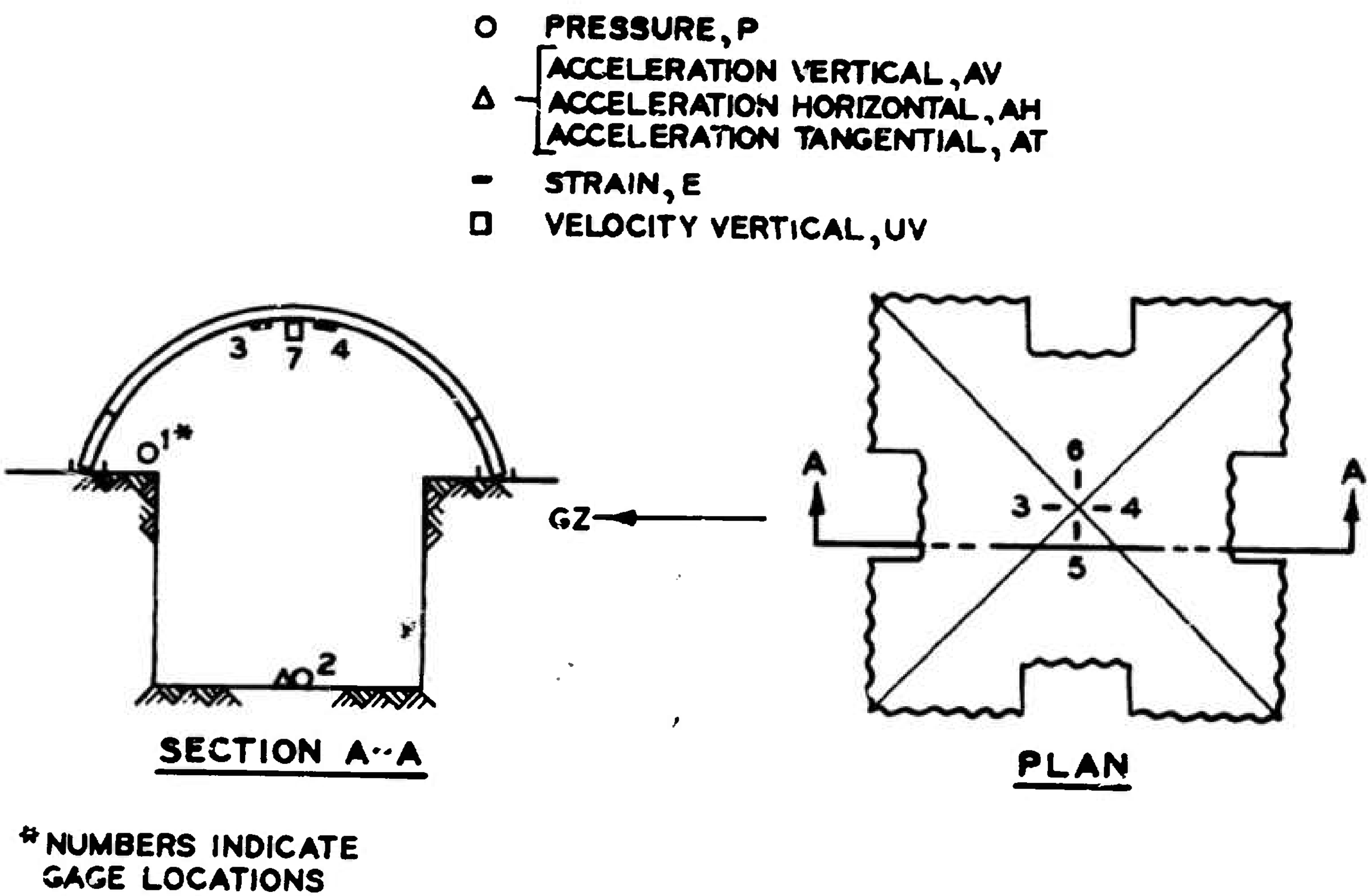

Figure 19. Instrumentation layout for Structures PS2a and b.

Figure 20. Interior view of Structure PS1a, postshot.

Figure 21. Base of shelter frame that has been driven into the ground.

a. Structure PS1a.

b. Structure PS1b.

Figure 22. Postshot views of shelter entranceways.

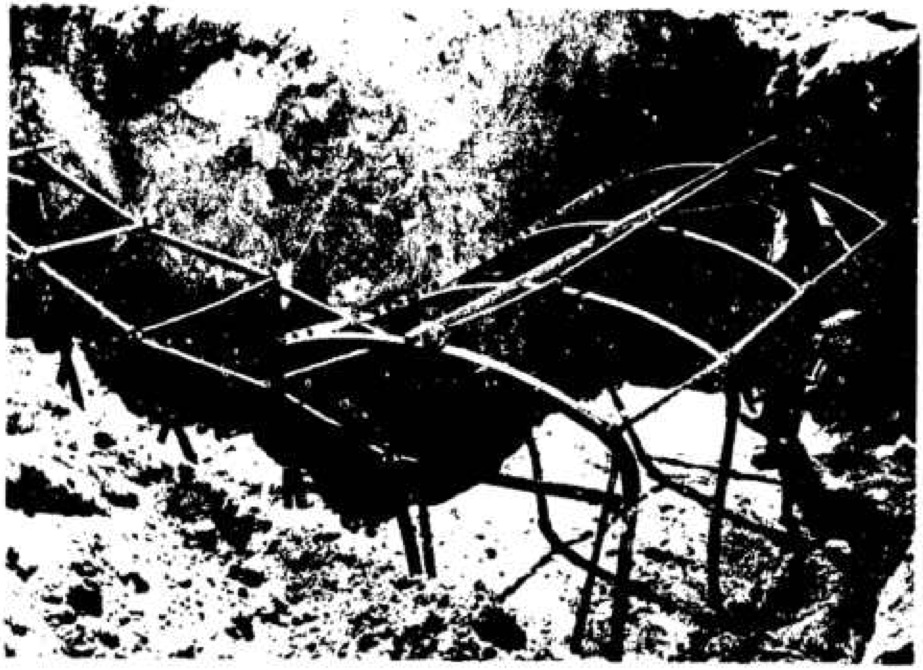

a. Dugout frame.

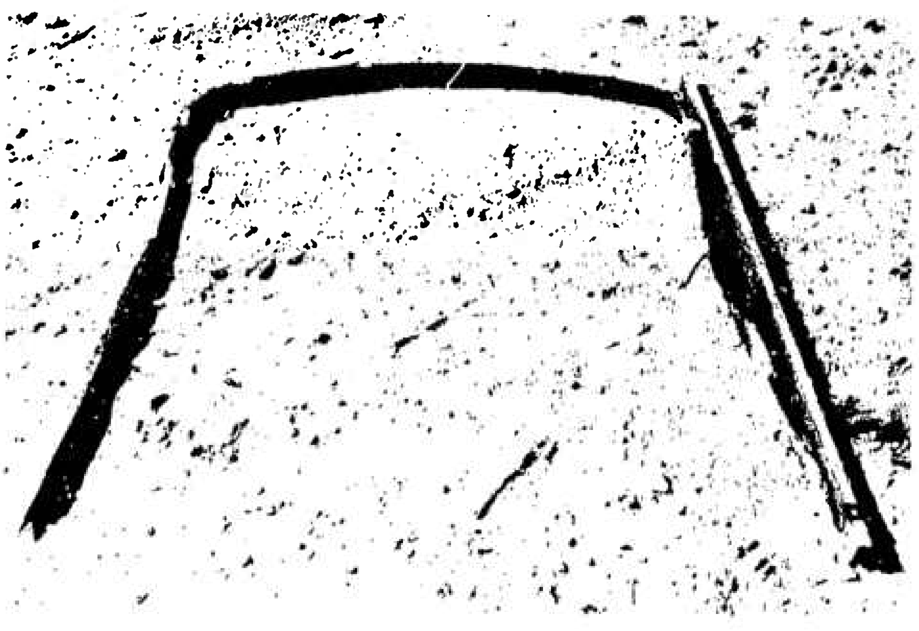

b. Permanent deflection of pickets.

Figure 23. Postshot views of Shelter PS4.

Figure 24. Damaged firing port cover, Structure PS2a.

Figure 25. Postshot view of Structure PS2b.

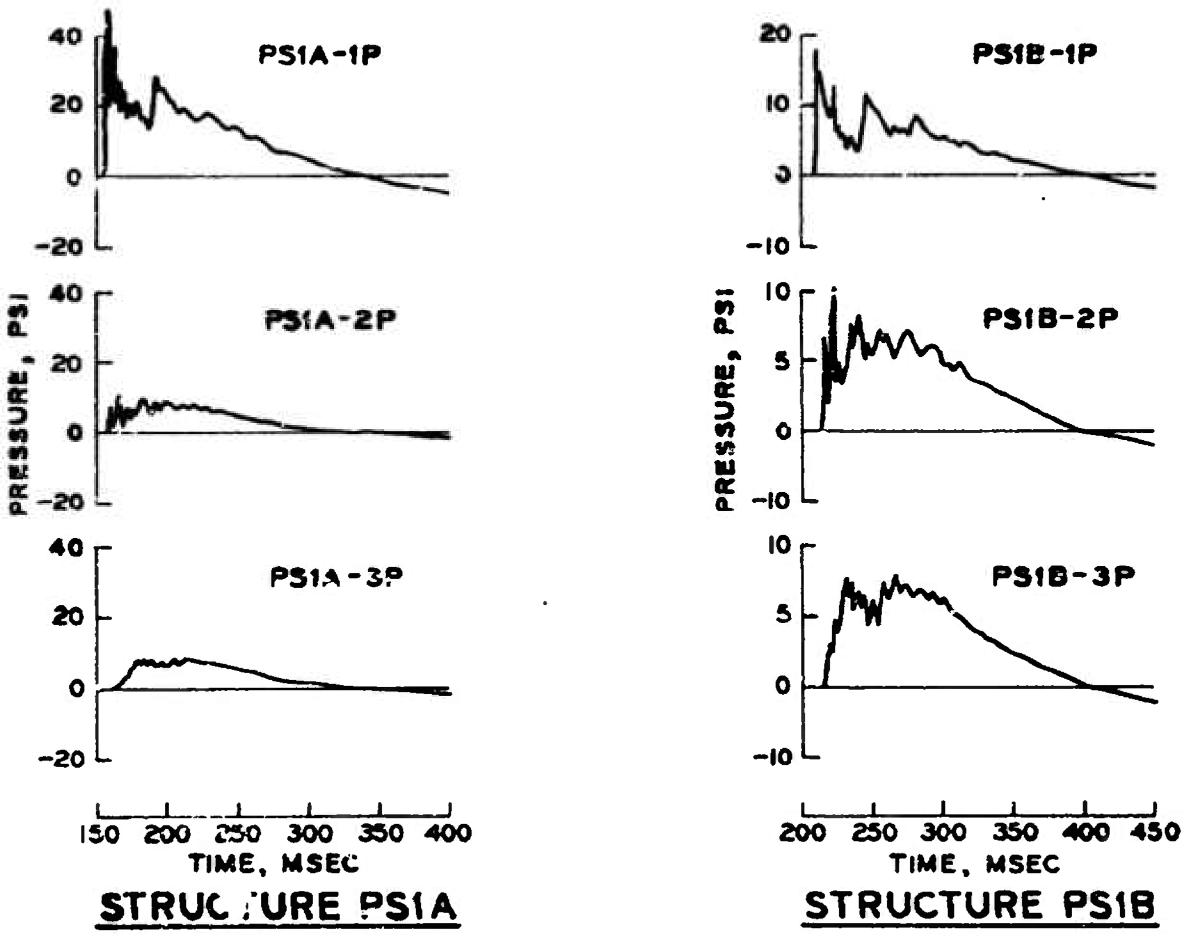

Figure 26. Pressure rise in Structures PS1a and b.

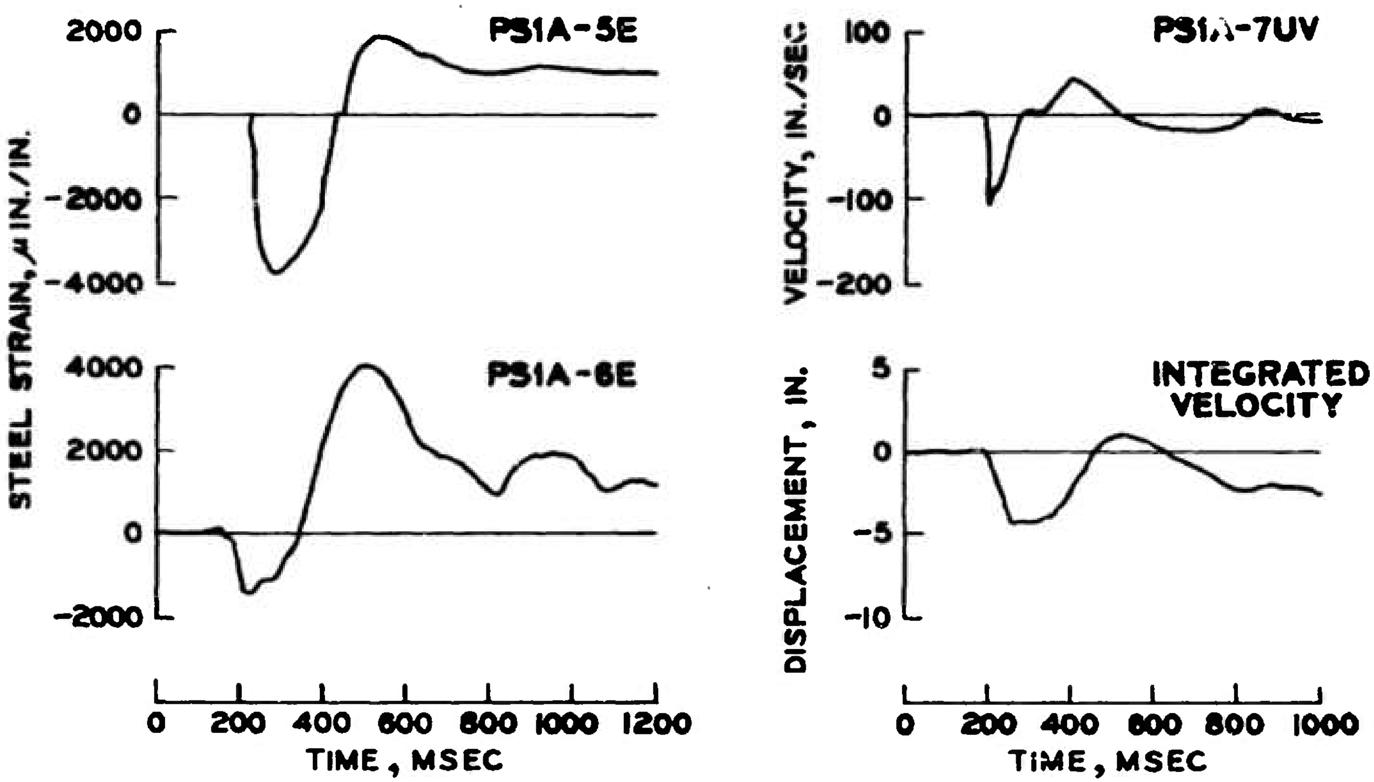

Figure 27. Strain and velocity measurements, Structure PS1a.
Note: To convert microinches per inch to millimetres per centimetre, multiply by 0.00001. To convert inches per second to centimetres per second, multiply by 2.54.

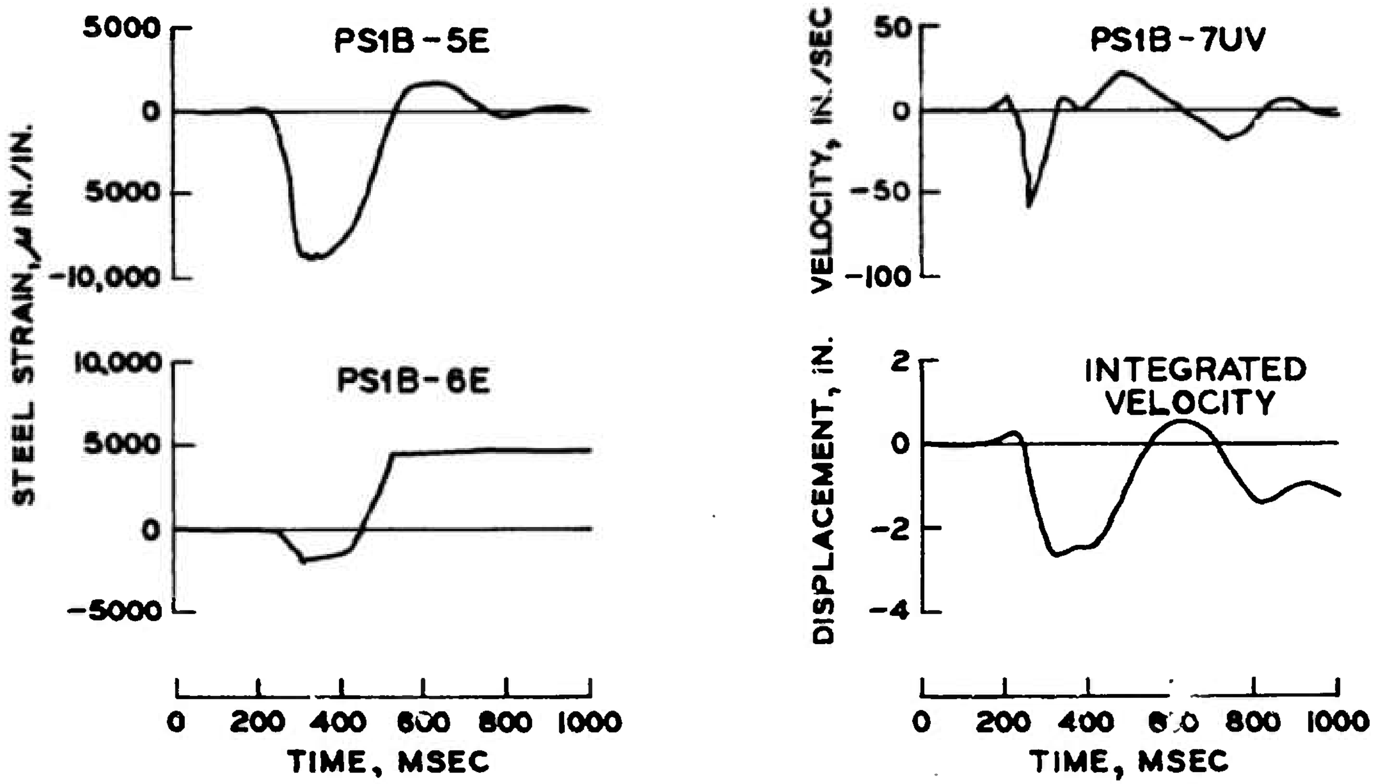

Figure 28. Strain and velocity measurements, Structure PS1b.

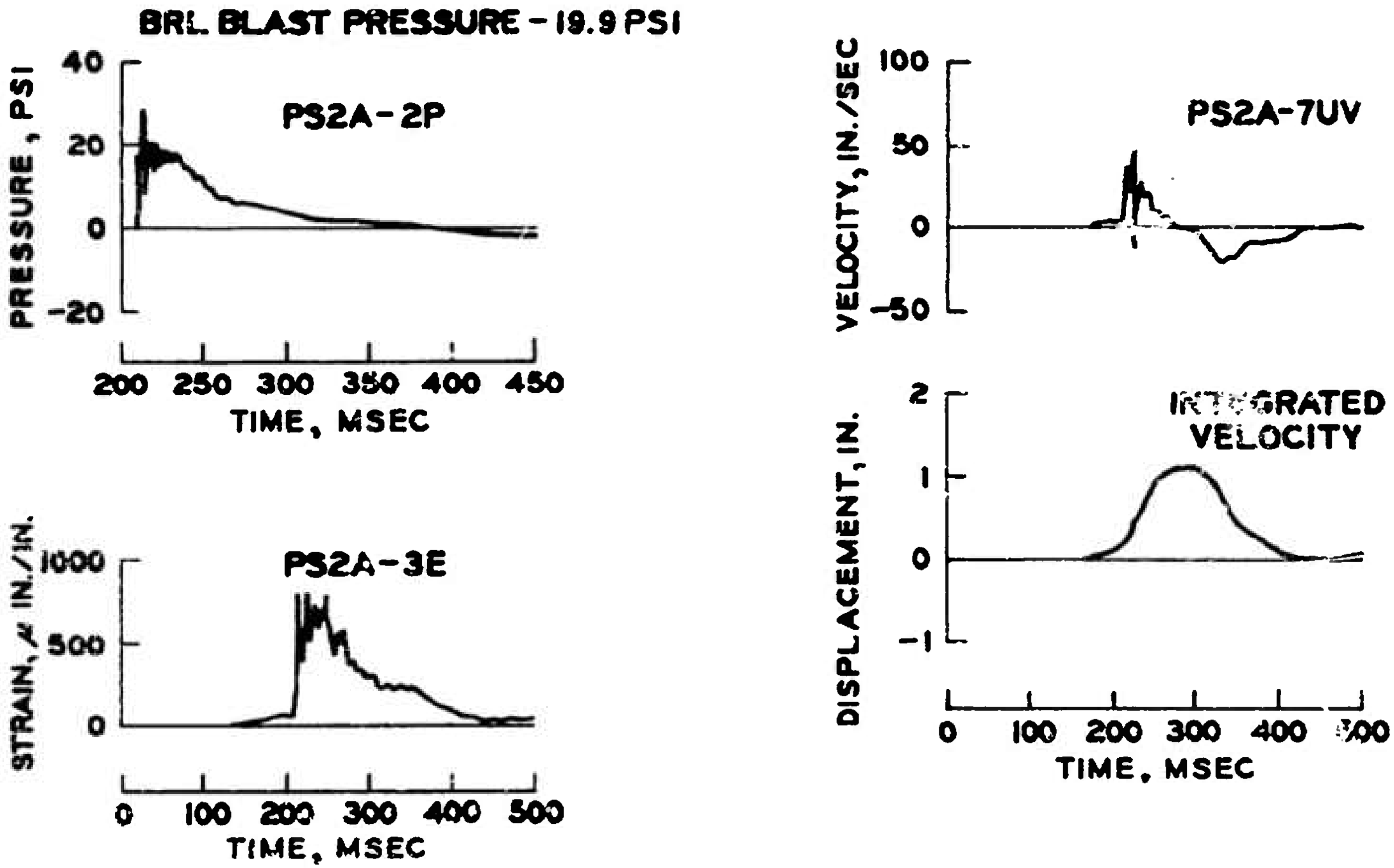

Figure 29. Pressure, strain, and velocity measurements, Structure PS2a.

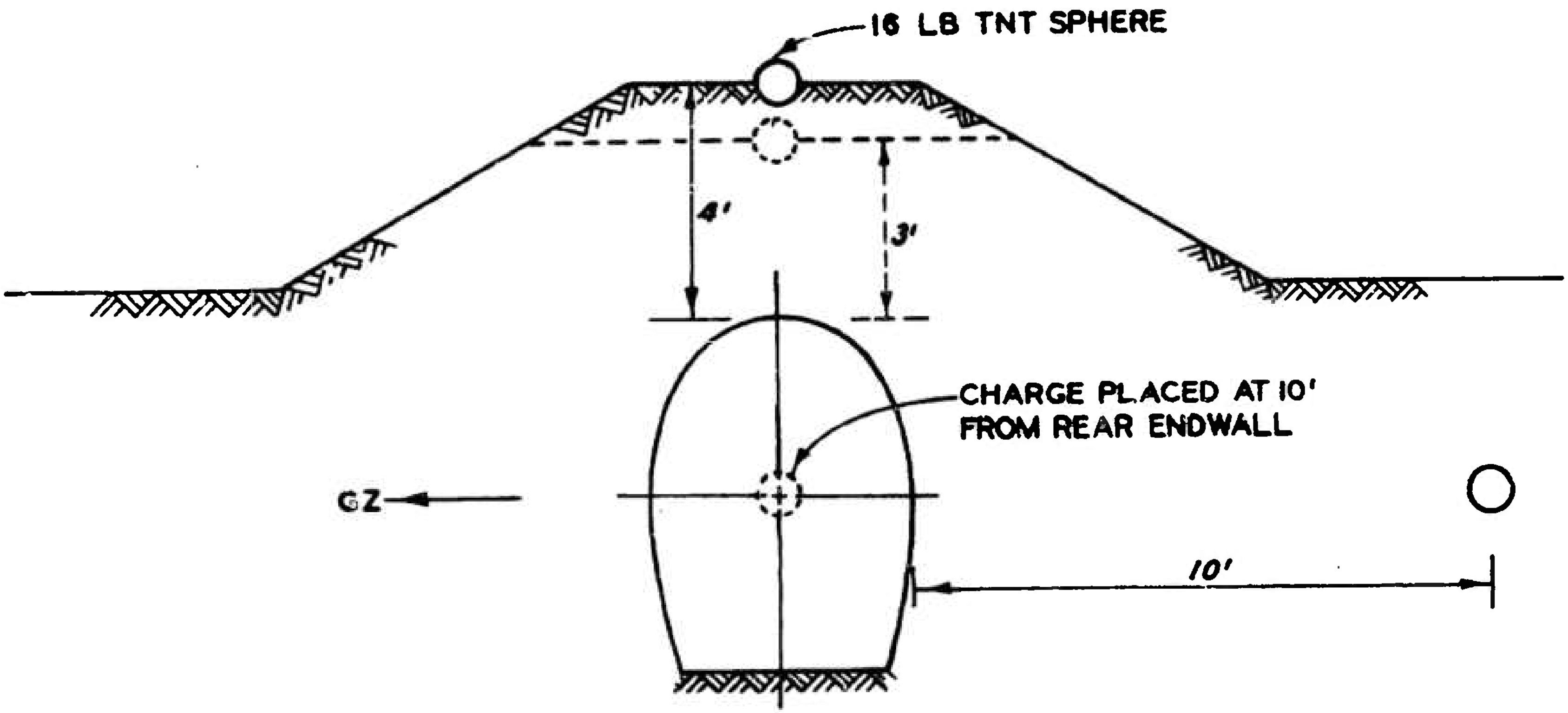

Figure 30. Charge locations for HE follow-on test.

Figure 31. Results of charge being detonated over crown of Structure PS1a with 0.9 metre (3 feet) of soil cover.

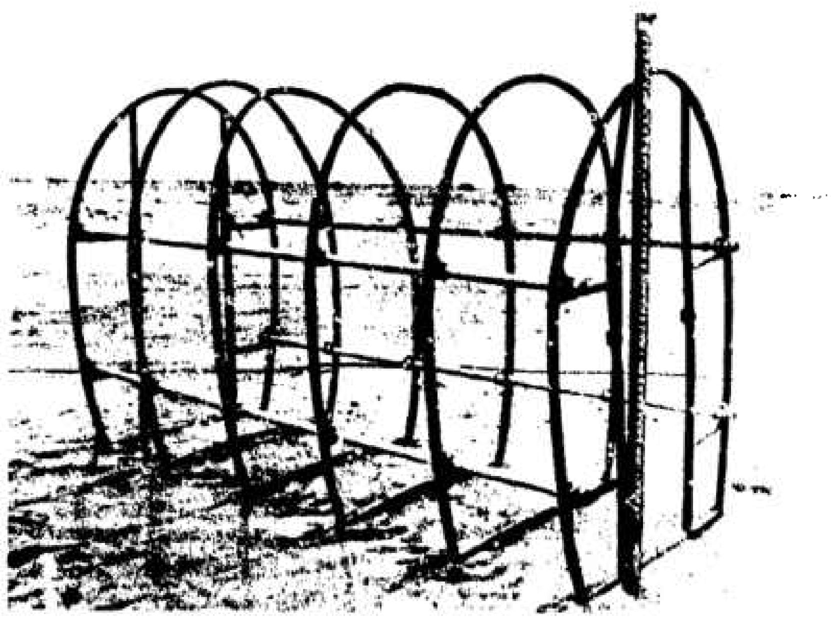

Figure 32. Framework of Structure PS1a at the conclusion of the HE test.

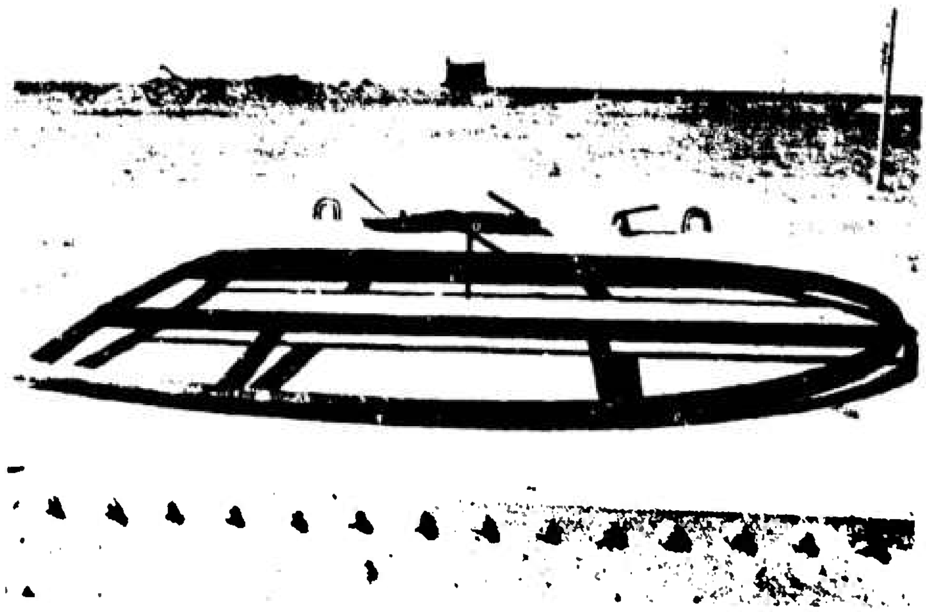

Figure 33. Rear endwall of Structure PS3.

Figure 34. Results of charge being detonated over crown of Structure PS3 with 0.9 metre (3 feet) of soil cover.

Figure 35. Damaged frame of Structure PS3 compared with undamaged frame.

Figure 36. Framework of Structure PS3 at conclusion of HE test.

APPENDIX A. TEST DATA

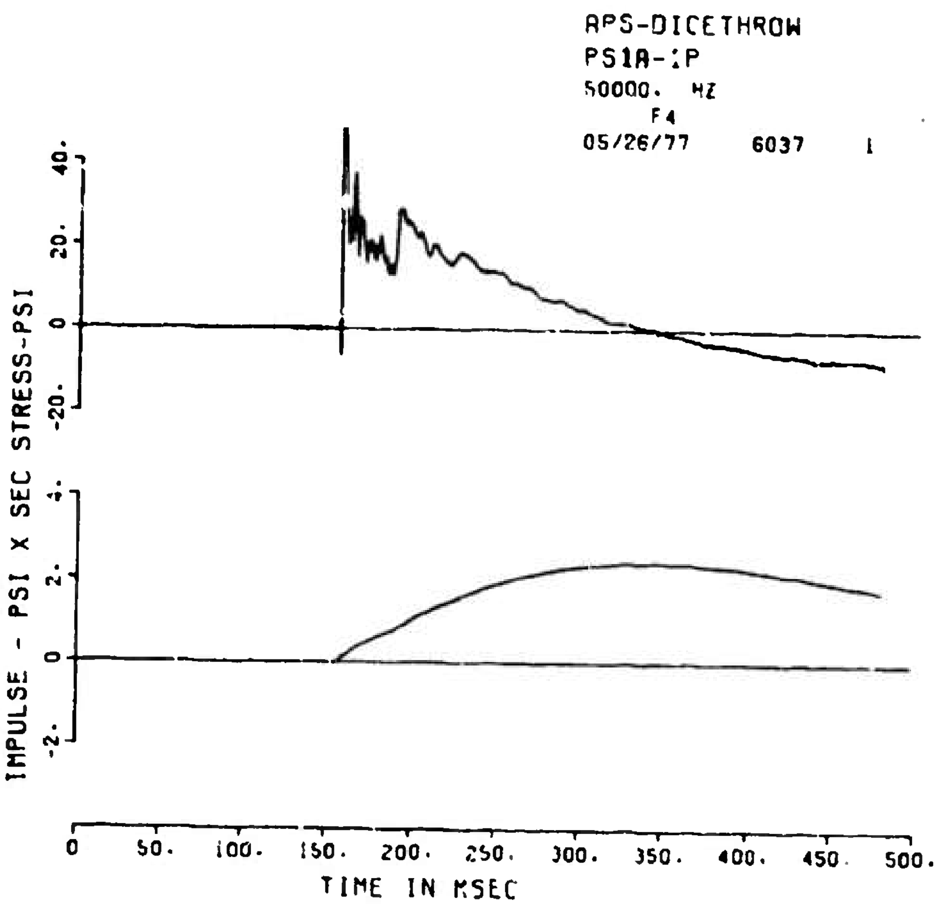

PRECEDING PAGE BLANK

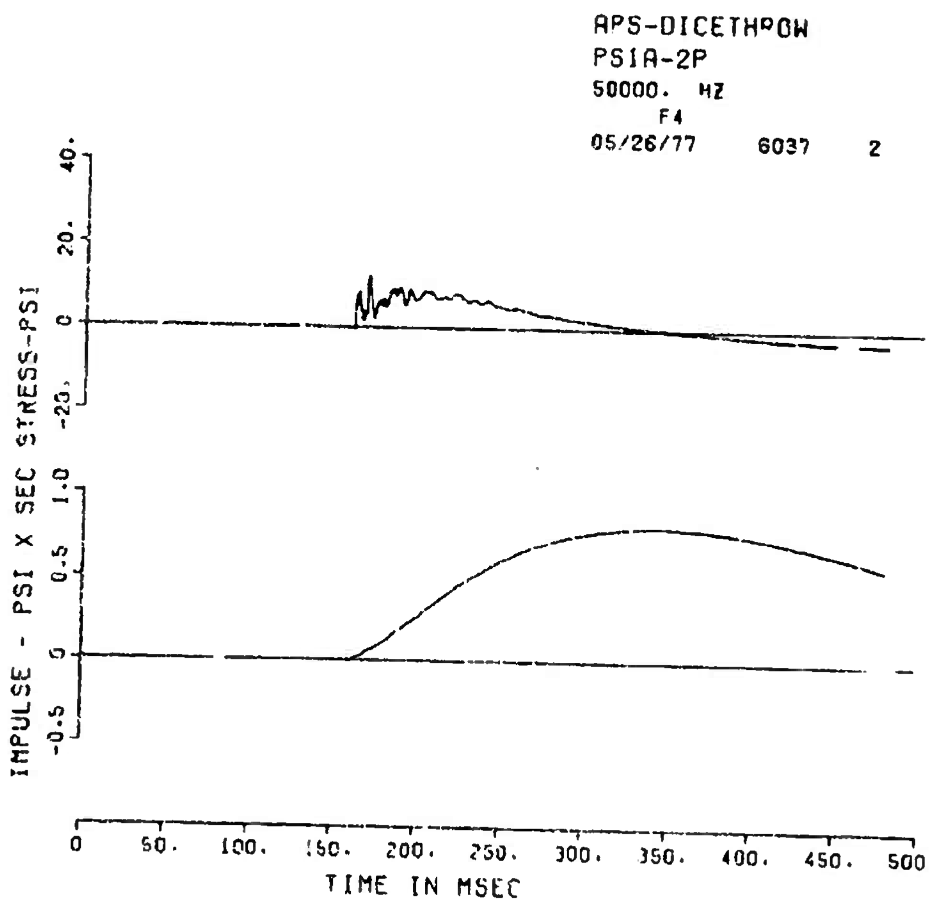

APS-DICETHROW
PSIA-2P
50000. HZ
F4
05/26/77 6037 2
STRESS-PSI
IMPULSE - PSI X SEC
TIME IN MSEC

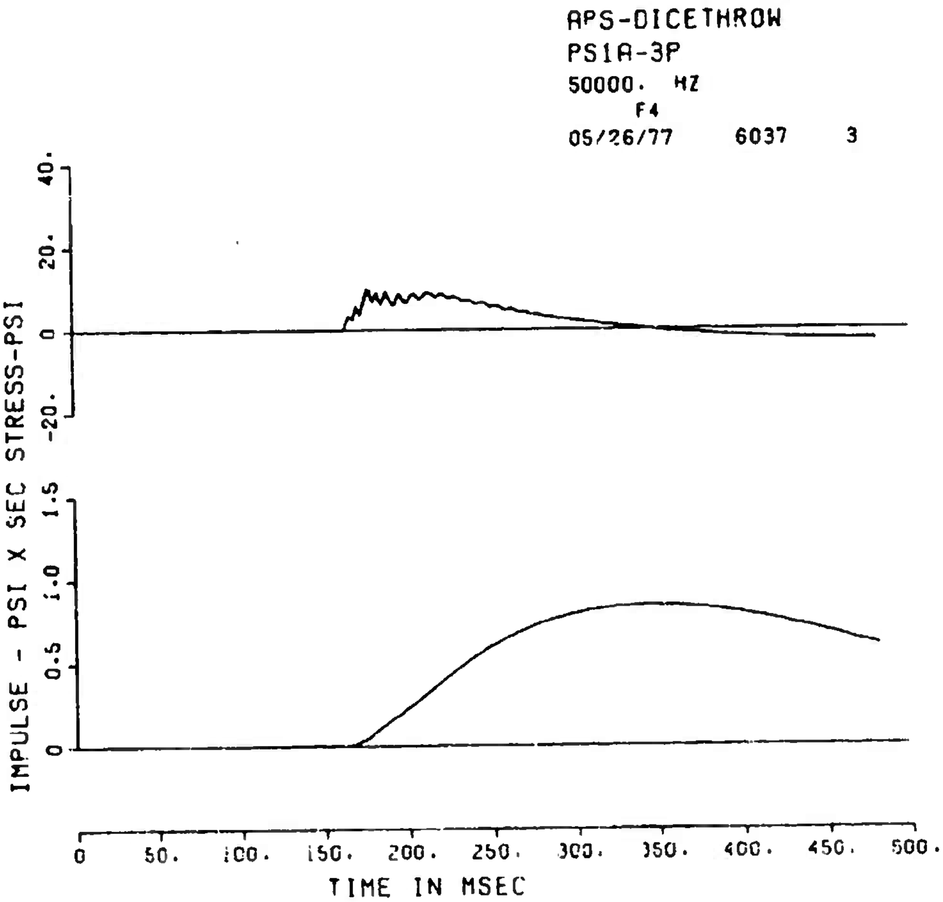
APS-DICETHROW
PSIA-3P
50000. HZ
F4
05/26/77 6037 3
STRESS-PSI
IMPULSE - PSI X SEC
40.
20.
0
-20.
1.5
1.0
0.5
0
0
50.
100.
150.
200.
250.
300.
350.
400.
450.
500.
TIME IN MSEC

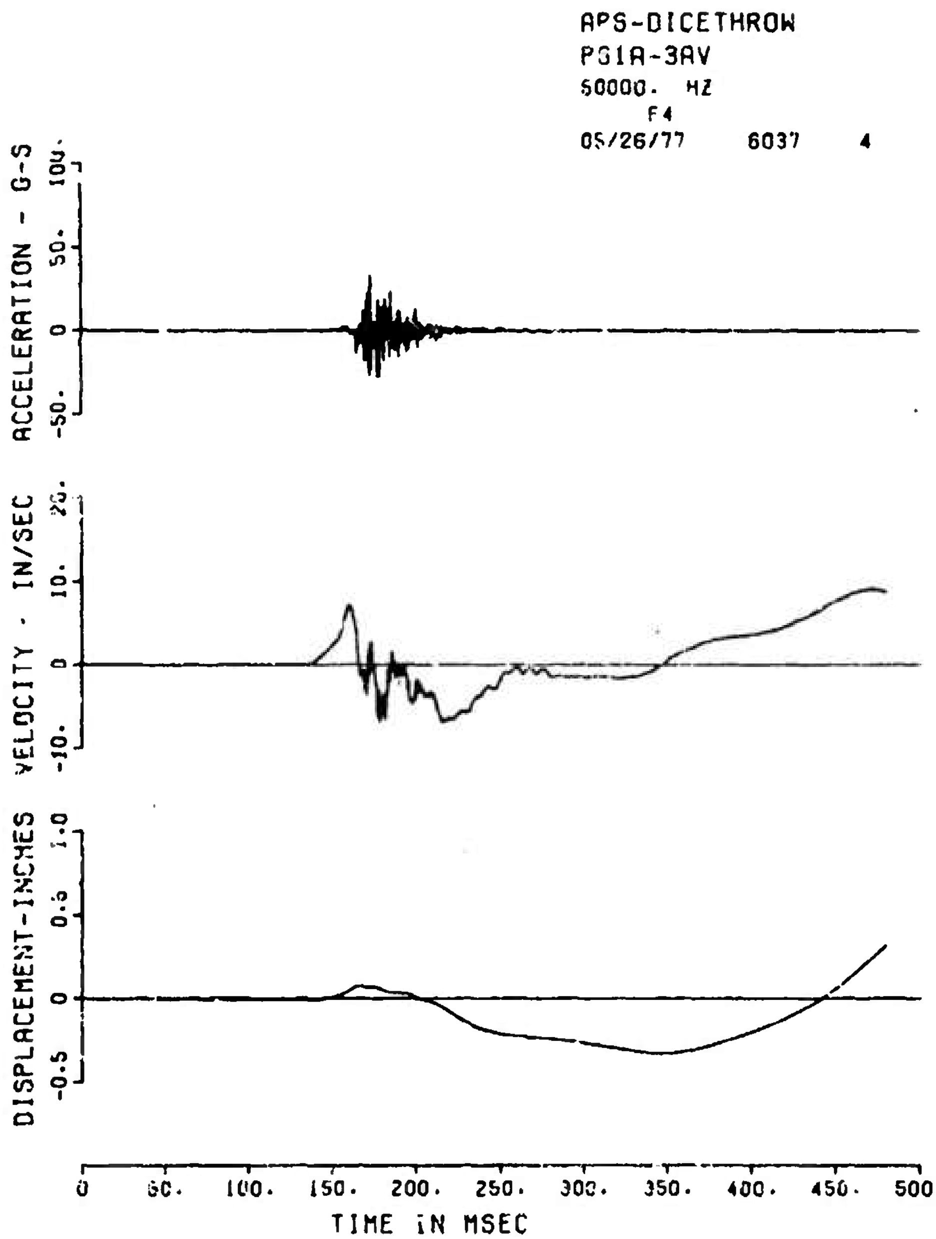
APS-DICETHROW
PG1A-3AV
50000. HZ
F4
05/26/77 6037 4
ACCELERATION - G-S
VELOCITY - IN/SEC
DISPLACEMENT-INCHES
0 50. 100. 150. 200. 250. 300. 350. 400. 450. 500.
TIME IN MSEC

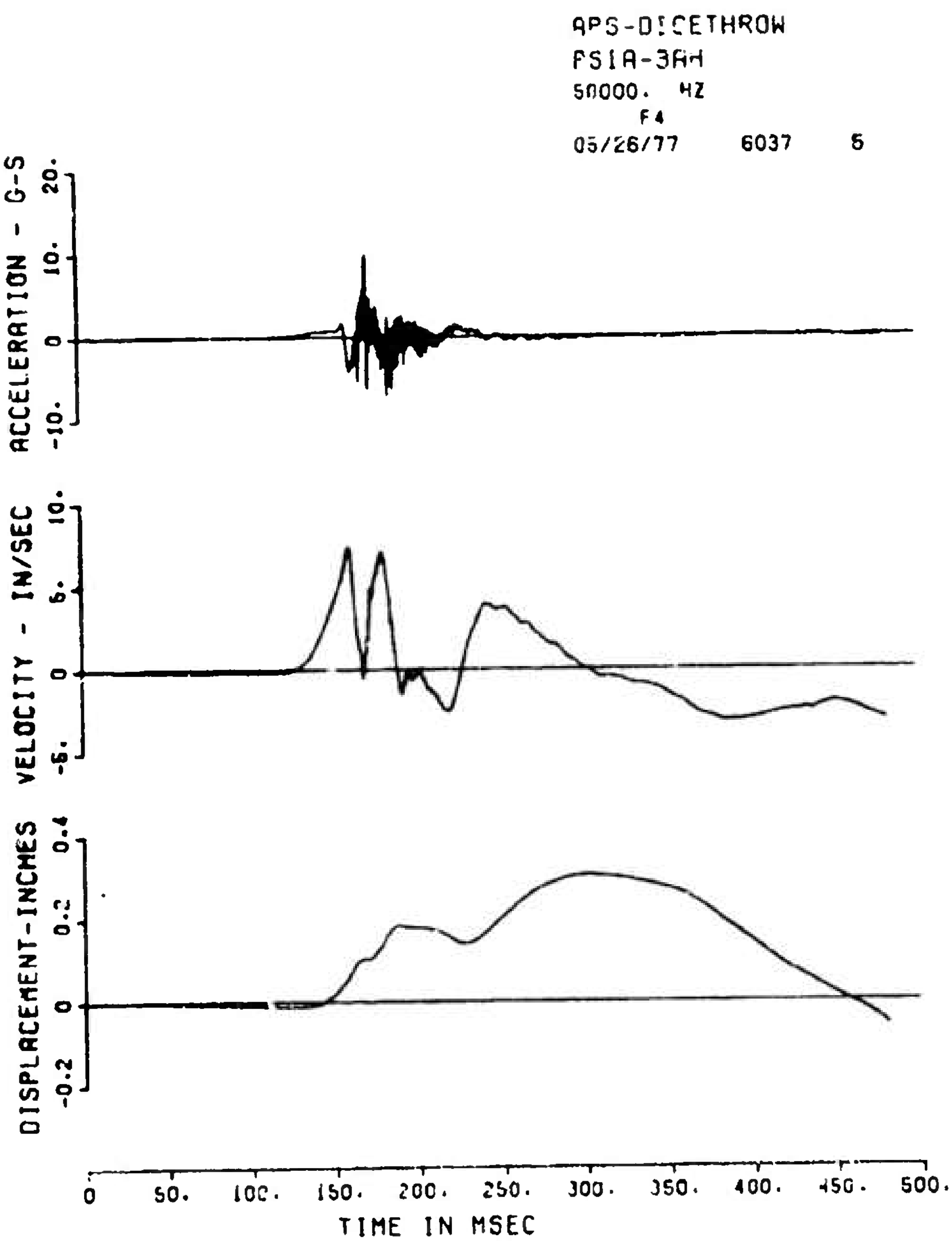

APS-DICETHROW
FSIA-3AH
50000. HZ
F4
05/26/77 6037 5
ACCELERATION - G-S
20.
10.
0
-10.
VELOCITY - IN/SEC
10.
5.
0
-5.
DISPLACEMENT-INCHES
0.4
0.2
0
-0.2
0
50.
100.
150.
200.
250.
300.
350.
400.
450.
500.
TIME IN MSEC

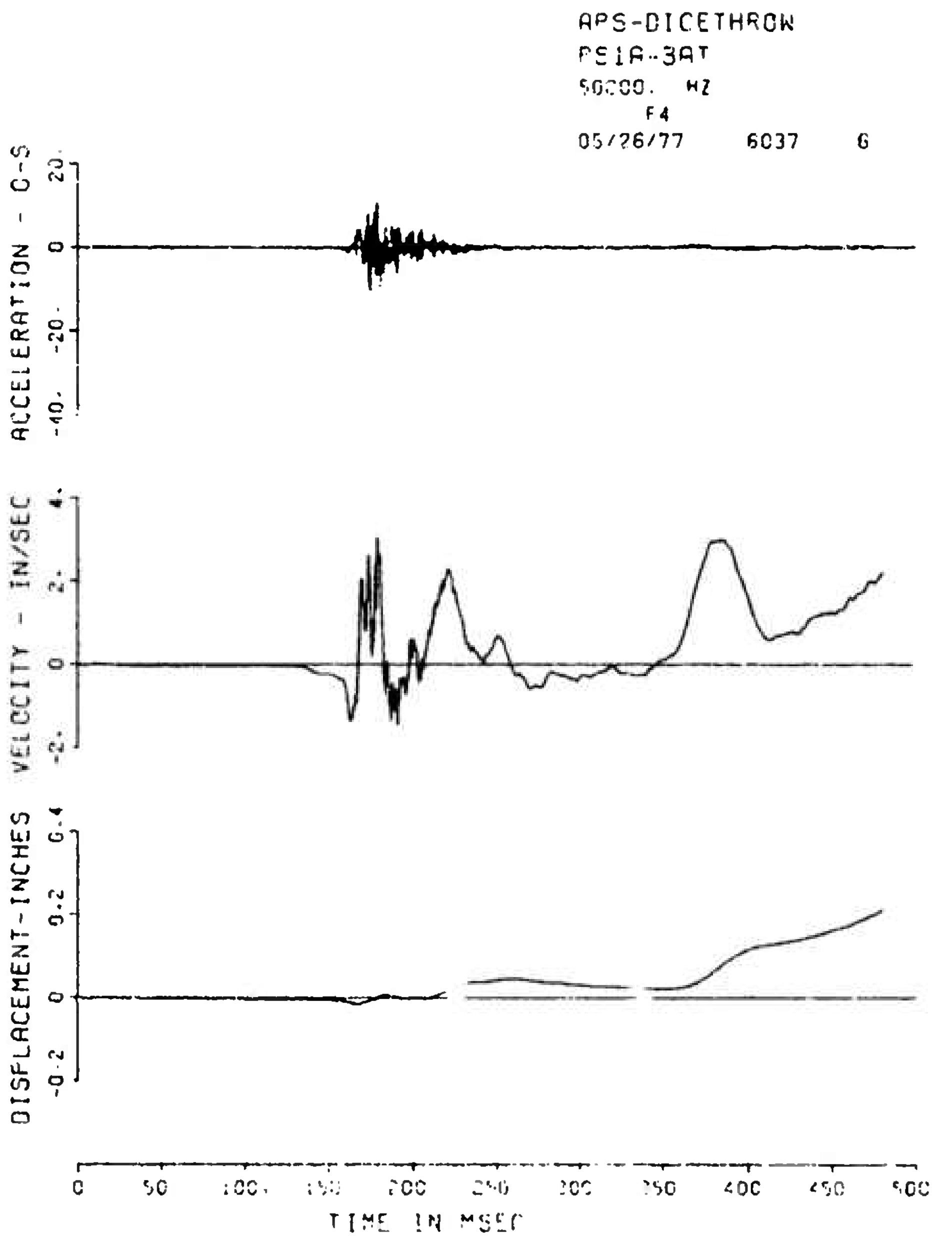

APS-DICETHROW
PS1A-3AT
50000. HZ
F4
05/26/77 6037 6
ACCELERATION - G-S
20.
0
-20.
-40.
VELOCITY - IN/SEC
4.
2.
0
-2.
DISPLACEMENT-INCHES
0.4
0.2
0
-0.2
0
50
100.
150
200
250
300
350
400
450
500
TIME IN MSEC

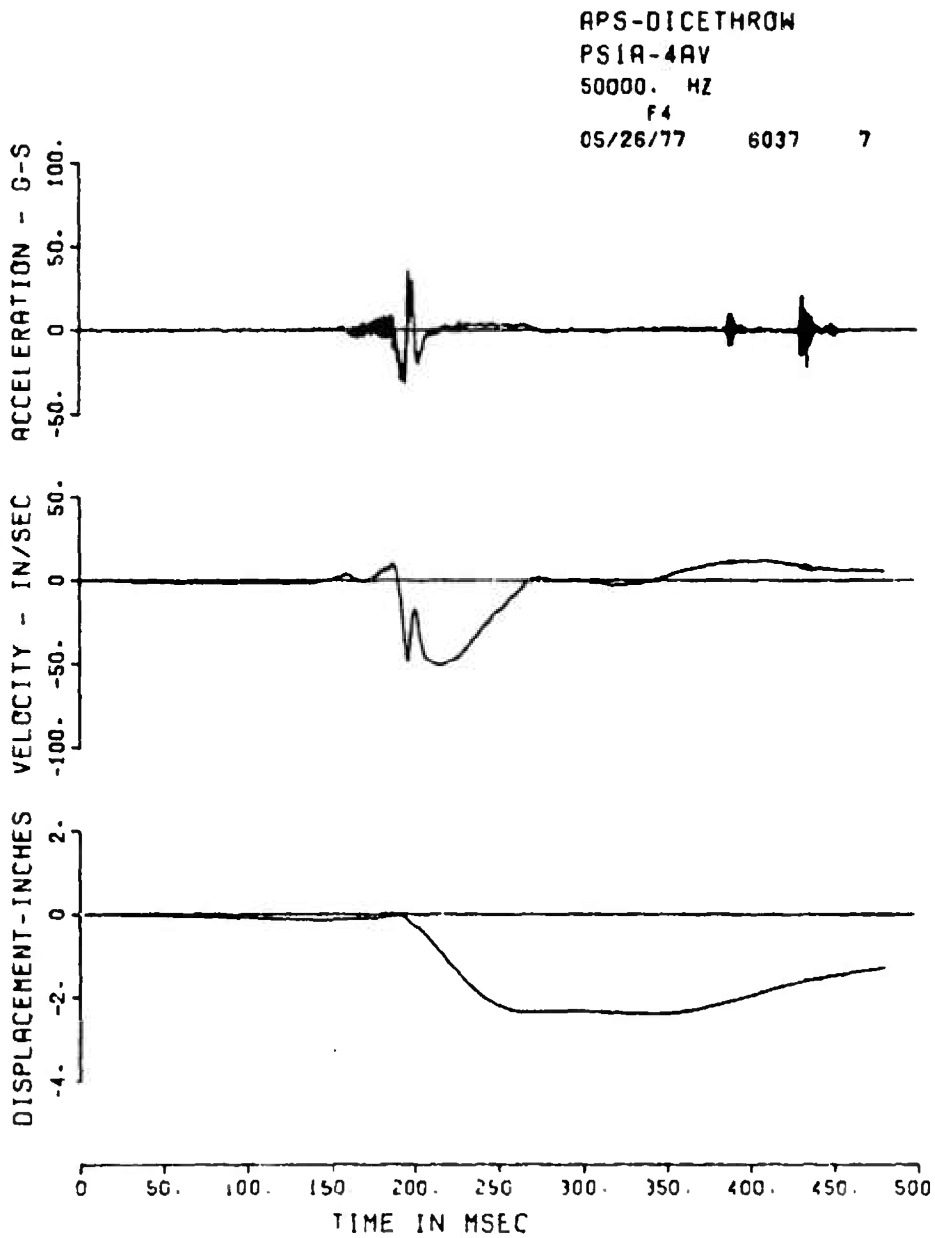
APS-DICETHROW
PSIA-4AV
50000. HZ
F4
05/26/77 6037 7
ACCELERATION - G-S
100.
50.
0
-50.
VELOCITY - IN/SEC
50.
0
-50.
-100.
DISPLACEMENT-INCHES
2.
0
-2.
-4.
0
50.
100.
150
200.
250
300.
350.
400.
450.
500.
TIME IN MSEC

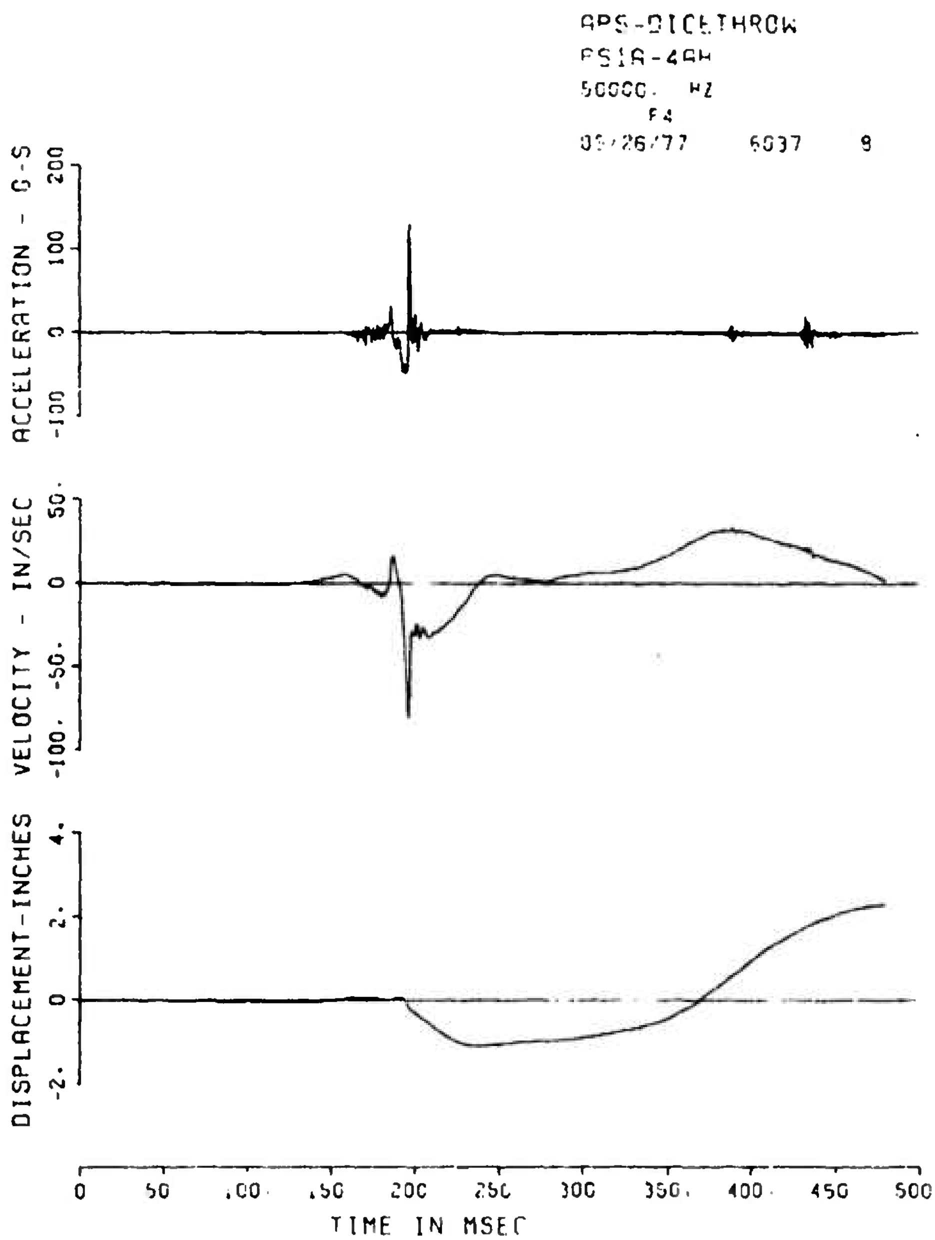

APS-DICETHROW
FS1A-4AH
50000. HZ
F4
09/26/77 6037 9
ACCELERATION - G-S
200
100
0
-100
VELOCITY - IN/SEC
50.
0
-50.
-100.
DISPLACEMENT-INCHES
4.
2.
0
-2.
0 50 100. 150 200 250 300 350. 400. 450 500.
TIME IN MSEC

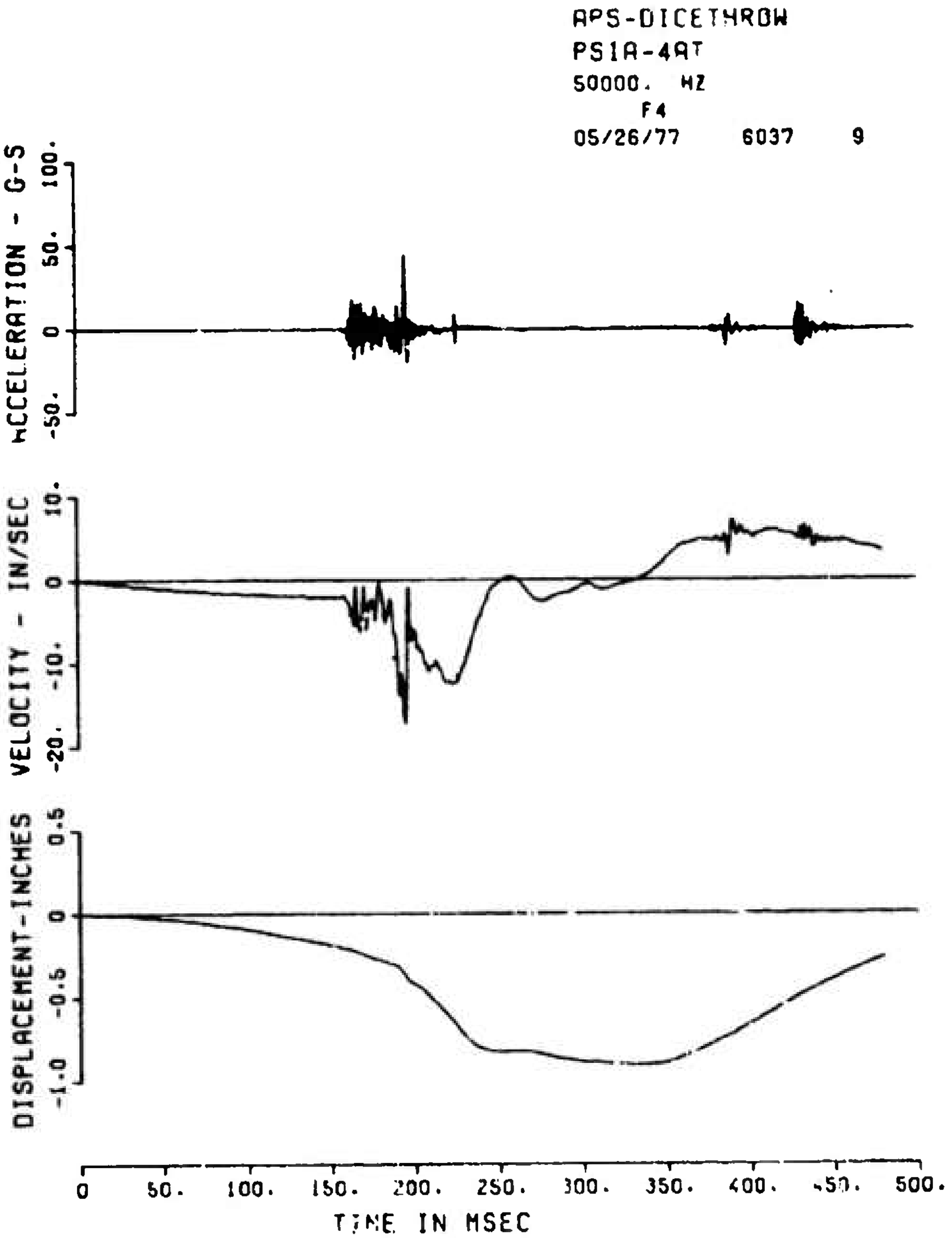

APS-DICETHROW
PSIA-4AT
50000. HZ
F4
05/26/77 6037 9
ACCELERATION - G-S
100.
50.
0
-50.
VELOCITY - IN/SEC
10.
0
-10.
-20.
DISPLACEMENT-INCHES
0.5
0
-0.5
-1.0
0
50.
100.
150.
200.
250.
300.
350.
400.
450.
500.
TIME IN MSEC

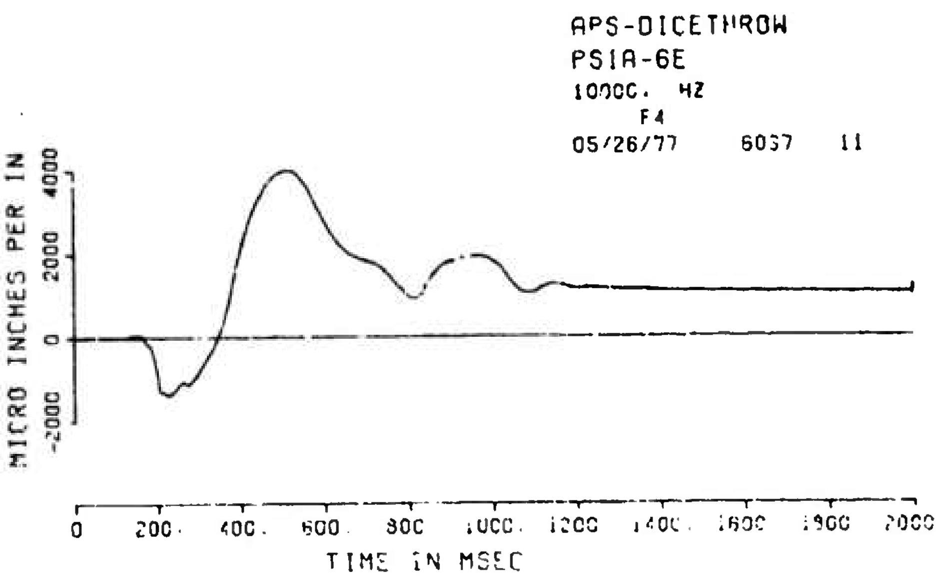
APS-DICETHROW
PSIA-6E
10000. HZ
F4
05/26/77 6037 11
MICRO INCHES PER IN
4000
2000
0
-2000
0
200.
400.
600.
800
1000.
1200
1400.
1600
1800
2000.
TIME IN MSEC

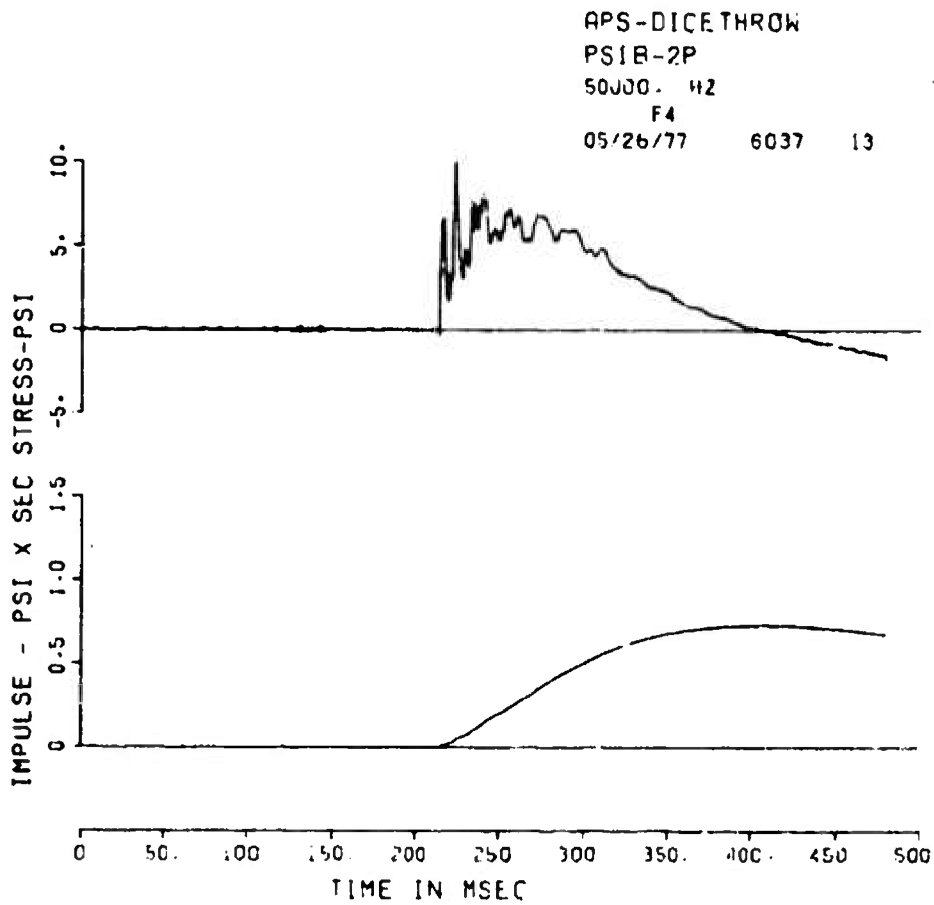

APS-DICETHROW
PSIB-2P
50000. HZ
F4
05/26/77 6037 13
IMPULSE - PSI X SEC STRESS-PSI
10.
5.
0
-5.
1.5
1.0
0.5
0
0
50.
100
150.
200
250
300
350.
400.
450
500.
TIME IN MSEC

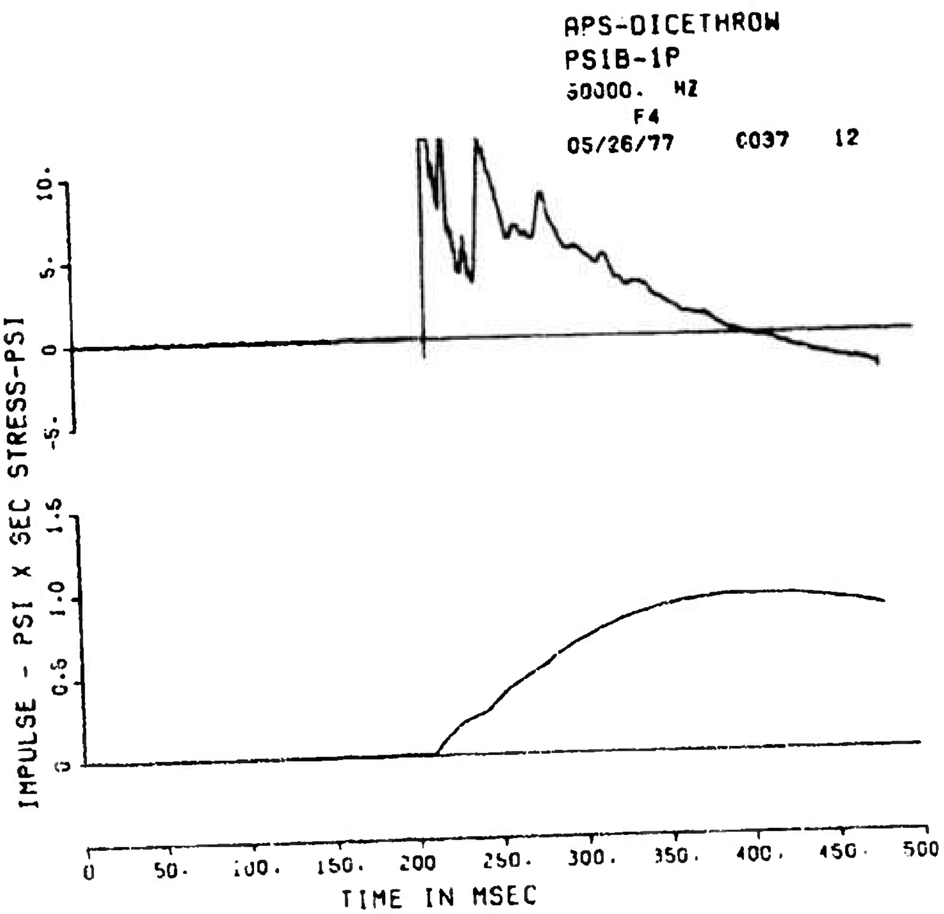

APS-DICETHROW
PS1B-1P
50000. HZ
F4
05/26/77 C037 12
STRESS-PSI
10.
5.
0
-5.
IMPULSE - PSI X SEC
1.5
1.0
0.5
0
0
50.
100.
150.
200
250.
300.
350.
400.
450.
500.
TIME IN MSEC

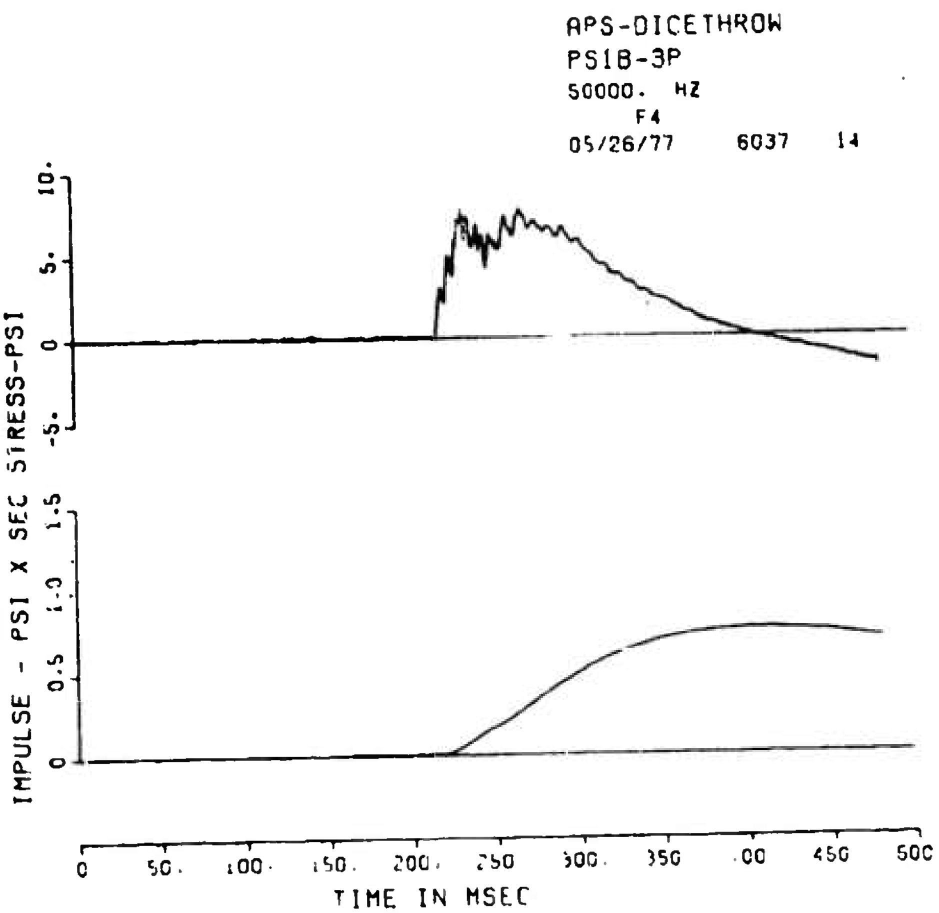
APS-DICETHROW
PS1B-3P
50000. HZ
F4
05/26/77 6037 14
STRESS-PSI
IMPULSE - PSI X SEC
TIME IN MSEC

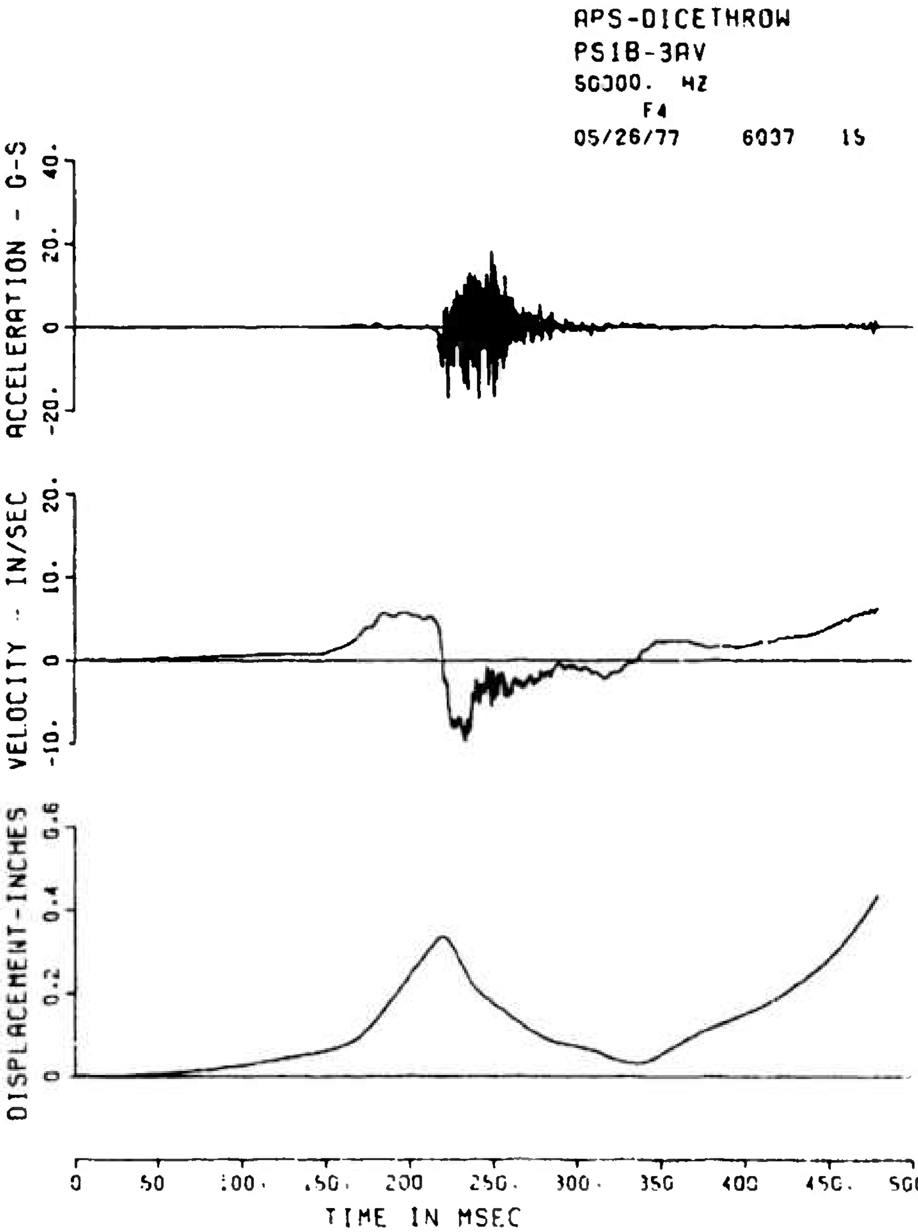
APS-DICETHROW
PSIB-3AV
50000. HZ
F4
05/26/77 6037 1S
ACCELERATION - G-S
40.
20.
0
-20.
VELOCITY - IN/SEC
20.
10.
0
-10.
DISPLACEMENT-INCHES
0.6
0.4
0.2
0
0
50
100.
150.
200
250.
300.
350
400
450.
500.
TIME IN MSEC

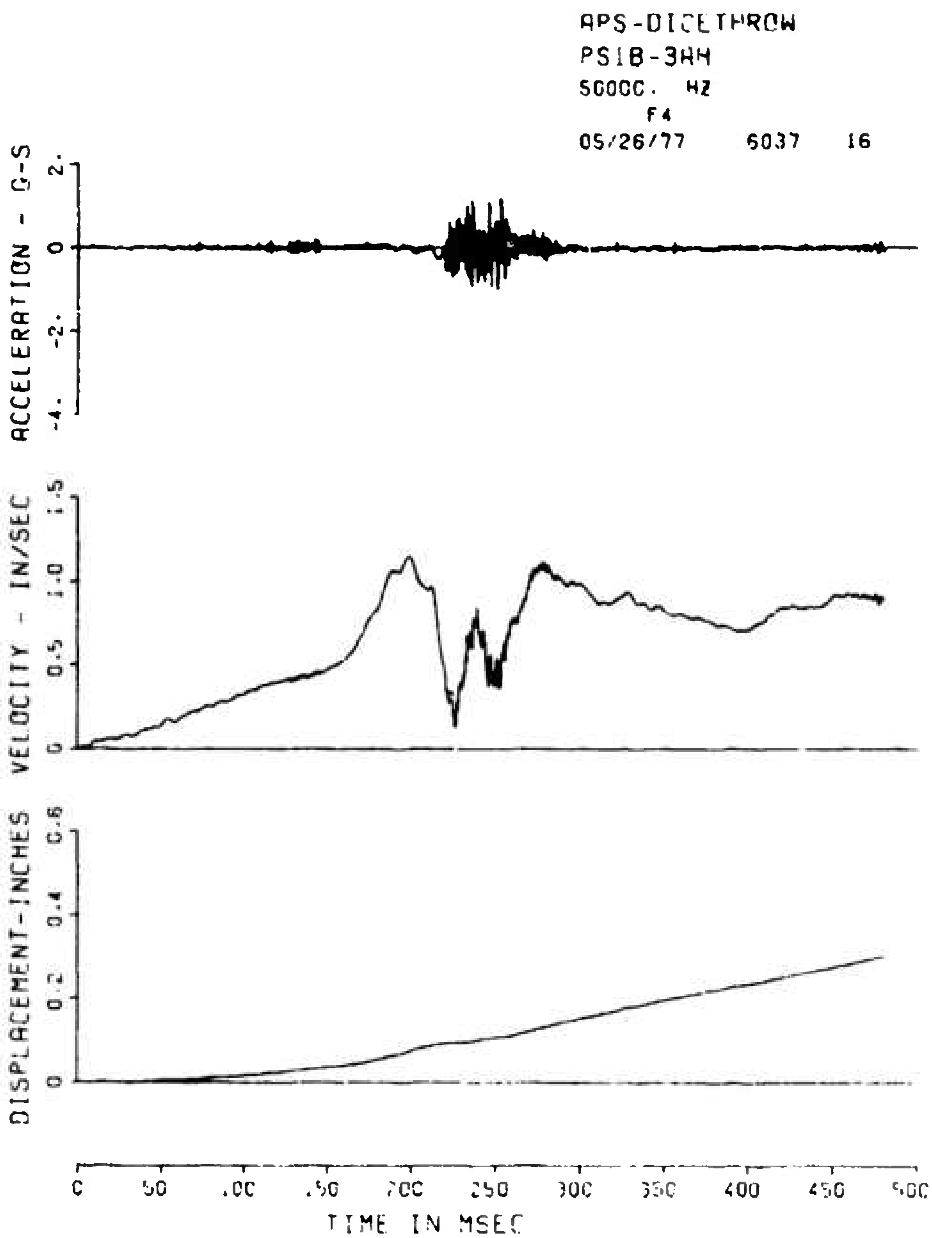
APS-DICETHROW
PS1B-3HH
50000. HZ
F4
05/26/77 6037 16
ACCELERATION - G-S
VELOCITY - IN/SEC
DISPLACEMENT-INCHES
TIME IN MSEC

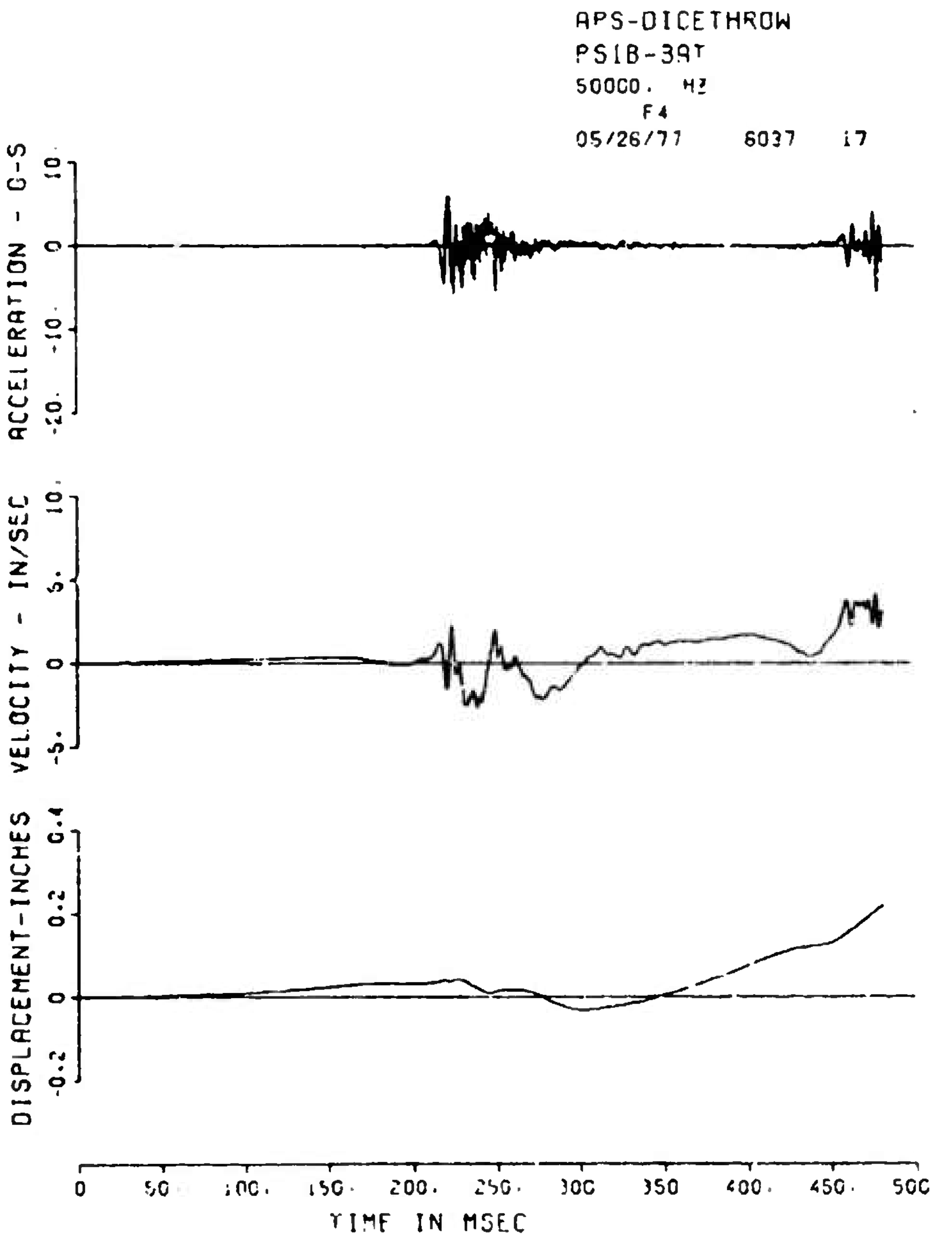
APS-DICETHROW
PSIB-39T
50000. HZ
F4
05/26/77 6037 17
ACCELERATION - G-S
10.
0
-10.
-20.
VELOCITY - IN/SEC
10.
5.
0
-5.
DISPLACEMENT-INCHES
0.4
0.2
0
-0.2
0
50
100.
150.
200.
250.
300
350
400.
450.
500
TIME IN MSEC

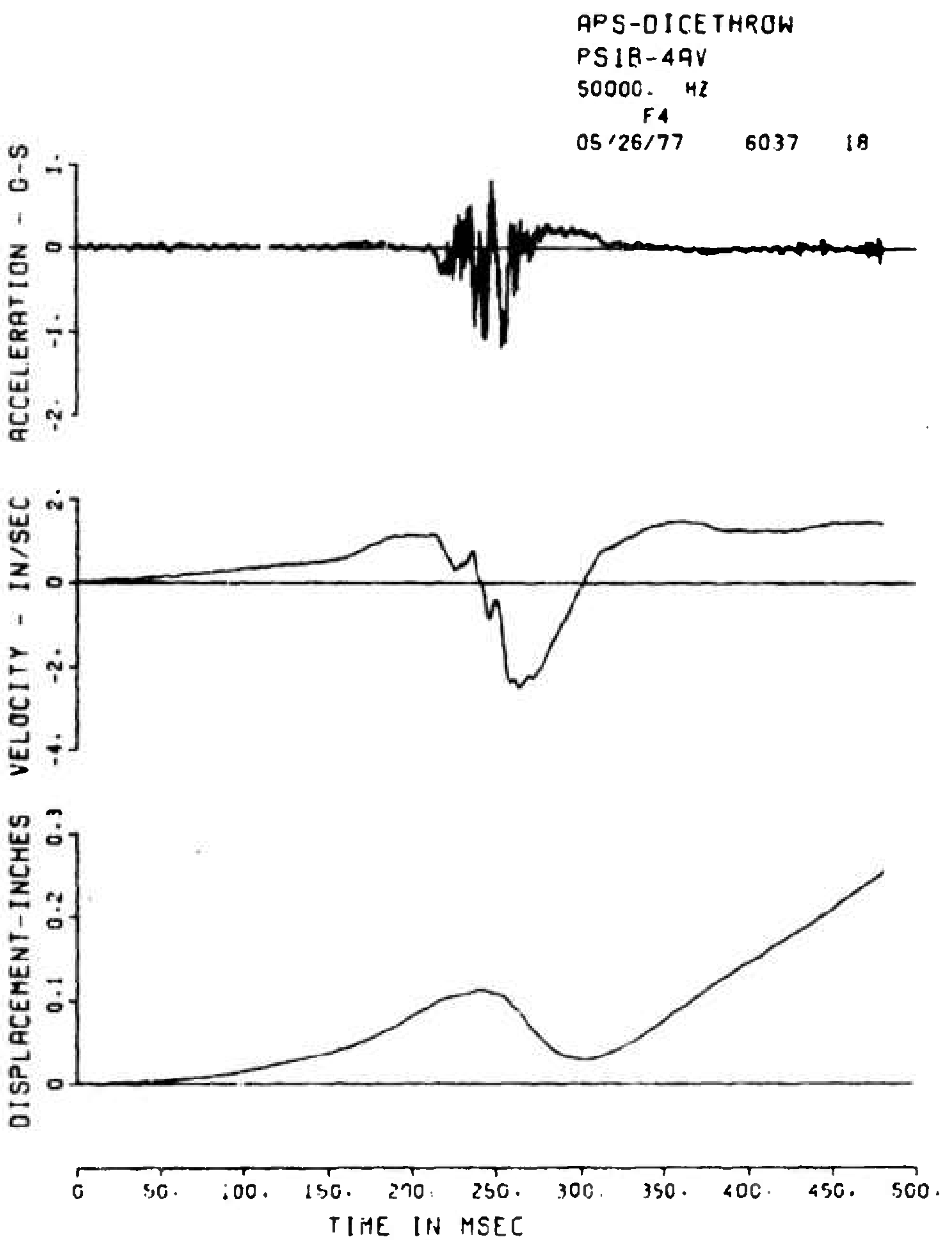

APS-DICETHROW
PS1B-4AV
50000. HZ
F4
05/26/77 6037 18
ACCELERATION - G-S
1.
0
-1.
-2.
VELOCITY - IN/SEC
2.
0
-2.
-4.
DISPLACEMENT-INCHES
0.3
0.2
0.1
0
0
50.
100.
150.
200.
250.
300.
350.
400.
450.
500.
TIME IN MSEC

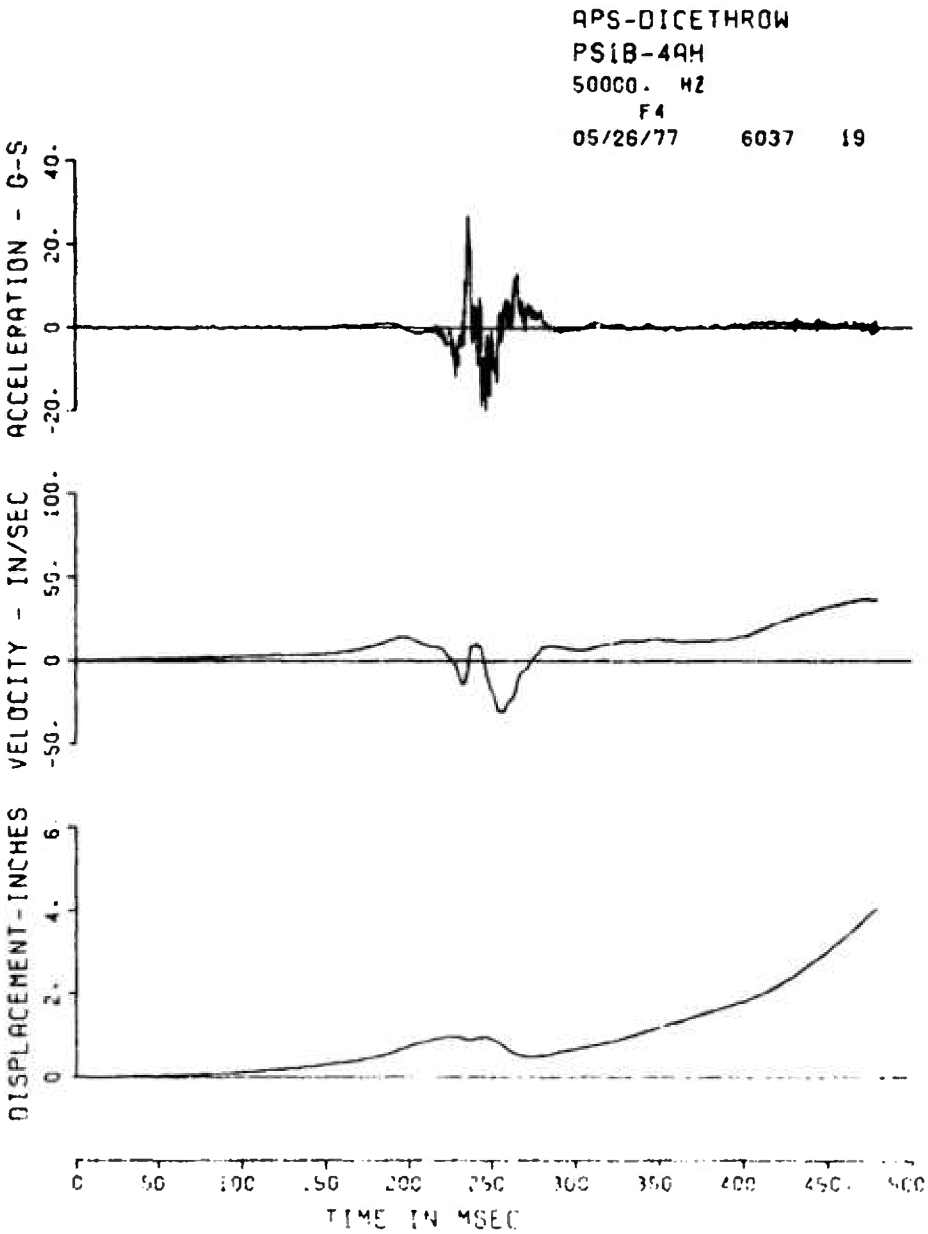
APS-DICETHROW
PSIB-4AH
50000. HZ
F4
05/26/77 6037 19
ACCELERATION - G-S
40.
20.
0
-20.
VELOCITY - IN/SEC
100.
50.
0
-50.
DISPLACEMENT-INCHES
6.
4.
2.
0
0
50
100
150
200
250
300
350
400
450
500
TIME IN MSEC

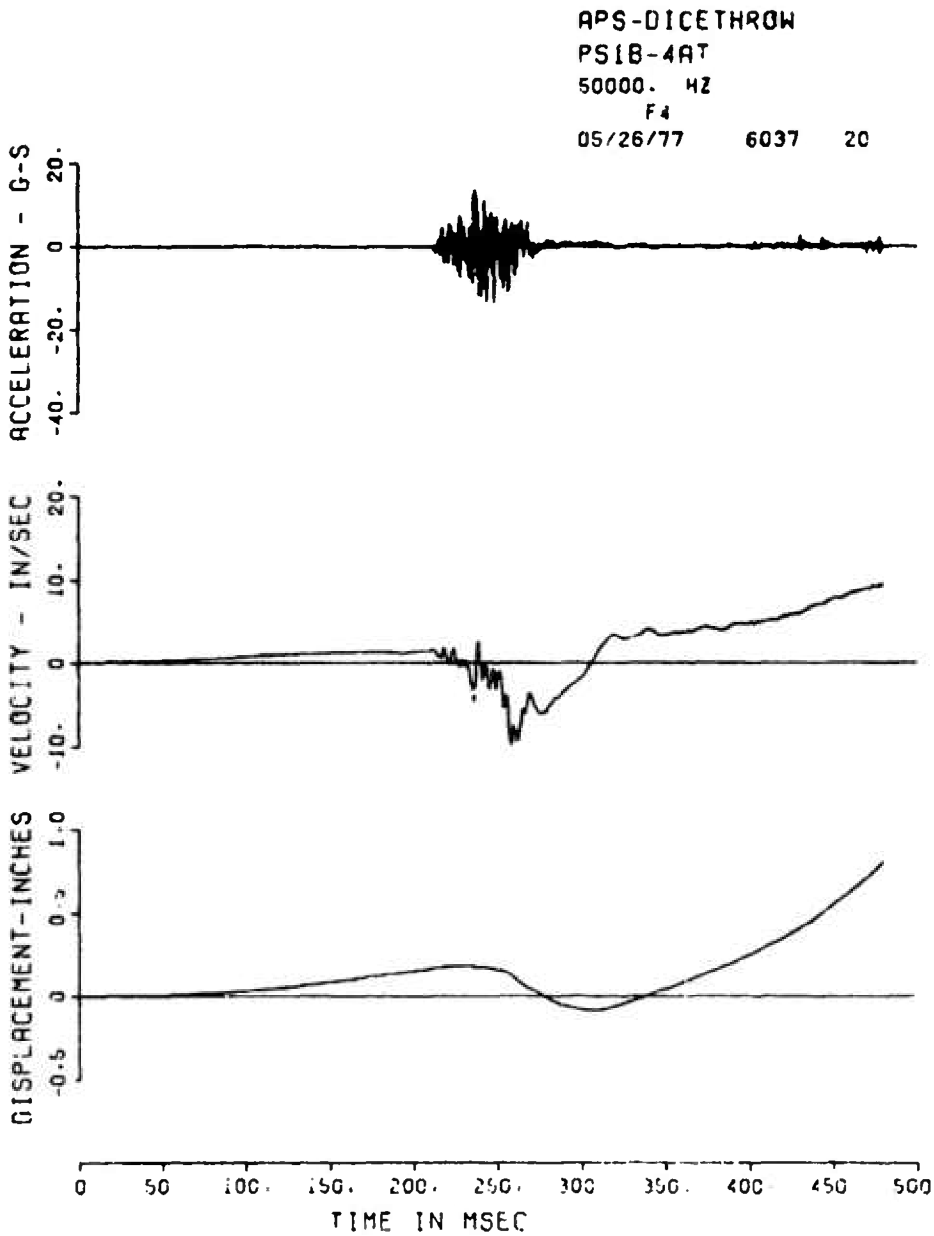

APS-DICETHROW
PSIB-4AT
50000. HZ
F4
05/26/77 6037 20
ACCELERATION - G-S
20.
0
-20.
-40.
VELOCITY - IN/SEC
20.
10.
0
-10.
DISPLACEMENT-INCHES
1.0
0.5
0
-0.5
0
50
100.
150.
200.
250.
300
350.
400
450
500.
TIME IN MSEC

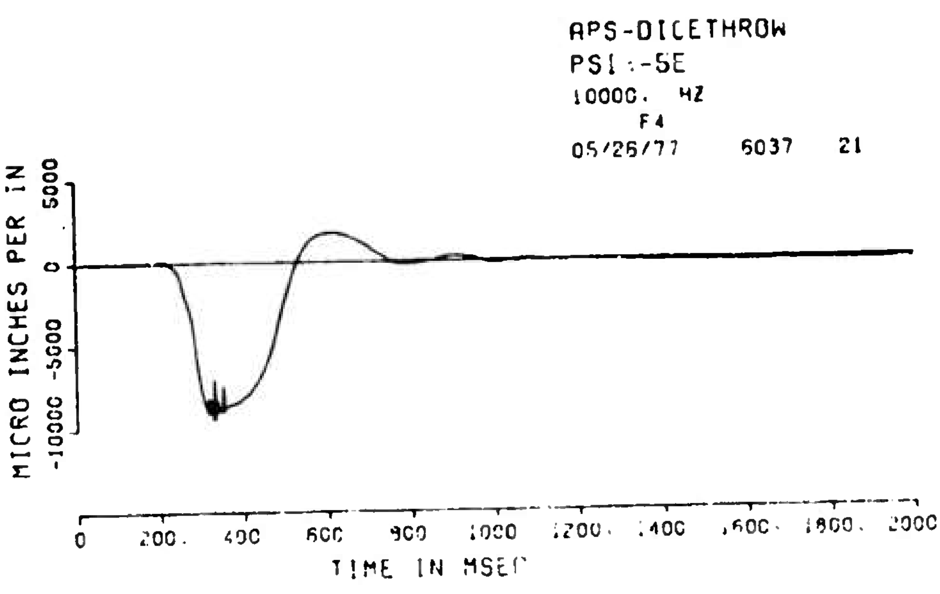

APS-DICETHROW
PSI :-5E
10000. HZ
F4
05/26/77 6037 21
MICRO INCHES PER IN
5000
0
-5000
-10000
0
200.
400
600
800
1000
1200.
1400
1600.
1800.
2000
TIME IN MSEC

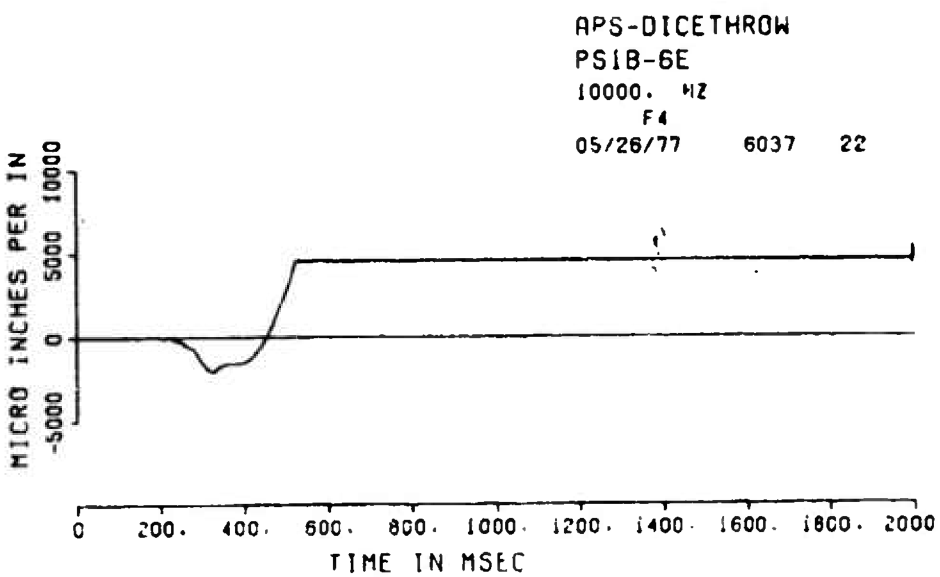

APS-DICETHROW
PSIB-6E
10000. HZ
F4
05/26/77 6037 22
MICRO INCHES PER IN
10000
5000
0
-5000
0
200.
400.
600.
800.
1000.
1200.
1400.
1600.
1800.
2000.
TIME IN MSEC

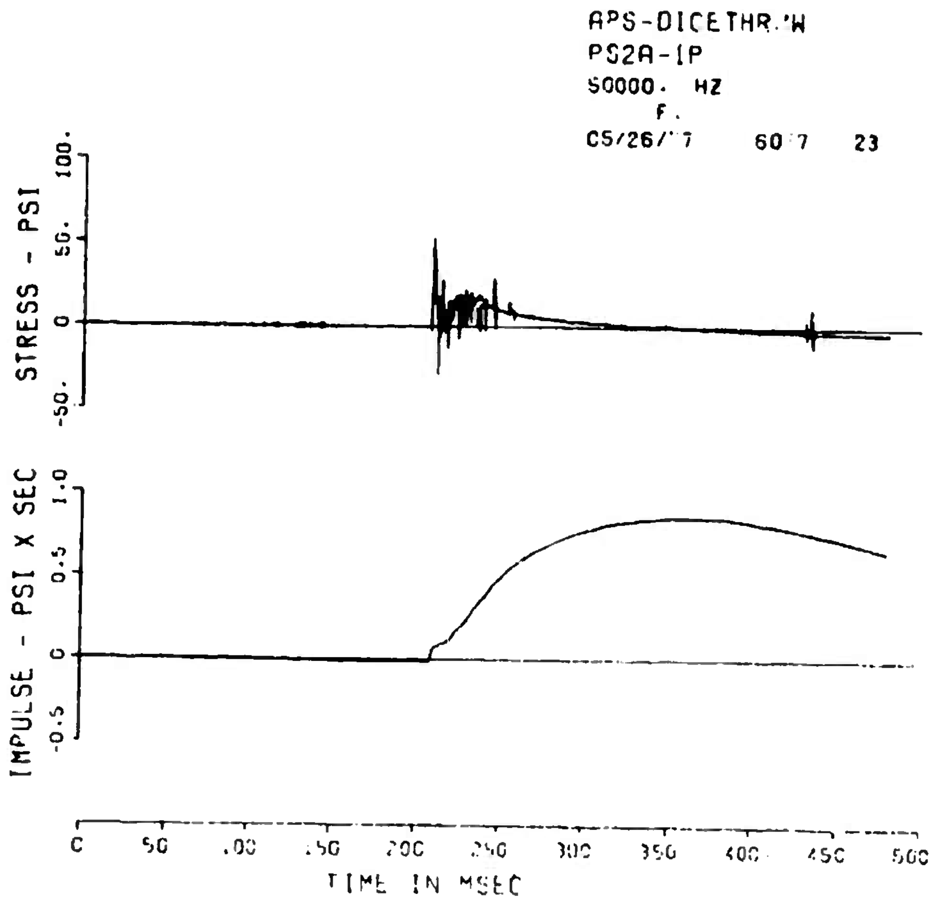

APS-DICETHR.'W
PS2A-IP
50000. HZ
F.
05/26/'7 60 7 23
STRESS - PSI
100.
50.
0
-50.
IMPULSE - PSI X SEC
1.0
0.5
0
-0.5
0
50
100
150
200
250
300
350
400
450
500
TIME IN MSEC

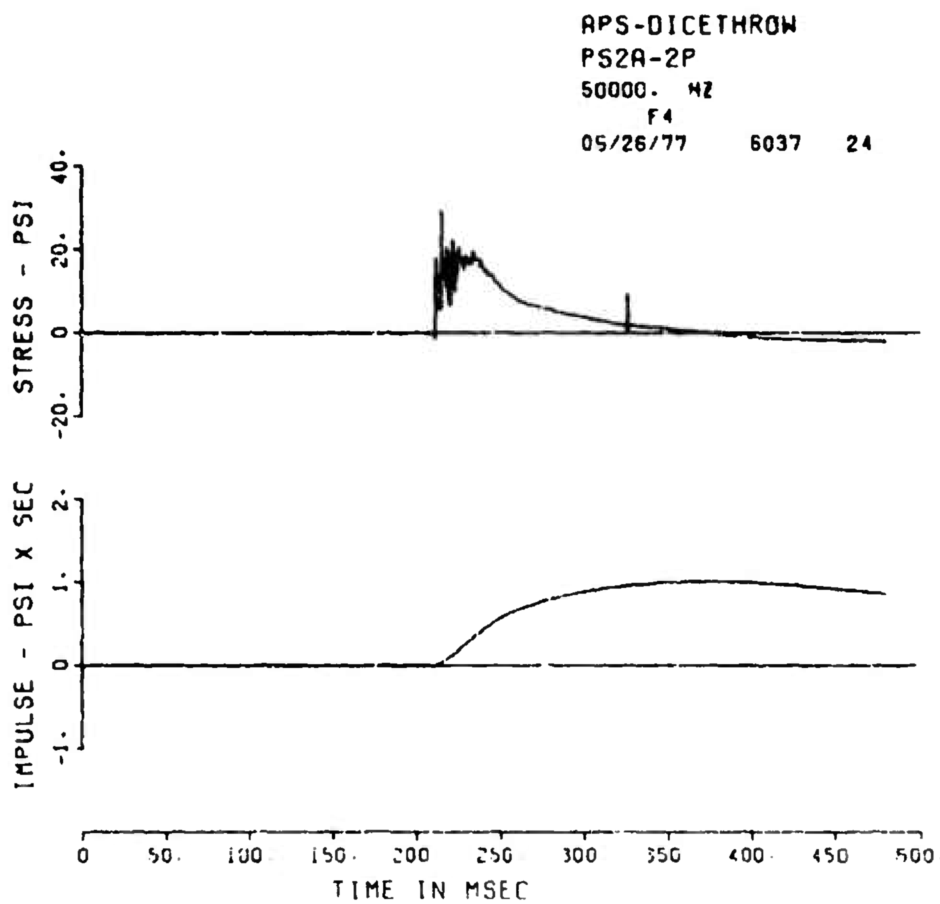

APS-DICETHROW
PS2A-2P
50000. HZ
F4
05/26/77 6037 24
STRESS - PSI
40.
20.
0
-20.
IMPULSE - PSI X SEC
2.
1.
0
-1.
0
50.
100
150.
200
250
300
350
400.
450
500.
TIME IN MSEC

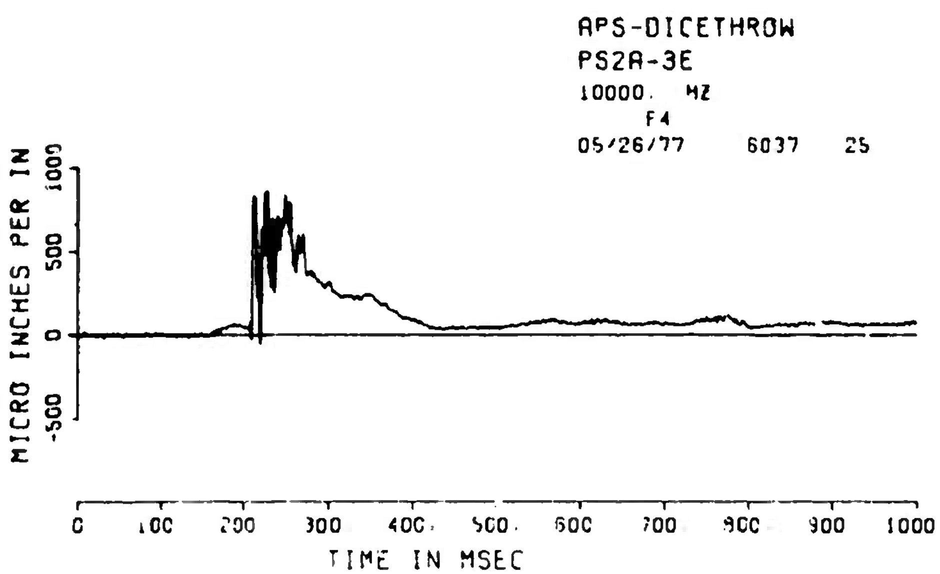
APS-DICETHROW
PS2A-3E
10000. HZ
F4
05/26/77 6037 25
MICRO INCHES PER IN
1000
500
0
-500
0
100
200
300
400.
500.
600
700
800
900
1000.
TIME IN MSEC

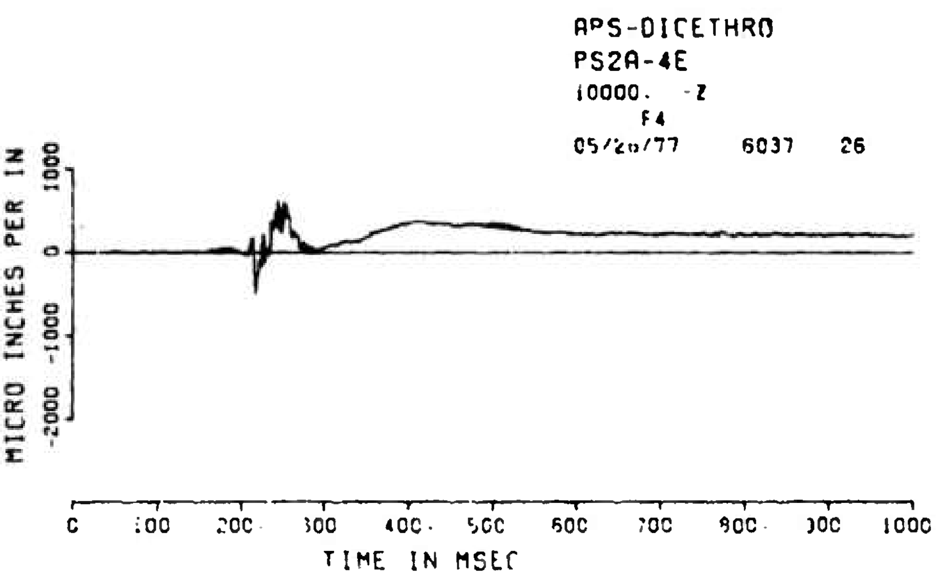
APS-DICETHRO
PS2A-4E
10000. -Z
F4
05/26/77 6037 26
MICRO INCHES PER IN
1000
0
-1000
-2000
0
100
200
300
400
500
600
700
800
900
1000
TIME IN MSEC

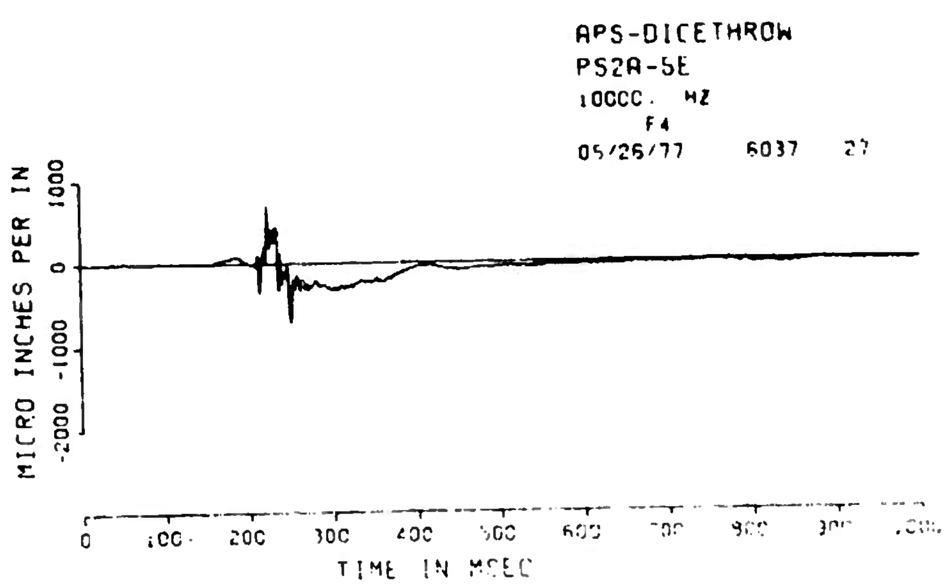
APS-DICETHROW
PS2A-5E
10000. HZ
F4
05/26/77 6037 27
MICRO INCHES PER IN
1000
0
-1000
-2000
0
100
200
300
400
500
600
TIME IN MSEC

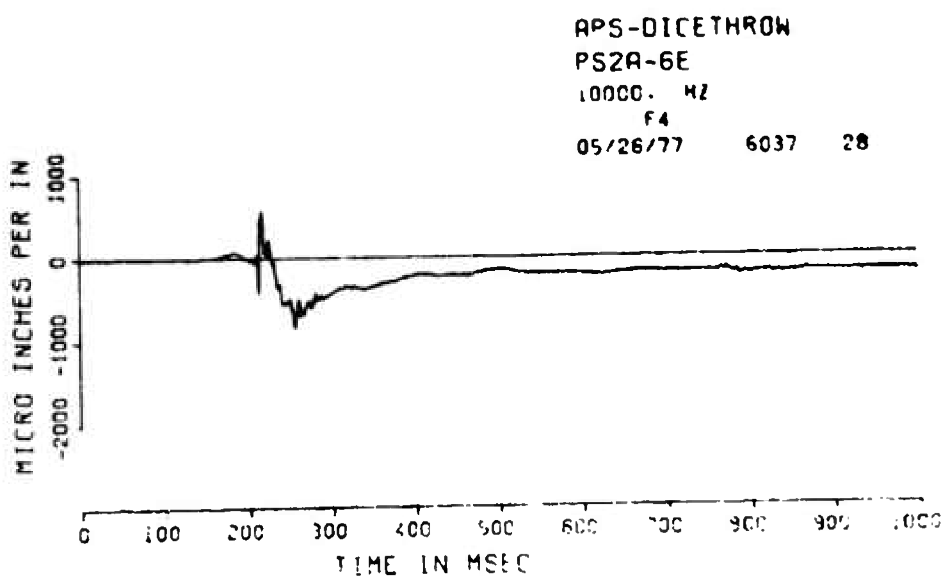

APS-DICETHROW
PS2A-6E
10000. HZ
F4
05/26/77 6037 28
MICRO INCHES PER IN
1000
0
-1000
-2000
0
100
200
300
400
500
600
700
800
900
1000
TIME IN MSEC

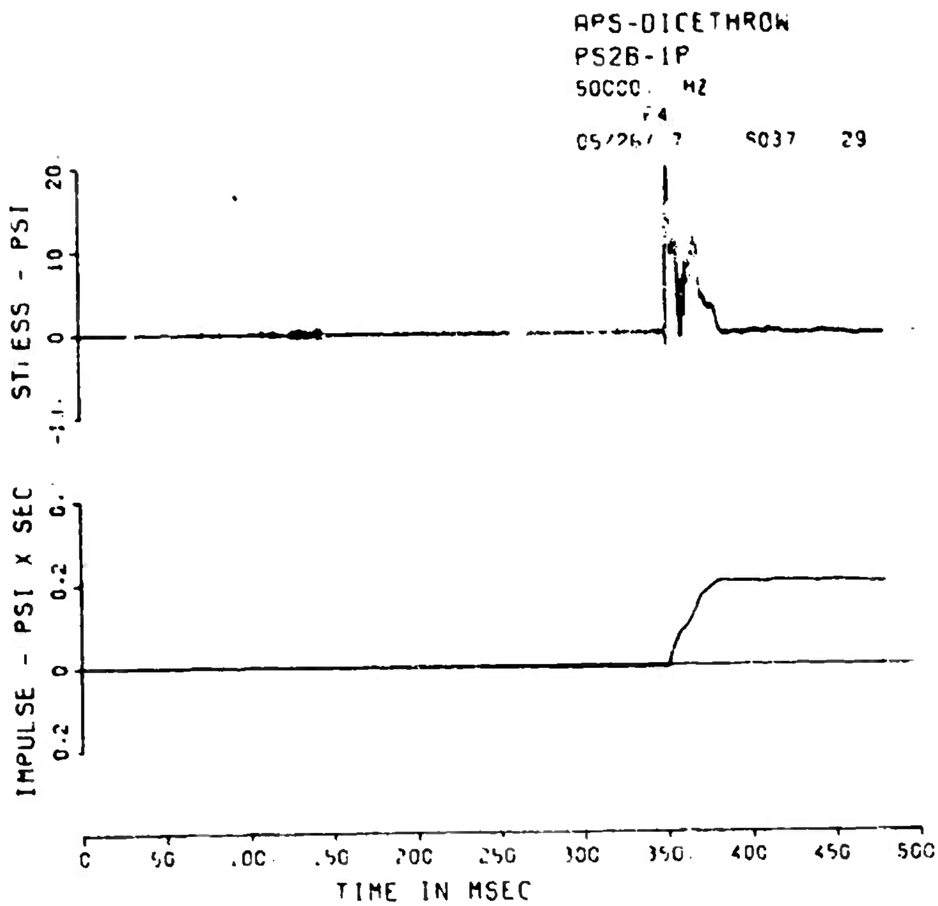

APS-DICETHROW
PS2B-1P
50CCC. HZ
STRESS - PSI
IMPULSE - PSI X SEC
TIME IN MSEC

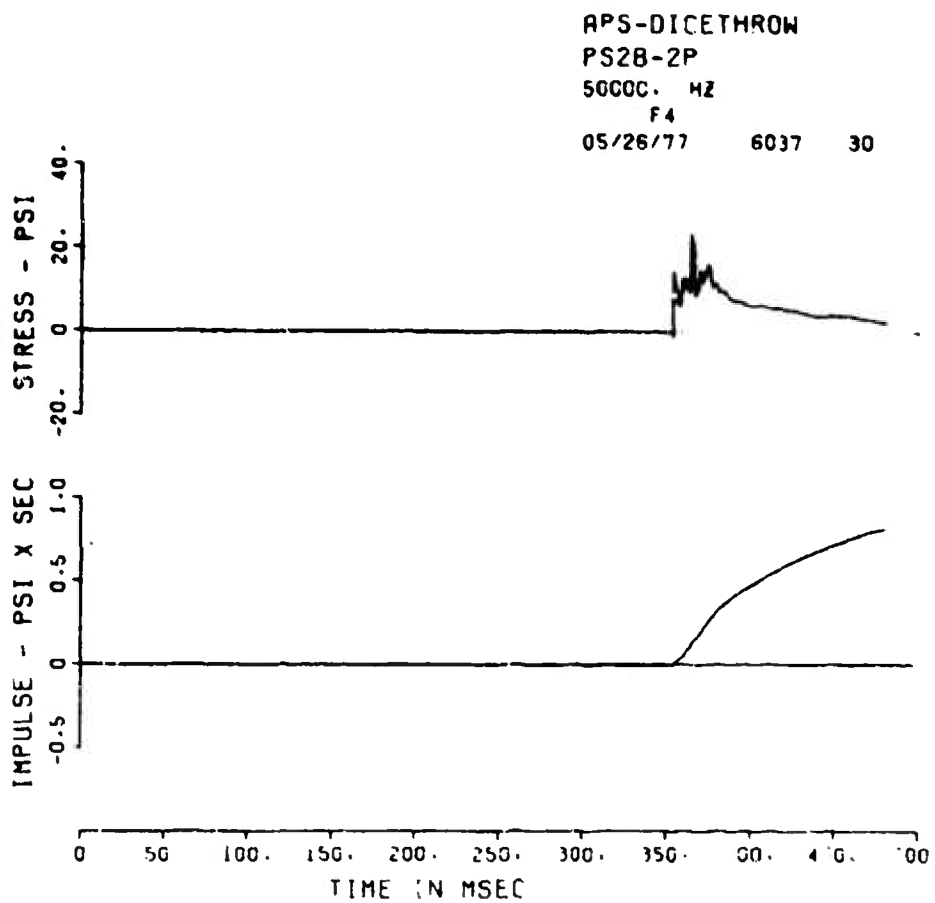
APS-DICETHROW
PS28-2P
50C0C. HZ
F4
05/26/77 6037 30
STRESS - PSI
IMPULSE - PSI X SEC
TIME IN MSEC

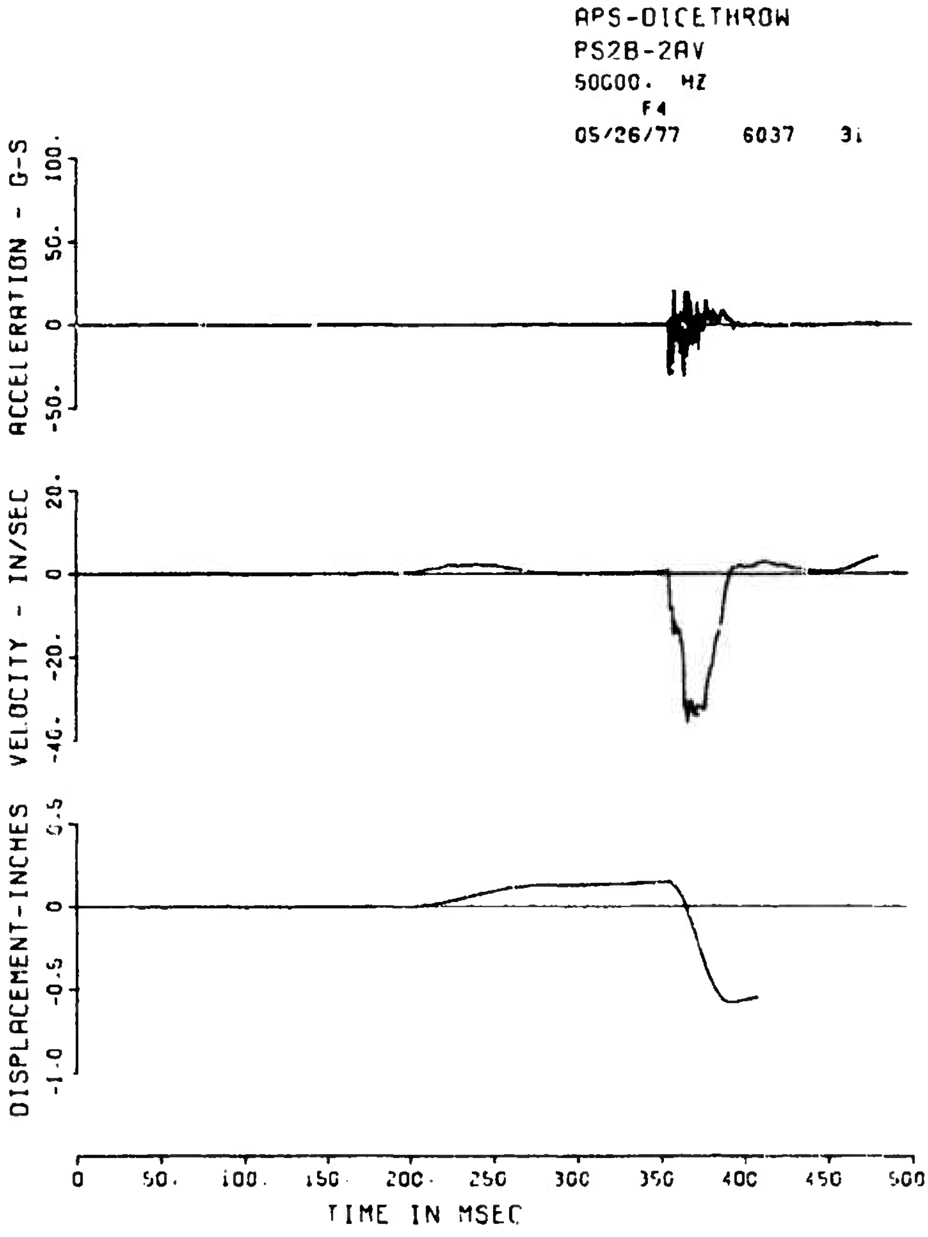
APS-DICETHROW
PS2B-2AV
50000. HZ
F4
05/26/77 6037 31
ACCELERATION - G-S
100.
50.
0
-50.
VELOCITY - IN/SEC
20.
0
-20.
-40.
DISPLACEMENT-INCHES
0.5
0
-0.5
-1.0
0
50.
100.
150.
200.
250
300
350
400
450
500.
TIME IN MSEC

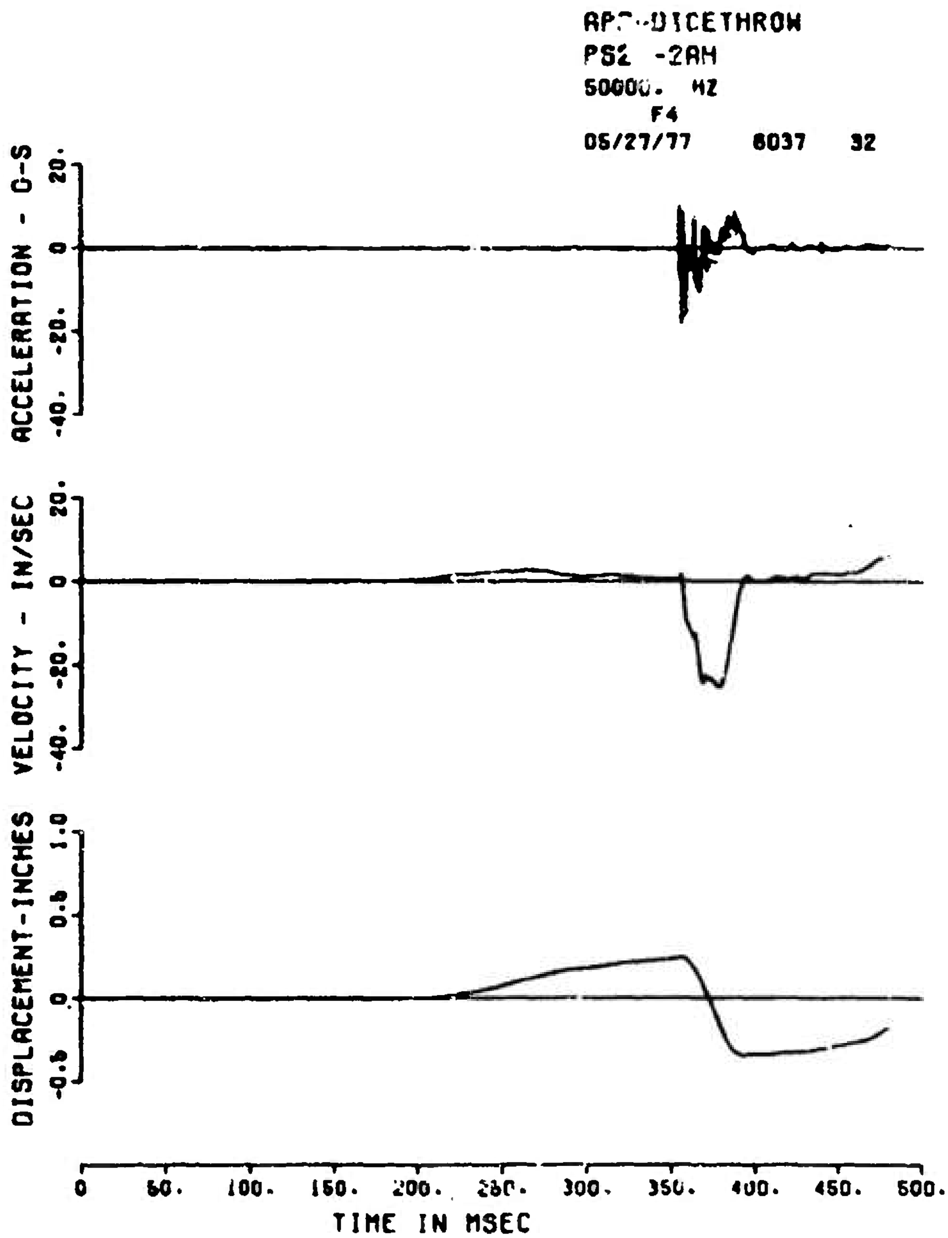

RP?-DICETHROW
PS2 -2AH
50000. HZ
F4
05/27/77 8037 32
ACCELERATION - G-S
20.
0
-20.
-40.
VELOCITY - IN/SEC
20.
0
-20.
-40.
DISPLACEMENT-INCHES
1.0
0.5
0.
-0.5
0
50.
100.
150.
200.
250.
300.
350.
400.
450.
500.
TIME IN MSEC

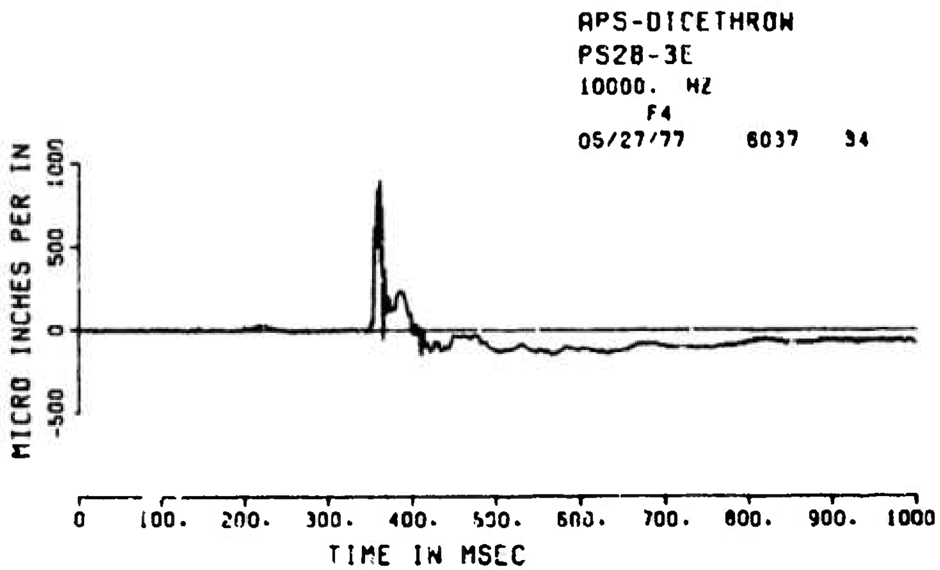
APS-DICETHROW
PS2B-3E
10000. HZ
F4
05/27/77 6037 34
MICRO INCHES PER IN
1000
500
0
-500
0
100.
200.
300.
400.
500.
600.
700.
800.
900.
1000.
TIME IN MSEC

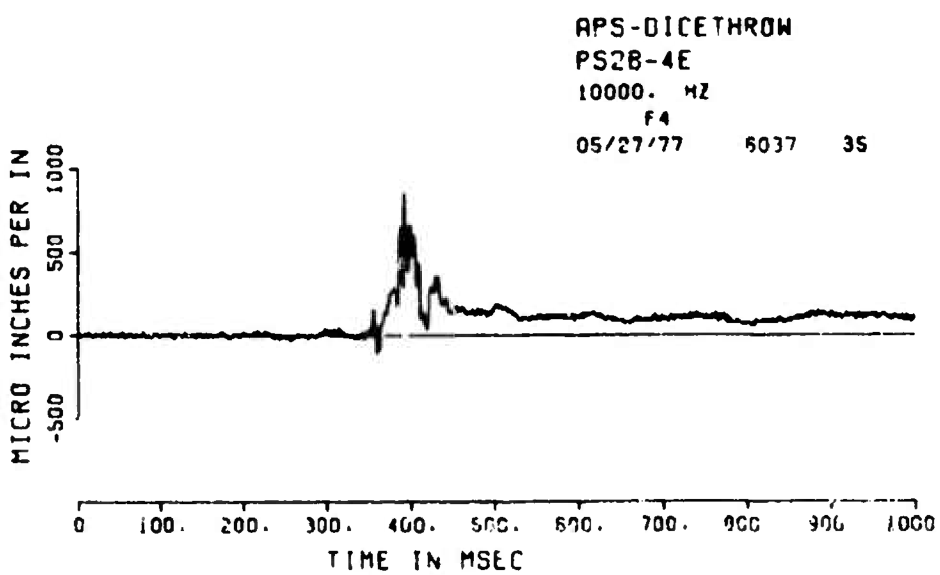
APS-DICETHROW
PS2B-4E
10000. HZ
F4
05/27/77 6037 35
MICRO INCHES PER IN
1000
500
0
-500
0
100.
200.
300.
400.
500.
600.
700.
800.
900.
1000.
TIME IN MSEC

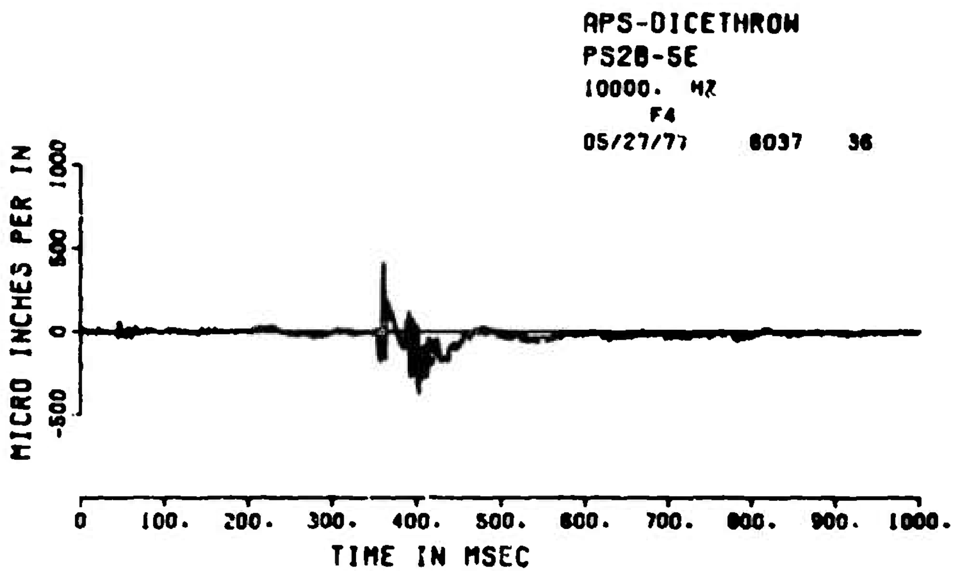
APS-DICETHROW
PS2B-5E
10000. HZ
F4
05/27/77 8037 36
MICRO INCHES PER IN
1000
500
0
-500
0
100.
200.
300.
400.
500.
600.
700.
800.
900.
1000.
TIME IN MSEC

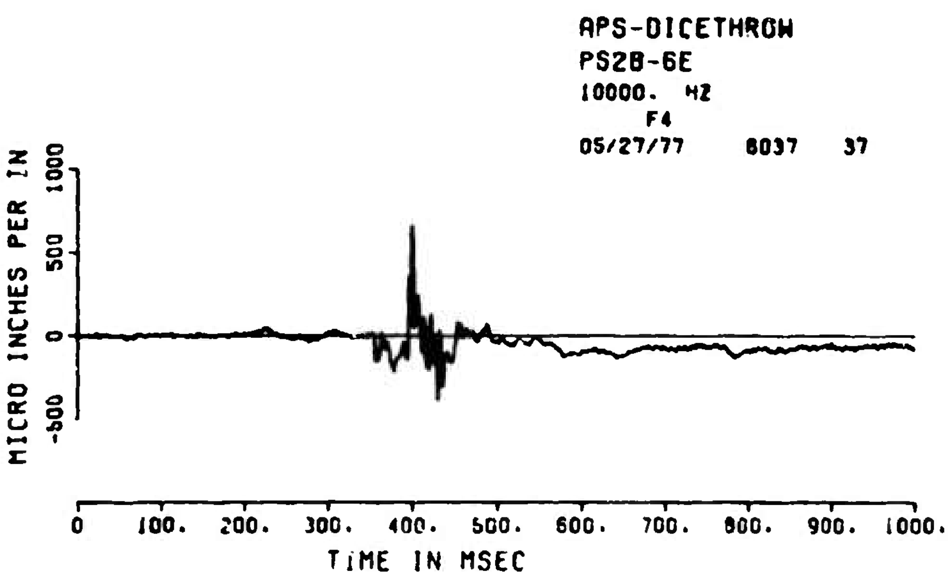
APS-DICETHROW
PS2B-6E
10000. HZ
F4
05/27/77 8037 37
MICRO INCHES PER IN
1000
500
0
-500
0
100.
200.
300.
400.
500.
600.
700.
800.
900.
1000.
TIME IN MSEC

DISTRIBUTION LIST

DEPARTMENT OF DEFENSE

Director
Defense Advanced Research Project Agency
ATTN: Strategic Tech. Office
ATTN: NMRO
ATTN: Technical Library

Director
Defense Communications Agency
ATTN: NMCSSC Code 510

Defense Documentation Center
Cameron Station
12 cy ATTN: TC

Director
Defense Intelligence Agency
ATTN: DT-1C Nuc Eng Branch
ATTN: DT-2 Wpns & Sys Div
ATTN: DI-7D

Director
Defense Nuclear Agency
ATTN: DDST
ATTN: TISI Archives
3 cy ATTN: TITL Technical Library
ATTN: STSP
ATTN: SPAS
ATTN: Maj William A. Alter
ATTN: Maj. E. Neal Gunby
ATTN: Tom Kennedy
ATTN: Maj. Edmund Mueller
ATTN: LTC Edwin T. Still
ATTN: SPSS
ATTN: SPTD

Director
Defense Research & Engineering
ATTN: S&SS (OS)
ATTN: AD/ET J. Persh

Commander
Field Command
Defense Nuclear Agency
ATTN: FCTMD
ATTN: FCTMOT
ATTN: FCTMOF
ATTN: FCPR
ATTN: FCT
ATTN: Capt. V.A. Alvarez
ATTN: Capt. R.G. DeRaad
ATTN: Noel Ganwick
ATTN: Lt. C. Klimmek
ATTN: LCDR J.D. Strode
ATTN: Maj. R.F. Bestgen

Director
Joint Strat Tgt Planning Staff JCS
ATTN: JLTW-2
ATTN: JPTM
ATTN: JPTP

Chief
Livermore Division Field Command DNA
Lawrence Livermore Laboratory
ATTN: FCPRL

Explosive Safety Board
ATTN: Dr. Thomas Zaker

The Pentagon
ATTN: J-5 Plans & Pol Planning & Prgm Div
ATTN: J-5 Plans & Policy Nuc Div

Studies Analysis and Gaming Agency
Joint Chiefs of Staff
ATTN: SFLB

Director
Defense Civil Preparedness Agency
ATTN: Michael A. Pachuta

Director
National Security Agency
ATTN: Edward Butala (R51)
ATTN: William DeBoy (R51)

Commander
902 Military Intelligence Group
ATTN: Col. Hassel L. Parker

DEPARTMENT OF THE ARMY

Director
BMD Advanced Tech Center
ATTN: ATC-T Melvin T. Capps
ATTN: Marcus Whitfield

Program Manager
BMD Program Office
ATTN: DACS-BMT John Shea
ATTN: DACS-BMC
ATTN: DACS-BMC-D Julian Davidson
ATTN: DACS-BMT Clifford E. McLain

Commander
BMD System Command
ATTN: BDMSC-TEN Noah J. Hurst

Deputy Chief of Staff for Rsch Dev & Acq
Department of the Army
ATTN: Technical Library

DEPARTMENT OF THE ARMY, continued

Deputy Chief of Staff for Operations & Plans
Department of the Army
 ATTN: Director of Nuclear Plans & Policy

Commander
U.S. Army Electronics Command
 ATTN: Robert Frieberg

Commander
SOC USAOCCS
 ATTN: Capt. Alexander F. Wojcicki

Commander
Harry Diamond Laboratories
 ATTN: DRXDO-RBH James H. Gwaltney
 ATTN: DRXDO-TI Robert B. Oswald, Jr.
 ATTN: DRXDO-TI, Technical Library
 ATTN: DRXDO-NP
 ATTN: L. Belliveau
 ATTN: W. Vault

Commander
Picatinny Arsenal
 ATTN: Al Loeb
 ATTN: SARPA-ND-C-T Donald Miller
 ATTN: SARPA-FR-I Louis Avrami
 ATTN: SMUPA-MD Henry Opat

Director
TRASANA
 ATTN: R.L. Dekinder, Jr.

Commander
White Sands Missile Range
 ATTN: Richard Dysart
 ATTN: Dale W. Green

Director
U.S. Army Ballistic Research Labs
 ATTN: J.H. Keefer, DRDAR-BLE
 ATTN: DRXBR-X, Julius J. Meszaros
 ATTN: DRXRD-BVL, William J. Schuman, Jr.
 ATTN: Richard Vitali
 ATTN: DRXBR-TB, J.T. Frasier
 ATTN: Robert E. Eichelberger
 ATTN: Technical Library, Edward Baicy
 ATTN: W.D. Allison
 ATTN: N. Ethridge
 ATTN: Col. R. Gomez
 ATTN: A. Gupta
 ATTN: J. Jacobson
 ATTN: V. King
 ATTN: C. Kingery
 ATTN: R. Mayerhofer
 ATTN: R. Pearson
 ATTN: R.L. Peterson
 ATTN: E. Quigley
 ATTN: R.J. Raley
 ATTN: R.I. Reisler
 ATTN: L. Roecker
 ATTN: D.L. Rigotti
 ATTN: R. Schumacher
 ATTN: R. Shelton
 ATTN: J. Sullivan
 ATTN: W. Taylor
 ATTN: G. Teel
 ATTN: G. Watson
 ATTN: M. Wiherle

Director
U.S. Army Engineer Waterways Experiment Station
 ATTN: Technical Library
 ATTN: James Ballard
 ATTN: Jimmy P. Balsara
 ATTN: William Flathau
 ATTN: William L. Huff
 ATTN: Adam A. Ruta
 ATTN: James Watt
 ATTN: LTC Ronald R. Kaufmann

Commander
U.S. Army Materiel & Mechanics Research Center
 ATTN: DRXMR-HH, John F. Dignam

Commander
U.S. Army Materiel Development & Readiness CMD
 ATTN: DRCDE-D, Lawrence Flynn
 ATTN: Technical Library

Commander
U.S. Army Missile Command
 ATTN: DRSMI-XS, Chief Scientist
 ATTN: DRS-RKP, W.B. Thomas
 ATTN: DRSMI-RRR, Bud Gibson

Commander
U.S. Army Nuclear Agency
 ATTN: MONA-SA
 ATTN: MONA-WE
 ATTN: CDC-NVA
 ATTN: ATCA-NAW
 ATTN: Maj. John Uecke
 ATTN: Maj. Alan Lind

U.S. Army Satellite Communications Agency
 ATTN: Eugene Caulifield

Commander
U.S. Army Armament R&D Command
 ATTN: Alvin Fluger (DRDAR-LCW)
 ATTN: Martin A. Ravotto (DRDAR-LCS-W)
 ATTN: Daniel Waxler (DRDAR-LCS-W)

DEPARTMENT OF THE NAVY

Chief of Naval Material
 ATTN: MAT 0323, Irving Jaffe

Chief of Naval Operations
 ATTN: Code 604C3, Robert Piacesi
 ATTN: Code 604C4, Robert A. Blaise
 ATTN: OP 62
 ATTN: OP 981

Chief of Naval Research
 ATTN: Technical Library

Director
Naval Research Laboratory
 ATTN: Code 2600, Technical Library
 ATTN: Code 7770, Gerald Cooperstein
 ATTN: Code 5180, Mario A. Persechino

Commander
Naval Sea Systems Command
 ATTN: 0333A, Marlin A. Kinna

DEPARTMENT OF THE NAVY, continued

Officer-in-Charge
Civil Engineering Laboratory
Naval Construction Battalion
ATTN: Technical Library

Officer-in-Charge
Naval Surface Weapons Center
ATTN: Code WA07, Carson Lyons
ATTN: Code WR10, Joseph Petes
ATTN: Code WA501 Navy Nuclear Programs Office
ATTN: Michael Swisdak
ATTN: Phillip Peckham

Commanding Officer
Naval Weapons Evaluation Facility
ATTN: Lawrence R. Oliver
ATTN: Peter Hughes
ATTN: Rudolf Friedberg

Director
Strategic Systems Project Office
ATTN: NSP-272

Commander
Naval Facilities Engineering Command Headquarters
ATTN: Technical Library

Naval Sea Support Center
Fleet Support Office
ATTN: LCDR E.W. Edgerton

DEPARTMENT OF THE AIR FORCE

Commandant
AF Flight Dynamics Laboratory, AFSC
ATTN: FXG

AF Geophysics Laboratory, AFSC
ATTN: Chan Touart

AF Materials Laboratory, AFSC
ATTN: LPH Gordon Griffith
ATTN: MBE George F. Schmitt
ATTN: MBC Donald L. Schmidt
ATTN: MAS
ATTN: T. Nicholas
ATTN: LTM

AF Rocket Propulsion Laboratory, AFSC
ATTN: RTSN G.A. Beale

AF Weapons Laboratory, AFSC
ATTN: DYS
ATTN: Al Sharp
ATTN: SAB
ATTN: DYT
ATTN: DYV
ATTN: Dr. Minge
ATTN: SUL
ATTN: Lt. Joel C. Bradshaw
ATTN: Susan Check
ATTN: Steve Melzer
ATTN: Charles Needham
ATTN: Maynard A. Plamondon
ATTN: LTC James Warren
ATTN: Harry Webster
ATTN: NTO
ATTN: Technical Review

Air Force Institute of Technology, AU
ATTN: Library, AFIT

Headquarters
Air Force Systems Command
ATTN: XRTO
ATTN: SDSS

Commander
Arnold Engineering Development Center
ATTN: XOA

Commander
ASD
4 cy ATTN: ENFS D. Ward

Commander
Foreign Technology Division, AFSC
ATTN: TQPTN
ATTN: PDBG
ATTN: TDFBD, J.D. Pumphrey

HQ USAF/RD
ATTN: RDQSM
ATTN: RD
ATTN: RDQ
ATTN: RDPM

HQ USAF/XO
ATTN: XOOSS

SAMSO/DY
ATTN: DYS

SAMSO/MN
ATTN: MNNH
ATTN: MNNR
ATTN: Capt. Thomas Edwards

SAMSO/RS
ATTN: RST
ATTN: RSS
ATTN: RSSE

Commander in Chief
Strategic Air Command
ATTN: XOBM
ATTN: XPQM
ATTN: Maj. Ronald W. Bushant
ATTN: XPFS
ATTN: DOXT

U.S. ENERGY RESEARCH & DEVELOPMENT ADMINISTRATION

Division of Military Application
ATTN: Doc. Con. for Res. & Dev. Branch

University of California
Lawrence Livermore Laboratory
ATTN: G. Staehle, L-24
ATTN: C. Joseph Taylor, L-92
ATTN: Joseph B. Knox, L-216
ATTN: Joseph F. Keller, Jr., L-125
ATTN: Bernard Hayes

U.S. ENERGY RAD ADM., continued

Los Alamos Scientific Laboratory
- ATTN: Doc. Control for Robert Skaggs
- ATTN: Doc. Control for R. Dingus
- ATTN: Doc. Control for John McQueen
- ATTN: Doc. Control for J.W. Taylor
- ATTN: Doc. Control for R.S. Thurston

Sandia Laboratories
Livermore Laboratory
- ATTN: Doc. Control for Technical Library
- ATTN: Doc. Control for [illegible]

Sandia Laboratories
- ATTN: Doc. Control for Thomas B. Cook
- ATTN: Doc. Control for R.R. Boade
- ATTN: Doc. Control for Albert Chabai
- ATTN: Doc. Control for M. Cowan
- ATTN: Doc. Control for Jack Reed
- ATTN: Doc. Control for Normal Breazeal
- ATTN: Doc. Control for Technical Library

Director
Oak Ridge National Laboratory
- ATTN: Dr. [illegible] Kearny, Bldg. 4500n

DEPARTMENT OF DEFENSE CONTRACTORS

Acurex Corporation
- ATTN: J. Huntington
- ATTN: J. Courtney
- ATTN: C. Nardo
- ATTN: R. Rindal

Aerospace Corporation
- ATTN: W. Barry
- ATTN: R. Mortensen
- ATTN: Richard Crolius, A2-Rm1027
- ATTN: H. Blaes
- ATTN: W. Mann
- ATTN: Robert L. Strickler
- ATTN: J. McClelland

Analytic Services, Inc.
- ATTN: Jack Selig

AVCO Research & Systems Group
- ATTN: John Gilmore, J400
- ATTN: Document Control
- ATTN: John E. Stevens, J100
- ATTN: William Broding
- ATTN: George Weber, J230

Battelle Memorial Institute
- ATTN: Technical Library
- ATTN: E. Unger
- ATTN: Merwyn R. Vanderlind

Boeing Company, The
- ATTN: Edwin York
- ATTN: Robert Holmes
- ATTN: Robert Dyrdahl
- ATTN: Brian Lempriere
- ATTN: Jay C. Pyle
- ATTN: Roland Carlson

Boeing Wichita Company
- ATTN: [illegible]

Brown Engineering Company, Inc.
- ATTN: Ronald Patrick

California Research & Technology, Inc.
- ATTN: Ken Kreyenhagen

Chrysler Defense Division
- ATTN: R.E. Smith

Calspan Corporation
- ATTN: M.S. Holden

Dayton, University of
Industrial Security Super KL-505
- ATTN: Hallock F. Swift
- ATTN: D. Gerdiman

Denver, University of
Colorado Seminary, Denver Research Institute
- ATTN: John Wisotski
- ATTN: Larry L. Brown

Effects Technology, Inc.
- ATTN: Richard Parisse
- ATTN: Robert Wengler

EG&G, Inc.
Special Projects Div.
- ATTN: Robert Ward

Electromechanical Systems of New Mexico, Inc.
- ATTN: R.C. Shunk

Ford Aerospace & Communications Operations
- ATTN: P. Spangler

General Electric Company
Space Division
- ATTN: A. Martellucci
- ATTN: Phillip Cline
- ATTN: G. Harrison
- ATTN: Daniel Edelman
- ATTN: Carl Anderson

General Electric Company
TEMPO-Center for Advanced Studies
- ATTN: DASIAC

General Electric Company
TEMPO-Center for Advanced Studies-Albuquerque
- ATTN: Gerald Perry

General Electric Company
TEMPO-Center for Advanced Studies-Bel Air
- ATTN: E.J. Bryant

General Research Corporation
P.O. Box 3587
- ATTN: T. Stathacopoulos

Institute for Defense Analyses
- ATTN: Joel Bengston
- ATTN: IDA Librarian

Ion Physics Corporation
- ATTN: Robert D. Evans

DEPT. OF DEFENSE CONTRACTORS, continued

Kaman Avidyne
Division of Kaman Sciences Corp
ATTN: E.S. Criscione
ATTN: Ray Ruetenick
ATTN: Norman P. Hobbs

Kaman Sciences Corporation
ATTN: Donald C. Sachs
ATTN: Thomas Meagher
ATTN: John R. Hoffman
ATTN: Frank H. Shelton
ATTN: John Keith

Ken O'Brien & Associates
ATTN: Richard Crum

Lockheed Missiles & Space Co., Inc. - Sunnyvale
ATTN: R. Walz, Dept. 81-14

Lockheed Missiles & Space Co., Inc. - El Segundo
ATTN: T.R. Fortune

Lockheed Missiles & Space Co., Inc. - Palo Alto
ATTN: F.G. Borgardt

Lovelace Foundation for Medical Education
and Research
ATTN: D.R. Richmond
ATTN: R.O. Clark
ATTN: E.R. Fletcher

Martin Marietta Aerospace
Orlando Division
ATTN: William A. Gray, MP-61
ATTN: Laird Kinnaird
ATTN: Gene Aiello
ATTN: James M. Potts, MP-61

McDonnell Douglas Corporation
ATTN: E.A. Fitzgerald
ATTN: R.J. Reck
ATTN: H. Hurwitz
ATTN: H.H. Berkowitz
ATTN: J.F. Garibotti
ATTN: L. Cohen

National Academy of Sciences
ATTN: National Materials Advisory Board
ATTN: Donald G. Groves

New Mexico, University of
Civil Engineering Research Facility
ATTN: Glen Jones
ATTN: Golden Lane
ATTN: Stephen Pickett

Northrop Corporation
ATTN: Don Hicks

Pacific-Sierra Research Corp.
ATTN: Gary Lang

Physics International Company
ATTN: Doc. Control for James Shea
ATTN: Doc. Control for Technical Library

Prototype Development Associates, Inc.
ATTN: John McDonald
ATTN: John Slaughter

R&D Associates
ATTN: F.A. Field
ATTN: Cyrus P. Knowles
ATTN: Paul Rausch
ATTN: Jerry Carpenter
ATTN: Harold L. Brode
ATTN: William R. Graham, Jr.
ATTN: Edward Chapyak
ATTN: Henry Cooper
ATTN: Albert L. Latter

RCA Corporation
ATTN: E. Van Keuren, Bldg. 13-5-2

RAND Corporation, The
ATTN: J.J. Mate

Raytheon Company
ATTN: Library

Science Applications, Inc.- La Jolla
ATTN: Olan Nance
ATTN: W. Yengst
ATTN: John Warner
ATTN: Duane Hove
ATTN: G. Ray

Science Applications, Inc. - El Segundo
ATTN: Carl Swain
ATTN: Lyle Dunbar
ATTN: G. Burghart

Science Applications, Inc. - McLean
ATTN: William R. Seebaugh
ATTN: William M. Layson
ATTN: Michael McDonnell

Southern Research Institute
ATTN: C.D. Pears

SRI International
ATTN: Philip J. Dolan
ATTN: D. L. Huestis
ATTN: George R. Abrahamson
ATTN: Herbert E. Lindberg
ATTN: Donald Curran
ATTN: Carl Wiehle
ATTN: Alan A. Burns

Systems, Science and Software, Inc
ATTN: G. A. Gurtman
ATTN: Russell E. Duff

Terra Tek, Inc.
ATTN: Sidney Green

TRW Defense & Space Systems Group - Redondo Beach
ATTN: Peter Brandt, E1-2006
ATTN: Peter K. Dai, R1/2170
ATTN: R.K. Plebuch, R1/2078
ATTN: Thomas G. Williams
ATTN: D.H. Baer, R1-2136
ATTN: I.E. Alber, R1-1008
ATTN: W.W. Wood

DEPT. OF DEFENSE CONTRACTORS, continued

TRW Defense & Space Systems Group - San Bernardino
ATTN: William Polich
ATTN: E.Y. Wong, 527/712
ATTN: L. Berger
ATTN: Earl W. Allen, 520/141
ATTN: V. Blankenship

FOREIGN

Royal Fortification Administration
Stockholm, Sweden
ATTN: Dr. Eddy Abrahamsson
ATTN: Brig. Gen. Gunnar Noren

National Defense Research Institute
Stockholm, Sweden
ATTN: H Axelsson

Defence Research Establishment Suffield
Ralston, Alberta, Canada
ATTN: Clayton Coffey
ATTN: Allen W.M. Gibb
ATTN: G.A. Grant
ATTN: R.M. Heggie

Infrastructure Staff
Federal Republic of Germany
ATTN: Col. Rottgerkamp
ATTN: LTC Hermann Pahl
ATTN: Eberhard Bachmann

Ernst-Mach Institute
Federal Republic of Germany
ATTN: Dr. Heintz Reichenbach
ATTN: Gerhard Gurke

Office of Test & Development
Norwegian Defence Construction Service
Oslo, Norway
ATTN: Arne Skjeltorp

National Defence HQ
Directorate of Maritime Activities and Research
Quebec, Canada
ATTN: Ole R. Bezemer

Technologisch Laboratorium (TNO)
Rijswijk, Netherlands
ATTN: H.J. Pasman

Federal Ministry of Defense
Federal Republic of Germany
ATTN: LTC D. Bruegmann
ATTN: R. Schilling
ATTN: [illegible] Hentschel

Military Attache Staff
Embassy of the Federal Republic of Germany
ATTN: Col. Rudolf Erlemann

Federal Republic of Germany Liaison Office
Alexandria, VA
ATTN: Herman Pfrengle

Admiralty Surface Weapons Establishment
Ministry of Defence
United Kingdom
ATTN: [illegible]

British Embassy
Washington, DC
ATTN: [illegible]

Embassy of Australia
Washington, DC
ATTN: Office of the Defence Science Attache